Report Date: April 2014 DOE/NV/25946--2012

NEVADA NATIONAL SECURITY SITE

Site-Directed Research & Development Fiscal Year 2013 Annual Report

- **Material Studies and Techniques**
- **Instruments, Detectors, and Sensors**
- **Computational and Information Sciences**
- **Photonics**

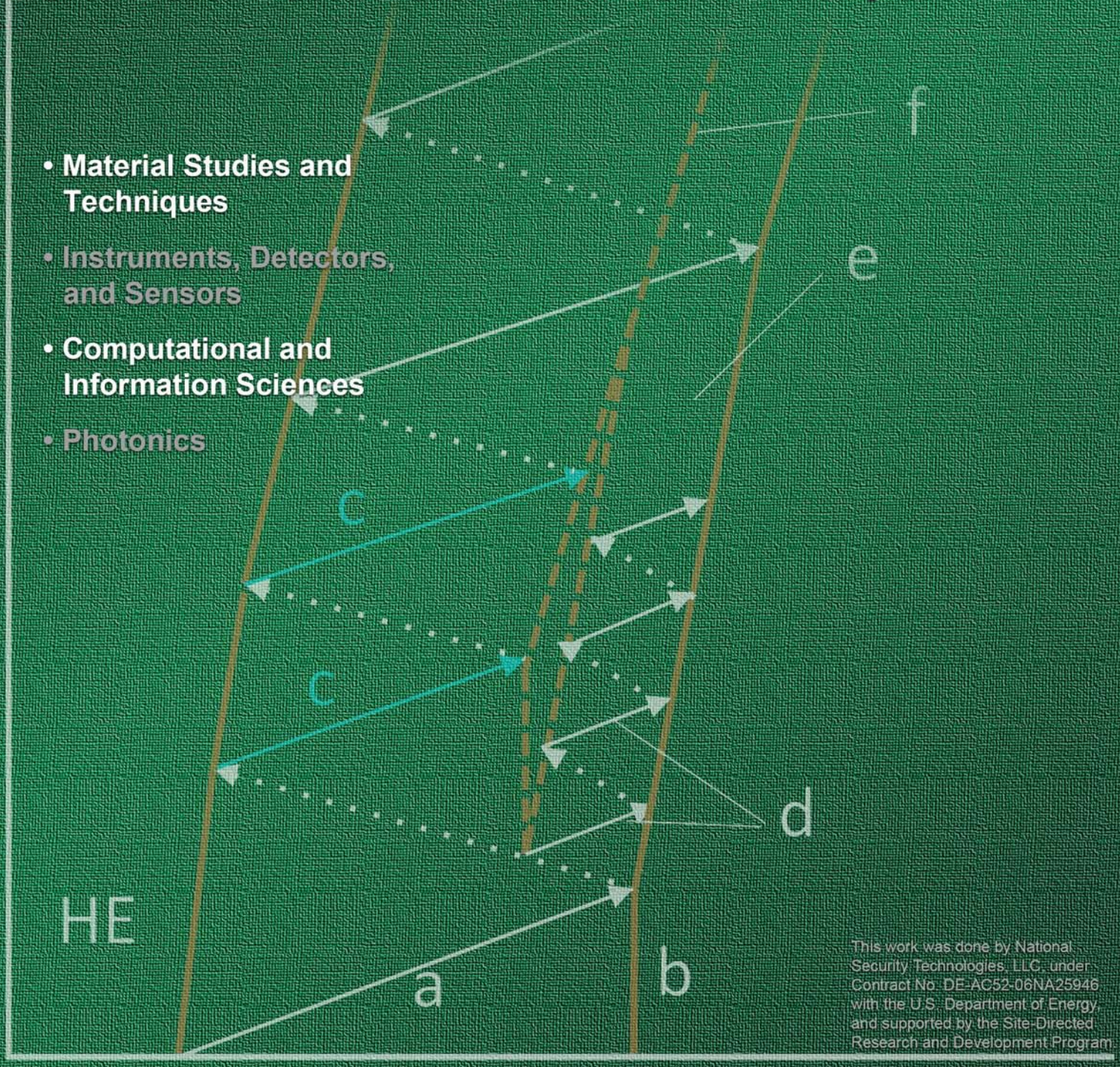

This work was done by National Security Technologies, LLC, under Contract No. DE-AC52-06NA25946 with the U.S. Department of Energy, and supported by the Site-Directed Research and Development Program.

SDRD
SITE-DIRECTED RESEARCH & DEVELOPMENT

Availability Statement

Available for sale to the public from—

U.S. Department of Commerce
National Technical Information Service
5301 Shawnee Road
Alexandria, VA 22312
Telephone: 800.553.6847
Fax: 703.605.6900
E-mail: orders@ntis.gov
Online ordering: http://www.ntis.gov/help/ordermethods.aspx

Available electronically at http://www.osti.gov/bridge

Available for a processing fee to the U.S. Department of Energy and its contractors in paper, from—

U.S. Department of Energy
Office of Scientific and Technical Information
P.O. Box 62
Oak Ridge, TN 37831-0062
Telephone: 865.576.6401
Fax: 865.576.5728
E-mail: reports@adonis.osti.gov
Online ordering: http://www.osti.gov/reportform.html

DOE/NV/25946--2012

Nevada National Security Site

Site-Directed Research and Development

Fiscal Year 2013 Annual Report

This work was done by National Security Technologies, LLC, under Contract No. DE-AC52-06NA25946 with the U.S. Department of Energy, and supported by the Site-Directed Research and Development Program.

Report Date: April 2014

Table of Contents

Foreword

"Ground Truth and Discovery"

"Ground truth and discovery"—this is the phrase that best describes NSTec for me. It captures the historical mission and reflects what we are still about at U1a, JASPER, the DAF, remote locations, and in global security. We provide "ground truth" via complex applied science and engineering expertise in rigorous experimental operations and "discovery" via state-of-the-art sensors and diagnostics. As the Stockpile Stewardship mission matures and our global security mission broadens, our "ground truth and discovery" footprint continues to expand well beyond the unique capabilities of the amazing Nevada National Security Site. Our ability to conduct operations and to field state-of-the-art sensors or diagnostics in harsh and extreme conditions is second to none. Likewise, we strive to bring the best possible value to our customers by creating advanced concepts, technologies, and analysis through our Site-Directed Research and Development program.

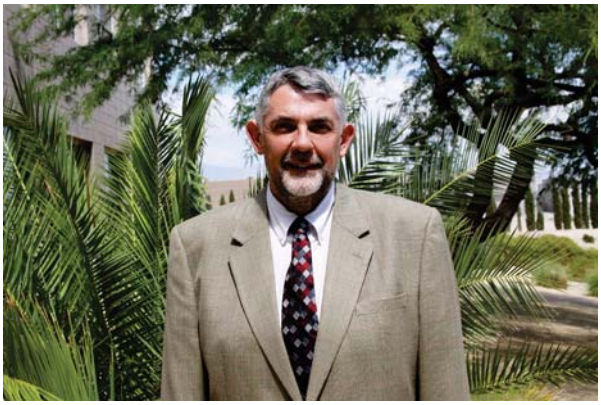

Our R&D program funding is relatively small, but thanks to the excellence of our technical staff and the leadership of the SDRD team, it has proven a major innovation engine for NSTec. This is recognized by our president, Dr. Ray Juzaitis. As the Chief Technology Officer, I am working with Ray, the Senior Management Team, and the SDRD team to strengthen our already outstanding SDRD program. Together we can ensure that we live up to the "technologies" moniker in our company name.

To strengthen SDRD, we need to:

1. Grow the program size without increasing our overall cost of doing business;
2. Continuously improve transparency by informing principal investigators who have received funded projects why they were awarded and also, importantly, improve the proposal pool by giving feedback and guidance to those who were not funded;
3. Frequently assess our project selection process to ensure relevancy; and
4. Strategically invest for the future and partner with others.

In addition, we use best-in-class business practices and partner internally for maximum efficiency. A new website dedicated to NSTec's technologies, based in the Chief Technology Office, will act as a communication hub for the technical workforce encompassing four states and eight individual locations. Also, before the end of the fiscal year, we will have a technology roadmap that will build on the recent strategic plans to add the driving muscle that will advance NSTec.

Please join me in thanking the entire staff and team that contributed to this report and recognizing the achievements of the SDRD Program. We are committed to making our SDRD Program the key element in NSTec's technically excellent future!

Christopher Deeney
Chief Technology Officer

This page left blank intentionally

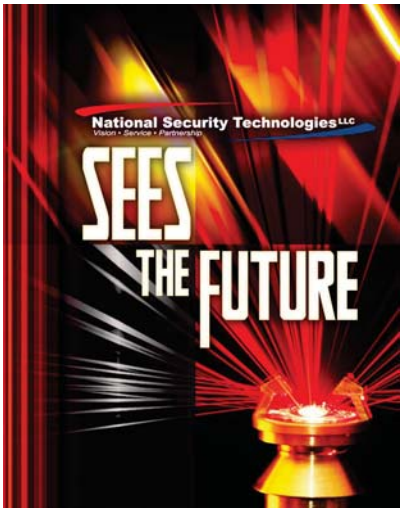

NSTec is *singular* in its focus to support national security, *efficient* to maximize fiscal resources, *effective* in achieving results for its customers, and *sustainable* for the long term to meet future challenges and fulfill its mission for the nation and the broader global community

Fiscal Year 2013 Program Overview

A hallmark of high-performance research and development is sustained achievement that endures. R&D organizations and laboratories have changed the course of technology and the world, and their innovations impact us for generations. At the center of the Nevada National Security Site's (NNSS) science, technology, and engineering (ST&E) mission is the Site-Directed Research and Development Program (SDRD), which, through sustained achievement, has had an indelible impact on our mission and altered some of our most important work for the foreseeable future.

The innovations created in the SDRD program have a remarkably high return on investment, and the SDRD program has helped raise the overall emphasis on the ST&E mission. In recent years the technology mission and its importance to the long-term vitality of the NNSS has been a prominent focus of National Security Technologies, LLC (NSTec). For example, NSTec created the Chief Technology Officer (CTO) position and filled it in August 2013 (see Foreword). SDRD was functionally realigned to report to the CTO concurrent with this change in leadership structure. A new corporate systems–based approach to strategic applied science and technology is starting to materialize, and expectations are that this shift of attention to technology innovation will bring about powerful outcomes for our mission and customers.

In FY 2013 SDRD program improvements primarily involved developing strategic initiatives and integrating SDRD innovations into programmatic efforts. As mentioned in the FY 2012 annual report, we reconvened the external advisory panel with other internal experts in January 2013 for a special look at strategic challenges in four main

FY 2013 marks the 12th annual SDRD report, an enduring archive of technical R&D

thrust areas: stockpile stewardship, treaty verification/arms control, nonproliferation/emergency response, and intelligence/information security. Based on red team–like exercises and follow-up deliberation and analysis, key technology gaps and needs were identified. This information was used to formulate specific strategic opportunity challenges, which will be the subject of the first Strategic Opportunity Research proposal call in 2014. Also of note was a first-of-its-kind integrated year-end review of SDRD projects, held in September 2013, where all principal investigators presented the status of their R&D efforts. Previously, due to the geographical separation of many of the NNSS sites, reviews were conducted independently at each site; this new approach was successful in bringing the investigators together and fostering a higher awareness among staff and program leadership of the value of SDRD. This venue brought new understanding and broader knowledge of all aspects of the ST&E capabilities and new opportunities for engaging and applying the innovations and knowledge being developed. To conclude the meeting multiple performance awards were given to SDRD participants based on their contributions to technology and program management.

Epilogue: MPDV Gemini Experimental Series Success

On December 5, 2012, the Pollux subcritical experiment was conducted at the NNSS by an integrated team from the NNSS, Los Alamos National Laboratory, and Sandia National Laboratories. This experiment was the culmination of a highly important test series that used the Gen-1 multiplexed photonic Doppler velocimetry (MPDV) based on the original SDRD innovation (see E. Daykin, "Advanced PDV Techniques: Evaluation of Photonics Technologies," FY 2010 SDRD Annual Report, 205–214; "SDRD to Stockpile Success," FY 2012 SDRD Annual Report, viii–xi). With this success, and subsequent development and analysis, the full impact this transformational technology is having on stockpile stewardship is now being fully realized. Next-generation MPDV systems (see "Next-Generation MPDV Systems Support Advanced Hydrotesting" on page x) are forging ahead with vast performance improvements and enhanced architectures allowing even more utility on wide ranging experiments relevant to national security.

"Diagnostic equipment fielded by our scientists resulted in more data collected in this single experiment than all other previous subcritical experiments. This type of data is critical for ensuring our computer simulations can accurately predict performance, and thus continued confidence in the safety of the nation's stockpile."

—Dr. Don Cook, NNSA Deputy Administrator for Defense Programs

Enhanced Gamma Directional Sensing with Advanced Covariance Techniques

It has long been recognized that Compton scattering of gamma rays can be exploited to infer the direction to a radiation source, but everyone has always assumed that detectors utilizing the phenomenon need to be complicated and expensive. An FY 2013 SDRD project shows that directional information can be obtained from two ordinary gamma detectors, provided that they "crosstalk" to each other, and that the crosstalk is processed in a certain way. The two ideas that make the simplification possible are the energy asymmetry of the crosstalk and a covariance filtering technique to extract that crosstalk from a very large background.

The covariance filtering technique uses fluctuations of signals from the two detectors to measure correlated events. The correlated events are the signals from the Compton recoil electron in one detector and the absorption of the Compton scattered gamma in the other detector. To maximize sensitivity, both detectors should view the radiation source, but that means that two scattering paths contribute to the correlations data. Because the Compton formula depends on the cosine of the scattering angle, the data possess a certain symmetry. This is because one path depends on +cos(θ), and the other path on –cos(θ). The energies are distributed over the two detectors in a very particular way, and analysis of that distribution is straightforward.

A covariance map shows the energy distributions for angles from the detector pair to the radiation source. The two axes of each covariance map represent energy in the two detectors, and the islands of covariance show a steady progression along a cross- diagonal in the maps (see "Covariance Processing of Energy Asymmetry of Compton Crosstalk for Directional Gamma Sensing," 137–148). Processing the location of the covariance islands along that cross diagonal produces the angle vs. asymmetry plot shown. Note the data are very well behaved, and the angular resolution is better than 1 degree of arc, quite extraordinary for a simple pair of 2" × 2" sodium iodide detectors.

Contributed by R. Trainham

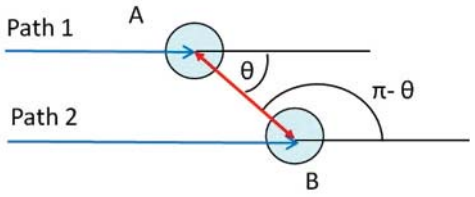

When both detectors are exposed to the gamma source, the Compton signal has a forward-scattering component along path 1 from A to B, and a backscattering component along path 2 from B to A

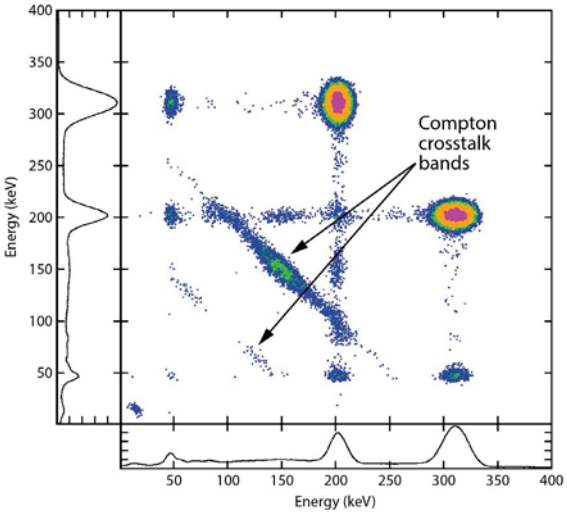

This covariance map shows islands of correlation linking the cascade gammas at 202 and 306 keV and characteristic x-rays. The cross-diagonal bands (arrows) are from Compton crosstalk between detectors, and the axes intercepts of the bands are at the full gamma energy. The direction to the radiation source can be derived from information contained within the crosstalk bands.

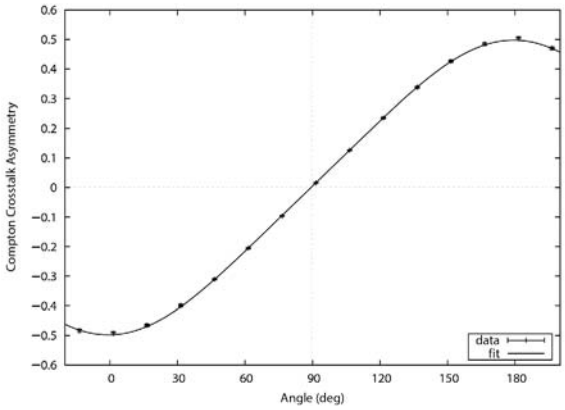

The curve of angle versus Compton crosstalk asymmetry derived from the experimental data for a ^{137}Cs source

High-Speed and Ultrafast Optical Diagnostics for Tomorrow's Needs

The NNSS perpetuates a legacy of deep experience and technical excellence at the cutting edge of high-speed optical diagnostics, stretching from "Doc" Edgerton's earliest photography through contemporary high-bandwidth MPDV suites. SDRD has made a strategic thrust to continue this legacy, and in 2013, 4 out of the 24 funded projects built on this strength: "Ultrafast All-Optical Framing Technology" (LAO-02-13, 207–213), "Electron Mobility Measurements in Scintillator Materials" (LAO-06-13, 1–9), "Study of Radiation-Induced Refractive Index Change in GaN for Ultrafast Scintillator Applications" (LAO-08-13, 201–206), and "Solid-State IR Fast Streak Based on Beam Deflection" (SO-01-13, 215–220).

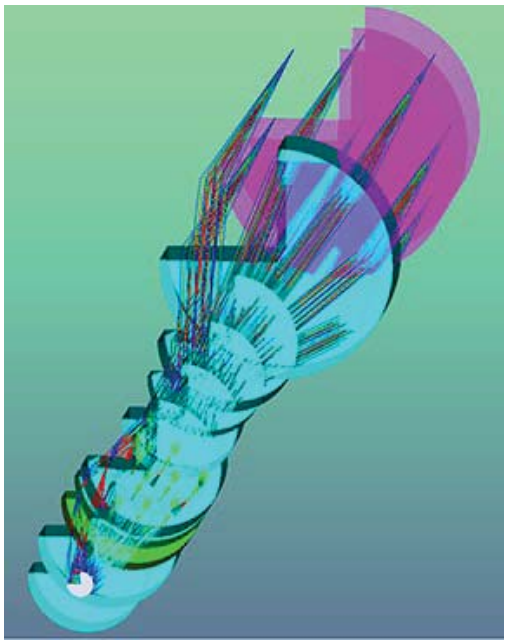

An illustration of the hyperchromatic lens, shown producing images at varying locations as a function of time

Two of these projects focused on the basic science of ultrafast detection. Charge carrier mobility has been demonstrated to be foundational to scintillator phenomenology. LAO-06-13, through probing the electron mobility of scintillator materials, sought better understanding of the fundamental mechanisms by which scintillators absorb ionizing radiation and emit optical radiation, with the possibility of new, faster scintillator materials in view. Lawrence Livermore National Laboratory (LLNL) has invested a significant amount of time, effort, and money developing high-speed diagnostics based on the radoptic effect for use at the National Ignition Facility. LAO-08-13 developed a strong collaboration with the original researchers at LLNL and leveraged this substantial investment to expand investigation of related materials to circumvent the temporal challenges of scintillators entirely.

The remaining two projects focused on leveraging more developed methodologies into novel diagnostic technologies. LAO-02-13 combined ultrafast laser physics, state-of-the-art 3-D cameras, and an innovative hyperspectral lens in the pursuit of high-frame-number imaging with variable recording times pushing into the THz regime. This technology may eventually allow for movies of experiments with picosecond phenomena using ultrafast laser sources or free electron lasers. SO-01-13 leveraged proprietary optical streaking technology developed by LLNL and a highly successful collaboration into a novel all-optical streak methodology in pursuit of data capture well beyond the temporal and spectral limitations of today's technology. This technology may see development into nanosecond near-infrared spectroscopy.

Contributed by D. Frayer

Diagnostic Techniques for Matter in the Extremes

Fundamental experimental work in matter in the extremes is another area where SDRD-funded research is also making a substantial difference. We are systematically reducing uncertainty in dynamic temperature measurements in shock physics studies to provide data with unprecedented accuracy in support of equation-of-state calculations. In addition, simple integral plate impact and high-explosive metal damage experiments are providing much needed verification and validation data for high-fidelity computer simulations. A strong collaborative approach with NNSA laboratories and universities is further enhancing the overall benefit of these efforts.

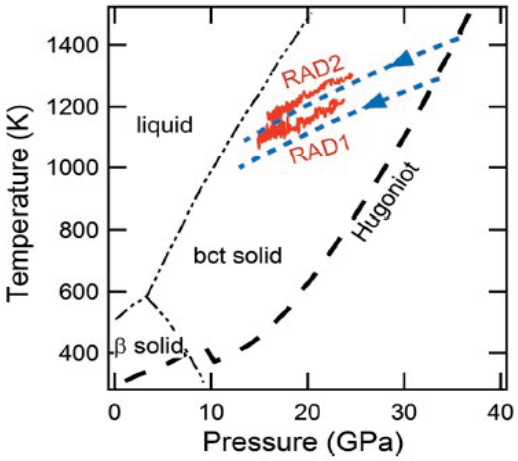

Measured temperature-stress release paths (red) for two experiments on shocked tin (La Lone et al., *J. Appl. Phys.* 114, 063506 [2013]). There is an immediate release from the Hugoniot shock stress to around 25 GPa when the shock releases into a LiF window, followed by a slower Taylor wave release to around 15 GPa. Calculated release isentropes (dashed blue lines) using the formalism presented by Mabire (*AIP Conf. Proc.* 505, 93 [2000]) are shown for comparison. The phase diagram and Hugoniot model from Mabire are also shown. The systematic difference of about 40 K between our measurements and the calculations is within the experimental uncertainties, and the slopes are identical.

RF Sensing Device Mini-Mira Finds Broad-Based Utility

Besides tremendous success in stockpile areas, SDRD has contributed enormously to our changing global security missions. The initial SDRD technology investment in the Advanced Microwave Antenna Array and Multiband Receiver (Mini-Mira) has yielded a unique system currently in use by various government agencies, with a return of investment nearly 20 times the original SDRD investment as of FY 2013. This newest system incorporates four discrete microwave bands, each with a dedicated processing chain. This architecture, along with custom software, differentiates "true threats" from benign signals. This SDRD technology development led to an NSTec performance award, and the innovative design led directly to significant new customers.

The Mini-Mira 3 detects signals of interest in a variety of bandwidths over an extremely wide frequency range covering the S, C, X, and K bands.

Next-Generation MPDV Systems Support Advanced Hydrotesting

In 2013, the 1st Generation (Gen-1) multiplexed photonic Doppler velocimetry (MPDV) system was described as "a novel optical diagnostic." It measured the motion of a surface along more than 100 rays, providing orders of magnitude more data than past experiments of this type. A recent publication by Los Alamos noted, "MPDV launched a new era in hydrodynamic experiments. The Laboratory can measure the shock physics properties of metal in unprecedented detail and resolution, gaining deeper insights as it reports on the condition of the nuclear arsenal and considers reusing older systems without nuclear testing." (*Experimental Physical Sciences*, Los Alamos National Laboratory, 2013)

Building on that success, designers continued their efforts on upgrading MPDV systems for higher performance in a variety of new experimental conditions. Successful as it was, the Gen-1 MPDV, built using a myriad of commercial components, was complex and fiber intensive. The Gen-2 system has a simplified architecture based on circuit board integration and modularized design. It incorporates many enhancements such as increased sensitivity, broader dynamic range, better power management and serviceability, and easier operational setup. Combined with a very powerful user-oriented software interface, it quickly and efficiently handles analysis for the copious data returned from the experiment.

Recent success using Gen-2 MPDV at the DARHT facility at LANL has further proven the utility of high-channel velocimetry data for many applications relevant to advanced hydrotesting. Improvements to yet newer-generation MPDV systems are under consideration, and ongoing developments are sure to rapidly advance this technology to help solve challenging problems in material science and other applications.

Contributed by D. Esquibel, L. Esquibel

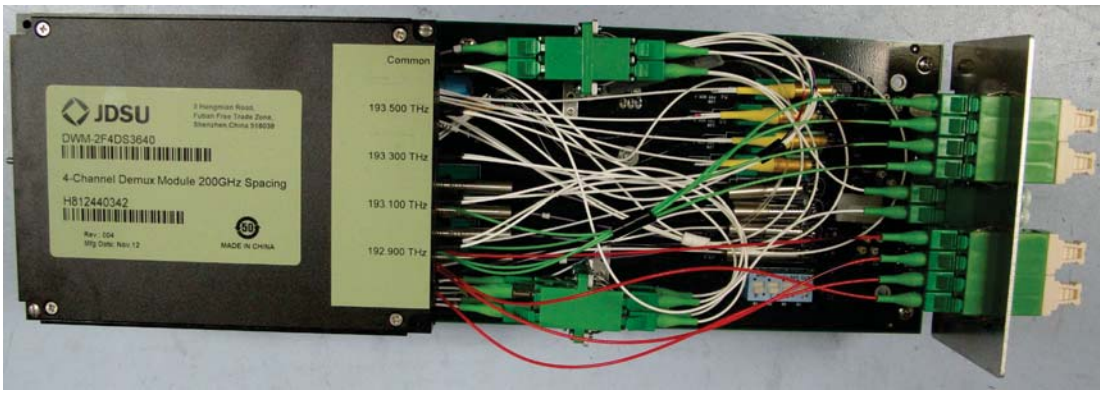

A new Gen-2 MPDV multichannel detector module. Combined with other improvements these systems have higher performance and overall lower cost.

Innovative Image Enhancement through Novel Statistical Techniques

One of the primary diagnostics in the National Security Laboratories (NSL) integrated experiments is x-ray radiography, an imaging method measuring photon attenuation through a dynamic scene. This technique allows experimentalists to calculate the densities of objects in the scene and locations of important features, but significant mathematical modeling and computational analysis are required to extract the information of interest. In collaboration with researchers at Los Alamos National Laboratory (LANL) and Sandia National Laboratories (SNL), we developed a breakthrough statistical formulation to image analysis that allows us to quantify uncertainties due to assumptions in the mathematical modeling and to measurement errors.

X-ray source shape analysis, deconvolution, and Abel inversion are the core of radiographic image processing. The shape and size of the x-ray source is important for understanding the spatial resolution of an imaging system, and, given the complete system response, deconvolution enhances the resolution. From an enhanced image, the Abel inversion technique calculates object density from the image's pixel intensities. Solving these three problems engages different physics, but they can all be formulated as ill-posed linear inverse problems, with slightly different formulations for Gaussian and Poisson noise models. The fact that they are ill-posed means that the corresponding equations cannot be solved directly and an additional assumption, known as regularization or a prior, must be included in the model. This assumption is often motivated computationally, not physically, resulting in solutions that do not correspond to the actual physics of the system.

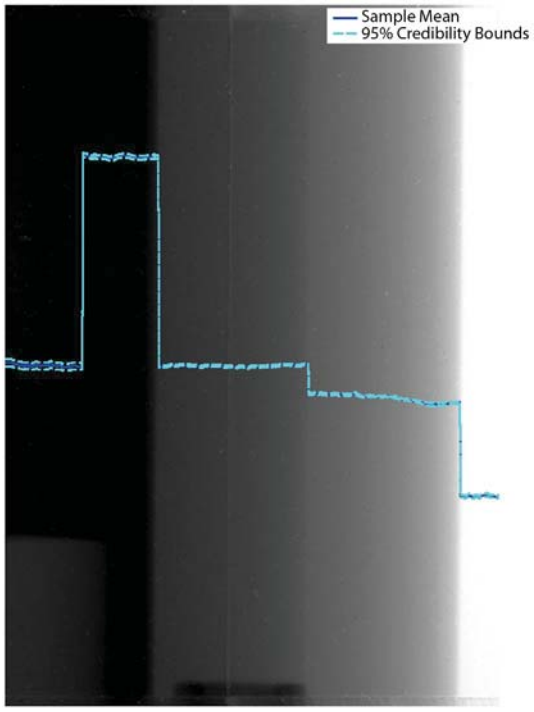

X-ray radiograph of an Abel cylinder used to test statistical techniques to extract areal density, edges, and other features with highest possible fidelity (see "Quantifying Uncertainty and Error Propagation in Radiography Image Processing," 161–170).

The focus of our work followed two parallel paths. The first was casting linear inverse problems in a Bayesian statistical formulation to compute a posterior distribution of solutions. We developed an innovative approach to sampling the prior, allowing our algorithms to drive the prior towards an assumption most consistent with the data and allowing us to assess whether our assumptions negatively impact the solutions. The second path was to develop new computational methods for computing solutions, called samples, from the posterior distribution. Markov Chain Monte Carlo (MCMC) methods were pioneered at LANL in the 1960s, but it is only recently that computer power has caught up with the statistical theory, making MCMC methods tractable. We designed state-of-the-art algorithms for computing samples using graphics processor unit computing, making our processing practical for immediate analysis of radiographs from integrated experiments.

The results of our efforts are now being implemented into the standard processing of x-ray radiographs at the NNSS and SNL, and the methods are also being adapted to proton radiography at LANL. The research is ongoing and is now being supported by the individual radiography programs.

Contributed by A. Luttman, M. Howard, and M. Fowler

SDRD Principal Investigators in the Spotlight

NSTec researchers publish significant works in peer-reviewed journals, and occasionally the research is of such interest that scientific organizations see something that might appeal to the broader community. Principal Investigator **Paul Guss**' research on nanostructure-based scintillators was featured in multiple press releases commenting on the potential breakthrough of this hybrid material, delivering both better performance and cost reduction over previous crystalline materials (Guss, P., R. Guise, D. Yuan, S. Mukhopadhyay, R. O'Brien, D. Lowe, S. Kang, H. Menkara, V. Nagarkar, "Lanthanum halide nanoparticle scintillators for nuclear radiation detection," *J. Appl. Phys.* **113** (2013), 064303–064303-6).

PI Brandon La Lone presents at the LDRD Program Update in June 2013

In June 2013, a special Laboratory Directed Research and Development (LDRD) Program update was held in Washington, D.C. to highlight significant research being conducted for the benefit of the DOE/NNSA and broader community. Three major subject areas, "Materials in the Extremes," "Big Data to Decisions," and "Energy Use Impacts and Mitigation," were chosen for the update program due to their importance and timeliness to challenges and issues facing national security sciences. **Brandon La Lone**, an invited speaker, discussed his SDRD work in precision temperature measurements for shock-compressed metals (La Lone, B. M., G. D. Stevens, W. D. Turley, D. B. Holtkamp, A. J. Iverson, R. S. Hixson, L. R. Veeser, "Release path temperatures of shock-compressed tin from dynamic reflectance and radiance measurements," *J. Appl. Phys.* **114**, 6 (2013) 063506–063506-14). **Steven Becker**, another NSTec researcher, along with collaborators from the University of Nevada, Las Vegas (UNLV), presented a poster comparing experimental and computational techniques for gas gun–driven material impact studies. **Ki Park**, also from the NNSS, presented on his cyber security techniques related to power grid control systems, of particular concern for future energy security.

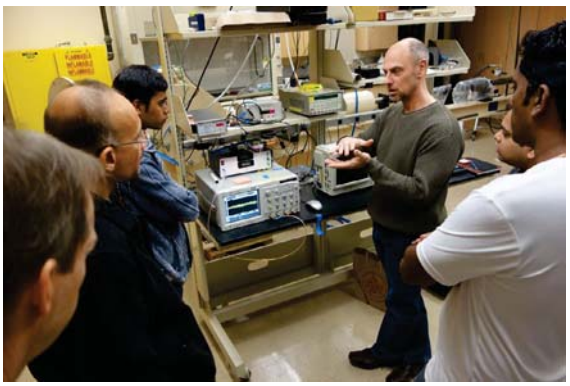

Ed Daykin, NSTec senior scientist and SDRD principal investigator, conducts tutorials on photonic Doppler velocimetry to students and staff at UNLV as part of ongoing experimental studies in dynamic material properties

FY 2013 Proposals & Projects

Projects selected in FY 2013 and reported here benefited from special pre-proposal guidance given to staff on areas of importance to our main mission areas. The result was a diverse sampling of proposals that covered multiple emphasis areas, including dynamic material needs, such as new ideas for detecting phase transitions, understanding dynamic temperature in shock-loaded metals, and physics associated with states of high pressure and high temperature. Sensor development figured prominently, generating ideas for advanced scintillator materials, concepts for enhanced spectroscopy, and algorithms to extract low-signal data. Other proposals sought techniques for geophysics modeling and monitoring, remote sensing applications, SCADA security, enhanced surveillance, secure communications, and specialized image processing. Overall the portfolio was a strong collection of innovative ideas and some exceptional avant-garde ideas, which made selection very difficult.

In total, 137 proposals were submitted and 24 were selected for funding, the same number as FY 2012. The selection rate stayed at about 1 in 6, still highly competitive, but with reasonable probability to ensure proposers that their ideas have a chance of acceptance. Technical review of proposals remains firmly grounded in peer review with established and comprehensive criteria. Our internal review team, supplemented by external advisors and subject matter experts, conducted an exhaustive review of all submissions. Proposals were evaluated on technical merit and innovation, probability of success balanced with technical risk, potential for mission benefit, and alignment with our mission directives to achieve the best possible outcomes.

FY 2013 costs were nearly the same as last year; the average project funding was about $230K. Total expenditures for the FY 2013 SDRD program were $6.5 million, with slightly less spent on administrative and management compared to FY 2012 due to cost-saving measures associated with delayed advisory board activities and more efficient integration efforts. Again, and as shown in some of our highlight features herein, this modest investment continues to provide incredible leverage and return based on successes and benefit to our mission and programs.

The NNSS *Technology Needs Assessment* document continues to be an effective tool for proposal submitters and reviewers. It provides a roadmap and guidance for addressing technology gaps and challenges facing mission areas. Our directed research emphasis areas were similar to last year, and they targeted key investment needs, including nuclear security, information security/assurance, high-energy density physics diagnostics, integrated experiments, advanced analysis, and safeguarded energy. The needs assessment is developed from a broad base of input from the national security complex, including the laboratories, NNSA, and other external agencies. Significant revisions to the assessment were made; most notably the “Emerging Areas and Special Opportunities” section was expanded, as were sections on new challenges and “Breaking Barriers” in cyber security, advanced radiography, energy security, and materials in the extremes (as mentioned above). The *Technology Needs Assessment* itself is now in the tenth year of revision, and its utility and effectiveness continues to improve year to year.

SDRD Performance Metrics

Measuring the performance or output of R&D programs is often the subject of much debate and can vary widely depending on the organization’s mission and purpose. In SDRD, we have continued to use a suite of basic metrics such as intellectual property, technology needs addressed, and technology transfer to programs. We

also consider the importance of other factors, such as follow-on programmatic or external funding received, new methods developed that effectively save costs, and overall enhanced staff capabilities. These are further indicators of innovation productivity and are also a direct measure of investment return. SDRD provides our staff with opportunities to explore and exercise creative motivations that ultimately lead to new knowledge and realized technologies. The traditional metrics we have used over the past years are tabulated below and are a broad measure of R&D performance.

Invention disclosures are the first step in our intellectual property pursuit and are often followed by patent applications when deemed appropriate. Traditionally SDRD has generated well over half of all inventions disclosed company-wide since the program began and continues to do so to this day. On average about one-third of our projects generate new invention disclosures, which is a reasonably high ratio given that projects can vary widely from basic concept, low technical readiness, to much higher more applied development efforts. In fact, our programs benefit from a high rate of technology utilization precisely due to this diverse mix of projects. A relatively high percentage of projects, roughly 40%, have technology that is subsequently adopted by a direct NNSS program. Another measure of program effectiveness and alignment with missions is how well projects address technology needs as identified in the annual NNSS *Technology Needs Assessment*. The ratio of needs addressed to total projects is also indicative of a trend that aligns efforts strategically with the NNSS mission. In addition, a small percentage of projects are targeting the emerging fields (introduced in the 2012 *Technology Needs Assessment* for the first time), which are new initiatives intended to incorporate higher risk and explore opportunities for enhanced mission outside of traditional NNSS areas of expertise.

We continue to strive to have SDRD effectively contribute new technology into key programmatic efforts as quickly as possible. New strategic efforts are also providing greater emphasis on forward-looking needs and efficiently coupling with long-term visionary goals. As always, SDRD looks to be “ahead of our time by design” and push for SDRD innovations to intersect future and evolving missions with the most impact possible.

SDRD Program Performance Metrics											
Year	FY03	FY04	FY05	FY06	FY07	FY08	FY09	FY10	FY11	FY12	FY13
Number of projects	41	57	55	50	37	27	23	25	26	24	24
Invention disclosures	11	12	21	11	9	6	11	9	7	8	7
	27%	21%	38%	22%	24%	22%	48%	36%	27%	33%	29%
Technology adopted by programs	15	18	12	8	8	8	10	10	9	10	9
	37%	32%	22%	16%	22%	30%	44%	40%	35%	42%	38%
Gap or need addressed*	11	14	18	17	18	15	15	13	13	11	14
	27%	25%	33%	34%	49%	56%	65%	52%	50%	46%	58%
“Emerging Area & Special Opportunity” effort*	Not applicable										3
	Not applicable										13%

*per *NNSS R&D Technology Needs Assessment*

FY 2013 Annual Report Synopsis

The reports that follow are for project activities that occurred from October 2012 through September 2013. Project life cycle is indicated under the title as well as the proposal number (in the following format: site abbreviation-ID #-originating fiscal year, e.g., LAO-02-13). Each of the reports describes in detail the discoveries, achievements, and challenges encountered by our principal investigators. As SDRD, by definition, invests in "high-risk" and hopefully "high-payoff" research, the element of uncertainty is inherent. While many of our efforts are "successful" and result in positive outcomes or technology utilization, some fall short of expectations, but cannot be construed as "failure" in the negative sense. The latter is a natural and valid part of the process of advanced research and often leads to unforeseen new pathways to future discovery. Regardless, either outcome advances our knowledge base and increases our ability to identify solutions and/or avoid costly and unwarranted paths for future challenges.

In summary, the SDRD program continues to provide an unfettered mechanism for innovation that returns multifold to our customers, to national security, and to the general public. The program is a vibrant R&D innovation engine, benefited by its discretionary pedigree, enhanced mission spectrum, committed resources, and sound competitiveness to yield maximum taxpayer benefit. The 24 projects described exemplify the creativity and ability of a diverse scientific and engineering talent base. The efforts also showcase an impressive capability and resource that can be brought to find solutions to a broad array of technology needs and applications relevant to the NNSS mission and national security.

Acknowledgments

A number of individuals contribute significantly to make SDRD successful year after year. Without their support much of this would not be possible. My sincere gratitude goes out to Michele Vochosky, Katharine Kelly Streeton, and Sierra Cory, for compiling, editing, and publishing this report; to Nancie Nickels for graphic design of the cover and dividers; to Linda Flaugher for efforts in cost accounting and Tom Graves for project management support; to Newell Ramsey and Kathy Gallegos for information system support; to Janet Lux and Cindy McIntosh for compiling financial data for reporting requirements; to Larry Franks, Rob Hixson, and Lynn Veeser for exceedingly valuable technical guidance and support; and to SDRD site representatives and review committee members, Frank Cverna, Daniel Frayer, Paul Guss, Mike Haugh, Eric Machorro, Michael Mohar, Sanjoy Mukhopadhyay, Cathy Snelson-Gerlicher, and Jerry Stevens. And special thanks again to members of our external advisory group, Larry Franks, Carl Ekdahl, Damon Giovanielli, Ralph James, Glenn Knoll, Dick Lynn, Paul Rockett, and Gerry Yonas, who graciously give their time and provide ongoing valuable recommendations.

Howard A. Bender III
SDRD Program Manager

This page left blank intentionally

National Security Technologies–Operated Sites

Los Alamos Operations (LAO)
P.O. Box 809
Los Alamos, New Mexico 87544-0809

Livermore Operations (LO)
P.O. Box 2710
Livermore, California 94551-2710

North Las Vegas (NLV)
P.O. Box 98521
Las Vegas, Nevada 89193-8521

Nevada National Security Site (NNSS)
P.O. Box 98521
Las Vegas, Nevada 89193-8521

Remote Sensing Laboratory–Andrews Operations (RSL-A)
P.O. Box 380
Suitland, Maryland 20752-0380
(Andrews Air Force Base)

Remote Sensing Laboratory–Nellis Operations (RSL-N)
P.O. Box 98521
Las Vegas, Nevada 89193-8521
(Nellis Air Force Base)

Sandia Operations (SO)
Sandia National Laboratories
P.O. Box 5800
Mail Stop 1193
Albuquerque, New Mexico 87185

Special Technologies Laboratory (STL)
5520 Ekwill Street
Santa Barbara, California 93111-2352

This page left blank intentionally

Acronyms and Abbreviations

A

AC	alternating current
A/D	analog-to-digital converter
^{107}Ag	silver-107
Al	aluminum
ALD	atomic layer deposition
AlGaAs	aluminum gallium arsenide
^{241}Am	americium-241
AM	amplitude modulation
AoA	angle of arrival
Ar	argon
ATD	arrival time distribution
AWG	arbitrary waveform generator

B

^{10}B	boron-10
bct	bicubic centered tetragonal
BGO	bismuth germanate
BPSK	binary phase-shift keying
Br	bromine

C

CAD	computer-aided design
Caltech	California Institute of Technology
CB	conduction band
CBRNE	chemical, biological, radiological, nuclear, and explosives
CCD	charge-coupled device
CCFET	capacitively coupled gate field-effect transistor
CCSD(T)	coupled-cluster singles and doubles plus perturbative triples method
Ce	cerium
$CeBr_3$	cerium tribromide
$CeBr_3:Ca^{2+}$	calcium-doped cerium tribromide
^{252}Cf	californium-252
CJ	Chapman-Jouguet
CLLB	$Cs_2LiLaBr_6:Ce$

CLLBC	$Cs_2LiLa(Br_6)_{90\%}(Cl_6)_{10\%}$:Ce
CLLC	$Cs_2LiLaCl_6$:Ce
CLYB	Cs_2LiYBr_6:Ce
CLYC	Cs_2LiYCl_6:Ce
CMOS	complementary metal oxide semiconductor
CNT	carbon nanotube
^{60}Co	cobalt-60
CPU	central processing unit
cRIO	Compact Real-Time Input Output (unit)
^{137}Cs	cesium-137
CSGM	complex spectrogram
CsI	cesium iodide
CsI:Na	sodium-doped cesium iodide
CsI:Tl	thallium-doped cesium iodide
CTH	A current SNL-developed radiation-diffusion hydrodynamics code derived from the 1-D 1969 "Chart D," which was extended to 2-D in 1975 (and named CSQ = $(\text{Chart D})^2$), and then to 3-D in 1987 (and renamed CTH = $(\text{CSQ})^{3/2}$).
CTO	Chief Technology Officer
CuW	copper tungsten
CVL	core-to-valence luminescence
CWA	chemical warfare agent
CZT	cadmium zinc telluride

D

DAQ	data acquisition
DARHT	Dual-Axis Radiographic Hydrodynamic test facility
DC	direct current
DD	deuterium-deuterium
DDR2	double data rate 2
DDS	direct digital synthesizer
DEZ	diethyl zinc
DFT	density functional theory
DFT+U	Hubbard U density functional theory
DOE	U.S. Department of Energy
DOS	density of state
DPF	dense plasma focus

DSC	differential scanning calorimetric
DSSS	direct-sequence spread-spectrum (modulation)
DT	deuterium-tritium
DU	depleted uranium

E

EBSD	electron backscatter diffraction
E_{coh}	cohesive energy
EEPROM	electrically erasable programmable read-only memory
EM	electromagnetic
ENOB	number of effective bits
EPROM	erasable programmable read-only memory
EOS	equation-of-state

F

FEA	finite element analysis
FET	field-effect transistor
FFT	fast Fourier transform
FLAG	(hydrocode developed at LANL)
FM	frequency modulation
FOM	figure of merit
FOV	field of view
FPGA	field-programmable gate array
fps	frame(s) per second
FWHM	full-width at half-maximum
FY	fiscal year

G

GaAs	gallium arsenide
$GaInO_3$	gallium indium oxide
GaN	gallium nitride
GaN:Mg	magnesium-doped gallium nitride
GB	gigabytes
$Gd_2Ti_2O_7$	gadolinium titanate
GEB	Gaussian energy broadening
GEE_n	gamma equivalent energy
GGA	generalized gradient approximation

GPa	gigapascal
GPS	global positioning system
GS/s	giga samples per second

H

H_2	hydrogen
H_2O	water
HCBS	High Confidence Block Shifts
He	helium
^3He	helium-3
HE	high explosive
HGFET	hanging gate field-effect transistor
HMAC	hash-based message authentication code
HPIV	holographic particle imaging velocimetry
HPLC	high-performance liquid chromatography

I

IAC	Idaho Accelerator Center
IC	integrated circuit
ICCD	intensified charge-coupled device
ICP-MS	inductively coupled plasma mass spectrometry
ICSP	in-circuit serial programming (interface)
ICV-E	integrity check value in EPROM
ICV-P	integrity check value in processor
ID	identification
IEEE	Institute of Electrical and Electronics Engineers
IFOV	instantaneous field of view
InGaAs	indium gallium arsenide
InP	indium phosphide
InP:S	sulfur-doped indium phosphide
I-NVM	invisible non-volatile memory
IpFFT	Interpolated fast Fourier transform
IR	infrared
IT	information technology

J

JASPER	Joint Actinide Shock Physics Experimental Research (facility)
JTAG	Joint Test Action Group

L

LANL	Los Alamos National Laboratory
LAO	Los Alamos Operations
^{6}Li	lithium-6
lidar	light detection and ranging
LiF	lithium fluoride
$LiInSe_2$	lithium indium selenide
linac	linear accelerator
LLNL	Lawrence Livermore National Laboratory
LO	Livermore Operations
LoS	line-of-sight
LPA	local polynomial approximation
lp/mm	line-pair per millimeter
LRE	L rolled edge
LS-DYNA	(general-purpose finite element program)
^{176}Lu	lutetium-176

M

MAC	message authentication code
MCA	multichannel analyzer
MCMC	Markov Chain Monte Carlo
MCNP	Monte Carlo N-Particle
MCNPX	Monte Carlo N-Particle Extended
MEMS	microelectromechanical systems
MISFET	metal insulator semiconductor field-effect transistor
MLE	maximum likelihood estimation
MOS	metal oxide semiconductor
MOSFET	metal oxide semiconductor field-effect transistor
MP2	Møller-Plesset perturbative theory
MPDV	multiplexed photonic Doppler velocimetry
MUX	multiplexer

N

N_2	nitrogen gas
n/γ	neutron/gamma
NaI	sodium iodide
NaI:Tl	thallium-doped sodium iodide

NASA	National Aeronautics and Space Administration
NH_3	ammonia
NI	National Instruments
NIF	National Ignition Facility
NIST	National Institute of Standards and Technology
NLV	North Las Vegas
NNSA	U.S. Department of Energy, National Nuclear Security Administration
NNSS	Nevada National Security Site
NO_2	nitrogen dioxide
NRS	neutron resonance spectroscopy
NSTec	National Security Technologies, LLC
NToF	neutron time of flight
NVM	non-volatile memory

O

1-D	one-dimensional
OFHC	oxygen-free high conductivity (copper)
OPA	optical parametric amplifier
OSCAR	Occluding Scintillator Crystal Array

P

PAGOSA	(a multi-dimensional, multi-material Eulerian hydrocode/computational fluid dynamics computer program developed at LANL)
PAS	power automation system
PAW	Projector-Augmented-Wave
PBE	Perdew-Burke-Ernzerhof
$Pb[Zr_{(x)}Ti_{(1-x)}]O_3$	lead zirconate titanate
PCB	printed circuit board
PDT	Pacific daylight time
PDV	photonic Doppler velocimetry
phe	PMT photoelectrons
PHY	physical (layer)
PKT	Peano kernel theorem
PMT	photomultiplier tube
PN	pseudorandom noise
PRONTO	transient-dynamics finite-element code (Sandia National Laboratories)
PSD	power spectral density

PSF	point spread function
PS-MA-PMT	position-sensitive multi-anode photomultiplier tube

Q

QE	quantum efficiency
QPSK	quadrature phase-shift keying

R

RAM	random access memory
R&D	research and development
RF	radio frequency
RMD	Radiation Monitoring Devices, Inc.
ROI	region of interest
ROM	read-only memory
RPI	Rensselaer Polytechnic Institute
RSL	Remote Sensing Laboratory
RSL-A	Remote Sensing Laboratory–Andrews
$Ru(bpy)_3^{2+}$	Tris(bipyridine)ruthenium(II) chloride

S

SBA	super bialkali
SBSF	statistics-based spline fitting
SCADA	supervisory control and data acquisition
SD	secure digital (card)
SDRD	Site-Directed Research and Development
SEM	scanning electron microscope
SGFET	suspended gate field-effect transistor
SHA	secure hash algorithm
SLIDER	serrated light illumination for deflection-encoded recording system
SNL	Sandia National Laboratories
SNR	signal-to-noise ratio
SPaSM	scalable parallel short-range molecular dynamics (a high-performance code for studying collective effects in large systems of interacting particles)
SPH	smoothed-particle hydrodynamics
SPI	serial peripheral interface
SSPM	solid-state photomultiplier
ST&E	science, technology, and engineering

STL	Special Technologies Laboratory
STP	standard temperature and pressure

T

2-D	two-dimensional
3-D	three-dimensional
TCP/IP	transmission control protocol/Internet protocol
TEM	transmission electron microscopy
Th	thorium
TIC	toxic industrial compound
TPM	trusted platform module
TV	total variation

U

U	uranium
^{235}U	uranium-235
^{238}U	uranium-238
UCl_3	uranium trichloride
UCLA	University of California, Los Angeles
UCSB	University of California, Santa Barbara
UO_2	uranium dioxide
U_3O_8	triuranium octoxide
UNLV	University of Nevada, Las Vegas
UQ	uncertainty quantification
USB	universal serial bus
UT	University of Tennessee, Knoxville
UTA	University of Texas at Austin
UV	ultraviolet

V

VASP	Vienna Ab-initio Simulation Package
VB	valence band
VISAR	velocity interferometer system for any reflector
V-NVM	visible non-volatile memory
VOC	volatile organic compound

Z

ZnO	zinc oxide
ZnS	zinc sulfide
ZrO_2	cubic zirconium dioxide

This page left blank intentionally

Material Studies and Techniques

Material Studies and Techniques

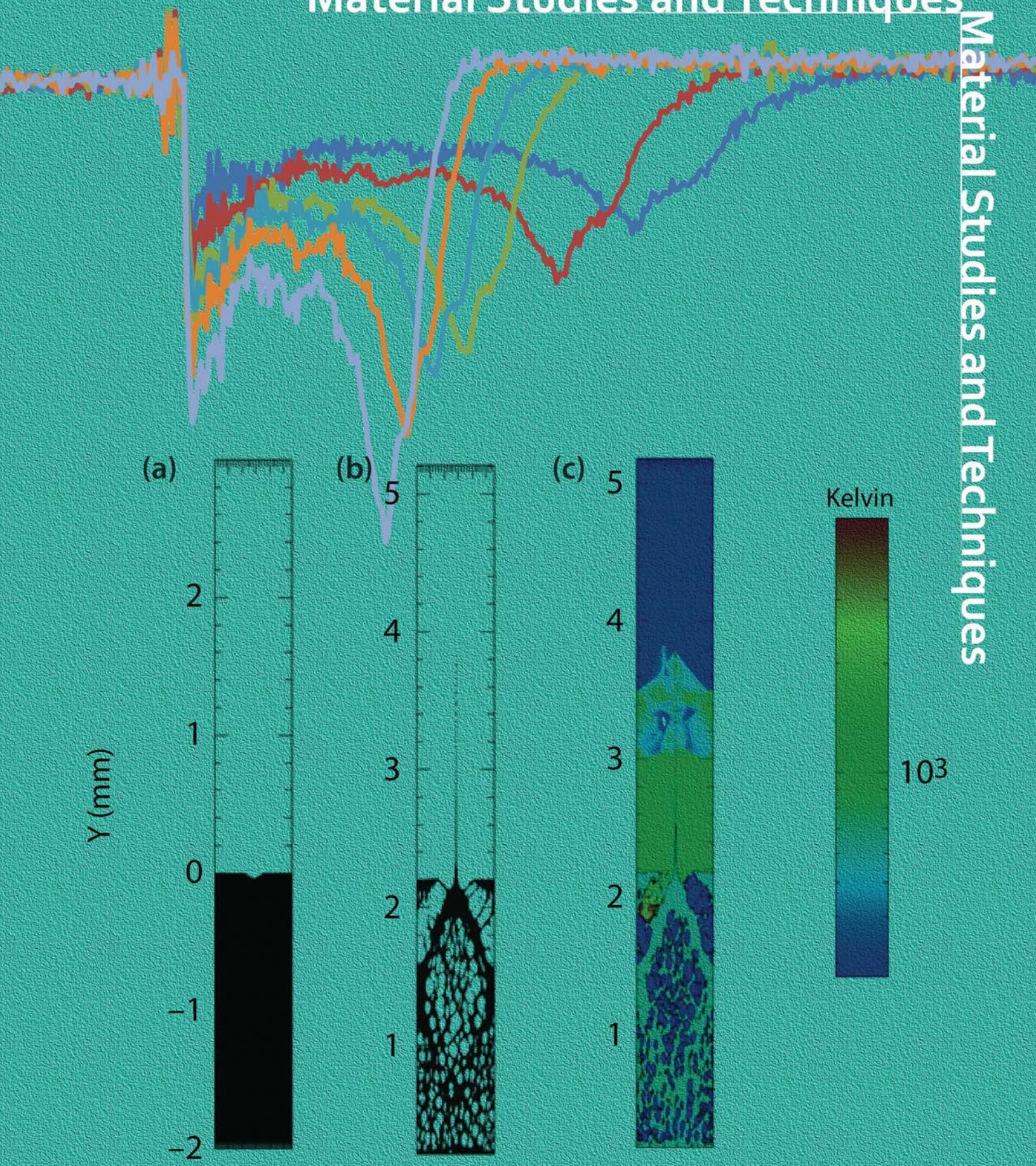

Electron Mobility Measurements in Scintillator Materials

LAO-06-13 | Continued from FY 2012 | Year 2 of 2

Alden Curtis,[1,a] James Tinsley,[b] Kristina Brown,[a] and Ken Moy[b]

Understanding the physical mechanisms that cause ionizing radiation to create an optical signal in scintillator materials is important for understanding the nonproportionality of scintillator response to different incident particle energies, and for providing a basis for identifying new scintillator materials. Charge carrier mobility has been shown to be particularly significant in these interactions. We used several types of ionizing radiation to create charge carriers in strongly biased, thin scintillator samples and then attempted to measure the transit times of the electrons across the material in order to calculate the electron mobility. We successfully demonstrated the viability of the technique using a cadmium zinc telluride sample. However, the substantial increase in resistivity of the dielectric scintillator over that of the semiconductor sample rendered measurements using the scintillator inconclusive.

[1] curtisah@nv.doe.gov, 505-663-2067
[a] Los Alamos Operations; [b] Special Technologies Laboratory

Background

Despite the use of scintillators for more than a half century (Hofstadter 1948), the basic physics underlying the operation of inorganic scintillators is poorly understood. To gain insight into their operation, attempts are being made (Li 2001, Setyawan 2009) to model the role of a number of processes believed to be involved. A key characteristic of these materials is the carrier mobility, which affects the energy transfer process and, in particular, the nonproportionality of light output. The measurement of mobility in scintillators is difficult at best and experimental values are rarely found in the literature. This difficulty arises from the fact that the characteristics of carrier mobility in insulators differs substantially from that inherent to semiconductors. In insulators the carriers are transported by Frenkel-Poole conduction—they move by hopping from trap to trap either by thermal excitation or tunneling. Electrons easily trapped in their localized states require random thermal fluctuations and an externally applied electric field to excite them into the conductions band for free movement, resulting in mobility values many orders of magnitude less than those of semiconductors.

Project

The project comprised two major tasks. The first task consisted of using different sources of ionizing radiation to measure electron mobility in the semiconductor cadmium zinc telluride (CZT). Electron mobilities measured in the CZT range from 700 to 1350 $cm^2/V{\cdot}s$ (Schlesinger 2001). By comparing our values to the measured values, we were able to gauge whether our techniques were appropriate. The second task was to use these same techniques to measure the electron mobility of cesium iodide (CsI), to be followed by additional scintillator materials.

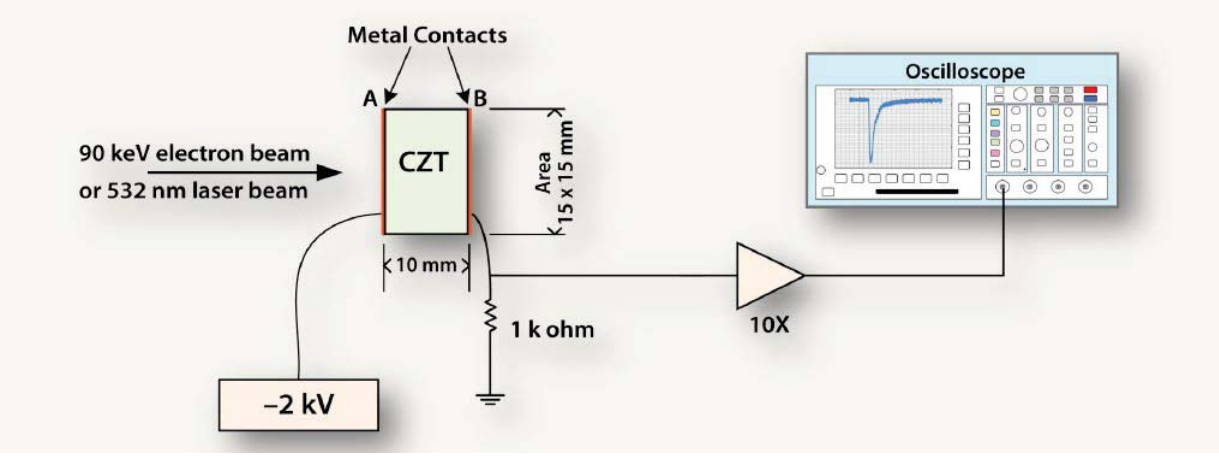

Figure 1. Schematic layout for CZT mobility tests

Figure 2. CZT mounted in a Pomona shielded box

CZT Tests

Because the physical parameters of CZT vary widely for different samples depending on the manufacturer, we first measured the electron mobility of our sample using laser excitation following the technique demonstrated by Burshtein (1993). By measuring the transit time, t_r, of charge carriers as they travel through the material, we are able to calculate the mobility, μ, using the formula,

$$\mu = \frac{d^2}{t_r \times V}, \quad (1)$$

where d is thickness of the sample and V is the applied bias. By varying the biases, we were able to demonstrate the repeatability of the method. This formula is applicable only when the trapping time is longer than the transit time.

The schematic layout for the experiment can be seen in Figure 1. In this case, a 10 ns, 532 nm laser pulse impinges on one face of the CZT sample, generating electron-hole pairs. The electrons are then swept across the sample by a negative bias applied to the same face. The CZT sample is a 15 × 15 × 10 mm crystal mounted in a Pomona shielded box (Figure 2). Both 15 × 15 mm sides have been evaporatively coated with 50 nm of gold soldered to electrical leads for biasing and signal readout. All other tested materials were similarly coated for bias and signal collection.

The results for the laser-generated electron mobility testing can be seen in Figure 3. The transit time was measured from the first peak to the second peak for each pulse response, as a function of bias voltage. The spread of the later peak is caused by the longitudinal diffusion of the electron pulse as it travels through the material; the peak indicates the highest electron flux at the cathode. With longer transit times, the charge cloud experiences increasing longitudinal dispersion, producing longer tails at lower biases (Fink 2006). Overexposure of the sample to laser intensity causes these tails to become significantly longer, leading to a small increase in peak-to-peak duration, indicating space charge saturation effects.

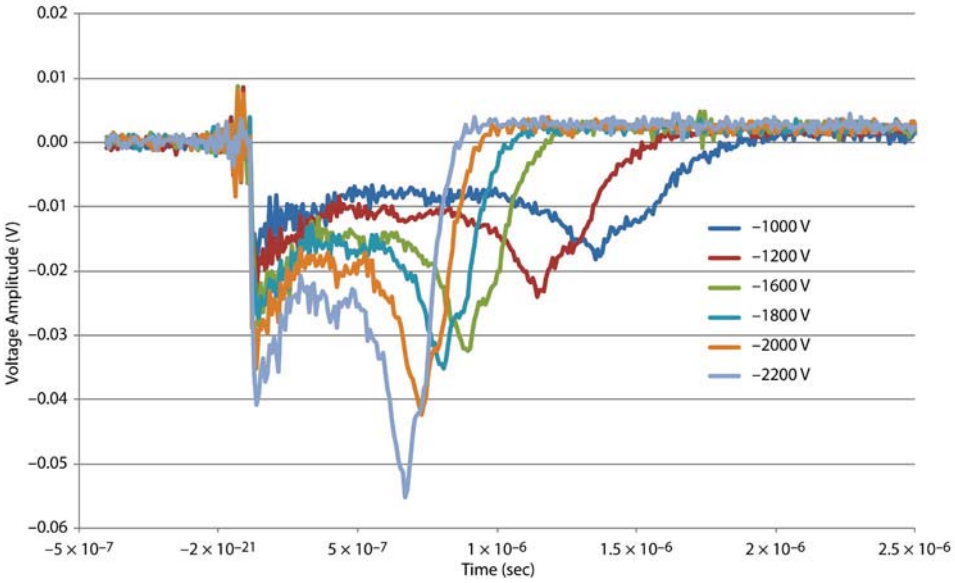

Figure 3. Current waveforms generated in CZT using optical excitation. The duration (mobility) measurements were made between the two peaks of the waveforms. Increasing longitudinal diffusion is also evident at lower biases.

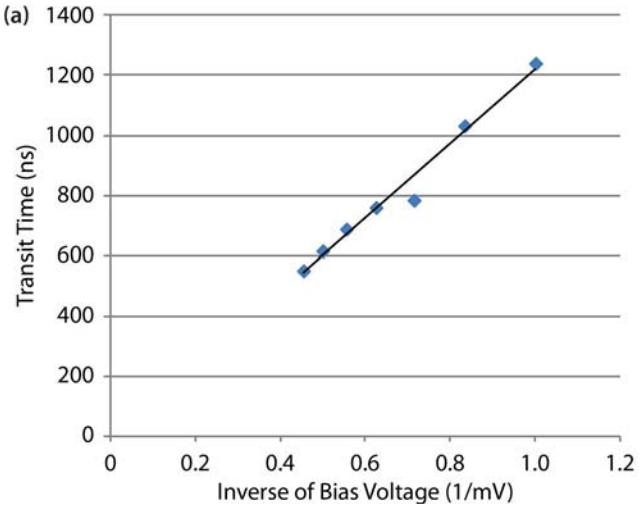

(b)

$$t_t = \frac{L^2}{\mu V}$$

Electron Time of Flight (ns)	Bias (–V)	Electron mobility* from formula ($cm^2/V \cdot s$)
552	2200	823
616	2000	811
688	1800	807
760	1600	822
784	1400	911
1032	1200	807
1240	1000	806

*Average electron mobility = 815

Figure 4. (a) A linear fit to the laser testing data of CZT shows good agreement for different biases; (b) the average of the different values is calculated, showing a 4.3% standard deviation

Measured transit times and a table of calculated mobilities for the sample are shown in Figure 4. The plot shows that the electron transit time varies approximately linearly with applied bias.

The average calculated value for the electron mobility is 815 $cm^2/V \cdot s$. The mobility values show good agreement, with a standard deviation of 4.3%, well within the 700–1350 $cm^2/V \cdot s$ range reported in the literature.

To demonstrate that our techniques were appropriate for scintillators, mobility measurements were taken using a variety of ionizing radiation sources, first on the CZT. The number of electron-hole pairs generated in a solid by incident radiation is strongly dependent on the band gap energy; i.e., the larger the band gap, the greater the energy required to generate an electron-hole pair. Because insulators such as CsI typically have band gaps of 5 eV or more, fewer pairs are generated per unit of energy absorbed compared to CZT at ~1.6 eV. These tests were shown to be repeatable on the CZT with electrons and x-rays from an electron linear accelerator (linac), and gamma and alpha radiation from material sources.

The first radiation test was performed using the electron linac located at National Security Technologies, LLC (NSTec), Los Alamos Operations (LAO). The experimental setup was very similar to that shown in Figure 1, except the CZT was mounted inside the vacuum enclosure to be in the electron beam path. The linac produced 2 ns, 90 keV electron pulses with around 0.5 A peak current per pulse in response to trigger signals varying from single-shot to 10 Hz. Results for several biases are shown in Figure 5. Although there are fewer data points, a linear fit is evident. The mobility value has changed for this measurement by 11% from 800 to 900 $cm^2/V{\cdot}s$. We believe this may be caused by space charge effects due to high linac current density incident on the CZT. The LAO linac has limited tunability when less than 0.5 A of current is used.

Another test was performed outside the linac target chamber using bremsstrahlung and characteristic line x-rays generated by the electron pulse on a copper tungsten (CuW) target as shown schematically in Figure 6. The x-rays then passed through a 10-mil-thick beryllium vacuum window and impinged on the sample in air. Figure 7 shows the resulting current pulses from the CZT. The mobility value of 827 $cm^2/ V{\cdot}s$ agrees well with the laser measurement discussed above, and the standard deviation of less than half of a percent shows good agreement for different biases. Unlike the previous direct electron exposure test, this configuration allowed for easier tunability of the energy deposited on the sample, via changing the distance between the target and the sample, allowing for unsaturated operation.

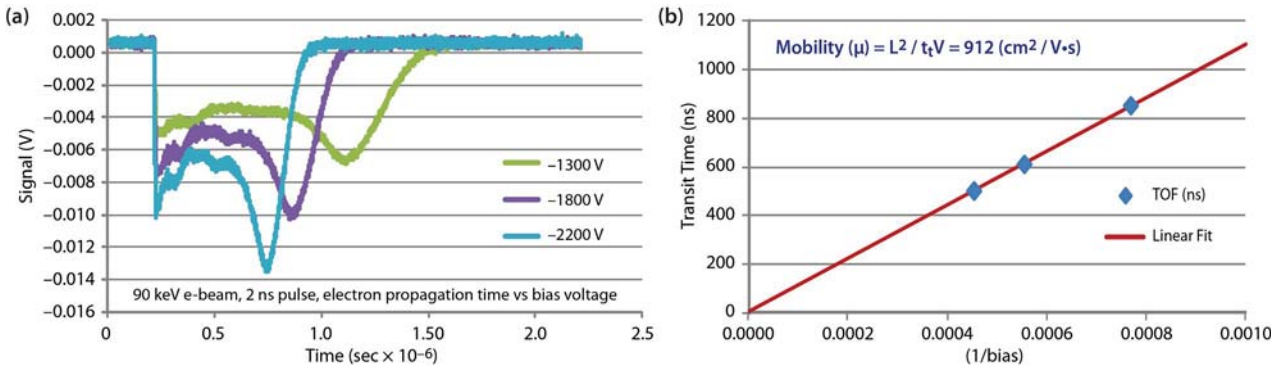

Figure 5. (a) Traces from electron impact CZT tests and (b) a plot showing good linear agreement for the three test points with the electron beam

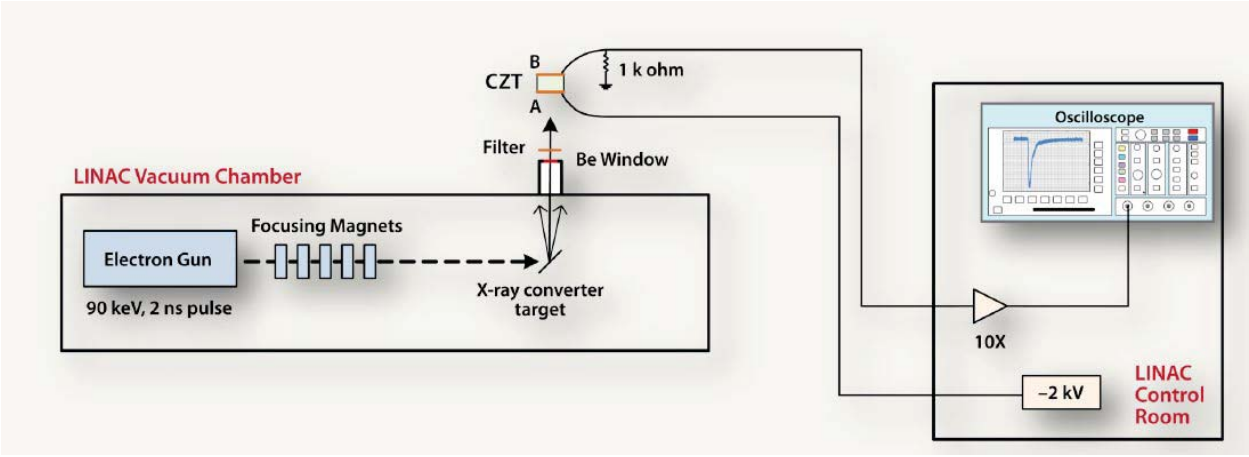

Figure 6. Experimental setup for bremsstrahlung and characteristic line x-ray tests for CZT

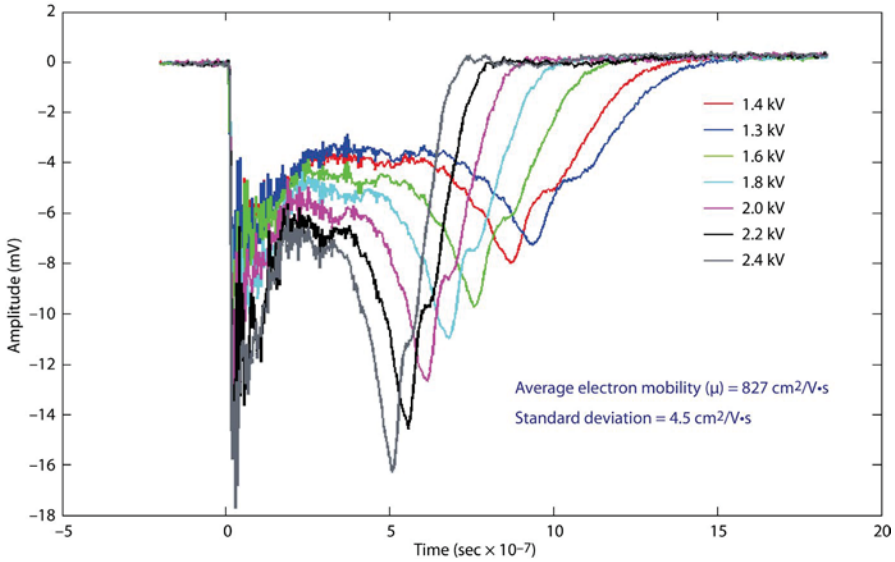

Figure 7. Traces for x-ray tests with CZT show a similar shape and duration to the laser test results shown in Figure 3

The test was also performed using a 5 μCi ^{137}Cs gamma source, a 5 μCi ^{243}Am alpha source, and 200 nm laser pulses, all identified as potential excitation sources for the dielectric materials. The resulting pulse shape and mobility values were the same as those shown above for the electron, x-ray, and 532 nm laser sources, and thus are not shown.

Scintillator Tests

Two different scintillator materials, CsI and bismuth germinate (BGO), were tested using a number of the sources mentioned above. BGO is a high-Z, non-hygroscopic scintillator with a 4.8 eV band gap. The BGO sample was 160 μm thick. CsI is one of the brightest known scintillator materials, with a 6.2 eV band gap. CsI is mildly hygroscopic, so the samples, which were not hermetically sealed, had to be handled with care to prevent oxides from forming on the edges that would skew measurements. We tested 0.25, 0.5, and 1 mm samples of CsI.

The samples were mounted in shielded boxes with BNC connectors attached to the leads on each crystal face, on which a very thin layer of gold was deposited. Radiation and electromagnetic shielding for the samples were required in all the testing environments. Electromagnetic pulses from the LAO linac or the Pockels cells in the Livermore Operations (LO) short-pulse laser laboratory were sufficient to create tens of mVs of noise when each device fired, more than overwhelming our expected signal. Combinations of aluminum foil and lead bricks were used to bring the noise down to a few mV.

Due to the noise problem at the LAO linac, which was only later more effectively filtered, the first scintillator tests were performed at the Pegasus Facility at the University of California, Los Angeles (UCLA). The electron pulses at this facility are created by a short-pulse laser generated in a different room and then transported to a photocathode rather than a thermionic cathode (as is done with the LAO linac). The samples were inserted into a vacuum chamber where a 2–3 ps electron pulse excited the negatively biased face. While no noise was evident with this setup, we were not able to see a signal with either scintillator or CZT. We believe the electron charge per pulse was too low to excite a measurable signal.

The next experiments occurred at the LO short-pulse laser laboratory, where we expected noise lower than at the LAO linac; also, a 200 nm laser should be able to excite carriers across the band gap of the CsI and BGO scintillators. The 250 μJ pulses can create enough carriers to observe a signal, and the 1 ps duration is short enough to approximate an impulse relative to the signals we expect to observe. The experimental setup is shown in Figure 8. The laser pulse is sent through a variable amount of attenuation before being focused

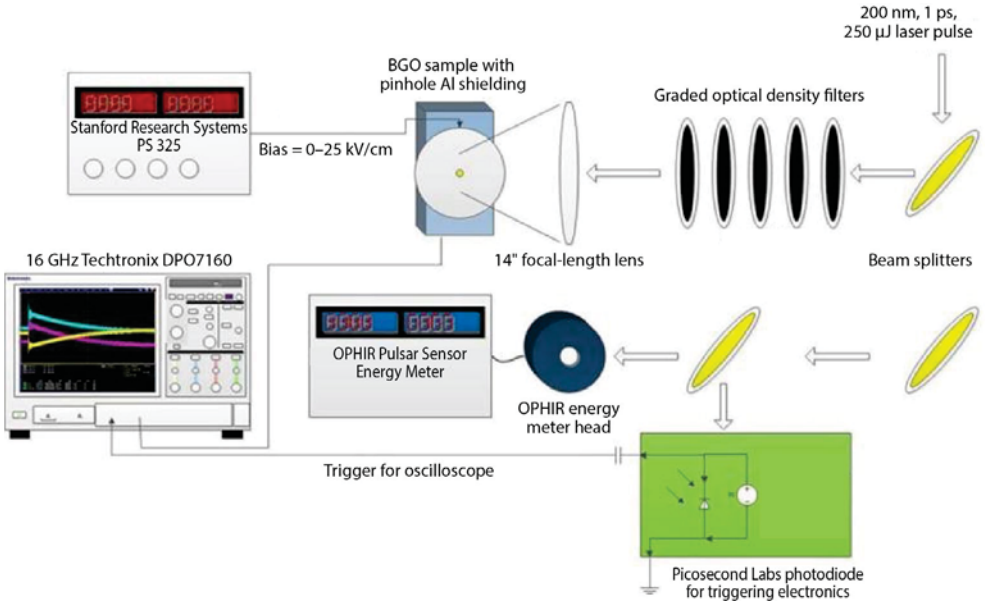

Figure 8. Schematic layout for scintillator testing at the LO short-pulse laser laboratory

on the sample. Part of the beam is picked off and sent to timing electronics as well as an energy meter to measure shot-to-shot energy variations.

The resulting waveforms for the BGO testing, shown in Figure 9, did not look like the CZT results. Although signal amplitude is seen to change as a function of bias, the decay time also increases at the largest bias values. A log plot of the same data revealed no second time constant in the decay. The data seem to be contaminated with the capacitive response of the circuit we used. Months after this series of tests was concluded, during a second series of tests at LO, we found that there was no apparent electrical continuity between the front face of the sample and the BNC bias connection. However, it is not possible to determine the integrity of the sample at the time these traces were taken.

The results for CsI, for samples that were electrically tested and appeared intact, are shown in Figure 10. Again we see that these traces are different from either of the previously shown waveforms. It should be noted that these waveforms could be repeated with samples of different thicknesses. It appears that for several CsI samples the electrodes had disconnected from the leads, as had occurred with the BGO. We saw similar capacitive signals with these CsI samples. This leads us to conclude that the waveforms shown in Figure 10 indicate what is physically going on in the biased dielectrics when a large population of charge carriers is excited on one face, and it is not just an artifact of the circuit.

We attempted to use the Hecht equation to extract a mobility-carrier lifetime (µτ) product from the above curves for BGO and CsI. The Hecht equation relates charge collection efficiency, $Q(t)/Q_0$, in semiconductor radiation detectors to charge carrier trapping conditions under a uniform field, and typically takes the form

$$Q(t) = Q_0 \left(\frac{\tau}{t_r} \right) \left[1 - e^{\left(\frac{t}{\tau} \right)} \right], \quad \textbf{(2)}$$

where τ is the carrier recombination time, t_r is the transit time of the charge carriers across the material, and t is time elapsed (Knoll 2010). The µτ product can be extracted from this formula by noting

$$t_r = \frac{L^2}{\mu \times V}, \quad \textbf{(3)}$$

a rearrangement of Equation 1 (no trapping before t_r has elapsed). We expect to find τ from the decay time of the waveform and then calculate µ.

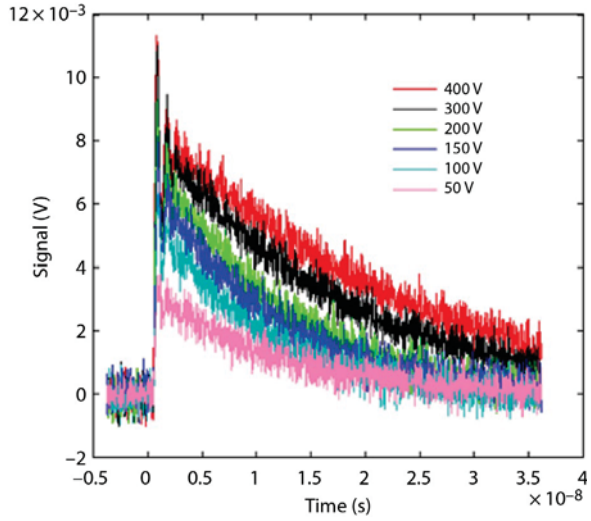

Figure 9. We were disappointed to see that the averaged response of the BGO sample at six different biases seems to only indicate a capacitive decay

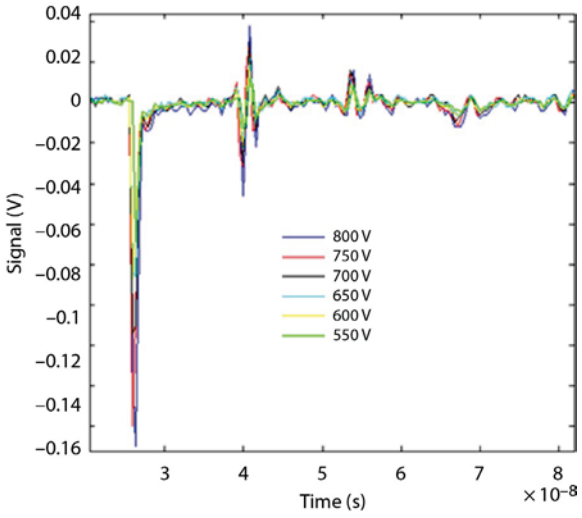

Figure 10. Waveforms generated by 250 µm thick CsI excited by 200 nm laser light at different biases in the configuration shown in Figure 8

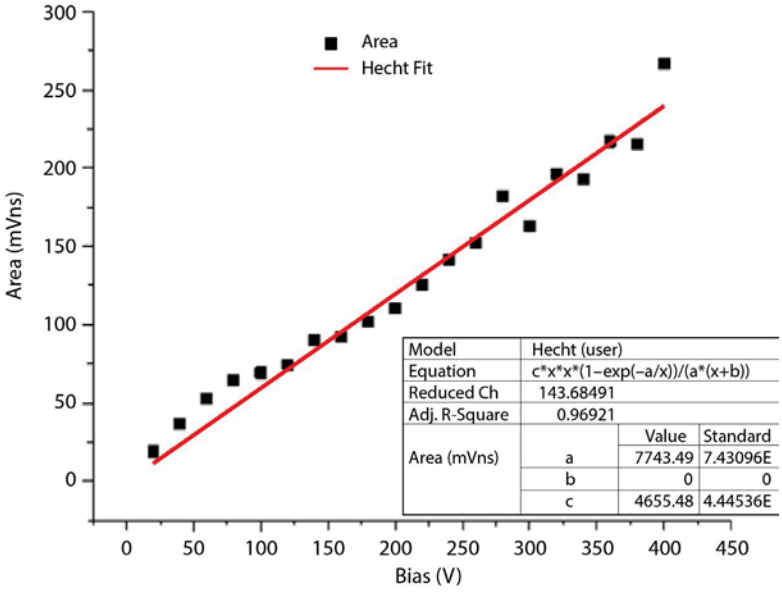

Figure 11. Results from BGO traces (shown in Figure 9), after being fit with the Hecht equation, show poor agreement with expected results

For the BGO sample, the $1/e$ decay time seen in the Figure 10 curves is around 10 ns before we start to see saturation effects at about 12.5 kV/cm. With the data fitted to the Hecht relation, the µτ product is 3×10^6 cm^2/V; the fit is shown in Figure 11. The resulting electron mobility is close to 300 cm^2/V·s. We believe this is not a realistic value; we are expecting values of 1–10 cm^2/V·s. The CsI data will be processed by Fisk University, and we are hopeful that a useful number for the µτ product can be calculated from the data in Figure 10.

Lithium Indium Selenide ($LiInSe_2$) Sample Tests

We received samples of $LiInSe_2$ from Fisk University. This material has the potential to be one of the first direct-conversion semiconducting neutron detectors.

$LiInSe_2$ should have a band gap near 3.8 eV, which is between the CZT and scintillator band gaps. The first sample we received was tested at LO in the configuration shown in Figure 8. We were unable to see a signal for this sample. The second sample, which the Fisk University lab claimed had fewer impurities, was tested during our last experimental run at the LAO linac. The results look similar to the waveforms shown in Figure 10 for CsI. We are waiting for the complete analysis of these tests.

Discussion

Although it is still possible that we will be able to derive a μτ product from the data, it is unlikely we will be able to isolate the charge carrier mobility for the CsI or $LiInSe_2$. There is no clear time constant in the traces in Figure 10 to use as a figure for the recombination time. Although further research could lead to measurement of recombination time for these materials, such research is not planned at this time. We plan to use the scintillation decay time in lieu of a more accurate measurement for CsI, and compare the results with those published by Aduev (1998).

We believe most of our difficulties with the scintillator materials were due to space charge effects. The sources we used created a large number of charge carriers at the surface of the material, three orders of magnitude more than would be created by the bias on the capacitance of the samples alone. This high concentration of charge carriers could have been enough to distort the electric field created by the bias. Once our electric field was no longer uniform, all of our assumptions using the equations above would have become invalid. The fact that the scintillators are dielectrics could have exacerbated this effect. Because of charge trapping near the cathode, the charge carriers were not able to diffuse as they did in the higher-mobility CZT.

Conclusion

We tested several semiconductor and dielectric materials to try to determine the electron mobility. We successfully measured the mobility in CZT with a number of methods, including laser, electron, x-ray, gamma, and alpha particle excitation. We were unable to measure the mobility in $LiInSe_2$, where the resistivity and band gap are much higher. This was possibly due to material impurities, as it has only recently been synthesized for the first time, and growth of the material is not a mature process. We were also unsuccessful measuring the mobility in the scintillators BGO and CsI. We believe that the dielectric nature of the materials and space charge effects prevented these measurements from succeeding. We may still be able to obtain a μτ product from the collected data and thereby estimate the mobility.

Acknowledgments

The authors thank Larry Franks (Keystone), Arnold Burger (Fisk University), Pietro Musumeci (UCLA), Andrew Mead (LO), Wendi Dreesen (LAO), David Schwellenbach (LAO), Vu Tran (LO), and Evan Threlkeld (UCLA) for their contributions. The gamma measurement was done with the help of William Quam and Bob Vogel at the Special Technologies Laboratory, the alpha test was done with the help of Arnold Burger and Mike Groza at Fisk University, and the laser measurement was done with the help of Andrew Mead at LO.

References

Aduev, B. P., E. D. Aluker, G. M. Belokurov, V. N. Shvayko, "Radiation-stimulated conductivity of some alkali halides induced by 50 ps electron pulse irradiation," *Physica Status Solidi B* **208** (1998) 137–143.

Burshtein, Z., H. N. Jayatirtha, A. Burger, J. F. Butler, B. Apotovsky, F. P. Doty, "Charge-carrier mobilities in $Cd_{0.8}Zn_{0.2}Te$ single crystals used as nuclear radiation detectors," *Appl. Phys. Lett.* **63**, 1 (1993) 102–104.

Fink, J., H. Krüger, P. Lodomez, N. Wermes, "Characterization of charge collection in CdTe and CZT using the transient current technique," *Nucl. Instrum. Methods Phys. Res. A* **560**, 2 (2006) 435–443.

Hofstadter, R., "Alkali halide scintillation counters," *Phys. Rev.* **74** (1948) 100–101.

Knoll, G. F., *Radiation Detection and Measurement*, 4th edition, John Wiley & Sons, Hoboken, New Jersey, 2010, 489.

Li, Q., J. Q. Grim, R. T. Williams, G. A. Bizarri, W. W. Moses, "A transport-based model of material trends in nonproportionality of scintillators," *J. Appl. Phys.* **109**, 12 (2011) 123716.

Schlesinger, T. E., J. E. Toney, H. Yoon, E. Y. Lee, B. A. Brunett, L. Franks, R. B. James, "Cadmium zinc telluride and its use as a nuclear radiation detector material," *Mat. Sci. Eng.* **R32**, 4–5 (2001) 103–189.

Setyawan, W., R. M. Gaume, R. S. Feigelson, S. Curtarolo, "Comparative study of nonproportionality in electronic band structures features in scintillator materials," *IEEE Trans. Nucl. Sci.* **56**, 5 (2009) 2989–2996.

This page left blank intentionally

Detection of Phase Transitions and Effusivity Changes through Isobaric Heating of Shock-Compressed Materials

STL-09-13 | Continued from FY 2012 | Year 2 of 2

Brandon La Lone,[1,a] Gene A. Capelle,[a] Dale Turley,[a] Gerald Stevens,[a] Mike Grover,[a] Robert S. Hixson,[b] Oleg Fatyanov,[c] Paul Asimow,[c] and Lynn Veeser[a]

We explored the use of shock-wave compression followed by laser heating in order to accomplish two important goals: the first goal was to locate high-pressure and temperature phase transitions in metals; the second was to determine thermal transport properties of shock-compressed materials. Both goals are critical for equations of state development for the Stockpile Stewardship Program. While neither goal was met entirely, significant progress was made on both fronts. Calculations were performed to show that continuous laser irradiance near 1 MW/cm² is needed for the phase-boundary identification measurements. A laser capable of this irradiance was located at Los Alamos Operations and moved to the Special Technologies Laboratory (STL), and is currently being refurbished for use at the STL explosives testing chamber (Boom Box). Preliminary work on thermal transport measurements, using short-pulsed-laser heating, began in FY 2012 and has been advanced by this work. The accuracy of the thermal transport measurement was improved under explosive loading, and the technique is currently being transitioned to a two-stage gas gun platform for measurements at higher shock-wave pressures. A new project, "New methods to quantify thermodynamic and phase properties of shocked materials," will begin in FY 2014 in collaboration with the California Institute of Technology, where two-stage gas gun measurements will be conducted.

[1] lalonebm@nv.doe.gov, 805-681-2046
[a] Special Technologies Laboratory; [b] Los Alamos Operations; [c] California Institute of Technology

Background

Material phase diagnostics and accurate temperature measurements are critical needs for equations of state (EOS) development within the weapons physics community. Currently, the principal diagnostic for identifying phase transitions in dynamic compression experiments is velocity measurements of wave profiles. Careful analysis of shock, ramp, and release wave profiles can reveal volume and compressibility changes caused by a phase transition. While widely used, this technique is limited to a narrow range of thermodynamic states, and the temperatures at the phase boundaries are not known experimentally. Because of the limitations of wave-profile measurements, many alternative techniques are being explored such as x-ray diffraction, sample preheating, complex loading, reflectivity, etc. All of these techniques have limitations, and there is an ongoing search for complementary methods of phase-change identification and experimental phase-boundary locators.

In addition to high-pressure phase identification, interior temperatures of dynamically compressed metals are needed for EOS development, and pyrometry is currently the most viable temperature measurement diagnostic. However, pyrometry measurements

of metals are restricted to measurements of the metal surface temperature, or metal-window interface temperature, since metals are opaque. The surface temperature differs from the interior temperature for a few reasons, as discussed previously (Grover 1974, Tan 2001, La Lone 2013a). One reason is the conduction of heat from the metal into the window. The temperature difference between the metal interior and the metal-window interface can be accounted for with knowledge of the thermal transport properties of the metal and the window. Specifically, for a metal at a temperature T_M in contact with a window at a temperature T_W, the interface temperature T_I is

$$T_I = T_M - \frac{T_M - T_W}{1 + \left(\frac{\kappa_M \rho_M C_M}{\kappa_W \rho_W C_W} \right)^{1/2}}, \quad \textbf{(1)}$$

where κ is the thermal conductivity, ρ is the density, and C is the specific heat at constant pressure; the subscripts M and W denote metal and window, respectively (Grover 1974). The quantity $(\kappa\rho C)^{1/2}$ is termed the thermal effusivity and is a measure of a material's ability to exchange heat with its surroundings.

Previous investigators (Gallagher 1996, Ahrens 1998, Holland 1998) have attempted to measure the thermal transport properties in dynamic compression experiments. The method they used was to shock load a thin film of metal sandwiched between two transparent windows. The metal film is heated by the shock wave to a higher temperature than the surrounding windows and then allowed to cool off by heat conduction into the windows. The temperature decay was measured with pyrometry and used to extract thermal transport properties of the windows. This method has drawbacks, as discussed by Tan and Dai (2001). The main drawback is that the amount of heat deposited into the film from shock-wave interactions must be calculated very accurately, and these calculations rely on the EOS (the properties they are attempting to measure). Also, the gap between the film and window must be known accurately as this causes additional heating due to a release-reshock cycle for material near the gap (however, no gap measurement was reported).

In the first year of this project (La Lone 2013b), we developed a method to measure the thermal transport properties of explosively compressed solids. The method utilized a pulsed laser to rapidly heat a thin layer of material at the interface between the metal of interest and a window. The temperature rise and decay of the heat pulse is recorded with pyrometry, and the thermal effusivity was extracted from the shape of the pulse. This method overcomes the major drawback of the metal sandwich method in that the amount of excess heat deposited at the interface can be accurately controlled by adjusting the laser power, and can also be accurately determined by measuring the laser fluence and surface emissivity. Although the pulsed-laser heating method was successfully demonstrated in FY 2012, several issues limited the accuracy of the measurements: (1) the single-channel pyrometer was overfilled and had a complicated response that was difficult to deconvolve, (2) the detector was not sensitive enough to make measurements on bare tin and required an emissive layer of chromium to be deposited between the sample and the window, and (3) the laser beam fluence was not well known.

In the second year of this project, we proposed to expand upon the FY 2012 work by using a shock followed by laser heating to pursue measurements of phase-boundary locations. The concept uses a continuous laser heating approach of the metal-window interface, as opposed to pulsed-laser heating. We also improved the accuracy of the short-pulsed heating technique and are working to transition the technique to a two-stage light gas gun for measurements on materials of interest to the weapons physics community.

Project

Long-Pulsed Laser Heating

The temperature response of a surface to rapid heating is dependent on the conductivity of heat away from the surface, the thermal conductivity, and the temperature change that corresponds to a change in the internal energy (the heat capacity). The heat capacity increases dramatically at a first-order phase transition, such as a melt boundary, because most of the thermal energy is consumed by the phase transformation as opposed to raising the temperature. Therefore, analogous to differential scanning calorimetry, if constant heating is applied to the surface with a laser, the rate of temperature increase should undergo a discontinuity at a phase boundary.

We simulated the temperature-time profile of the interface between a shock-compressed tin sample and a glue layer heated with a continuous laser. In this calculation, the thermal transport properties for tin were set to their room-temperature values, κ = 67 W/m*K, and C = 0.21 J/g*K. The heat of fusion of the tin melt boundary was set to its ambient value of 59 J/g, and the melt temperature was set to 1660 K, which corresponds to a pressure on the melt boundary of around 25 GPa (Mabire 2000). Calculations were performed with and without melting, and the results are shown in Figure 1. In the calculation with melt, a clear break in the temperature-time slope is present at the 1660 K melt temperature; this break should be observable in a pyrometry experiment. Therefore, we should be able to experimentally identify the melt temperature; the corresponding melting pressure would be the interface pressure, which can be obtained from velocity measurements.

The laser heating method has potential advantages over other techniques of phase-boundary identification. Because the heating is accomplished with a laser, a complex pressure-loading path is not needed to access the melt boundary. In principle, the melt boundary can be accessed with this method at any pressure below where the shock Hugoniot intersects the melt curve. Also, unlike velocity, x-ray, and most other phase-boundary diagnostics, the temperature at the phase transition is measured directly.

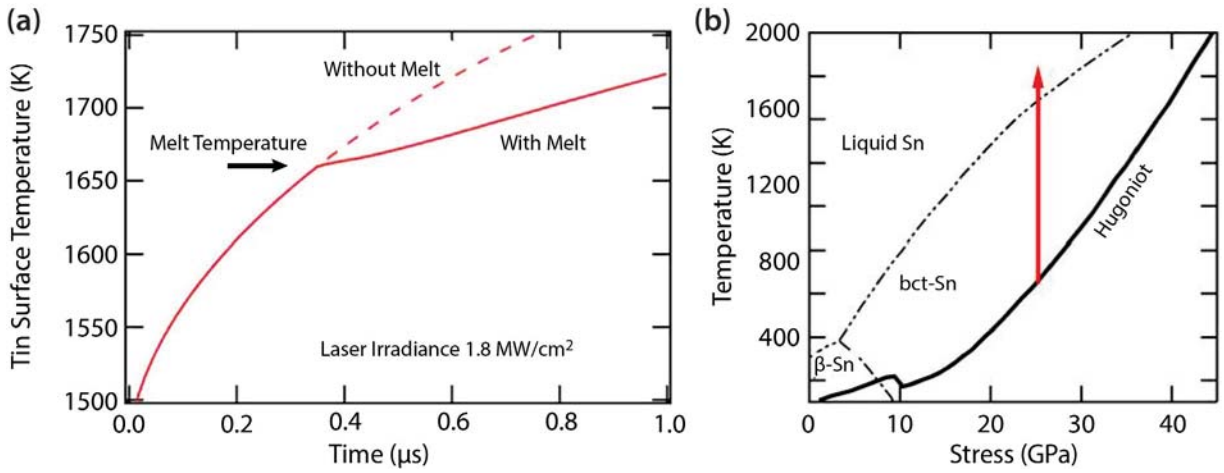

Figure 1. (a) Calculated surface temperature for tin (Sn) undergoing heating from continuous laser irradiation. Calculations were performed with and without a melt boundary at 1660 K. The melt temperature is identified as a break in the slope of the temperature-time curve. (b) The red arrow indicates the path in phase space taken for tin shock compressed to 25 GPa and laser heated. The pressure-temperature path is overlaid on the theoretical phase diagram developed by Mabire and Héreil (2000).

The laser irradiance levels used in the simulations shown in Figure 1 are over 1 MW/cm^2. This was required in order to heat the surface to a high enough temperature to observe melt on the time scale of a shock-wave experiment (~1 µs). To meet this laser irradiance requirement, we located a long-pulsed laser at Los Alamos Operations that has previously output up to 10 joules of energy at a 1064 nm wavelength in a single pulse, with a variable pulse width up to 50 µs. Because the laser was not in use, we moved it to the Special Technologies Laboratory (STL) for the current project. Presently, the laser is undergoing refurbishment and will be operational in FY 2014 for testing at the STL explosives testing facility (Boom Box).

Short-Pulsed Laser Heating

In order to increase the accuracy of the thermal effusivity measurements, several improvements were made to the experimental design used in the FY 2012 short-pulsed laser heating campaign. Figure 2 is a schematic of the short-pulsed heating experiments; the improvements to the experimental design are circled in the figure and discussed below.

Beam Profiler

A major limitation from the FY 2012 campaign was the inability to quantify the beam fluence. In FY 2013, part of the beam was picked off and sent into a laser beam profiler for quantification of the laser beam fluence. The beam profile analyzer used is a WinCamD 1M4, made by DataRay Inc.

Larger Area Detector

In the FY 2012 project, a single detector for the pyrometry measurement was used: an amplified InGaAs detector (model TTI-TIA950, made by Terahertz Technologies Inc.). This fiber-coupled detector could only accept a maximum fiber diameter of ~200 µm before overfilling complicated the response. The fiber diameter limited the amount of thermal radiance that could be collected during an experiment. This limitation prevented us from making measurements on bare

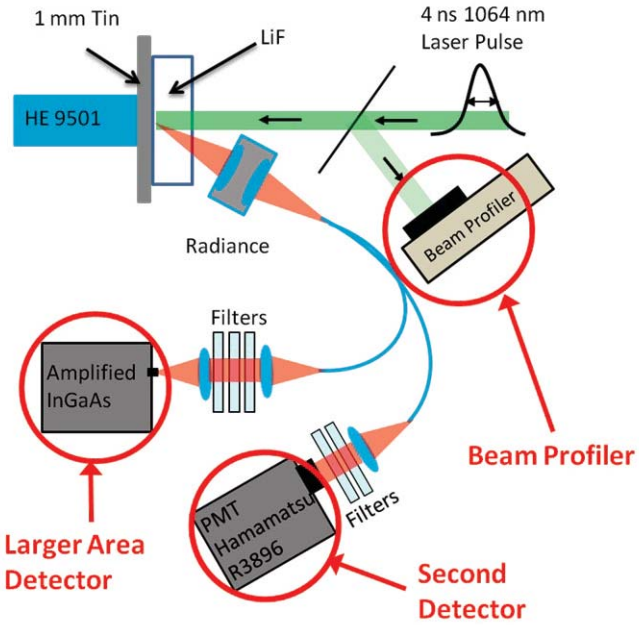

Figure 2. Configuration used for the short-pulsed laser heating experiments. Detonation of a 12 × 12 mm right-cylinder of PBX-9501 high explosive (HE) drives a shock wave into a 1 mm tin sample backed by a lithium fluoride (LiF) window glued to the tin surface. A short-pulsed laser is used to heat the tin-glue interface, and the temperature profile of the heat pulse is recorded with pyrometry. The items circled in red are upgrades to the system that were not part of the laser heat experiments performed in FY 2012.

tin due to the low emissivity of the surface, and only experiments performed using a highly emissive layer of vapor-deposited chromium on the tin surface gave sufficient signals.

In the FY 2013 project, we investigated several detector-amplifier combinations and settled upon using a 300 µm diameter InGaAs detector, made by Fermionics, coupled to a TTI-TIA525 amplifier (10,000 V/W) to replace the detector from FY 2012. Using free-space coupling, we were able to couple light from a 600 µm diameter fiber without overfilling issues. This modification resulted in a 10x improvement in signal-to-noise ratio compared with the previous detector and with comparable signal rise times (~3 ns). The filters used to define the band pass (1150–1700 nm) and to remove the 1064 nm laser light were identical to those in FY 2012.

Second Detector

For additional accuracy of the pyrometry measurement, we added a second detector channel with a 650–800 nm band pass. This detector was a photomultiplier tube (PMT) (model R3896 from Hamamatsu).

Dynamic Experiment at the Boom Box

Using the upgraded configuration shown in Figure 2, a dynamic experiment was performed on explosively compressed tin without a chromium layer. Both detectors were calibrated using a high-temperature blackbody source. The pulsed-laser energy was set to 18 mJ for this experiment. A photograph of the target package, including both detector probes and a photonic Doppler velocimetry (PDV) probe, is shown in Figure 3. Unfortunately, the PDV system did not trigger in this experiment and was not recorded. It is assumed here that the shock-wave stress at the interface between the tin and LiF window was about 25 GPa, based on previous experiments and a high degree of reproducibility for similar experiments.

Detector voltages under both ambient conditions and during the dynamic event are shown in Figure 4. Because neither pyrometer detector is sensitive to temperatures below ~800 K, any signal seen under ambient conditions is a result of either laser-light contamination (bleed through or around the filters) or electrical noise. In the InGaAs TTI detector, this background light contamination had an amplitude of ~1 mV and was subtracted from the signal in the dynamic experiment (Figure 4a). Overall, the signals from the TTI detector had an excellent signal-to-noise ratio of ~30. The shape of the radiance signal in the TTI detector is consistent with previous pyrometry experiments on explosively compressed tin (La Lone 2013a),

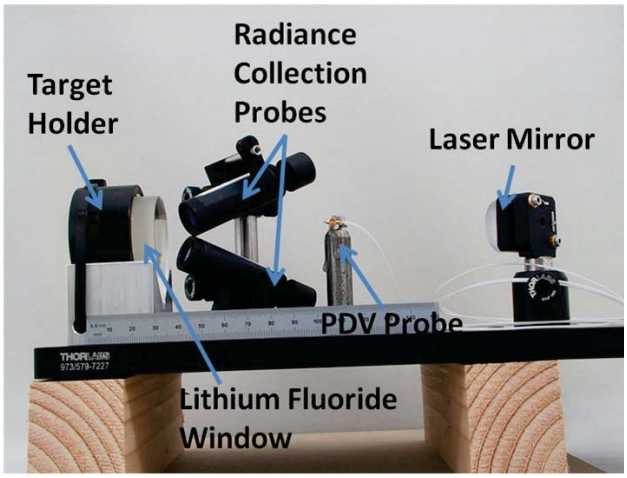

Figure 3. Photograph of the target for the short-pulsed laser-heating experiment on explosively compressed tin, with key features labeled

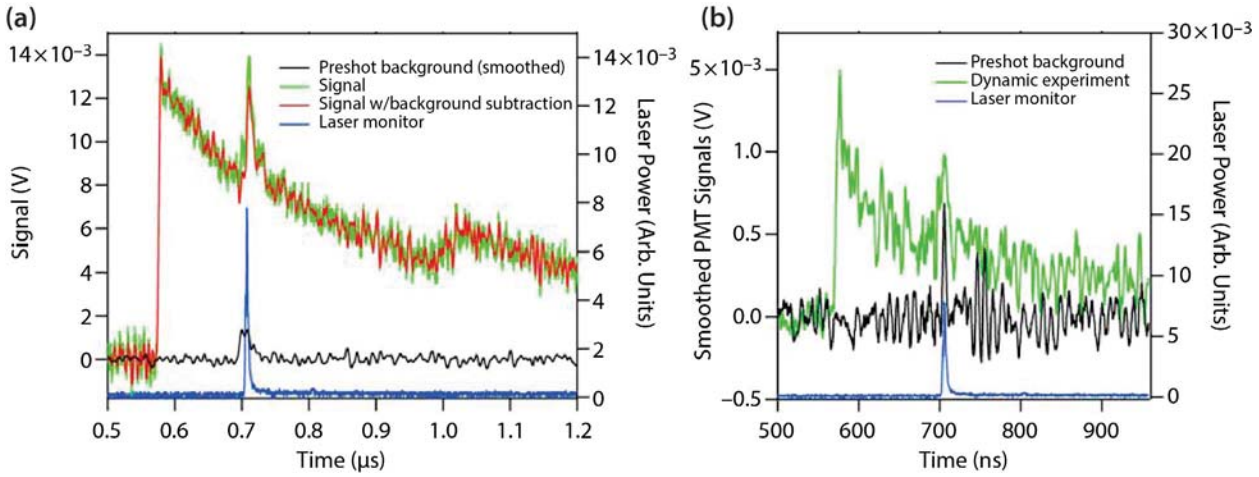

Figure 4. Radiance signals from the (a) TTI detector and the (b) PMT detector. The black traces were recorded with the laser firing under ambient conditions; the green traces were recorded in the dynamic experiment. The blue traces are from the laser-pulse monitor. The red trace in (a) was calculated by subtracting the background (black) from the dynamic experiment trace. The background-subtracted trace was used for the temperature analysis.

and the heating signature from the laser pulse is clearly visible beginning about 130 ns after shock breakout (shock breakout occurs at 0.56 µs). The pyrometry signals on the PMT detector had a poor signal-to-noise ratio of ~4 but have the correct gross features nonetheless. No attempt was made to subtract the background signals for the PMT detector because we did not want to increase the noise even further. The PMT signals shown in Figure 4b were smoothed over a 4 ns boxcar window for clarity.

Beam Profile

As mentioned, a small percentage of the laser beam was picked off and sent to the laser-beam profiler. To account for beam divergence, we set the profiler at a distance from the laser source that matched the laser-to-target distance. With the existing profiler, we were not able to capture the beam image during a dynamic experiment (only about 1 in 10 laser pulses are successfully captured). However, we found that the beam shape was very reproducible and could be characterized on a separate pulse using the same laser settings as in the dynamic experiment. Because the beam image is larger than the 6.2 × 5.3 mm sensor, we calibrated the beam at the target plane by measuring the energy that passes through a 1 mm pinhole. Several measurements were made near the center of the beam, which gave an average fluence of 62 mJ/cm^2 in the central region. The calibrated beam image shown in Figure 5 was scaled such that the central 2.5 × 2.5 mm region matched the pinhole measurements (62 mJ/cm^2). Because the beam fluence has spatial fluctuations of ~16% in this region, we estimate that the calibration uncertainty is 16%. An additional ~16% of uncertainty is also present because of uncertainty in the spatial location of the pyrometry probes relative to the laser pulse. The combined laser fluence uncertainty at the location of the measurement was ~23%. Therefore, we report the beam fluence on the tin surface at the location of the pyrometry probes as 62 ±14 mJ/cm^2. The uncertainty in the laser-beam fluence dominates the effusivity measurement uncertainty for shock-compressed tin. We will be able to greatly reduce the calibration uncertainty with a camera sensor that captures the entire beam, since the entire beam energy can be accurately measured. However, the beam variations, clearly visible in Figure 5, will continue to be problematic in the future.

Conclusion

Analysis

The dynamic temperatures calculated from the detector signals are shown in Figure 6. Emissivity values for shock-compressed tin from La Lone (2013a) were used for the temperature calculations and for the laser

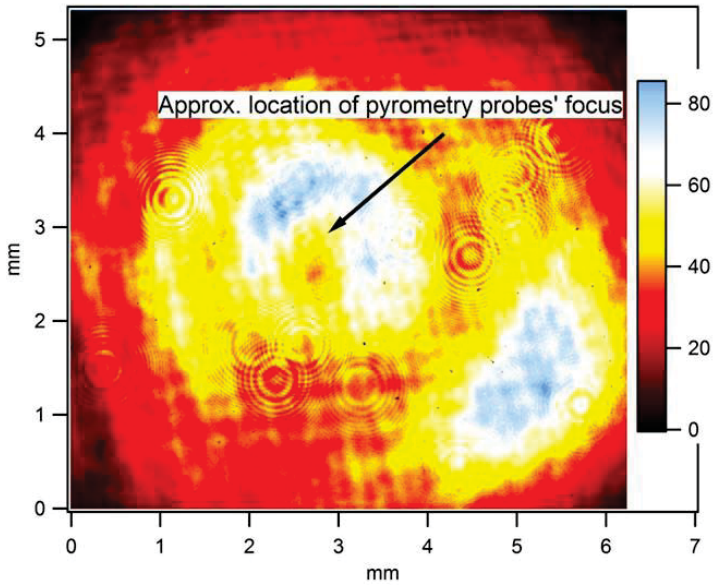

Figure 5. Calibrated laser-beam profile of the short-pulsed laser incident on the tin surface during the dynamic experiment. The color scale has units of mJ/cm^2. The arrow indicates the approximate location where the laser beam intersects both the target surface and the foci of the pyrometry probes. The circular rings are diffraction from dust on a neutral density filter in front of the beam profiler and are not present in the target beam.

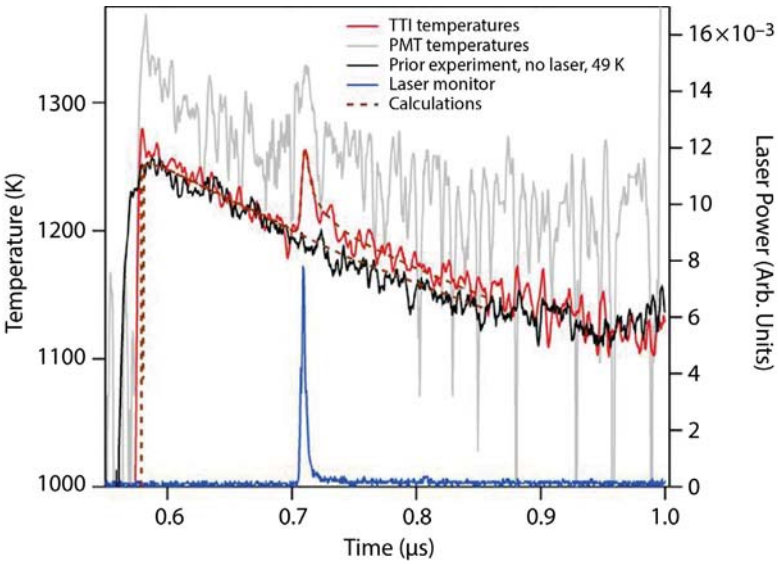

Figure 6. Measured temperatures from the TTI (red) and the PMT (gray) detectors in the pulsed-laser heating measurement on shock-compressed tin. The black curve is a previous temperature measurement without laser heating that was lowered by 49 K to match the breakout temperature in this year's experiment. The dashed brown curves are temperature simulations with and without laser heating, and were fit to the laser heating data by adjusting the thermal effusivity of tin.

absorption calculation. The temperatures recorded by the PMT detector are unrealistically high based on many prior pyrometry experiments on tin and indicate a systematic error; this channel was thus omitted from the effusivity analysis. Also shown in Figure 6 are temperatures from a prior pyrometry experiment without laser heating; the temperatures in that experiment were lowered by 49 K to match the temperatures in this year's experiment.

We used the MATLAB computer code, thermalconduct_isentropic2, to model the 1-D heat conduction at the tin-glue interface during the dynamic experiment. The code was written for this project and accounts for heat conduction, isentropic pressure release (with two linear pressure-time segments), and pulsed-laser heating. Calculated temperature-time profiles with and without laser heating are plotted in Figure 6 together with the experimental data. For the laser-heating experiment, the tin effusivity was varied to find the calculated temperature-time profile that best fits the heat signature from the laser pulse. A 4 ns boxcar smoothing function was applied to the calculated data before fitting to approximate the detector convolution. The best fit resulted in an effusivity value of 17,400 ±4500 $J*m^{-2}K^{-1}s^{-1/2}$. The uncertainty estimate is dominated by the uncertainty in the laser fluence. Although the uncertainty is large, it is a significant improvement in the uncertainty from the FY 2012 campaign, which was 50%. The measured effusivity value is a 70% increase over the ambient value of 10,200 $J*m^{-2}K^{-1}s^{-1/2}$ and likely represents an increase in the thermal conductivity of shocked tin (at 25 GPa stress and 1250 K) by about a factor of 2 over the ambient pressure and temperature thermal conductivity. The effusivity value measured in this year's work is consistent with the measurements we made in FY 2012.

California Institute of Technology (Caltech) Experimental Campaign

We have been working toward performing the laser-heating experiments on a gun platform for two reasons. First, in order to perform experiments on materials of broader interest, such as lithium fluoride or iron, we need to be able to access higher shock pressures. Second, we hope these laser heating techniques will eventually be used at facilities such as JASPER, and transitioning to a gas gun is an important step toward this goal.

We have partnered with scientists Oleg Fatyanov and Paul Asimow, from Caltech's Lindhurst Laboratory for Experimental Geophysics, who operate a two-stage light gas gun and several other guns on the Caltech campus. In FY 2014 a new project, "New methods to quantify thermodynamic and phase properties of shocked materials," will investigate the effusivity

of shock-compressed LiF windows in collaboration with partners at Caltech. The first experiments are scheduled for fall 2014.

References

Ahrens, T. J., K. G. Holland, G. Q. Chen, "Shock temperatures and the melting point of iron," *AIP Conf. Proc.* **429** (1998) 133–136.

Gallagher, K. G., T. J. Ahrens, "Ultra-high pressure thermal-conductivity measurements of griceite and corundum," in *Shock Waves: Vol. 2*, B. Sturtevant, J. E. Shepherd, H. G. Hornung, eds., World Scientific, Singapore, 1996, 1401–1406.

Grover, R., P. A. Urtiew, "Thermal relaxation at interfaces following shock compression," *J. Appl. Phys.* **45**, 1 (1974) 146–152.

Holland, K. G., T. J. Ahrens, "Properties of LiF and Al_2O_3 to 240 GPa for metal shock temperature measurements," *Geophys. Monogr. Series* **101** (1998) 335–343.

La Lone, B. M., G. D. Stevens, W. D. Turley, D. B. Holtkamp, A. J. Iverson, R. S. Hixson, L. R. Veeser, "Release path temperatures of shock-compressed tin from dynamic reflectance and radiance measurements," *J. Appl. Phys.* **114**, 6 (2013a) 063506–063506-14.

La Lone, B. M., W. D. Turley, G. D. Stevens, G. A. Capelle, M. Grover, "Dynamic conductivity of shocked materials," *Site-Directed Research and Development*, FY 2012, National Security Technologies, LLC, Las Vegas, Nevada, 2013b, 21–30.

Mabire, C., P. L. Héreil, "Shock induced polymorphic transition and melting of tin," *AIP Conf. Proc.* **505** (2000) 93–96.

Tan, H., C. Dai, "Problems of shock temperature measurements for metals by using optical radiometry method," *High Pressure Res.* **21** (2001) 183–214.

Ejecta Breakup Dynamics

STL-03-13 | Continued from FY 2012 | Year 1 of 1

Gerald Stevens,[1,a] Brandon La Lone,[a] Gene A. Capelle,[a] Mike Grover,[a] Thomas Tunnell,[b] and Dale Turley[a]

Validation and verification of weapons simulations requires ejecta transport measurements for input and comparison. In addition, refining these transport models will require data concerning the effects of background gas on ejecta production, transport, and evolution. In FY 2012, we studied the effects of reactive gases with ejected material spectroscopically and using holographic techniques. Simulations of high-mach-number particle breakup suggested that such breakup might occur on time scales that are dependent on particle size (i.e., micron particles break up in several nanoseconds). This year, using high-resolution holographic particle imaging velocimetry, we executed dynamic experiments to determine the time scale and properties of particle breakup in a vacuum and in a partial pressure of helium. Results indicate a highly uniform distribution of particle sizes as a function of velocity.

[1] stevengd@nv.doe.gov, 805-681-2219
[a] Special Technologies Laboratory; [b] Los Alamos Operations

Background

Shocked metal surfaces produce a cloud of fine particles commonly referred to as ejecta. Ejecta may originate from surface defects, machine markings, inclusions, metal grain boundaries, and other small-scale (micron to sub-micron) deviations from a smooth plane. In a vacuum, shocked metal initially leaves the surface in the form of fine tips and tendrils that break up into individual particles. In a gas, the individual particles continue to break into finer particles as they travel through the gas at high-mach-number velocities. The initial formation process of ejecta from periodic structures machined into a metal surface is described by Richtmyer–Meshkov instability (Buttler 2012), and has been modeled both analytically and by Eulerian continuum hydrodynamics codes such as Los Alamos National Laboratory's (LANL's) PAGOSA, or with a molecular dynamics code such as LANL's SPaSM (Dimonte 2011). The presence of a gas is an added complication that has pronounced effects on the formation, production, and evolution of ejecta. Gases will slow the ejecta through viscous drag. Additionally, shocked gases reach high temperatures (10^3–10^4 K) and may react with the metal. Analytic models with closed form solutions are available to calculate individual particle drag in gases. However, these models are not easily incorporated into hydrodynamic calculations due to the extremely fine time and mesh-scale requirements for tracking individual particles. LANL scientists have recently reported on a detailed ejecta model that combines an arbitrary Lagrangian-Eulerian code with a multiphase particle in-cell treatment for ejecta transport through gases in their FLAG code (Fung 2013). Our experiments will provide additional information to refine such a model.

Many ejecta models require key assumptions such as spherical particles; low Reynolds numbers; self-similar, collisionless expansion; and the absence of mass-velocity correlations (Oro 2012). These assumptions are necessary because data from radiographic and piezoelectric-pin-based experimental diagnostics measure integrated mass in a manner that is

insensitive to individual particle evolution. However, important transport phenomena are highly dependent on single particle dynamics. Liquid particle breakup has been studied in supersonic gas flows (Theofanous 2004) but not at the pressures and time scales present in a shocked metal experiment. By developing new techniques that look at ejecta on a particle-by-particle basis, we will improve our understanding of ejecta formation, transport, and breakup.

Particle Imaging Velocimetry

Single-pulse holographic techniques have successfully characterized ejecta size distributions from shocked metals (Sorenson 1996). The ejecta particles observed in a hologram have undergone a long (~18 µs in our experiments) history of formation, breakup, and interaction with a background gas. However, single-pulse holography can only provide average particle velocities, which gives limited information about the evolution.

Holographic particle imaging velocimetry (HPIV) is a modified in-line Fraunhofer holographic technique where part of the laser pulse is split off from the main beam, sent through a delay leg, and recombined with the original beam in order to produce a double-exposed hologram. By applying HPIV to ejecta studies, we will improve our understanding of short time scale particle breakup of ejecta caused by viscous and reactive gases. An example of this breakup, as predicted by CTH calculations, is shown in Figure 1, which shows a 3 µm liquid particle traveling at 2 km/s in standard temperature and pressure air at three different times (a), and a solid particle at 10 ns for comparison (b).

Another phenomenon that HPIV should enable us to observe is the process by which small particles become entrained in the shocked gas ahead of the metal free surface. Figure 2 shows the calculated rate of slowing of aluminum particles in air (Lemmon 2004). Small particles simply cannot maintain high speeds relative to a surrounding gas. Looking at particle velocity versus size using HPIV may show evidence of particle entrainment. Direct optical observation of ejecta (by holography, for example) has a limit to the minimum resolvable particle diameter below which particles are not observable. By observing breakup processes at sizes just above the resolution limit, we may begin to model how particles transition and feed into this unresolved and undetected portion of a distribution.

Project

Experimental Design

We chose to characterize ejecta jets produced by a 40 × 140 µm (120° full angle) v-groove on the free surface of a tin sample. We have previously acquired holographic data for samples with these v-grooves. Our experimental package was composed of a polycarbonate sample holder that holds a 2 mm thick × 40 mm

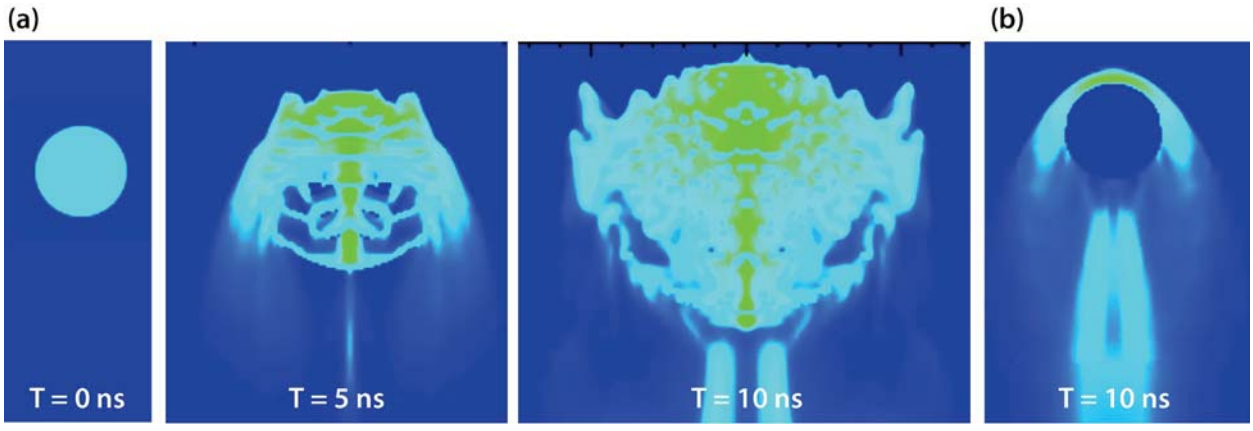

Figure 1. False-color temperature images showing (a) the breakup of a liquid aluminum particle, and (b) the gas bow shock of a similar, but solid, particle at 10 ns

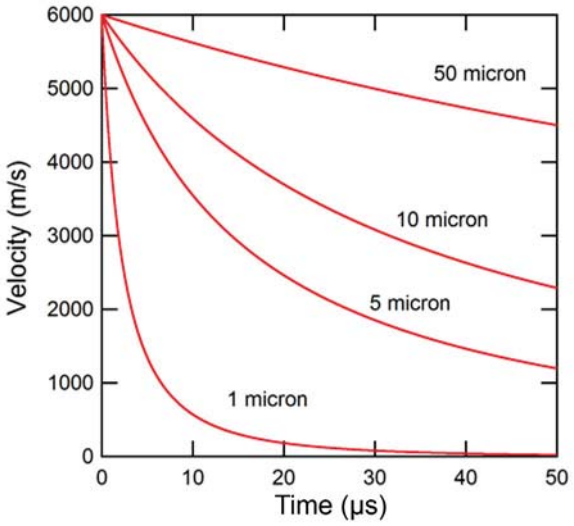

Figure 2. Viscous drag calculation of the velocity of various-diameter aluminum particles in air as a function of time, with an initial velocity of 6000 m/s

diameter tin sample within a larger windowed package that contains a background gas or a vacuum. A half-inch right-cylinder of PBX 9501 high explosive (HE), initiated with an RP-1 detonator (Teledyne RISI, Inc.), is used to drive a shock wave into the tin sample. The free surface velocity of the target is measured, using photonic Doppler velocimetry (PDV), to be around 2 km/s. Peak stress in the shock-compressed tin is about 30 GPa, and is calculated from the free surface velocity using the Rankine-Hugoniot jump conditions.

A jet of ejecta is formed when the shock wave breaks out of the bottom of the v-groove. Figure 3 is a sketch of a typical experimental package.

Results

A total of three experiments were performed with the HPIV system: two in a vacuum, and one in 0.5 atm helium gas. The second vacuum experiment's delayed laser pulse was not properly balanced, and data from that experiment will not be discussed. The first vacuum experiment recorded a double-exposure hologram 18 µs after shock arrival at the free surface, with a delay of 7 ns between exposures. The helium experiment recorded a double-exposure hologram 21 µs after shock arrival at the free surface, with a delay of 8.8 ns between exposures.

The recorded hologram was optically reconstructed using a 355 nm laser and a high-resolution microscope on a computer-controlled positioning stage. A complete dataset for a full holographic plate is typically on the order of 500 GB of data, which is difficult to analyze. We chose to analyze several strips of sub-images along the ejecta trajectories. Because each particle moves between exposures, they appear as particle "pairs" in the reconstructed image. Particle pairs were fit with a 2-D Gaussian shape duplicated at a distance from the first exposure of the particle that best fits the image. This gives the distance the particle has moved

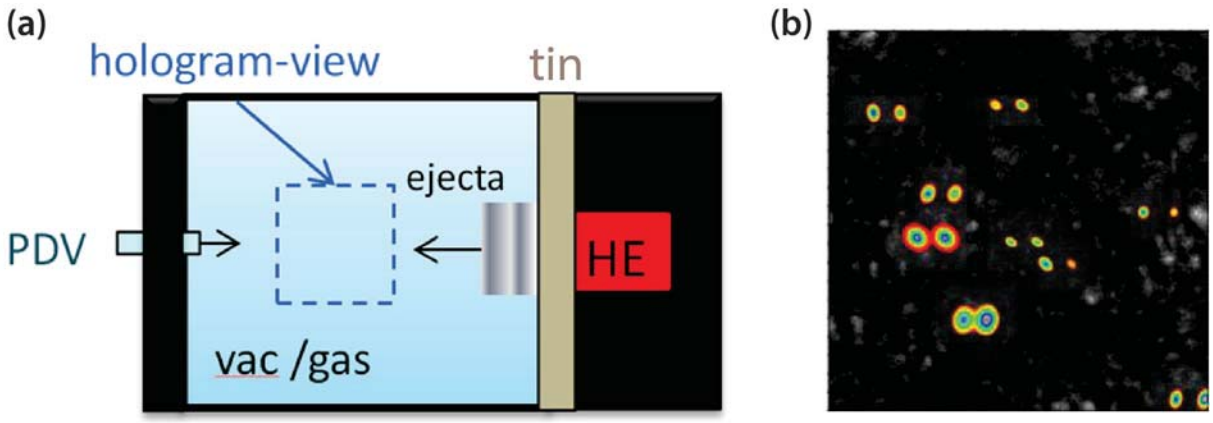

Figure 3. Diagram of an HPIV experiment. (a) Our holographic lens provides a 5x magnification of an approximately 10 mm cubic volume. (b) A 1 mm × 1 mm portion of the reconstructed hologram shows "double-exposed" particles that appear as pairs. A color overlay highlights fitted particle pairs. The separation of the fitted pair is proportional to the instantaneous velocity of that particle.

between exposures. The fitted separation distance divided by the laser delay gives the "instantaneous" particle velocity, V_inst. Additionally, the distance between the particle and the free surface divided by the exposure time (first laser pulse) relative to the shock breakout time gives the average velocity of the particle, V_avg. Figure 4a shows a plot of V_inst versus V_avg for the first vacuum experiment. The blue line labeled "slopeone" is a plot of V_avg = V_inst, which represents the case where particles originate at shock breakout time and move with a fixed, unchanging velocity. Our analysis indicates that the particles we examined have not experienced events (e.g., drag, collisions) that significantly alter their velocity for the 18 μs after shock wave breakout. This suggests a dilute, self-similar expansion, similar to what is assumed in many ejecta models.

Figure 4b shows the calculated particle volume versus V_inst and V_avg. Particle volume is calculated for an ellipsoid with radii given by the Gaussian fit, where the out-of-plane particle radius is chosen to be the average of the two in-plane radii. This plot suggests there is a fairly uniform distribution of particles at all velocities (both V_avg and V_inst) in a vacuum. In a gas, we expect the velocity distribution to narrow in time, eventually peaking at a velocity just ahead of the free surface as the particles slow and become entrained in the gas.

We chose to repeat the vacuum experiment with the addition of 0.5 atm of helium gas. Figure 5 shows velocity and size plots for the helium experiment. The observed distributions were surprisingly similar to those in vacuum, suggesting minimal gas-related effects. While evidence of the effects of gas on the ejecta velocities is hard to discern, the hologram we acquired does show a marked difference from the vacuum experiment. Particle pairs were much harder to identify, possibly due to larger transverse velocity components shifting the second particle out of the focus plane of the first. We developed a custom "focusing" algorithm, using image kurtosis (or peakedness) in order to select the best focused image from the stack of images along the laser path. This algorithm was not needed for particle identification in the vacuum experiment.

A CTH calculation of jet formation and transport was performed to predict the effects of a light gas on the sheet of ejecta from the defect. Figure 6 shows the results for this calculation in vacuum (black and white figures) and helium (temperature color scale figure on the right). The peak velocity of the jet does not slow appreciably in the 3 μs of the calculation (consistent with our experiments), and we just begin to see signs of particle breakup in helium at the front of the ejecta (tiny green "spike" on the upper left of the gas-shock front). In hindsight, we might have expected to find a

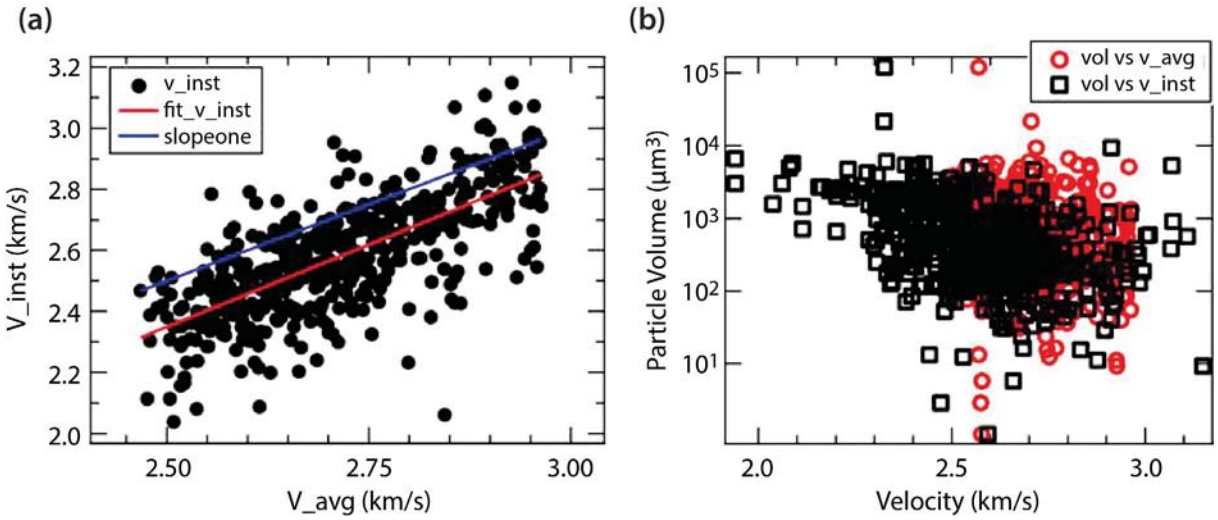

Figure 4. Results from ejecta experiment in vacuum, showing (a) instantaneous velocity (V_inst) versus average velocity (V_avg) and (b) calculated particle volume versus velocity (both V_inst and V_avg)

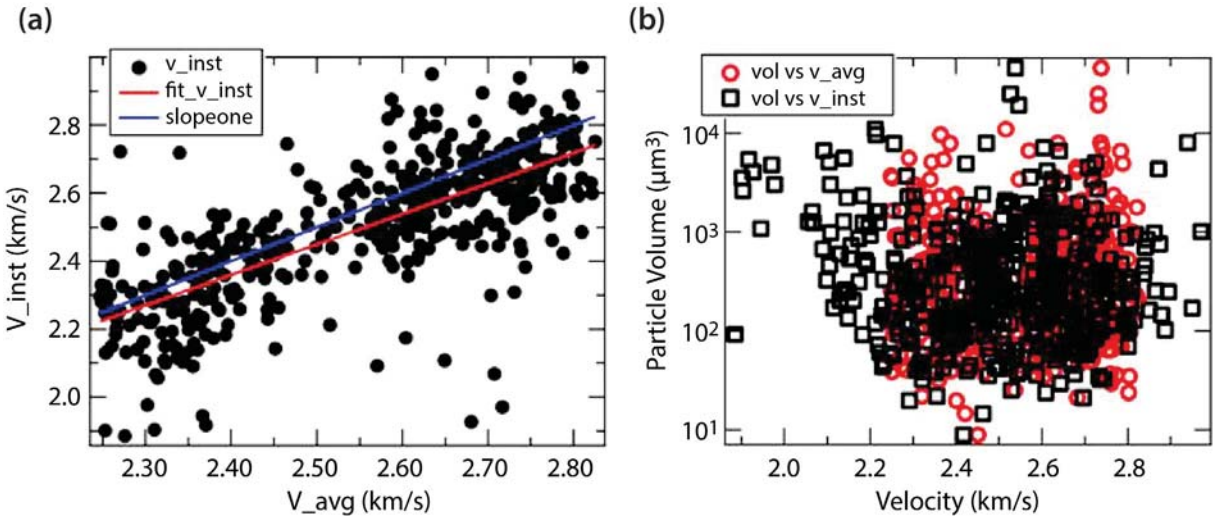

Figure 5. Results from ejecta experiment in helium, showing (a) instantaneous velocity (V_inst) versus average velocity (V_avg) and (b) calculated particle volume versus velocity (both V_inst and V_avg); particle pairs are harder to identify compared to the vacuum experiment

general lack of discernible drag effects on the ejecta size and velocity distributions in our helium experiment. We regularly employ helium in place of a poor vacuum in order to suppress light emission (both thermal and shocked gas). Temperature measurements of ejecta in helium and vacuum using a gated mid-wave IR camera showed only slight (~100 K) heating of the ejecta by the gas. For comparison, 1 atm of nitrogen was enough to heat the ejecta near its boiling point, and caused the in-line holographic technique to fail, resulting in a dark shadowgram. In this study, we did not attempt ejecta experiments in higher helium pressures or for denser gases because in-line Fraunhofer holography is predicted to fail due to phase distortion of the unscattered reference beam by the shocked gas.

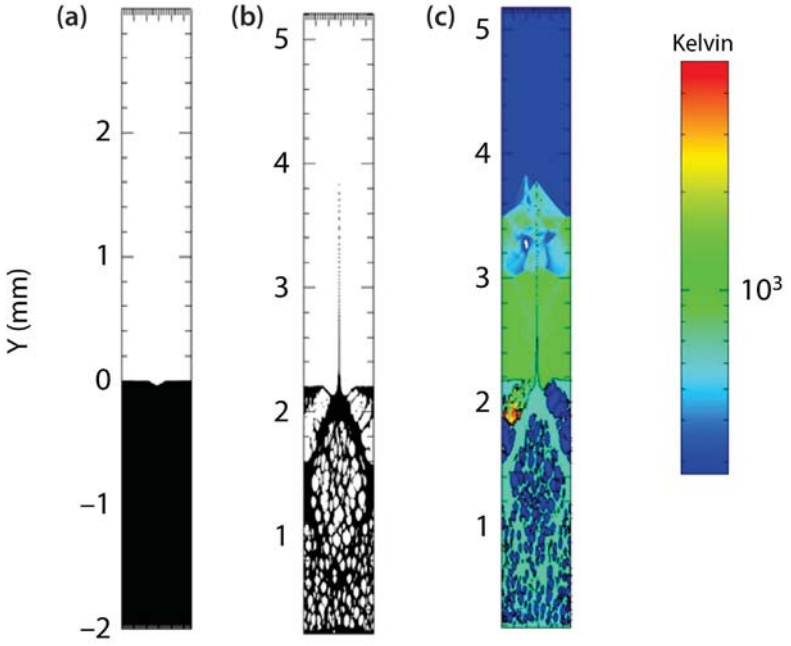

Figure 6. CTH jet model in vacuum (black and white images) and 0.5 atm of helium gas (right, color plot): (a) initial groove defect dimensions, (b) jet after 3 µs, (c) temperature plot of the jet in 0.5 atm of helium gas (also at 3 µs). The color scale is in units of Kelvin.

Other Particle Imaging Velocimetry Techniques Investigated

Despite significant improvements in the alignment and fielding aspects, HPIV is a cumbersome technique to implement. As a side investigation, we looked at using plenoptic imaging with a light-field camera (Raytrix R11) to provide high-resolution, 3-D, high-depth-of-focus data. In order to function optimally, the F/8 numerical aperture of the lenslet array needs to be filled. Using a 180 mm F/2.8 telephoto lens on the R11 and a 35 mm F/1.4 video-lens objective combination gave the maximum magnification (5.1x) achievable while matching the numerical aperture of the Raytrix. This was not enough magnification to resolve the small, several-micron particles we observed in the holographic experiments. Further, reconstructed "total focus" images of tin particles embedded in a transparent target showed very poor image contrast. This limitation may have to do with imaging through a transparent media, and may be ameliorated by future revisions to the camera's reconstruction algorithms.

Conclusion

We have demonstrated an HPIV system that is capable of resolving sub-micron particles with km/s velocities. Results from experiments in vacuum and a partial pressure of helium indicate a surprisingly uniform distribution of particle sizes as a function of velocity—an important finding for ejecta model development.

Acknowledgments

The authors would like to thank Billy Buttler and Danny Sorenson from LANL P-23 for collaborating on this work. Pete Pazuchanics and Robert Malone were also essential contributors to the HPIV experiments.

References

Buttler, W. T., et al., "Unstable Richtmyer–Meshkov growth of solid and liquid metals in vacuum," *J. Fluid Mech.* **703** (2012) 60–84.

Dimonte, G., G. Terrones, F. J. Cherne, T. C. Germann, V. Dupont, K. Kadau, W. T. Buttler, D. M. Oro, C. Morris, D. L. Preston, "Use of the Richtmyer–Meshkov instability to infer yield stress at high-energy densities," *Phys. Rev. Lett.* **107** (2011) 264502.

Fung, J., A. K. Harrison, S. Chitanvis, J. Margulies, "Ejecta source and transport modeling in the FLAG hydrocode," *Computers & Fluids* **83** (2013) 177–186.

Lemmon, E. W., R. T. Jacobsen, "Viscosity and thermal conductivity equations for nitrogen, oxygen, argon, and air," *Int. J. of Thermophys.* **25**, 1 (2004) 21–69.

Oro, D. M., J. E. Hammerberg, W. T. Buttler, F. G. Mariam, C. L. Morris, C. Rousculp, J. B. Stone, "A class of ejecta transport test problems," *Shock Compression of Condensed Matter–2011: AIP Conf. Proc.* **1426** (2012) 1351–1354.

Sorenson, D., R. Malone, B. Frogget, C. Ciarcia, T. Tunnell, R. Flurer, "Particle distribution measurements using in-line Fraunhofer holography," LA-UR-96-3510, Los Alamos National Laboratory, Los Alamos, New Mexico, October 1996.

Theofanous, T. G., G. J. Li, T. N. Dinh, "Aerobreakup in rarefied supersonic gas flows," *Trans. ASME* **126** (2004) 516–527.

Understanding Damage Anomalies in Shocked Metals

STL-05-13 | Continued in FY 2014 | Year 1 of 1

Dale Turley,[1,a] Robert S. Hixson,[b] Brandon La Lone,[a] Gerald Stevens,[a] Lynn Veeser,[a] Ellen Cerreta,[c] Darcie Dennis-Koller,[c] Paulo Rigg,[c] and Rusty Gray[c]

We undertook this study to learn more about spall mechanisms for small, nearly planar explosive-driven shocks, a topic that has not been studied extensively and is of great importance to our mission. When a sample is subjected to a tension wave in a shock experiment, a spall scab or damaged region can separate from the sample and move ahead of and faster than the remaining target material. Combined with early-time velocimetry measurements, post-shot sample recovery and metallurgical analysis are methods to characterize the damage process and sample condition. However, multiple processes during the shock-wave experiment, such as spall and recompression, may obscure the features of the initial damage in the recovered samples. For example, it was previously observed that a sample with a free surface velocity profile indicating complete spall did not show the anticipated spall damage, or even voids, in the recovered sample (Koller 2005). In our study, we discovered that in some cases the unspalled bulk sample can be reaccelerated and overtake the scab fast enough to recompress the sample at the spall plane; this observation may explain the previous anomalous results. An additional goal was to learn how well CTH, the hydrodynamic modeling code that we use extensively, reproduces the recompression process.

[1] turleywd@nv.doe.gov, 805-681-2239
[a] Special Technologies Laboratory; [b] Los Alamos Operations; [c] Los Alamos National Laboratory

Background

Tensile damage formed in materials subjected to dynamic loads remains an important field of study. In particular, the mechanism of recompression of damaged material remains an area of open debate. Tensile stresses can appear in dynamic loading when release waves interact. One important example is when a triangular-shaped pressure pulse, such as from an explosive detonation, encounters a free surface. The release wave reflected from the target free surface propagates back into the already releasing pressure in the triangle wave, immediately creating a state of tension, which increases as the reflection moves farther from the free surface. If large enough, this tension can cause the material to break apart, or spall. Following this process, the same free surface release wave can reflect again, from the interface with the explosive gas products back into the sample, adding another velocity component to that part of the sample. If complete spall separation has occurred, the remaining target material can subsequently impact the spall scab and cause a recompaction shock to be formed (shown in red in Figure 1).

To study the spall failure phenomena, conditions of tension leading to spall are frequently created in the laboratory using shock-wave experiments either with flat-top or triangular-wave profiles. The principal difference between these two kinds of experiments is the amount of time the sample material spends at pressure; this is important because the amount of

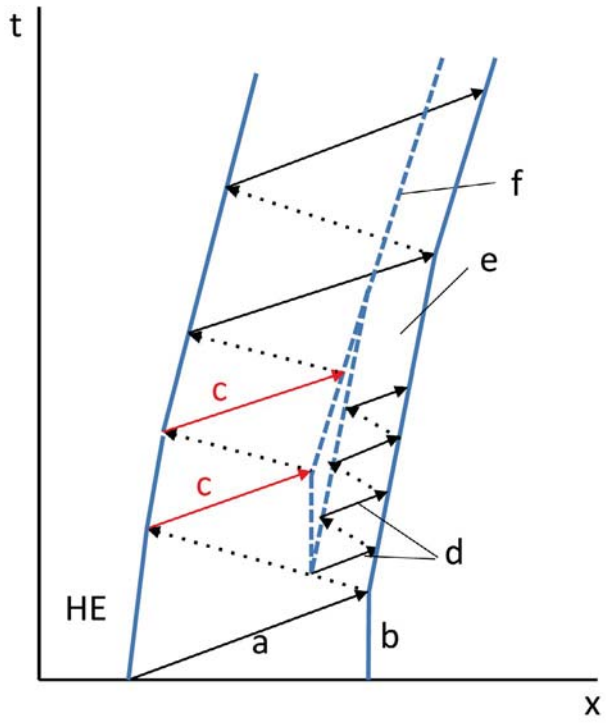

Figure 1. Notional position (x) versus time (t) diagram for metal driven by high explosives (HE), showing (a) detonation wave from HE, (b) free surface, (c) recompaction waves (in red), (d) initial ringing in spall scab, (e) scab, and (f) spall "plane"

work hardening in a metal such as copper depends upon the amount of time available for plastic processes such as dislocation multiplication and glide to occur (Gray 2004). For ductile materials, the principal failure mechanism is ductile void nucleation followed by void growth and possibly coalescence of the voids into a complete spall plane. For brittle materials, there can be some ductile damage, but new mechanisms, including crack nucleation and propagation, are present. The amount of time a material element spends at peak stress has been shown by Gray (2004) to be important, as longer times allow increased substructural development in the form of dislocation storage that leads to work hardening. This is important because work hardening causes the material to be more brittle and can lower the spall strength. In addition, longer duration pulses allow more time for stress concentrations to form, in turn leading to more sites for void nucleation. Conversely, for triangular-wave shapes, very little time is spent at peak stress, so the material remains relatively ductile and can have a higher spall strength (Hixson 2004, Koller 2005). For completeness we note that another difference between typical triangle-wave and flat-top spall experiments is that triangle-wave experiments are typically done using high explosives (HE) drive, in which there can be late-time push from expanding product gases.

The degree of spall and damage formation is also highly dependent upon the peak stress, tensile strain rate, material microstructure, and impurity location. When there is complete spall or a very extensive plane of damage in a sample, an acoustic wave is trapped in the spall scab and it rings, leading to oscillations in the velocity profile of the sample free surface. This ringing period is typically twice the thickness of the spall scab divided by the sound speed. For samples that do not spall or damage extensively, there can be similar ringing, but in this case it is consistent with the full sample thickness. For shock stresses too low to spall completely, sample recovery methods have shown various degrees of void formation, sometimes accompanied by a free surface velocity wave profile similar to that for complete spall. These observations suggest that a free surface velocity measurement is not always a reliable indicator of complete spall separation.

In previous studies (Hixson 2004, Koller 2005) it was reported that copper targets subjected to compressive and tensile loading from gas gun flyer impacts using flat-topped shocks exhibit free surface velocity profiles (VISAR) indicative of spall (ringing of a trapped acoustic wave). Post-shock metallurgical analysis of copper samples for various experimental stresses and release rates reveals a variety of conditions ranging from tiny voids to complete spall, and the damage plane locations are consistent with the ringing periods in the velocity profiles. In these studies, triangular waves were created using a layered flyer concept, and results showed that complete spall is observed at moderate stress, and multiple spall layers were observed in many experiments.

However, when similar experiments were done by driving a triangle wave into copper with the explosive Baratol, results were unexpected (Koller 2006). No

ductile voids were observed in the recovered copper samples in spite of the fact that the measured wave profiles showed a ringing signature indicative of a spall plane. Subsequent experiments (Koller 2006) with a more energetic explosive, PBX 9501, showed multiple spall and damage layers consistent with the velocity profile. It was postulated that different Taylor release rates may provide an explanation for this response, but these have not been accurately measured, and this result is still not well understood. It is worth noting here that the soft-recovery technique exhibits the result of the entire process the sample has been subjected to, from the moment the shock enters it until it is recovered. Recovery techniques are not capable of providing any time resolution of the sample loading and unloading history.

Researchers at Lawrence Livermore National Laboratory (Becker 2007) suggested that the damaged zone could be recompressed during the experiment by compressional waves that arrive after the initial tension is generated. Becker (2007) hypothesized that if a recompression wave follows the tension, the recompression can drive the damaged layers back together, causing the voids to collapse. Becker (2007) also postulated that collapsed voids might not be readily apparent in subsequent metallurgical analysis of the soft-recovered sample. Becker's experiments with gas guns support this hypothesis in spite of the fact that there have been questions raised about the quality of the recovery process. To further test this concept, we have executed a set of explosive experiments in parallel with detailed hydrocode simulations.

Project

We have studied the dynamics of the recompression process in copper using optical velocimetry and pulsed x-ray radiography on planar, or nearly planar, shots driven by HE. Also, in collaboration with Los Alamos National Laboratory (LANL), samples of these dynamic experiments were recovered and analyzed using traditional 2-D metallographic techniques (optical and electron microscopy) as well as 3-D x-ray microtomography.

The copper targets were nominally 40 mm in diameter and 2 mm thick. To help mitigate effects of edge waves for the 25 mm diameter HE drive, the center of the target was a 10 mm diameter disk that was press fit into a ring of copper (40 mm outside diameter, 10 mm inside diameter) with a measured gap no greater than 20 µm. After assembly, the target was polished flat. The outer ring forms a momentum trap for edge releases, allowing planar compression but not radial tension, and thereby minimizing 2-D perturbations in the central sample. All targets were prepared from 99.999% pure oxygen-free high-conductivity (OFHC) copper. The center 10 mm portion was prepared by LANL from a sample annealed under vacuum at 600°C for 1 hour with a resulting average grain size of 40 µm.

The experimental configuration is shown in Figure 2. Samples were shocked using either a six-layer stack of 25 mm diameter × 1.8 mm thick sheets of Detasheet or, for increased shock stress, a disk of PBX 9501 (25 mm in diameter × 8.9 mm thick). The explosive was axially detonated, yielding a slightly divergent shock wave in the sample. Both photonic Doppler velocimetry (PDV) and VISAR velocimetry techniques were used to measure the free surface velocity profile of the samples—the VISAR to obtain high-resolution velocimetry around shock breakout and spall, and the PDV for late-time data, up to 20 µs. A single-pulse flash x-ray system provided a radiographic image of the target 100 µs after detonation to verify shape and trajectory of the 10 mm center of the target, which flew free of the surrounding copper ring and subsequently entered the soft recovery chamber. Samples were stopped in a layered stack of water-saturated felt. The water helped cool the sample to keep residual shock temperature rise from self-annealing microstructural features due to the shock processing of the material.

As a control we also executed a Detasheet experiment with a solid 40 mm diameter copper sample. The sample stretched radially, and the x-ray showed extensive curvature at late times. We did not recover the sample for metallography because it was assumed that the results would not be of sufficient interest to justify the analysis efforts. We also repeated the Detasheet

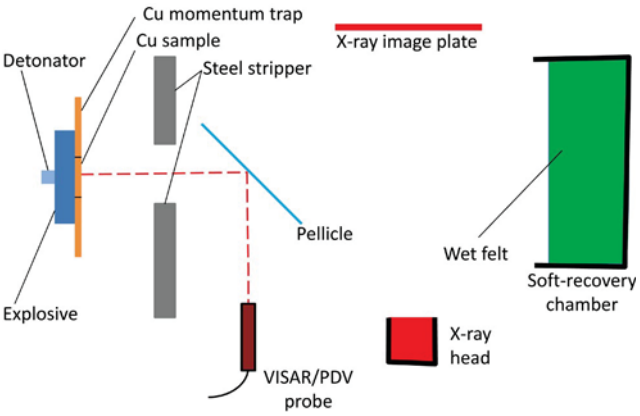

Figure 2. Schematic diagram of the experimental setup. For the early shots we did not have the steel stripper between the sample and pellicle.

momentum-trap shot with a stripper to keep the momentum ring away from the soft-recovery can. Our momentum-trapping scheme is yielding samples that still show signs of late-time perturbations or 2-D effects, so we are working to improve this part of the experiments. Subsequent metallographic characterization of the damage in the recovered samples included optical microscopy as well as electron backscatter diffraction (EBSD) and transmission electron microscopy as previously described, all done at LANL.

Figure 3 shows x-ray images from two experiments. Figure 3a shows the result without a stripper. Although the momentum-trapping scheme nicely separates the sample center, considerable debris is flying behind and can cause sample damage during soft recovery. Figure 3b, taken with the stripper in place, shows a much better result, with only an intact sample in the field of view. The other target debris is trapped behind the stripper and does not interfere with the recovery process. Nevertheless the soft-recovery technique still has issues. Figure 3c shows an x-ray of the sample from Figure 3b after recovery. It was held in the same position as seen in the x-ray in Figure 3b. After recovery, the sample shape has changed slightly; furthermore, not seen in the x-ray are what appear to be imprints of the felt on its surface. We are working to improve our soft-recovery methods.

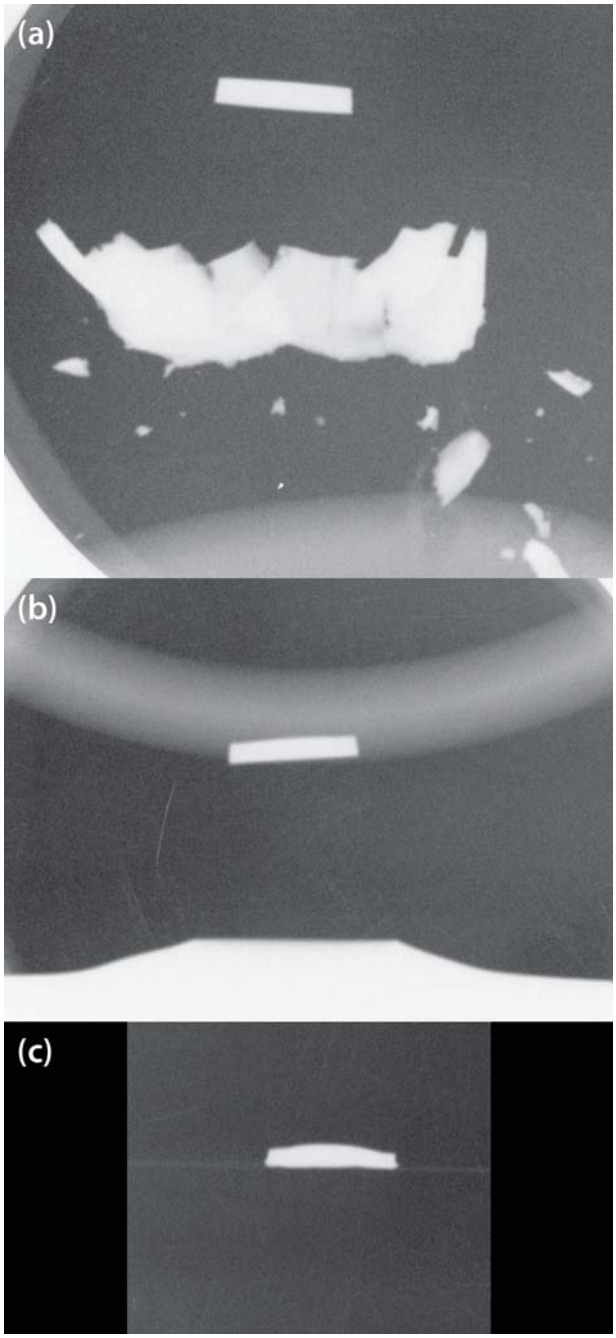

Figure 3. X-ray images from (a) an experiment that did not use a stripper and (b) an experiment using a stripper to remove the debris, passing only the sample center through the stripper hole. (c) Static x-ray of the same sample as in (b) but after recovery; the sample shape was changed slightly between the dynamic x-ray and the recovery.

Low-Stress Velocity Measurements

Figure 4 shows free surface velocity profiles collected from a target shocked by a detonation wave from a stack of Detasheet layers. Figure 4a is the velocity record extended out to nearly 18 µs after first motion. The wave profile shows the characteristic release associated with a Taylor wave drive, followed by pullback and spall ringing that damps out to leave a nearly constant velocity until a recompression wave arrives at 6.2 µs. Figure 4b shows the early-time pullback and the ringing associated with the reverberation of the wave in the spall layer, which is, of course, thinner than the shock-compressed full sample thickness. The peak velocity of 1020 m/s can be used to calculate a peak stress of 21 GPa. The 165 m/s free surface velocity decrease between the peak velocity and the first minimum implies a spall strength of 3.18 GPa, which is much larger than copper spall stresses of about 1.3 GPa measured in flyer plate experiments using flat-topped shocks (for example, see Hixson [2004] and Escobedo [2011]). This result is consistent with shock dwell time effects discussed in Gray (2004). It is much closer to the 2.68 GPa result for Baratol (Koller 2006). The 175 ns ring time indicates a spall thickness of 420 µm. These results and results for the other experiments, including the one driven by PBX 9501, are summarized in Table 1.

A key point here is that the period of ringing observed in the velocimetry records increases to be consistent with the full thickness of the sample after the recompression wave is observed. This is very compelling evidence for the "merging" together of the spall scab and the still-accelerating remains of the sample, which sees a late-time push from the HE products.

Figure 5 shows the same data compared with CTH calculations. We are able to calculate the velocity between spall and recompaction as well as the recompaction time fairly well, but the spall-strength parameter in the code is much smaller than we measure (see Table 1). Alternatively, with a larger spall-strength parameter, we can match the spall but not the velocity before recompaction (not shown).

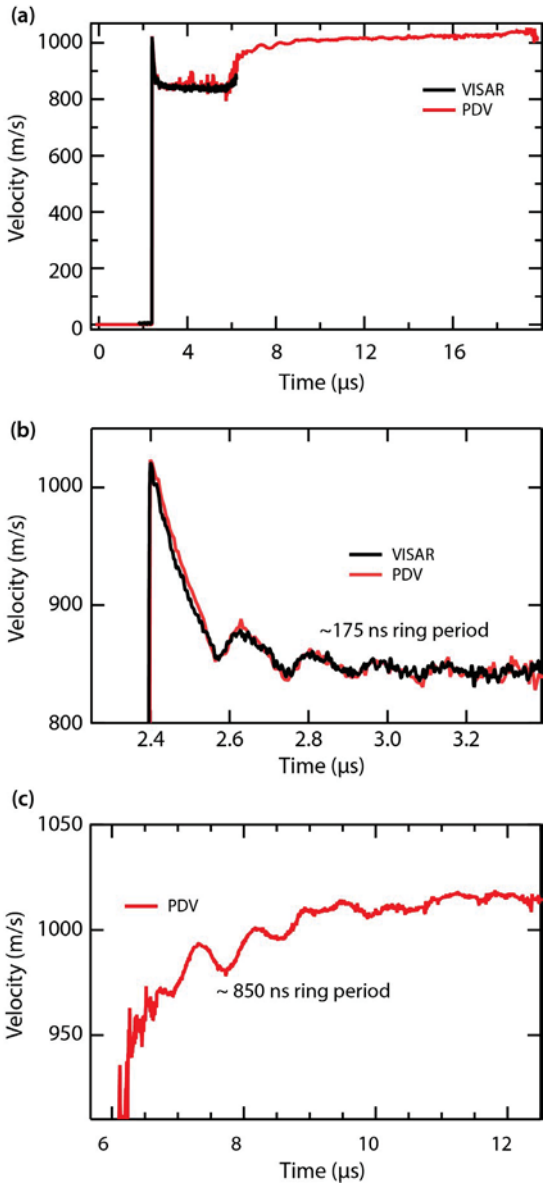

Figure 4. Free surface velocity profiles of a copper sample shocked by Detasheet explosive, with (b) and (c) showing the information on expanded time scales. We used both VISAR and PDV diagnostics to obtain early-time high fidelity (<1 µs) as well as long time (>10 µs) velocity records. (a) The shock breaks out of the sample at 2.4 µs. At 6.2 µs, the arrival of a second wave suggests the bulk target material was accelerated after the initial damage and is catching up to the spall layer. (b) The velocity record starts with the classic spall signature of release (2.4 µs), pullback (2.4–2.6 µs), and short interval ringing (2.6–3.3 µs). (c) At 6.2 µs there is an abrupt velocity increase accompanied by an increase in the ringing interval. This new period matches the roundtrip time of a sound wave in the compressed full sample, suggesting sufficient healing of the damaged sample to allow sound waves to pass through the damaged region. Hydrodynamic modeling of these experiments also suggests void collapse and recompression of the damaged sample.

Table 1. Experimental velocimetry results and estimated peak stress, spall strength, and thickness

Experiment	Δu_{fs} (m/s)	Release Rate (m/s^{-2})	Spall Strength (GPa)	Peak Stress (GPa)	Estimated Spall Thickness (mm)	Time Spacing in 1st Spall Ring (ns)
Control (Shot 130109)	172	1.04×10^9	3.32	22	0.39	164
Detasheet (Shot 130306)	165	9.89×10^8	3.18	21	0.42	175
Detasheet + stripper (Shot 130813)	145	9.73×10^8	2.79	23	0.36	149
Baratol (Koller 2006)	139	6.95×10^8	2.68	22	1.04	439
PBX 9501 (Shot 130313)	161	1.04×10^9	3.10	33	0.35	145
PBX 9501 (Koller 2006)	158	--	3.05	36	0.38	--

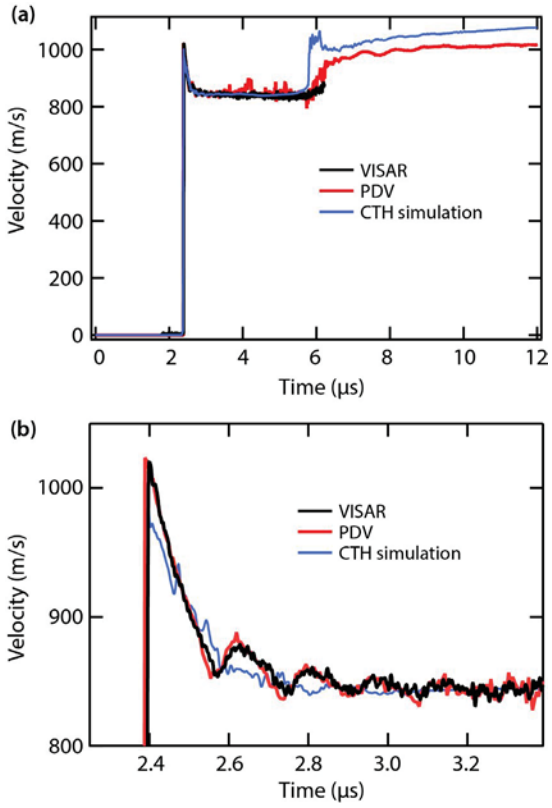

Figure 5. (a) Measurements compared with hydrocode (CTH) simulation results for the Detasheet-driven shock in copper shown in Figure 4, with (b) details of the early time history. The simulation uses an elastic-plastic, fracture formulism (called PMFRAC in CTH) that spreads the spall fracture over several time steps in the calculation to simulate ductility. The spall signature, the first minimum, occurs at 2.55 μs. Then the shock rings in the scab, as shown by the dips at 2.55, 2.75, and 2.9 μs. Even after spall, the free surface continues to slow until about 3.0 μs. The spall strength used in the CTH model is too small to calculate the first spall minimum correctly. Increasing the spall strength to get the proper time and velocity for the spall and subsequent ringing causes the velocity to continue to decrease for too long, making the calculated velocity plateau between the end of damage too slow and, consequently, the recompaction wave to arrive too early.

It is worth noting here that a recent look at the results of the LANL Baratol-based experiments shows a recompression wave very similar to that observed in our Detasheet experiments. Figure 6 shows data from that experiment as reanalyzed recently (Rigg 2013). The same wave structures were observed when the experiments were done. The late-time (~17 μs) increase in particle velocity was ignored at that time, believed to be caused by late-time edge release.

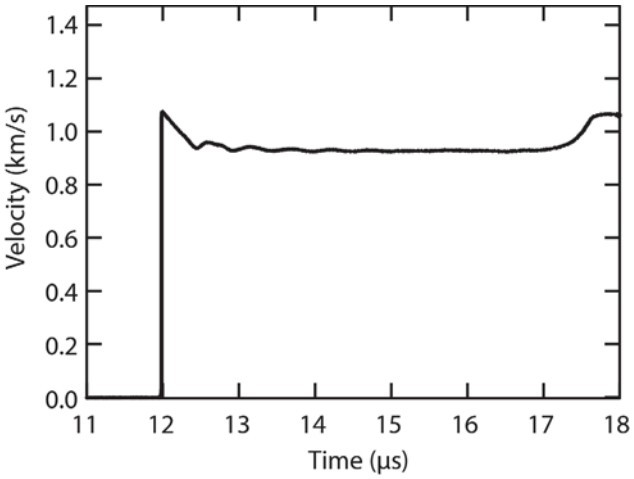

Figure 6. Data from P022 (Baratol) lens on OFHC copper, LANL shot 8-972

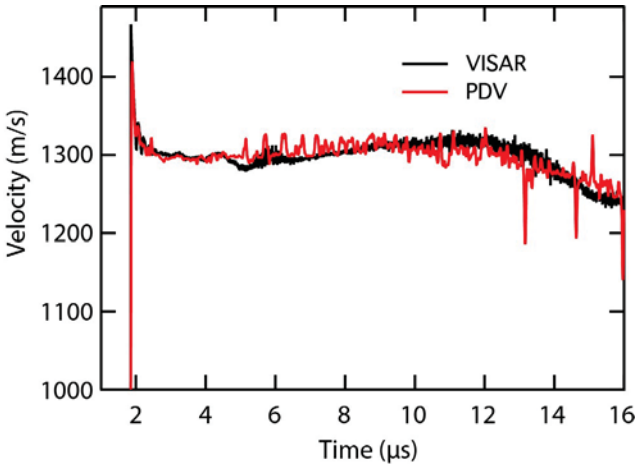

Figure 7. Measured free surface velocity for a PBX 9501–driven shock in copper. No recompaction is evident.

Higher-Stress Velocity Measurements

Our experiment driven with PBX 9501 shows little or no evidence in the time-resolved data of a recompaction event, and so differs in this respect from the experiments done with Detasheet. CTH simulations show only a small recompaction wave, but we have not been able to get a satisfactory CTH calculation reproducing the peak stress, spall, or lack of a significant recompaction wave. Figure 7 shows the measurements.

Metallography

Post-loading metallurgical analysis of shock-loaded samples has proven to be a powerful tool in understanding the details of the material response to such loading. This provides a valuable complement to the time-resolved data obtained from VISAR or PDV. These analyses were done on all experiments except the control shot.

Reanalysis of LANL Baratol/Copper Experiment

Post-shot metallurgical analysis was done on the P022 (Baratol) experiment done at LANL in 2003. At the time (2003), no evidence for ductile void nucleation, growth, or coalescence onto a spall plane was observed. What was found in the photomicrographs was a feature at the correct location in the sample (as compared to thickness of the spall scab from the VISAR data) that was interpreted to be shear localization. This is shown in Figure 8.

The black bands in Figure 8 were imaged at higher magnification. The details of the structure of these bands are shown in Figure 9. The bands primarily comprise individual crystallites that are difficult to index at lower magnifications and therefore appear black in Figure 8. In Figure 9, it is clear that there are no obvious voids or cracks present within these bands. Figure 10 is a transmission electron microscopy (TEM) image within the band region. The actual size and substructure of these crystallites are revealed. This substructure is consistent with significant plasticity occurring in this region as well as initial stages of recrystallization.

There are at least two possible explanations for the structures observed in these images. First among these is that significant plastic flow, driven by substantial shear stress, caused this localized heating. The second is that the sample did spall to at least some degree (enough to explain the VISAR data), and then the back of the target impacted the spall scab later, causing a recompaction of the damaged region. These data alone are not able to distinguish between these possibilities. However, further evidence that might support

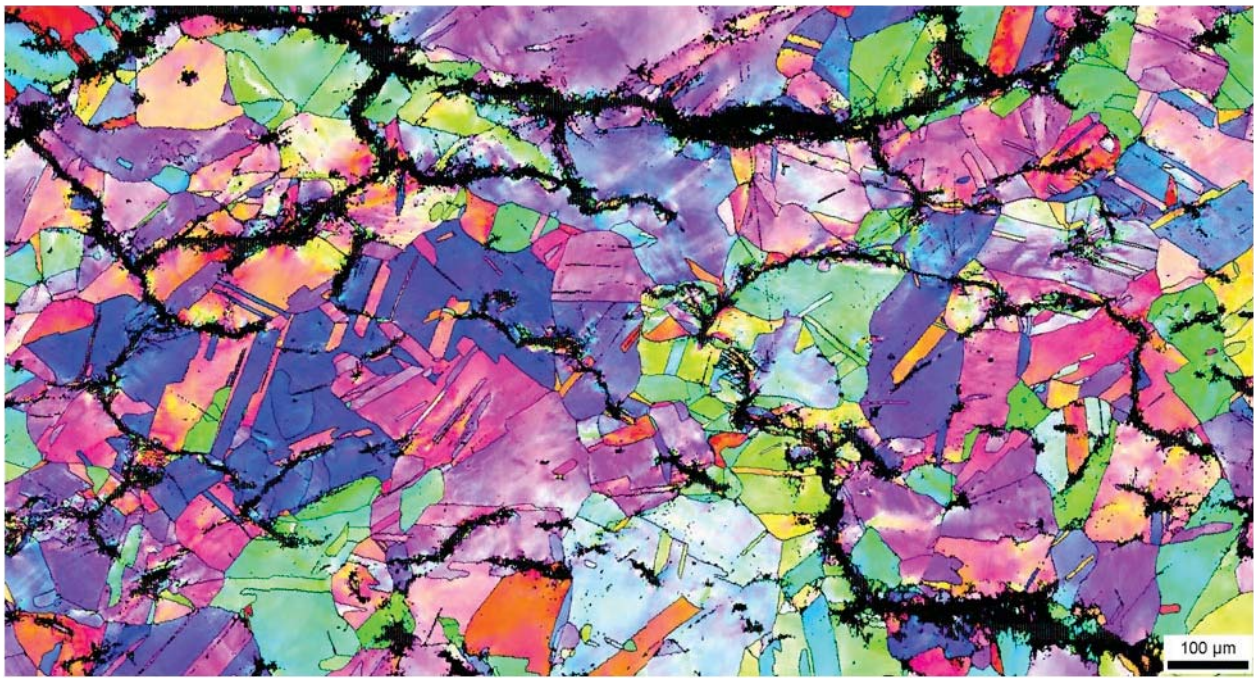

Figure 8. Images from the P022/copper experiment fired in 2003. Note the black bands, which indicate voids, running across the image, even through individual grains. Different colors indicate different grain orientations.

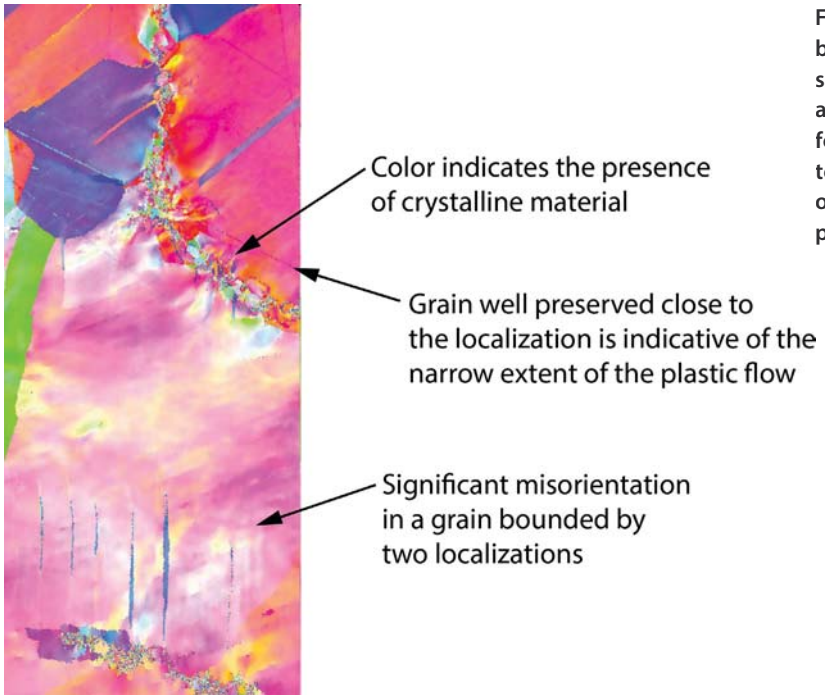

Figure 9. Evidence for recrystallization in the black band regions as shown in Figure 8. This shows direct evidence for adiabatic heating in a region of localized plastic flow that was then followed by recrystallization. It is important to note that the postmortem nature of this observation provides no evidence for when processes occurred.

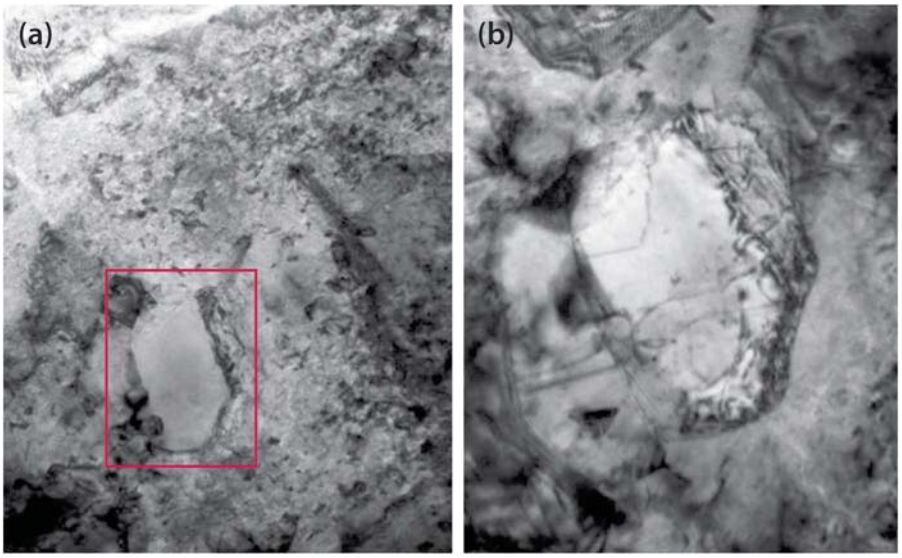

Figure 10. (a) TEM image and (b) close-up area in box in (a) of a recrystallized grain within the heavily deformed banded region in the copper target subjected to HE loading with a Baratol plane wave lens

the possibility of a localized temperature increase is seen in a detailed look at the substructure, shown in Figure 10b. This image shows a recrystallized grain, indicating that it has been subjected to a relatively high temperature excursion, as would happen if voids were shock compressed, or there was significant localized plastic deformation.

Detasheet/Copper

This work involved post-shot metallurgical analysis of the sample recovered from the center-initiated Detasheet explosive shot without a stripper, described earlier, as contrasted to the Baratol experiment, which used a plane wave lens. Microstructural analysis was done at LANL. Figure 11 shows both optical imaging and EBSD results. We note that these results are similar to those for the Baratol/copper experiment. But there is more evidence for recrystallization, and some voids are still present, which appear as fine regions shown in black in these images. This supports the idea that there was at least some ductile void nucleation and growth in this experiment.

PBX 9501/Copper

This experiment used a very high performance explosive with a CJ pressure that was significantly higher than either the Detasheet or Baratol experiments discussed above. Both the time-resolved data and the post-experiment metallurgical analysis indicate that considerable ductile damage was created in the loading/unloading history for this sample. Figure 12 is a cross-sectional view of this sample showing that considerable damage is still present. In addition, the CTH simulations show that there is a late-time, very gentle recompaction event, with a very small recompaction stress as compared with the Detasheet and Baratol experiments. A possible reason we do not see a clearly separated spall plane(s) in this experiment is that the pieces were pushed back together in the recompaction process, although this could also have happened during the recovery process. To better understand this, we really need to refine our recovery process.

Higher magnification images (Figure 13) show more detail on the existence of voids.

Conclusion

A clear hypothesis is emerging from this research, especially when combined with previous results from the community. The hypothesis is that in all of these experiments, considerable damage was done in the target immediately following the reflection of the triangular-shaped shock wave at the copper sample free surface. It would be very surprising if damage were not created in this wave reflection process given

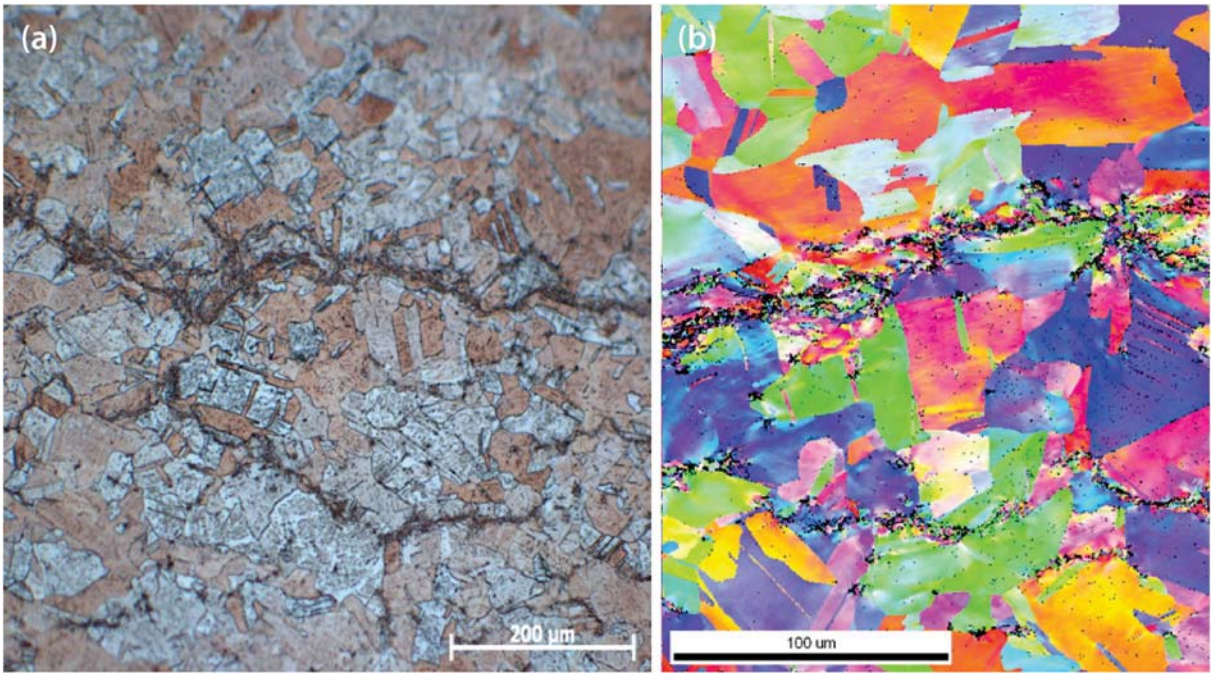

Figure 11. (a) Optical imaging and (b) EBSD microscopy results for Detasheet/copper experiment. This experiment is an important complement to the previous Baratol-based experiment, and pushed us even further in the direction of exploring the recompaction hypothesis.

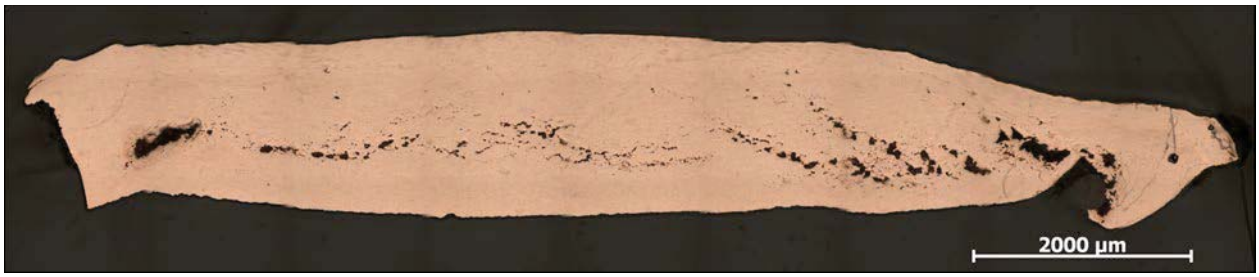

Figure 12. Cross section of the PBX 9501/copper sample showing clear evidence of damage. The feature at the right end is not seen in the radiograph and therefore was likely caused during the recovery process.

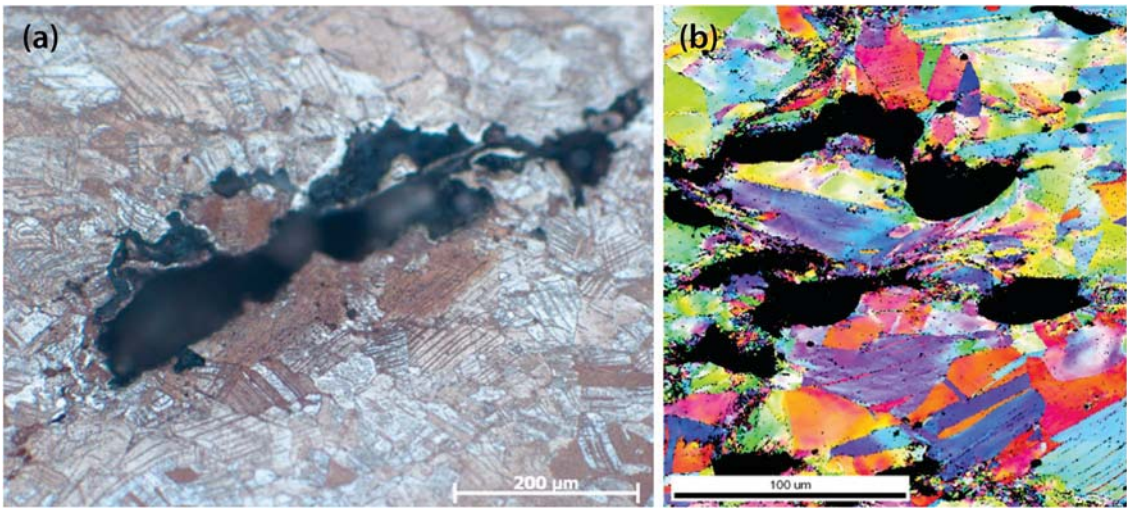

Figure 13. (a) Optical imaging and (b) EBSD microscopy images of damage in the PBX 9501/copper experiment

the peak stresses involved (~200–400 kbar) and the relatively low spall strength of annealed OFHC copper (14–35 kbar). This damage zone is then recompressed a short (few microseconds) time later because the spall scab is moving at a constant velocity, but the remaining target material is being accelerated by the HE product gases. This recompaction event causes the sample and scab to be compressed back together, which in turn generates heat and localized recrystallization in the damaged regions. For the highest performance HE used (PBX 9501, with a CJ pressure of ~375 kbar) the recompaction event was very minor and did not completely "weld" the sample and scab back together. For completeness, we note here that we have only observed this process in planar or nearly planar HE-driven experimental geometries. For more complex geometries, such as sweeping waves, this process remains to be explored.

This is a compelling story but is only a hypothesis. Therefore, we will continue this line of research in FY 2014 with a new 1-year SDRD project (Dynamic Recompression of Damaged Materials, STL-04-14) that emphasizes adjustment of the arrival time, rise time, and amplitude of the recompression wave. Our goal is to determine the recompression conditions required and physical mechanisms for void collapse, if present. We also intend to continue the hydrodynamic modeling of this system, as the model results are not in complete agreement with our measured results. As well, we will use several PDV probes to improve our alignment with the detonation axis. All samples will be recovered and sent to our LANL colleagues for analysis, and we will continue to improve our recovery process.

References

Becker, R., M. M. LeBlanc, J. U. Cazamias, "Characterization of recompressed spall in copper gas gun targets," *J. Appl. Phys.* **102**, 9 (2007) 093512.

Escobedo, J. P., D. Dennis-Koller, E. K. Cerreta, C. A. Bronkhorst, "Effects of grain size and boundary structure on the dynamic tensile response of copper," *J. Appl. Phys.* **110**, 3 (2011) 033513.

Gray, G. T., N. K. Bourne, B. L. Hendrie, J. C. F. Millett, "Influence of shock-wave profile shape (triangular - "Taylor-wave" versus square-topped) on the spallation response of 316L stainless steel," *J. Phys. IV* **110** (2003) 773–778.

Gray, G. T., N. K. Bourne, J. C. F. Millett, M. F. Lopez, "Influence of shock-wave profile shape ("Taylor-wave" versus square-topped) on the shock-hardening and spallation response of 316L stainless steel," *AIP Conf. Proc.* **706** (2004) 461–464.

Hixson, R., G. T. Gray, P. A. Rigg, L. B. Addessio, C. A. Yablinsky, "Dynamic damage investigations using triangular waves," *AIP Conf. Proc.* **706** (2004) 469–472.

Koller, D. D., R. S. Hixson, G. T. Gray III, P. A. Rigg, L. B. Addessio, E. K. Cerreta, J. D. Maestas, C. A. Yablinsky, "Influence of shock-wave profile shape on dynamically induced damage in high-purity copper," *J. Appl. Phys.* **98**, 10 (2005) 103518.

Koller, D. D., R. S. Hixson, G. T. Gray III, P. A. Rigg, L. B. Addessio, E. K. Cerreta, J. D. Maestas, C. A. Yablinsky, "Explosively driven shock induced damage in OFHC copper," *AIP Conf. Proc.* **845** (2006) 599.

Rigg, P. A., private communication, 2013.

This page left blank intentionally

Instruments, Detectors, and Sensors

Instruments, Detectors, and Sensors

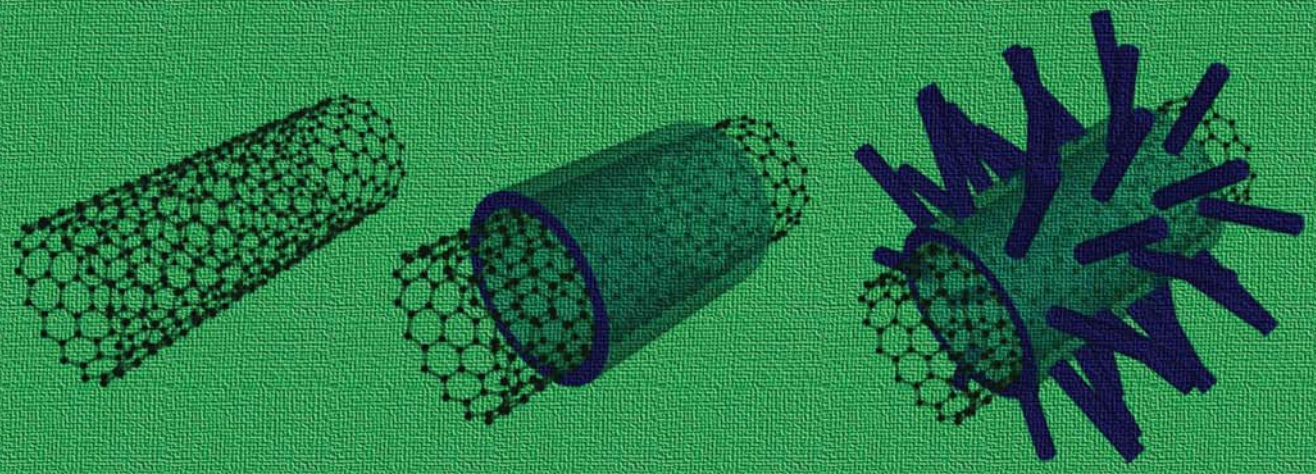

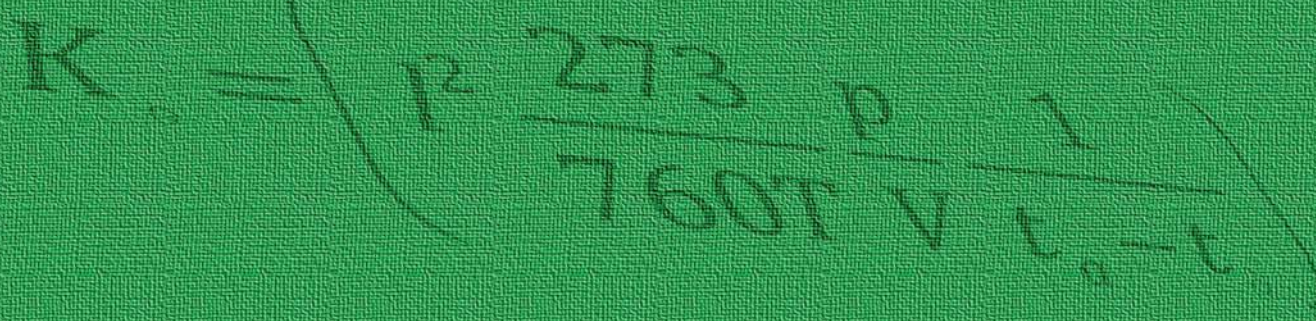

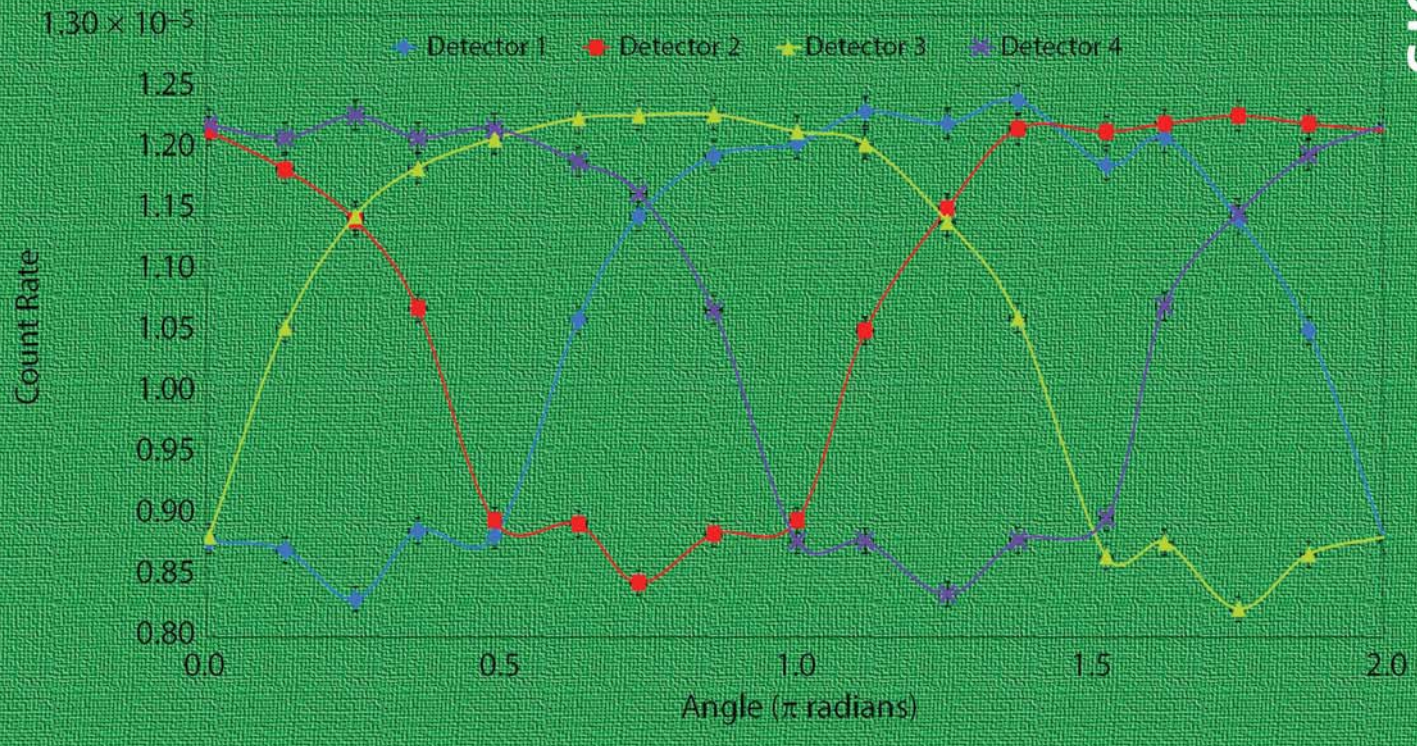

Plastic Deformation Study Using a Light Gas Gun

NLV-33-13 | Continued in FY 2014 | Year 1 of 2

Steven Becker,[1,a] Robert S. Hixson,[a] Michael Peña,[a] Edward Daykin,[a] Eric Machorro,[a] Carlos Perez,[a] Tim Meehan,[a] Nathan Sipe,[a] Kristen Crawford,[a] Steven Gardner,[a] Mohamed Trabia,[b] Brendan O'Toole,[b] Shawoon Roy,[b] Deepak Somasundaram,[b] Jagadeep Thota,[b] Richard Jennings,[b] and Melissa Matthes[b]

The goal of this research was to explore the plastic deformation behavior of metallic plates using a two-stage light gas gun at the University of Nevada, Las Vegas. Developing computational codes for predicting this kind of behavior accurately at such high impact was also an important goal of this project. The experiments shot cylindrical Lexan projectiles at steel plates, with velocities ranging from 4.5 to 5.7 km/s, by pressurizing the gun with hydrogen or helium gases. Single-point or multiplexed photonic Doppler velocimetry diagnostic systems were used to measure the velocities of selected points on the back surface during impact. These results were corroborated using a high-speed imaging system. Additionally, physical measurements were taken of the impact crater and back surface bulge of the target plates after sectioning. Recommendations for accurately simulating these experiments using LS-DYNA smoothed-particle hydrodynamics code and CTH hydrocode are presented. The results of these simulations are in generally good agreement with experimental results.

[1] beckersa@nv.doe.gov, 702-295-0612
[a] North Las Vegas; [b] University of Nevada, Las Vegas

Background

One of the most common techniques to study high-velocity impact is the two-stage light gas gun (Chhabildas 2005), which has been used extensively in aeroballistics and impact dynamics (Doolan 2001). Historical development of this type of gun has been presented by Swift (2005). The shock wave pressure resulting from the projectile-target impact at such high velocity is similar to the pressures created by explosions, detonations of nuclear weapons, or large meteorite collisions with the earth's surface (Holmes 2000).

Deformation of metallic plates under high-velocity impacts has been studied for decades (Goldsmith 1965, Børvik 2004, Rosenberg 2012) but without using multichannel time-resolved velocimetry diagnostic tools. Under high-velocity impact conditions, thin plates tend to stretch and bend around the impact area, absorbing a significant part of the projectile's kinetic energy though these deformations happen before perforation occurs. On the other hand, thick plates experience several failure modes during perforation, such as spalling, petalling, discing, and plugging (Rosenberg 2012). These failure modes depend on several factors—the impact velocity, the properties of the plate material, and the loading geometry, to name a few. Børvik (2004) studied ballistic penetration of aluminum plates of varying thicknesses using a compressed gas gun. In all tests, residual and initial velocities of the projectiles were measured to find the ballistic limit for varying thickness targets. All the data were compared to analytical models. Goldsmith (1965) also studied the perforation of aluminum plates with a hard steel cylindrical-nose projectile. Elastic-plastic

plate deformation and perforation were described analytically. Merzhievskii and Titov (1975) studied thin plate perforation and deformation of steel plates at a velocity range of 3–9 km/s and described an analytical method to relate debris particles to impact velocity.

Because impact studies of the plate perforation are conducted with expensive experimental devices and equipment, computational modeling and numerical simulation have become an acceptable way to investigate materials behaviors, with the goal of having a predictive capability for these kinds of impact events. Numerical solutions and computational modeling of plate perforation problems have been described by several researchers. Børvik (1999, 2001) used a constitutive material model of viscoplasticity with ductile damage in LS-DYNA to computationally simulate the perforation phenomena. Chen (2003, 2008, 2009) extensively studied plate perforation with different projectile nose shapes, providing analytical and computational models to compare results. Ductile spall fracture and post-spall behavior of a circular plate was simulated using the PRONTO finite element code (Eftis 1992). Impact dynamics is a complex phenomenon, and a solution of computational model depends on selection of the proper physics models and input parameters (Zukas 1990). A high-speed projectile impact on a target generates an enormous amount of pressure and heat, resulting in a large deformation of both objects (Rolsten 1965). Recently, several computational packages based on hydrocode methods have been used for penetration modeling. Also, the Lagrangian-based smoothed-particle hydrodynamics (SPH) method is gaining popularity to simulate impact penetration problems (Shah 2008, Swaddiwudhipong 2010, O'Daniel 2011, Kalameh 2012).

Several researchers have conducted experimental and computational investigations of long-rod penetrators into metallic and composite targets (Bond 1976; Anderson 1995a, 1995b, 1996; Cullis 1995; Hayhurst 1995; Rosenberg 1996, 1998; Littlefield 1997; Espinosa 1998; Normandia 1999; Walker 1999; Forrestal 2000; Westerling 2001; Yadav 2001). Metallic materials used in these studies included 4340 alloy steel and rolled homogeneous armor steel, tungsten, and aluminum. Some of the work focused on modeling the behavior of ceramic tiles under hyper-velocity impact, but they also included useful experimental data and computational material model properties for the metallic materials. Most of the work relied on post-test evaluation of the targets to determine the extent of plastic deformation. A few studies discuss the plastic deformation of metallic plates instead of complete penetration. Plastic deformation of metallic plates depends on impact velocity. Beynet and Plunkett (1971) studied the plastic deformation in thin aluminum plate impact experiments at a velocity range of 25.4–254 m/s. Moire fringes were recorded using a streak camera in transverse direction to study displacements and stress patterns; plastic deformation in impact direction was not considered.

This project was initiated because research is still needed to study plastic behavior of materials in high-velocity impact and to develop computational models that can accurately predict this phenomenon. In the current research, cylindrical Lexan projectiles are shot into A36 steel target plates at a velocity ranging between 4.5 and 5.7 km/s. Under these conditions, the projectile partially penetrates the target plates and creates a small bulge on the back of the target. CTH hydrocode and LS-DYNA SPH solver were used to simulate this behavior.

Project

Two-Stage Light Gas Gun Facility at the University of Nevada, Las Vegas (UNLV)

The gun at UNLV (Figure 1) was manufactured by Physics Applications, Inc. Major components of this gun are the propellant breech, pump tube, central breech, launch tube, blast tank, and target chamber. The cartridge filled with gunpowder is fired with a solenoid pin. Gunpowder (IMR 4064) in the powder breech then burns, which drives a cylindrical piston (20 mm diameter and 120 mm length) in the pump tube. Hydrogen or helium gas is used as a propellant in the pump tube. So the moving piston pressurizes the propellant gas, which eventually bursts the petal valve.

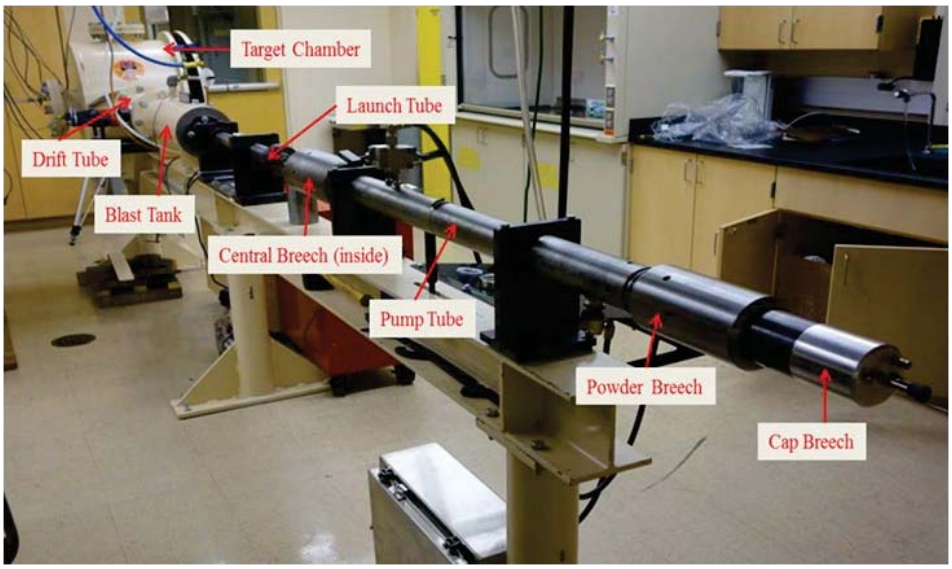

Figure 1. Major components of the gun at UNLV

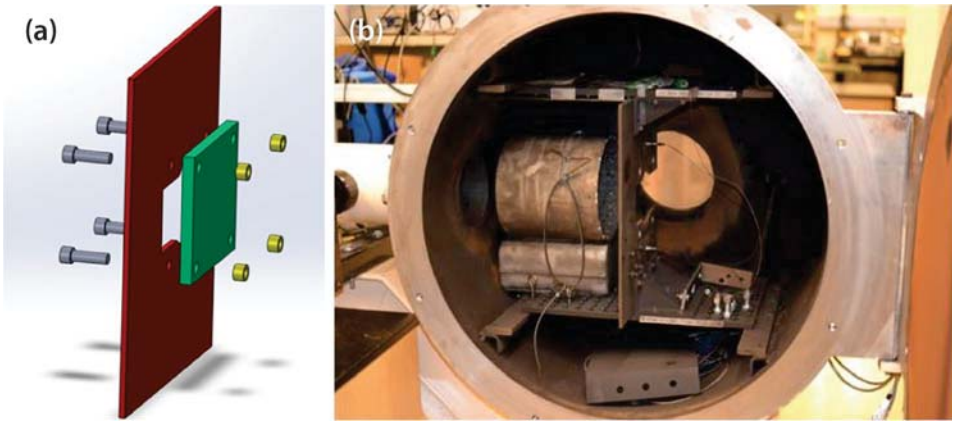

Figure 2. Target setup, showing (a) the target mounting plate and (b) the target chamber assembly

High pressurized gas then accelerates the projectile in a launch tube through the blast tank and drift tube until it impacts the target in the target chamber.

Materials

Cylindrical Lexan projectiles with a diameter of 5.6 mm and a height of 8.6 mm are used in all our gun experiments. ASTM A36 steel plates are used as targets, as the material is readily available, and material characteristics under the testing conditions are well documented. Target plates are cut into a dimension of 152.4 × 152.4 × 12.7 mm. All targets are bolted on a mounting plate inside the target chamber assembly of the gun, as shown in Figure 2.

Data Acquisition and PDV/MPDV Systems

A laser intervalometer system was used to measure projectile velocity. A photonic Doppler velocimetry (PDV) system was used to measure the deformation of the back surface of the target plate. PDV is an interferometric optical velocimetry diagnostic system. Velocity of a point is determined by measuring the Doppler shift of light reflected from the moving surface. A PDV system is capable of measuring frequency up to 20 GHz. Separate experiments using single-probe PDV (Figure 3), 9-probe multiplexed PDV (MPDV), and 25-probe MPDV systems were conducted. The PDV/MPDV systems were triggered 85 μs after the start laser triggered the intervalometer. At this stage, the optical probe/probes began collecting the signal and

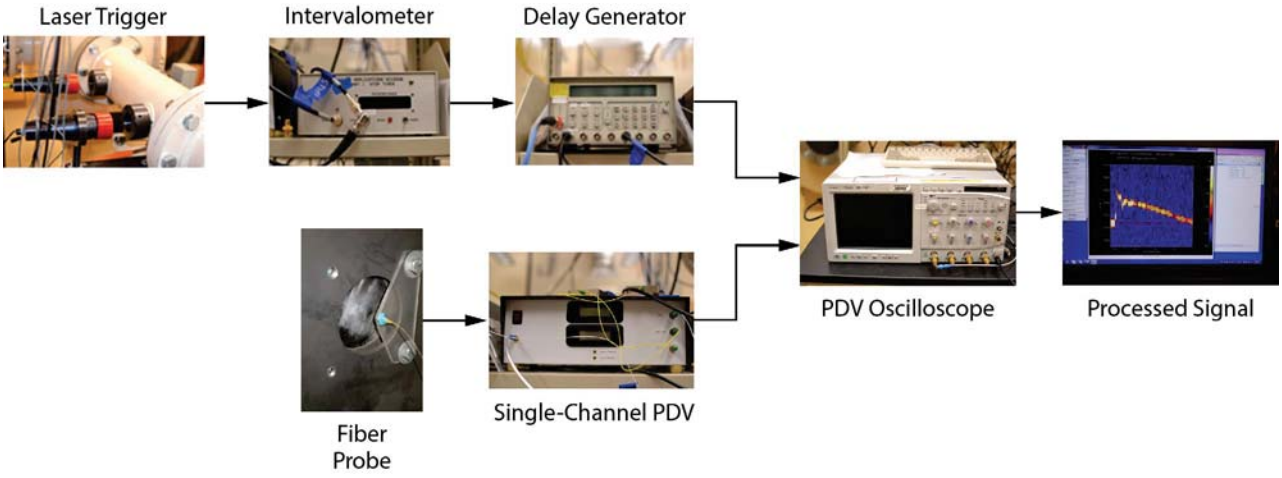

Figure 3. Schematic flowchart illustrating instruments used on a typical single-probe PDV impact experiment

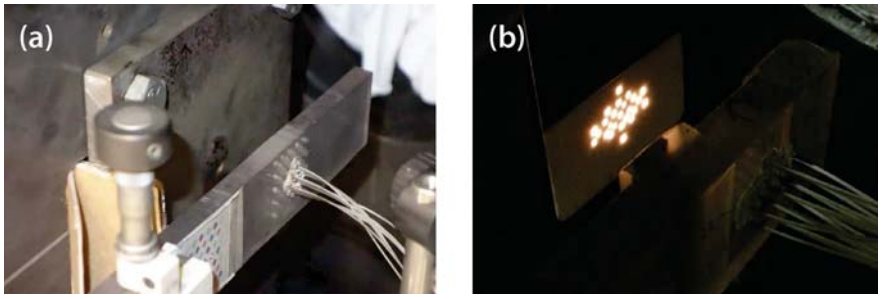

Figure 4. Typical MPDV (a) 9-probe holder and (b) 25-probe arrangement on target

sending it to PDV/MPDV oscilloscopes to record the frequency data. Data were collected at a sampling rate of 10 GS/s in all cases. Raw data were processed using FFT to obtain the velocity profile.

Compared to a single-probe PDV, the MPDV systems can obtain surface deformation information for a large area. MPDV probes were placed on a probe holder designed by NSTec staff (Figure 4). The probes in the MPDV system covered areas with diameters of 12 mm and 25 mm, respectively.

Results

In all experiments, a small crater with a bulge on the back side of the target plate was created as a result of impact (Figure 5). Projectiles disintegrated due to the enormous heat generated upon impact with the target surface.

Spalling

The initiation of spalling in the target plates was another characteristic feature in all our experiments. Compressive shock waves generated in the targets are reflected as releases from the back surface of the plate and then interact with the rest of the oncoming release to generate a region of high tensile stress, which eventually leads to spalling of material off the back surface of the plate. After experiments, some of these target plates were cut in half to confirm that initiation of spall fracture of the steel plates had begun (Figure 6).

Physical Measurement

Impact crater dimensions (diameter of the crater and depth of penetration) were measured using slide calipers. Three measurements were taken for each parameter and an average value was considered for the final parameter. The distance between the flat

Figure 5. (a) Front and (b) back sides of a typical target plate after impact from a 9-probe MPDV experiment

Figure 6. A sectioned target (Test ID 1000-016) plate confirmed spall fracture had occurred

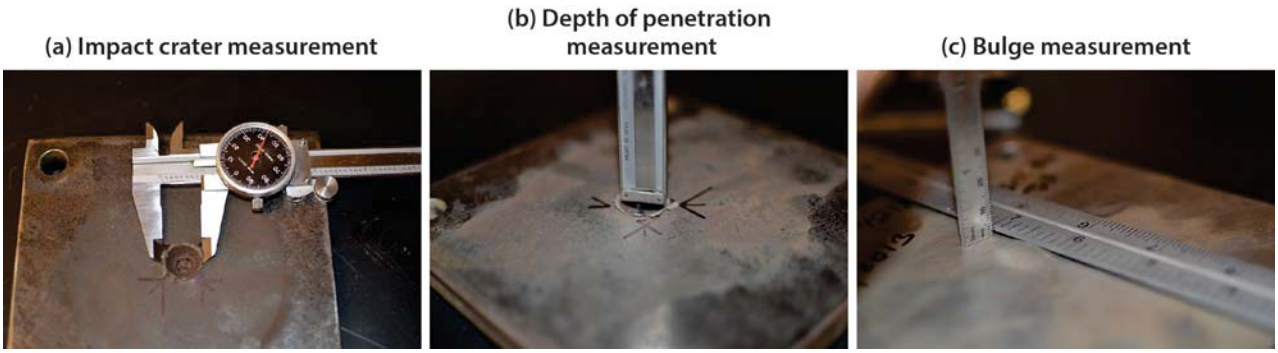

Figure 7. Physical measurements of impacted plate, showing (a) impact crater diameter measurement, (b) depth of penetration measurement, and (c) bulge measurement

surface of the plate and peak point of the bulge was considered as the height of the bulge. Rulers were used to measure this distance, and finally an average was considered. All the measurements were taken in inch scale and then converted to millimeter scale. Figure 7 shows how physical measurements were made of the impacted plates.

Free Surface Velocity Measurement

Figures 8–10 show typical velocity profiles for the PDV and MPDV systems. In general, the surface velocity shows clear evidence for a two-wave structure in compression. The data show that the initial shock wave arrives at the various probe locations according to the distance from the impact point. This is not totally consistent, which may be due to the spalling effects on the shock wave progression.

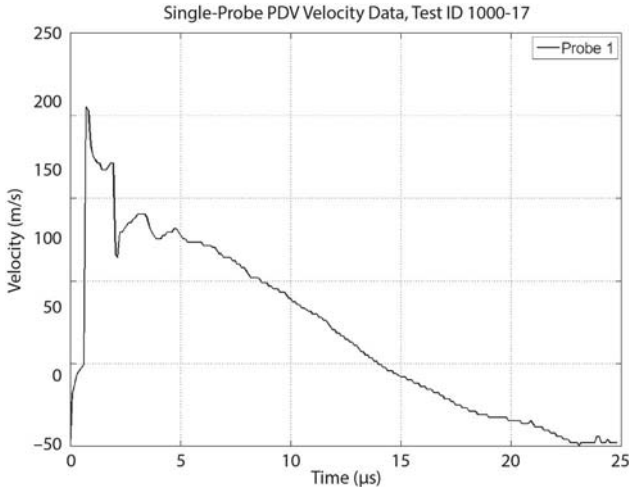

Figure 8. Typical velocity profiles for the single-probe PDV

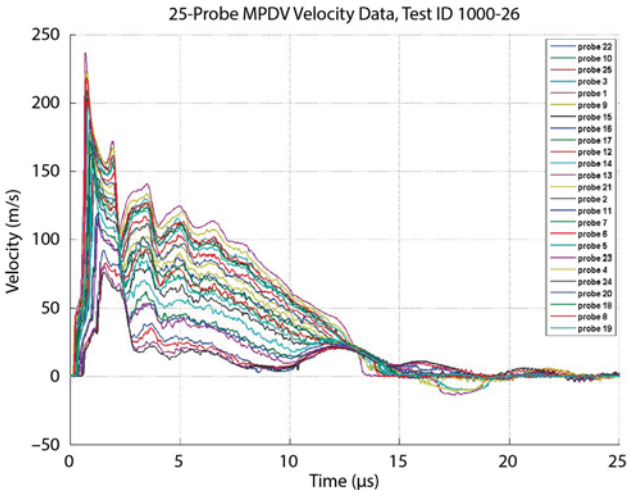

Figure 10. Typical velocity profiles for the 25-probe MPDV

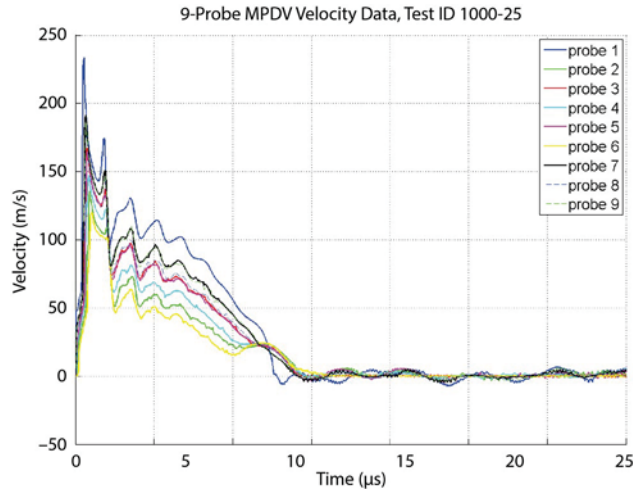

Figure 9. Typical velocity profiles for the 9-probe MPDV

Simulation of the Experiments

One of the major challenges of this project was to simulate the impact phenomena computationally. The commercially available finite element analysis (FEA) software program LS-DYNA was used by the UNLV team while the NSTec team used the CTH hydrocode. Both programs were capable of simulating the experiments. Two different types of comparisons were made: (1) deformed shape of the plate and (2) free surface velocity of the target back surface.

Material Models

When performing dynamic simulations of this kind, material models must be chosen for each material in the simulation. Both computational techniques used in this study consisted of choosing three material models: (1) equation of state (EOS), (2) material strength in compression, and (3) material strength in tension. All the particular material models chosen for this project are described below.

EOS

All materials in this kind of simulation require definition of an EOS. Materials under shock-wave loading need a shock model that can account for the sudden pressure, temperature, internal energy, and density changes in front of shock waves. Different forms of the EOS describe different types of materials and how their volumetric compression (or expansion) behaves. Mie-Grüneisen EOS models were chosen for all materials used in this work. In both LS-DYNA and CTH, different sets of EOS parameters are available to simulate different phenomena. To simulate materials under high-impact loading, the *EOS_GRUNEISEN card is used in LS-DYNA.

Grüneisen parameters for both Lexan projectiles and A36 steel target plates are listed in Table 1. These were used in both LS-DYNA and CTH simulations.

Table 1. EOS parameters for projectiles and targets

Parameter	Projectile (Lexan) (Steinberg 1996)	Target (A36 steel) (Elshenawy 2013)
ρ (kg/m^3)	1190	7890
C (m/s)	1933	4659
S_1	1.42	1.49
γ	0.61	2.17

Table 2. Johnson-Cook material properties for projectiles and targets

Parameter	Lexan Projectile (Littlewood 2010)	A36 Target (Seidt 2007)
A	75.8 MPa	286.1 MPa
B	68.9 MPa	500.1 MPa
C	0	0.022
M	1.85	0.917
N	1.004	0.2282
T_m	533 K	1811 K
γ	0.344	0.26
D_1	0	0.403
D_2	0	1.107
D_3	0	–1.899
D_4	0	0.00961
D_5	0	0.3

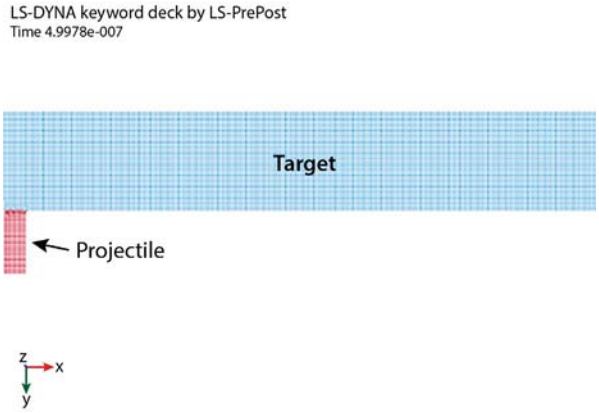

Figure 11. 2-D axisymmetric SPH model of projectile and targets

Strength in Compression

The Johnson-Cook material model is one of the most effective and commonly used material models for simulating high strain and large deformation problems (Katayama 1995, Seidt 2007, Littlewood 2010, Elshenawy 2013). All Johnson-Cook model parameters for Lexan projectiles and A36 steel target plates are given in Table 2.

Strength in Tension (Spall Model)

In both LS-DYNA and CTH, spall failure is invoked when the tensile stress exceeds a certain pressure cutoff (i.e., P_{min}) value. Based on the literature, the P_{min} value for the Lexan projectiles and the A36 steel targets was taken as 160 MPa (Steinberg 1996) and 700 MPa (Zurek 2003), respectively.

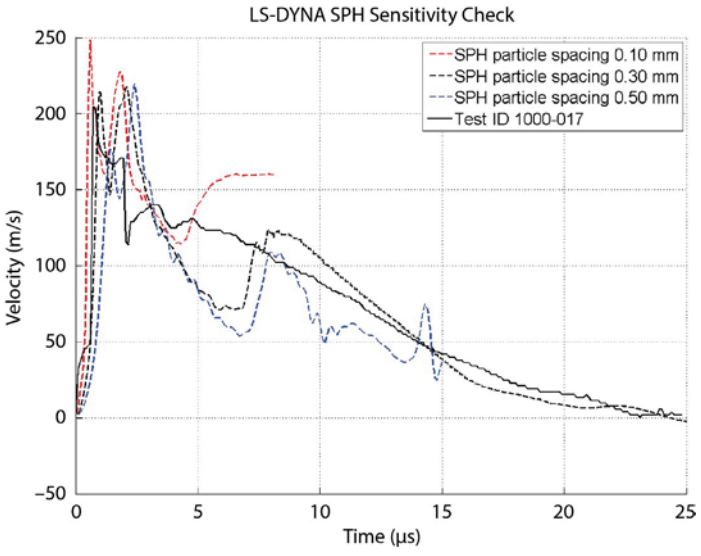

Figure 12. LS-DYNA SPH model particle sensitivity tests show that simulations vary with particle spacing

LS-DYNA Simulation

SPH Method

The Lagrangian-based SPH method was used in LS-DYNA to simulate the experiment. SPH is a meshless numerical technique used to model the fluid equations of motion (i.e., large distortions).

SPH Model Development and Boundary Conditions

A 2-D axisymmetric SPH model was created for both projectiles and target plates (Figure 11). In a 2-D axisymmetric model, the target plate was a circular disk with a radius of 76.2 mm and a thickness of 12.7 mm. SPH particle density was one of the key problems in developing the model. Three different types of SPH particle spacing were considered: very dense (0.1 × 0.1 mm), medium dense (0.3 × 0.3 mm), and coarse dense (0.5 × 0.5 mm). Because the very fine and coarse dense spacings gave poor results, all simulation models were created with the medium dense (0.3 × 0.3 mm) SPH grid (Figure 12). No boundary conditions were implemented as the impact is a localized phenomenon.

CTH Simulation

CTH is a Eulerian hydrodynamics computer code developed and maintained by Sandia National Laboratories. It is well known that zone size (Figure 13) in this kind of simulation can have an effect upon the results. CTH simulations were also done in a 2-D axisymmetic (cylindrical) geometry. Tracer particles were placed at various target locations to collect physics information, including close to the back surface of the target where the velocimetry data are collected. Tracers were set slightly off center radially to stay away from on-axis numerical instabilities. Several parametric studies were done using CTH simulations.

In this study, coarse zone size was 0.5 × 0.5 mm, medium was 0.5 × 0.3 mm, and fine was 0.3 × 0.3 mm. The sensitivity of the simulated velocity profiles with zone size is the reason we continued reducing zone size even more to find a terminal zone size below which the simulation results do not change. These simulations also capture some physical details of the cratering and even the penetration process. Figure 14 is a simulation plot for this same experiment later in time showing the crater and the existence of considerable spall damage.

Another question for this research is the selection of A36 steel as the target: Can we confirm that it undergoes the α-ε phase change that is well known to happen in pure iron and low alloy steels (e.g., 1018 CRS) at 13–15 GPa? Because no existing literature has yet answered this question, most simulations are done without enabling the target to undergo this transformation. It should be noted that even if the target does

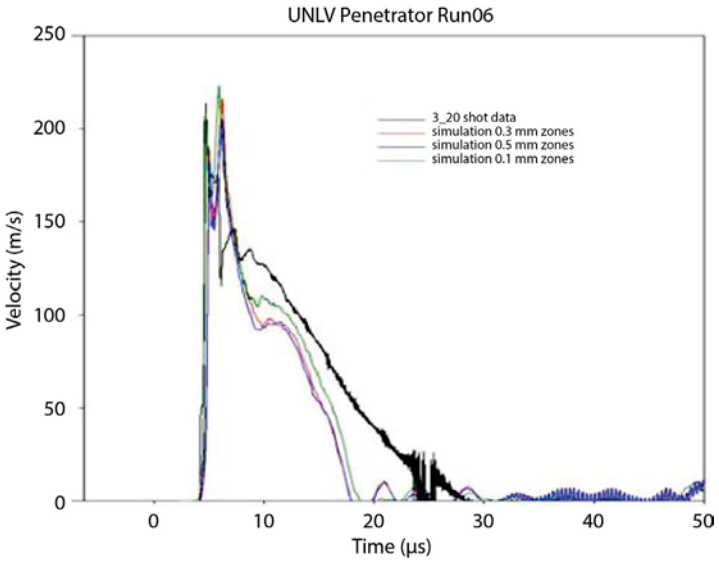

Figure 13. Initial zone size study in CTH for Test ID 1000-017 shows that the simulations vary with zone size

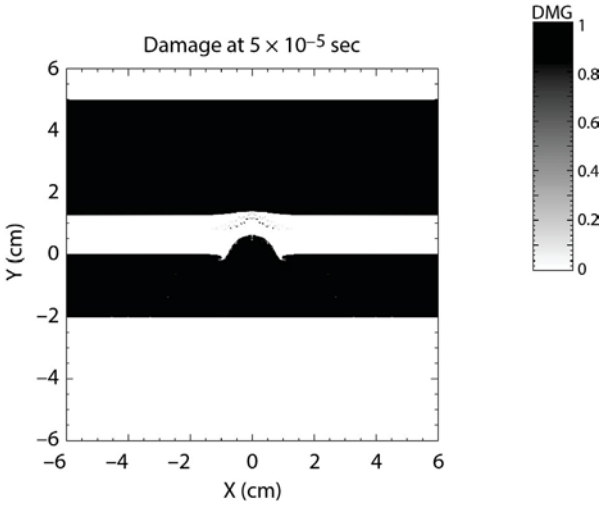

Figure 14. Details of cratering and spall processes in CTH simulation indicate that the physical models need improvement before simulations can better match the data

show phase transition, even for the highest velocity experiments, the entire target will not show this transition.

The general features of the simulation agree with data, including peak particle velocity, but some details do not agree well. This indicates we need to improve our understanding of how various physical effects interact in the experiment and what improvements are required for the physics models in the simulation to obtain better agreement.

FEA Results Comparison

The computationally predicted deformation after impact along with the target plate back surface velocity both agree well with experimental data. Crater and bulge measurements were taken in all FEA simulations to compare with the physical measurements. Table 3 lists a comparison between experimental and LS-DYNA simulated crater dimensions and bulge.

Figure 15 shows velocity versus time for a point on the back surface of the target plate from experiment 1000-017. Experimental data are plotted along with both LS-DYNA and CTH predictions. The overall prediction for both simulation methods is good, but there are some anomalies. The simulated velocity profile provides a good prediction of the peak velocity, but both methods show a double peak as the velocity rises. This double peak was not evident in the experimental data. This difference is consistent with comparisons of the other experiments as well. Experimental velocity curves were also compared to LS-DYNA and CTH simulations for the 9-probe and 25-probe MPDV experiments, and similar observations were made (Figures 16 and 17).

Table 3. Comparison of experimental results with LS-DYNA simulation

Test ID	Crater Diameter (mm)		% Error	Penetration (mm)		% Error	Bulge (mm)		% Error
	Experimental	LS-DYNA Simulation		Experimental	LS-DYNA Simulation		Experimental	LS-DYNA Simulation	
1000-016	17.01	17.02	0.06	6.32	7.35	14.01	2.32	3.65	57.33
1000-017	16.86	15.90	5.69	5.76	5.04	14.22	2.36	2.17	8.05
1000-024	17.17	17.08	0.52	6.64	7.02	5.37	3.13	3.16	0.96
1000-025	15.37	16.20	5.40	4.83	4.14	16.75	1.42	1.39	2.11
1000-026	15.14	16.30	7.66	4.84	4.67	3.71	1.48	1.54	4.05
1000-027	16.90	16.88	0.12	5.40	4.91	9.98	2.33	1.86	20.17
1000-028	15.90	16.68	4.91	5.17	5.21	0.83	1.67	1.97	17.96
Average Error (%)			**3.48**			**9.27**			**15.81**
Standard Deviation			**3.16**			**6.07**			**19.81**

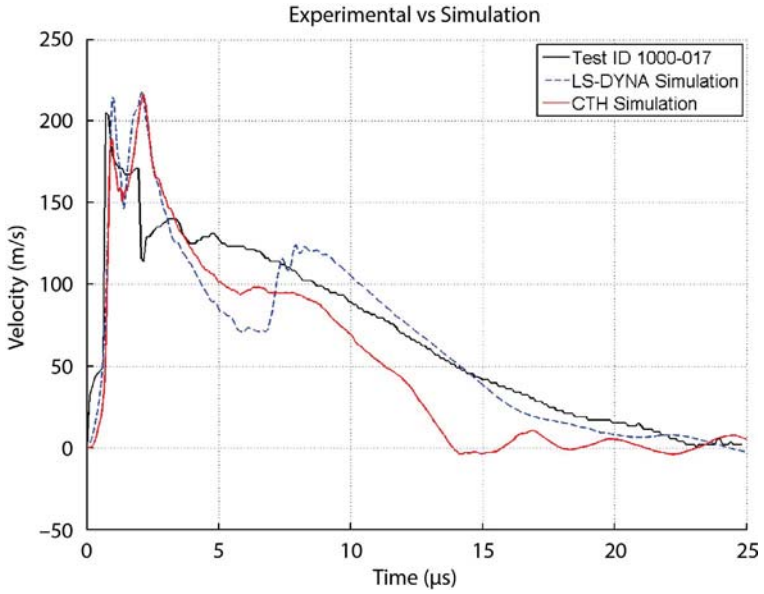

Figure 15. Typical single-probe PDV velocity profile compared with LS-DYNA and CTH simulated velocity shows a double peak that was not present in the experimental data

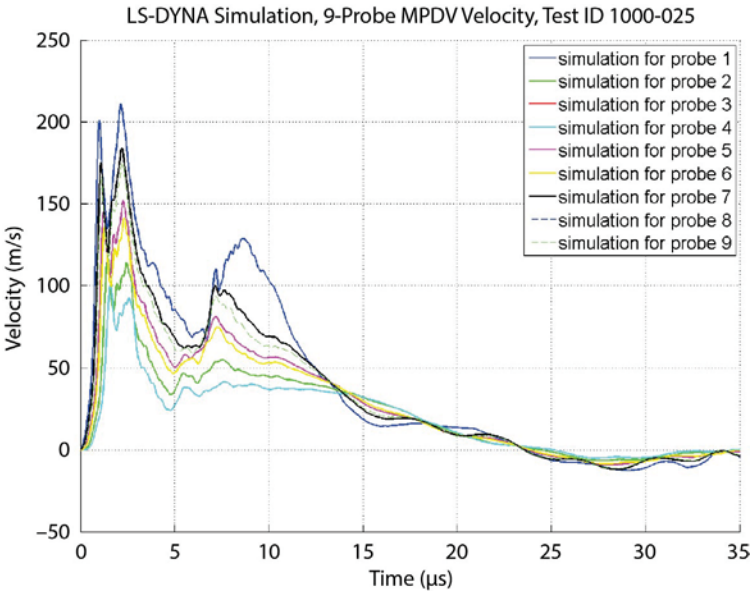

Figure 16. Typical 9-probe MPDV velocity profile from LS-DYNA simulation

Conclusion

Gun experiments were performed to monitor the plastic deformation of steel plates during hypervelocity conditions. Velocity of the back surface of the plate was measured using PDV and MPDV systems. Simulation models developed in LS-DYNA SPH solver and CTH hydrocode were used to simulate the experiments. The simulation results show that the physical measurements of cratering resulting from the impacts were in reasonable agreement with simulation results, but differences in details still exist. The simulations were also able to predict the velocity profiles of the probes of the PDV and MPDV experiments, again with some differences observed. Additional experiments and tuning of the simulation models, including the use of more accurate material models and simulation parameters, are needed to further refine the simulation results.

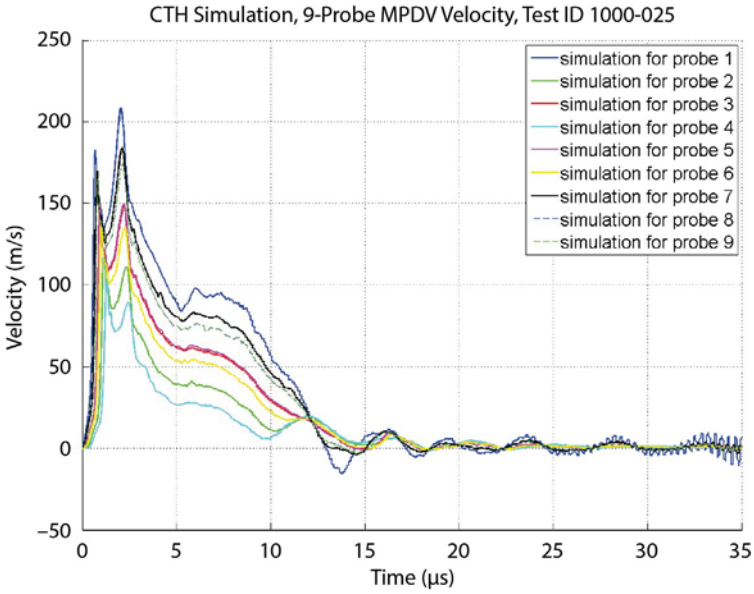

Figure 17. Typical 9-probe MPDV velocity profile from CTH simulation

So far, good progress has been made on initial experimental and computational results in this project. To bring the simulations into better agreement with the actual data, the next step is to identify the primary cause behind the observed differences. There are two possible sources of difference that can be identified. First, computational effects such as differencing schemes, zone size, and artificial viscosity can contribute. Additionally, the actual physics models, which are empirical in nature, will cause differences between the experiment and the simulation. For our second year of research, we will focus on determining the source of the largest disagreement. This will involve performing calculations in which we vary input parameters for both the computer code and the physics models in a logical way to find where sensitivites exist.

References

Anderson, C. E., Jr., V. Hohler, J. D. Walker, A. J. Stilp, "Time-resolved penetration of long rods into steel targets," *Int. J. Impact Eng.* **16**, 1 (1995a) 1–18.

Anderson, C. E., Jr., J. D. Walker, S. J. Bless, T. R. Sharron, "On the velocity dependence of the L/D effect for long-rod penetrators," *Int. J. Impact Eng.* **17**, 1–3 (1995b) 13–24.

Anderson, C. E., Jr., J. D. Walker, S. J. Bless, Y. Partom, "On the L/D effect for long-rod penetrators," *Int. J. Impact Eng.* **18**, 3 (1996) 247–264.

Beynet, P., R. Plunkett, "Plate impact and plastic deformation by projectiles," *Experimental Mechanics* **11**, 2 (February 1971) 64–70.

Bond, J. W., "Hypervelocity-impact shock-induced damage to steel armor," Report 2174, U.S. Army Mobility Equipment Research and Development Command, Fort Belvoir, Virginia, 1976.

Børvik, T., M. Langseth, O. S. Hopperstad, K. A. Malo, "Ballistic penetration of steel plates," *Int. J. Impact Eng.* **22**, 9–10 (1999) 855–886.

Børvik, T., O. S. Hopperstad, T. Berstad, M. Langseth, "Numerical simulation of plugging failure in ballistic penetration," *Int. J. Solids and Structures* **38**, 34–35 (2001) 6241–6264.

Børvik, T., A. H. Clausen, O. S. Hopperstad, M. Langseth, "Perforation of AA5083-H116 aluminium plates with conical-nose steel projectiles—experimental study," *Int. J. Impact Eng.* **30**, 4 (April 2004) 367–384.

Chen, X. W., Q. M. Li, "Perforation of a thick plate by rigid projectiles," *Int. J. Impact Eng.* **28**, 7 (August 2003) 743–759.

Chen, X. W., Y. B. Yang, Z. H. Lu, Y. Z. Chen, "Perforation of metallic plates struck by a blunt projectile with a soft nose," *Int. J. Impact Eng.* **35**, 6 (June 2008) 549–558.

Chen, X. W., X. Q. Zhou, X. L. Li, "On perforation of ductile metallic plates by blunt rigid projectile," *European Journal of Mechanics - A/Solids* **28**, 2 (March–April 2009) 273–283.

Chhabildas, L. C., M. D. Knudson, "Techniques to launch projectile plates to very high velocities," in *High-Pressure Shock Compression of Solids VIII*, L. C. Chhabildas, L. Davidson, Y. Horie, eds., Springer Berlin Heidelberg, 2005, 143–199.

Cullis, I. G., N. J. Lynch, "Performance of model scale long rod projectiles against complex targets over the velocity range 1700–2200 m/s," *Int. J. Impact Eng.* **17**, 1 (1995) 263–274.

Doolan, C., "A two-stage light gas gun for the study of high speed impact in propellants," DSTO-TR-1092, Department of Defence, Defence Science and Technology Organization, Salisbury, Australia, 2001.

Eftis, J., J. A. Nemes, "Modeling of impact-induced spall fracture and post spall behavior of a circular plate," *Int. J. Fracture* **53**, 4 (1992) 301–324.

Elshenawy, T., Q. M. Li, "Influences of target strength and confinement on the penetration depth of an oil well perforator," *Int. J. Impact Eng.* **54** (April 2013) 130–137.

Espinosa, H. D., S. Dwivedi, P. D. Zavattieri, G. Yuan, "A numerical investigation of penetration in multilayered material/structure systems," *Int. J. Solids and Structures* **35**, 22 (1998) 2975–3001.

Forrestal, M. J., A. J. Piekutowski, "Penetration experiments with 6061-T6511 aluminum targets and spherical-nose steel projectiles at striking velocities between 0.5 and 3.0 km/s," *Int. J. Impact Eng.* **24**, 1 (January 2000) 57–67.

Goldsmith, W., T. W. Liu, S. Chulay, "Plate impact and perforation by projectiles," *Experimental Mechanics* **5**, 12 (December 1965) 385–404.

Hayhurst, C. J., H. J. Ranson, D. J. Gardner, N. K. Birnbaum, "Modelling of microparticle hypervelocity oblique impacts on thick targets," *Int. J. Impact Eng.* **17**, 1–3 (1995) 375–386.

Holmes, N., "'Shocking' gas-gun experiments," *Science & Technology Review* (September 2000) 12–19.

Kalameh, H. A., A. Karamali, C. Anitescu, T. Rabczuk, "High velocity impact of metal sphere on thin metallic plate using smooth particle hydrodynamics (SPH) method," *Frontiers of Structural and Civil Engineering* **6**, 2 (2012) 101–110.

Katayama, M., S. Kibe, S. Toda, "A numerical simulation method and its validation for debris impact against the whipple bumper shield," *Int. J. Impact Eng.* **17**, 4–6 (1995) 465–476.

Littlefield, D. L., C. E. Anderson, Jr., Y. Partom, S. J. Bless, "The penetration of steel targets finite in radial extent," *Int. J. Impact Eng.* **19**, 1 (January 1997) 49–62.

Littlewood, D. J., "Simulation of dynamic fracture using peridynamics, finite element modeling, and contact," in *Proc. ASME 2010 International Mechanical Engineering Congress and Exposition*, British Columbia, Canada, 2010.

Merzhievskii, L. A., V. M. Titov, "Perforation of plates through high velocity impact," *Zhurnal Prikladnoi Mekhaniki i Tekhnicheskoi Fiziki* **16**, 5 (1975) 102–110.

Normandia, M. J., M. Lee, "Penetration performance of multiple segmented rods at 2.6 km/s," *Int. J. Impact Eng.* **23**, 1 (December 1999) 675–686.

O'Daniel, J., K. Danielson, N. Boone, "Modeling fragment simulating projectile penetration into steel plates using finite elements and meshfree particles," *Shock and Vibration* **18**, 3 (2011) 425–436.

Rolsten, R. F., H. H. Hunt, "Phenomena resulting from hypervelocity impact," *J. Spacecraft* **2**, 1 (1965) 38–43.

Rosenberg, Z., E. Dekel, "A computational study of the influence of projectile strength on the performance of long-rod penetrators," *Int. J. Impact Eng.* **18**, 6 (September 1996) 671–677.

Rosenberg, Z., E. Dekel, "A computational study of the relations between material properties of long-rod penetrators and their ballistic performance," *Int. J. Impact Eng.* **21**, 4 (April 1998) 283–296.

Rosenberg, Z., E. Dekel, "Plate perforation," in *Terminal Ballistics*, Springer Berlin Heidelberg, 2012, 109–153.

Seidt, J. D., A. Gilat, J. A. Klein, J. R. Leach, "High strain rate, high temperature constitutive and failure models for EOD impact scenarios," in *Proc. 2007 SEM Annual Conference and Exposition on Experimental and Applied Mechanics*, Society for Experimental Mechanics, Inc., Springfield, Massachusetts, 2007.

Shah, Q. H., Y. A. Abakr, "Effect of distance from the support on the penetration mechanism of clamped circular polycarbonate armor plates," *Int. J. Impact Eng.* **35**, 11 (November 2008) 1244–1250.

Steinberg, D. J., "Equation of state and strength properties of selected materials," UCR-MA-106439, Change 1, Lawrence Livermore National Laboratory, Livermore, California, 1996.

Swaddiwudhipong, S., M. J. Islam, Z. S. Liu, "High velocity penetration/perforation using coupled smooth particle hydrodynamics-finite element method," *Int. J. Protective Structures* **1**, 4 (2010) 489–506.

Swift, H. F., "Light-gas gun technology: A historical perspective," in *High-Pressure Shock Compression of Solids VIII*, L. C. Chhabildas, L. Davison, Y. Horie, eds., Springer Berlin Heidelberg, 2005, 1–35.

Walker, J. D., "A model for penetration by very low aspect ratio projectiles," *Int. J. Impact Eng.* **23**, 1 (1999) 957–966.

Westerling, L., P. Lundberg, B. Lundberg, "Tungsten long-rod penetration into confined cylinders of boron carbide at and above ordnance velocities," *Int. J. Impact Eng.* **25**, 7 (August 2001) 703–714.

Yadav, S., E. A. Repetto, G. Ravichandran, M. Ortiz, "A computational study of the influence of thermal softening on ballistic penetration in metals," *Int. J. Impact Eng.* **25**, 8 (September 2001) 787–803.

Zukas, J. A., *High Velocity Impact Dynamics*, John Wiley & Sons, New York, 1990.

Zurek, A. K., J. Mata, E. Cerreta, C. P. Trujillo, "Experimental study of A36 steel spall fracture," *Journal de Physique IV* **110**, 1 (September 2003) 863–867.

This page left blank intentionally

Dense Plasma Focus Magnetic Mirror Experiment

LAO-30-13 | Year 1 of 1

Michael Berninger,[1,a] Tim Meehan,[b] Mark Morey,[c] Roderick Tiangco,[c] Wayne Word,[d] Rick Cummings,[d] Doug McBride,[d] Scott Myers,[b] Brian Cata,[a] Martin Palagi,[b] Kevin McGillivray,[b] Joe Delash,[e] Chris Hagen,[b] Daniel Lowe,[b] Larry Robbins,[b] Thomas Tunnell,[a] and Steve Molnar[f]

A magnetic mirror can be created in the dense plasma focus (DPF) in the regions of the plasma where there are large magnetic-field gradients. When a charged particle moves from a region of low magnetic-field strength to one with a high field, it can be reflected back, as with a mirror. In a DPF machine, these magnetic field gradients are a loss mechanism with the potential to limit fusion yields by forcing ionized deuterium away from the hottest regions of the pinch. This drift would only be exacerbated as charging voltages are increased. However, hydrodynamics calculations of the DPF plasma predict that the maximum gradients would be about 1.0×10^6 G/cm—three orders of magnitude too low to significantly affect the density distribution of deuterium within the pinch. To verify this result, solid-state pinhole cameras were installed in the DPF to collect images of the deuterium pinch while step-range spectrometers simultaneously collected proton-energy data. The deuterium-plasma images show that as the DPF charging voltage was increased, rather than being dissipated by field gradients, the plasma-pinch column became longer and more organized with a segmented structure along the pinch axis. The proton-energy spectrum appeared to vary little with charging voltage and showed the plasma had an approximately Maxwellian distribution with a peak energy of 3.4 ±0.3 MeV. Although the spectrum is Maxwellian, this peak energy is more indicative of a field-driven fusion process.

[1] berninmj@nv.doe.gov, 505-663-2032
[a] Los Alamos Operations; [b] North Las Vegas; [c] Special Technologies Laboratory; [d] Nevada National Security Site; [e] Livermore Operations; [f] Powder River Geophysical

Background

In a dense plasma focus (DPF) machine, nested cylindrical electrodes are installed inside a chamber centered on the same axis, hence we call this coaxial assembly a "coax." One end of the coax is sealed, electrically insulated, and connected to a capacitor bank through the chamber wall, while the other end is open and suspended within the chamber. The empty volume in the chamber is filled with a uniform density of gas such as argon, helium, deuterium, or tritium.

The DPF operation may be described by the so-called "snow-plow" model (Butler 1969). In this model, the plasma is initiated by the bank of capacitors discharging into the gas. Electric fields at the insulating end of the coax ionize the deuterium gas between the electrodes and form a thin annular plasma sheath. Current flowing through the ion layer creates azimuthally circulating magnetic fields, and the $\vec{J} \times \vec{B}$ ($\vec{J}$ is current density and $\vec{B}$ is magnetic field) reaction forces the plasma sheath to propagate down the length of

the electrodes, collecting and ionizing deuterium atoms along the way. At the open end of the coax, the plasma overlaps the inner conductor, collapses radially inward, and pinches on the central axis near the inner conductor. During a pinch with deuterium or tritium, an intense pulse of neutrons is generated. Strong electrical fields then force the low-density plasma cloud away from the inner conductor.

In the deuterium fusion reaction, two branches occur with approximately equal probability:

$$ {}_1D^2 + {}_1D^2 \rightarrow {}_2He^3 + {}_0n^1 \rightarrow {}_1T^3 + {}_1H^1. \quad (1) $$

On the first branch, a ^{3}He ion is created with a single neutron. On the second, a tritium isotope is created with an ~3 MeV proton. Neutrons are difficult to detect, but protons are easily detected with solid-state detectors. Due to the equal probability that protons will be produced in deuterium-deuterium (DD) fusion, images of the DPF plasma obtained through proton measurement are representative of neutron images. However, detecting protons at the DPF is not trivial. Their particle trajectories are modified by the strong magnetic fields that exist in and around the DPF plasma pinch.

A neutron yield plateau, ~1 × 10^{12} neutrons per pulse, has been ubiquitously observed in focus machines for about four decades but has never been adequately explained (Krall 1973, Lee 1996). The challenge for increasing the yield with DD fusion in a plasma focus is that the plasma properties are nonlinear and there are numerous possible mechanisms for reducing the neutron yield. These possibilities include various types of instability such as self-focusing (Bennett 1934, 1955; Vikhrev 2007), kinks, and "sausage" (Miller 1982, Vikhrev 2007). Plasma flows away from the fusion regions (Keck 1962, Butler 1969, Potter 1971); relaxation occurs with the Hall effect (Sudan 1978, Turner 1986, Auluck 2011); and axial fields (Krauz 2012) exist with filamentary current flow (Bernard 1975).

NSTec has two DPFs; one produces DD fusion and the other deuterium-tritium (DT) fusion. These DPFs are important platforms for developing diagnostics intended for use with the National Center for Nuclear Security, the National Ignition Facility, and the Z machine. The neutron yields produced by NSTec's DPF machines will also be useful for effects studies at the NNSS. NSTec has identified a priority with improving the neutron yield generated by NSTec's DPFs that use deuterium and tritium gases. Our goal was to investigate the influence on deuterium fusion of magnetic field gradients produced by the DPF plasmas.

Project

The hydrodynamics code ALEGRA (Robinson 2008) was used to calculate field gradients in a plasma pinch with the initial conditions from a DPF that produces DD fusion. In the calculation (Figure 1) where the charging voltage was 35 kV, the drift speed of the plasma sheath prior to plasma pinch was found to be approximately $\vec{V}_{drift} \approx 1 \times 10^7$ *cm/s,* where the electrical field was $\vec{E}$ = *57 statV/s*, and maximum magnetic field was $|\vec{B}_\theta|$ = *–2.5 × 10^5 G*. The magnitude of these field quantities was consistent with prior calculations (Potter 1971).

The equation for drift velocity due to field gradients is

$$ V_{z\nabla B_X\,-\,drift} = \frac{w_\perp c}{q B_\theta^{\,2}} \nabla_\perp B_\theta, \quad (2) $$

where $w_\perp$ is the perpendicular kinetic energy, c is the speed of light, q is the charge, B_θ is the azimuthal magnetic field, and $\nabla_\perp B_\theta$ is the field gradient normal to the shock front. After taking the inverse of the gradient lineout (Figure 1c) we can insert the maximum (10 tesla/pixel) with proper unit conversion into the equation for $V_{z\nabla B_X - drift}$ and obtain $V_{z\nabla B_X - drift}$ = 29 cm/s. In 1 µs, this additional component of drift would only force a single deuterium ion Δz = 0.29 µm along the z-axis. For the gradients to have a significant influence on the plasma distributions, the ions would have to be moved a distance on the order of *millimeters*. Because the neutron-yield plateau effects are observed experimentally with a charging voltage only twice that of the charging voltage in the calculation, it is unlikely that the gradients would become sharp enough at 70 kV to produce a three-order-of-magnitude change in the

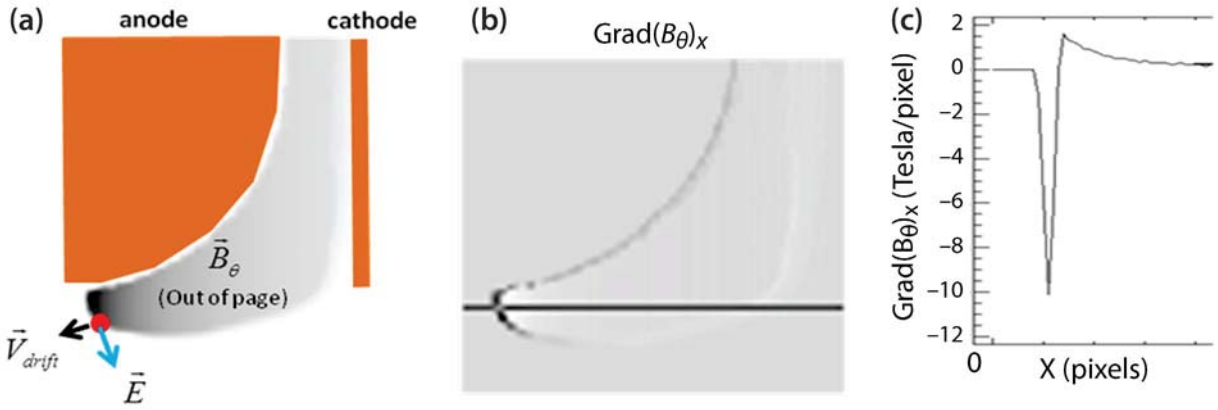

Figure 1. (a) An ALEGRA calculation with the charging voltage at 35 kV, (b) a 2-D profile of the numerical profile of the magnetic fields, and (c) the line profile of the gradient

drift velocities. Thus, to the first order, field gradients (the mirror effect) do not play a significant role in modifying the ion density distribution in the plasma leading up to and during the plasma pinch.

Recognizing the highly nonuniform nature of the DPF pinch, we collected data to evaluate the efficacy of using a first-order approximation.

Proton Range Spectrometer and Pinhole Cameras Experiment

Solid-state track-etch detectors were fabricated with proton spectrometers (Jager 1985, Seguin 2012) and pinhole cameras (Jager 1985, Zakaullah 1999) for this experiment. Track detectors have the advantages of being insensitive to photon radiation and electrons, while having 100% detection efficiency with protons and deuterons with energies greater than a few tens of eV (Fleischer 1965). In a track detector, an energetic particle penetrates a solid (e.g., Lexan, quartz, or cellulose nitrate) and leaves a damage track, losing energy as it does so. If the solid-state detector is thick enough, the particle will lose all of its energy in the detector material. Thus, the amount of damage is proportional to the energy of the particle. However, the tracks tend to be only angstroms in diameter. The solid-state detector must be etched in a sodium hydroxide or potassium hydroxide bath to develop or widen the damage tracks so they can be observed under a microscope. The damage tracks are then recorded with a digital imaging system.

The spectrometers were of the step-range type, where the energetic particles must traverse filters (Al) of different thicknesses that are laid next to each other on a single piece of plastic. The filters were arranged in order from thinnest to thickest that resemble a set of "steps." The filters face the radiation source. Only deuterons and protons with enough energy to penetrate completely through a foil-step and produce a damage track in the underlying solid-state detector would be recorded. Thus, steps of increasing thickness filter out increasingly higher energies of protons. The spectrum is obtained by subtracting the track count under the respective foil filter from the track count with the next thinner step to obtain the number of protons in the energy range defined by the different thicknesses of filter.

The physical spectrometers in the DPF had 11 slots (22 × 2 mm and 3 mm deep) of which ten were covered completely with differing thicknesses of aluminum foil (Goodfellow, Inc.) and the eleventh had no filter. Table 1 summarizes the foil features of each channel with the nominal stopping energy for the given thickness. All channels were backed with a single piece of 0.9 mm thick CR-39 (Jager 1985, Dörschel 1997) plastic from Landauer. The foil thicknesses were measured with weight-density method and verified with a Gage-2000 Reflex gage table (Brown & Sharpe). The energies were derived from the National Institute of Standards and Technology (NIST) proton stopping power tables for aluminum generated with P-Star (NIST 2013).

Table 1. Aluminum foil thickness for each channel and nominal proton range energy

Channel	Average Thickness (μm)	Error (±μm)	%Error	Proton Range Energy (keV)
A2	12.75	0.33	2.55	936.2
A3	18.97	0.44	2.32	1203.7
A4	27.60	0.29	1.04	1546.8
A5	37.30	0.41	1.09	1875.9
A6	46.92	0.28	0.59	2143.0
A7	56.88	1.28	2.26	2362.3
A8	70.42	1.02	1.44	2787.5
A9	86.20	1.58	1.83	3122.1
A10	99.13	2.90	2.93	3396.7
A11	116.38	0.40	0.35	3711.9

In the pinhole cameras, a 1-inch disc of CR-39 plastic was seated within a cylindrical housing about 2.5 inches long and about 1.25 inches in diameter. The magnification was 0.23, and the resolution was limited by the 200 μm diameter of the pinhole in a 0.05 mm thick piece of tungsten (purchased from Lenox Laser). In about half the shots, 25 μm of aluminum foil covered the plastic detector. The plastic detector and foil appeared to be undamaged.

The pinhole cameras and spectrometers (Figure 2) were installed on a carousel in three pairs under a shield. The rotating carousel allowed the detectors to be protected by the shield while the DPF was prepared.

The center of the spectrometer was 20 cm from the expected center of the pinch (a point about 15 mm below the center of the anode) at a viewing angle 22° away from the z-axis of the pinch. The spectrometer had an acceptance angle of 6.8° relative to the expected center of the pinch. The pinhole cameras were fielded about 15 cm from the expected center of the pinch. The center of each pinhole was on a line of sight 38.5° off the z-axis, but the base of each camera was rotated up in polar angle around the center point of the pinhole by about 5° to view a larger region under the anode.

Each DPF pulse typically produced a significant amount of copper spall. Although the exterior of both types of detector were damaged by spallation, only the spectrometer channels with the thinnest foils had significant damage and the pinhole apertures survived intact (preventing spallation products from reaching the detector surface in significant quantities).

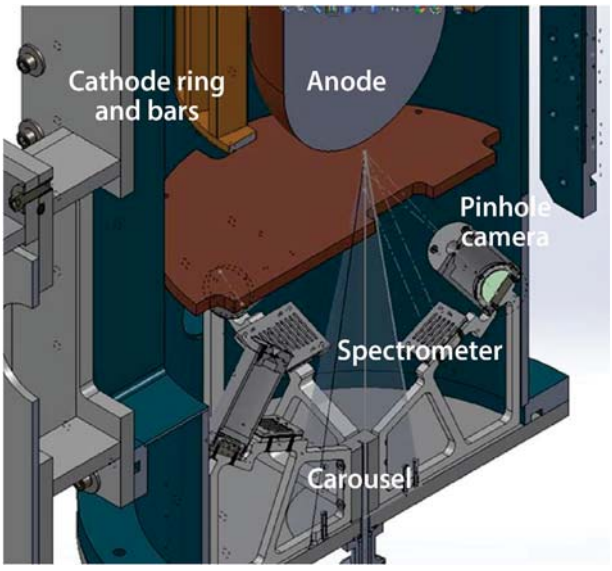

Figure 2. The location of the pinhole cameras and spectrometers with the DPF anode

Results

Figure 3 shows a plot with the range of yields versus the charging voltages over the course of this experiment. The yields were measured with a silver activation foil. This plot shows that the yield increased monotonically with charge voltage.

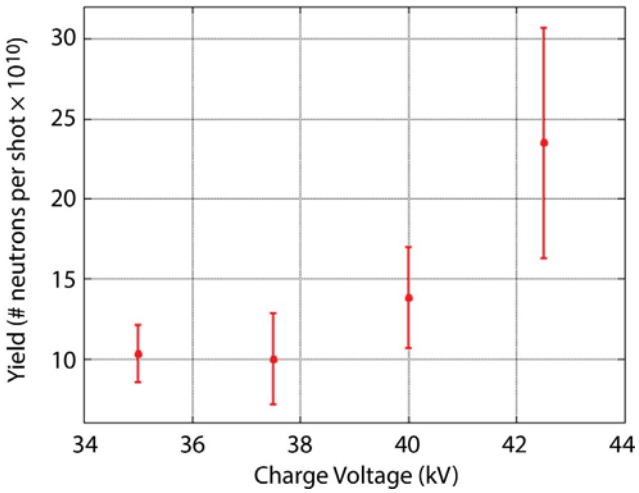

Figure 3. The dependence of neutron yield with charge voltage over the shot series in this experiment indicates the measured neutron yields (dot with error bars) increased monotonically with charge voltage

Examples of the deuterium pinch images are seen in Figure 4. These time-integrated images show a stack or column of dark droplet features. In Figure 4b, the pinhole detector was tilted an extra 5° to compensate for magnetic field effects; thus, the top of the column appears closer to the top of the image near the label. The dark, sausage-shaped droplet feature nearest the top of each column in both images is identified with the primary pinch because after demagnification and projection scaling, they are about 1 cm long. In this instance, the primary pinch is the portion of the plasma that pinches first, about 1 cm under the anode, and is typically observed to be 1 cm long in agreement with the above measurements. Unfortunately, because the images are time-integrated, the timing of the formation of the other droplet features in the images cannot be determined.

In both images, the deuterium pinch has a much larger diameter, from ~2.5 to 3 mm, than the expected ~1 mm diameter. In Figure 4a the pinch is about 2 cm long, and the pinch in Figure 4b is 3.2 cm long. Linear and circular features around the center of Figure 4b appear to be associated with the circular base of the cathode and the cathode bars. The diffuse grey scatter is suggestive of deuterium spray off both the anode and cathode.

The pinch lengths from the pinhole images can be correlated with neutron doses. The plot in Figure 5 compiles the average length of the plasma column from the entire set of pinch images with the average length of the primary pinch for various neutron yields. While the length of the primary pinch (first droplet feature) remains relatively constant with increasing yields, the total length of the plasma column increases. The pinhole data (Figure 4) suggest that at lower charge

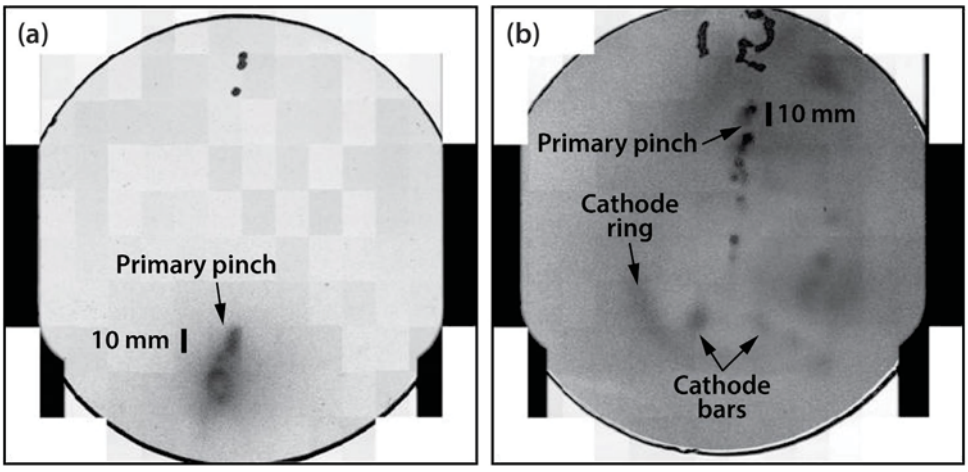

Figure 4. Two pinhole images of deuterium pinches, which produced (a) 8.8×10^{10} neutrons and (b) 3.27×10^{11} neutrons. The detector labels, 1 and 15, visible near the 12 o'clock positions, should not be confused with the images of the pinch.

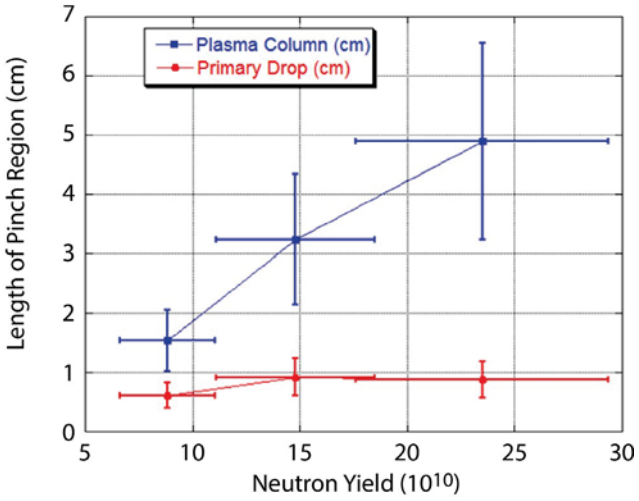

Figure 5. While the length of the primary pinch (first droplet feature) remains relatively constant with increasing yields, yields appear to be correlated with the total length of the plasma column yield

voltages and yields the plasma has a diffuse "pear-like" shape. With higher yields, the pinch is nominally cylindrical and shows more clearly delineated features in the form of a stack of discrete "droplets." The droplets and the long narrow cylindrical shape indicate the plasma is constrained by higher magnetic fields that are distributed in a periodic manner along the length of the plasma column. Although it is not clear from these images where (or when) the fusion is occurring in the pinch, it would appear that the yield depends upon the overall total length scale and distribution of the fields supporting the plasma.

A spectrometer was fielded with each pinhole camera. Figure 6 shows a typical example of the raw spectrometer data. Each energy channel, labeled from left to right A11–A1, appears as a vertical gray bar where the damage-track density is shown by a corresponding gray level. Closer inspection with 50x magnification (Figure 6b) shows that the gray level in each bar is actually a spatial distribution of light circles caused by proton-track damage. The thickness of each foil is listed with each channel in Table 1. The proton track-density in the plastic appeared to be mildly angle dependent over the acceptance angle of the spectrometer, with the higher track density on the side closest to the z-axis of the DPF. The reason for this angle dependence is that the plasma pinch produces a highly directional deuterium cone-beam along the axis of the DPF. This beam has a nominal opening angle of about 10°, but the boundary is not sharp.

The filter foils were progressively thinner from left to right in Figure 6a (channel A1 was directly exposed to the plasma beam), but, corresponding with this trend, the number of proton tracks behind the filters should have increased from left to right because a greater number of low-energy protons would have been able to penetrate into the CR-39 plastic. However, a "peak" in the track densities appears in channels A9 and A8, and the tracks are not visible in channel A6 in the center of the spectrometer.

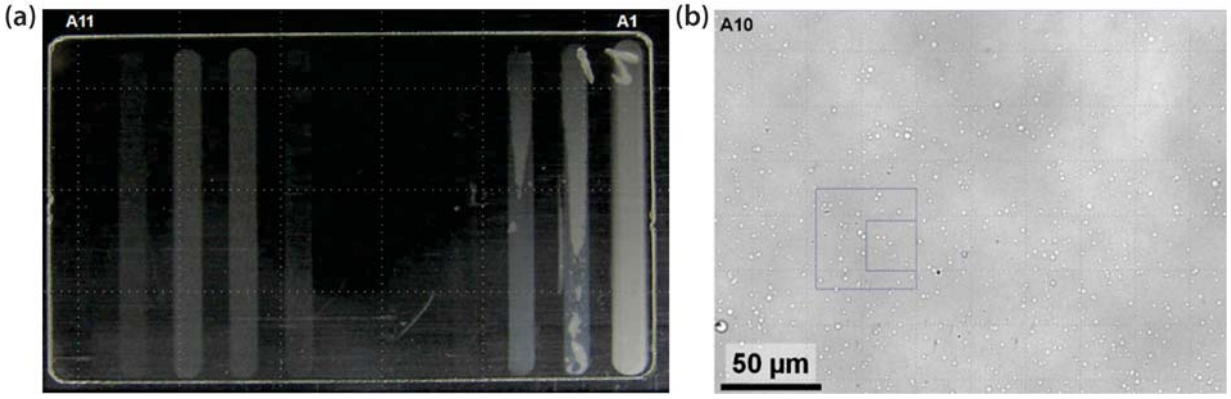

Figure 6. (a) A sample of the raw spectrometer data and (b) a 50x magnification of the tracks in column A10 with reflecting illumination. The sample was etched in a 22% concentration solution of sodium hydroxide.

This peak effect occurred because the spectrometer was intentionally under-etched; an incomplete etch was done to preserve the data under the thicker Al steps where the highest-energy protons were slowed to energies between 300 to 800 keV. If etched too long, these low-energy tracks would merge, making them hard to count. Another advantage of solid-state detectors is that the track damage is preserved over time and after multiple etch baths. Further etching will reveal currently invisible tracks in channels A6–A2. (At the time of this report, the high-energy channels were being analyzed. After these data are analyzed, a follow-on etch will be done to fully reveal the track density in the lower-order channels.)

A peak due to deuterons is seen in channels A4–A1. These tracks appear in the channels with the thinnest foils because the deuterons have much lower energies (35–100 keV) than the fusion protons. There is clear evidence of spall damage in channels A1–A3, and the analysis of the deuterium spectrum is doubtful.

Despite an incomplete set of data with the spectra, information can still be gleaned about the proton spectrum. Figure 6a shows that there is very little signal in channel A11; the first channel nearby with a significant track density is channel A10. Referencing the stopping energies for these channels in Table 1, we conclude that the maximum energy in the proton spectrum is between 3.4 and 3.7 MeV. Additionally, the step difference in the track count between channels A11 and A10 constrains the fall of the high-energy slope of the peak. Due to the very small signal in channel A6, we conclude from the etch calibrations (Jager 1985, Dörschel 1997) that all the particle energies are above 2.0 MeV. Assuming a Maxwellian source, we predict the proton spectrum will have a Gaussian shape with a mean of about 3.4 MeV and a sigma of about 300 keV.

To better validate our hypothesis regarding the normal distribution of the energy spectrum, we ran an MCNPX (Pelowitz 2008) calculation in which a proton source was defined with a Gaussian energy distribution where the mean energy was 3.4 MeV and the sigma was 300 keV. The source particles propagated in parallel through Al parallelepipeds defined with the

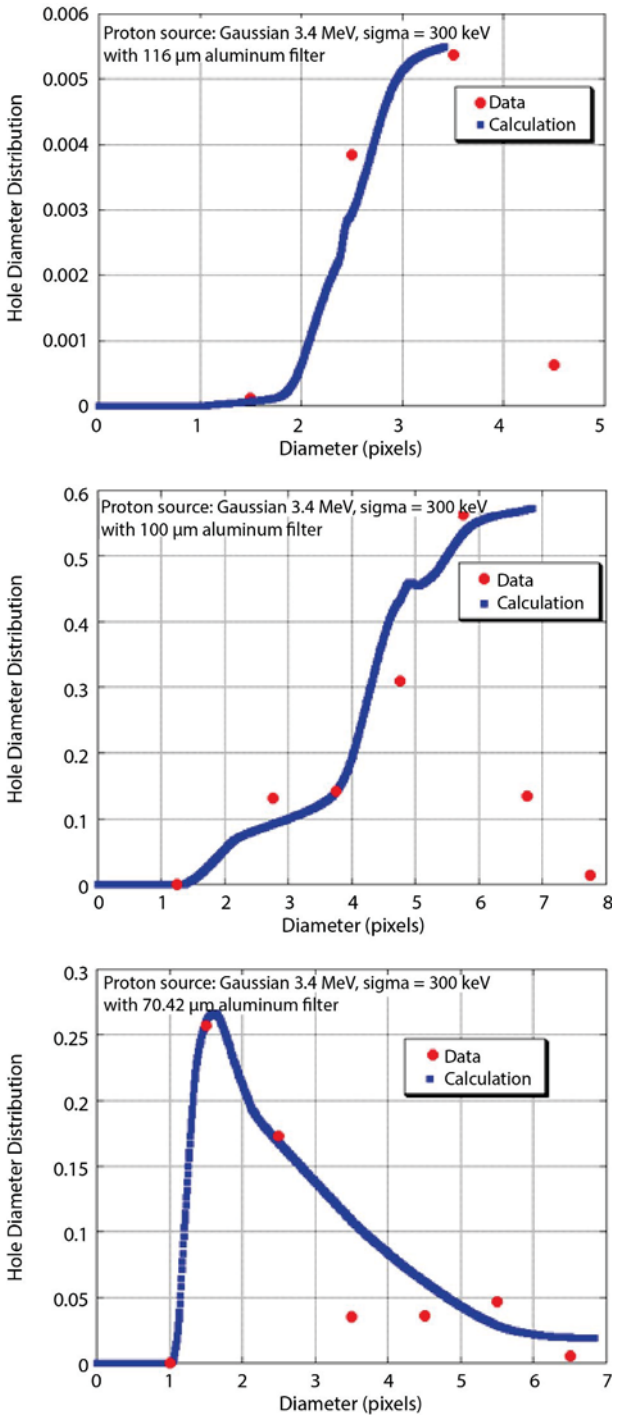

Figure 7. Calculations of the hole distribution for three channels assuming a Gaussian proton source with a 3.4 MeV mean energy and sigma of 300 keV compared with a histogram of the hole sizes for these channels from the spectrometer data

thicknesses listed in Table 1. The energy spectra on the downstream side of the Al were tallied. These spectra were then combined with proton-track calibrations with CR-39 plastic (Jager 1985, Dörschel 1997) to obtain histograms of hole-diameter distributions that are unique for each of the channels.

The calculated histograms are compared with histograms obtained from the data in Figure 7. Although track data have coarse resolution, there appears to be good agreement between the data and the predicted histograms across the entire set of spectra in the spectrometer channels. This good agreement verifies that the protons produced by the DPF have a nominally Maxwellian (thermal) distribution with an average peak energy close to 3.4 MeV that then rapidly falls to 3.7 MeV.

Variations can be seen in the histogram data with track diameters greater than ~3.5 pixels. This range of tracks is weighted with the protons that had less than or equal to 800 keV remaining after penetrating the aluminum filters. The presence of these tracks suggests there was an asymmetric low-energy tail in the proton spectrum below 3.4 MeV (consistent with spectra published by Jager [1985]). Thus, the plasma is only approximately Maxwellian.

Conclusion

In the DPF magnetic mirror project, we hypothesized that as the plasma collapses onto the pinch state consistent with the snow-plow model, magnetic field gradients would form a mirroring effect that would redistribute the deuterium ions toward the cooler regions, and this drift would increase significantly with increasing charging voltages and currents. Hydrodynamics calculations were run to determine the role these magnetic field gradients might play in the plasmas formed by the DPF. These calculations predicted that the maximum field gradients perpendicular to the collapsing plasma sheath prior to the pinch would be about 1.2×10^6 G/cm, which is not high enough to significantly influence the plasma density distributions. Deuterium pinhole images support this result, showing that as neutron yield increased with increasing currents, the plasma column actually became less diffuse, longer, and more concentrated with a stacked droplet structure on the pinch axis. MCNPX simulations were run to obtain an independent measure of the spectrum to compare with the subtractive method. Proton energies appear to be approximately Maxwellian with a 3.4 ±0.3 MeV peak and a low-energy tail.

References

Auluck, S. K. H., "Evaluation of Turner relaxed state as a model of long-lived ion-trapping structures in plasma focus and Z-pinches," *Phys. Plasmas* **18** (2011) 32508-1–32508-6.

Bennett, W. H., "Magnetically self-focusing streams," *Phys. Rev.* **45** (1934) 890–897.

Bennett, W. H., "Self-focusing streams," *Phys. Rev.* **98** (1955) 1584–1593.

Bernard, A., A. Coudeville, A. Jolas, J. Launspauch, J. de Mascureau, "Experimental studies of the plasma focus and evidence for nonthermal processes," *Phys. Fluids* **18** (1975) 180–194.

Butler, T. D., I. Henins, F. C. Jahoda, J. Marshall, R. L. Morse, "Coaxial snowplow discharge," *Phys. Fluids* **12** (1969) 1904–1916.

Dörschel, B., D. Fülle, H. Hartmann, D. Hermsdorf, K. Kadner, Ch. Radlach, "Measurement of track parameters and etch rates in proton-irradiated CR-39 detectors and simulation of neutron dosemeter responses," *Radiation Protection Dosimetry* **69** (1997) 267–274.

Fleischer, R. L., P. B. Price, R. M. Walker, "Solid-state track detectors: Applications to nuclear science and geophysics," *Annu. Rev. Nucl. Sci.* **15** (1965) 1–28.

Jager, U., L. Bertalot, H. Herold, "Energy spectra and space resolved measurements of fusion reaction protons from plasma focus devices," *Rev. Sci. Instrum.* **56** (1985) 77–80.

Keck, J. C., "Current distribution in a magnetic annular shock tube," *Phys. Fluids* **5** (1962) 630–632.

Krall, N. A., A. W. Trivelpiece, *Principles of Plasma Physics,* 1st edition, McGraw-Hill, New York, 1973, 37–38.

Krauz, V. I., K. N. Mitrofanov, M. Scholz, M. Paduch, P. Kubes, L. Karpinski, E. Zielinska, "Experimental evidence of existence of axial magnetic field in plasma focus," *Europhysics Letters* **98** (2012) 45001, 1–6.

Lee, P., A. Serban, "Dimensions and lifetime of the plasma focus pinch," *IEEE Trans. Plasma Sci.* **24** (1996) 1101–1105.

Miller, R. B., *An Introduction to the Physics of Intense Charged Particle Beams,* 1st edition, Plenum Press, New York and London, 1982, 154–170.

Pelowitz, D. B., editor, "MCNPX User's Manual," Version 2.6.0, LA-CP-07-1473, Los Alamos National Laboratory, Los Alamos, New Mexico, 2008.

Potter, D. E., "Numerical studies of the plasma focus," *Phys. Fluids* **14** (1971) 1911–1924.

NIST, "P-Star, Stopping power and range tables for protons," http://physics.nist.gov/PhysRefData/Star/Text/PSTAR.html, accessed September 10, 2013.

Robinson, A. C., et al., "ALEGRA: An Arbitrary Lagrangian-Eulerian multimaterial, multiphysics code," presented at AIAA-2008-1235, Proceedings of the 46th AIAA Aerospace Sciences Meeting, Reno, Nevada, 2008, 1–39.

Seguin, F. H., et al., "Advances in compact proton spectrometers for intertial-confinement fusion and plasma nuclear science," *Rev. Sci. Instrum.* **83** (2012) 10D908-1–10D908-3.

Sudan, R. N., "Stability of field-reversed, force-free, plasma equilibria with mass flow," *Phys. Rev. Lett.* **42** (1978) 1277–1281.

Turner, L., "Hall effects on magnetic relaxation," *IEEE Trans. Plasma Sci.* **14** (1986) 849–857.

Vikhrev, V. V., V. D. Korolev, "Neutron generation from Z-pinches," *Plasma Phys. Rep.* **33** (2007) 356–380.

Zakaullah, M., I. Akhtar, G. Murtaza, A. Waheed, "Imaging of fusion reaction zone in plasma focus," *Phys. Plasmas* **6** (1999) 3188–3193.

This page left blank intentionally

Time-Resolved Hyperspectral Frequency-Modulated Spectroscopy: Raman Scattering and DFT of Excited States

STL-51-13 | Continued from FY 2012 | Year 1 of 1

Gene A. Capelle,[1,a] John Di Benedetto,[a] and Mary D. O'Neill[a]

The scope of work for this project was to demonstrate the application of a new beat frequency frequency-modulated spectroscopy technique both to Raman scattering of excited states of selected materials and also to remote sensing of materials in outdoor scenarios. While the excited-state Raman measurements were not successful, the remote sensing application was very successful, as demonstrated by field tests in the Mojave Desert with measurements at distances up to ½ km during daylight hours.

[1] capellga@nv.doe.gov, 805-681-2252
[a] Special Technologies Laboratory

Background

A new frequency-domain measurement technique for measuring both spectral signatures and approximate lifetimes of fluorescent materials has been developed over the last few years with SDRD support (Di Benedetto 2012a, Capelle 2013). The basic technique has been described in detail in a recent publication (Di Benedetto 2012b). Since its initial demonstration, the technique, time-resolved hyperspectral frequency-modulated beat frequency spectroscopy (or the beat frequency technique for short) has been applied to a number of different scenarios; it has also been tested for efficacy as an alternate and potentially superior measurement technique to currently used methods. The beat frequency technique was first successfully demonstrated for materials in the laboratory, with controlled ambient light environments and distances up to a meter. The second successful demonstration was in microscopy, where it was shown that spectra and approximate lifetime could easily be collected from a 14-micron-diameter particle on a microscope slide (the size limitation was a function of available lenses for the particular microscope at our disposal; considerably smaller particles could have been measured with different optics).

This year, we investigated two other possible applications of the technique: as a method for measuring excited-state Raman scattering, and as an alternative to time-domain methods for outdoor remote sensing measurements at large standoff distances. These two applications will be treated separately below.

Project

Excited-State Raman Measurements

We used two lasers and a modification of the beat frequency technique to detect excited-state Raman scattering signals from samples of interest. The first laser, or pump laser, operates at frequency f_1 in either the standard 50% duty factor mode or a short-pulse mode, and at a wavelength that creates an excited-state population in the material being studied. The second, or probe, laser operates at a different wavelength and in a short-pulse mode, nominally 10 ns wide in the experiments described herein, at frequency f_2. The detector gate is timed to be 10 ns wide and simultaneous with the probe laser pulse. Because Raman scattering is prompt, it will be present

only when the probe laser beam is present. Therefore, keeping the probe laser and detector gate simultaneous and of short duration discriminates against background fluorescence for the materials we are investigating, which have radiative lifetimes typically much longer than 10 ns. Excited-state Raman scattering signal(s) should be recognizable by their presence only when the probe laser is present and simultaneously when there is an excited-state population present from which to scatter. Because of this, the excited-state Raman signal should have a component at the difference (beat) frequency, $f_1 - f_2$. A number of different lasers at different wavelengths, all known to produce excited-state populations in the materials being tested, were used as the pump source, including a pulsed laser at 355 nm, a modulatable laser at 402 nm, and both a modulatable and a pulsed laser at 532 nm. The probe laser provided a short pulse at 355 or 532 nm. The 402 nm laser output was 250 mW or less; the pulsed 355 and 532 nm lasers produced 6 and 30 mJ per pulse, respectively, at 10 Hz.

Remote Sensing Measurements

In early fall of 2012, a trailer-mounted measurement system was deployed for approximately one week at the Cuddeback dry lake bed in the Mojave Desert, a location that allowed us to make measurements at long standoff distances in an outdoor setting (Figure 1). This trailer-mounted system, which was for the most part built in FY 2012 and described in last year's SDRD final report (Capelle 2013), consists of five 402 nm diode lasers as the excitation source and a 14-inch-diameter light-collection telescope coupled by fiber-optic bundle to an intensified charge-coupled device (ICCD)/spectrograph combination for detection, all mounted on an accurately and remotely controllable gimbal. The five lasers are mounted on the outer diameter of the telescope; each one can be fine-tuned in elevation and azimuth to account for parallax errors as the target standoff distance changes. Additional support equipment includes computers for gimbal and ICCD control and data collection, power supplies, signal generators, and diesel-powered generators for operation in the field where no electrical hookups are available. Two video cameras provide visual displays; one is mounted at the telescope diameter edge to aid in approximate alignment of the telescope to distant targets, and the other looks through the telescope to provide more precise pointing of the gimbal and to allow visual alignment of each of the 5 lasers on the distant targets. The total average emitted laser power is typically 1.25 W with all lasers operating at 50% duty factor. Spectra can be collected simultaneously from 350 to 750 nm with 3–4 nm resolution over the entire region. The system was operated in the manner previously described for use on the Special Technologies Laboratory outdoor laser range (Capelle 2013), with the lasers driven at frequency f_1 to produce square-wave output at 50% duty factor. The detector was gated at frequency f_2, also with a 50% duty factor; f_1 was slightly faster than f_2, such that the difference between the two gave a beat frequency of 0.5 Hz, the beat that we measure.

Three targets were used in the outdoor field tests, and each one was applied to a 48" × 48" × ¼" white enameled aluminum honeycomb panel, chosen for its light weight and stiffness. The first target was a fluorescent red paint, obtained at a local hardware store and sprayed on a panel; it was used primarily for initial location of the laser beams at long distances, and for subsequent alignment of the five beams to a center point. The second target was ruby sand (approximately 1.5 kg of synthetic ruby scrap, crushed to a coarse sand consistency, provided courtesy of Chatham Created Gems & Diamonds, San Francisco, California) mixed into a UV-transmitting epoxy and painted onto a panel. The third was a phosphor material (YOSR05 from PhosphorTech, Kennesaw, Georgia), also mixed in the epoxy and painted onto the panel (Figure 2). All targets give visible fluorescence when excited by a 402 nm laser; the paint is "prompt" (radiative decay time less than 10 ns). The ruby radiative decay time is near 3 ms, while the phosphor is near 350 µs. Targets were mounted in the back of a flatbed truck so we could easily move them any distance (Figure 3a). The diode lasers were individually optically corrected to better than 1 mrad divergence, full angle, so they gave a spot less than 1 meter (longest axis) at 1 km distance (Figure 3b).

Figure 1. Trailer-mounted system stationed in the Mojave Desert. The small "dot" near the end of the road in the distance is a flatbed truck with one of the 48" square targets at 1 km.

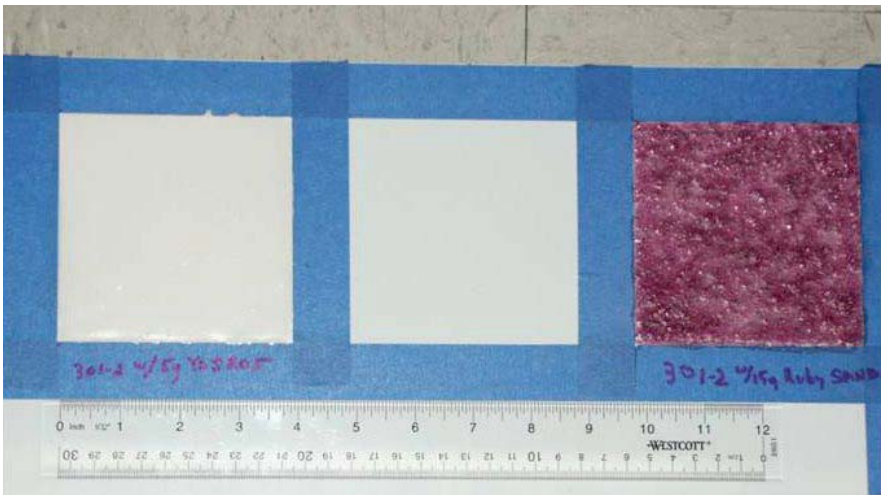

Figure 2. Smaller versions of targets (from left to right: phosphor, blank, and ruby) on aluminum honeycomb; actual targets were 48" × 48" × ¼"

Data and Results

Raman Measurements

For initial system tests, we began by measuring ground-state Raman signals from a number of (non-fluorescent) materials, including diamond, zircon, and sapphire, using 532 nm excitation and 50% duty factor on the laser output. The signal from the diamond material is shown in Figure 4.

Upon transitioning to targets from which we hoped to detect excited-state Raman signals, we found that even the ground-state Raman signals were swamped by sample fluorescence. While many Raman measurements use laser excitation at long wavelengths to avoid this fluorescence problem (longer wavelengths tend to produce less fluorescence and position the resulting Raman lines at wavelengths longer than the emission band of any fluorescence that may be produced), this was not an option to us. This limitation resulted because we intentionally used shorter laser

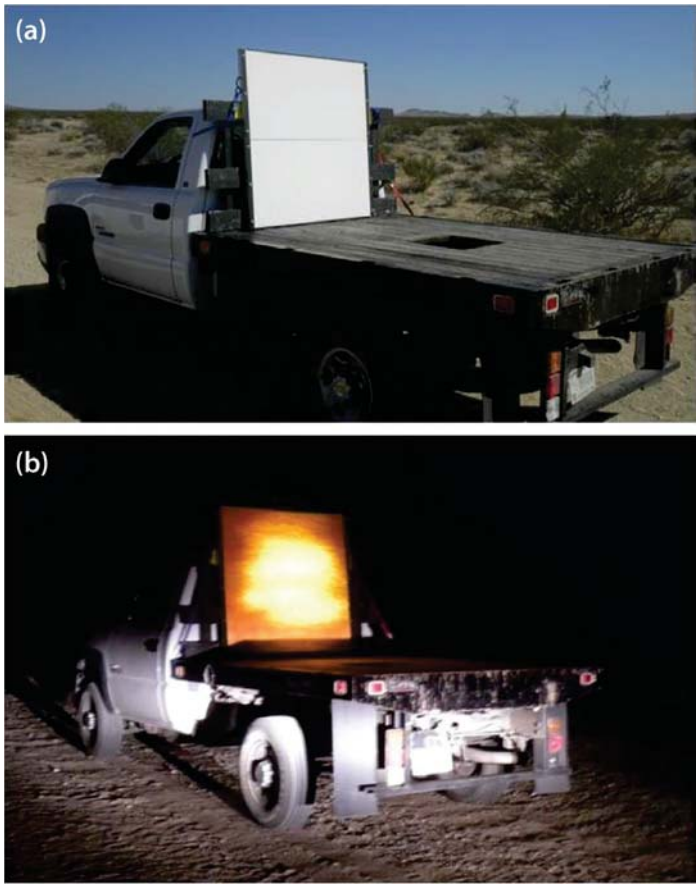

Figure 3. (a) Phosphor target mounted on flatbed truck. (b) Truck-mounted ruby target at night, illuminated by car headlights and by the five lasers at 1 km distance.

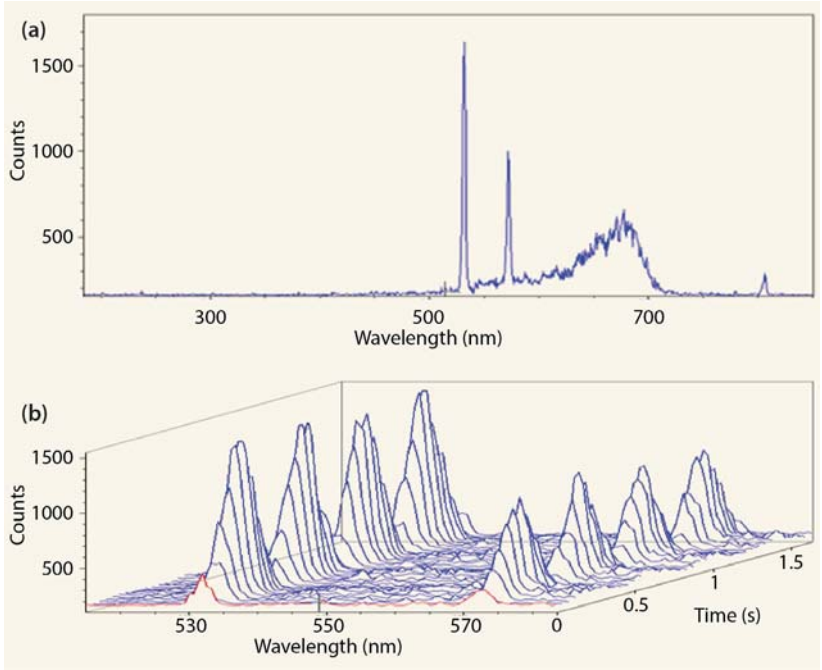

Figure 4. (a) Single-frame Raman signal from the diamond material; the two sharp lines are, from left, a 532 nm excitation line (reduced 5 to 6 orders of magnitude by a notch filter) and a diamond Raman line. (b) 40 frames of the curve in (a) containing laser and Raman lines, showing beat waves at 2 Hz = $f_{laser} - f_{detector}$ for both the laser and the (prompt) ground-state Raman signal.

wavelengths to produce an excited-state population from which we hoped to demonstrate Raman scattering; as well, our ICCD detector was not sensitive to wavelengths longer than 750 nm.

To mitigate the fluorescence problem, we changed from a 50% duty factor for the probe laser and detector to a short-pulse technique with a 10 ns wide detector gate centered on a 10 ns laser pulse. This change enabled us to detect ground-state Raman signals from the targets we were using, including a naturally occurring phosphor-containing mineral (Figure 5) and another phosphorescent sample as well as from a sample of $Ru(bpy)_3^{2+}$ in acetonitrile at 6.7×10^{-4}M concentration and contained in a 1 cm pathlength quartz cuvette. Confirmation of some of the ground-state Raman lines were confirmed by comparison with literature reports (Schoonover 1998, RRUFF 2012).

When the natural mineral, the green phosphor sample, and the $Ru(bpy)_3^{2+}$ solution were irradiated with 532 or 355 nm, strong luminescence was produced (with lifetimes on the order of 5 microseconds, several hundred microseconds, and less than 1 microsecond for those samples, respectively). This strong luminescence indicates a significant excited-state population was created in each case. When looking for excited-state Raman scattering after the pump was added to each of the phosphor-containing materials (532 nm probe, observe near 532 nm, and add pump at 355 nm; and 355 nm probe, look near 355 nm, and add pump at 532 nm), no additional lines were detected. However, there were some subtle spectral changes with the $Ru(bpy)_3^{2+}$ solution, which could be due to excited-state Raman scattering. Unfortunately, this was discovered late in the fiscal year and could not be further pursued.

Remote Sensing Measurements

Tests of the beat frequency technique as a remote sensing tool were carried out during full afternoon sun (shining directly on the target) as well as near sunset. Measurements were made with the targets at 50, 200, 500, and 1000 meters. Data were analyzed as described previously, yielding both phase shift and radiative lifetime as a function of frequency. The frequency was varied over a number of discrete values chosen to yield phase shifts both less than and greater than 45° for each target; for the ruby the frequency range was 20–800 Hz, and for the phosphor it was 50–4000 Hz.

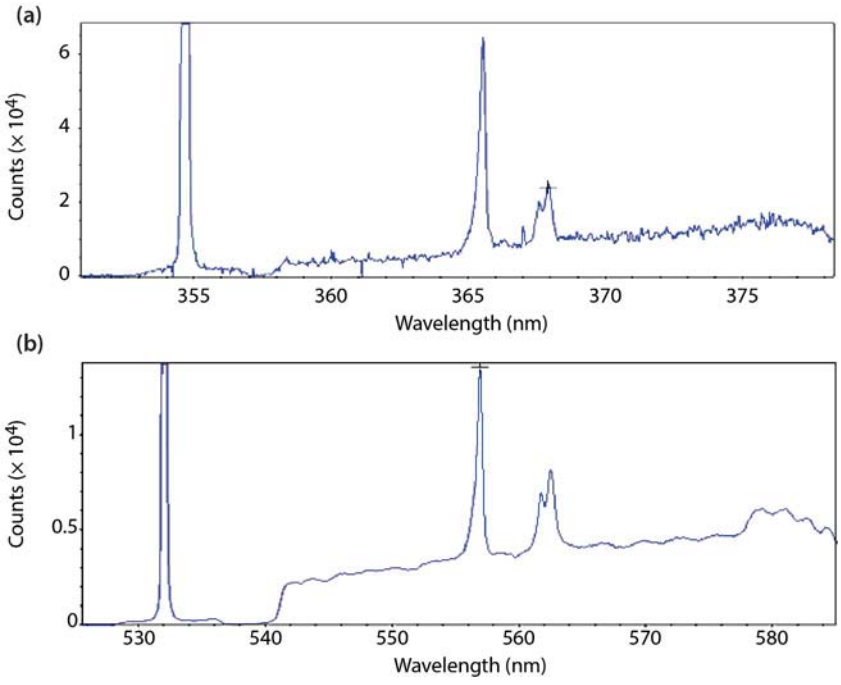

Figure 5. Ground-state Raman spectra for the mineral phosphor with (a) 355 nm excitation and (b) 532 nm excitation

Figure 6 is a sample of the raw data collected for the ruby target in full afternoon desert sun at a 200 meter distance; it shows the full spectrum collected over 120 camera frames (z axis). The (clipped) triangle wave at the left of Figure 6 is the collected laser return at 402 nm, as is the second order of the laser at 804 nm. The feature at 695 nm is the strongest feature of the ruby emission. From the figure, it is clear that the ruby signal is modulated and phase shifted (the frame in red is at the peak of the ruby emission, but significantly shifted from the peak of the 402 nm excitation beat wave). While the ruby beat wave is also increasingly demodulated with increasing frequency, the larger part of the unmodulated component of the ruby signal is due to solar stimulation of the ruby emission. This solar stimulation, with its inherent noise, is one of the primary factors limiting the maximum distance at which this technique works in daylight. (Solar-induced atmospheric turbulence is also a significant factor at longer distances.) Figure 7 shows the lifetime calculated from the 200-meter data as a function of excitation frequency. The calculated lifetime is reasonably accurate until the frequency reaches sufficiently high values where demodulation excessively reduces the signal level. Figure 8 shows the return signal from the ruby target at 6:15 PM (sun low on horizon, target in shadow) with the target at a 0.5 km distance and with 100 Hz excitation frequency (also over 120 frames). Note the improved signal-to-noise ratio in the absence of strong solar stimulation. The phase shift is slightly higher in this data set due to the higher excitation frequency. These data also yielded the correct estimate of lifetime at excitation frequencies up to several hundred hertz.

Data sets were also collected using the phosphor target placed at distances of 200 and 500 meters in daylight. The phosphor target was more difficult to see than the ruby, due to its weaker response and strong solar excitation. Nevertheless, reasonable results were obtained at the 200-meter standoff distance, including a reasonable estimate of the magnitude of the lifetime. Collected spectra are shown in Figure 9.

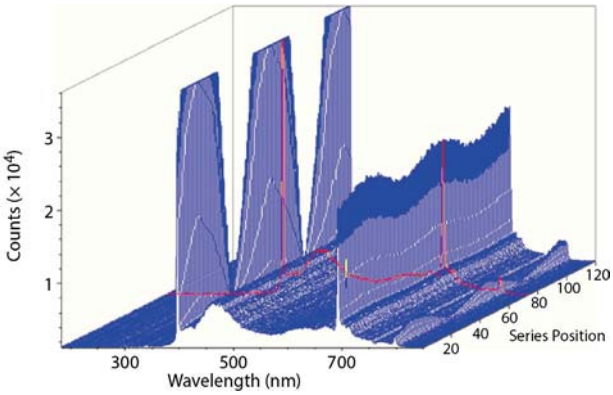

Figure 6. Ruby target at 200 meters, 2:30 PM, with target in full sun; 50 Hz with 0.5 Hz beat frequency; 120 CCD frames

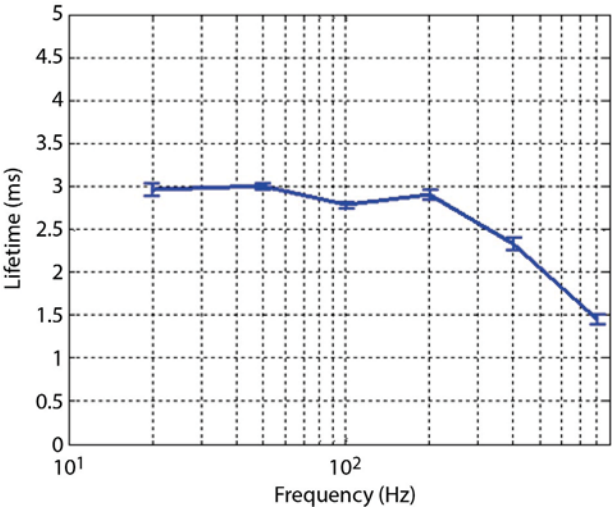

Figure 7. Lifetime of the ruby target, as a function of excitation frequency, at 200 meters in full sun (calculated from collected data)

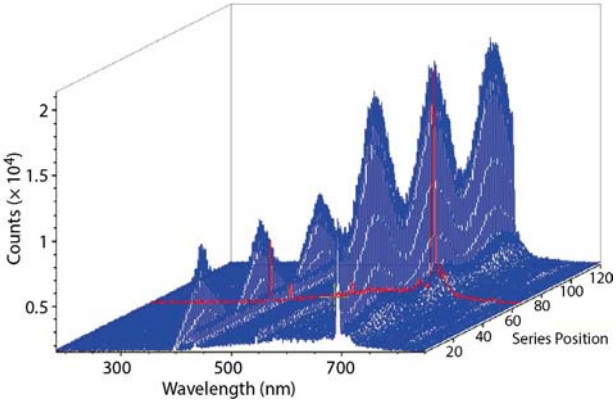

Figure 8. Ruby target at 0.5 km, 6:15 PM, with target in shade; 100 Hz with 0.5 Hz beat frequency; 120 CCD frames

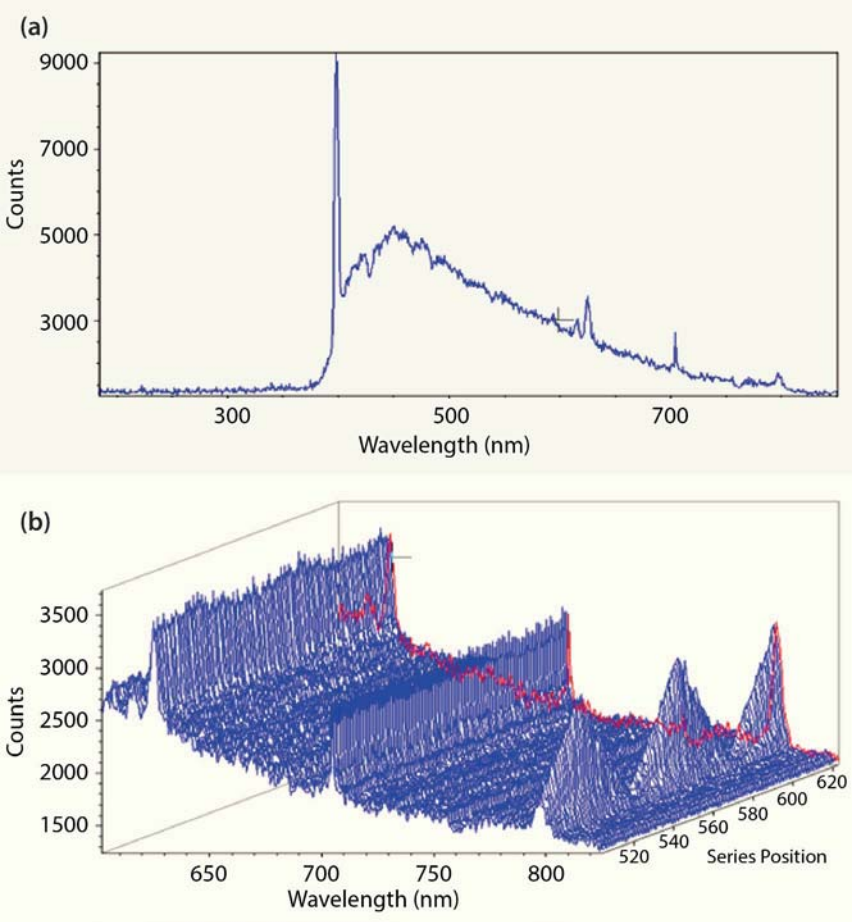

Figure 9. Phosphor target at 200 meters, 3:00 PM, 50 Hz with 0.5 Hz beat. (a) One frame showing laser return near 400 nm and phosphor lines near 625 nm (there is a hot pixel near 700 nm and a second-order laser line near 800 nm). (b) Expanded version of the region between phosphor lines and second-order laser line showing 120 CCD frames; modulation in the phosphor signal is clearly visible despite a high solar-stimulated component.

Conclusion

Our attempts to detect excited-state Raman scattering from phosphor-containing compounds have so far been unsuccessful. To be successful with these materials, it appears that, at a minimum, better equipment and considerably more effort would be necessary. Specifically, because of the short laser and detector pulse widths, weakness of the excited-state Raman signal, and the fact that any attempt to increase the laser power on target led to burning of the sample, the most helpful improvements would be (1) much higher repetition-rate lasers (at least 100x or more, depending on material lifetime), (2) a spectrograph with even less scattered light (for such experiments, a triple monochromator is typically used [Schoonover 1998]), and (3) a quieter, more red-sensitive detector.

The remote sensing field test demonstrated the beat frequency technique to be a viable method for making visible spectral and approximate lifetime measurements of fluorescent materials at relatively large standoff distances during sunlit conditions. While both samples could be measured in full sunlight at 200 meters and one at 500 meters with our first-generation field system, we believe that detection at much longer distances (many kilometers) can be achieved after sunset. These demonstrations, however, must await the second field test, which we plan to carry out in cooperation with another project.

Acknowledgments

We would like to thank Steve Jones for his help in solving some challenging software problems.

References

Capelle, G. A., J. Di Benedetto, M. O'Neill, "Time-resolved hyperspectral fluorescence spectroscopy using frequency-modulated excitation—applications," *Site-Directed Research and Development*, FY 2012, National Security Technologies, LLC, Las Vegas, Nevada, 2013, 67–76.

Di Benedetto, J., G. A. Capelle, M. O'Neill, "Time-resolved hyperspectral fluorescence spectroscopy using frequency-modulated excitation," *Site-Directed Research and Development*, FY 2011, National Security Technologies, LLC, Las Vegas, Nevada, 2012a, 87–96.

Di Benedetto, J., G. A. Capelle, M. O'Neill, "Time-resolved hyperspectral fluorescence spectroscopy using frequency-modulated excitation," *J. Appl. Phys.* **112**, 1 (2012b) 013109.

RRUFF Project database, "Raman spectra for autunite," Department of Geosciences, University of Arizona, http://rruff.info, accessed June 17, 2012.

Schoonover, J. R., G. F. Strouse, "Time-resolved vibrational spectroscopy of electronically excited inorganic complexes in solution," *Chem. Rev.* **98**, 4 (1998) 1335–1356.

Development of an X-Ray Radar Imaging Technique for 3-D Scene Scanning

LAO-09-13 | Continued in FY 2014 | Year 1 of 2

Wendi Dreesen,[1,a] Mark Browder,[b] Rick Wood,[b] Carl Carlson,[a] Nick Kallas,[a] Craig Kruschwitz,[a] David Schwellenbach,[a] Sara Thiemann,[c] and Aric Tibbitts[a]

The goal of this project is to develop a 3-D imaging technique called x-ray radar, a concept recently patented by Lockheed Martin and experimentally studied by NSTec using the Los Alamos Operations (LAO) 2 MeV electron linear accelerator (linac). X-ray radar combines radar techniques with the penetrating power of x-rays. The radio frequency (RF) microstructure of the x-ray pulse is exploited to process x-ray signals using radar techniques. This technology has multiple advantages over current 3-D imaging technologies, such as one-sided access to the scene and improved signal-to-noise ratio over other detection schemes, and it uses the versatility of the LAO linac to perform differential imaging. In the first year the majority of the work involved modifications to the linac to meet experimental requirements and to run basic experiments to verify the ability to derive distance from changes in the phase of a moved x-ray detector. Results show linac performance issues and low signal to noise in the detectors, but also show promise. The second year of the project will include ensuring the phase distance measurements are accurate and repeatable, performing detector studies, and proof of concept experimentation to extract 3-D data from a scene.

[1] dreesewm@nv.doe.gov, 505-663-2050
[a] Los Alamos Operations; [b] Lockheed Martin; [c] Keystone International, Inc.

Background

A U.S. patent on the concept of x-ray radar was recently awarded to Lockheed Martin (Wood 2013). The technology uses radar signal processing techniques on a signal produced by radio frequency (RF) modulated x-rays rather than the standard RF electromagnetic (EM) waves used by traditional methods. X-rays can penetrate metal walls, whereas standard EM waves at radio frequencies would reflect off metal walls. Using an impulse radar technique (Azevedo 1996) and frequency domain techniques, we have modeled our experiment and compared the model to measurements taken using the Los Alamos Operations (LAO) electron linear accelerator (linac).

An example of the application of ranging techniques to discriminate structures in a given volume is a modulated light detection and ranging (lidar) system constructed by Lockheed Martin. The detector measures the amplitude of the modulated light signal, and this signal is stored. The stored signal is compared with the stored transmitted reference signal, and the phase difference between the two signals is computed and stored. This phase difference is proportional to the range delay in the reference image. The phase information can be plotted in the same scanning format in which the signal was collected to form a range image, where black represents near range, white represents far range, and intermediate ranges take on a grayscale value. Figures 1 and 2 show ranging images where the

Figure 1. Near-range gated image of scene, in which black is mapped to shortest range in gate and white to the longest. The two vehicles are poorly identified.

Figure 2. Far-range gated image of scene, in which two vehicles appear as distinct from other objects in the scene at different ranges

vehicles are outside (Figure 1) and inside (Figure 2) the ranging values, respectively. As these figures show, the ranging technique can improve the signal-to-noise ratio for imaging. X-ray radar relies on the same range delay technique, but it will be implemented using modulated x-rays rather than light. Once the preliminary phase/distance measurements prove the basic physics, the next phase of the project will seek to evaluate and select image-forming techniques.

Project

Experiment Definition

The goal of this project is to experimentally verify implementation of the x-ray radar concept. Objects of interest are placed in the field of view of an x-ray pulse from the linac, and the scene is flooded with RF modulated x-rays (Figure 3). An array of detectors measures the reflected backscatter signal. By implementing radar signal processing techniques, enough information is available to form a 3-D image. Initial experimentation is in transmission mode to simplify the system in order to refine the techniques through basic first-principles measurements.

Radar uses a ranging and detection algorithm that relies on time delays of a signal reflected off of an object.

$$d = \frac{ct}{2} \quad (1)$$

The radar equation in one-dimension gives a distance (d) based on the speed of light (c) and the time of flight (t) divided by two, to compensate for the distance traveled to and from the backscattered object. Because the relative phase of a signal is related to the time of flight, radar techniques include methodologies using time domain analysis and frequency domain analysis. More sophisticated models can be used to extract 2-D and 3-D information.

The LAO linac can generate electrons with energies ranging from 100 keV to approximately 2 MeV. Long- and short-pulse bursts of electrons can be generated; however, each type requires a different radar processing technique. For short-pulse electron bursts, the accelerator generates a 1 ns pulse that is accelerated through the RF cavities, and the 2.856 GHz RF waveform is superimposed on the pulse. A time-based radar ranging technique can be applied to analyze the backscattered waveform. The technique we selected, impulse radar (Azevedo 1996), transmits a short pulse and receives one or more reflections. The delay of each reflection is then correlated with distance. As the phase ambiguity limits distance measurements to one wavelength, impulse radar makes slight time delays on each transmitted pulse that essentially equates to a range sweep over the volume of interest. Using fast photodiodes to detect the reflected x-rays, we can deconvolve the signal and generate a depth map of the volume being scanned.

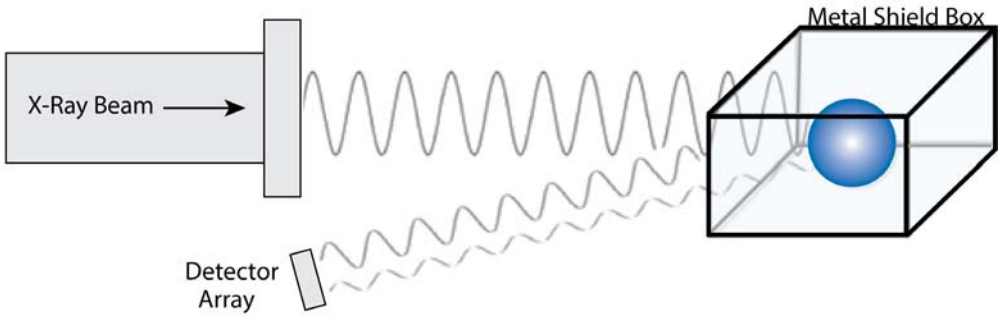

Figure 3. Conceptual diagram of the experimental setup

Using the linac in long-pulse mode drives the use of a frequency-based radar approach. Accelerating a 100 ns pulse through the RF cavity creates a 100 ns pulse with a 2.856 GHz microstructure superimposed on the long pulse. We then use the intra-pulse modulation signal to analyze the scanned volume. When using a long pulse, we use a frequency domain technique that uses an FFT of the x-ray signal generated by the long pulse. This FFT gives us the magnitude and phase of the x-ray signal with respect to the frequency domain; phase can be used to calculate the range.

Linac Hardware

This project experienced several technical challenges during the initial experiments. Hardware improvements were made to the linac in order to attain the operational stability required for these experiments. Additionally, this project called for new linac operating parameters to meet the tight timing and low jitter requirements inherent in our x-ray radar experiments.

The first hardware issue to be addressed involved an electron gun failure. We found the cause of the problem was metal fatigue in the gun adapter assembly. It was repaired and put back into service.

The second hardware issue pertained to the injector control system, which makes adjustments to amplifiers, power supplies, and other components that are floated at 100 kV. The original three-channel analog control system for the injector was failing, and it was operated in open-loop mode, which did not meet the precise adjustment needs of x-ray radar experiments. We replaced the analog system with a National Instruments (NI) Compact Real-Time Input Output

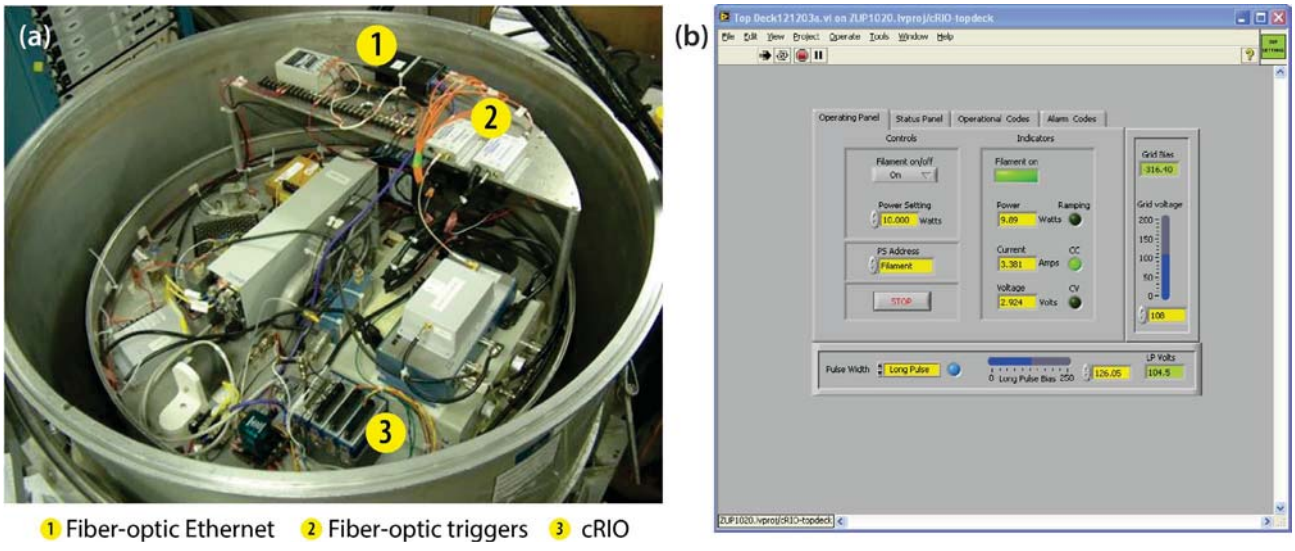

1 Fiber-optic Ethernet 2 Fiber-optic triggers 3 cRIO

Figure 4. The (a) upgraded top deck and the (b) LabVIEW interface for injector control

(cRIO) unit and wrote LabVIEW software to control the system. The new system is shown in Figure 4a, and the software user interface is in 4b.

RF Solution Evaluation

The next challenge was to determine our jitter requirements and find hardware that could perform better than the specifications. In order to maintain pulse-to-pulse stability on the linac and meet the goal for sub-centimeter-range resolution ($\Delta d = c\Delta t/2 = c$ 10 ps/2 = 0.15 cm), a system was needed to generate the 2.856 GHz RF for the accelerator and the logic pulses synchronized to the RF; the maximum acceptable jitter was 10 ps. An additional requirement for a phase-synchronized 219.69 MHz signal, a sub-harmonic of the 2.856 GHz, was included for future implementation of the sub-harmonic buncher on the linac. We evaluated three RF products from Agilent, NI, and Tektronix. The Agilent and NI solutions did not meet the jitter requirements for this project.

The Tektronix 7122C arbitrary waveform generator (AWG) was the most promising candidate because it claimed sub-picosecond jitter between the 0° phase of the RF frequency and either of the digital signals out, which Tektronix refers to as a digital marker. The AWG shows DAQ noise, which was initially unacceptable, but after adding an analog low-pass filter the signal met the requirements for this project. We tried three different measurement techniques using a Tektronix four-channel 20 GHz oscilloscope; measurements ranged from 0.7 to 3 ps, all within our specified jitter parameter. The AWG generates two programmable RF waveforms and four digital markers. The cost of purchasing an AWG was prohibitive, so we leased a unit for 4 months. Alternate systems for time synchronization as well as rental of the AWG are being considered for next year. Figure 5 shows the output of the Klystron versus the digital marker in comparison to a low-pass filtered AWG output.

Detector Evaluation

Using x-ray detectors capable of resolving 3 GHz–modulated x-rays was a significant challenge for this project. The fastest commercial x-ray detector identified at the beginning of the project was the Optodiode AXUVHS6 coupled with a Picosecond Pulse Labs 5530/5543 bias tee. The 50 ps rise time of this detection system was dominated by the Opto Diode Corp. detectors. Because the estimated width of the microstructure pulses from the linac is 30 ps, this detection system cannot give full temporal information about the x-ray pulse. However, these detectors can resolve the 350 ps (2.856 GHz) microstructure spacing.

With the initial experimental setup complete, and without amplification, the diodes read from 5 to 14 mV, requiring the highest gain setting on the 20 GHz oscilloscope. In these experiments, we directly measured x-ray intensity close to the x-ray source. Future measurements at greater distances and reflected x-rays will require the use of high-quality amplifiers.

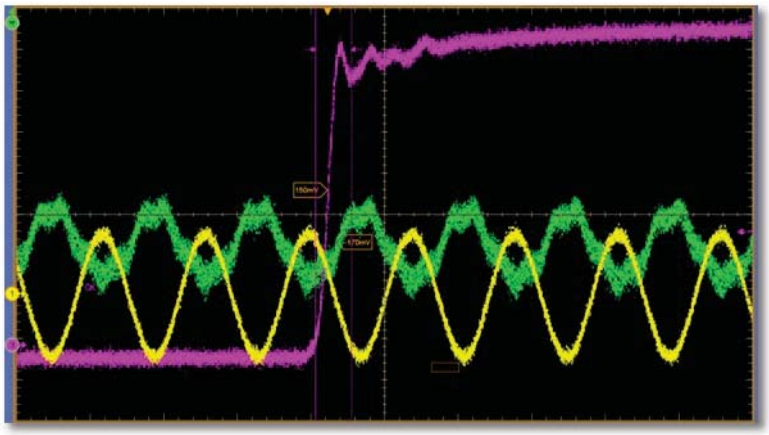

Figure 5. Visual representation of jitter using infinite persistence on the oscilloscope. The AWG marker (purple) was used as the trigger. The jitter is measured relative to the marker of the 2.856 GHz RF signal generated by the AWG and filtered (yellow). The output of the klystron (green) is driven by an unfiltered output of the AWG.

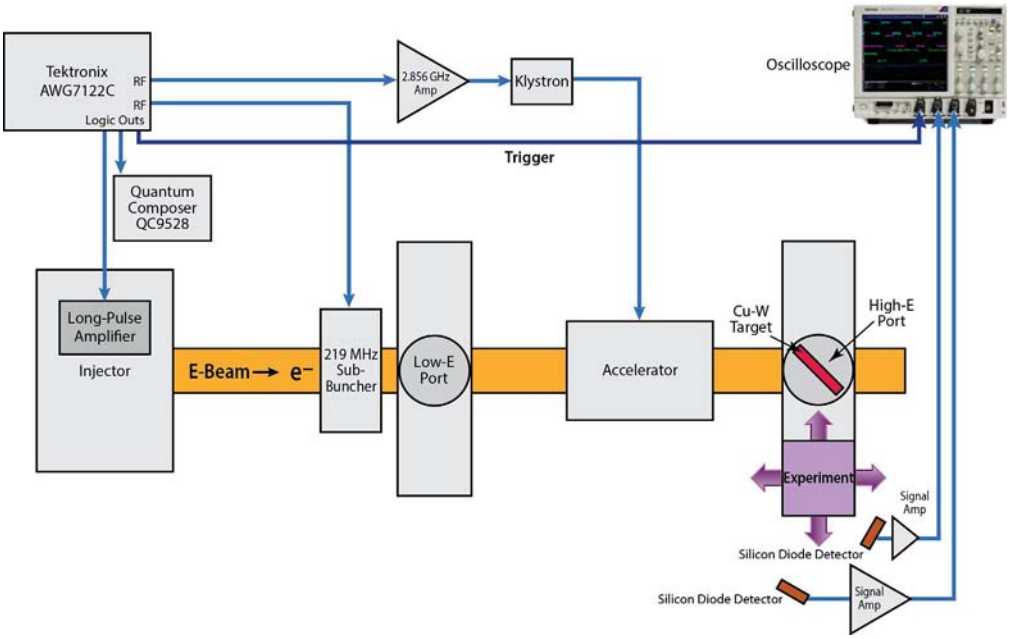

Figure 6. System diagram and experimental setup for accelerator operation includes synchronization of RF with injected electron pulse and with oscilloscope for data acquisition

Furthermore, when we send a long pulse through the accelerator and modulate it at 2.856 GHz, the Faraday cup sees the full depth of modulation, but the diodes will not, due to their longer recovery time. We have acquired faster Opto Diode detectors with rise times of 2 ps that will be evaluated in FY 2014. We have also discussed other possible candidates, such as fast scintillators or vacuum Compton diodes, and plan to explore any additional commercially available higher bandwidth detectors that were not available at the onset of this project.

Building a New System for Running and Triggering the Accelerator

Figure 6 shows the system diagram of the experimental setup indicating synchronization of the linac's electron gun with the RF burst. The klystron supplies a fixed 4 µs burst of RF energy, and the electron pulse must be injected at a stable, flat-topped region within that burst. The injector has considerable volume for installing bench-top amplifiers and delay units for firing the electron gun. In its current configuration, the injector has a short-pulse amplifier that fires 1 ns electron pulses triggered by a rising edge. It also houses a long-pulse amplifier capable of different pulse lengths ranging from 40 ns to 1 µs. The system's master clock is a Quantum Composer trigger delay unit capable of triggering up to eight channels. The Tektronix AWG is controlled by the master clock to generate a 2.856 GHz sinusoidal 4 µs burst to the klystron. The klystron feeds its (1 MW) energy into the waveguides to the accelerator. We investigated using the 90 keV low-frequency port for these experiments, but the penetration energy was too low. We then moved to the high-energy port that we estimate is running about 1 MeV. We do not currently have a spectrometer to measure the exact energy. At this port we can make transmission and backscatter measurements; our ultimate goal is to make backscatter measurements to extract 3-D information from one side of a scene.

Modeling

MCNPX

In parallel with preparing the accelerator to handle derived range measurements, we also prepared software models of the x-ray flux and the basic backscatter approach to transmitting and receiving the

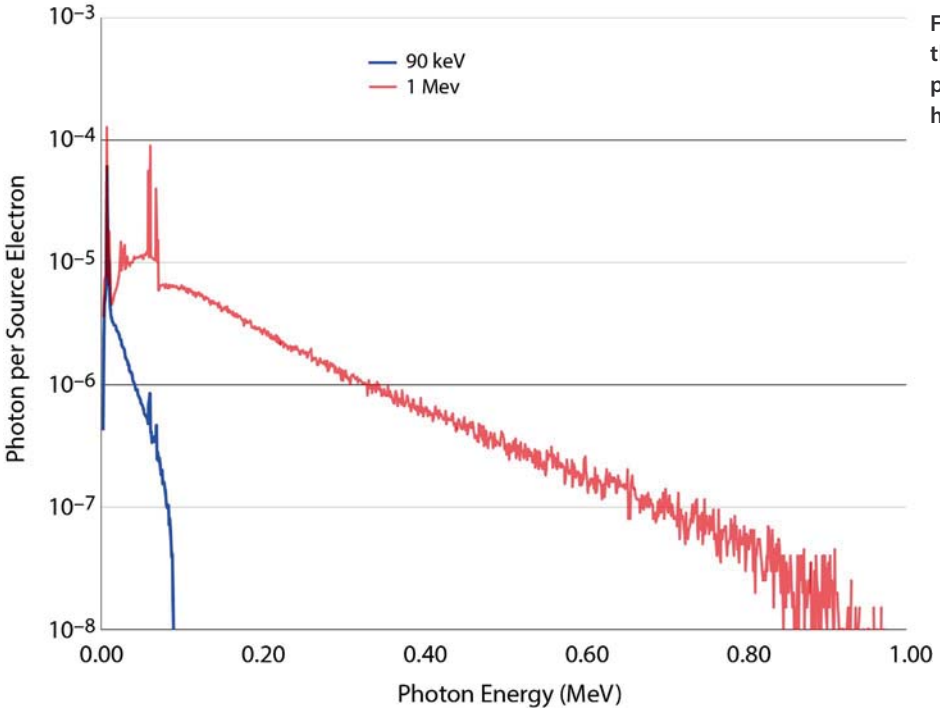

Figure 7. MCNPX model of the photons generated vs. photon energy at the high-energy port

signal. MCNPX simulations were performed to determine our x-ray energy spectrum electron energies of 90 keV and 1 MeV, as shown in Figure 7. These simulations were consistent with experimental results on the low-energy port, showing that we did not have sufficient energy for penetrating metals expected to be used in imaging tests. This result, combined with the higher modulation frequency available, makes the high-energy port the primary x-ray source for experiments.

Impulse Radar

The model includes two scenarios: operation of the linac at the low-energy port or the high-energy port. Modeling low-energy port operation meant that lower frequencies would be used. Lower frequencies, with corresponding longer wavelengths, meant that we can only detect down to centimeter sizes using hundreds of megahertz modulation frequencies, and so the low-energy model was dubbed the large box scenario. Modeling the higher-energy port after the RF acceleration portion of the linac allowed for pulses modulated at 2.856 GHz, and so the high-energy model was dubbed the small box scenario.

In the small box scenario, there are three infinite planes located at 3, 5, and 7 cm in the model. The pulse train is transmitted and essentially convolved to show the reflected interaction with the three planes. Figure 8b shows the anticipated reflected signals detected by the photodiode or other photodetector. Figure 8a shows a zoomed in portion of the received pulse train to show the derived distance of the reflection planes for one transmitted pulse. The tallest pulse is the transmitted pulse, which can be filtered out, and two of the reflections are clearly seen at 3 and 5 cm. There is uncertainty of the position of the third reflection at 7 cm, as it is at the edge of the resolution of the model.

Referring back to Figure 1, a single pixel in that scaled scene (the vehicle scene being greatly reduced in size) could represent the 3 cm range return signal shown in Figure 8a. After scanning all the pixels, the various ranges from ~0 cm to just beyond 3 cm would be mapped in grayscale from black (0) to white (3), resulting in the image in Figure 1. By moving the range mapping window to start at 3 cm and end just beyond 5 cm, the scaled scene in Figure 2 could be realized.

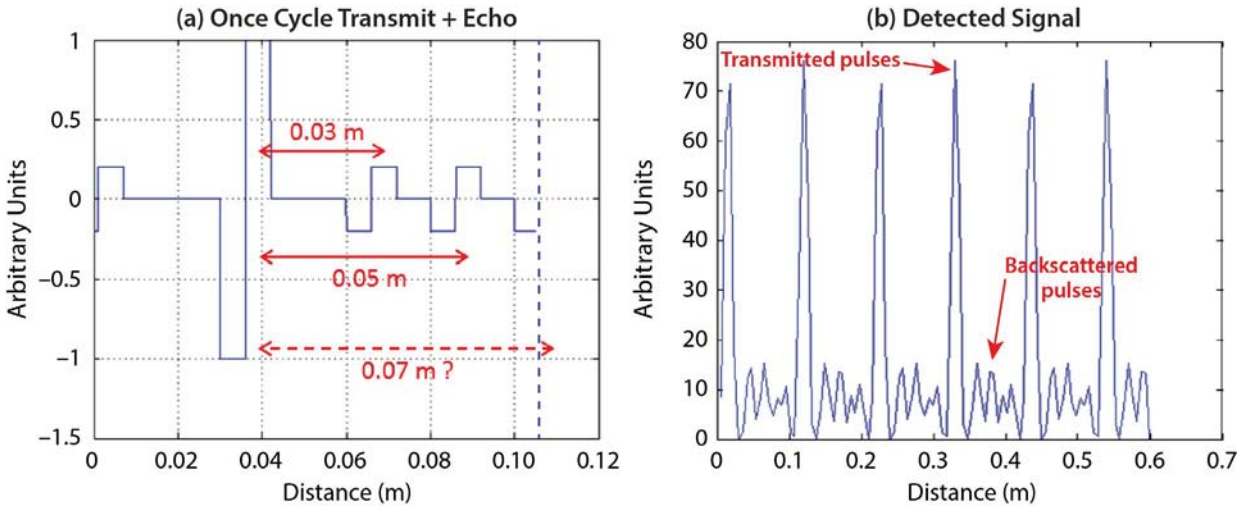

Figure 8. Model results of running the small box scenario showing (a) zoom of received pulse train with the derived distance of the reflection planes for one transmitted pulse, and (b) detected signal received by the photodiode or photodetector

Experimental Setup

Even though the model was built based on a time-based impulse response mode, our experiments had to use a frequency analysis technique to measure phase because of the better signal-to-noise ratio of the phase technique. Before we were ready to make derived range measurements in the backscatter mode, we first needed to verify the capability to measure basic phase changes as we moved two detectors in a transmission mode setup using FFT of the data. One photodiode was set up as a fixed diode placed near the beam port, as shown in Figure 9.

The second diode is movable, sliding toward and away from the beam port on an optical rail. The diodes were mounted using plastic holders and screws to decrease scatter from the mounting mechanisms. We placed the fixed diode approximately 16.8 cm from the copper-tungsten target in the electron beam line as a fixed phase reference. The position of the moveable diode was adjusted from the position of the fixed diode from 5 cm back to 10 cm in 1 cm increments.

Range can be derived using the following equations:

$$\Delta\theta = \left(\theta_{fixed} - \theta_{movable}\right)_{position\,0} - \left(\theta_{fixed} - \theta_{movable}\right)_{position\,1} \quad (2)$$

$$Range(f) = \frac{c \cdot \Delta\theta}{f \cdot 360.0^{o}} \quad (3)$$

We were well within the 10.5 cm range maximum (wavelength = c/frequency) before which we would expect to see phase wrap. We had data from the FY 2012 feasibility study, and we compared the results. At a distance change of 3 cm and 2.856 GHz, one would expect 103° of change using the following formula:

$$\Delta\theta(degrees) = 360^{o}\frac{\Delta d}{\lambda}. \quad (4)$$

The phase values we saw were much more stable shot-to-shot than before, but we did not see the expected 103° jumps. For each 1 cm increment, we were expecting 34.3° of relative phase change, but this effect was not clearly seen in the data. We replaced potentially bad cables and connectors, and we moved the oscilloscope to the accelerator cell to reduce line attenuation and RF pickup, but still obtained inconsistent results. We also took measurements on the Faraday cup, which is used to measure the temporal behavior of the electron beam directly. These measurements showed unexpected noise inconsistent with past linac performance. We identified an out-of-phase component between the two traces that would indicate RF leakage or some other source of interference. From

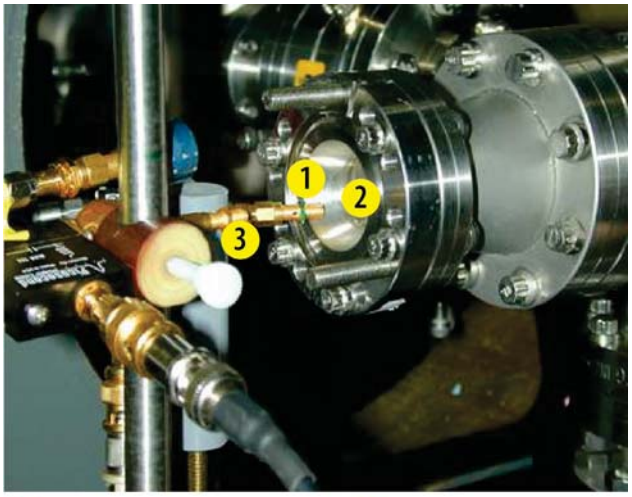

1 Fast diode #1 (stationary) 2 X-ray window
3 Fast diode #2 (movable)

Figure 9. The position of the fast photodiodes is shown relative to the x-ray window. The x-ray target is in the beam line, approximately 15 cm behind the x-ray window.

the perspective of accelerator operations, we believe there may be a problem with the accelerator tuning that allows for spiraling of the electron beam. An inadvertent stray beam will cause multiple x-ray beams to emanate from the beam pipe and could be causing these measurement problems.

We measured the phase and calculated the derived range at the first and second fundamentals or harmonics of the FFT. Figure 10 shows a calculated range measurement with the detector at four positions, from 1 to 4 cm. At the first harmonic, the calculated range measurement falls short of the expected values. The second harmonic falls short as well, but at 4 cm seems to be more predictable. We expect that when the interference problem is resolved, the measured values will agree with predictions. We plan to refine our measurements and retest next year.

Conclusion

Measurements to verify the x-ray radar concept have proven challenging. The LAO linac required modifications and repairs to improve its stability for making these sensitive measurements. The stability of the injector and the time jitter have been improved to the level required for x-ray radar measurements. The tuning stability and the RF noise challenges remain. Diagnostic measurements will continue early in FY 2014 to define the linac and data acquisition stability as well as to refine the data analysis techniques. Once confidence in the techniques has been established, 1-D backscatter studies will be performed to validate the capabilities of x-ray radar. Due to the expected weak

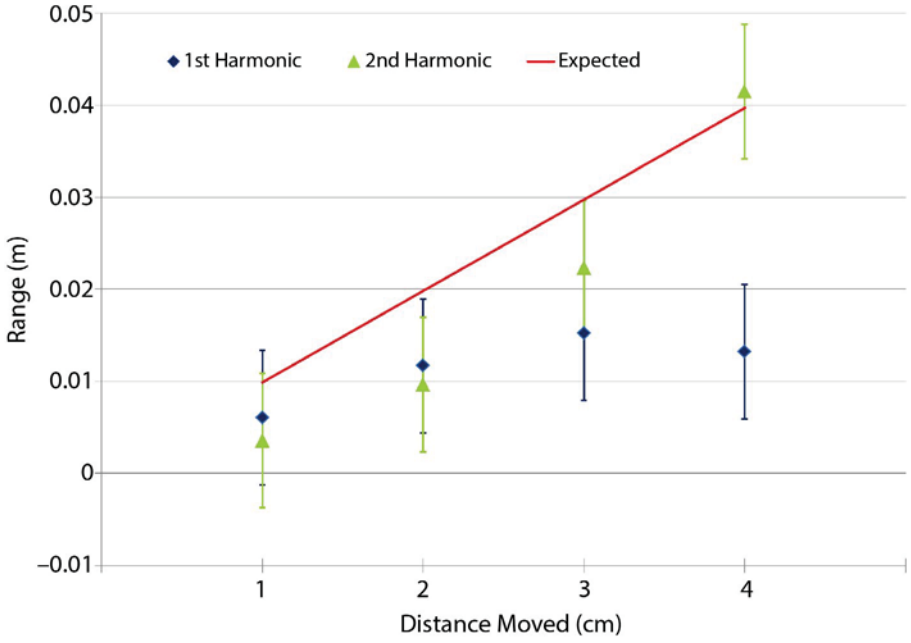

Figure 10. Derived range measurement showing calculated range vs. distance moved. The red line shows the expected values while the blue and green show the calculated values based on the phase measured. Only the 4 cm position agrees with the predicted value.

signal, stable, high-gain RF amplifiers will need to be identified and procured for the backscatter experiments. With successful 1-D backscatter experiments, an array of detectors will be built to test the feasibility of imaging using x-ray radar.

X-ray detectors with higher bandwidth and higher sensitivity will be identified and tested in parallel to improve the signal-to-noise ratio on all experiments. MCNPX simulations of the x-ray scattering will be performed and compared to experiments to improve the x-ray radar models and to better understand the expected signal at the detectors. Because the signal-to-noise ratio on the reflected signal is expected to be poor, an accurate prediction of this signal through modeling will be important. Accurate models will help us to choose proper amplifiers and to process the x-ray signal.

References

Azevedo, S., T. E. McEwan, "Micropower impulse radar," *Science & Technology Review* (January/February 1996) 16–29.

Wood, J. R., "X-ray radar," U.S. Patent 8,433,037 B1, filed October 23, 2009, and issued April 30, 2013.

This page left blank intentionally

Secure Sensor Networks Using Direct-Sequence Spread-Spectrum

STL-33-13 | Continued in FY 2014 | Year 1 of 1

Martin Fay,[1,a] Kelly Painter,[a] Sean Gordoni,[a] and Steve Lyon[a]

The goal of this project was to develop a secure, direct-sequence spread-spectrum (DSSS) modulation PHY (physical) layer for national security applications. There is an ongoing need for sensors that can be rapidly deployed and present in a denied environment with minimal risk of being discovered. Discovery should not compromise security of any remaining sensors. This year a novel Eigenvector technique was investigated to determine, in real-time, the despread for a DSSS system. This technique would allow each sensor to have its own unique spread code. MATLAB simulations demonstrated the feasibility of the technique. Continuation of the work in FY 2014 will focus on implementing the technique in a field-programmable gated array–based hardware platform.

[1] faymt@nv.doe.gov, 805-681-2445
[a] Special Technologies Laboratory

Background

Commercial technologies do not, in general, provide the level of waveform security required by other government agencies' applications. The standards utilized are published and therefore subject to discovery and exploitation. A need exists for a sensor-flexible network that resists discovery, sets up rapidly, and requires a minimum of advance configuration. Further, if a unit is compromised, it is desirable that other units in the field are not.

We worked on a direct-sequence spread-spectrum (DSSS) receiver in which the spread code is never turned off for synchronization purposes. Instead, the spread code is determined by a mathematical Eigenstructure technique. This technique, which does not require a priori knowledge of the spread code, allows for dynamic code assignment.

Project

Traditional DSSS receivers periodically turn off randomized data to aid in pseudorandom-noise (PN) code synchronization. The periodic portion of the signal presents a discrete spectra signature that can be detected. If the PN code is known, a correlation receiver can be used to direction find (detect and locate) the transmission from very long distances. The Eigenstructure technique investigated in this effort was described by Mangalvedhe (1997). Not only does this PN code not require exposure, the spread code need not be known in advance. This technique provides superior performance in low signal-to-noise conditions, allowing the transmit power to be lowered (thereby further reducing the sensor's profile). Due to the adaptive nature of the algorithm, multipath and Doppler shift effects are compensated for. The primary disadvantages of the technique are the longer training-sequence requirements and the high level of computing power required.

The primary focuses of this project in FY 2013 were to develop the despreader and demodulator, as these are the most difficult aspects of a DSSS system.

We developed a state-of-the-art, programmable, radio-development platform that allows for maximum flexibility and performance. This platform was only used to test development efforts for this project, but will prove invaluable in future digital communications endeavors.

The Eigenstructure-based demodulator as a component in a DSSS receiver can be broken down into the simplified block diagram shown in Figure 1.

The Eigenstructure despreader is implemented via the following algorithm. First, individual complex signal samples are frequency channelized as

$$\mathbf{x}(t) = x(t) \cdot e^{-j2\pi k f_r t}, \quad (1)$$

where $k = 0..N-1$ (N is the number of chips in the PN sequence), and f_r is the repetition frequency of the PN sequence. The autocorrelation matrix is found from $\mathbf{x}(t)$ as

$$\hat{\mathbf{R}}_{\mathbf{xx}} = < \mathbf{x}(t) \cdot \mathbf{x}^H(t) >_T. \quad (2)$$

From the autocorrelation matrix, the dominant mode of $\hat{\mathbf{R}}_{\mathbf{xx}}$ is computed by solving for the maximum eigenvalue, $\boldsymbol{\lambda}_{max}$, and associated eigenvector, $\mathbf{w}_{max}$, from

$$\hat{\mathbf{R}}_{\mathbf{xx}} \cdot \mathbf{w} = \lambda \cdot \mathbf{w}. \quad (3)$$

The despread code is found by averaging $\mathbf{w}_{max}$ over multiple sample measurements. We can now despread in the frequency or time domain using $\mathbf{w}_{max\_avg}$.

Frequency domain:

$$\hat{d}(t) = \mathbf{w}_{max\_avg}{}^H \cdot \mathbf{x}(t). \quad (4)$$

Time domain:

$$\hat{d}(t) = \mathcal{F}^{-1}\left\{\mathbf{w}_{max\_avg}{}^H\right\} \cdot x(t). \quad (5)$$

The despread mode chosen is based on the system requirements. If Doppler shift and/or multipath effects are anticipated, the frequency domain method makes more sense because $\mathbf{w}_{max\_avg}$ is likely to be derived from a moving average due to changing conditions. If, however, static conditions are present, the time domain method would require less computation because the time domain despread code given by $\mathcal{F}^{-1}\left\{\mathbf{w}_{max\_avg}{}^H\right\}$ would be static and can be replayed cyclically.

An example of how the despread improves as $\mathbf{w}_{max}$ measurements are averaged is shown in Figure 2.

The output of the despreader can have a frequency error equal to $\pm f_r/2$. A frequency estimator is needed to provide this frequency offset to the Costas Loop demodulator. We have investigated a zero-crossing-based frequency estimator; a block diagram of it is shown in Figure 3. The estimator requires data removal that, for quadrature phase-shift keying (QPSK), involves raising the signal to the 4th power.

This approach, first described by Liao (2011), uses a state machine to log where I and Q (in-phase and quadrature) cross a set point, α, that relates to the phase of the complex signal and the time. These data are used to update tracking variables for a running least squares analysis. The phase points, φ_i, correspond to 0, $\frac{\pi}{2}$, π, and $\frac{3\pi}{2}$ radians. An example of the

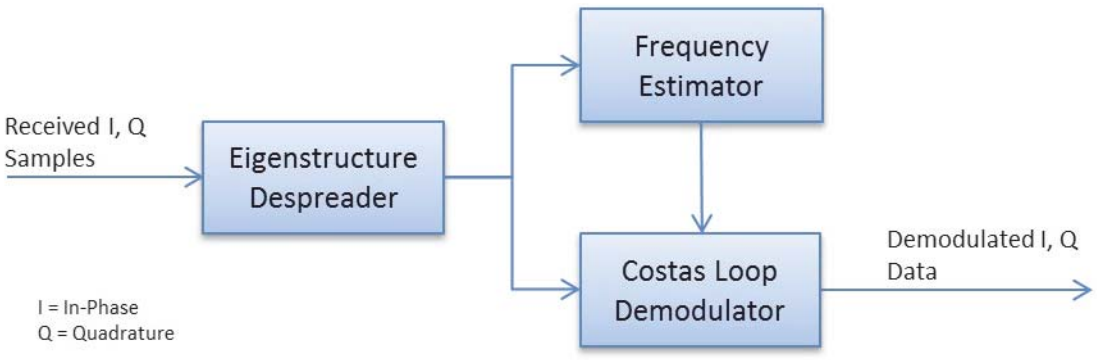

Figure 1. DSSS receiver demodulator block diagram

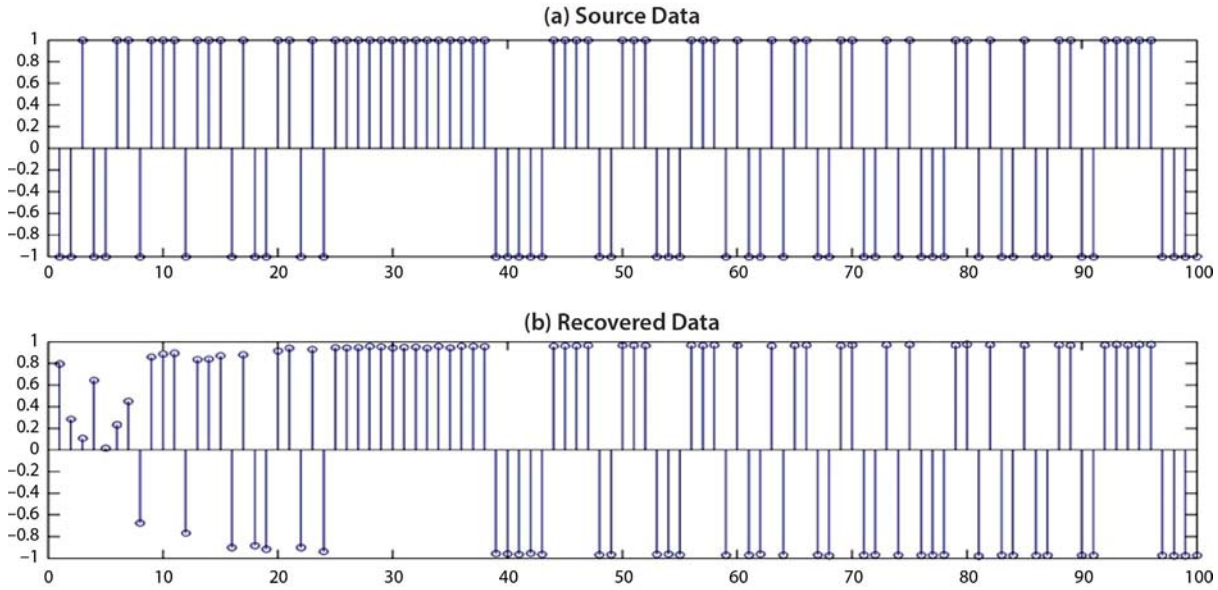

Figure 2. Recovered data stream with increasing $\mathbf{w}_{max}$ measurements shows (a) source data and (b) recovered data converging with multiple applications of the algorithm. Note successful recovery of data as evidenced by matching stem patterns.

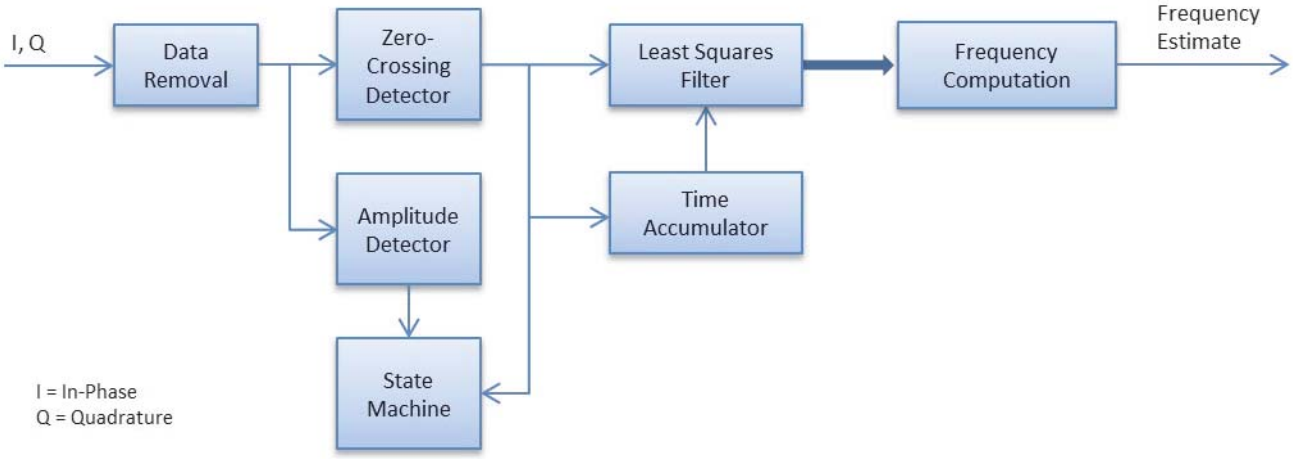

Figure 3. Block diagram of zero-crossing frequency estimator

zero crossings and their normalized phases are shown in Figure 4a. The tracking variables *a, b, c, d,* and *e* are updated with the point (t_i, φ_i).

$$a = a + t_i^2 \quad (6)$$

$$b = b + 1 \quad (7)$$

$$c = c + t_i \quad (8)$$

$$d = d - t_i(\varphi_i + m) \quad (9)$$

$$e = e - (\varphi_i + m) \quad (10)$$

The phase unwrap index, m, refers to the cycle number as tracked by the state machine. Using these tracking variables, the y-intercept and slope correspond to phase, φ_o, and frequency offset, f_o, and are given by Equations 11 and 12, respectively.

$$\phi_o = \frac{-(ea - cd)}{(ba - c^2)} \quad (11)$$

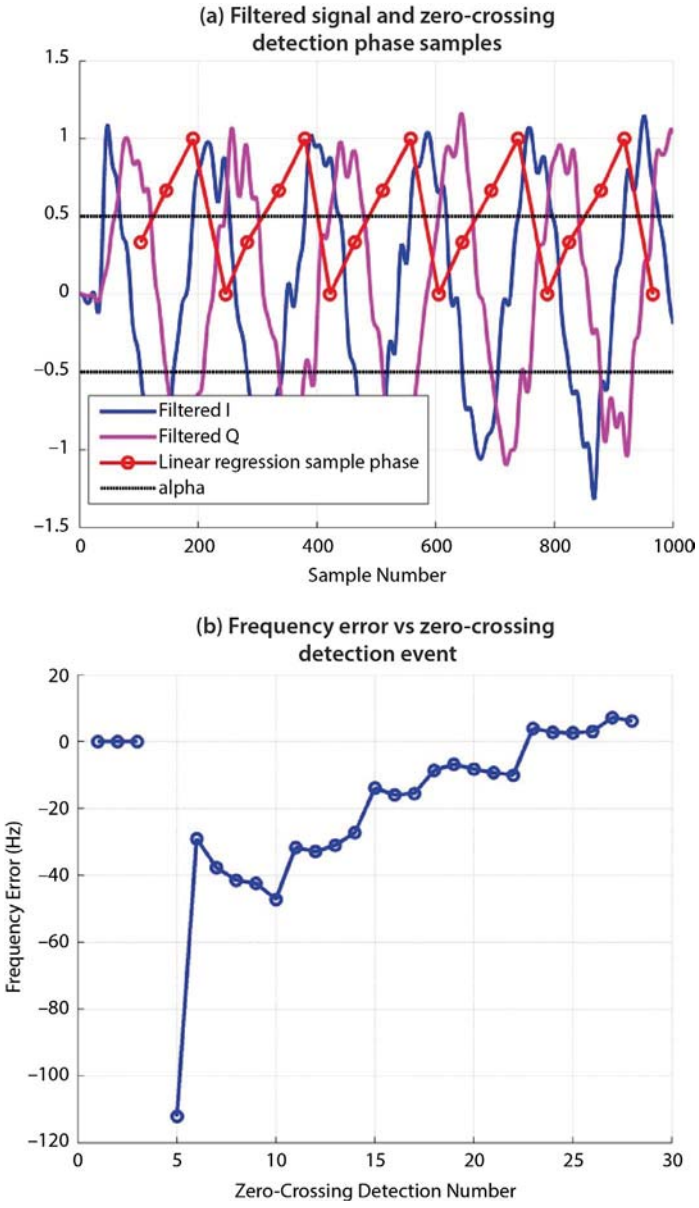

Figure 4. (a) Zero crossing and phase points illustrating measurement points applied to the algorithm (as indicated in Equations 5–10); (b) frequency estimate convergence with increasing measurement data through application of Equations 11 and 12

$$f_o = \frac{-(c\phi_o - d)}{2\pi a T_s} \quad \textbf{(12)}$$

Figure 4b shows a typical frequency convergence error as a function of crossing detections. We have implemented the zero-crossing detector in Simulink and are in the process of transitioning the design into Xilinx's System Generator for DSP. Initially we attempted to implement this module using a relatively new tool called Vivado High-Level Synthesis (also by Xilinx) in which C++ code can be used to design hardware. This effort did not produce the desired result in this case. The exercise was still worthwhile, however, as the technique may prove useful for other designs.

The implementation we are currently working on has added enhancements such as ignoring data during an amplitude fade. This had proven problematic because AM-to-FM conversion can occur, thus introducing errors into the frequency estimate. Logic circuitry was also developed that looks at the rate of change of the frequency estimate to analyze if the estimator is converging to a stable result or not. This is important in high-noise conditions. If, after an appropriate integration time, no valid result was produced, the tracking variables are dumped and the process starts over. If, on the other hand, the estimator is converging to a stable result, the frequency estimate value is locked until the end of the transmission.

Final demodulation of the despread signal is accomplished via a Costas Loop, as shown in the simplified block diagram in Figure 5. We have implemented this block in System Generator for DSP and are currently optimizing its performance. The data filters, $H_d(z)$, are z-domain implementations of a first-order Butterworth low-pass filter. The cutoff frequency is set to the symbol rate. The sideband suppression filters, $H_{sb}(z)$, are also first-order Butterworth filters, but the cutoff frequency is set to five times the loop bandwidth. This filter was found to be necessary as the loop filter, $H_{lf}(z)$, is a proportional-integral filter and the output proportional term was throwing the loop out of lock with any large transitions. This sideband filter reduces this effect and smooths out operations.

The design equations used for the loop filter are given in Equations 13–17. The loop bandwidth, BW_{Loop}, is typically set to around 100 Hz. The gain of the DDS (direct digital synthesizer), K_v, is set based upon the sample rate, R_s. The gain of the phase detector, K_d, can be made to be 0.5 if automatic gain control is used to force the incoming signal to have an amplitude of 1.

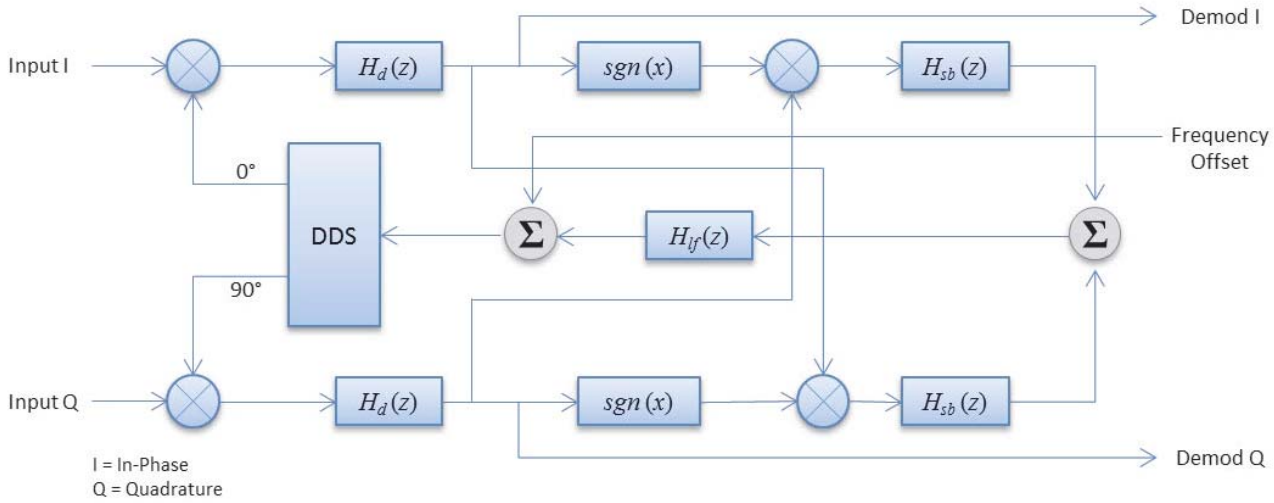

Figure 5. Costas Loop capable of demodulating binary phase-shift keying (BPSK) and QPSK

Finally, the proportional term, α, and integrator term, β, are determined from Equations 16 and 17. The damping factor, ζ, is set to make a fairly lethargic loop. We are currently using $\zeta = 3$.

$$\omega_n = 2\pi BW_{Loop} \quad (13)$$

$$K_v = \pi R_s \quad (14)$$

$$K_d = \frac{A_1 A_2}{2} = \frac{1}{2} \quad (15)$$

$$\alpha = \frac{2\pi\zeta}{K_v K_d} \quad (16)$$

$$\beta = \frac{\omega_n^2}{R_s K_v K_d} \quad (17)$$

Our collaboration with the University of California, Santa Barbara (UCSB), was in place late in FY 2013. As frequency estimation is such a prevalent issue in the design of communications systems, at our request UCSB began to investigate and determine the feasibility of another approach: frequency estimation using simultaneous correlation with a set of frequency-distorted segments of a preamble. This concept could potentially be used in place of the frequency estimator and would have the added benefit of determining both timing offset and frequency error. This technique would work with traditional DSSS PN code synchronization as well as in non-spread systems. UCSB successfully produced a MATLAB simulation of the technique in operation; we continue to analyze their findings and are evaluating the ramifications.

As a test platform was going to be needed, we designed a PCB early on in which we attempted to incorporate everything we thought we could ever possibly need (Figure 6). This board is based around a very large, state-of-the-art Kintex-7 Series field-programmable gate array (FPGA) (by Xilinx) coupled with an AVR32 microcontroller. Among the features of the board are two completely independent Lime Microsystems 300 MHz–3.8 GHz transceivers with 2 W output power amplifiers; GainSpan 801.11b Wi-Fi interface; remote key fob interface; GPS with reference oscillator output; accelerometer; temperature sensors; microSD card; real-time clock; and USB interface. Additionally, the board uses four MICTOR connectors as a logic analyzer interface for debugging and a slot for a 128 MB DDR2 RAM for capturing samples in real time.

Our board design is very technologically advanced, and has generated a great deal of interest. We have tested a good portion of the board's functions and, as yet, have not found any defects. We have been testing the Costas Loop demodulator on this platform, and are using a Lime Microsystems transceiver to receive an RF signal.

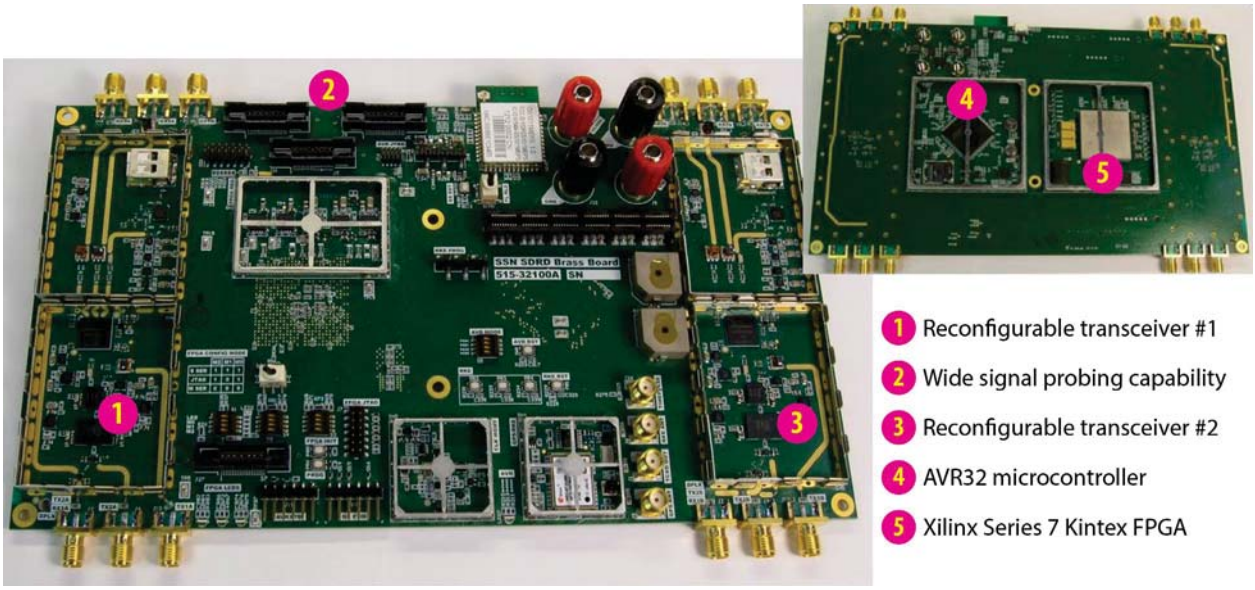

Figure 6. The advanced digital radio test platform measures 9"× 5"; inset shows the underside of the board

Conclusion

Simulations have shown that the Eigenstructure technique is a viable mechanism for despreading DSSS signals without requiring synchronization or knowledge of the despread code. We have developed an FPGA-based Costas demodulator, a workable design of a zero-crossing-based frequency estimator, and a working model of a correlation-based frequency estimator that also determines timing error. Finally, we have developed an advanced digital radio development PCB platform.

In the second year, development will focus on the physical implementation of the Eigenstructure algorithm in an FPGA to form a practical DSSS receiver. The primary challenge will be to determine and implement an optimum method for computation of the dominant-mode eigenvector in near-real time.

Acknowledgments

We would like to thank Forrest Brewer, Wei Tang, and Vincent Radzicki of the University of California, Santa Barbara, for their contributions to this work.

References

Liao, Y., "Phase and Frequency Estimation: High-Accuracy and Low-Complexity Techniques," Thesis, Worcester Polytechnic Institute, 2011, 45–67.

Mangalvedhe, N. R., J. H. Reed, "Analysis of an Eigenstructure Technique for DSSS Synchronization," in *Wireless Personal Communications: Advances in Coverage and Capacity*, J. H. Reed, T. S. Rappaport, B. D. Woerner, eds., Springer Science+Business Media, New York, 1997, 201–214.

Novel Deployment of Elpasolites as a Dual Gamma–Neutron Directional Detector

RSLN-06-13 | Continued in FY 2014 | Year 1 of 3

Paul Guss,[1,a] Thomas Stampahar,[a] Sanjoy Mukhopadhyay,[b] Joshua Lee,[c] Kanai Shah,[c] Michael R. Squillante,[c] and William Higgins[c]

Some applications in the area of radiological search, localization, and identification require detection of both neutron and gamma radiation, and usually two detectors are used to detect neutrons and gammas separately. In the first year of this three-year effort, we have investigated a new type of neutron/gamma (n/γ) directional detection capability, exploring a new class of scintillator: cerium (Ce)-doped Elpasolites such as Cs_2LiYCl_6:Ce (CLYC), $Cs_2LiLaCl_6$:Ce (CLLC), Cs_2LiYBr_6:Ce (CLYB), $Cs_2LiLaBr_6$:Ce (CLLB), or $Cs_2LiLa(Br_6)_{90\%}(Cl_6)_{10\%}$:Ce (CLLBC). These materials can provide energy resolution as good as 2.9% at 662 keV (FWHM). Because they contain ^6Li, Elpasolites can also detect thermal neutrons. In the energy spectra, the full energy thermal neutron peak appears near or above 3 MeV gamma equivalent energy (GEE_n). Thus, very effective pulse height discrimination is possible. In addition, the core-to-valence (CVL) luminescence provides Elpasolites with different temporal responses under gamma and neutron excitation, and possibly may be used for effective pulse shape discrimination. The n/γ discrimination capability of Elpasolite detectors may be optimized by tuning the Ce doping content for maximum effect on n/γ pulse shape differences. The resulting Elpasolite detectors have the ability to detect neutron and gamma radiation simultaneously, with excellent discrimination. Further, an array of four of these Elpasolite detectors will perform directional detection in both the neutron and gamma channels simultaneously.

[1] gusspp@nv.doe.gov, 702-295-8095
[a] Remote Sensing Laboratory–Nellis; [b] Remote Sensing Laboratory–Andrews; [c] Radiation Monitoring Devices, Inc.

Background

A new class of Elpasolite materials appears to be very promising for dual neutron/gamma (n/γ) detection (Shah 2010). Scintillators are an important class of materials that emit light when excited by radiation. This property makes scintillators a good means for detecting x-rays, gamma rays, and neutrons. A good scintillator material should have high density (for large radiation stopping power), high light output and energy resolution, fast decay time, and be available in large single crystals. These properties are related to the fundamental material properties, i.e., band gap (important for the light output); carrier transport efficiency (relevant to scintillation decay); and optical, chemical, and structural properties (Biswas 2012). Scintillators for dual n/γ detection should not only detect gammas and neutrons and their energy spectra, but also should reliably distinguish between them and their angles of origin. Although some materials can detect both types of radiation, so far none of them have performed well enough to be widely practical.

Elpasolites, by using pulse height or pulse shape discrimination (Glodo 2009a, Shah 2010), show promise to perform good n/γ discrimination simultaneously

and to obtain gamma spectra that have better energy resolution than the thallium-doped sodium iodide (NaI:Tl) detectors commonly used. While pulse height is a good method of particle detection, pulse shape discrimination is the preferred method, as it allows for energy spectra generated by both types of radiation to overlap, which is often the case. The physics problem reduces down to separating the light output of photons (gamma energy) from that of other charged particles, primarily alpha particles that are a neutron interaction product of $^{6}Li(n,\alpha)^{3}H$.

As a matter of fact, desirable characteristics for future detectors include (1) low-cost, high-resolution gamma scintillators sensitive to neutrons; (2) good n/γ discrimination capability; (3) ability to collect neutron and gamma data simultaneously with excellent discrimination; and (4) the ability to accomplish directional detection in both the neutron and gamma channels simultaneously with the same detector (array). The properties evidenced by Elpasolite detectors indicate their potential for use in nuclear detection systems.

The general formula of Elpasolites is $A^{+}B^{+}B'^{3+}X^{-}$ (Figure 1). Here X^{-} is a halogen ion (F, Cl, Br, or I). A^{+} and B^{+} are typically (but not limited to) alkali metal ions. B'^{3+} can be a rare-earth, transition metal, or other trivalent ion. It can be quickly seen that there are hundreds of Elpasolites. Elpasolites are attractive as scintillators because a large number of them are cubic (double perovskite structure), ideal for crystal growth from melt; the B' site is well suited for the doping of Ce^{3+}, whose *5d* and *4f* states can trap electrons and holes for radiative recombination; the large number of elements that can be incorporated into them offers the opportunity of finding desired material properties for scintillation applications; and besides gamma-ray detection, neutron detection is also possible when neutron-conversion elements are incorporated (e.g., ^{6}Li on the B site).

The first Elpasolite material that was considered for dual neutron/gamma detection was cerium (Ce)-doped Cs_2LiYCl_6:Ce (CLYC). CLYC was originally proposed as a neutron scintillator by Combes (1999). Its properties were studied later by the Delft University

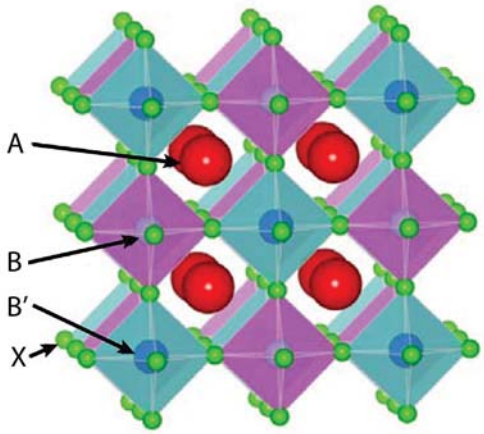

Figure 1. The general formula of Elpasolites is $A^{+}B^{+}B'^{3+}X^{-}$ (Biswas 2012)

of Technology, Delft, the Netherlands (van Loef 2002; Bessiere 2004, 2005) and Radiation Monitoring Devices, Inc. (RMD) (van Loef 2005, Glodo 2008). It was shown that this material is capable of providing effective pulse shape discrimination. CLYC also exhibits a very good energy resolution, as good as 4.3% at 662 keV (Glodo 2009b). While an excellent material, there are other Elpasolite crystals that demonstrate even better energy resolution due to higher light yield. One of these materials is Ce-doped $Cs_2LiLaCl_6$:Ce (CLLC), luminescent properties of which were already studied by Rodnyi (2000). They showed that in addition to Ce^{3+} emission, the crystal also shows core-to-valence (CVL) luminescence and measured its decay time to be 1.4 ns. The main advantage of CLLC over CLYC is its higher light yield. While CLYC exhibits approximately 20,000 ph/MeV, the light yield of CLLC can be as high as 35,000 ph/MeV (Glodo 2009a, Shah 2010). As a result, CLLC shows better energy resolution for gamma-ray spectroscopy. At 662 keV, the CLLC FWHM was measured to be as good as 3.4% (Shah 2010, Glodo 2011), better than that provided by CLYC or by NaI:Tl.

The presence of ^{6}Li in the crystal structure of Elpasolites enables detection of thermal neutrons. The gamma equivalent energy (GEE_n) of the neutron full energy peak is approximately 3 MeV. With such a high GEE_n value, the n/γ discrimination can be achieved using pulse height discrimination for gamma energies below 3 MeV. Because CLLC and CLYC exhibit the type

of ultrafast CVL emission that is present only under gamma excitation, effective pulse shape discrimination is achievable.

Table 1 summarizes some of the key parameters obtained from the literature, mostly by principal investigators based at RMD. The Elpasolite $Cs_2LiLaBr_6$:Ce (CLLB) scintillator detector is interesting, particularly for the fact that its resolution appears to exceed the 4.3% reported recently for CLYC (Bessiere 2004, Glodo 2009b). Shirwadkar (2011) and Glodo (2011) are reporting that a 2.9% value is achievable with CLLB. It appears from this work that 10% Ce is desirable (Shirwadkar 2011). A reported 2.9% gamma energy resolution (Glodo 2009a, 2011; Shirwadkar 2011) for CLLB and up to a 2.6% resolution on the thermal energy neutron peak reported for some Elpasolites (Glodo 2009a) brings into focus the tantalizing prospect that

Table 1. List of properties relevant to n/γ spectroscopy and discrimination

Detector	% Ce	Decay Time (τ, ns)	Gamma Equivalent Energy (GEE_n) (MeV)	Energy/Pulse Shape Discrimination/ Photon Yield ph/MeV)	Energy Resolution at 662 keV (R, %)
NaI:Tl	0	415 (Shah 2010)	--	38,000 (Shah 2010)	6%–7%
CsI:Tl	0	540 (Shah 2010)	--	52,000 (Shah 2010)	6%–7%
$LaBr_3$:Ce	1	360 (Shah 2010)	--	>63,000 (Shah 2010)	3%
$CeBr_3$	0	371 (Shah 2010)	--	68,000 (Shah 2010)	4%
SrI_2:Eu	0	1200 (van Loef 2009)	--	120,000 (van Loef 2009)	3%
CLYC	0.5	600, 6×10^6 (Combes 1999) 85 (Bessiere 2004) 55 (Glodo 2008)	3.50 (Shah 2010) 3.2 (Glodo 2008) 70 kph (0.1% Ce) (Shah 2010, Bessiere 2004, Glodo 2008)	pulse shape discrimination = 10^{-3} (Glodo 2009b) 20,000 (Glodo 2009a) 21,000 (Shah 2010) 4,500 phe*/MeV (Glodo 2008)	4.5% (Shah 2010) 5.1% (Glodo 2008) 8% for 0.1% Ce (Bessiere 2004) 4.3% (Glodo 2009b) 3.9% (Glodo 2011)
CLLC	0.1	2 (5%) 50 (25%) 450 (70%) (Glodo 2009a)	3.04 (Glodo 2009a) 110 kph (Shah 2010)	35,000 (Glodo 2009a, Shah 2010) 7,500 phe*/MeV (Glodo 2008)	3.4% (Shah 2010, Glodo 2011)
CLLB	10	55 (Shirwadkar 2011)	3.2 MeV (Shah 2010) 180 kph (Shah 2010)	50,000 (Shirwadkar 2011) 60,000 (Shah 2010) 9,500 phe*/MeV (Glodo 2008)	3.0% (Shah 2010) 2.9% (Shirwadkar 2011, Glodo 2011)
CLYB	1	85, 2.5×10^6 (Bessiere 2004)	88 kph (Bessiere 2004)	23,600 (Bessiere 2004)	8.5% (Bessiere 2004)

* phe = photomultiplier (PMT) photoelectrons

a single detector array may be built that has very high resolution in the gamma channel and simultaneously provides excellent gamma and neutron detection sensitivity.

A measure of the success for our investigation will be the n/γ discrimination record. Ultimately, in this study, a detector that can distinguish neutrons, as well as gammas, is sought. Techniques have been well established for doing this with Elpasolites (Whitney 2011, Glodo 2012). The reported value for neutron false postives per gammas of 1 per 1000 for the CLYC (Glodo 2009b) is an excellent start. Other metrics relevant for n/γ discrimination are reported in Table 1.

Tables 2–4 and Figure 2 illustrate some of the key characteristics of Elpasolites (Shah 2010). Critical are the time profile and pulse shape for gammas and neutrons. The effect of Ce content on the time profile has been well illustrated for the CLLC detector (Glodo 2009a). Data for the CLLC detector (Glodo 2009a, Shah 2010) are shown in Figures 2 and 3. Figure 3 affirms that the Ce content impacts the detector performance. The investigation of Trefilova (2007) appears to indicate that a 0.1% Ce concentration is optimal. Looking at Figure 4, one sees the dependencies of afterglow I/I_0, radioluminescence yield Y_{RL}, light yield L, and energy resolution R on Ce content, or Ce mass-percentage (mas%), in the CLYC crystal (Trefilova 2007), indicating there is only a narrow band of acceptable Ce percent-mass content. Table 5 summarizes the results from RMD on the effects of Ce content on the time profile for the CLLC. The CVL appears critical to good pulse shape discrimination. It has been associated with the 2 ns decay component (see Table 5 [Glodo 2009a]).

The CVL is illustrated in Figure 5 (Glodo 2009a). Figure 6 shows the variation of CVL relative to the emission spectrum as a function of Ce content (Glodo 2009a), depicting wavelength intensity as a function of Ce doping (Glodo 2009a). As the Ce doping content is increased, a relatively smaller amount of the light occurs in the wavelengths associated with CVL (i.e., the higher energy realm is associated with inner atomic shells). Using data in the literature (Glodo 2011), an evaluation plan was made regarding which Elpasolite would perform the neutron discrimination function best. A very recent development in the published literature (D'Olympia 2012) establishes the basis for further optimizing this Elpasolite array for fast neutron spectroscopy. A diagram of the prototype detector array is shown in Figure 7.

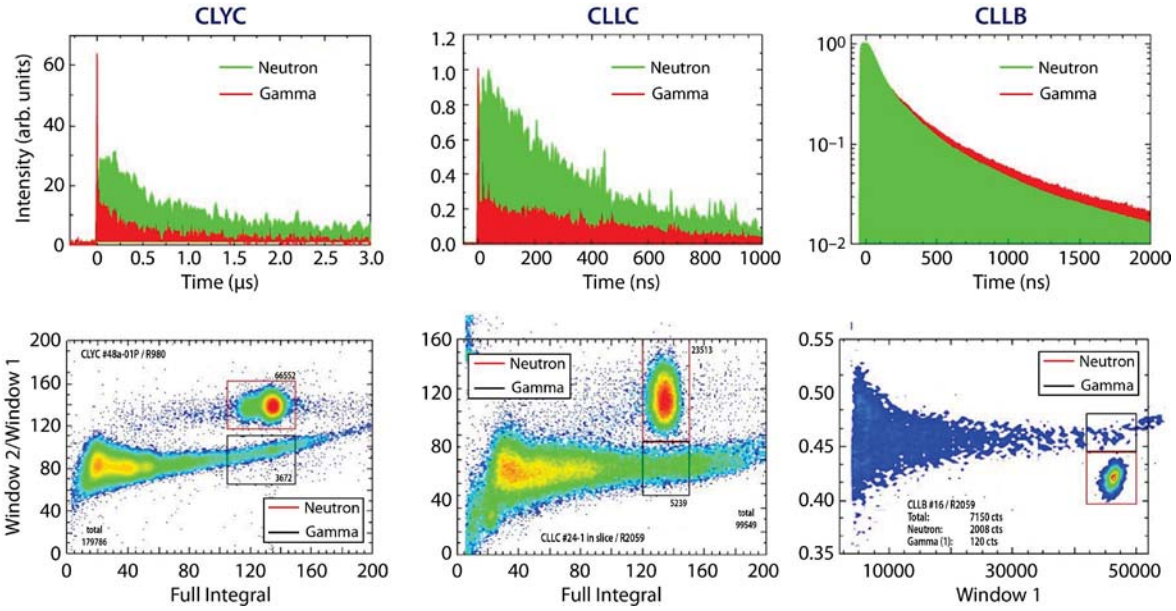

Figure 2. A pulse shape discrimination comparison indicates that in each case criteria may be specified on the electronic signal that will segregate signals due to neutrons (Shah 2010)

Table 2. Gamma characteristics (14–1256 keV) of select gamma scintillators (Shah 2010)

Material	Light Yield (photons/MeV)	Emission (λ max, nm)	Energy Resolution at 662 keV (R, %)	Non-Proportionality (ΔL, %)	Principal Decay Time (ns)
NaI:Tl	38,000	415	6–7	15	230
CsI:Tl	52,000	540	6–7	13	1000
$LaBr_3$:Ce	>63,000	360	3	10	17
$CeBr_3$	68,000	371	4	2	17
CLYC	20,000	370	4	2	1** 50 ~1000
CLLC	35,000	400	3.4	2	1**, 60, >400
CLLB	60,000	410	3	2	~ 55, 270

Table 3. Detection characteristics of select neutron scintillators (Shah 2010)

Material	Dopant	Emission (nm)	Light Yield (ph/MeV)	Light Yield (ph/n)	Decay Time (ns)	Pulse Shape Discrimination
Li-Glass	Ce	395	4000	6000	75	N
LiI	Eu	470	12,000	50,000	1400	N
LiF/ZnS	Ag	450	75,000	160,000	1000	N
CLYC	Ce	300*, 390	21,000	70,000	1*, 50, 1000	Y
CLLC	Ce	300*, 400	35,000	110,000	1*, 60, >400	Y
CLLB	Ce	410	60,000	180,000	55, >270	Y

*CVL

Table 4. Summary of scintillator properties (Shah 2010)

	CLLC	CLLB	CLYC
Density (g/cm^3)	3.5	4.2	3.3
Emission (nm)	290 CVL, 400 Ce^{3+}	410 Ce^{3+}	290 CVL, 390 Ce^{3+}
Decay time (ns)	1 CVL, 60, >400	55, >270	1 CVL, 50, ~1000
Maximum light yield (ph/MeV)	~35,000	~60,000	~20,000
Light yield (ph/n)	~110,000	~180,000	~70,000
GEE_n (MeV)	~3.1	3.2	~3.1
Best energy resolution at 662 keV	3.4	2.9	3.9
Pulse Shape Discrimination	Excellent	Possible	Excellent

Table 5. Summary of decomposition of time profiles for CLLC (Glodo 2009a)

Crystal Doping Percent	Decay Time* (ns)	Intensity	Decay Time (ns)	Intensity	Decay Time* (ns)	Intensity	Decay Time (ns)	Intensity
Undoped	2	9%	40	11%	450	80%	--	--
0.10%	2	5%	50	25%	450	70%	--	--
0.50%	2	2%	60	27%	450	71%	--	--
0.5%–1.0%**	2	0.60%	160	14%	450	15%	1500	--
1%***	--	--	85	23%	450	22%	1300	55%

* fixed ** 7 ns rise time for all components except the first *** 12 ns rise time for all components

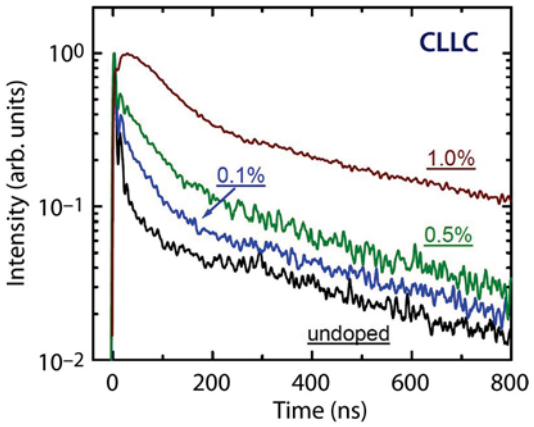

Figure 3. CLLC time profile vs. Ce content shows greater CVL signatures relative to the overall signal profile for lower Ce doping values (Glodo 2009a)

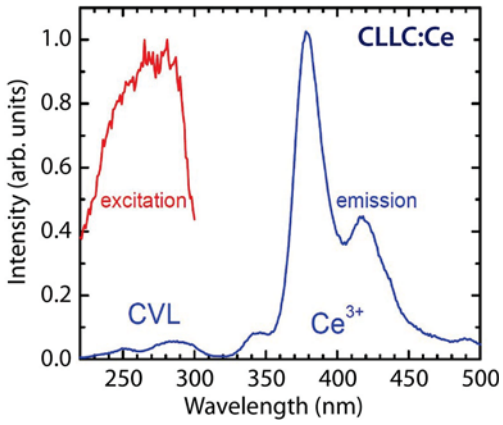

Figure 5. Radioluminescence spectrum of CLLC:0.5%Ce (blue) and Ce^{3+} emission excitation spectrum in CLLC (red) (Glodo 2009a)

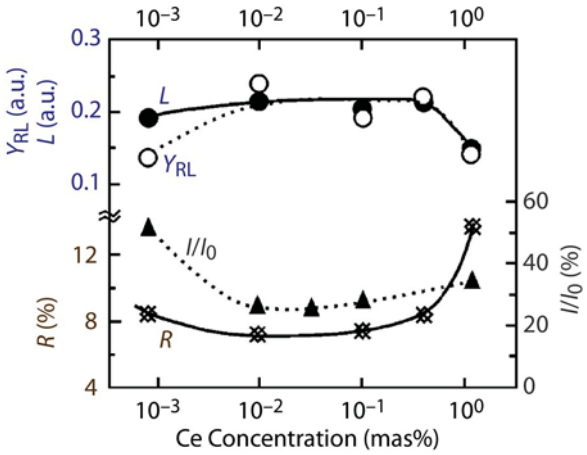

Figure 4. The dependencies of afterglow I/I_0, radioluminescence Y_{RL}, light yield L, and energy resolution R on Ce content in the CLYC crystal (Trefilova 2007)

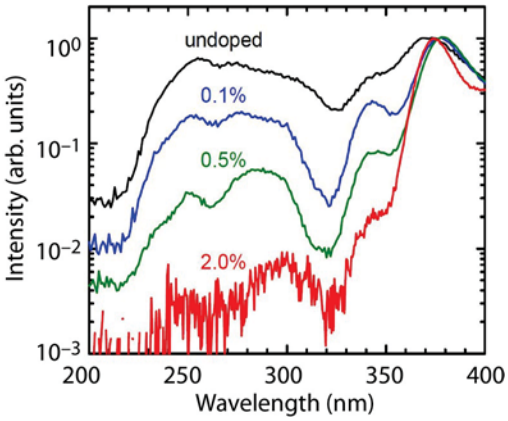

Figure 6. Emission spectra as a function of Ce content for the CLLC detector (Glodo 2009a)

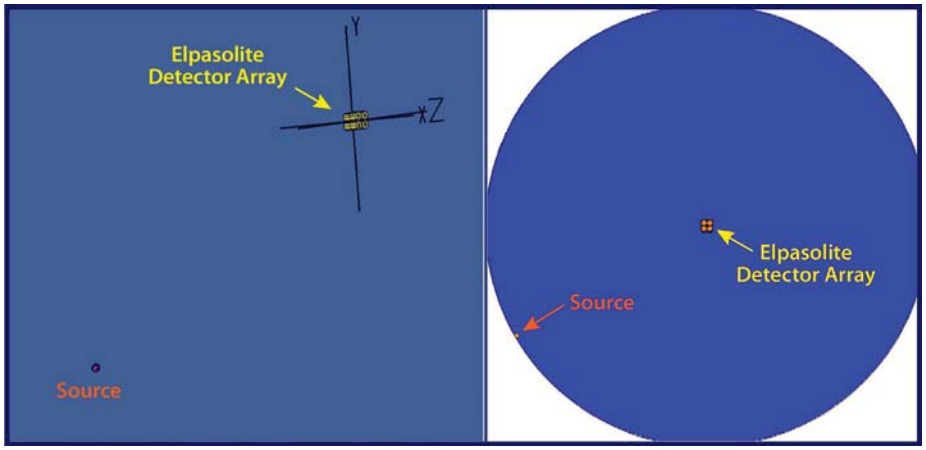

Figure 7. Basic geometry for the 4-crystal Elpasolite directional detector capable of directional detection and spectroscopy functions for neutron and gamma channels simultaneously. The array (left) stands upright in the *y–z* plane and (right) *x–y* plane. The red ball contains a source of radiation, located 1 m away at Θ = [7/6]π. The source is successively moved to different positions in the *x–y* plane, with the source to detector (centroid) distance held constant at 1 m, and then new detector count rates are calculated with MCNPX for each position. Count rate results are shown for each angle, relative to the +x axis in the next figure.

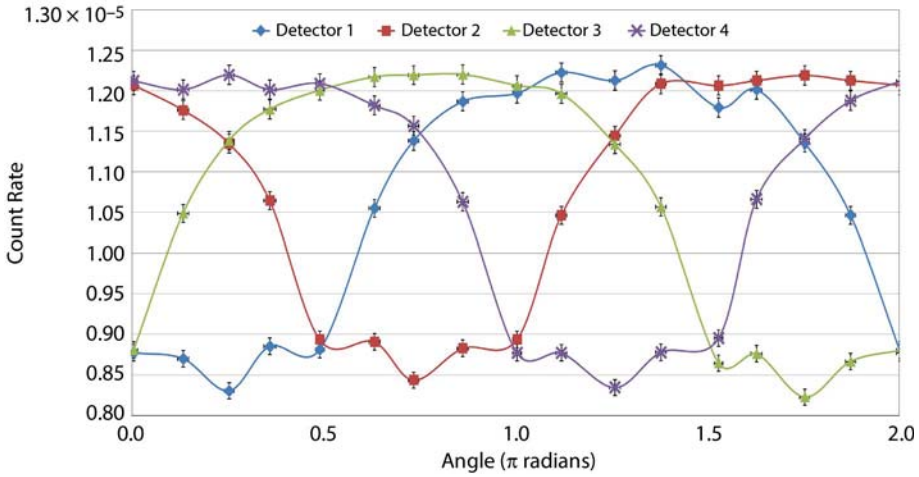

Figure 8. MCNPX determination of the gamma count rate for each of the four Elpasolite detectors as a function of angle. The geometry is defined in Figure 7. The angle may be determined by analysis of the detector count rate asymmetries.

Project

We performed MCNPX modeling and analysis of the candidate detector configurations to predict sensitivities and directional detection capacities for the gamma and neutron channels. Figure 7 depicts the geometry employed in the MCNPX calculations. Projected results based on the MCNPX models for determining the directionality of a gamma radiation source are shown in Figure 8 for a four-detector array. With this set of count rate data, it is easy to specify the angle of the incoming radiation, which depends on the relative detector count rates.

Detector Evaluations

RMD performed detector synthesis, crystal growth, and packaging. We are now evaluating the properties of two detector materials provided by RMD—CLYC and CLLBC.

CLYC Detector

A high-quality 1" × 1" CLYC crystal, doped with a 0.5% Ce^{3+} concentration, was mounted to a 2-inch PMT, and the detector package was hermetically sealed, as the crystal is hydroscopic (Figure 9). We chose to use a Hamamatsu super bialkali (SBA) R6231-100 PMT. This SBA photocathode has peak quantum efficiency (QE) of 35%, close to the peak wavelength for our scintillator. Sources were carefully set up 30 cm from the front face of the CLYC detector. The CLYC scintillator/PMT system achieved much better than the 8% energy resolution at 662 keV, the 20,000 ph/MeV for gammas, and the 70,000 photons/n (which were all reported by Bessiere 2004), and better than the 1-to-1000 n/γ energy discrimination reported earlier (Glodo 2009b).

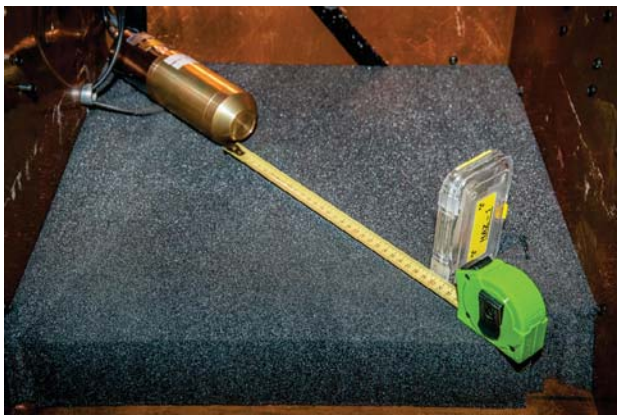

Figure 9. CLYC detector, source, and CLYC detector geometry

The oscilloscope traces for neutrons and gammas in Figure 10 show the neutron signature (associated with the $^6Li(n,\alpha)^3H$ alpha and triton particle energy losses in the detector or the $^6Li(n,\gamma)^7Li^*$ ion recoil energy resulting from neutron capture by the detector's lithium nuclei) is stronger in magnitude than the gamma signature. Furthermore, not only is the decay time for the gammas shorter, but also there is slight evidence in this trace of a CVL with a decay time of much less than 100 ns. Each division on Figure 10 is 100 ns, with a full scale range of ±1 μs.

CLLBC Detector

A high-quality 12 × 18 × 3 mm^3 hybrid Elpasolite $Cs_2LiLa(Br_6)_{90\%}(Cl_6)_{10\%}$:Ce (CLLBC) crystal composed of cesium, lithium, lanthanum, bromine, and chlorine was prepared for evaluation. The CLLBC material detects gamma photons and neutrons. Two neutron interactions exist: one with the ^6Li atom (thermal neutrons) and a second with the chlorine atom (fast neutrons). The crystal was mounted to a 2-inch PMT, and the detector package was hermetically sealed. Again, the super bialkali PMT was used. The CLLBC scintillator/PMT system achieved at least a 4% energy resolution at 662 keV and the 180,000 photons/n, and 50,000 ph/MeV for gammas, which all were reported by Shah (2010) for the CLLB. It also achieved a better than 1-to-1000 n/γ energy discrimination. Notice that the CVL, seen for the CLYC, is not evident in the CLLBC, consistent with earlier CLLB results (Shah 2010, Glodo 2011, Shirwadkar 2011). Results are shown in Figure 10. CLLBC pulse shape discrimination (Figure 11) relies on the pulse decay time. One can define a pulse shape discrimination figure of merit (FOM) as (Knoll 2000):

$$FOM = \frac{centroid_n - centroid_\gamma}{FWHM_n + FWHM_\gamma}. \quad \textbf{(1)}$$

Using this formalism, the pulse shape discrimination spectrum may be analyzed and the experimental setup tuned or modified to enhance the FOM, and thereby the discrimination between neutron and gamma signatures in the Elpasolite detector. Using this discrimination to gate a differential pulse-height spectrum may yield selectivity for a spectrum associated with either the detected gammas or the detected (thermal) neutrons. The energy spectrum associated with the detected neutrons will be dominated by the GEE_n peak. This peak energy is determined by what Bessiere (2004) defines as the γ-equivalent factor F_γ

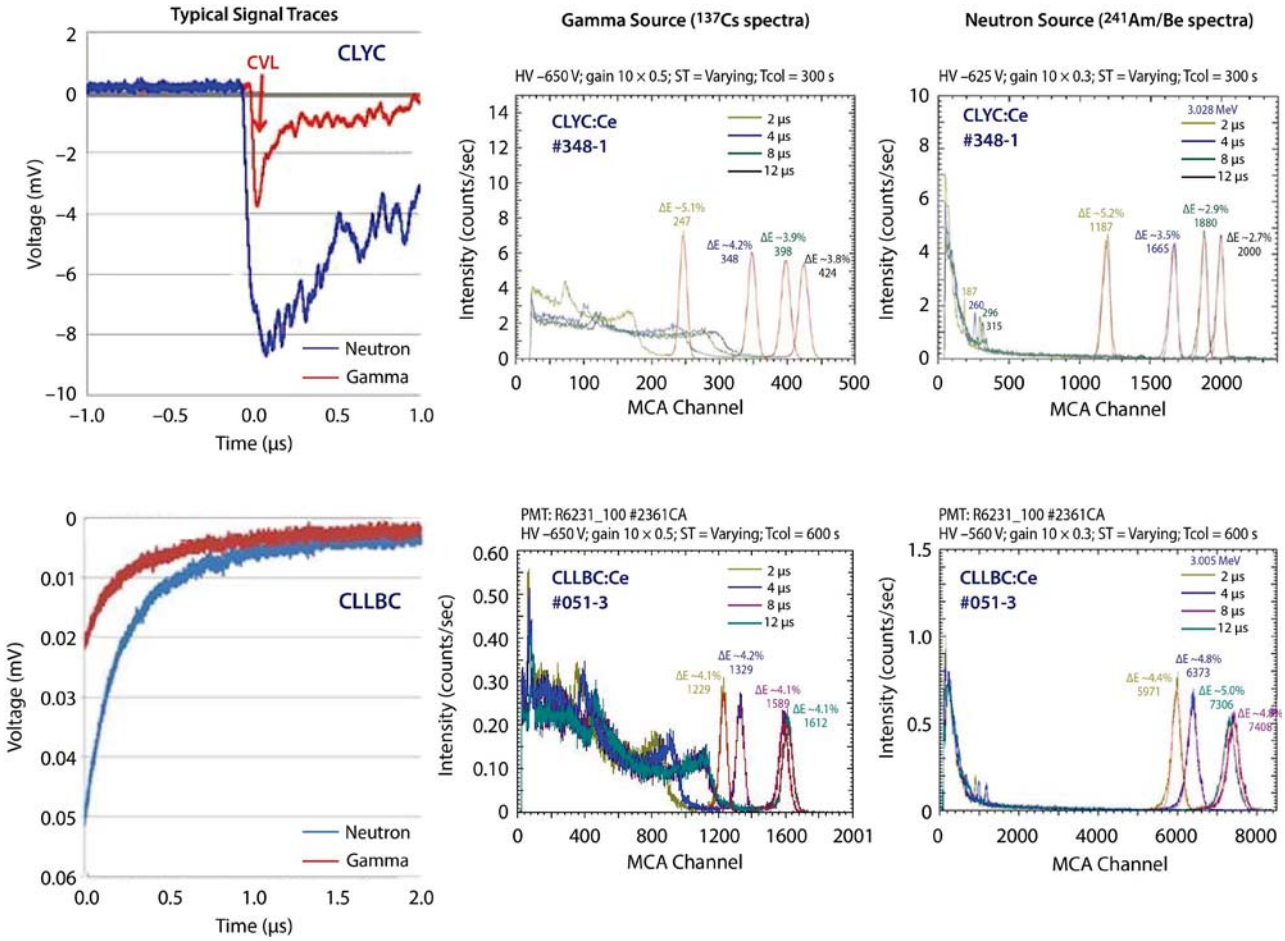

Figure 10. (left) Typical gamma and neutron signal traces on oscilloscope using the CLYC (upper) and CLLBC (lower) detectors. It is likely that the larger signal is due to neutrons, which result in the production of both an alpha particle and a triton in the detector media. (center) CLYC and CLLB spectra of ^{137}Cs source acquired for various shaping times; (right) CLYC and CLLB spectra of ^{241}AmBe source acquired for various shaping times.

$$F_\gamma = \frac{E_\gamma(4.78\ \mathrm{MeV})}{(4.78\ \mathrm{MeV})},$$

where $E_\gamma(4.78\ \mathrm{MeV})$ is the gamma equivalent energy of the neutron peak, GEE_n. The 4.78 MeV value arises from the reaction

$$^{6}_{3}\mathrm{Li} + {}^{1}_{0}\mathrm{n} \rightarrow {}^{3}_{1}\mathrm{H} + {}^{4}_{2}\alpha + 4.78\ \mathrm{MeV}. \quad (3)$$

The α particle and triton share a kinetic energy of 4.78 MeV. Significantly, this detector can be set up to simultaneously obtain energy spectra in the gamma and neutron channels.

(2) Conclusion

Elpasolites can be used in pulse height discrimination mode to do n/γ discrimination (limited by neutron peak). Elpasolites can also be used in pulse shape discrimination mode to do n/γ discrimination. Elpasolites have good energy resolution for gamma rays. In the first year of this project, we have determined specifications for the first detector, a CLYC with 0.5% Ce^{3+} doping content, for the directional detector array. MCNPX calculations were used to characterize the directional detector array response. We have also determined the material content to use as a hybrid

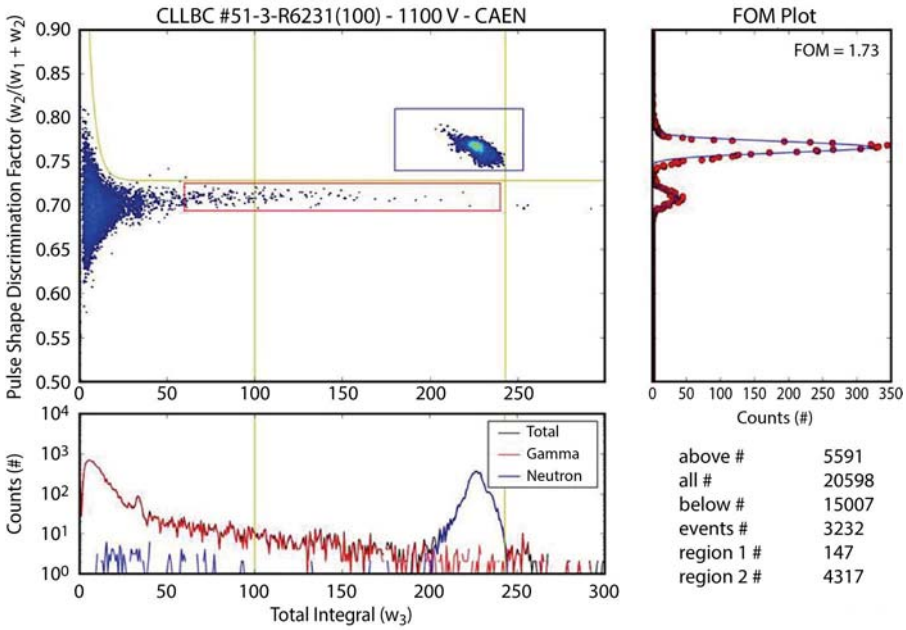

Figure 11. Pulse shape discrimination can effectively and reliably separate both types of radiation detected by the CLLBC

CLLBC for improved sensitivity to a broader energy range of neutrons, using decay times for pulse shape discrimination.

Future work will include quantifying the characteristics and luminescence properties of the Elpasolite detectors. Selection of the best detector material for the NNSS mission space requires further evaluation of the properties of the various types of Elpasolites, along with impact of different cerium doping content. We will proceed to investigate the best methods to engineer an array of Elpasolites that performs n/γ directional detection. We will proceed to prepare and demonstrate the components of this system in the laboratory. In the final phases of the project, we shall fabricate the final package for n/γ directional detection and will perform static source benchmarking, testing, and evaluation. The preliminary results of the work so far have been presented at the 2013 SPIE conference in San Diego, California. (Guss 2013).

Acknowledgments

The authors acknowledge the professional staff of RMD, Watertown, Massachusetts, for the production of the detectors, for providing these detectors to the Remote Sensing Laboratory, and for their support and advice. We would like to thank Ja'lon Sisson and John O'Donoghue for their contributions.

References

Bessiere, A., P. Dorenbos, C. W. E. van Eijk, K. W. Krämer, H. U. Güdel, "New thermal neutron scintillators: Cs_2LiYCl_6:Ce and Cs_2LiYBr_6:Ce," *IEEE Trans. Nucl. Sci.* **51**, 5 (2004) 2970–2972.

Bessiere, A., P. Dorenbos, C. W. E. van Eijk, K. W. Krämer, H. U. Güdel, "Luminescence and scintillation properties of Cs_2LiYCl_6:Ce for gamma and neutron detection," *Nucl. Instrum. Methods Phys. Res. A* **537** (2005) 242–246.

Biswas, K., M.-H. Du, "Energy transport and scintillation of cerium-doped Elpasolite Cs_2LiYCl_6: Hybrid density functional calculations," *Phys. Rev. B* **86** (2012) 014102.

Combes, C. M., P. Dorenbos, C. W. E. van Eijk, K. W. Krämer, H. U. Güdel, "Optical and scintillation properties of pure and Ce^{3+}-doped Cs_2LiYCl_6 and Li_3YCl_6:Ce^{3+} crystals," *J. Lumin.* **82** (1999) 299–305.

D'Olympia, N., et al., "Optimizing Cs_2LiYCl_6 for fast neutron spectroscopy," *Nucl. Instrum. Methods Phys. Res. A* **694** (2012) 140–146.

Glodo, J., W. M. Higgins, E. V. D. van Loef, K. S. Shah, "Scintillation properties of 1 inch Cs_2LiYCl_6:Ce crystals," *IEEE Trans. Nucl. Sci.* **55** (2008) 1206–1209.

Glodo, J., R. Hawrami, E. van Loef, W. Higgins, U. Shirwadkar, K. S. Shah, "Dual gamma neutron detection with $Cs_2LiLaCl_6$," *Proc. SPIE* **7449** (2009a) 74490E-1.

Glodo, J., W. M. Higgins, E. V. D. van Loef, K. S. Shah, "Cs_2LiYCl_6:Ce scintillator for nuclear monitoring applications," *IEEE Trans. Nucl. Sci.* **56**, 3 (2009b) 1257–1261.

Glodo, J., E. V. D. van Loef, R. Hawrami, W. M. Higgins, A. Churilov, U. Shirwadkar, K. S. Shah, "Selected properties of Cs_2LiYCl_6, $Cs_2LiLaCl_6$, and $Cs_2LiLaBr_6$ scintillators," *IEEE Trans. Nucl. Sci.* **58**, 1 (2011) 333–338.

Glodo, J., R. Hawrami, E. van Loef, U. Shirwadkar, K. S. Shah, "Pulse shape discrimination with selected Elpasolite crystals," *IEEE Trans. Nucl. Sci.* **59**, 5 (2012) 2328–2333.

Guss, P., S. Mukhopadhyay. "Dual Gamma Neutron Directional Elpasolite Detector" *Proc SPIE* **8854** (August 28, 2013) 885402-1.

Knoll, G. F., *Radiation detection and measurement*, 3rd edition, John Wiley & Sons, New York, 2000, 680.

Rodnyi, P. A., V. B. Mikhalik, G. B. Stryganyuk, A. S. Voloshinovskii, C. W. E. van Eijk, G. F. Zimmerer, "Luminescence properties of Ce-doped $Cs_2LiLaCl_6$ crystals," *J. Lumin.* **86** (2000) 161–166.

Rodnyi, P. A., "Progress in fast scintillators," *Rad. Meas.* **33** (2001) 605–614.

Shah, K. S., J. Glodo, E. van Loef, W. Higgins, R. Hawrami, U. Shirwadkar, S. Mukhopadhyay, "New detectors for gamma and neutron studies," DOE SBIR Phase II. http://science.energy.gov/~/media/np/pdf/sbir%20sttr/presentations/shah_np_gamma_neutron_scintillators_1.pdf (2010), accessed May 1, 2013.

Shirwadkar, U., J. Glodo, E. V. van Loef, R. Hawrami, S. Mukhopadhyay, A. Churilov, W. M. Higgins, K. S. Shah, "Scintillation properties of $Cs_2LiLaBr_6$ (CLLB) crystals with varying Ce^{3+} concentration," *Nucl. Instrum. Methods Phys. Res. A* **652** (2011) 268–270.

Trefilova, L., et al., "The inertia properties of Cs_2LiYCl_6:Ce scintillation crystals," *Rad. Meas.* **42** (2007) 572–575.

van Loef, E. V. D., P. Dorenbos, C. W. E. van Eijk, K. W. Krämer, H. U. Güdel, "Scintillation and spectroscopy of the pure and Ce^{3+}-doped Elpasolites: Cs_2LiYX_6 (X = Cl; Br)," *J. Phys. Condens. Matter* **14** (2002) 8481–8496.

van Loef, E. V. D., J. Glodo, W. M. Higgins, K. S. Shah, "Optical and scintillation properties of $Cs_2LiYCl_6:Ce^{3+}$ and $Cs_2LiYCl_6:Pr^{3+}$ crystals," *IEEE Trans. Nucl. Sci.* **52** (2005) 1819–1822.

van Loef, E. V., C. M. Wilson, N. J. Cherepy, G. Hull, S. A. Payne, W.-S. Choong, W. W. Moses, K. S. Shah, "Crystal growth and scintillation properties of strontium iodide scintillators," *IEEE Trans. Nucl. Sci.* **56**, 3 (2009) 869–872.

Whitney, C., C. Stapels, E. Johnson, E. Chapman, G. Alberghini, J. Glodo, K. Shah, J. Christian, "6-Li enriched Cs_2LiYCl_6:Ce based thermal neutron detector coupled with CMOS solid-state photomultipliers for a portable detector unit," *Proc. SPIE* **7961** (2011) 79610U.

This page left blank intentionally

Solid-State Neutron Detectors Using Uranium Oxides

LAO-22-13 | Continued in FY 2014 | Year 1 of 3

Craig Kruschwitz,[1,a] David Schwellenbach,[a] Sanjoy Mukhopadhyay,[b] Thomas Meek,[c] Jerrad Auxier,[c] Brandon Shaver,[c] and Taylor Cunningham[c]

This project aims to develop and test a new type of solid-state neutron detector fabricated from uranium compounds. It has been known for many years that UO_2 and U_3O_8 as well as other uranium compounds exhibit semiconducting characteristics with a broad range of electrical properties. This project seeks to exploit these characteristics to make a direct-conversion semiconductor neutron detector. In such a device a neutron interacts with a uranium nucleus, inducing fission. The fission products deposit their energy, producing detectable electron-hole pairs. The high energy of the fission products indicates that the noise discrimination of such a device would be excellent. This project uses depleted uranium (DU), making it sensitive to high-energy neutrons, though the small amount of ^{235}U present in DU means the device would maintain some thermal neutron sensitivity. In FY 2013 we performed MCNPX modeling of potential UO_2 device performance, and fabricated and tested some simple single-crystal, Schottky-type UO_2 diodes. In FY 2014, we will continue to build upon the FY 2013 results and attempt to fabricate and test p-n junction devices.

[1] kruschca@nv.doe.gov, 505-663-2023
[a] Los Alamos Operations; [b] Remote Sensing Laboratory–Andrews; [c] University of Tennessee, Knoxville

Background

Highly efficient neutron detectors are required for a wide variety of applications ranging from homeland security to astronomy. The well-known shortage of ^3He gas has recently driven a search for new neutron detector materials to replace ^3He-based detectors. Solid-state devices are one such alternative, with the advantages over ^3He gas detectors of being compact and not requiring high voltages to operate. Solid-state neutron detection devices are classified as one of two types: indirect-conversion devices and direct-conversion devices.

In an indirect-conversion device (Figure 1a), a layer of a neutron-reactive substance (usually ^{10}B or ^6Li) is placed in contact with a separate detector material, typically a silicon diode. A neutron interacting in the reactive layer produces energetic reaction products, some of which deposit energy in the detector material, generating electron-hole pairs and hence a signal. Devices of this type have been produced by a variety of groups recently (e.g., McGregor 2009). A key shortcoming of such devices is that only some of the reaction energy can be deposited in the detecting medium; the rest is either absorbed in the reactive material or moves away from the detecting medium to conserve momentum in the reaction. Use of etching technologies to create complex structures in the silicon detector, in which the neutron-reactive material is then embedded, have led to significant increases in the neutron sensitivity for such devices. These devices are more expensive to fabricate, however.

In a direct-conversion device, the neutron-reactive material and the detector material are one and the

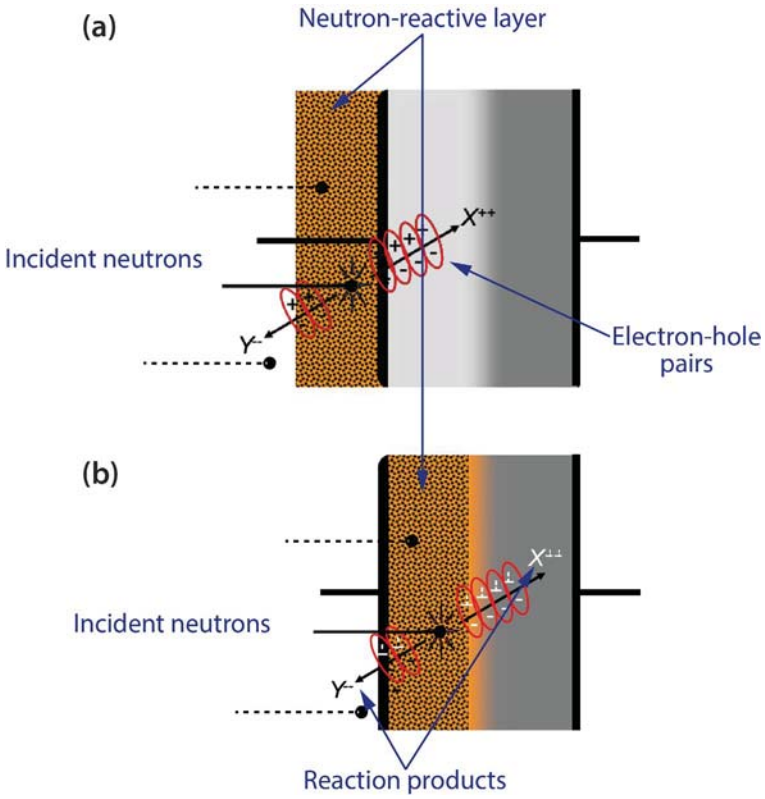

Figure 1. In a semiconductor (a) planar geometry indirect-conversion neutron detector, a neutron-induced reaction occurs in the reactive layer, creating energetic reaction products, some of which deposit energy in the semiconductor. (b) The semiconductor material of a direct-conversion detector is also neutron-reactive (Caruso 2010).

same—virtually all of the reaction energy is available for detection. But materials suitable for direct-conversion devices are relatively rare, and their properties are often poorly understood. A case in point is boron carbide; although it seems to be an ideal material for a direct-conversion detector, it has underperformed (Caruso 2010). More recently, groups at Fisk University (Tupitsyn 2012) and Radiation Monitoring Devices (Kargar 2011) have investigated $LiInSe_2$, which shows some potential for a direct-conversion thermal neutron detector material.

We proposed to produce a direct-conversion device from uranium oxides (primarily UO_2), which have hitherto been overlooked as neutron detector materials, despite being known to have semiconducting properties and to be neutron reactive. We proposed to use depleted uranium (DU) for this work, which consists primarily of ^{238}U. The fission cross section of ^{238}U for slow neutrons is small, unlike that of ^{235}U; for >1 MeV energy neutrons, however, such as from a fission source, the ^{238}U fission cross section approaches that of ^{235}U, making a DU-based detector suitable for fast neutron detection. A fast neutron incident on a ^{238}U nucleus induces fission, releasing >165 MeV of energy (Caruso 2010). This energy is deposited locally, creating copious electron-hole pairs, which are detectable as an electrical signal in the detector.

UO_2 has some fascinating properties, which make it an interesting material not only for radiation detection, but also as a general-purpose semiconductor material. The band gap is 1.3 eV, putting it in between silicon and GaAs, and making it suitable for room-temperature operation. The resistivity of intrinsic UO_2 is about 1.5×10^{-3} Ω-cm at room temperature, which is similar to silicon and GaAs. Additionally, UO_2 can withstand much higher temperatures (~2600 K) than silicon (~473 K), and because UO_2 is a ceramic material it is more resistant to radiation damage than many other materials (Meek 2001).

Professor Thomas Meek from the Materials Science and Engineering Department at the University of Tennessee, Knoxville (UT) was our collaborator on this project. Professor Meek has studied uranium

Table 1. MCNPX results for neutron interaction in 2 µm and 1/16" thick UO_2 samples

Neutron Energy	Fissions per Source Neutron	
	2 µm thick sample	1/16" thick sample
Thermal	8.6×10^{-6}	6.6×10^{-3}
1 MeV	8.3×10^{-8}	6.3×10^{-5}
10 MeV	4.9×10^{-6}	3.7×10^{-3}
^{252}Cf spectrum	7.0×10^{-9}	5.3×10^{-6}

oxide compounds and their properties for some time (Meek 2002, 2008). He has succeeded in fabricating p-n junctions and even a simple p-n-p transistor from UO_2 deposited in thin films using the sol-gel process. Professor Meek has also investigated the effects of various dopants on the electrical characteristics of UO_2.

In this first year of the project, we attempted to build upon Professor Meek's previous work and investigate various dopants and dopant levels for UO_2 and also for U_3O_8, which has been less studied but is known to be an intrinsic n-type semiconductor. The goal was to develop a solid-state detector suitable for neutron detection using intrinsic and doped UO_2 and possibly U_3O_8 or other uranium-based compound to create a Schottky, p-n or p-i-n heterostructure device. Simulations were performed using MCNPX to study neutron detection characteristics of fabricated devices.

Project

This project has three main components. The primary components are the fabrication and testing of uranium oxide–based devices as neutron detectors. A secondary component involves simulations of neutron sensitivity. Professor Meek and his group at UT have fabricated some simple UO_2 devices for testing. MCNPX was used to perform simulations of neutron sensitivity and to approximately model fission fragment energy deposition in the samples.

MCNPX Simulations

MCNPX was used to simulate neutron sensitivity of the UO_2 samples fabricated by UT. We expected there to be two types of samples made this year: thin film samples made using a chemical deposition coating technique (or sol-gel technique), and relatively thick single-crystal samples made using an arc-fusion technique in previous work by the UT group. As discussed in the next section, sol-gel samples were not available for experimental testing by the end of the year, but the simulation results will be discussed.

The following parameters were used in the MCPNX simulations:

- DU sample size:
  - Approximately 0.5" diameter
  - Sol-gel samples: 2 µm thick
  - Single-crystal samples: 1/16" thick
- Density: 10.97 g/cc
- Composition: 99.7% ^{238}U, 0.3% ^{235}U; these are fairly typical numbers for DU (natural uranium has ~0.7% ^{235}U)
- Neutron source:
  - Uniformly distributed, monoenergetic beam of neutrons normal to surface
  - ^{252}Cf point source 10 cm away
- Energies: Thermal, 1 MeV, 10 MeV, and ^{252}Cf spectrum

Simulation results are summarized in Table 1. Interestingly, efficiencies for thermal and 10 MeV neutrons are expected to be comparable—while there is very little ^{235}U in DU, the cross section for thermal neutron fission in ^{235}U is so much higher (580 barns) than the cross section for MeV neutron fission in ^{238}U (1–2 barns) that the overall efficiency ends up

being comparable. Efficiencies for the ^{252}Cf source are significantly lower, primarily because it is an isotropic source, so most of the neutrons never enter the sample (Figure 2).

Fabrication of UO_2 Samples

Our intention was to fabricate samples using the sol-gel chemical deposition technique. This technique is an inexpensive and effective way of depositing thin films on a substrate. The maximum film thickness that we can likely obtain with this method is on the order of a few microns. While this is most likely too thin to be of much practical use for neutron detection, it should prove sufficient for testing the concept. Because of difficulties in obtaining the required equipment, however, fabrication of the sol-gel samples was only just commencing at the end of FY 2013, so we did not have the opportunity to test any such samples. This effort will continue in FY 2014.

The UT group provided more than 40 single-crystal UO_2 samples from earlier work, from which we made some simple devices that we tested. The single-crystal samples were fabricated using an arc-fusion technique. The samples varied in size, but most were approximately 0.5" in diameter and 1.0–1.5 mm thick. The majority of the single-crystal samples were doped with different dopant materials in different concentrations at each of the sample faces. Gold and silver pastes were used to make electrode coatings on a surface of the samples in an attempt to make Schottky-type surface diodes. Ideally, such electrode coatings would be deposited using a sputtering apparatus, but a suitable sputterer was not obtained until near the end of the year. Therefore, we proceeded to test devices made using the pastes and in FY 2014 plan to test devices after coatings have been applied to them with the sputtering apparatus.

The devices made from the single-crystal UO_2 samples had a couple of shortcomings. First, the use of pastes to form the electrode contacts was problematic in that we encountered some difficulty forming a Schottky contact. The result was that these devices acted more like resistors than diodes. The second issue was that these were surface diodes (i.e., both electrodes were on the same surface) rather than bulk diodes where the electrodes are on opposite surfaces. This was primarily challenging in that it is unclear how to expect such a device to behave when attempting to count the pulses resulting from neutron-induced fission reactions. The electric field in the device is more complex than

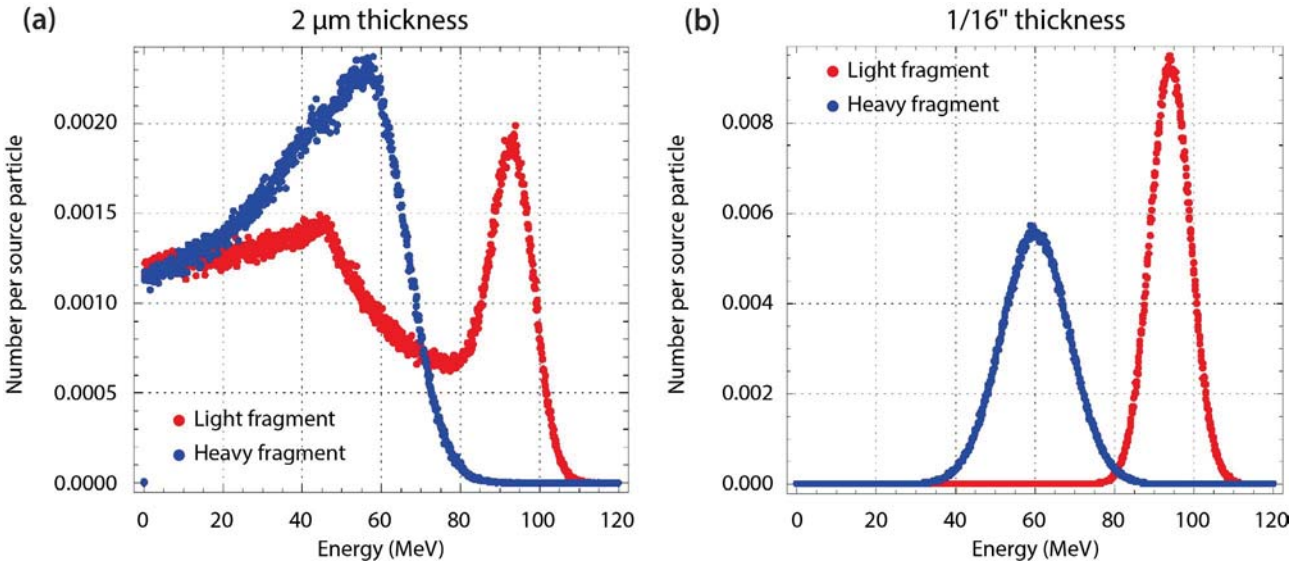

Figure 2. MCNPX modeling results approximating fission fragment energy distribution in (a) 2 µm thick and (b) 1/16" thick UO_2 samples. For the 2 µm sample, a significant fraction of the fragments escape the sample. For the thicker sample essentially all the fragment energy is deposited in the sample.

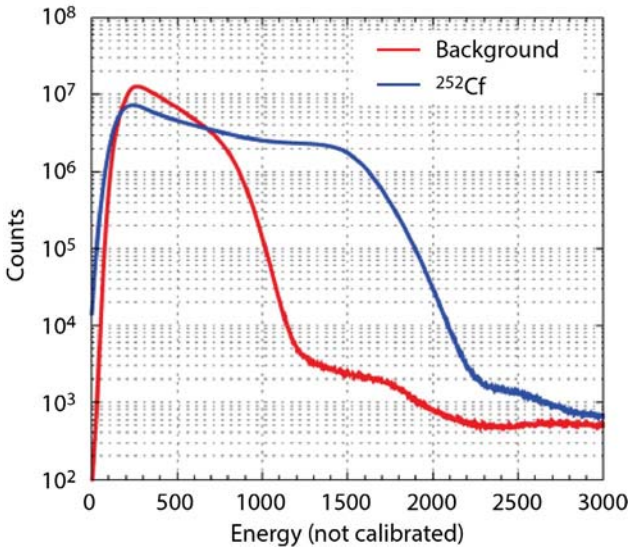

Figure 3. Pulse-height spectrum for phosphorous-doped single-crystal UO_2 sample. There is a clear difference between the background spectrum and the spectrum collected in the immediate proximity of the ^{252}Cf source.

in a parallel plate bulk diode geometry, and neutron reactions in different parts of the device could possibly lead to different pulse-heights, making the expected signal ambiguous. This ambiguity does not exist with bulk diodes. Nevertheless, several of the single-crystal devices were tested as potential fission neutron detectors. The results of these tests are discussed in the next section.

Experimental Testing of UO_2 Samples

Several of the single-crystal samples fabricated at UT were tested in laboratory facilities at the UT department of Nuclear Engineering. A ^{252}Cf source, with an approximate activity of 470,000 neutrons/second was used. In addition, an ORTEC high-voltage power supply (model 556), an ORTEC preamplifier (model 142), an ORTEC amplifier (model 527A), and an ORTEC multichannel analyzer (model 926) were part of the experiment setup.

Pulse-height spectra were obtained for an intrinsic sample and for samples doped with phosphorous and boron. Background spectra were collected away from the ^{252}Cf source for one hour. Another hour-long spectrum was collected with the sample 10 cm away from the source. A background spectrum and the spectrum collected near the source for the phosphorous-doped sample are shown in Figure 3. Spectra for the other samples tested look similar to that shown in Figure 3, and the spectra were very consistent across several integrations. There is clearly a significant difference between the two spectra, with the ^{252}Cf source spectrum exhibiting higher energy pulses. Unfortunately, the clear spectral features we anticipated are not present—one would expect to see a clear high energy peak, well separated from the background signal, corresponding to neutron induced fission. We deduce this is due in large part to the rather poor quality of the devices tested, as alluded to in the previous section. Nevertheless, the fact that the ^{252}Cf pulse-height spectra look significantly different from the background spectra is promising in that it indicates that even these non-ideal devices are effective as neutron detectors.

Conclusion

During this project we established a collaboration with UT to fabricate several UO_2 Schottky-type devices. Because of logistics complications, thin-film chemical deposition coating samples could not be made in this FY. However, a few single-crystal UO_2 surface "diodes" have been fabricated and successfully tested for neutron sensitivity, with the results indicating that UO_2 holds some potential as a direct-conversion neutron detector material. In addition, two papers are being prepared for the 2014 Materials Research Symposium in San Francisco. In FY 2014, we will continue with the fabrication and study of various doped thin-film samples. We will also pursue alternate fabrication methods if possible, such as pulsed laser deposition, chemical vapor deposition, and tape casting.

Acknowledgments

We would like to thank Larry Franks for useful discussions, particularly near the beginning of the project.

References

Caruso, A. N., "The physics of solid-state neutron detector materials and geometries," *J. Phys. Condens. Matter* **22**, 44 (2010) 443201.

Kargar, A., J. Tower, H. Hong, L. Cirignano, W. Higghins, K. Shah, "Lithium and boron based semiconductors for thermal neutron counting," *Proc. SPIE* **8142** (2011) 81421P.

McGregor, D. S., W. J. McNeil, S. L. Bellinger, T. C. Unruh, J. K. Shultis, "Microstructured semiconductor neutron detectors," *Nucl. Instrum. Methods Phys. Res. A* **608**, 1 (2009) 125–131.

Meek, T., M. Hu, M. J. Haire, "Semiconductive properties of uranium oxides," Waste Management 2001 Symposium, http://web.ornl.gov/~webworks/cpr/pres/108263_.pdf (2001), accessed October 9, 2012.

Meek, T. T., B. von Roedern, "Semiconductor devices fabricated from actinide oxides," *Vacuum* **83**, 1 (2008) 226–228.

Tupitsyn, E., P. Bhattacharya, E. Rowe, L. Matei, M. Groza, B. Wiggins, A. Burger, A. Stowe, "Single crystal of $LiInSe_2$ semiconductor for neutron detector," *Appl. Phys. Lett.* **101** (2012) 202101-1–202101-3.

An Experimental and Theoretical Investigation into the Chemical Properties of Uranium and Thorium Ions in the Gas Phase and on Surfaces

STL-19-13 | Continued in FY 2014 | Year 1 of 3

Manuel J. Manard[1,a]

The design of an instrument that embeds a variable temperature, high-pressure drift/reaction cell between two quadrupole mass analyzers for investigating gas-phase interactions of uranium (U) and thorium (Th) ions with neutral reactant species is described. This was accomplished during the first year of a 3-year collaborative effort involving Special Technologies Laboratory and the University of California, Santa Barbara, to probe the interactions of U and Th ions both in the gas-phase and deposited on surfaces. With this design, ions generated will be mass selected by the first quadrupole for injection into the drift/reaction cell. When built, the cell will measure 4 cm in length, have a uniform electric field supplied by eight ring electrodes situated inside the cell body, will be variable in pressure up to 5 Torr, and will range in temperature from 80 to 800 K. Ions exiting the cell will then be mass selected by the second quadrupole and detected by an electron multiplier. The instrument has been designed to examine the thermodynamic and kinetic properties of U and Th ions when reacting with ligands of interest in the gas phase. We also used density functional theory to theoretically model the systems studied to elucidate the complex factors involved with these bonding interactions.

[1] manardmj@nv.doe.gov, 805-681-2121
[a] Special Technologies Laboratory

Background

A deeper understanding of the chemical properties of uranium (U) and thorium (Th) compounds could lead to advancements in techniques used to detect these compounds for nuclear nonproliferation. A detailed investigation into the fundamental chemical interactions that occur, for example, when these materials are exposed to the atmosphere or spilled on the ground could unearth new proliferation signatures or generate new methodologies for remote detection. By comparing/contrasting experimental data collected on the gas-phase interactions of U and Th with select ligands to the data gathered from depositing those analytes on surfaces, and combining these findings with theoretical calculations using density functional theory, we expect to further our knowledge about the fundamental chemical properties of these systems. Additionally, we hope the results obtained by this study will uncover novel chemical signatures that can be exploited for the purpose of treaty verification and nonproliferation.

Studies involving mass-selected, ion-neutral interactions have the potential to elucidate some of the complex factors involved with the bonding processes of this species. By experimentally determining the fundamental physical properties of these molecules, such as bond dissociation energies, association entropies, molecular geometries, and reaction energetics (to name a few), a deeper understanding of these processes will be gained, leading to the possibility of

manipulating their chemistry for a specific outcome. These results can also be used as an experimental point of reference to verify the accuracy of theoretical methods used to predict these properties for more complicated systems.

Project

Instrument Design

An overview of the instrument is shown in Figure 1. The design details of the components that make up the various regions of the instrument are discussed in the following sections. The mechanical design of the system was generated using SolidWorks, while ion trajectory simulations were performed using Simion 8 to determine optimal electrode configuration and electric field strengths for efficiently guiding the ion beam through the system.

Ion Source

The instrument was designed to allow for the use of various types of ionization sources, depending on the nature of analytes being studied. These ion source methods include electron impact ionization, glow discharge ionization, and laser vaporization ionization. Given that the target analytes of this project are U and Th, the primary ionization methodology is expected to be laser vaporization. Accordingly, metal ions will be generated using pulsed laser vaporization of a translating/rotating metal rod in a high-pressure argon (Ar) bath gas. The desorbed metal plasma will be entrained in the Ar to collisionally cool the plasma and, if desired, generate clusters. The laser light will enter the vacuum chamber via a laser window positioned perpendicular to the axis of the instrument. A pulse valve will be used to generate the Ar pulse, and a delay generator will be used to synchronize it with the laser pulses. An isolation valve will be positioned between the source chamber and rest of the instrument to allow sample changes without the need to vent the entire system.

First Quadrupole and Transfer Lenses

Ions exiting the source enter a three-element lens system designed to focus the ion beam into the first quadrupole for mass selection. An xy-steering element is also incorporated near the start of the lens system. The quadrupole is made up of ¾-inch rods and has a mass range of 4–4000 amu (made by Extrel Core Mass Spectrometers). Ion kinetic energies through the quadrupole can be varied; higher ion energies lead to higher sensitivity and ion transmission through the quadrupole, while lower kinetic energies maximize the mass resolution. Similar steering/focusing elements are positioned directly after the first quadrupole.

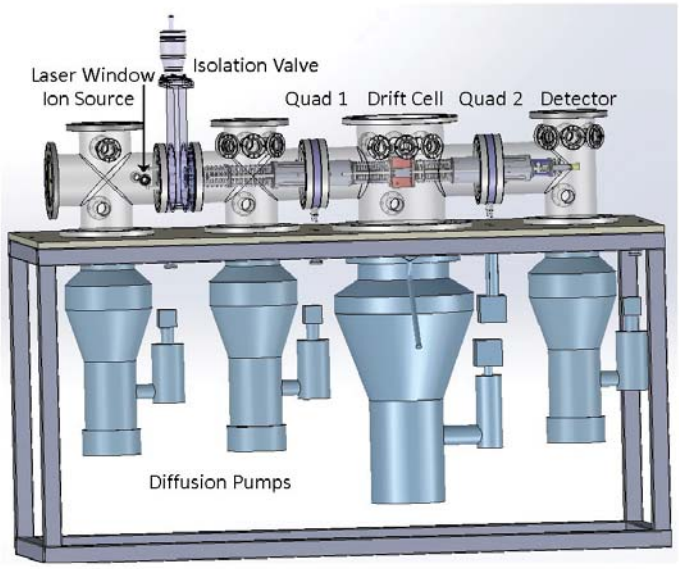

Figure 1. A model of the instrument as generated with SolidWorks. The vacuum chambers are shown transparently so the internal components of the instrument can be viewed.

These electrodes will be used to focus the mass-selected ion beam into the drift/reaction cell. A Simion 8 simulation of this section is shown in Figure 2.

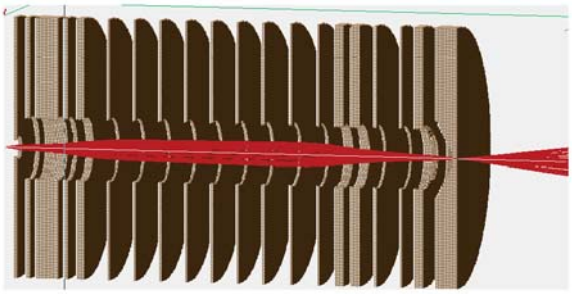

Figure 2. A 3-D cross section of an ion trajectory simulation, generated by Simion 8, of the pre-cell steering/focusing assembly. The simulation is used to determine the magnitude of the electric fields required to yield 100% ion transmission into the drift/reaction cell.

Drift/Reaction Cell

A schematic of the drift/reaction cell is shown in Figure 3. The cell is based on the design of Kemper and Bowers (1990) and will consist of a cylindrical copper shroud that contains the heating/cooling passages, an end cap that is electrically isolated from the shroud, and eight ring electrodes that provide the uniform drift field through the cell. A precision resistor chain will deliver the proper potentials to the individual drift rings. The ions will be drawn though the cell under the influence of the electric field, which will be sufficiently weak so as not to significantly perturb the thermal energy of the ions. The drift volume will be 4 cm long by 1.5 cm in diameter, with entrance and exit orifices measuring 0.5 mm in diameter. This arrangement will allow for a maximum operating pressure of 5 Torr. Pressure in the cell will be monitored using a capacitance manometer. Separate gas inlet connections will be made to the helium (He) buffer gas, the reactant gas, and the pressure monitor. The experimental temperature range of the cell can be varied from 80 to 800 K. Temperatures greater than 300 K will be achieved by resistive heating of tantalum resistors embedded in the cell body, while temperatures below 300 K are reached by flowing nitrogen gas cooled in liquid nitrogen through channels inherent in the cell body. The temperature will be monitored by three thermocouples placed at various locations on the cell. This is a means of determining whether significant temperature gradients across the cell exist and whether errors in the temperature reading are present.

Second Quadrupole/Detector Assembly

A schematic of the quadrupole/detector assembly is shown in Figure 4. Ions exiting the cell will be accelerated and focused into a second quadrupole using a set of transfer lenses identical to the steering/focusing elements situated prior to the first quadrupole. The second quadrupole is also identical to quadrupole one (made by Extrel Core Mass Spectrometers), again consisting of ¾-inch rods and having a mass range of 4–4000 amu. Upon exiting the second quadrupole, the ions will pass through a final steering/focusing lens combination and will be detected using a conversion dynode and an electron multiplier. The resulting quadrupole mass scans will then be collected on a multichannel scaler capable of 100 ns resolution (made by ORTEC MCS Plus).

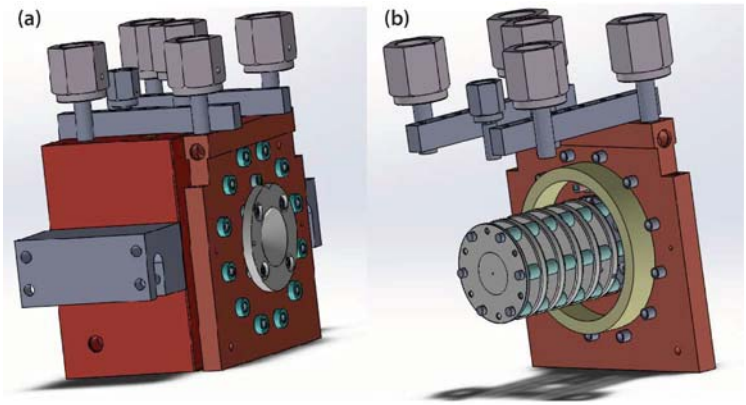

Figure 3. A model of the drift/reaction cell as generated with SolidWorks, showing (a) the complete cell assembly and (b) the cell assembly with shroud removed so the drift rings, which are mounted to the end cap, are visible

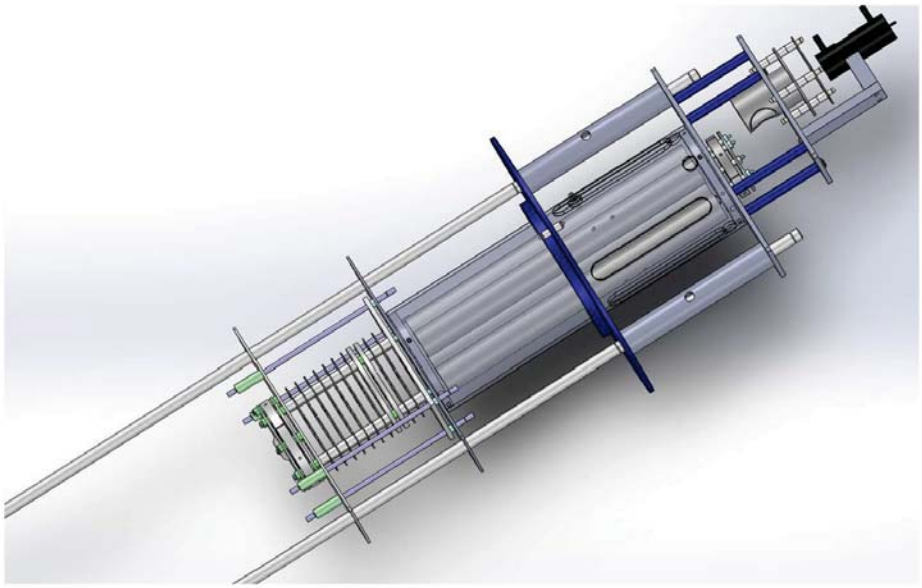

Figure 4. A model of the second quadrupole/detector assembly as generated in SolidWorks. The quadrupole shroud is transparent so the internal ¾-inch rods are visible. The detector is the small element shown in black.

Vacuum Design

The vacuum system will consist of four chambers containing the various components that make up the instrument: the ion source chamber, the first quadrupole chamber, the main chamber (housing the cell), and the second quadrupole/detector chamber. The main chamber will measure 10 inches in diameter and will be pumped by a 10-inch diffusion pump. All other chambers will measure 6 inches in diameter and will each be pumped by 6-inch diffusion pumps. With the exception of the source diffusion pump, all diffusion pumps will share a common foreline driven by a single mechanical pump. The source chamber will be backed by a second mechanical pump to isolate the source and simplify the process of exchanging samples within the chamber.

The pressure differential between the cell and the main chamber will depend on the pressure inside the cell. However, given the 0.5 mm cell apertures, the maximum operating cell pressure will be approximately 5 Torr. This will generate an operating main-chamber pressure of approximately 10^{-4} Torr. The conductance-limiting orifices between the main chamber and the two quadrupole chambers are provided by the exit aperture of quadrupole one and the entrance aperture of quadrupole two. Both apertures measure 0.3 inches in diameter. This will give rise to an operating pressure of approximately 5×10^{-6} Torr in each quadrupole chamber. Additionally, the shroud of each quadrupole will be vented to allow for more efficient pumping in the quadrupole chambers. Finally, a conductance-limiting orifice measuring 0.3 inches in diameter will be situated between the source chamber and the first quadrupole chamber. The operating pressure of the source chamber will depend on the duration of the Ar pulses provided by the pulse valve. However, the operating pressure of the chamber will likely not exceed 10^{-4} Torr.

Experimental Methods

The instrument described above is slated to be assembled in FY 2014. Thus, no experimental data have been collected to date. A brief description follows of the experimental methods that will be used to analyze the data the system is expected to generate, as well as the physical properties it can measure when completed.

Equilibrium Reactions

Equilibria will be rapidly established in the cell for successive association reactions of neutral ligands to the core ions (Equation 1).

$$M_m^{+/-}L_{n-1} + L \rightleftarrows M_m^{+/-}L_n \quad \textbf{(1)}$$

Integrated peak areas of the various $M_m^{+/-}L_n$ ions will be recorded. These values, along with the pressure of the ligating gas (P_L) in Torr, are used to determine an equilibrium constant (K_p°) for each reaction using Equation 2.

$$K_p^\circ = \frac{\left[M_m^{+/-}L_n\right]}{\left[M_m^{+/-}L_{n-1}\right]} * \frac{760}{P_L} \quad (2)$$

The equilibrium constants can then be used to calculate the standard Gibbs free energies for the reactions,

$$\Delta G_T^\circ = -RT\ln\left(K_p^\circ\right). \quad (3)$$

The values obtained for ΔG_T° plotted versus the temperature are used to obtain ΔS_T° and ΔH_T° for each reaction using Equation 4:

$$\Delta G_T^\circ = \Delta H_T^\circ - T\Delta S_T^\circ. \quad (4)$$

The resulting plots will be linear over the experimental temperature range. A least-squares fitting procedure will be used to obtain slopes and intercepts of each line. The slopes will be used to determine the association entropy (ΔS_T°) for Equation 1, and the intercepts will give the corresponding ΔH_T° values.

Ion Mobility

In order to obtain the mobility data, a pulse of mass-selected ions are injected into the He-pressurized cell. A weak, homogeneous electric field is applied across the cell, causing the ion packet to drift toward the small exit orifice. The ion packet is rapidly thermalized by collisions with the buffer gas. Ions exiting the cell are then detected as a function of time in order to establish an arrival time distribution (ATD). The mobility of the ions, $K_\circ$, is given by Equation 5 (Mason 1988),

$$K_\circ = \left(l^2 \frac{273}{760T}\frac{p}{V}\frac{1}{t_a - t_\circ}\right), \quad (5)$$

where l is the length of the drift cell, T is the temperature in Kelvin, p is the pressure of the He buffer gas in Torr, V is the drift voltage, t_a is the arrival time of the ions acquired from the center of the ATD peak, and $t_\circ$ is the time the ions spend outside of the cell. A plot of t_a versus p/V has a slope inversely proportional to $K_\circ$, which yields the collision cross section from Equation 6 (Mason 1988),

$$\sigma = \frac{3e}{16N_\circ}\left(\frac{2\pi}{\mu\, k_b T}\right)^{1/2}\frac{1}{K_\circ}, \quad (6)$$

where $N_\circ$ is the number density of He at standard temperature and pressure, e is the charge of the ions, μ is the ion-He reduced mass, k_b is Boltzmann's constant, and T is the temperature in Kelvin.

Conclusion

The design of an instrument that embeds a variable-temperature, high-pressure reaction cell in between two quadrupole mass analyzers for the purpose of studying gas-phase, ion-neutral reactions/interactions of U and Th ions has been described. The instrument has been designed to examine the thermodynamic and kinetic properties of U and Th ions when reacting with ligands of interest in the gas phase. As part of a future effort to facilitate collaboration with the University of California, Santa Barbara (UCSB), a partnership has been established between Special Technologies Laboratory and Professor Michael Bowers of UCSB. This partnership will be used to conduct the surface science experiments in the near future using facilities available at the university. Assembly of the instrument is scheduled to begin during the first quarter of FY 2014. Accordingly, both quadrupole mass spectrometers and the associated power supplies were acquired during the last quarter of FY 2013 and are ready for instrument assembly.

References

Kemper, P. R., M. T. Bowers, "A hybrid double-focusing mass spectrometer—high-pressure drift reaction cell to study thermal energy reactions of mass-selected ions," *J. Am. Soc. for Mass Spectrom.* **1**, 3 (1990) 197–207.

Mason, E. A., E. W. McDaniel, *Transport Properties of Ions in Gases*, John Wiley & Sons, New York, 1988.

This page left blank intentionally

Neutron Resonance Spectroscopy

NLV-22-13 | Year 1 of 1

Tim Meehan,[1,a] Chris Hagen,[a] Daniel Lowe,[a] Steve Molnar,[b] and Robert O'Brien[c]

The goal of this project was to perform a neutron resonance spectroscopy (NRS) experiment to measure the temperature of various known metal samples in order to determine the ultimate accuracy that an NRS temperature measurement could achieve. This work was preliminary to performing a dynamic NRS experiment using the deuterium dense plasma focus (DPF) machine to measure the temperature of a shocked target, and was to provide a bulk temperature measurement for equation-of-state models of experimental data. We designed and built an oven that would handle selected material samples. Testing of metal samples revealed that changes in the bulk temperature were subtle, and therefore the experiment at the DPF would not be feasible.

[1] meehanbt@nv.doe.gov, 702-295-0490
[a] North Las Vegas; [b] Powder River Geophysical; [c] University of Nevada, Las Vegas

Background

Pyrometry combined with emissivity can now measure shocked metal surface temperatures above 1200 K to < 2% (La Lone 2013). However, there remain substantial uncertainties in relating a surface temperature to that of the bulk material in the sample behind the shock front because of uncertainties in the thermal conductivities of the metal, window, and glue between them. A temperature measured by neutron resonance spectroscopy (NRS) is a bulk temperature, instead of a surface temperature. Even a rough NRS temperature measurement might make a useful validation of a pyrometry measurement and extrapolation to the interior temperature, and NRS measurements of a few percent or better would provide data good enough to guide the thermal conductivity work.

Project

Material Study

The materials used in this project—tungsten, tantalum, and silver—were chosen because they had neutron resonances from 1 to 20 eV with cross sections of 10^4 barns or larger. Previous experiments with NRS had used tungsten, tantalum, silver, and indium (Yuan 2005). Although tungsten and tantalum have high melting points, they rapidly oxidize in air hotter than 500°F. Unfortunately, this was found experimentally. Indium's low melting point, 313°F, and much lower in-air oxidation temperature prevents us from using heated indium foils to make NRS measurements. Luckily, silver does not have a rapid oxidization reaction with air and has a melting point of 1763°F; with the experimental setup we are using, this melting point is high enough for us to observe changes in the width of the resonance due to thermal broadening. Any oxidization would be small enough that we would be unable to detect changes in the mass of the sample. Furthermore, oxygen does not interfere with the resonance spectrum in the epithermal region, as we would be using only be a thin coating of material, and the total neutron cross section is about an order of magnitude lower than that for ^{6}Li (Rose 1991).

Oven

In order to see measurable differences in the temperature broadening of the neutron resonance spectrum of a sample, the sample has to be heated in excess of 1000°F in an oven that does not interfere with the epithermal neutron flux used to probe the sample. This is problematic because the same insulation that would be used to keep a constant temperature in our sample oven would interfere with the epithermal neutron flux. Therefore, we knew that we would have to procure or build an oven capable of reaching high temperatures but having insulation that would not interfere with the epithermal flux.

The oven used in the Los Alamos National Laboratory (LANL) NRS experiments was a tube furnace that essentially uses air as an insulator. A tube furnace heats the center of a long ceramic tube. The sample is placed in the center of the tube, and the tube is placed so that the epithermal neutron flux passes along the axis of the ceramic tube. This arrangement is beneficial in that there is minimal matter in the path of the epithermal neutrons that would interfere with the neutron resonance spectrum. A major drawback of this furnace is that the largest diameter of the ceramic tubes available is about 4 inches. Hence, samples are never larger in diameter than 4 inches, which reduces the amount of filtered epithermal neutron flux that can be recorded by the detector array. Other limitations are that the tube furnace is expensive, and the bulk of the machine and its insulation and heating elements not only make it hard to position, but also make it produce a large scattering signal component in the detector array. In addition to being unsuitable for our experiment, the LANL oven had been stored poorly; repairing it would have been more costly than replacing it.

Therefore, we designed and fabricated an oven specifically for this experiment. Although we investigated an oven that would heat samples in an inert environment, we rejected the concept as being too expensive and risky, and chose a more simple and robust design. The oven design chosen used commercial-off-the-shelf components and had a 12-inch-diameter mouth, as shown in Figure 1. Several tests indicated that the oven would require insulation in the axial direction in order to get to temperatures that would provide measurable broadening of the resonance in the sample. Aluminum foil was chosen as an insulator for several reasons: (1) it would not oxidize or melt at the experimental temperatures, (2) it minimized air currents in the heated volume and therefore stabilized temperature by eliminating the convective losses from inside of the heated air volume, and (3) aluminum has a low enough neutron scattering cross section to be effectively transparent to the epithermal neutron flux—about 1 barn in the energy range of 1–100 eV (Rose 1991).

Figure 1. NRS sample oven, shown with the aluminum foil removed on the front, exposing the heating element inside

Denoising Study

The neutron resonance spectra often have noise that obscures the resonance dips. Filtering or denoising the data makes the resonance dips more observable in the data but does not improve the fitting of the resonance peaks to determine the bulk temperature. Because the purpose of this project was to determine the ultimate accuracy of the temperature measurement, it was important to understand the role filtering has in the analysis process.

Over time, the filtering or denoising process has evolved from common, simple averaging techniques, where the averaging was done to make the signal "look better," to the more rigorously designed H1 regularization technique that we are using now, which chooses a regularization parameter based on the measured noise in the scope trace before the signal begins. First, we begin with the H1 regularization functional, where we find the signal, μ, that minimizes the noise in the actual signal, y, with respect to the regularization parameter, α,

$$L(t;\mu,\mu') = \underset{\mu}{\operatorname{argmin}} \|\mu - y\|^2 + \alpha\|\mu'\|^2 = \underset{\mu}{\operatorname{argmin}} \int_\Omega (y-\mu)^2 + \alpha(\mu')^2 \, d\Omega. \quad (1)$$

In order to find the signal, μ, that minimizes this functional, we use the Euler-Lagrange differential equation

$$\frac{\partial L}{\partial \mu} - \frac{d}{dt}\left(\frac{\partial L}{\partial \mu'}\right) = 0. \quad (2)$$

After we compute the derivatives, we are left with a differential equation, relating the known signal, y, to the denoised signal, μ,

$$-\alpha\mu'' + \mu = y. \quad (3)$$

In order to solve this numerically for an input signal that is regularly sampled, we use a discrete second-order derivative (three-point stencil; h is the time step),

$$-\frac{\alpha}{2h^2}(\mu_{k-1} - 2\mu_k + \mu_{k+1}) + \mu_k = y_k. \quad (4)$$

The boundary condition that produces the lowest overshoot at the ends is the "anti-reflective" boundary condition.

With a regularization technique as described above, we still have to determine what the regularization parameter should be, based on the noise in the data. The method chosen for this work, known as the discrepancy principle (Hansen 2006), is

$$\|y - u\|_2 = \tau\sigma_{noise}, \quad (5)$$

where y is the signal, u is the denoised signal, and σ_{noise} is the noise standard deviation. The constant τ is ordinarily specified to be in the range of 2 to 5. The noise standard deviation can be determined from the scope trace containing the data because prior to the arrival of the NRS signal, the digitizer records a few microseconds of the quiescent signal present on the channel. This gives a range of regularization parameters that optimize the smoothness of the denoised signal; a sample of this is shown in Figure 2.

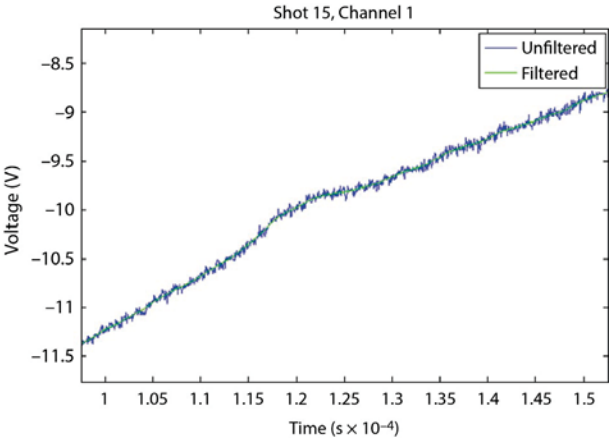

Figure 2. Example of denoised data showing the 5 eV resonance in ^{107}Ag

Data Fitting Study

The most straightforward way of determining the temperature-broadened resonance data for the nuclides of interest was to use the data in the MCNPX 2.7 data libraries. Robert O'Brien at the University of Nevada, Las Vegas, generated temperature-broadened resonances for 300, 600, 900, and 1200 K. These tables were then used to create a parametric function in MATLAB that takes rundown time, moderator-detector distance, sample thickness, and sample temperature as input parameters. The function is then used to do a nonlinear least squares fit to the experimentally observed data in order to estimate the target temperature.

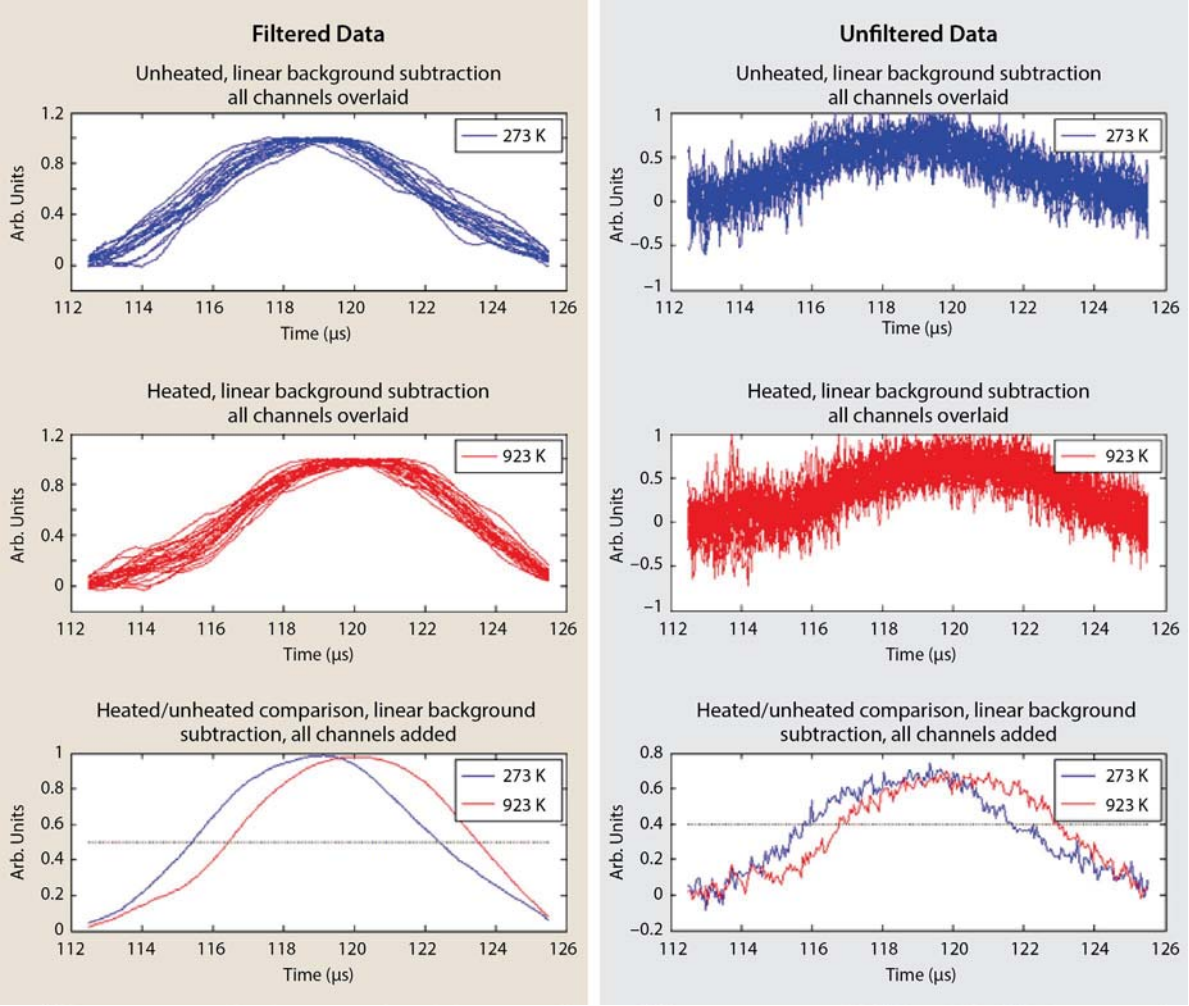

Figure 3. An analysis of the broadening of the 5 eV resonance in silver for heated (red) and unheated (blue) silver targets, with and without filtering applied to the resonance. In the images above, the resonances were background subtracted and normalized to unit height, and then the FWHM of the resonance was measured. In the bottom images, the heated and unheated data are averaged together for comparison.

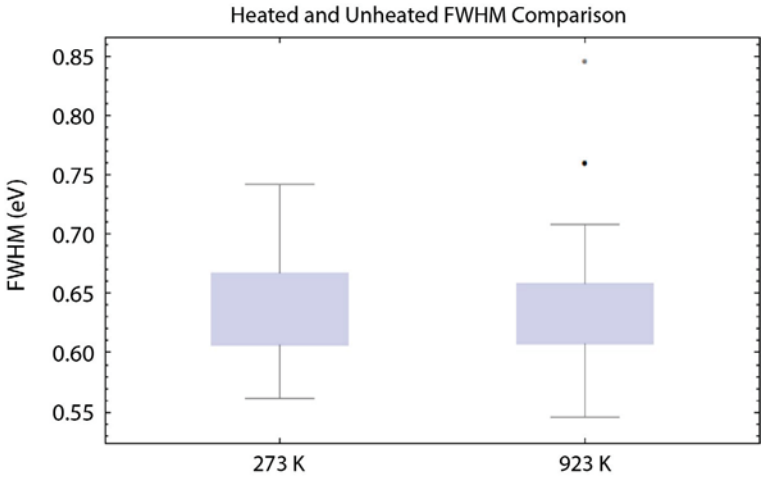

Figure 4. Box-and-whisker plot for the heated and unheated data. The experimental data do not indicate that there is a statistical difference in the widths of the resonance peaks.

The functional form of the NRS signal we were using to estimate the temperature and locate the resonances is somewhat convoluted to describe. It is important to understand that the signal is an absorption measurement, and furthermore, the neutron flux probing the higher energy resonances is larger than that available for probing the lower energy resonances. In our model the background signal depends on the neutron yield of the shot, the environment that the detectors are in, and a neutron resonance signal that is multiplied onto the background signal, where the resonances will appear as dips. While not included in the parametric function, the following factors are important: the broadening effects caused by the moderator, the fluorescence lifetime(s) of the scintillator, and the solid angle subtended by the target at the moderator. If these effects are not removed, the parametric fitting function would represent the resonances as being broader, and higher-energy resonances would be much less visible due to the blurring effect.

Figure 3 displays data taken for a natural silver foil at room temperature and at 923 K. The 5 eV resonance was located and subtracted from the linear background to allow for determination of the FWHM of the resonance in energy. For comparison, both the denoised and raw data are shown. The median FWHM of the unheated sample was 0.633 eV, and the median FWHM of the heated sample was 0.637 eV. An analysis of the variance in the sample, also shown in Figure 4, shows that from the FWHM data alone we cannot conclude that the FWHM increased due to the temperature change in the sample.

Detector Study

During the planning phase, we were looking for thermal-neutron-sensitive scintillators that might be more sensitive than the ^{6}Li glass that had been used in the past. We did a literature survey and found that Eljen Technologies sells boron-loaded plastic and ^{6}Li-loaded ZnS. ^{10}B has a capture cross section for

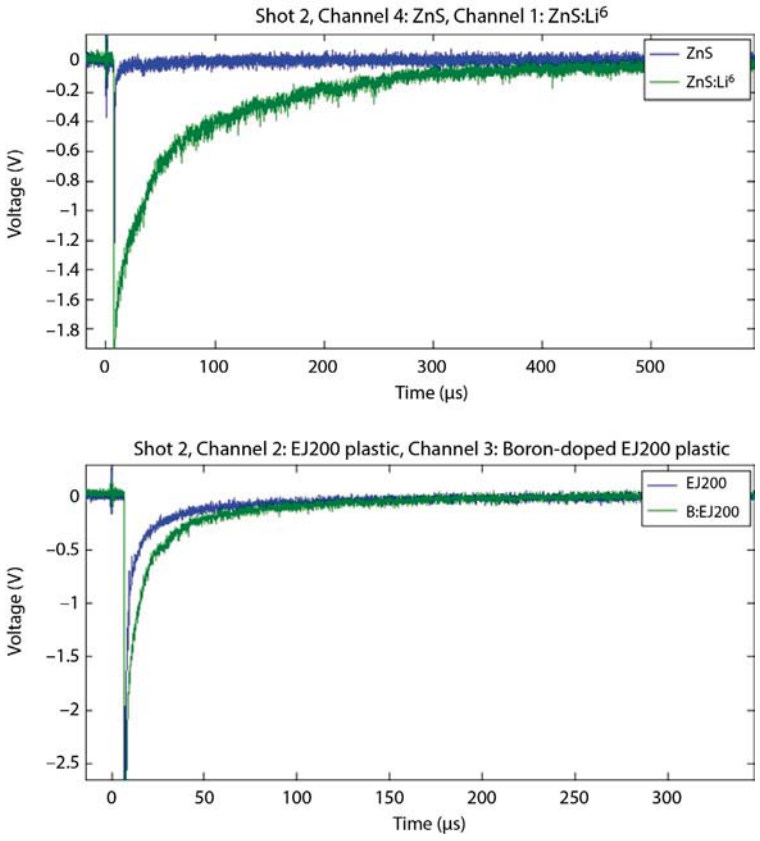

Figure 5. New scintillator material comparisons. In the top plot, the insensitivity of ZnS to gamma flux is shown. In the bottom plot, the relative sensitivity of EJ200 to gamma flux is shown.

thermal neutrons that is roughly four times that of ^{6}Li below 100 eV (Rose 1991). Based on experimental data, the thin ^{6}Li glass, the boron-loaded scintillating plastic, and the ^{6}Li-loaded ZnS all performed poorly compared to the thick ^{6}Li glass that LANL had used in the original experiment. No conclusive reason was determined for this.

Qualitatively, as seen in Figure 5, the ZnS did show a dramatic difference in signals between the ^{6}Li-loaded ZnS and the ZnS. This indicates that the ZnS is very gamma-insensitive, and that the ^{6}Li loading causes it to be sensitive to the neutron flux. Unfortunately, the fluorescence time of the ZnS was quite long, which washed out any resonances that would have been there. The ^{6}Li glass performed much better. In the lower graph, boron-loaded plastics were compared to non-boron loaded plastics. Boron was chosen because it had a large thermal capture, but we see in Figure 5 that the boron-loaded plastic is not significantly brighter than the non-boron-loaded plastic on the same shot.

Conclusion

As illustrated in Figure 4, the FWHM resonance data did not indicate that it was possible to measure the temperature of the sample using the deuterium dense plasma focus (DPF) located at the A-1 High Bay Extension in North Las Vegas. The changes in the width of the resonance are subtle, and even adding together a number of shots was not sufficient to reduce the noise in the signal to the level that the subtle widening effect with temperature could be measured. It is hoped that with larger neutron yields available with the deuterium-tritium DPF, the resonance signal would be increased relative to the noise, and the measurement would then be possible.

Acknowledgments

The authors wish to thank the DPF group for assistance in setting up the experiment, helping with shielding design and data acquisition, as well as helpful insights into how to design the sample oven. Thanks to Irene Garza for quality checking the photomultiplier tubes used in the experiment and monitoring tube bases for problems during the experiment. The authors also thank Aaron Luttman and Marylesa Howard for supporting the statistical analysis of the data and assistance in designing and implementing the denoising algorithm used in this experiment. We are grateful for Dennis Daley's ability to turn our simple design drawings into real objects made of metal.

References

Hansen, C., J. G. Nagy, D. P. O'Leary, *Deblurring Images: Matrices, Spectra, and Filtering*, SIAM, Philadelphia, 2006.

La Lone, B. M., G. D. Stevens, W. D. Turley, D. B. Holtkamp, A. J. Iverson, R. S. Hixson, L. R. Veeser, "Release path temperatures of shock-compressed tin from dynamic reflectance and radiance measurements," *J. Appl. Phys.* **114**, 063506 (2013).

Rose, P. F., ed., "ENDF/B-VI Summary Documentation," Cross Section Evaluation Working Group (CSEWG), National Nuclear Data Center, Brookhaven National Laboratory, Upton, New York, 1991.

Yuan, V. W., J. D. Bowman, D. J. Funk, G. L. Morgan, R. L. Rabie, C. E. Ragan, J. P. Quintana, H. L. Stacy, "Shock temperature measurement using neutron resonance spectroscopy," *Phys. Rev. Lett.* **94**, 12 (April 2005) 125504.

Handheld Directional Gamma-Ray Radioisotope Identifier

RSLA-08-13 | Year 1 of 1

Sanjoy Mukhopadhyay,[1,a] Stephen Mitchell,[b] Paul Guss,[c] Rusty Trainham,[d] and Alden Curtis[e]

Our objective was to design and build a prototype, light-weight, handheld, gamma-ray spectrometer with directional sensitivity. It is important for first responders in a radiological emergency to have an easy-to-use gamma spectrometric detection system that determines the incident gamma-ray energy along with the relative angular position of a point-like radioactive source in a near-field measurement (≤3 meters from the source). The technical challenge of this project, driven by search scenarios for monitoring crowds in national special security events, was to determine the relative angle of a gamma-ray-emitting source (50 μCi strong) at a distance of 3 meters from the detector in 3 minutes. We designed and built three types of small, portable, light-weight, directional, gamma energy spectrometers using three types of light collection media, namely an ordinary photomultiplier tube with a bi-alkaline photocathode, a solid-state photomultiplier, and a position-sensitive multi-anode photomultiplier. All three spectrometers showed remarkable (ΔΘ = ±2°) sensitivity to relative angular position of the source in near-field laboratory measurements.

[1] mukhops@nv.doe.gov, 301-817-3319
[a] Remote Sensing Laboratory–Andrews; [b] North Las Vegas; [c] Remote Sensing Laboratory–Nellis;
[d] Special Technologies Laboratory; [e] Los Alamos Operations

Background

The prototype device is designed for the first responders—it is ruggedized, fast and responsive (with quasi real-time data output in a visual mode), handheld, easy to use, light-weight, low-power, easy to replace, and will provide spectroscopic and angular information of the target gamma-ray emitting source with reference to the detector. In terms of the form factor, it conforms to the size and shape of an identiFINDER, commercially available from FLIR Corporation (FLIR 2013). The identiFINDER is the industry standard handheld spectrometer. The proposed detector far exceeds the capability of an identiFINDER by providing a larger opening angle and angular position information.

Currently available NA-42 backpack detector systems do not provide adequate angular position information of the target radiation source or gamma energy spectral information. Recently developed imaging systems, such as the Domestic Nuclear Detection Office's standoff radiation detection systems (McKenna 2011), Pacific Northwest National Laboratory's Gamma Tracker (Batdorf 2009), or the Radiation Monitoring Devices, Inc. (RMD) RadCam (RMD 2010), are bulky, slow, and cannot provide search and angular position information simultaneously.

In a render safe scenario, high-sensitivity spectrometers are deployed, but they cannot gather any spatial or spectral information about multiple point-like gamma emitters or gamma source distribution. Having this information may reveal a great deal about the threats posed by the source(s). The handheld spectrometer we are developing can also help the NNSA Accident Response Group localize and identify the radioactive

components of a device. For second line of defense application, a quick systematic scan of a container will easily reveal the presence of discrete point-like or distributed sources.

Physics Principles

Careful placement and orientation of individual detectors with reference to other detectors in an array can provide improved angular resolution for determining the source position by occlusion mechanism. By evaluating photopeak area values and uncertainties, efficiencies, branching ratio, peak area correction factors, and the correlations between these quantities, one can determine the precise activity of a particular radioisotope from a mixture of radioisotopes that have overlapping photopeaks that are ordinarily hard to deconvolve. This spectral coincidence technique, often known as covariance spectroscopy, examines the correlations and fluctuations in data that contain valuable information about radiation sources, transport media, and detection systems. Covariance spectroscopy enhances radionuclide identification techniques, provides directional information, and makes weaker gamma-ray emission—normally undetectable by common spectroscopic analysis—detectable, by virtue of the fact that signal from Compton continua can be remapped into photopeaks.

Covariance spectroscopic data collection boils down to collecting multichannel analyzer data for all available channels (1K) in list mode for a short time interval from each of the sensor elements in an array. In the analysis phase, one looks at positive and negative correlations between two significant elements in the array (viz., adjacent sensors for emphasizing Compton effect or diametrically opposite sensors for establishing occlusion) by requiring software coincidence (for positive correlation) or anticoincidence (for negative correlation) within short time intervals.

In typical coded aperture imaging systems, high-Z materials are used as masks of particular geometric forms to block gamma-ray incidence on the imaging plane (Gehrels 1985). The information carried by the gamma rays absorbed by the mask is lost. By using responsive detector materials (for masking) similar to those in the imaging plane, information carried by the blocked gamma ray can be saved. This technique is called active masking. The Remote Sensing Laboratory–Andrews (RSL-A) has used large blocks of NaI:Tl as an active masking agent in building the Occluding Scintillator Crystal Array (OSCAR). The geometric occlusion of one sensor by another member in a symmetric array of sensors creates patterns in the passage of gamma rays that reveals angular information.

Size of the detection elements is important. Depending on the gamma-ray energy, a relatively small sensor would afford more Compton scattering angular information than a large one; plus, because the system is handheld, it needs smaller crystals.

Project

MCNPX Simulations

The MCNPX code was used to obtain gamma energy spectral and gross gamma-ray count rates from detectors under different geometric settings using nominal check sources (^{137}Cs, ^{60}Co, ^{241}Am) of 100 µCi strength at a distance of a meter from the detector array center. The isotope mix was chosen to cover the large dynamic range of gamma energy (59–1332 keV).

To simulate ^{241}Am, ^{137}Cs, and ^{60}Co sources of 100 µCi, the following prescription was used:

1. Obtain basic x-ray and γ-ray (daughters, alpha emissions, etc.) photon per yield and energy line data for each isotope from the Lawrence Berkeley Laboratory website (Firestone 2000). This information was also conveniently formatted and saved in simple comma-separated value formatted files from PeakEasy software maintained by Los Alamos and Sandia National Laboratories.

2. Divide the energies into 1000 bins, combine contributions from all isotopes, and sort from smallest to largest energies to represent the MCNPX source information card.

3. Combine the photon yields and associate them with each incident gamma-ray energy to represent the MCNPX source probability card. This information and the source information card definitions represent the energy distribution.

Tallies

F8 or pulse height energy information from the detectors was used to tally and estimate observed detectable counts in each crystal detector. There are 3.7 × 10^4 disintegrations per second from 1 µCi of a gamma-emitting source; therefore, for 100 µCi source activity, the tally for each crystal is multiplied by 3.7 × 10^6 to estimate each detector count per second. Also, to simulate the CsI:Tl energy resolution response of approximately 7% (e.g., 0.07 ΔE at FWHM at the ^{137}Cs 0.662 MeV energy line), the MCNPX Gaussian energy broadening (GEB) modifying card was used in conjunction with each F8 pulse height detector as

F8: p (2<6[1, 1, 0] <8), **(1)**

FT8 GEB −0.00789 0.07 0.21159. **(2)**

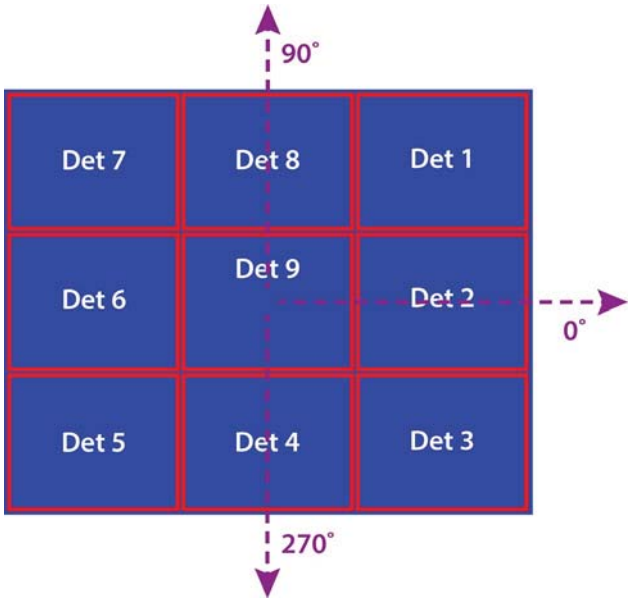

Figure 1. The 9-element detector array was arranged as shown. The assignment of detector numbers is important in calculating the asymmetry function using Equation 3.

Figure 1 displays the distribution of the CsI:Tl elements in the 9-element array.

The asymmetry function $A_y(\theta)$ for the 9-element detector array was defined as

$$A_y(\theta) = \frac{\sum_{1,7,8} N_j - \sum_{3,4,5} N_k}{\sum_1^9 N_i}, \quad \textbf{(3)}$$

where N_i is the count rates for individual detector elements, i.

Experimental Methodology

Experimentally we used detector arrays with different numbers of scintillator elements to obtain best possible angular resolution. We also tried different light collection media, from photomultiplier tubes (normal and position sensitive and multi-anode) to solid-state photomultipliers (SSPMs), and varied the scintillator media viz., thallium-doped sodium iodide (NaI:Tl), thallium-doped cesium iodide (CsI:Tl), and sodium-doped cesium iodide (CsI:Na) to best utilize high quantum efficiency, high gain, and low noise level; maximize photon yield/incident electrons; and best match the maximum emissivity wavelength to the photon wavelength generated. We considered CMOS compatibility to keep production cost low. We optimized the number of scintillator elements to best utilize the Compton scattering, occlusion, and compact geometry, paying attention to the volume and weight of the system. A quad scintillator system with a close-packed form with a position-sensitive multi-anode photomultiplier tube (PS-MA-PMT) response provided the best form factor and quickest response time; the electronics are very fast—capable of a 250 kHz rate—and it had an input pulse height dynamic range of 84 decibels.

We modeled and evaluated some 6-element non-close-packed sensors to see how the relative geometric configurations change the gamma gross count response. Compact geometries having built-in symmetry among the array elements provided better

angular information in laboratory measurements; therefore, all spectrometers built for this study were close-packed forms.

The simulation studies led to the development of three spectrometers (Table 1). The first spectrometer was an array of multi-element detectors (3-, 4-, and 6-elements) made of NaI:Tl scintillators in a close-packed form capable of recording spectral data and angular position determination from a gamma-ray-emitting material. The motivation for the remaining two spectrometers came from several recent application developments, an SSPM (Becker 2013) and a PS-MA-PMT (Belcari 2004). Inspired by the success of these photodetectors in the medical imaging field, we designed two small spectrometer systems: one 9-element system with CsI:Tl crystals (16 × 16 × 20 mm) mounted on a commercially available SSPM array, and one 4-element system with CsI:Na crystals (25.4 × 25.4 × 38.1 mm) mounted on a Hamamatsu H8500 PS-MA-PMT (Hamamatsu 2011). Table 1 describes the combinations of scintillator materials, photosensitive materials, dimensions of individual sensors, and number of sensors in an experimental array, along with the comparison of the maximum emissivity wavelengths (in nm) of the detection materials and maximum light response wavelengths of the photosensitive elements.

Figure 2. Three NaI:Tl crystals (50.8 × 50.8 mm) sit vertically with crystals facing the table. The combination of check sources were moved on the arc of a 50.8 cm radius around the center, and data were obtained in long dwell mode (10 minutes at each angle) to calculate gamma count rate from individual crystals and a summed spectrum; individual amplifier gains were matched before the data run.

Table 1. Detector elements combinations tested

Scintillator Materials	Photosensitive Materials	Maximum Emissivity/ Response Wavelength (Detector Material/ Photodetector) (nm)	Detector Element Array Size and Quantity	Measured Items/ Calculated Items
NaI:Tl	Bi-alkaline photocathode	385/415	50.8 × 50.8 mm cylinder, 3 each	Individual count rate and energy spectrum/ Asymmetry
			50.8 × 50.8 mm cylinder, 4 each	
			50.8 × 50.8 mm cylinder, 6 each	
CsI:Na	PS-MA-PMT, Hamamatsu H8500	415/420	25.4 × 25.4 × 38.1 mm, 4 each	
CsI:Tl	SSPM, silicon	540/480	16 × 16 × 20 mm, 9 each	Individual count rate/ Asymmetry
NaI:Tl	Bi-alkaline photocathode	385/415	50.8 × 50.8 mm cylinder, 6 each	Individual count rate, successive pulse height data for short time interval in list mode/Covariance spectroscopic data

Results

Spectral and gross count data from each individual sensor were collected from the elements of an array. Figure 2 is a 3-element array of 50.8 × 50.8 mm NaI:Tl sensors in a laboratory setting. The asymmetry function is defined as

$$A_y(\Theta) = \frac{N_2 - N_1}{\sum_1^3 N_i}, \quad \textbf{(4)}$$

where N_i is the count rate in an individual detector, i. The asymmetry function, calculated as the angle changes between the source and the detector center, is plotted in Figure 3. The angular position can be determined from a linear relationship with a high degree of accuracy.

The experimental setup for a 9-element pixellated CsI:Tl crystal array with SSPM is shown in Figure 4. Figure 5 shows the asymmetry as a function of the angular position of the source with respect to the center of the detector for the 9-element detector array. We obtained excellent position information from the SensL Corporation's Matrix SM-9 SSPM array of 12 × 12 pixels. Spectral information was not readily available, and work is being done to extract the energy information from the SSPM array.

A 4-element (50.8 × 50.8 mm) NaI:Tl crystal configuration and calculated asymmetry function are shown in Figure 6. Equation 4 describes the formula used to calculate the asymmetry function as a function of individual count rates from the detector elements.

The asymmetry $A_y(\Theta)$ is defined by

$$A_y(\Theta) = \frac{N_1 + N_3 - N_2 - N_4}{\sum_1^4 N_i}, \quad \textbf{(5)}$$

where N_i is the count rate from individual detector i.

Covariance Spectroscopy

The experimental methods of covariance spectroscopy use fluctuations in signals to uncover information encoded in correlations that are usually lost when signal averaging occurs. In gamma-ray spectroscopy the technique could be thought of as a generalization of the coincidence technique with user-selectable coincidence time windows. The method is gaining acceptance in extracting signal from uncorrelated noise, separating overlapping spectral peaks, and identifying escape peaks, as well as reconstructing spectra from Compton continua and generating unique secondary spectral fingerprints (Trainham 2013).

The data analysis involves processing second-order moments of data to obtain information that is usually absent from average spectra. Correlations and fluctuations in data reveal information about gamma-ray sources, transport media, and detection systems.

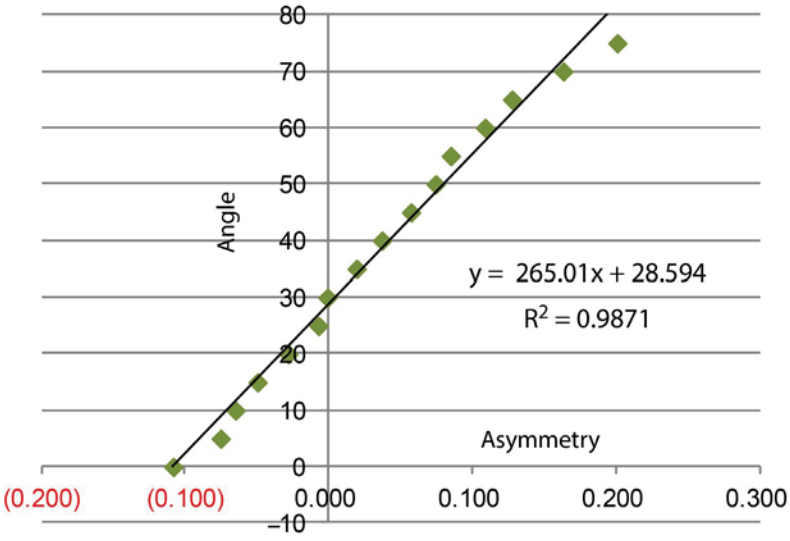

Figure 3. The asymmetry is a unique linear function of the angular position of the source with respect to the center of the array

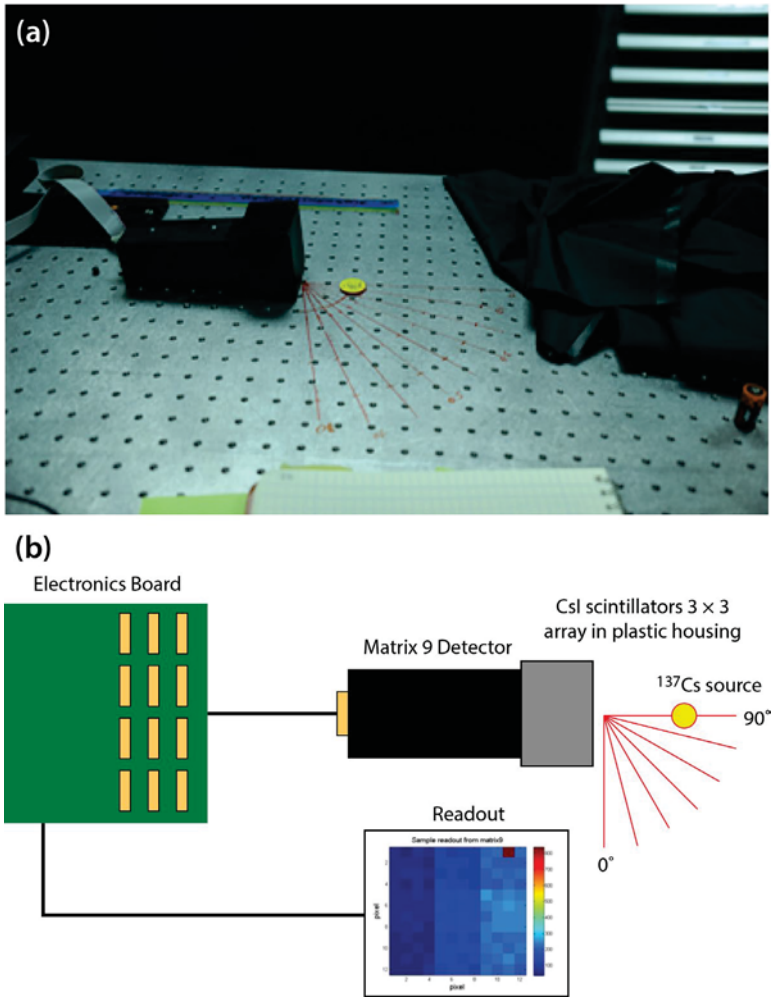

Figure 4. (a) The experimental setup consists of nine rectangular crystals of CsI:Tl, measuring 16 × 16 × 20 mm, mounted and centered on a Matrix 9 SSPM with a mechanical guide. The data output is in the form of a 12 × 12 matrix. Each crystal encompasses an array of 4 × 4 pixels of the SSPM; the counts from each of these 16-pixel elements were summed and attributed to the crystal. The source used to collect the colored image was ^{137}Cs. (b) The color-coded output in the readout screen shot shows highest counts in the pixel nearest to the source location.

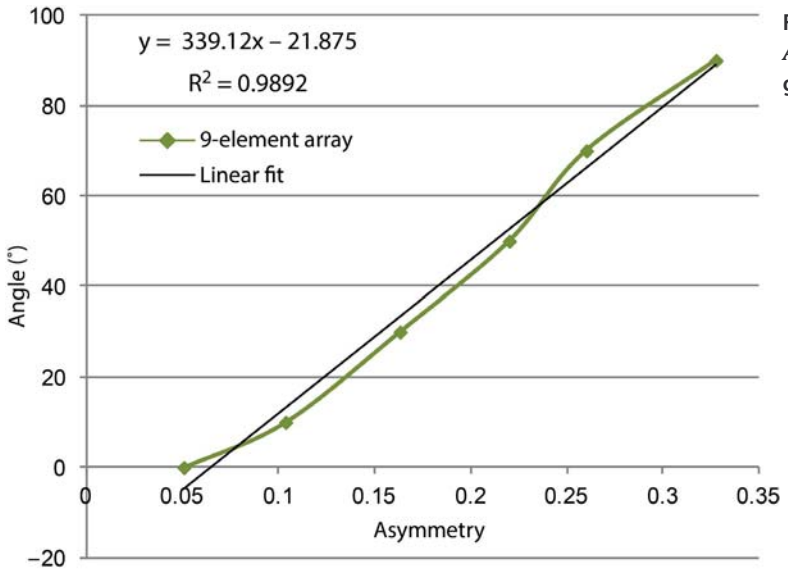

Figure 5. The measured asymmetry function $A_y(\Theta)$ is shown as a function of the incident gamma-ray angle Θ for a 9-element array

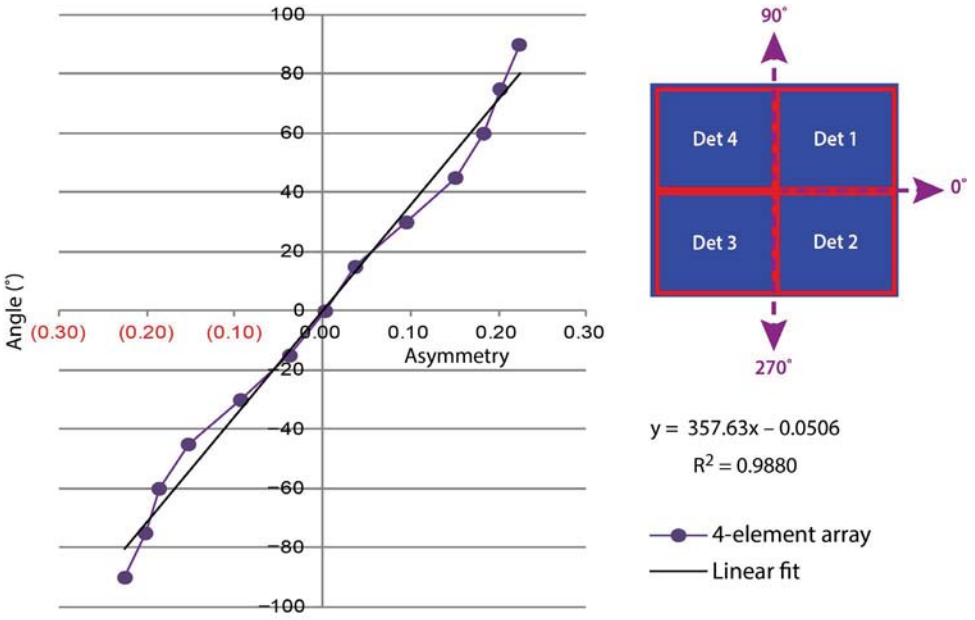

Figure 6. The calculated asymmetry (using the individual count rates as shown in Equation 5) is linear with the incident gamma-ray angle for a 4-element array

Correlations existing at the source level are particularly valuable because many radioactive isotopes emit correlated gammas and neutrons. This helps to identify gamma emitters with cascading photon energies. Correlations also arise from interactions within detector systems and from scattering in the environment. In particular, correlations from Compton scattering and pair production within a detector array can be usefully exploited even in scenarios where direct measurement of source correlations would be unfeasible (Trainham 2011).

Using covariance gamma spectroscopy measurements from a 6-element array in which list mode spectral data were recorded from each of the six 50.8 × 50.8 mm NaI:Tl sensors, we selectively introduced coincidence with user-selectable windows of coincidence. The data obtained from using a 100 µCi ^{137}Cs source at a distance of 3 meters are shown in the 2-D plot of the gamma energy deposited in two adjacent scintillators in Figure 7. Figure 8 shows the crosstalk between the same two detectors in the form of 1-D energy spectrum, and Figure 9 accentuates the difference in terms of gamma energy of the photons taking path A to B compared to the reversed pathway (B to A), where A and B are two detectors.

Measurements and Results for Covariance Spectroscopy

The covariance map in the 2-D plot (Figure 7) represents energy correlations between spectral features for two detectors. The cross-diagonal band is of particular interest; it exists because of Compton scattering cross-talk: when a gamma is Compton scattered in one detector and leaves the Compton electron energy in that

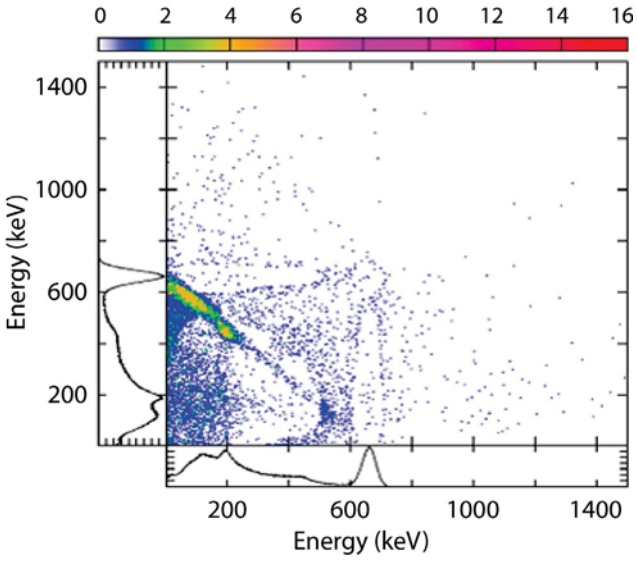

Figure 7. 2-D energy plots for two adjacent detectors in the 6-element array. The projected plot on each axis shows the 1-D ideal spectrum for the ^{137}Cs source used.

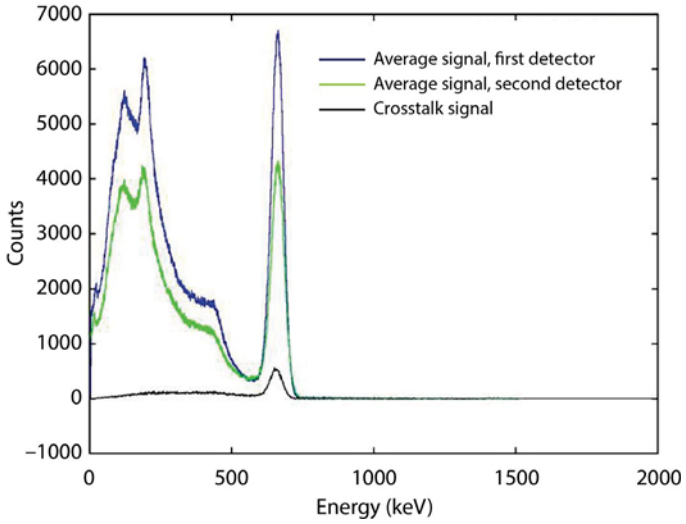

Figure 8. Positive crosstalk between two adjacent detectors

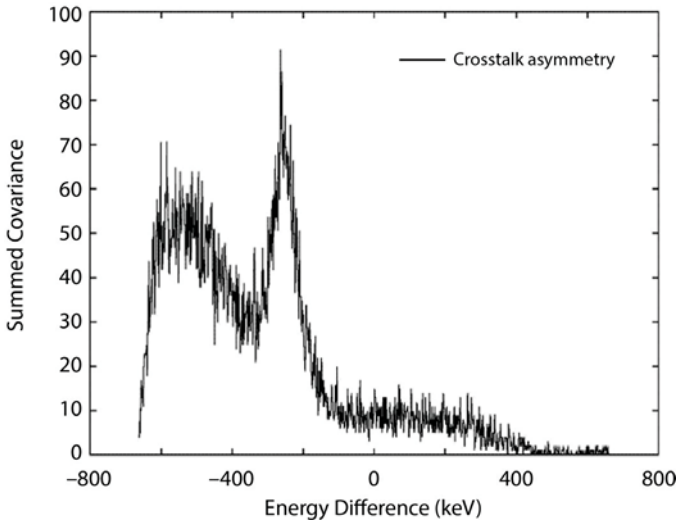

Figure 9. A plot of the Compton crosstalk covariance band seen in Figure 7 clearly identifies the asymmetry; the two peaks indicate the two scattering paths the gammas may take

detector, the red-shifted gamma is subsequently absorbed by the second detector. The Compton formula connects those energies to a scattering angle, and the Klein-Nishina formula weights contributions over a range of angles; consequently the covariance band of the crosstalk is asymmetric. That asymmetry can be used to infer the Compton angle and, consequently, the direction from which the gamma arrived.

Directional information is contained within the correlations between the spectra (Figure 8). Summing signals averages away most, if not all, of the directional information, so the average signals of the two detectors look very similar. The covariance of the crosstalk, however, recovers information from the Compton continuum, and Figure 8 shows how much the correlated signal can be extracted from the Compton continua. In Figure 8 the blue line represents the average pulse height spectrum summed over a period of time for the first scintillator; the green line represents the same for the second scintillator, whereas the black line represents the crosstalk effect between the two scintillators.

Figure 9 is a plot of the Compton crosstalk covariance band seen in Figure 7. The asymmetry is clearly evident, and the two bumps are due to the two scattering paths that gamma rays may take. One path has the gamma scattered from detector A to detector B (scatter angle = Θ). The other path has the scatter occur

from detector B to detector A (scatter angle = π − Θ). The asymmetry allows both paths to be combined into a single angle analysis.

Conclusion

We have designed and constructed a working, directional, portable gamma detector. This detector is not sensitive to variations in source distance, background count rates, polar angle, or photon energy. Summed, the detector elements function as a sensitive, azimuthally symmetric gross count detector. This technique will generally apply to a wide range of detector geometries and types of radiation detections, including neutron detection.

Through simulations and experimental measurements, we encompassed a large parameter space (size, geometry, scintillator materials, light collecting media, and relative orientation between detection elements in an array) of gamma-ray detectors. In general, we found that it is better to have built-in geometric symmetry in the array configuration and, with everything being equal, it is better to have more elements than fewer. Although the SSPM system performed very well, obtaining gamma energy directly from this array may not be practical, as it would need elaborate calibration. Ideally the number of pixels triggered is proportional to the incident gamma energy, but that is true for glancing incidence, and we have not proven this is the case for normal incidence. Finally, in order to achieve manageable size, weight, form factor, and sophistication of light handling, position sensitivity, and spectral data capability, the 4-element system with a PS-MA-PMT performed best.

Acknowledgments

Joshua Jahn (RSL-A) collected data from all angular measurements with NaI:Tl scintillators, and Jack Meade (RSL-A) provided graphic drawings for publications and presentations. Stuart Baker and Kristina Brown (LAO) assisted with packaging and measurements of the 9-element CsI:Tl array with a 12 × 12 Matrix SM-9 SSPM.

References

Batdorf, M. T., W. K. Hensley, C. E. Seifert, L. J. Kirihara, L. E. Erikson, D. V. Jordan, "Isotope identification in the Gamma Tracker handheld radioisotope identifier," *Nuclear Science Symposium Conference Record (NSS/MIC), IEEE* (2009) 868–872.

Becker, E. M., A. T. Farsoni, A. M. Alhawsawi, B. Alemayehu, "Small prototype gamma spectrometer using CsI(Tl) scintillator coupled to a solid-state photomultiplier," *IEEE Trans. Nucl. Sci.* **60**, 2 (2013) 968–972.

Belcari, N., M. Camarda, A. Del Guerra, D. Herbert, A. Motta, A. Vaiano, G. di Domenico, G. Zavattini, "Detector development for a novel Positron Emission Mammography scanner based on YAP:Ce crystals," *Nucl. Instrum. Methods Phys. Res. A* **525** (2004) 258–262.

Firestone, R. B., "The Berkeley Laboratory Isotopes Project's Exploring the Table of Isotopes," http://ie.lbl.gov/education/isotopes.htm (2000), accessed December 2012.

FLIR Corporation, identiFINDER–Portable, Handheld Radiation Detection, http://gs.flir.com/detection/radiation/handhelds/identifinder, accessed September 6, 2013.

Gehrels, N., T. L. Cline, A. F. Huters, M. Leventhal, C. J. MacCallum, J. D. Reber, P. D. Stang, B. J. Teegarden, J. Tueller, "A coded aperture imaging system optimized for hard X-ray and gamma ray astronomy," *19th Intern. Cosmic Ray Conf.* **3** (1985) 303–306.

Hamamatsu, "Flat Panel Type Multianode PMT Assembly H8500 Series/H10966 Series," http://www.hamamatsu.com/resources/pdf/etd/H8500_H10966_TPMH1327E02.pdf (2011), accessed September 10, 2013.

McKenna, C., "DHS Demonstrates Next-Gen Radiation Detection Systems at Race Track," http://www.emergencymgmt.com/safety/DHS-Radiation-Detection-Systems-Race-Track.html (2011), accessed June 11, 2013.

RMD Instruments Corp., "RMD RadCam–Spectroscopic Gamma-Ray Imaging System," https://www.dndkm.org/DOEKMDocuments/GetMedia/Technology/828-RadCam.pdf (2010), accessed May 9, 2013.

Trainham R., J. Tinsley, R. Keegan, W. Quam, "Covariance spectroscopy applied to nuclear radiation detection," *Proc. SPIE* **8142** (2011) 81420Q.

Trainham, R., J. Tinsley, "Covariance analysis of gamma ray spectra," *Rev. Sci. Instrum.* **84** (2013) 013502.

Passive Method to Characterize Atmospheric Turbulence

STL-10-13 | Year 1 of 1

Mary D. O'Neill,[1,a] David Terry,[b] Alex Potter,[a] and Ian McKenna[a]

The Special Technologies Laboratory and Remote Sensing Laboratory have been involved in remote sensing of materials using both passive and active illumination. Atmospheric effects reduce the ability to make these measurements since they add spatial and spectral scintillation. As part of this project, we conducted a thorough review of current methods to measure and compensate for atmospheric turbulence. While methods for compensating for turbulence effects exist for vertical paths (from space), reliable methods to compensate and/or measure turbulence for horizontal paths do not exist. The first step to compensation is a reliable measurement. We examined the mathematical basis for new methods to measure the strength of turbulence. We collected a large quantity of video imagery, which was used to confirm our new, passive method that characterizes the strength of the atmospheric turbulence. This work is ready to extend to atmospheric compensation. This compensation is applicable to hyperspectral sensing (which is a large part of the DOE nonproliferation R&D portfolio) along with long-range imagery, which has significant implications for future work with other government agencies.

[1] oneillmd@nv.doe.gov, 805-681-2477
[a] Special Technologies Laboratory; [b] Fifth Gait Technologies, Santa Barbara

Background

There are three major effects of the atmosphere on a propagating wave: absorption, scattering, and refractive-index fluctuations (optical turbulence). Turbulence remains an important unsolved problem of classical physics. Atmospheric scintillation uses the same statistical models that are used for turbulent motion in fluids. Applied mathematician Horace Lamb reportedly said at a meeting of the British Association for the Advancement of Science, "I am an old man now, and when I die and go to Heaven there are two matters on which I hope for enlightenment. One is quantum electrodynamics, and the other is the turbulent motion of fluids. And about the former I am really rather optimistic."

Atmospheric-turbulence-induced image degradation presents a significant problem in extended range surveillance and signal processing. In many applications, atmospheric turbulence is more restrictive to viewing resolution than the diffraction limit. Algorithms used to mitigate image degradation and analyze signals are increasingly dependent upon the character and strength of the turbulence. As such, accurate methods to measure in situ line-of-sight (LoS) turbulence levels along terrestrial horizontal or slant paths are quite important.

Currently, an active laser scintillometer presents the best and most reliable option for measuring horizontal atmospheric turbulence strength in real time. These devices typically work by correlating cross-polarized or bi-chromatic laser spots at range and inferring the index of refraction structure constant, c_n^2, from the statistics thereof. However, the scintillometer has its

drawbacks: marginal portability, critical laser beam alignment, eye safety issues, and instrument cost. The device requires instrumentation at both ends of its LoS measurement, and there is a maximum path length to the measurement that is often restrictive.

Methods to produce a reliable passive c_n^2 measurement have long been investigated. The leading contenders can be placed into three general categories: (a) pointing and angle of arrival statistical methods (Zamek 2006, Espinola 2012), (b) radiosonde (Sterenborg 2005), and (c) point source spatial filtering and point source power spectrum methods (Beckers 1993, Renhorn 2013). To date, passive methods have simply been inadequate, require special setup, or are not applicable to horizontal paths. The scintillometer device remains the gold standard for measuring turbulence.

Project

The goal of this project was to develop a passive method to measure the index of the refraction structure constant, c_n^2. This is the first step to reliable image degradation compensation for imaging through long-range horizontal paths. This section is separated into the following parts: *Turbulence Theory*, *Data Collection*, *Spatial/Temporal Power Spectrum Method of Turbulence Characterization*, and *Angle of Arrival (AoA) Method of Turbulence Characterization*.

Turbulence Theory

Atmospheric turbulence effects are seen in active and passive sensing. Turbulence is strongest when there is a large temperature differential between the earth (ground) and the surrounding air. When the earth is warmed by the sun, the energy is injected back into the air via the wind mixing the buoyant warm bubble of air with the surrounding cooler air. The energy dissipates into the next layer; thus, cell size reduces from larger to smaller. The larger cells act as refractive elements, and the smaller cells act as diffractive elements. In general, the smallest and largest cells determine the inner (l_0) and outer (L_0) scales of turbulence. A diagram of these effects is given in Figure 1 (Max 2010).

In one dimension, Kolmogorov's ansatz (Kolmogorov 1941) is characterized by the correlation function for a stationary random process, $B(r)$, following a ⅔-power law

$$B(r) = c_r^2 r^{⅔}. \quad \textbf{(1)}$$

The correlation function is replaced in turbulence theory by the structure function due to the non-stationary nature of turbulence. The index of refraction structure function is related to the covariance of the atmospheric index of refraction at two points separated by a distance, r, and relates to $B(r)$ as

$$D_n(r) \equiv 2[B(0) - B(r)] = c_n^2 r^{⅔}. \quad \textbf{(2)}$$

The 3-D power spectral density (PSD) of the turbulence is defined as the Fourier transform of the index of refraction structure and is proportional to the index of refraction structure constant, c_n^2 (Robinson 1993). This PSD is the Kolmogorov power spectrum valid in the inertial subrange, which includes spatial frequencies above the outer scale frequency ($1/L_0$) and below the inner scale frequency ($1/l_0$) (Tatarskii 1971). The latter is less of a concern, buried in typical imaging. The modified atmospheric spectrum (related to the Von Karman spectrum) considers the inner and outer scale effects (Tatarskii 1993, Andrews 2001). This 3-D power law log-normal distribution has a −11/3 slope, as shown in Figure 2.

The 1-D PSD is computed from $D_n(r)$ as

$$V(k) = \frac{c_n^2}{2}\int_{-\infty}^{\infty} r^{2/3} e^{-ikr} dr = \frac{c_n^2}{(2\pi)^{3/2}}\Gamma\left(\tfrac{5}{3}\right) \cdot \sin\left(\tfrac{\pi}{3}\right) k^{-5/3}. \quad \textbf{(3)}$$

In cases of isotropy, the 3-D PSD can be related directly to the derivative of the 1-D PSD (Tatarskii 1967). This PSD is the basis for the power spectrum method described in this paper.

Fried's atmospheric coherence length, r_0, (Fried 1967) is the standard parameter used to characterize the point spread function for imaging through the

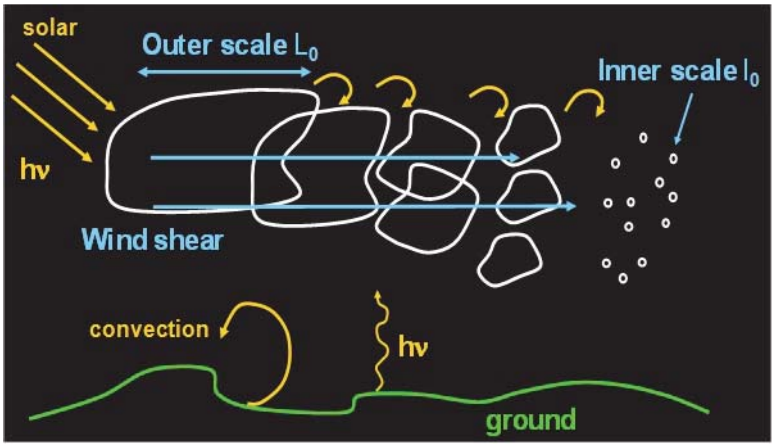

Figure 1. Diagram of effects that create a turbulent atmosphere. The smallest cells determine the inner scale, l_0, and the largest scales the outer scale, L_0. The energy of the photons from the earth and the sun are represented by Plank's constant times the photon frequency shown as hν (Max 2010).

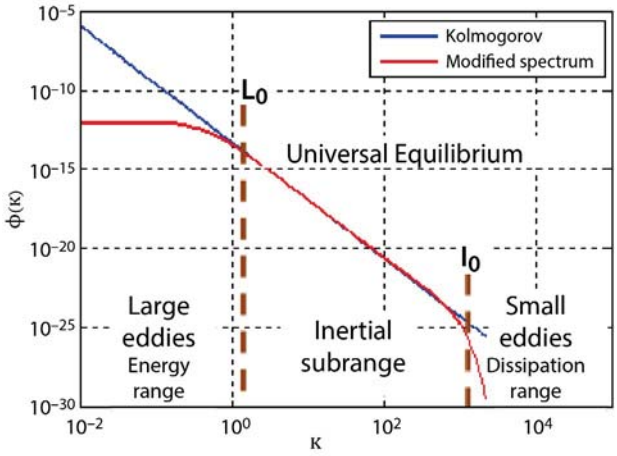

Figure 2. 3-D PSD of turbulence (Andrews 2005). The blue line is the PSD based on Kolmogorov's ansatz; the red line is the modified (Von Karman) spectrum that includes inner and outer scale effects. The method presented in this paper takes advantage of the proportionality of c_n^2 to the 1-D spectrum.

atmosphere (*seeing* conditions, Martinez 2010). This can be computed from the path-length integrated c_n^2 as

$$r_0^{-5/3} \equiv \frac{2.91}{6.88}\left(\frac{2\pi}{\lambda}\right)^2 \int_0^L \left(1-\frac{z}{L}\right)^{5/3} c_n^2\, dz \equiv \frac{2.91}{6.88}\left(\frac{2\pi}{\lambda}\right)^2 \left(\frac{3}{8}\right)\left\langle c_n^2 L\right\rangle. \quad (4)$$

Here, λ is the monochromatic wavelength, L is the integrated LoS path length, and we have defined the "constant-equivalent" average index of refraction structure constant $\langle c_n^2 L\rangle$ as if c_n^2 were indeed constant along the entire path—which it is often not. This is the quantity measured by a scintillometer, and this is the level of atmospheric turbulence that will distort an image at constant range L. In particular, it is often convenient to scale Fried's parameter by the observation aperture diameter, D, to create the dimensionless "turbulence strength" parameter

$$D/r_0 \sim \left\langle c_n^2 L\right\rangle^{3/5}. \quad (5)$$

A typical diurnal cycle (sun goes up, atmosphere heats, c_n^2 increases until slightly after solar zenith) is illustrated by the measurement reported in Figure 3.

Figure 4 contains an image of an Air Force target taken during the day as the sun heated the atmosphere and LoS turbulence increased. Charts like the one in Figure 4 are created by focusing the camera early in the day when the turbulence is low. Even though the image is not monochromatic, it is extremely clear that perceived image quality correlates with D/r_0. In practice, we find $D/r_0 \sim 20$ ($c_n^2 \sim 10^{-12}$) produces images that have insufficient high-spatial-frequency detail and cannot be improved by image processing. This is the utility of the seeing parameter relative to c_n^2—no such intuitive numerical scaling is available with the turbulent structure parameter itself. The second method of measuring turbulence (AoA method) takes advantage of this relationship.

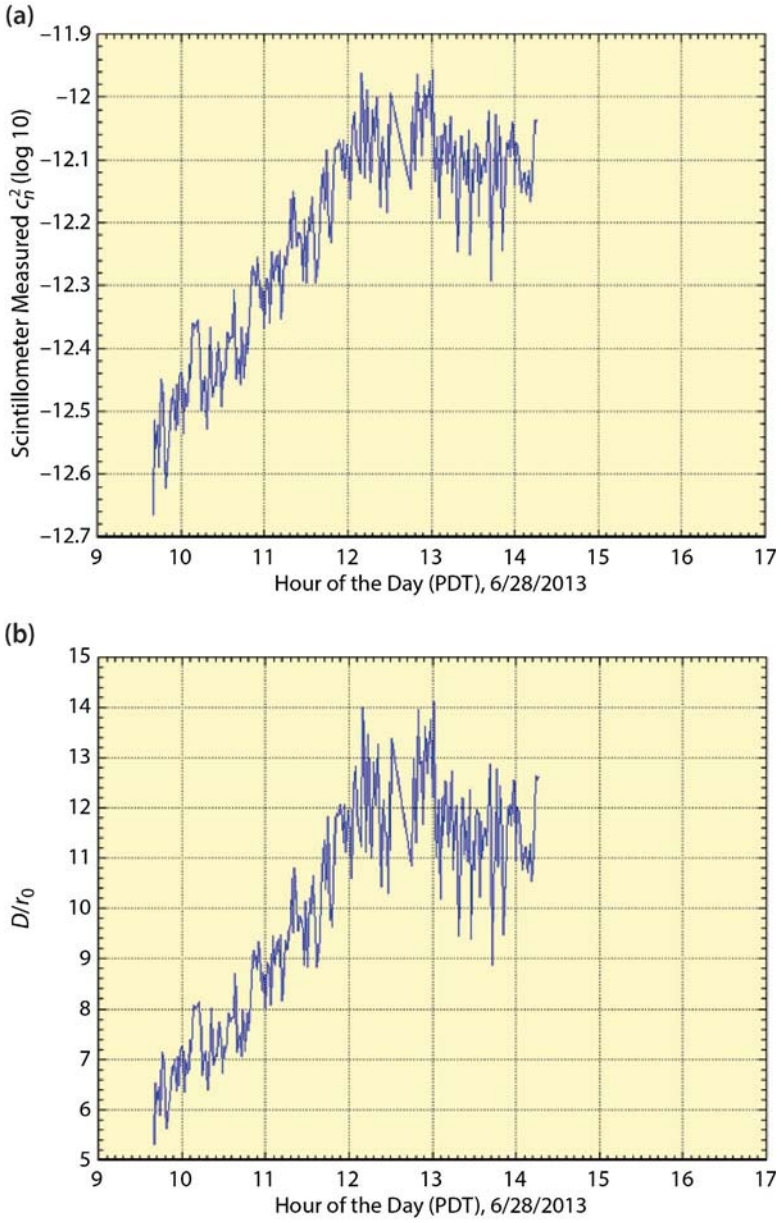

Figure 3. (a) Scintillometer measured c_n^2 and (b) computed D/r_0 on a sunny day in Santa Barbara, California, near summer solstice (sun zenith angle was approximately 34° at 1300 hours Pacific Daylight Time [PDT])

Data Collection

In order to create a data set suitable for verifying the possible measurement techniques, we planned and executed a data collection exercise in the Special Technologies Laboratory (STL) parking lot on a sunny, hot summer day. The goal of this collection was to provide a data set that would allow us to:

- Determine c_n^2 from imagery.
- Verify c_n^2 computed from imagery with scintillometer data.
- Compare mathematical analysis of scaling factors using wind speed and high-frame-rate data in conjunction with high-resolution data, in order to get from spatial to temporal frequencies.
- Determine if c_n^2 variations due to path length can be determined from video data.

The diagram of this collection activity is shown in Figure 5. The equipment list for this data collect is given in Table 1.

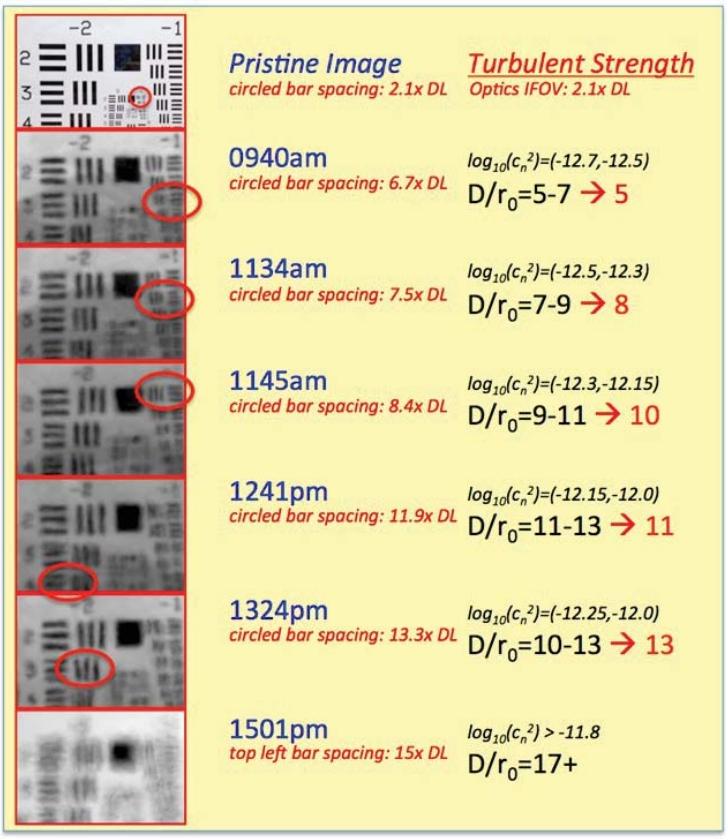

Figure 4. Turbulence strength chart. The target is taken throughout increasing levels of turbulence, measured by D/r_0 shown on the right.

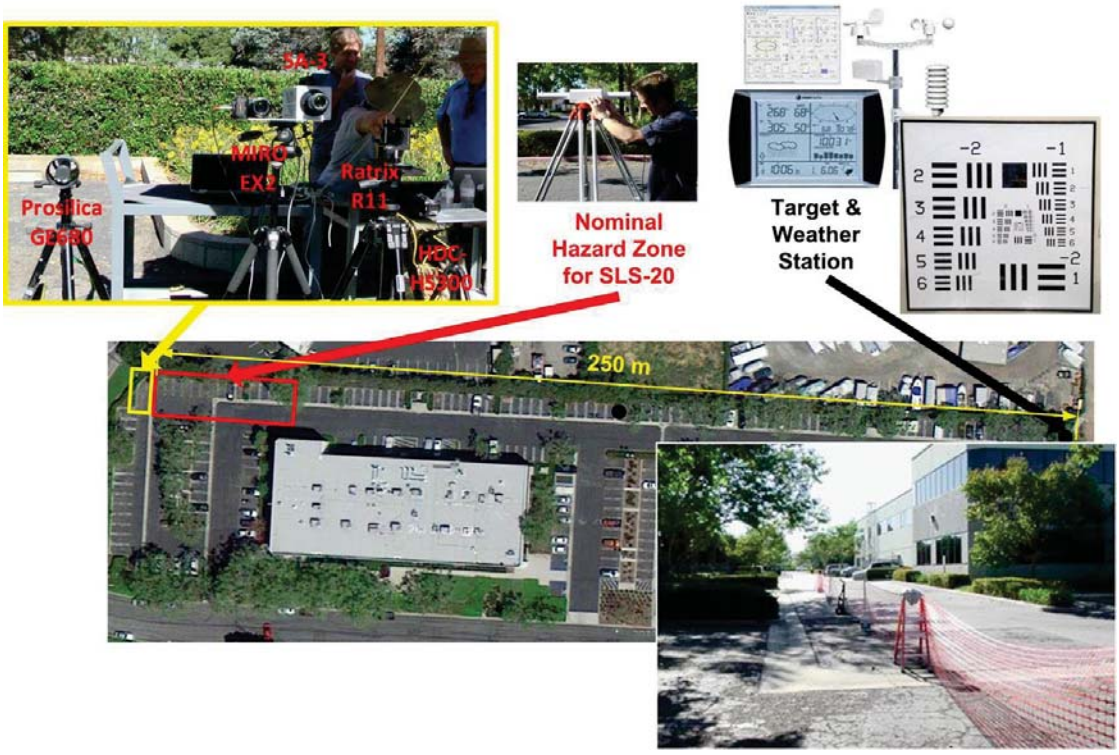

Figure 5. Parking lot data collection. Included in this collect were six cameras, a Scintech SLS20 scintillometer, and a weather station.

Table 1. Atmospheric scintillation equipment list

Quantity	Description	Manufacturer	Part/Model Number
2	HDD HD camcorder	Panasonic	HDC-HS300
1	High-speed video camera	Prosilica	GE680
1	High-speed video camera	Vision Research	Miro-EX2
1	High-speed video camera	Photron	SA-3
1	Scintillometer	Scintec	SLS20
1	Wireless home weather station	Ambient Weather	WS-1090
1	Lightfield camera	Raytrix	R11

At the east end of the parking lot (yellow box in Figure 5), six cameras were set up to view an Air Force target placed 250 meters away. The two Panasonic camcorders were set with a narrow 1.5° and a wide 3.75° field of view (FOV). In addition, an Ambient Weather WS-1090 weather station provided a measure of the metrology data during the collect. A Scintec SLS20 scintillometer was set up in the area shown in the red box. This scintillometer provided truth data for comparison with our completely passive methods. While not all cameras were used in the subsequent analysis, we collected data with as many cameras as possible to allow for future analysis and algorithm development.

Spatial/Temporal Power Spectrum Method of Turbulence Characterization

The spatial/temporal power spectrum method (hereafter referred to as the power spectrum method) of turbulence characterization is based on measuring the PSD spatially using a variance that is measured over a stack of frames (temporally). This method strives to measure the strength of turbulence using only a low-end camera with or without a target board in the scene. It is important to note that $D(r)$ and thus B_R and the normalized intensity are related. Given an intensity measurement imaged onto a focal plane at pixel at location x, y, at time t, and based on proportionality to Kolmogorov's ansatz, we define the scintillation index as the normalized variance over all pixels on the focal plane over a period, Δt, as

$$\sigma^2(x,y,t) \approx B_R(x,y,t) = \frac{\left\langle I(x,y,\tau)^2 \right\rangle_{\tau=t \text{ to } t+\Delta t} - \left\langle I(x,y,\tau) \right\rangle^2_{\tau=t \text{ to } t+\Delta t}}{\left\langle I(x,y,\tau) \right\rangle^2_{\tau=t \text{ to } t+\Delta t}}. \quad (6)$$

Because σ^2 is computed for each pixel, an image that contains the atmospheric structure is generated that is relatively tolerant to tripod instability. For each row, r, or column, c, in the image, we compute the Fourier transform to obtain the 1-D PSD of turbulence, noted as $V(k)$. In practice, we use the fast Fourier transform, defining k as the spatial frequency in cycles/meter and the estimated 1-D PSD for each row, r, as:

$$\hat{V}(k_x, y=r,t) = \sum_{n=1}^{N} \sigma^2(x, y=r, t) \cdot e^{-i2\pi(k-1)(n-1)/N}, \quad (7)$$

and

$$\Delta k = \frac{2\pi}{N\Delta x} \text{ and } k = \left\{ -\frac{N\Delta k}{2}, -\frac{(N-1)\Delta k}{2}, \ldots \frac{(N-1)\Delta k}{2}, \frac{N\Delta k}{2} \right\}. \quad (8)$$

The ⅔-power law indicates that $c_n^2 \sim c_r^2$; however, in practice and based on theory they are not equal. Because of the proportionality of these two constants, we can fit the ensemble average of many strips of 1-D PSD data to a −5/3 power law and extract c_n^2 up to an overall constant such that

$$\hat{c}_n^2 = \frac{a \cdot \hat{V}(k)}{k^{-5/3}} = a' \Delta x \left(\hat{V}(k) / N \right) k^{5/3}. \quad (9)$$

The scaling constant, a', must be determined experimentally but should be independent of optics or image features. Determination of this constant mathematically is not trivial and is a future exercise. In addition, there is a weak dependence on L for a scene that includes near- and far-field data. This dependence needs to be examined more thoroughly.

Using the Panasonic narrow and wide FOV data, we examined the power spectrum method to measure atmospheric turbulence strength. Figure 6a shows the Panasonic narrow image, 6b the scintillation index image, and 6c the 3-D PSDs for the ensemble average of the vertical (red) and horizontal (blue) compared to the theoretical modified (green) PSD.

Videos of the scene were taken throughout the day, typically every 15 to 30 minutes. Unfortunately, due to battery issues, there is no Panasonic data for the period from 1130 to 1230. During the entire test, the scintillometer data were compiled.

Figure 7 shows the results of the power spectrum method compared to the scintillometer data.

The scale factor for both camera setups was the same (10^{-10}), confirming the theory presented earlier in this paper. The scintillometer-measured c_n^2 (cyan) and the 1-D passive power spectrum method (blue) compare well at higher turbulence levels. Due to the size of the isoplanatic patch versus instantaneous FOV (IFOV) the method had larger errors at the lower turbulence levels. Data for a narrower FOV needs to be collected to verify the limits of this algorithm. One difficulty of the power spectrum method is the L dependence, albeit very weak. Analyzing the spectra of targets of mixed length will introduce more uncertainties. We can use the AoA method to compute the proportionality constant, as discussed in the next section.

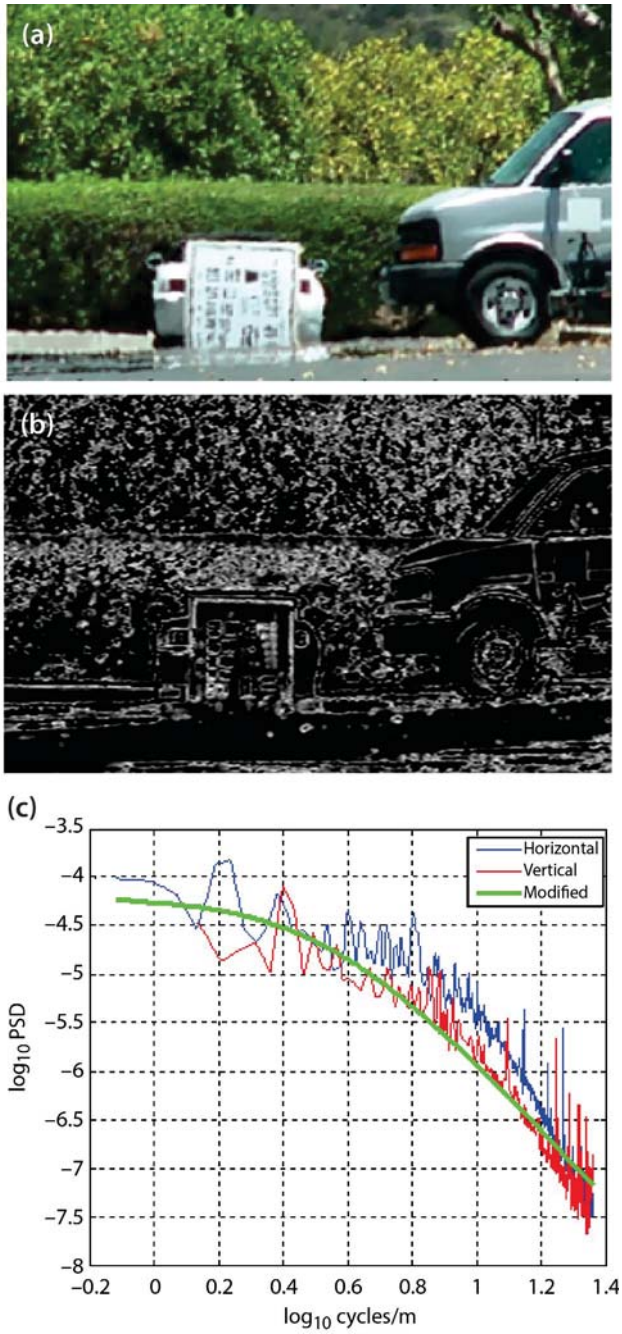

Figure 6. (a) Panasonic narrow image, (b) scintillation index image, and (c) 3-D PSD for the ensemble average of the vertical (red) and horizontal (blue) compared to the theoretical PSD

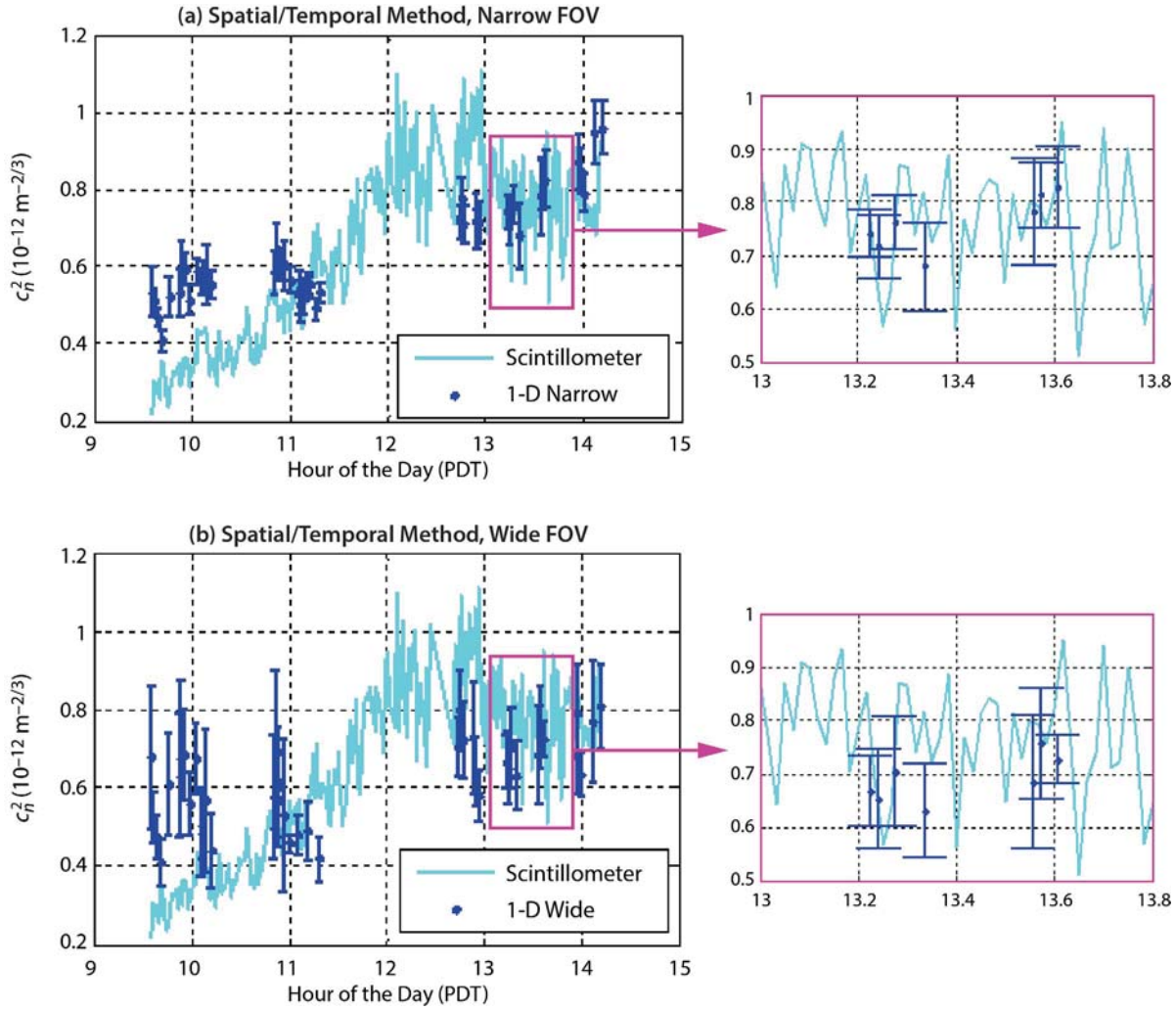

Figure 7. Results of the power spectrum method for the (a) narrow FOV camera and (b) wide FOV camera. The scintillometer-measured $\mathbf{c_n^2}$ (cyan) and the 1-D passive power spectrum method (blue) compare well at higher turbulence levels.

Angle of Arrival (AoA) Method of Turbulence Characterization

The AoA method is based on the absolute phase of the wavefront. It requires a higher-end camera, one that does at least 100 frames per second (fps). The AoA relationship (Andrews 2005), relating the phase structure function D_S and c_n^2, is

$$\sigma_\beta^2 = \frac{D_S(D,L)}{(kD)^2} = (2.91)\xi c_n^2 L D^{-1/3}. \quad \textbf{(10)}$$

We use the Rytov variance to relate D_S to c_n^2 (right-hand side of equation), where

$$\xi = \begin{cases} 1 \text{ for } \Omega \ll 1 \text{ (plane wave)} \\ 0.4 \text{ for } \Omega \gg 1 \text{ (spherical wave)} \end{cases}$$

$$\Omega \equiv \frac{\pi D^2}{4\lambda L} \quad \text{Fresnel Number.} \quad \textbf{(11)}$$

This represents the AoA variance in radians as a function of aperture diameter, D, and path length, L, where k is the wave number ($2\pi/\lambda$). In spite of using "weak fluctuation" theory, this expression has been found valid in both weak and strong turbulence (Andrews 2005). In the image plane we have

$$\sigma_{pixel}^2 = \frac{\sigma_\beta^2}{IFOV^2} = \frac{\sigma_\beta^2 D^2}{\lambda^2 N_{ifov}^2}$$
$$N_{ifov} \equiv \frac{IFOV}{\left(\lambda/D\right)} \text{ effective pixel size relative to } D.L \quad (12)$$

Combining Equations 3, 9, and 11, and evaluating the constants gives

$$D/r_0 = \left[\left(1.467\xi^{-\frac{1}{2}}\right) N_{ifov} \left(\sigma_{pixel}^2\right)^{\frac{1}{2}}\right]^{6/5}. \quad (13)$$

Unlike the power spectrum method, this method is based on the phase of the wavefront such that all scale factors are easily determined mathematically. This difference makes these two methods perfect complements of each other, and we hope to combine these methods in the future. Also note that ξ is a dimensionless function of only the Fresnel number. We use Hufnagel's empirical result. The analytic function is a combination of integrals of confluent hypergeometric functions that is not very tractable; the empirical relationship claims ~10% accuracy (Hufnagel 1978):

$$\xi(\Omega) \approx 0.4 / \left[\frac{\Omega}{2.5+\Omega} + \frac{0.4}{1+8\Omega}\right]. \quad (14)$$

We call our AoA method High Confidence Block Shifts (HCBS), which allows the algorithm to automatically determine the best regions in the scene for determination of D/r_0. Previous AoA methods for determining the strength of turbulence do not take into account Hufnagel's empirical result, and they require the user to pick the best pixels in the image to be processed prior to the determination of c_n^2 (Zamek 2006). To implement HCBS, we decompose an image into many small blocks (typically 16 × 16 or 32 × 32 pixels, depending on image content). The Fifth Gait Technologies Q-metric is computed on each block, the blocks are sorted by this metric, and the top two dozen are tracked as a function of time. Whenever a block's correlation coefficient along with its reference metric falls below a threshold (typically 0.75), the track dies and that block's tracking discontinues. After a macroscopic amount of time (e.g., some seconds of video frames), the surviving tracks yield a set of pixel variances of each surviving block's motion. Ensemble outliers are removed from the set, and the set's mean variance is used.

Both horizontal and vertical block shift statistics are kept separately, and the minimum of either set's mean variance is used for σ_{jitter}^2. Tripods are used for the video, and very often one axis (either *x* or *y*) is more susceptible to platform motion. This is sometimes obvious from the video, as will be shown below. The actual equation used thus becomes

$$D/r_0 \approx c\left[\max\left(0, \sigma_{pixel}^2 - \sigma_{platform}^2\right)\right]^{3/5}, \quad (15)$$

where $c = c(N_{ifov}, \Omega)$ is a known constant. In the simplest implementation we approximate the platform variance with a small constant (say, 0.5 pixels^2).

Using Prosilica GE680 video data (100 fps, N_{ifov} = 2.12, Ω = 64, ξ = 0.43, c = 6.492) taken over a 5-hour period in the STL parking lot on June 26, 2013, we obtained the results shown in Figure 8.

These plots resulted from processing approximately 100 video clips of 1500 frames each. The video is 12-bit monochromatic, and we used a wavelength of 555 nm for these calculations. In practice, however, we find the assumption of constant platform motion for the entire experiment is inadequate. We estimate platform motion using

$$\sigma_{platform}^2 = \max\left(0.25, \min\left(\text{var}\left(x_j - x_{j-1}\right), \text{var}\left(y_j - y_{j-1}\right)\right)\right). \quad (16)$$

By using the difference between jth frame shift and j – 1th, we are essentially using velocity of pixel motion. Without appreciable motion, we revert to the constant platform motion estimate. By using the minimum of x or y motion, we are consistent with using $\sigma_{pixel}^2 = \min(\sigma_x^2, \sigma_y^2)$ and require only one "stable" platform axis for D/r_0.

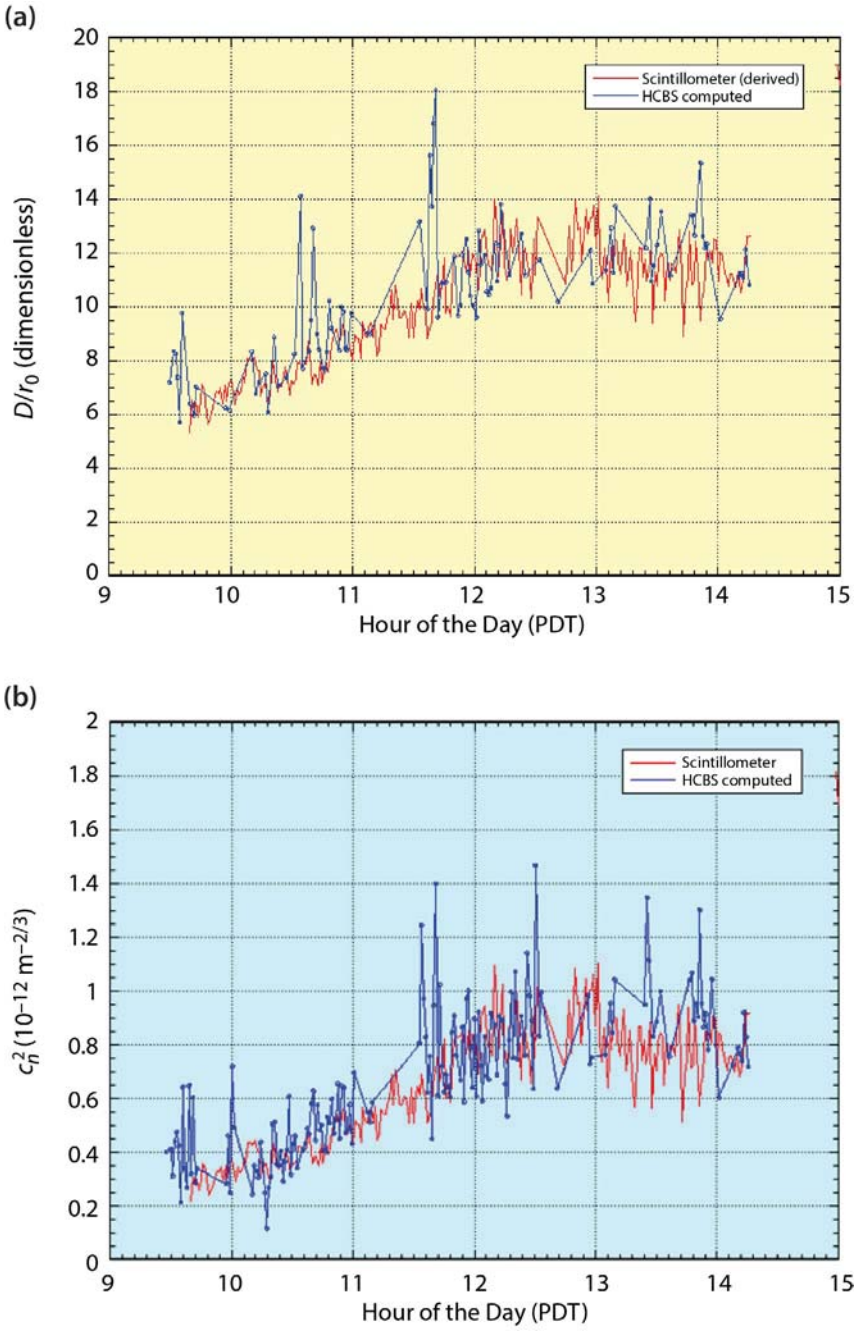

Figure 8. Results of the HCBS method with (a) D/r_0 and (b) c_n^2; data collected June 26, 2013, in the STL parking lot

Conclusion

We have devised two methods to measure the strength of atmospheric turbulence for horizontal paths. While both methods are more robust than other passive methods found in literature, the combination of the two methods should result in a very robust method to measure atmospheric turbulence strength. We can combine the power spectrum method of turbulence characterization—fitting the 1-D PSD of the scintillation index—with the HCBS method. The former requires evaluation of a proportionality constant, provided by the latter, and is most accurate when the path length, L, to the target is constant. The latter method relies on a complex algorithm to remove platform motion, which is not always accurate and may fail altogether

when platform motion is on the order of global pointing jitter. Using error bars provided by the variance in the set of 1-D PSD spectra helps determine when the HCBS method itself is valid. In the first and second quarter of FY 2014, we will implement this combination of algorithms. Further, we can leverage Fifth Gait Technologies' QPID software to compute both power spectrum and HCBS turbulence methods in real time and output $D/r_0(t)$ and $c_n^2(t)$.

References

Andrews, L. C., R. L. Phillips, C. Y. Hopen, *Laser Beam Scintillation with Applications*, SPIE Press Monograph, Bellingham, Washington, 2001.

Andrews, L. C., R. L. Phillips, *Laser Beam Propagation through Random Media*, 2nd edition, SPIE Press Monograph, Bellingham, Washington, 2005, 65.

Beckers, J. M., "Adaptive optics for astronomy: Principles, performance, and applications," *Ann. Rev. Astron. Astrophys.* **31** (1993) 13–62.

Espinola, R. L., S. Aghera, R. Thompson, J. Miller, "Turbulence degradation and mitigation performance for handheld weapon ID," *Proc. SPIE* **8355** (2012) 83550S.

Fried, D. L., "Optical heterodyne detection of an atmospherically distorted signal wavefront," *Proc. IEEE* **55**, 1 (1967) 57–77.

Hufnagel, R. E., "Propagation through atmospheric turbulence," in *The Infrared Handbook*, W. L. Wolfe, G. J. Zissis, eds., U.S. Government Printing Office, Washington, D.C., 1978.

Kolmogorov, A. N., "The local structure of turbulence in incompressible viscous fluid for very large Reynolds numbers," *Dokl. Akad. Nauk SSSR* **30**, 4 (1941) 301–305.

Martinez, P., J. Kolb, M. Sarazin, A. Tokovinin, "On the difference between seeing and image quality: When the turbulence outer scale enters the game," *European Southern Observatory Messenger* **141** (2010) 5–8.

Max, C., Lecture 3 of Astronomy 289C: Adaptive Optics and its Applications, University of California, Santa Cruz, April 8, 2010.

Renhorn, I. G. E., T. Svensson, G. D. Boreman, "Experimental observation of spatial correlation of scintillations from an extended incoherent source," *Opt. Eng.* **52**, 2 (February 2013) 026001-1–026001-6.

Robinson, S., J. S. Accetta, D. L. Shumaker, *The Infrared and Electro-Optical Systems Handbook, Volume 8: Emerging Systems and Technologies*, Infrared Information Analysis Center, Ann Arbor, Michigan, and SPIE Optical Engineering Press, Bellingham, Washington, 1993.

Sterenborg, M. G., J. P. V. Poiares Baptista, S. Bühler, "Determining the refractive index structure constant using high-resolution radiosonde data," http://www.sat.ltu.se/members/sab/publications/pedro_scint/scint_paper.pdf (2005), accessed December 19, 2013.

Tatarskii, V. I., *The Effects of the Turbulent Atmosphere on Wave Propagation*, Israel Program for Scientific Translations, Jerusalem, 1971.

Tatarskii, V. I., A. Ishimaru, V. U. Zavorotny, *Wave Propagation in Random Media (Scintillation)*, SPIE Optical Engineering Press, Bellingham, Washington, and Institute of Physics Publishing, Techno House, Bristol, England, 1993.

Zamek, S., Y. Yitzhaky, "Turbulence strength estimation from an arbitrary set of atmospherically degraded images," *J. Opt. Soc. Am. A* **23**, 12 (December 2006) 3106–3113.

This page left blank intentionally

Covariance Processing of Energy Asymmetry of Compton Crosstalk for Directional Gamma Sensing

STL-43-13 | Year 1 of 1

Rusty Trainham[1,a] and James Tinsley[a]

Compton scattering of gammas within an array of detectors encodes information that can be used to infer the direction to a radioactive source. Covariance processing of the data streams extracts correlated signals from detector pairs to match energy-shifted Compton gammas with their companion Compton recoil electrons. On a covariance map these signals appear as cross-diagonal bands with axes intercepts at the full photopeak energy. The covariance technique allows useful data to be collected without the need for detector masking or shadowing, so sensitivity is not sacrificed in order to obtain directional information. The covariance algorithm for processing inter-detector Compton crosstalk to infer direction can handle data streams in real time using modest computing capability, and an angular resolution of better than 1° of arc is possible for directional gamma sensing.

[1] trainhcp@nv.doe.gov, 805-681-2248
[a] Special Technologies Laboratory

Background

The angular dependence of the Compton energy shift is a consequence of conservation of energy and momentum. The principle was first published by Compton (1923), and the simple form of Equation 3 in that article is often rewritten equivalently (Davisson 1952, Evans 1982) as

$$\frac{\nu'}{\nu} = \frac{1}{1+\alpha(1-\cos\theta)}, \quad (1)$$

where ν' is the energy down-shifted Compton gamma, ν is the energy of the initial gamma, θ is the scattering angle, and $\alpha = h\nu/m_e c^2$ is the ratio of the initial gamma energy to the rest mass energy of the electron. When Compton scattering occurs inside a gamma detector, the Compton gamma is usually lost, and it is the energy of the recoil electron that is actually measured by the detector. This effect produces a continuum spectrum that is superimposed upon the photo-absorption line spectra of the detector. Figure 1 shows an idealized energy spectrum for a ^{137}Cs source including both photo-absorption and Compton scattering. The photo-absorption peak is located at 662 keV, and the Compton component is the continuum extending from nearly 0 keV up to 477.7 keV. The labels in the figure indicate the correspondence between the energy of the recoil electron and the scattering angle. Small-angle Compton scattering generates detector signal at low energy, and the maximum energy component of the continuum is the result of 180° backscattering. The small amount of signal seen in the region between the Compton edge at 477.7 keV and the photopeak at 662 keV is the result of multiple Compton scatterings within the detector. Also visible within the Compton continuum is a small bump at 184.3 keV, which is called the backscatter peak. It arises from Compton backscattering outside of the detector for which the energy down-shifted Compton gamma is subsequently absorbed by the detector.

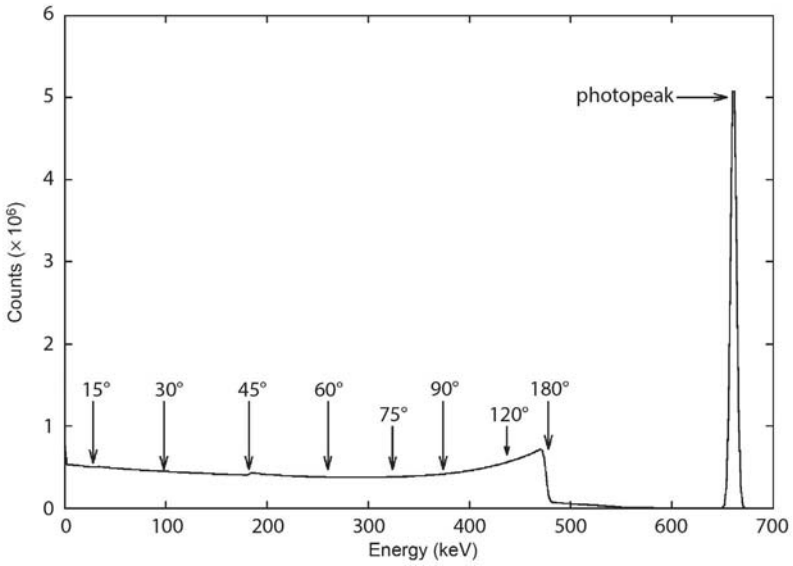

Figure 1. An idealized average gamma spectrum of ^{137}Cs shows the photo-absorption peak at 662 keV, and the Compton continuum extending from 0 keV to 477.7 keV. The markers indicate the energies of the recoil electrons for particular Compton scattering angles.

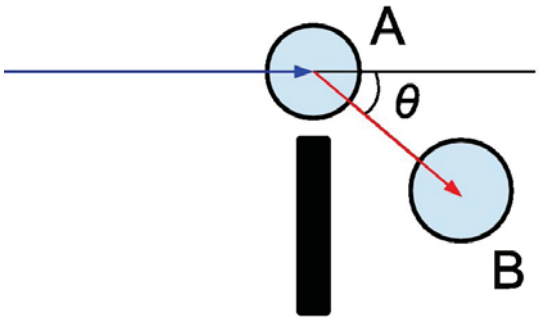

Figure 2. The shielded detector B receives only Compton gammas scattered from detector A. The spectrum for A is shown in Figure 1, and the spectrum for B is shown in Figure 3. If the shield blocking the source from B were not in place, then B's spectrum would be virtually identical to that of A, and only the correlations between the spectra of A and B would permit extraction of the spectrum seen in Figure 3.

If we consider the detector configuration shown in Figure 2, in which the Compton scattering site is located within the detector labeled A, and the Compton gamma is subsequently absorbed by detector B, then the spectrum for detector A would be that of Figure 1, and the spectrum for detector B would be that shown in Figure 3. These spectra are from a simulation of a 45° angle between the initial gamma direction and the axis detector centers, and the detectors are 2" × 2" cylinders of NaI. The broadness of the spectrum in Figure 3 is due to the range of angles for Compton scattering subtended by the geometry of the detectors.

To maximize detection sensitivity one would like to remove the barrier shielding detector B from the radiation source, but doing so would produce a spectrum for B virtually identical to that of detector A. The peak in Figure 3 is about three orders of magnitude smaller than the continuum spectrum in Figure 1, so the signal of the Compton-scattered gammas would get lost in the average signal. In addition, removing the barrier would further complicate the spectra by opening a new path for Compton scattering. This is illustrated in Figure 4, where both detectors are exposed to the radiation source. For a source in the far field, a forward path of Compton scattering would follow path 1 from A to B, and a backscattering path would follow path 2 from B to A. Signal from both paths would be measured by detector B, so it might seem that teasing information out of the data would be impractical. Fortunately, the information is accessible, because the higher energy signals concentrate in detector B. This is because forward scattering depletes the gamma energy only slightly, and backscattering depletes it maximally, so detector B would receive more energy for both scattering paths. When the scattering angle

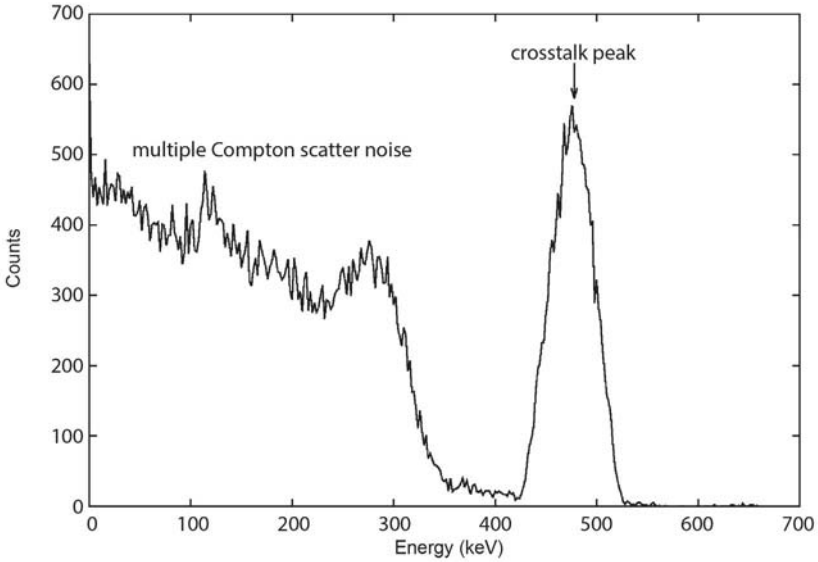

Figure 3. The spectrum measured by detector B for Compton-scattered gammas arriving from detector A. The peak is centered at the expected Compton energy of the gamma, in this case for a 45° scattering angle. The broadness of the peak is largely due to the range of scattering angles intercepted by detector B. The skewness depends partly upon the variation of the Klein-Nishina cross section over the range of angles, and partly upon the non-uniform penetration gammas into detector A that scatter into B.

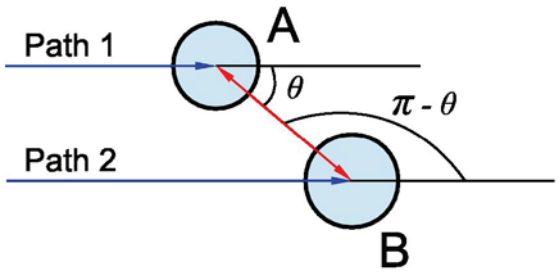

Figure 4. When both detectors are exposed to the gamma source, the Compton signal has a forward-scattering component along path 1 from A to B, and a backscattering component along path 2 from B to A. The two components can be identified from a covariance map, as explained in the text.

approaches 90°, the energies are equal; when the scattering angle is greater than 90°, detectors A and B reverse roles.

The problem, therefore, is to extract Compton scattering spectra from the average spectra overlaying them, and to account for the different energy components of both scattering paths. This is where the covariance approach (Frasinski 1989, Trainham 2013, Trainham 2014) becomes quite useful, because the signal from the recoil electron measured in one detector is correlated in energy and time with the signal from the energy down-shifted gamma absorbed by the other detector. The pair of events occurs on a sub-nanosecond timescale, and the energies of the pair sum to the full energy of the initial gamma. A coincidence technique could be used to gate and discriminate the events, but the covariance technique offers greater flexibility of signal handling and superior noise rejection.

The distinctive feature to look for on a covariance map of the spectra is a cross-diagonal band of correlation with axes intercepts at the full photopeak energy, which makes identification of the Compton crosstalk straightforward. Figure 5 illustrates several useful features of a covariance map. The false color scale represents magnitude of covariance, where red is maximum covariance and blue is minimum. Underneath and to the left of the covariance map are plots of the average spectra for the two detectors. Those plots are visual aids to link features in the covariance map to peaks and continua structure within the average spectra. The gamma source shown in Figure 5 is from a ^{176}Lu source measured by eight detectors treated as a single meta-detector. Islands of covariance show the correlation of cascade gammas at 202 and 306 keV, and those covariance islands are further linked to characteristic atomic x-rays emitted in conjunction with the nuclear gammas. The vertical and horizontal bands in the covariance map are features that we refer to as "ordinary" Compton bands. They are from correlations between a cascade gamma photopeak in one detector with the Compton continuum of the companion cascade gamma in another detector. For our present

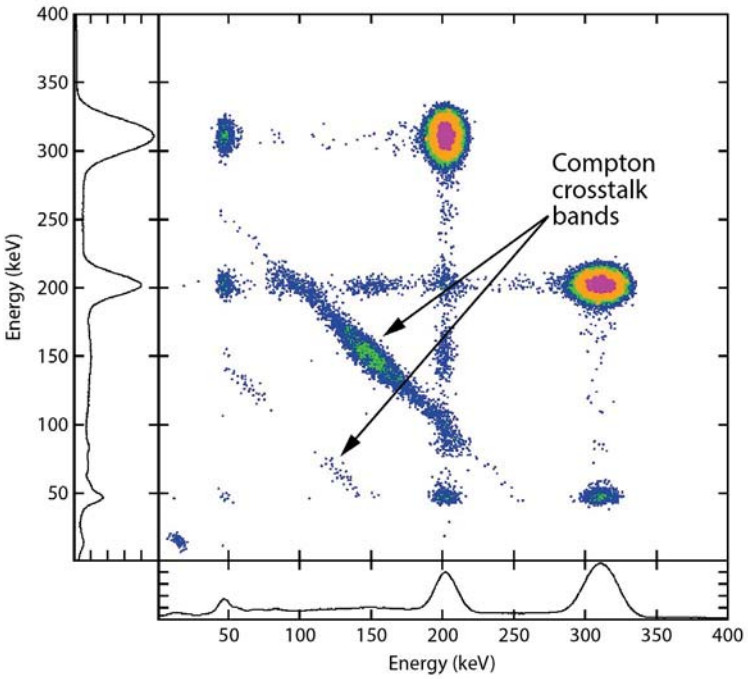

Figure 5. This covariance map of a ^{176}Lu energy spectrum as measured by eight detectors shows islands of correlation linking the cascade gammas at 202 and 306 keV. Correlations of those gammas to the characteristic x-rays are also evident in the map. The cross-diagonal bands indicated by the arrows are from Compton crosstalk between detectors, and the axes intercepts of the bands are at the full gamma energy. The direction to the radiation source can be derived from information contained within the crosstalk bands.

purpose the features that particularly interest us are the cross-diagonal bands whose axes intercepts are at the full photopeak energies—in other words, the x and y components of any point within the crosstalk band sum to the photopeak energy distribution of the original gamma. The crosstalk bands are created by gammas that undergo Compton scattering in one detector and are subsequently absorbed by another detector. For any pair of detectors, the covariance features fill in only a segment of the crosstalk band consistent with the range of scattering angles for that particular pair. The bands shown in Figure 5 are filled in by treating all eight detectors as a single meta-detector spanning a large range of scattering angles.

Project

Directional information for locating a radioactive source is obtained from a covariance map by quantifying the location of the signal along the Compton crosstalk band. Since the crosstalk band contains components for both forward scattering and backscattering, its profile tends to be bimodal. Figure 6 illustrates this for a ^{137}Cs source measured by a pair of NaI detectors in a 30° forward (and 150° backward) Compton scattering angle. The covariance map in Figure 6a is from a GEANT4 (Agostinelli 2003) simulation of the configuration, and the crosstalk band shows a distinct bimodal structure. The structure is more obvious by plotting the intensity of the band, shown in Figure 6b. The x-axis has an energy difference scale, and the y-axis is the intensity of the covariance. The broad continuum from −662 keV to +500 keV is from the forward scatter component, and the sharper peak, seen at −275 keV, is from the backscatter component.

Because we are interested in quantifying a location along the Compton crosstalk band, the choice of an appropriate variable is almost immediately obvious—the difference of energies between detectors. Furthermore, if we divide that energy difference by the initial full gamma energy, we have a normalized scale ranging from −1 to +1. We will call that variable x, and it is a measure of energy asymmetry between detectors. The range of x is easily identified. For a covariance point in the crosstalk band at the y-axis on the left of the covariance map, the $x = -1$. On the lower right side of the map, at the x-axis intercept of the covariance map, $x = +1$. At the center of the crosstalk band, on the main diagonal of the covariance map, $x = 0$.

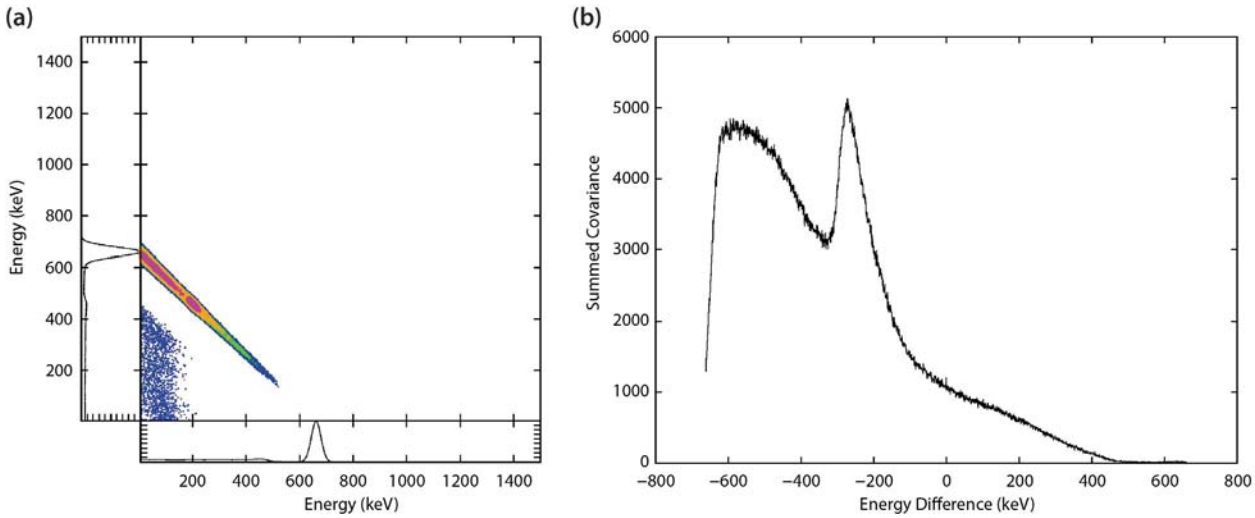

Figure 6. This GEANT4 simulation of a ^{137}Cs source at a 30° forward scattering angle shows the bimodal structure of the Compton crosstalk band. The covariance map (a) shows the concentration of correlation along the band, and (b) is the energy spectrum of that band. The spectrum is constructed by summing across the band to create a one-dimensional array. The scale of the x-axis of (b) is the difference of the energies along the crosstalk band, i.e., the value of x – y of the location of a point within the crosstalk band within the covariance map in (a). The broad distribution from –662 to +500 keV is from the forward Compton scattering component of the crosstalk. The sharp feature located at –275 keV is from the Compton backscatter component of the crosstalk.

The Compton formula of Equation 1 can be rewritten in terms of the asymmetry variable x, as follows:

$$x_1 = \frac{E_{A_1} - E_{B_1}}{v} = \frac{\alpha(1-\cos\theta)-1}{\alpha(1-\cos\theta)+1}. \quad (2)$$

Here, we have added a subscript 1 to x to indicate scattering along path 1 (see Figure 4). The equivalent Compton formula of Equation 1 for path 2 is

$$x_2 = \frac{E_{A_2} - E_{B_2}}{v} = \frac{1-\alpha(1+\cos\theta)}{1+\alpha(1+\cos\theta)}. \quad (3)$$

Solving for the scattering angle is straightforward, and for path 1 we have

$$\cos\theta = 1 - \frac{1}{\alpha}\left(\frac{1+x_1}{1-x_1}\right), \quad (4)$$

and for path 2 we have

$$\cos\theta = -1 + \frac{1}{\alpha}\left(\frac{1-x_2}{1+x_2}\right). \quad (5)$$

Components from forward scattering and backscattering paths both contribute to the crosstalk signal, and their intensities depend upon the Klein-Nishina cross sections for their respective angles (Klein 1928, 1929; Nishina 1929; Evans 1982). In Figure 7 we have plotted the asymmetry variables x_1 and x_2 as a function of θ for the 662 keV gamma of ^{137}Cs. The dashed curves show θ versus x_1 (forward) and x_2 (reverse), and the solid curve is the result of summing x_1 and x_2 using the Klein-Nishina cross sections as weighting factors.

The plots in Figure 7 represent results that would be obtained for detectors whose separation is large compared to that of the detector dimensions. A

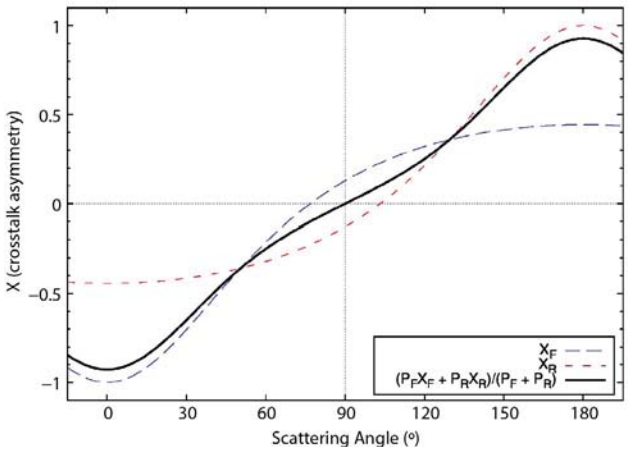

Figure 7. The energy asymmetry parameter as a function of the forward Compton scattering angle for 662 keV gammas

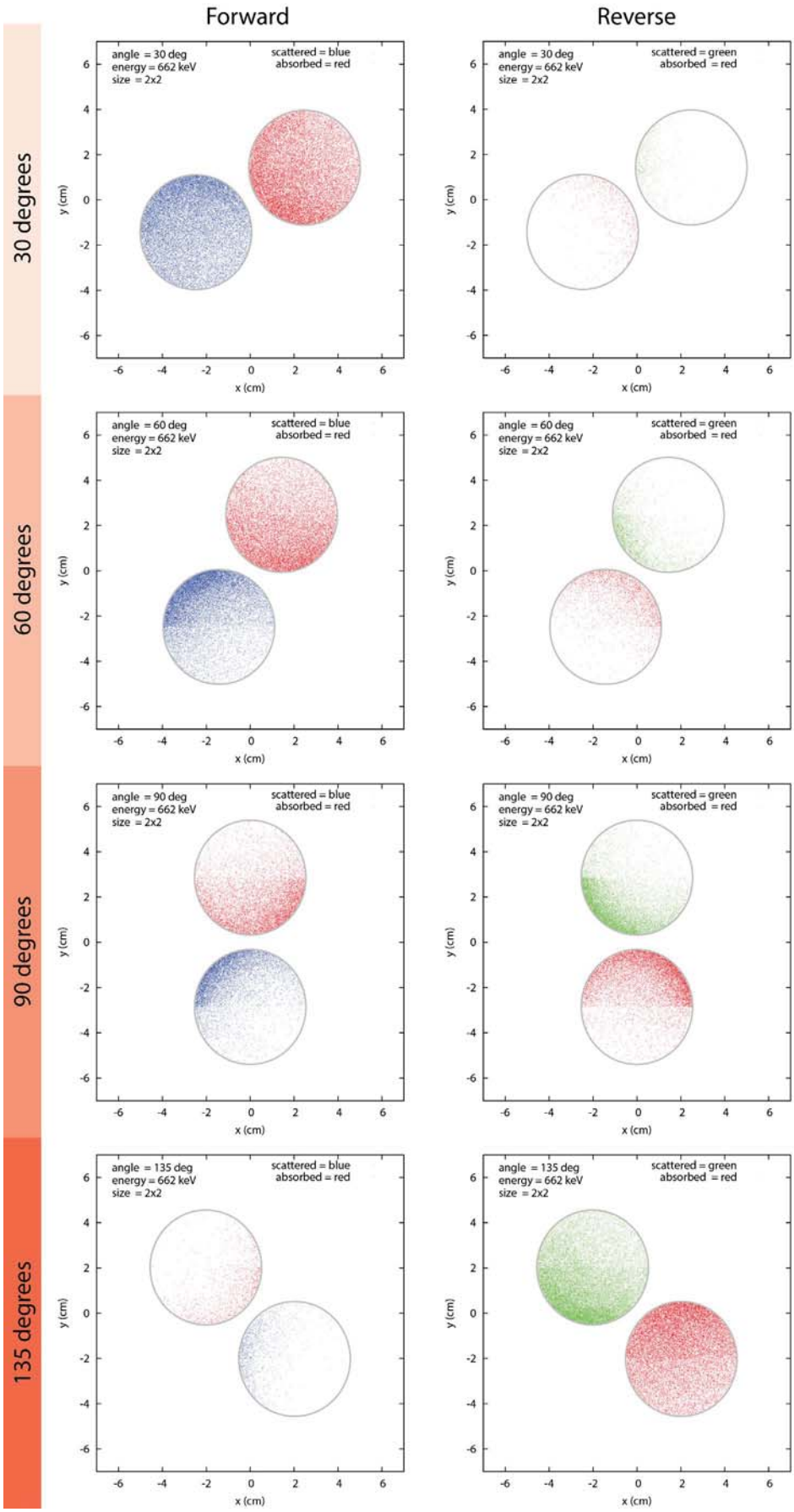

Figure 8. Some results of a semi-analytical model used to investigate the effects of detector geometry upon the angular resolution of the Compton crosstalk directional method. See the text for further explanation.

Angle Distributions

Energy Distributions

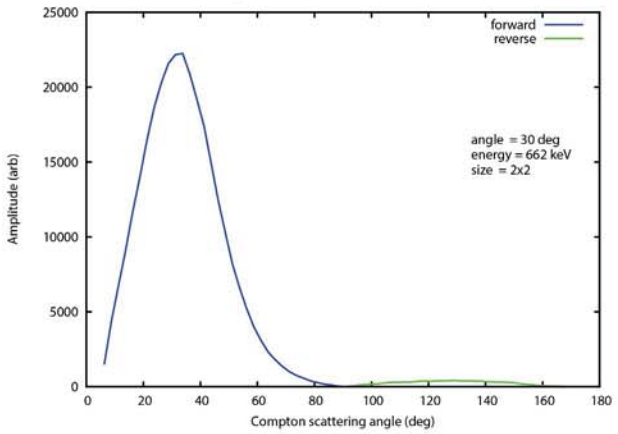

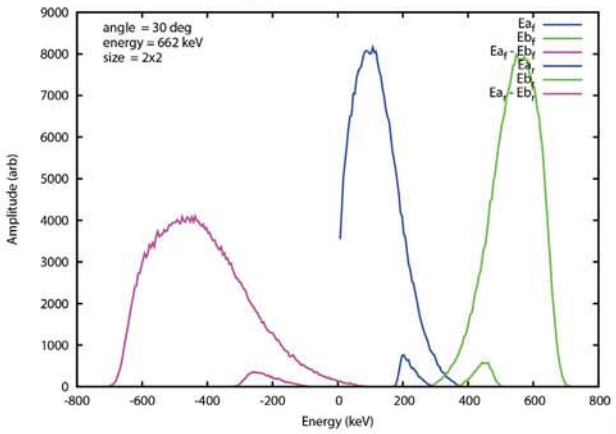

30 degrees

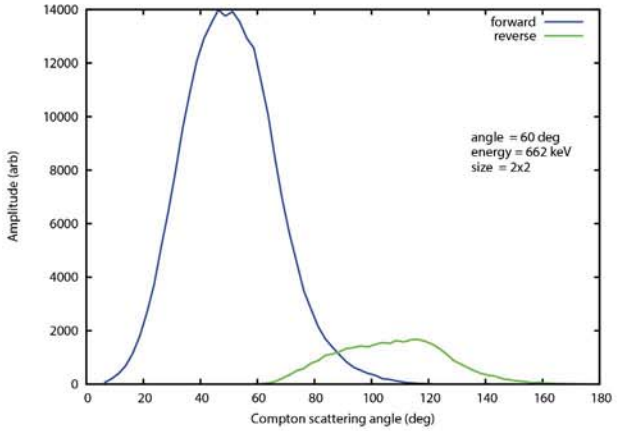

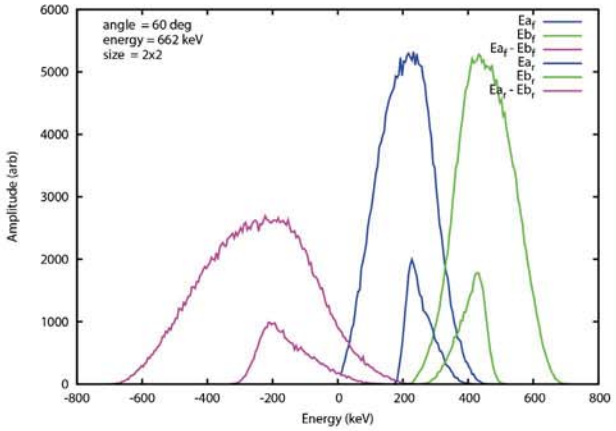

60 degrees

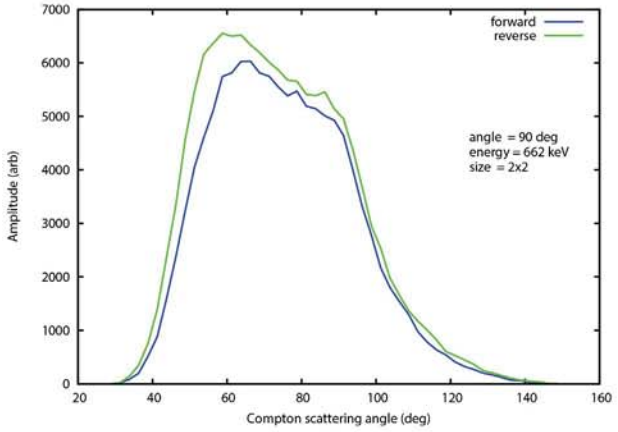

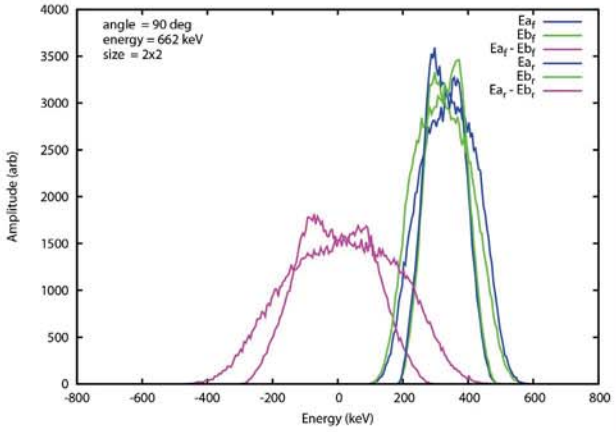

90 degrees

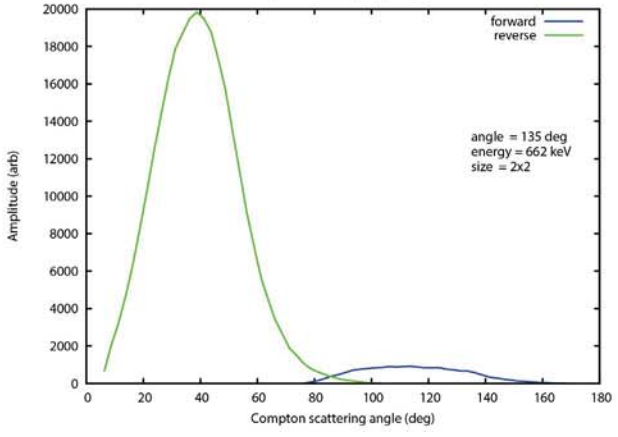

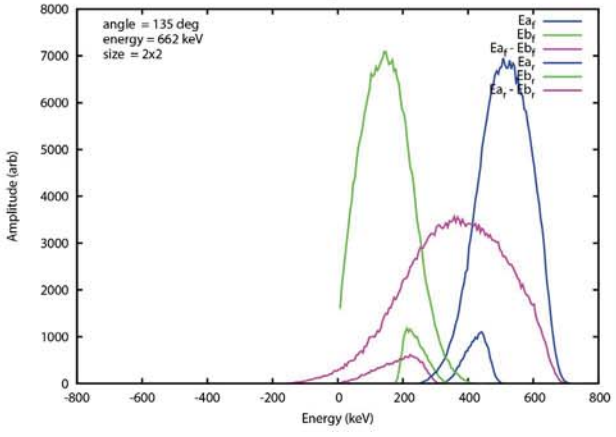

135 degrees

practical device, however, would be as compact as possible, so the scattering angle would, in fact, be over a range of angles that could be as large as 90° (e.g., when detectors physically touch one another). The distribution for the covariance signal along the Compton crosstalk band would then broaden dramatically, and one might assume that such a device would have extremely poor directional capability, but this is not the case. The broadening of the crosstalk distributions reduces the dynamic range of the averaged crosstalk energy asymmetry, but the directional capability remains quite good for relevant detector configurations.

To assess the effects of detector geometry upon the crosstalk energy asymmetry, we have written a C program of a semi-analytical model based upon the Compton formula, the Klein-Nishina cross sections, and the volume integrations of the two detectors. With this model detector we can investigate the effects of detector size and separation for arbitrary gamma energy, and we can construct full response curves for the crosstalk asymmetry over a range of angles in a few seconds. The model also calculates Beer's law attenuation of the gamma flux for penetration into scatter sites as well as penetration into absorption sites. Inter-detector shadowing is also accounted for in cases for which scatter angles have one detector partially blocking the view of the source from the other detector. The Beer's law attenuation in the model uses logarithmic interpolation of values of mass attenuation coefficients loaded into lookup tables. The volume integrations over six dimensions are performed by the MISER Monte Carlo algorithm (Press 1990), and error bars of the results are estimated. The program of the semi-analytical model makes use of the Gnu Scientific Library (GSL 2013) for random number generation and for the Monte Carlo integrations.

Figure 8 shows some of the results of the semi-analytical model for a ^{137}Cs source measured by a pair of 2" × 2" NaI detectors. The plots in column one are of density gradients for gamma penetration into the scattering and absorption sites. Forward scattering sites are marked in blue, and absorption sites are marked in red. Column two of Figure 8 shows the reverse scattering sites, marked in green, and the absorption sites, marked in red. Figure 8 column three shows plots of angular distributions of Compton scattering for several orientations of source and detectors. Both forward scattering and backscattering distributions are plotted together. Finally, Figure 8 column four shows plots of energy distributions for forward scattering and backscattering in addition to the difference distributions, which constitute the energy asymmetries. The magenta curves are of the energy asymmetry distributions. Although the distributions are broad, their central tendencies (i.e., the mean and the median) are well defined, and those central tendencies of the asymmetry are quite precise.

Figure 9 summarizes the results of the semi-analytical model for the source and detector configuration presented in Figure 8. In Figure 9 the asymmetry parameter is plotted as a function of the angle from the gamma source to the detector pair. To construct this curve the detector hits are energy subtracted and then normalized by the initial gamma energy. The result is a realization of the asymmetry parameter x, and the mean of the set of realizations of the asymmetry parameter is computed for each source-to-detector angle. The plot in Figure 9 covers a range of angles from −15° to 195°. The "data" points are from the semi-analytical model, and the continuous curve joining them is a fit to a second order polynomial in $\cos\theta$. The curve is very well behaved and well characterized, and its precision is better than 1° of arc.

The semi-analytical model does not fully account for the physics of the problem because it makes no attempt to simulate radiation transport. For example, it does not calculate multiple scattering or any other physical process beyond Beer's law attenuation. In order to confirm the validity of the semi-analytical model, we have also performed full radiation transport simulations using GEANT4 (Agostinelli 2003) and collected laboratory data. The results of the GEANT4 simulations agree with the general trends of the semi-analytical model, although the GEANT4 simulations produced somewhat lower dynamic ranges of the

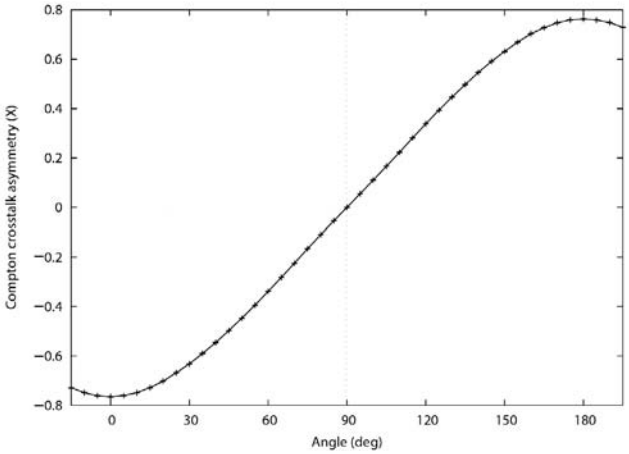

Figure 9. The Compton crosstalk asymmetry curve, as calculated by the semi-analytical model, suggests that excellent angular resolution is possible by the covariance approach

asymmetry parameter. The dynamic range reduction is caused primarily by a lower level discriminator energy cutoff used in the GEANT4 simulations, which is not included in the semi-analytical model. The simulations provide the same type of information as the semi-analytical model, but the simulations require a couple days of running time on a cluster computer, rather than the few seconds on a single-processor desktop computer required by the semi-analytical model.

The final test of the covariance analysis of Compton crosstalk asymmetry is provided by laboratory data. Figure 10 shows covariance maps for data from a 307 µCi source of ^{137}Cs measured by a pair of 2" × 2" NaI detectors at a distance of 1 meter. The data were collected for source-to-detector angles ranging from −15° to 195° in 15° increments, and the data collection time for each angle was 1000 seconds. Data acquisition was performed with ORTEC digiBASE-E digitizers operating in list-mode, and the dwell window for covariance sampling was 1 µs.

The Compton crosstalk covariances of the results shown in Figure 10 have been reduced to central tendencies of individual asymmetry values and are plotted in Figure 11. The error bars of the data points have been calculated according to the methods discussed in Trainham (2013). The propagated error bars are somewhat larger than what one would obtain by assuming a simple Poisson variable and using counting statistics estimates. For the 1000-second data collections plotted in Figure 11, the error bars on the data points are, nevertheless, smaller than the symbols used to represent the data points. This means that in Figure 11 we have used more data than absolutely necessary. In fact, much of the curve shown in Figure 11 can be constructed with 10 times less data. The solid curve through the points is from a fit to a second order polynomial in $\cos\theta$. The angular resolution derived from these data is approximately 0.6° of arc. To get a practical feel for the precision of this technique, we note that the change in the asymmetry parameter for an angular increment of 1° falls in the second decimal place of x, and the standard deviation falls in the third decimal place.

The covariance technique can be implemented using very modest computing hardware. Our algorithm stores only the part of the covariance table containing the Compton crosstalk band. We can, however, define multiple crosstalk bands for several gamma energies. Indexing into the covariance table segments for each band is relatively straightforward, and multiple gamma energies can be implemented simultaneously. To test the algorithm we used a prototype gamma detection array called Janus, which comprises eight 3" × 3" NaI detectors. For the eight detectors there are 28 distinct detector pairs. The algorithm can process all 28 covariance tables and can compute direction updates, using an Intel Atom Z530 processor, at a cadence of 10 updates per second in real time without performance degradation.

Finally, we must mention that the covariance approach does come at a cost. The time required for data collection is significantly longer than that required for average spectra. Since the covariance approach is a second order technique, the efficiencies of detection enter at second order. This includes the solid angle contribution; for example, if the detection efficiency for singles is 10%, the covariance efficiency is on the order of 1%. For the eight-detector prototype, the covariance data rate is approximately 50 times slower than the singles collection rates. This may seem prohibitive, but it is

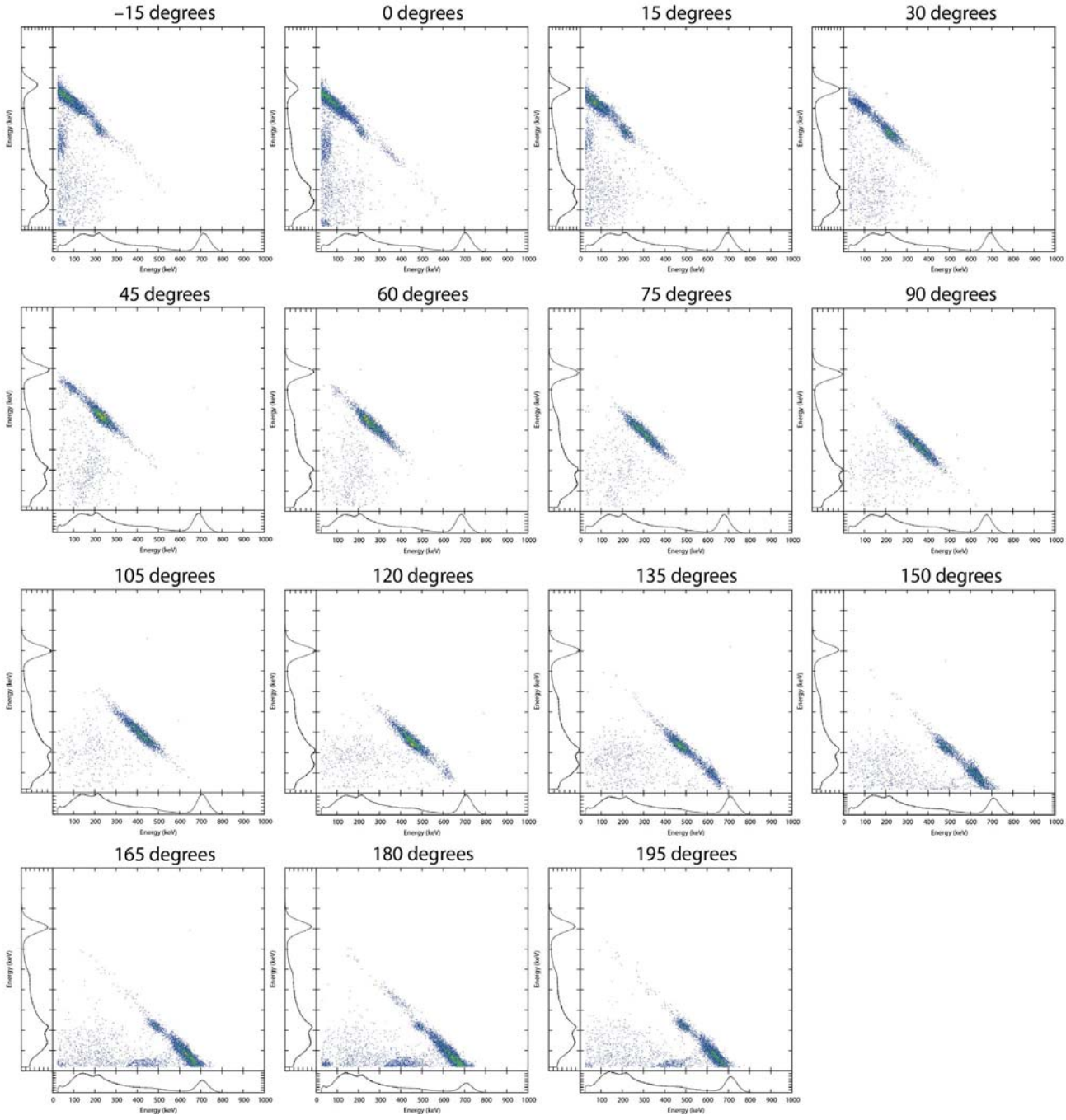

Figure 10. Covariance maps for data from a 307 µCi ^{137}Cs source measured by a pair of 2″ × 2″ NaI detectors at 1 meter. The progression of the covariance distributions down the cross-diagonal band of Compton crosstalk, as a function of angle, is distinct and well characterized.

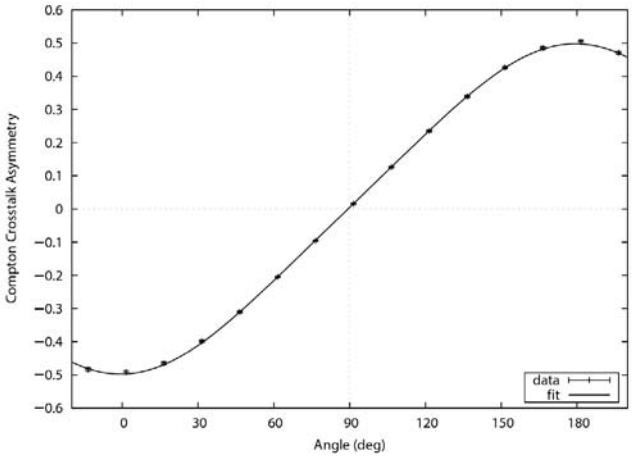

Figure 11. The curve of angle versus Compton crosstalk asymmetry derived from the experimental data shown in Figure 10 for a ^{137}Cs source

not extreme. Each data point shown in Figure 11 was collected in 1000 seconds, and the angular resolution is excellent. Ten times less data could have sufficed, and the curve would be nearly identical.

Conclusion

The basic concept of inferring the direction to a gamma source by use of covariance analysis of the energy asymmetries of Compton crosstalk is valid. Preliminary modeling suggested that the angular resolution could be excellent, and data collected by a pair of 2" × 2" NaI detectors from a ^{137}Cs gamma source shows an angular resolution of better than 1° of arc. Because the covariance approach is a second-order technique, using fluctuations of signals rather than averages of signals, there is a price to be paid in the time dedicated to data acquisition. In that light, traditional shadowing techniques for gamma directionality should also be exploited when the geometry allows for it. Nonetheless, the covariance approach to Compton crosstalk asymmetry is highly relevant to a number of applications where precise gamma directional information is important. The time required for meaningful data acquisition is not prohibitive, and the algorithm for processing data streams can execute in real time on modest computing hardware, such as those found in netbooks, tablet computers, and smart phones.

Acknowledgments

We would like to thank Bill Quam, Sanjoy Mukhopadhyay, and Howard Bender for several valuable discussions and very helpful suggestions.

References

Agostinelli, S., et al., "GEANT4 – A simulation toolkit," *Nucl. Instrum. Methods Phys. Res. A* **506**, 3 (2003) 250–303.

Compton, A. H., "A quantum theory of the scattering of x-rays by light elements," *Phys. Rev.* **21**, 5 (1923) 483–502.

Davisson, C. M., R. D. Evans, "Gamma-ray absorption coefficients," *Rev. Mod. Phys.* **24**, 2 (1952) 79–107.

Evans, R. D., *The Atomic Nucleus*, Robert E. Krieger Publishing Company, Malabar, Florida, 1982, 672–694.

Frasinski, L. J., K. Codling, P. A. Hatherly, "Covariance mapping: A correlation method applied to multiphoton multiple ionization," *Science* **246**, 4933 (1989) 1029–1031.

"GSL–Gnu Scientific Library," http://www.gnu.org/software/gsl/, accessed November 2013.

Klein, O., Y. Nishina, "The scattering of light by free electrons according to Dirac's new relativistic dynamics," *Nature* **122** (1928) 398–399.

Klein O., Y. Nishina, "Über die Streuung von Strahlung durch freie Elektronen nach der neuen relativistischen Quantendynamik von Dirac," *Z. Phys.* **52**, 11–12 (1929) 853–868.

Nishina, Y., "Die Polarisation der Comptonstreuung nach der Diracschen Theorie des Elektrons," *Z. Phys.* **52**, 11–12 (1929) 869–877.

Press, W. H., G. R. Farrar, "Recursive stratified sampling for multidimensional Monte Carlo integration," *Comput. Phys*. **4**, 2 (1990) 190–195.

Trainham R., J. Tinsley, "Covariance analysis of gamma ray spectra," *Rev. Sci. Instrum.* **84**, 1 (2013) 013502.

Trainham R., J. Tinsley, "Directional gamma sensing from covariance processing of inter-detector Compton crosstalk energy asymmetries," submitted to *Rev. Sci. Instrum.,* December 2013.

This page left blank intentionally

Chemically Activated Quiescent Persistent Sensors

STL-25-13 | Continued in FY 2014 | Year 1 of 2

Stephan Weeks,[1,a] Shayla Sawyer Armand,[a,b] and Harold McHugh[c]

Persistent monitoring for low-level chemical transients in denied areas is an unsolved mission problem. Robust, chemically activated sensors that can be covertly deployed for long periods of time (>1 year) may act as switches to turn on autonomous remote sensing networks when specific chemicals of interest are present. Our approach relies on "smart" semantic sensor nodes and micropowered processors to sense the chemical switch, turn on the sensor node to assess the scenario and wake up the network, and then exfiltrate information only when the target chemical and its threat scenario are detected, thereby prolonging battery and remote sensing system life. We have identified and evaluated low-power (<10 µA) sensor types and micropowered sensor node platforms. Results on carbon nanotube/zinc oxide thorn-like and ferrocene/ferrocenium materials and their device development for the detection of toxic industrial compounds, such as ammonia and hydrogen fluoride, are presented. The study of specific surface chemistries enabling the transduction of target analyte interactions into signals will continue in FY 2014.

[1] weekssj@nv.doe.gov, 805-681-2262
[a] Special Technologies Laboratory; [b] Rensselaer Polytechnic Institute; [c] Keystone International, Inc.

Background

There are mission-relevant observations of intermittent, transient, and very-low-level chemical emissions that can only be detected by persistent, in situ sensors. There is, therefore, high mission interest in extreme-low-power, multi-year battery, chemical sensing. Passive, chemically activated sensors for continuously operating autonomous sensor networks do not exist. Zero- or near-zero-power, gas-phase chemical sensors that trigger sensor network nodes would allow the sensor network to operate in the low-power sleep mode until something of interest occurs. Miniaturized platforms with micropowered processors that control sensors and network nodes are available. They can periodically interrogate the no- or low-power sensor(s) and report sensor and system "health" and still allow prolonged (>1 year) coin cell battery life for many strategic applications, such as covert deployment in denied areas. An autonomous sensor network would send an alarm to an external communications network only when a chemical of interest was detected in confirmed application scenarios. Critical to developing persistent ground-based remote sensing capabilities is the understanding of surface chemistry and structure effects at the nanoscale level; developing chemically functionalized, application-specific materials; and integrating these materials into device substrate surfaces for signal extraction. The nanofabrication of stable, low-power, selective, and sensitive chemical sensors is an emerging technology enabling the deployment of persistent remote sensing semantic networks for wide-area monitoring applications.

Chemical warfare agents (CWAs), improvised explosive devices, and toxic industrial compounds (TICs) are, unfortunately, necessary to monitor. Chemicals associated with their production and use may require

persistent, stealthy, and normally quiescent sensors that can "lie in wait" for prolonged periods, and then awaken to detect events of interest and exfiltrate information. For multiple mission reasons, durable, miniature, coin cell battery–operated sensor nodes are required for ground-based, wide-area remote sensing networks. Chemically activated sensors operating at near-zero power are required for these and other applications. Ideally, zero-power (change in resistance) chemical sensors were sought to use as a switch to power on sensor node electronic circuitry, which would then activate the node sensors and possibly wake up the sensor network to assess the scenario to determine whether to send an alarm signal.

Project

Our project initially looked at the types of devices that are considered emerging in the commercial market, as well as the materials, substrates, and devices being researched and developed. A clear vision for developing miniature, low-power sensors and sensor nodes was then established. Attention then turned to developing the materials and devices that can be nanofabricated to produce sensitive, selective (ideally specific), stable, and robust sensors for our target applications. The details of the project are organized by a review of current gas sensing technologies followed by the identification of a potential commercial sensor platform to incorporate novel devices. Finally, investigative results of fabricated materials for gas sensing and their initial device characteristics are demonstrated.

Literature Review of Ultra-Low-Power Gas Sensor Technologies

Low-power (<100 µA), long-lived (>1 year) chemical sensors and sensor development were reviewed. Considerable international research and development is taking place. However, the very few low-power sensors that are commercially available detect only a limited number of chemicals, and typically even these sensors have many cross sensitivities. Many commercial low-power sensors, such as metal oxides, are generally heated to higher than ambient temperatures and have a warm-up period in order to achieve stability and good sensitivity, which requires more power and therefore shortens their lifetime in automated persistent monitoring networks. Current research has been directed toward the development of low-power sensors. Table 1 shows the advantages and disadvantages of technologies for gas sensing.

Figure 1 demonstrates the general research pathways for gas-phase chemical detection. With the design constraints of compact and low-power sensing, the focus of the project lies entirely in electrical methods where changes in either resistance or capacitance are

Table 1. Material and device considerations for low-power sensors

Material or Device	Sensing Parameters	Advantages	Disadvantages	Commercial Status
Metal oxide semiconductor (MOS)	Conductivity dielectric	▪ Mature, versatile ▪ Many targets ▪ Long lifetime	▪ Requires heater ▪ Low sensitivity	Mature
Hanging gate field-effect transistor (FET)	Work function of gate via dielectric change	▪ High sensitivity ▪ Small size ▪ Very low power	▪ New technology	Limited; few products on the market
Polymer capacitive	Dielectric change	▪ Good sensitivity ▪ Small size ▪ Low cost	▪ Instability ▪ Irreversibility ▪ Poor selectivity	Products on the market
Polymer resistive	Conductivity change	▪ Low power	▪ Low selectivity	Products on the market
Optical	Refractive index, opacity, color spectroscopy	▪ High sensitivity ▪ High selectivity ▪ Stable in environment	▪ High power ▪ Large size	Mature
Microelectromechanical systems (MEMS)	Mass detection via piezo resonator	▪ Quartz device ▪ Low power	▪ New device ▪ High cost	Very early

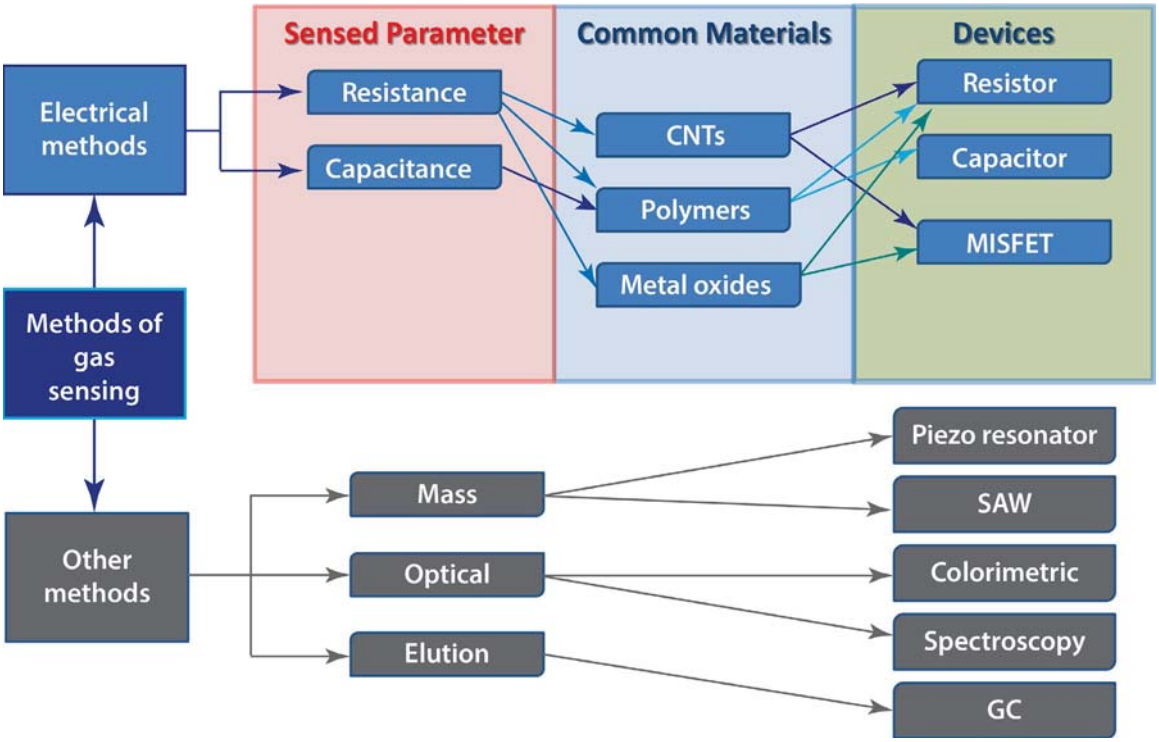

Figure 1. Pathways to low-power sensors

sensed. We have taken a parallel approach: commercial devices and sensor platforms are investigated and leveraged, while new application-specific materials and devices are developed through research collaboration.

Lifting the requirement of zero-power to allow micropowered chemically activated devices greatly increases the flexibility of sensor options, or types, in order to cover the wide range of target chemicals. Smart chemical sensing for application scenarios requires autonomous sensor nodes be controlled by micropower-processor integrated circuits (ICs). This approach meets the intent of the chemically activated quiescent persistent switch and provides the path forward for integrating the "switch" into mission applications requiring continuous chemical, biological, radiological, nuclear, and explosives remote sensing.

Commercial Micronas Sensor Platform and MISFET Devices

Micronas Corporation developed sensors and an integrated sensor platform that provides a compact, low-power solution. Presently only H_2- and NH_3-sensitive sensors are available, although NO_2 and volatile organic compound (VOC) sensors are nearly ready for production. Micronas offers a fully integrated HGFET-type gas sensor that operates on 1 µA of current and is controlled via a digital serial peripheral interface (SPI). The platform contains integral temperature and humidity sensors. Their devices illustrate the potential of this type of device as a very-low-power sensor technology that could be utilized in the development of a stealthy sensor network. The schematic of the sensor platform is shown in Figure 2. This IC is a complete system-on-a-chip, having a built-in data acquisition circuit and a serial digital interface to connect it to an external network.

This type of sensor platform can accommodate multiple sensors with different chemical detection capabilities. If specific chemical sensors are unavailable, pattern recognition or neural net algorithms can be used to train a selected chemical array system. This platform illustrates the potential for developing a very-low-power sensor system on a network node

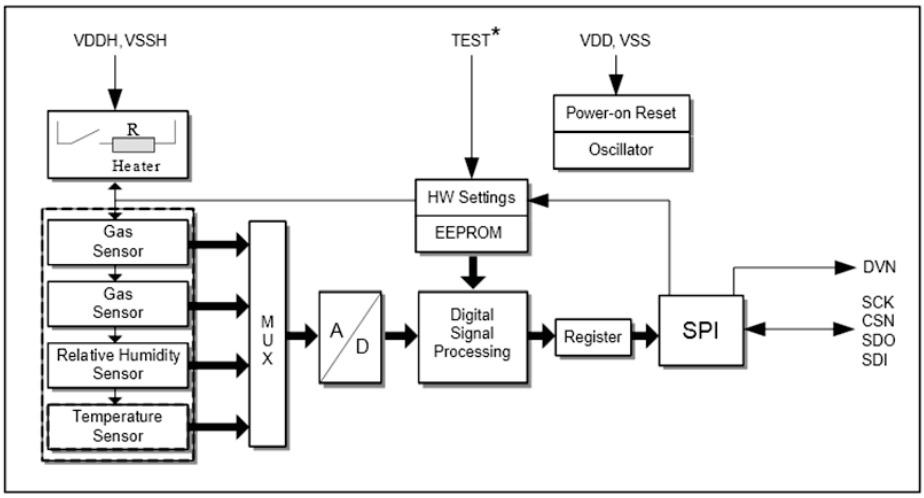

Figure 2. The Micronas 86xyb gas sensor IC platform (Micronas 2013)

that could be used in a semantic sensor network. Therefore, the path forward relies primarily on creating devices for targeted chemical detection that are compatible with current nano- and microfabrication technologies to integrate into an already mature ultra-low-power, commercial or custom, signal processing and communication system.

The Micronas sensors responding to NH_3 and H_2 gases were exposed to ammonia vapor and changes in humidity and temperature. The devices are a development of FET technology. Specifically, they are a subcategory of metal insulator semiconductor FETs (MISFETs) where instead of silicon dioxide, their insulator is air. The top electrode with sensing material is bonded using flip-chip technology to the rest of the FET structure so it forms an air gap. Typically, FET devices offer significant advantages over simple resistive or capacitive sensors due to their inherent signal gain. The basic device structure can be seen in Figure 3.

The devices were obtained and functioned as expected. Though the sensors were found to have chemical cross sensitivities, they were affected by temperature and humidity changes. Therefore, they will require temperature and humidity corrections, plus calibration of their relative chemical response decay times.

Polymer-Resistive, Capacitive, and Carbon Nanotube (CNT) Devices

MEMS-based resistive and capacitive platforms using arrays of sensors coated with specific chemically sensitive polymers can be adapted to address a wide variety of low-power chemical sensing applications, such as the detection of VOCs, CWAs, explosives, or TICs. Each chemiresistor or chemicapacitor in the array responds selectively to the chemical components in the sample gases. Because they simply provide a resistive or capacitive response, they could easily be incorporated into a quiescent persistent switch. Selectivity can be enhanced by developing an array of chemiresistors with different chemical adsorptivities, then using pattern recognition for identification and quantitation.

Considerable effort has been expended in the research and development of sensors that use single-walled and multiwalled CNTs; nanowires, nanobelts, and nanochannels are also being developed for detection purposes. CNTs offer an extremely large surface-to-volume ratio for gas adsorption as well as greater modulation of electrical properties (resistance, capacitance) due to nanoscale physics. FETs can be configured from CNTs with the addition of metallic contacts such as gold or palladium, turning these devices into P-channel chemFETs with much higher sensitivity

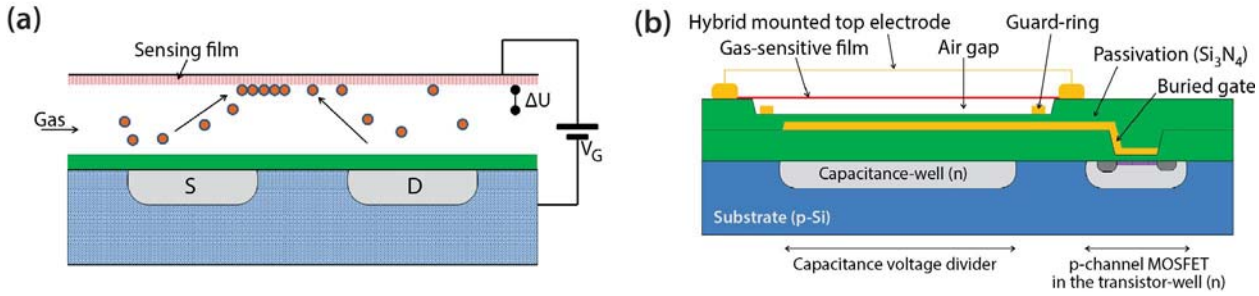

Figure 3. (a) General schematic (Fleischer 2013) and (b) detailed schematic of HGFET show the floating gate structure through which gas passes (Iskra 2008)

than simple chemiresistors. CNTs can also be used to enhance the sensitive coatings used on chemiresistors or FET sensors. The efforts to make CNT detectors appear promising, but few of these devices are commercially available at this time.

The National Aeronautics and Space Administration (NASA) Ames Research Center has developed a multisensor array utilizing CNTs for very-low-power gas sensing, but it has not been commercialized yet. It was originally intended for space applications and as such is a low-power device. It has been developed for emergency responder applications under the U.S. Department of Homeland Security's Cell-All Program (Li 2012). It could also have potential application for in situ monitoring and battlefield deployment. Currently it has been successfully tested using NO_2, NH_3, and VOCs in the ppm region. NASA Ames envisions using this device in conjunction with other MEMS devices to obtain improved selectivity.

No commercial sensor systems were found that satisfied our low-power and small size requirements. It typically takes 1 to 2 years to develop robust, selective, sensitive sensors that are commercially available. It is, therefore, very important to leverage emerging commercial chemical sensing products and take the parallel approach to develop ultra-low-power, application-specific materials and devices. Integrating chemically activated switches into sensor nodes enables mission-specific, long-term, continuous semantic network remote sensing.

Fabricated Material and Device Research Results

Large surface-to-volume ratios for gas adsorption, as well as greater modulation of electrical properties (resistance, capacitance) due to nanoscale physics, is the avenue for low-power gas sensing in compact electronic devices. Considerable effort has been expended in the research and development of chemical sensors utilizing CNTs, various metal oxide nanowire and nanoparticle materials, and polymers. From these materials, resistors, capacitors, and FETs can be created. The key to further development for our mission-specific applications is finding methods to functionalize these materials for selective/specific chemical response, then integrating them onto the surfaces of these low-thermal-mass, large-surface-area nanoscale devices, which transduce the chemical response into an informational signal measurement. The following are the results of two material investigations. The first is a unique metal oxide material with a large surface area (paper-like), and the second is a thin film of ferrocence materials.

Thorn-Like ZnO-CNT Hybrid Paper Materials

Metal oxides are well known for their gas-sensing capability, though they are typically limited by the requirement for heating. Some devices have been demonstrated at room temperature with the use of surface coatings, hybridization, and/or nanostructures (Lao 2007, Kuang 2008, Tulliani 2011, Yi 2011).

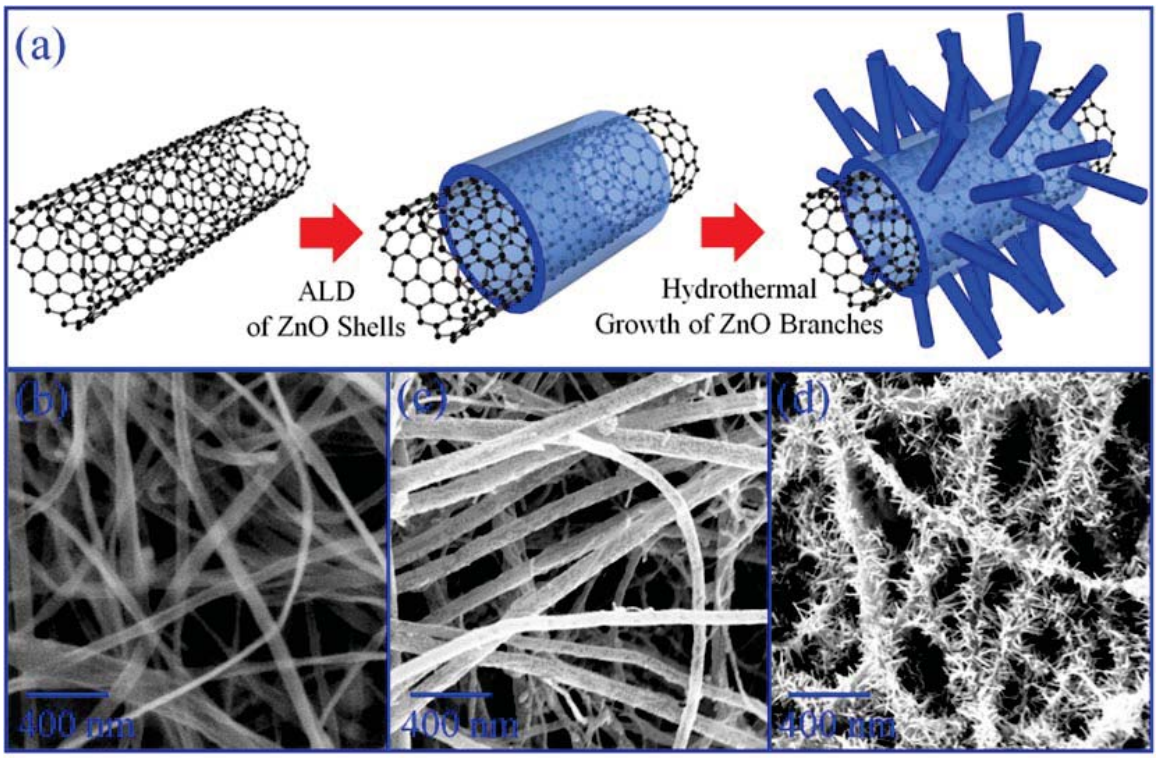

Figure 4. (a) The fabrication process of the flexible thorn-like ZnO-CNT hybrid paper. The high-resolution scanning electron microscope (SEM) images of sample in each fabrication step are presented in (b) pure CNT paper, (c) CNT paper with ZnO shells fabricated via ALD, and (d) thorn-like ZnO-CNT hybrid paper after hydrothermal growth.

A schematic illustration of flexible thorn-like ZnO-CNT hybrid paper is shown in Figure 4. First, ZnO nanostructures were grown directly on CNT paper (Buckeye Composites, Inc.) using a rotary atomic layer deposition (ALD) reactor. For the ZnO ALD, diethyl zinc ($Zn(CH_2HC_3)_2$) and high-performance liquid chromatography (HPLC)–grade H_2O were obtained from Sigma-Aldrich. ZnO ALD is performed using alternating $Zn(CH_2HC_3)_2$ and H_2O exposures:

(A) $ZnOH^* + Zn(CH_2CH_3)_2 \rightarrow ZnOZn(CH_2CH_3) + CH_3CH_3$

(B) $Zn(CH_2CH_3)^* + H_2O \rightarrow ZnOH^* + CH_3CH_3$,

where the asterisks represent the surface species. By repeating these reactions in an ABAB... sequence, ZnO quantum dots can be deposited with atomic layer control. The ZnO ALD reaction sequence was (i) dose diethyl zinc (DEZ) to 1.0 Torr for 120 seconds, (ii) evacuate reaction products and excess DEZ, (iii) dose N_2 to 20.0 Torr for 60 seconds and then evacuate N_2 (repeat five times), (iv) dose H_2O to 1.0 Torr for 120 seconds, (v) evacuate reaction products and excess H_2O, and (vi) dose N_2 to 20.0 Torr for 60 seconds and then evacuate N_2 (repeat five times). This sequence constitutes one AB cycle of ZnO ALD. The ZnO ALD was performed at 150°C with 50 cycles.

Second, ZnO nanowire branches were grown on the CNT-ZnO hybrid paper using a hydrothermal method. In a typical process, ammonium hydroxide (28 wt%) was added dropwise into 0.1 M zinc chloride solution until the pH was 10–11 and the solution was clear. Subsequently, the transparent solution was transferred to a Teflon-lined autoclave (Parr, USA) and the CNT-ZnO hybrid paper was suspended in the solution at 95°C for 14 hours in a regular laboratory oven. Then the growth solution was cooled down to room temperature naturally. The resulting substrate was thoroughly washed with deionized water and absolute ethanol several times and dried in air at room temperature (Figure 5).

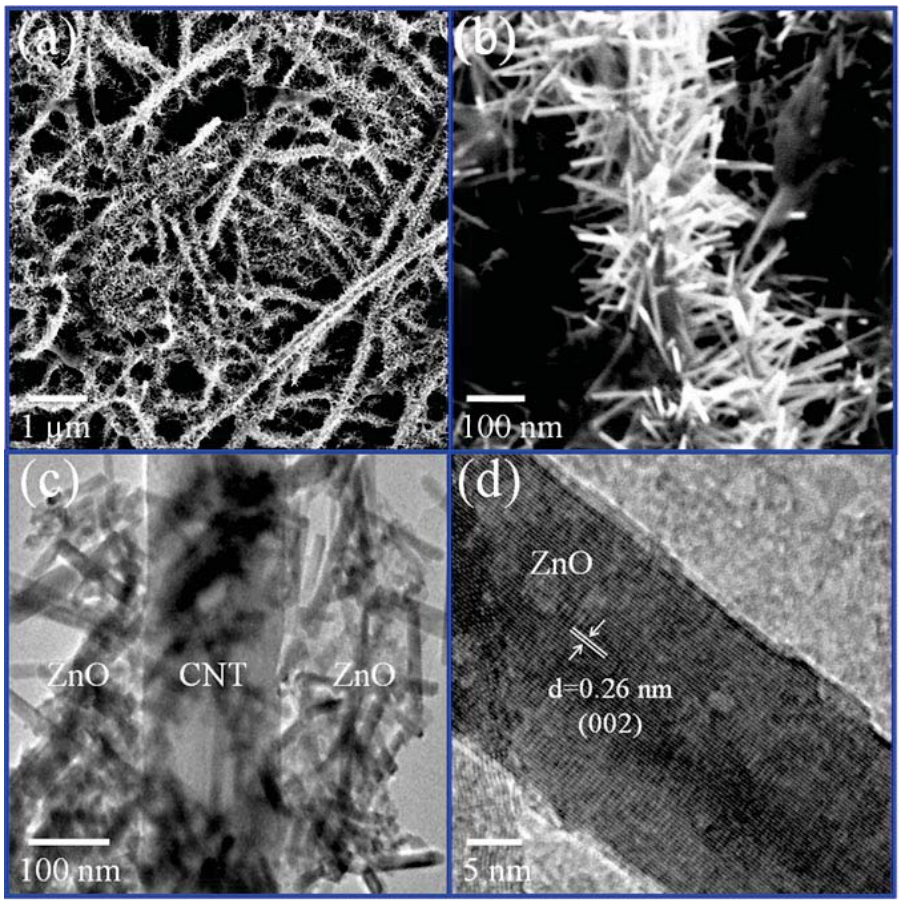

Figure 5. (a)–(b) High-resolution SEM images of the flexible thorn-like ZnO-CNT hybrid paper, (c) transmission electron microscope (TEM) image of a single ZnO-CNT hybrid structure, and (d) high-resolution TEM image of a ZnO nanowire branch grown on the CNT paper

The urchin thorn-like ZnO/CNT paper was mounted on a glass substrate for current voltage testing. A probe station was used to measure the current voltage characteristics first without and then with exposure to NH_3 (Figure 6). The resistance increased with exposure to NH_3 almost immediately; however, after removing the chemical, the resistance remained the same. Resistance increase with NH_3 exposure has been previously reported to be due to the change in oxidation or reduction process (Tulliani 2011). Specifically, oxygen adsorbed on the film surfaces and grain boundary surfaces accepts electrons to become O_2–, O–, or O^2, resulting in a decrease in carrier concentration and/or a decrease in mobility. The ZnO response may be because (1) ammonia gas is directly adsorbed on the sensor surface, accepting electrons available for conduction, and (2) the adsorption of atmospheric oxygen is enhanced by exposure to ammonia gas (Nanto 1986). Though a change was found immediately upon exposure, the time needed for the resistance to return to its original value is unknown at this time. The test should be repeated and time response determined. External factors such as heating the device and contact thickness will also be investigated.

Ferrocene Materials Development

Ferrocene is an organometallic material that undergoes electron transfer via reduction and oxidation (redox) with exposure to gases (Figure 7). Thus far in literature this charge transfer is best demonstrated by changes in conductivity in the conductive material it modifies (polymers, CNTs, etc.) (Shadaran 1997, Radhakrishnan 2007).

The initial ferrocene films created at Rensselaer Polytechnic Institute (RPI) show the individual crystal structures in Figure 8. The film consists of multiple crystals that are not conductive in nature. A covalent bond to a conductive film is required to connect crystal "islands" together. Without a covalent bond,

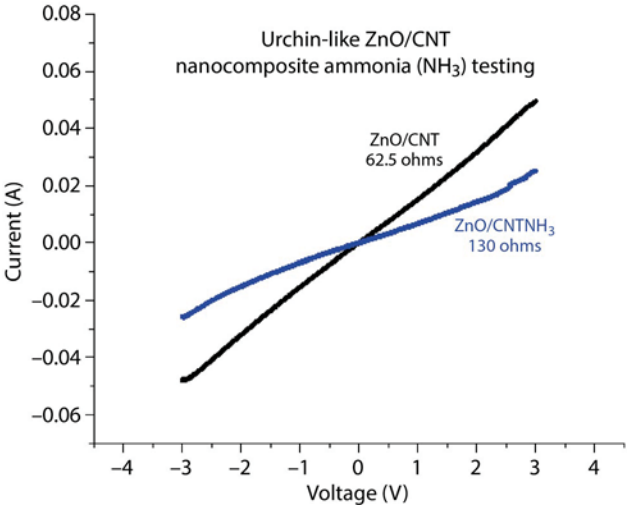

Figure 6. Current voltage characteristic of ZnO/CNT paper on a glass substrate with ($ZnO/CNTNH_3$) and without (ZnOCNT) ammonia exposure, demonstrating a resistance or conductivity change

ferrocene evaporates over time in ambient conditions. This kind of film can be doped silicon, CNTs, or metals. Though changes in conductivity with gas exposure can be measured, capacitance changes would be ideal for this material. The ferrocene-functionalized surface can be integrated into a HGFET device configuration.

Ferrocene Thin Film Deposition and Crystal Growth Processes

Ferrocene is an extremely volatile compound. It is available in powder form in high purity from Sigma-Aldrich. However, converting the powder into a thin film is a major challenge. It cannot be vacuum evaporated for deposition because, even at a vacuum level of 10^{-2} Torr, it evaporates at room temperature. Heating ferrocene for thermal evaporation is also a challenge. The vapor pressure is difficult to control even at temperatures around 75°C at normal atmospheric pressure in the presence of inert gases.

Different processes to deposit thin films of ferrocene on glass substrate with predeposited metal contacts were investigated. We developed a process for slow deposition of morphologically smooth ferrocene thin films (2–50 µm thickness) using inert gas flow (N_2, Ar, or H_2) in a two-zone furnace. The temperature gradient between the source (powder ferrocene) and the

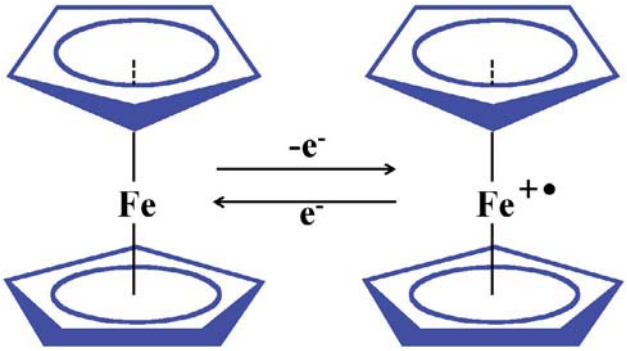

Figure 7. The ferrocene/ferrocenium redox couple (Neuse 2008)

substrate for obtaining smooth film was found to be in the range of 5°C–7°C. The most suitable source temperature was found to be in the range of 70°C–75°C. However, films deposited were not mechanically stable. They immediately peeled off from the substrate after the deposition process. This problem could be solved by having textured substrates or by using adhesive layers prior to deposition. However, that would lead to alteration in the electrical contacts between the ferrocene layers and the metal contacts.

Hence, an alternative process that led to thicker layers and crystals of ferrocene was developed. Solution crystal growth of ferrocene was employed using colloidal ferrocene solutions. Ferrocene has good solubility in organic solvents such as acetone, methanol, ethanol, hexane, etc. However, films deposited by solution evaporation are discontinuous and form films

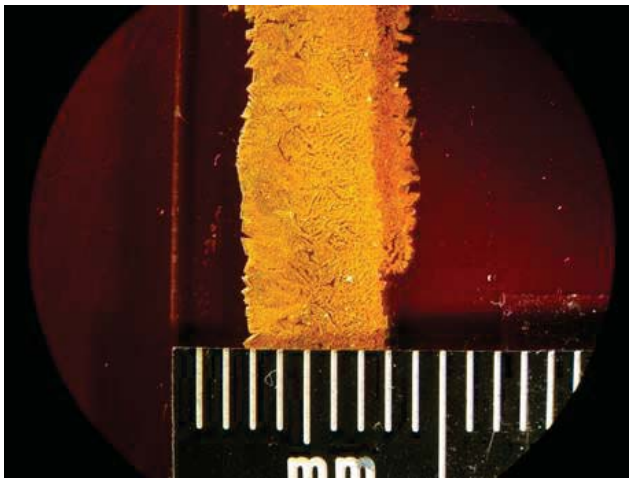

Figure 8. Ferrocene crystals deposited on a quartz substrate

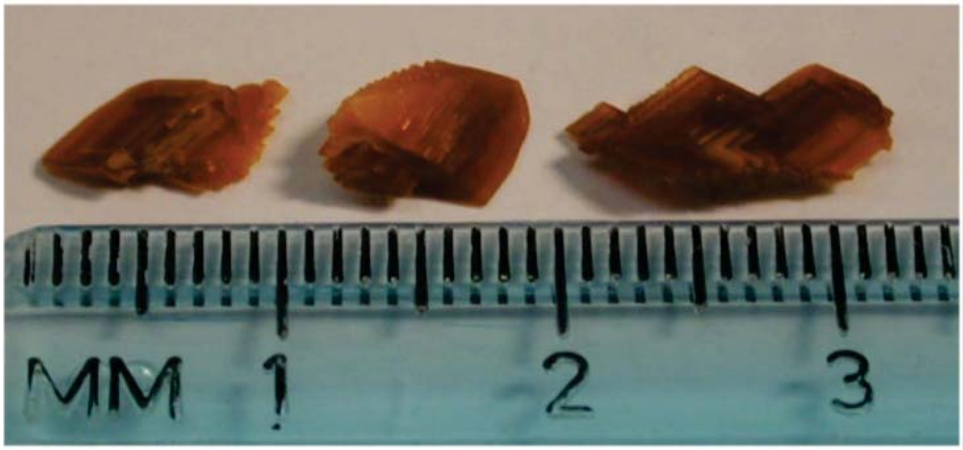

Figure 9. Ferrocene crystals grown from organic colloidal solution (crystal sizes up to 1 cm in length)

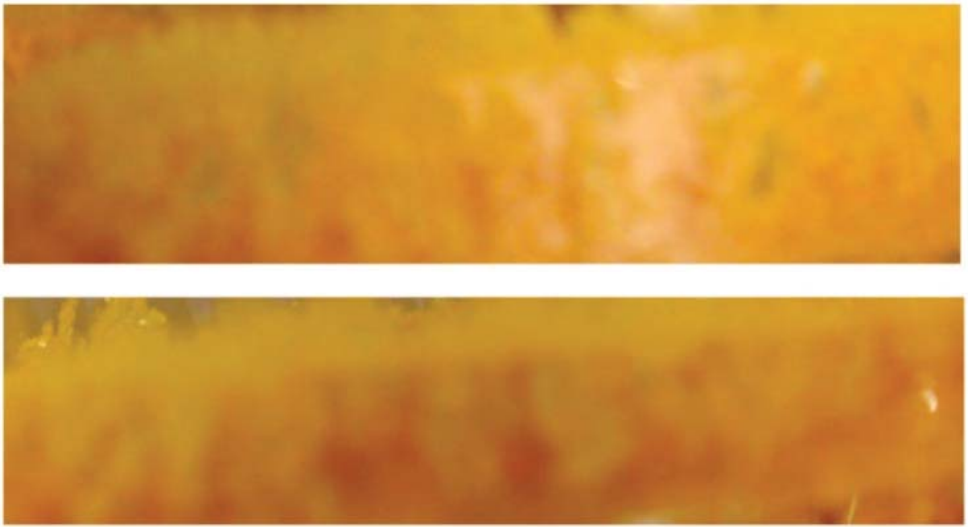

Figure 10. Ferrocene thin films deposited from organic colloidal solution

that continuously evaporate along with the solvent. To solve this problem, we developed a novel method for creating a two-phase solution of polar and non-polar solvents in various ratios for creating a colloidal solution of ferrocene. A variety of solutions, such as a water-acetone-methanol mixture with dissolved ferrocene, was used for growing crystals (Figure 9) and thick films (100–500 µm) on glass substrates (Figure 10). These films and crystals were found to be mechanically more stable than those deposited from vapor transport using gas. With the colloidal solution we used a two-zone temperature furnace to slowly evaporate the solution under a specific over-pressure of the evaporated solvent. This led to slow growth of films and crystals of ferrocene on glass. The crystals grown had morphologically flat surfaces on which measurements could be made. However, due to the fragile nature of ferrocene crystals, they are difficult to handle. To solve this issue in the future, we need to grow ferrocene crystals using our process inside porous media such as silica, zeolites, or other polymeric matrices. Alternatively, we could create ferrocene-polymer sheets wherein the exposed ferrocene molecules could be used for any chemical sensing.

Future Work

HGFET Sensor Development Platform Flip-Chip Technology

Although HGFET technology offers tremendous low-power detection possibilities, it is difficult to develop coatings for these devices in a small laboratory,

and the alternative is expensive collaboration with a sensor manufacturer. However, flip-chip technology can lower the cost of developing sensors in the laboratory by eliminating the time and expense of packaging the FET die into an IC each time a new coating test is being evaluated. In the flip-chip approach, an unpackaged FET or MOSFET die is mounted to a printed circuit board using flip-chip techniques, maintaining a space between the board and the gate of the device for gas flow. The surface of the board is coated with the chemical sensing compound being developed. A spacing of approximately 2 µm between the coating and the gate is typical in this application as it is sufficient to permit gas flow while minimizing the gap that reduces sensitivity of the device (there is no gap in a general purpose FET). Because the air gap greatly reduces the gain of the FET, the geometry of the FET must be optimized with different parameters than those of typical FETs. The ratio of the gate width to length must be greatly increased from about 5 to over 500, minimizing the opportunity that commercially available FET die meeting these requirements can be obtained. A second FET must also be mounted on the substrate to provide a temperature compensation reference.

Physical Implementation of an Ultra-Low-Power Persistent Sensor

The key to any stealthy persistent sensor is a micropower processor that can control the power supplied to all sensor components and interpret the output data. Any sensing device that has no appreciable warm-up time can be turned off when not needed, permitting periodic sampling of sensors with significant power consumption to be powered by miniature coin cell batteries. Sensors with micropower heaters can also be used, especially if their warm-up period is short. Figure 11 illustrates the potential components of an ultra-low-power persistent sensor that can communicate by a cell phone RF IC in the case of an alarm and remain deployed for multiple years. A single sensor module could contain multiple sensors with unique gas responses. The processor can use pattern recognition to identify analytes and send the ID data to an external network, or the data can be relayed to a network for further evaluation based on the response of other sensors in the network.

Conclusion

The electronic components needed to support long-term deployment of stealthy gas sensors are available commercially. Low-power sensor development is much less mature at the present time, but recent research offers much potential for the future deployment of miniature chemiresistors, chemicapacitors, and chemFETs. CNT technology promises to greatly expand this field in the near future; the development of a wide range of coatings to the nanotubes can enable these sensors to detect chemicals of interest. In addition, recent advances in HGFETs offer greatly enhanced sensitivities that allow the use of CNT and other emerging technologies to provide a highly sensitive suite of low-power sensors for mission-specific applications. New materials functionalized to interact specifically with targeted analytes can be designed by a better understanding of how nanoscale physics enhances chemical sensing interactions at surfaces. These surfaces, both material and device structures, must be electronically designed for efficient extraction

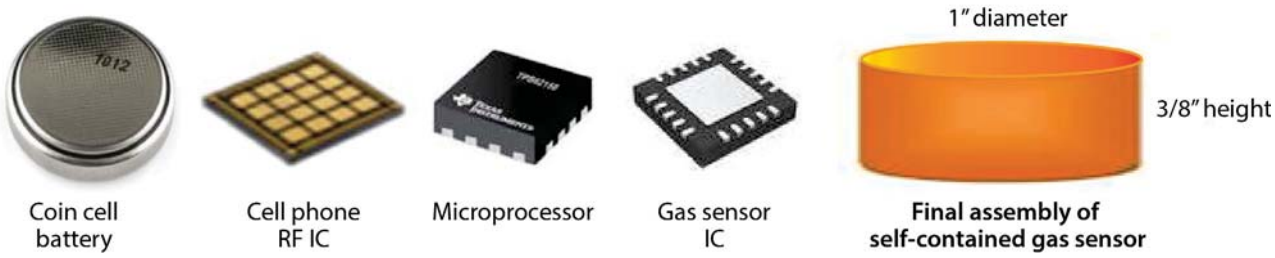

Figure 11. Possible configuration of components in an ultra-low-power persistent sensor

of charge carriers and must have large surface to volume ratios for gas adsorption. Again, a better understanding of nanoscale physics will allow greater modulation of electrical properties (resistance, capacitance) and be the avenue for low-power gas sensing in compact electronic devices. Then, the path forward entails developing efficient processes for integrating the chemically specific devices into existing microscale sensor platforms.

Acknowledgments

We would like to thank Dali Shao (RPI), Prof. Partha Dutta (RPI), Ron Justin (Special Technologies Laboratory [STL]), Tony Botello (STL), and Rod Tiangco (STL) for their contributions to this work.

References

Fleischer, M., R. Pohle, O. von Sicard, "Signal quality of field effect transistor-based humidity sensors or gas sensors," U.S. Patent 8373205 B2, filed September 24, 2009, and issued February 12, 2013.

Iskra, P., C. Senft, D. Kulaga-Egger, T. Sulima, I. Eisele, "A GasFET concept for high temperature operation," *Sensors, 2008 IEEE* (2008) 1301–1304.

Kuang, Q., C.-S. Lao, Z. Li, Y.-Z. Liu, Z.-X. Xie, L.-S. Zheng, Z. L. Wang, "Enhancing the photon- and gas-sensing properties of a single SnO_2 nanowire based nanodevice by nanoparticle surface functionalization," *J. Phys. Chem. C* **112**, 30 (2008) 11539–11544.

Lao, C. S., Q. Kuang, Z. L. Wang, M.-C. Park, Y. Deng, "Polymer functionalized piezoelectric-FET as humidity/chemical nanosensors," *Appl. Phys. Lett.* **90**, 26 (2007) 262107–262107-3.

Li, J., G. Yu, Y. Lu, C. Hsiung, A. Hannon, D. Kim, S. Dennis, "Nanotechnology based cell-all phone-sensors for extended network chemical sensing," *Sensors, 2012 IEEE* (2012) 1–4.

Micronas, "Digital Gas Sensor Platform," http://www.micronas.com/en/products/gas-sensors/gas-86xyb, accessed September 30, 2013.

Nanto, H., T. Minami, S. Takata, "Zinc-oxide thin-film ammonia gas sensors with high sensitivity and excellent selectivity," *J. Appl. Phys.* **60**, 2 (1986) 482–484.

Neuse, E. W., "Synthetic polymers as drug-delivery vehicles in medicine," *Metal-Based Drugs* **2008** (2008) 469531.

Radhakrishnan, S., S. Paul, "Conducting polypyrrole modified with ferrocene for applications in carbon monoxide sensors," *Sens. Actuators B* **125**, 1 (2007) 60–65.

Shadaran, M., J. Martinez, F. Garcia, D. Tavares, "Sensing ammonia with ferrocene-based polymer coated tapered optical fibers," *Fiber and Integrated Optics* **16**, 1 (1997) 115–122.

Tulliani, J.-M., A. Cavalieri, S. Musso, E. Sardella, F. Geobaldo, "Room temperature ammonia sensors based on zinc oxide and functionalized graphite and multi-walled carbon nanotubes," *Sens. Actuators B* **152**, 2 (2011) 144–154.

Yi, J., J. M. Lee, W. I. Park, "Vertically aligned ZnO nanorods and graphene hybrid architectures for high-sensitive flexible gas sensors," *Sens. Actuators B* **155**, 1 (2011) 264–269.

This page left blank intentionally

Computational and Information Sciences

Computational and Information Sciences

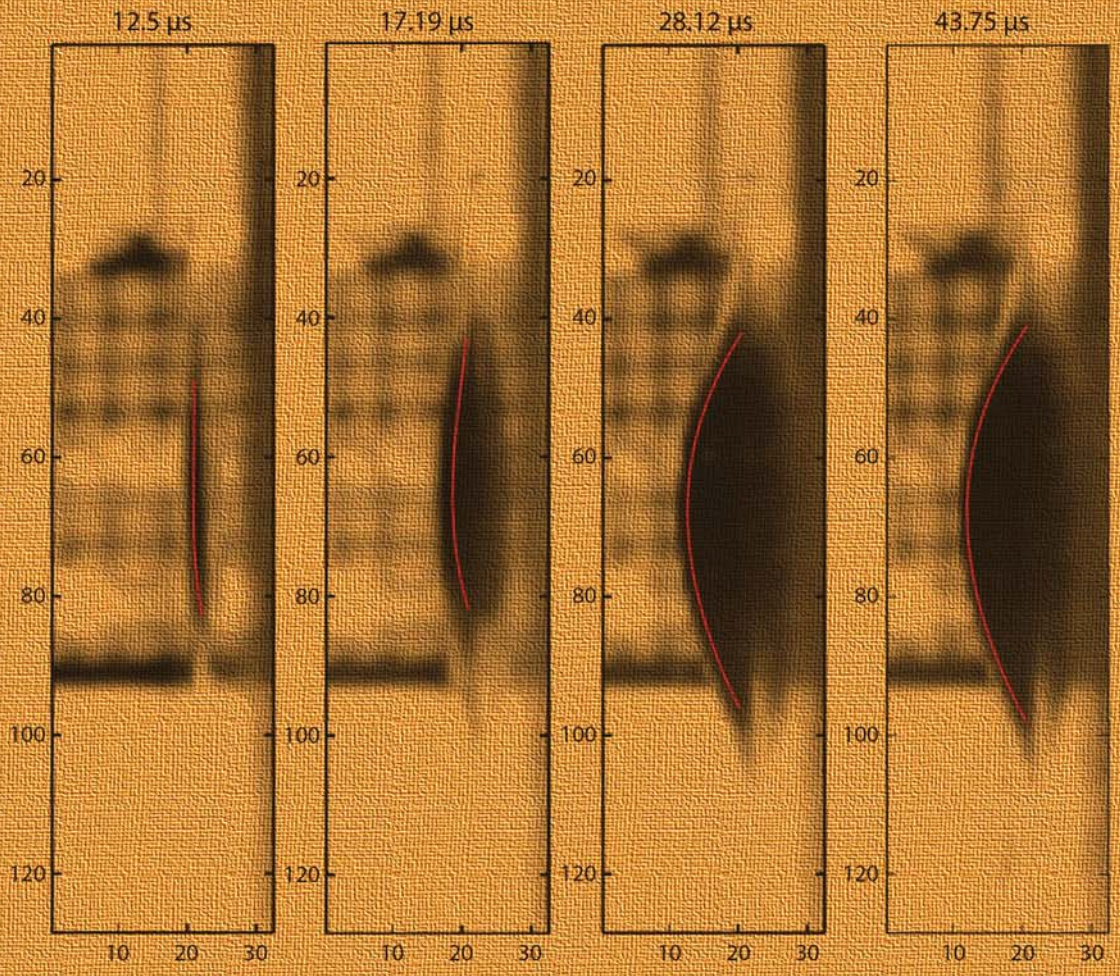

$$x_{LTV} = \arg\min_{u} \int_{\Omega} |Au - b|^2 d\Omega + \lambda \int_{\Omega} |\nabla u| d\Omega$$

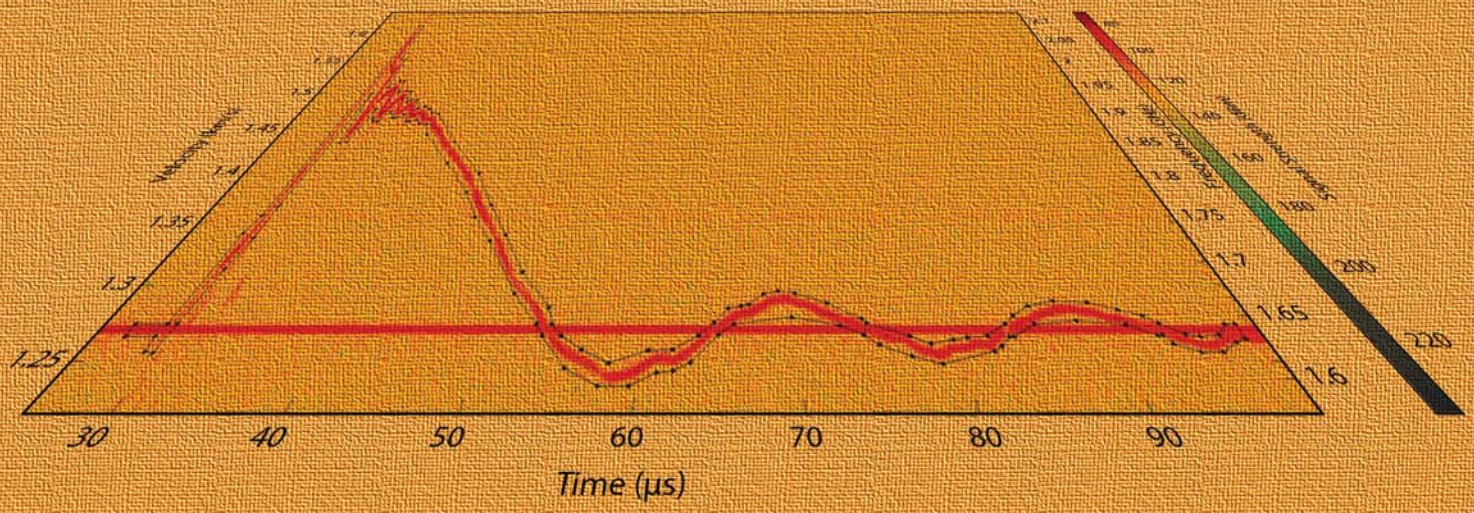

Quantifying Uncertainty and Error Propagation in Radiography Image Processing

NLV-11-13 | Year 1 of 1

Aaron Luttman,[1,a] Marylesa Howard,[a] Michael Fowler,[a] and Stephen Mitchell[a]

In imaging applications that focus on quantitative analysis—such as x-ray and proton radiographies in the security sciences—it is necessary to be able to reliably estimate the uncertainties associated with the processing algorithms applied to the image data. Deconvolution, Abel inversion, and x-ray spot reconstruction are three important processes used in radiography image analysis, and they can all be mathematically formulated as linear inverse problems solved within a Bayesian framework using Markov Chain Monte Carlo (MCMC) methods. This approach gives a statistical technique for quantifying uncertainties in the calculation and provides a natural method to impose scientific priors on the computed solutions. In this work we detail the Bayesian formulation and a new approach to MCMC sampling that allows construction of credibility bands on the reconstructions by sampling not only from the posterior density of the reconstruction but also from a posterior distribution on the prior density. Thus we quantify the uncertainty in our solution and the uncertainty in our scientific priors. The results are presented on real data captured from x-ray imaging facilities, showing the effectiveness of this novel approach.

[1] luttmaab@nv.doe.gov, 702-295-0303
[a] North Las Vegas

Background

Radiography is a primary diagnostic in the nation's subcritical nuclear experimentation program, and, as such, the certification of the U.S. nuclear weapons stockpile depends heavily on the information it provides. The two primary radiography diagnostics used are x-ray radiography (Smith 2005, 2007), which is ubiquitous throughout the DOE research complex, and proton radiography (Ziock 1998, Clarke 2013), which is an important diagnostic for research at Los Alamos National Laboratory (LANL). Though the physics behind the two diagnostics are fundamentally different, they both result in data that must be heavily processed in order to extract the information of interest from the images, such as object densities or feature locations. To ensure that the processing algorithms do not systematically bias the computed values of quantities of interest, it is essential to be able to associate mathematically rigorous and statistically justified error bars to the calculations.

Given measured data b, which in the case of radiography is an image, and a linear operator A, such as a convolution operator or the Abel transform, the most common approach to solving an ill-posed inverse problem of the form $Ax = b$ is to solve the optimization problem

$$x = \underset{u}{\operatorname{argmin}} \|Au - b\|^2 + \lambda R(u), \tag{1}$$

where $R(u)$ is a regularization, which numerically stabilizes the problem and allows one to impose prior assumptions on the solution, and λ is the regularization parameter, which serves as a weighting factor

between the regularization and the data fidelity. In this case x is the solution we seek, which is an uncontaminated or untransformed version of the measured data. Alternatively, if the noise in the signal comes from a counting process, one can instead solve the associated Poisson maximum likelihood estimation problem

$$x = \underset{u}{\operatorname{argmin}} \int_{\Omega} (Au + \gamma) - b \log \times (Au + \gamma)\, d\Omega + \lambda R(u), \tag{2}$$

where γ is the strictly positive signal background or dark field (Bardsley 2009). All of the applications studied in this work can be solved in either optimization formulation. The value of this formulation is that it leads to methods that give excellent results. There are two drawbacks of the optimization approach: (1) the optimal value of the regularization parameter is not generally known a priori, and (2) it gives no direct way to estimate the errors in the calculation.

In order to quantify the uncertainties in image processing, the classical Bayesian approach is to assume a prior distribution on the quantity of interest and to derive the form of the associated posterior distribution (Gelman 2004). One then develops a computational approach for sampling from the posterior distribution in order to understand its variation (Gamerman 1997). The most difficult component of this formulation is designing a prior that allows for spatially varying image properties. For example, a common prior would be to assume that the image is smooth. While radiographs often have regions that are smooth, they also often have sharp edges that are not smooth but are features of importance. Therefore, it is necessary to design a prior that allows for spatial variations. Some work has been done in this direction (Bardsley 2013), but we have developed a straightforward method for using the results of optimization techniques described above as a prior for the stochastic approach. This is demonstrated below using the Poisson optimization as a prior for image deconvolution.

One problem that both the optimization-based methods and the sampling methods have in common is that one must assume a form for the regularization or prior, respectively. In order to fully understand the potential errors in our image reconstructions, however, we must also understand the bias errors associated with assuming a particular prior. To this end, we have developed a new technique within the Bayesian framework for estimating uncertainty in the prior assumption. This novel approach, estimating the uncertainty in the least squares optimization prior for Abel inversion and for reconstructing the spot shape of an x-ray radiation source, is demonstrated below.

Project

The main objective of the project was to develop new techniques for radiography image processing that incorporate statistically justified uncertainty quantification (UQ). Two new sampling schemes were developed, and they are presented in the following sections with applications to image deconvolution and Abel inversion.

Feature-Enhancing Deconvolution with UQ

Radiographs are images that have been contaminated by measurement noise in the system but also by the systematic blur caused by optics, scintillation, scatter, and the fact that an x-ray source is not a point source. The mathematical model for convolution is

$$Ax := \int_{\Omega} a(s - t)x(s)\, ds = b(t), \tag{3}$$

where a is the so-called point spread function (PSF), which measures the system impulse response, and $\boldsymbol{s},\boldsymbol{t} \in \mathbf{R}^d$, where $d = 1$ or $d = 2$. There is extensive literature on solving this problem for x, given b (e.g., Vogel 2002, Hansen 2006, and their bibliographies). One of the primary goals is to reconstruct x, with the understanding that the data will have strong edges as a result of jump discontinuities in the signal. In this case, the deconvolution formulation is given by

$$x = \underset{u}{\operatorname{argmin}} \int_{\Omega} (Au + \gamma) - b \log (Au + \gamma)\, d\Omega + \lambda \int_{\Omega} |\nabla u|\, d\Omega. \tag{4}$$

The regularization term is known as the total variation (TV) of the function u. This approach to deconvolution, called Poisson-TV in what follows, was explored in detail in Bardsley (2009).

In the Bayesian formulation, the goal is to compute the maximizer of the posterior probability $p(u|b)$, where again u represents the desired solution x. A Taylor series approximation to the Poisson likelihood gives

$$p(b|u) \propto \exp\left(-\frac{1}{2}\left\|C^{-1/2}(Au - b + \gamma)\right\|^2\right), \quad \textbf{(5)}$$

where C is the diagonal matrix whose entries are the elements of b. The prior density is given by

$$p(u) \propto \exp\left(-\frac{\lambda}{2}u^T L u\right), \quad \textbf{(6)}$$

where λL is the precision matrix, which is the inverse of the data covariance. In order to compute an L that will capture the edge data in the imagery, we compute the solution of the Poisson-TV formulation. Given that solution, denoted x_{PTV},

$$L = D_x^T M D_x + D_y^T M D_y, \quad \textbf{(7)}$$

where

$$M := \operatorname{diag}\left(\frac{1}{\sqrt{(D_x x_{PTV})^2 + (D_y x_{PTV})^2 + \eta}}\right), \quad \textbf{(8)}$$

where η is a numerical regularization to overcome the nondifferentiability of the total variation seminorm, taken to be 10^{-4} in our examples. The matrix M captures the edge information in the Poisson-TV solution, and L encodes that into the diffusion operator.

We must also assume a prior distribution on λ, and, in order that the posterior distribution remains normal, we choose λ to follow a prior conjugate to the normal likelihood, which is a gamma distribution with parameters α and β. Thus,

$$\begin{aligned} p(\lambda) &\propto \lambda^{\alpha-1}\exp(-\lambda\beta) \\ p(u|\lambda) &\propto \lambda^{n/2}\exp\left(-\frac{\lambda}{2}u^T L u\right), \end{aligned} \quad \textbf{(9)}$$

and applying Bayes' Theorem gives the final posterior density

$$\begin{aligned} p(u,\lambda|b) &\propto p(b|u)p(u|\lambda)p(\lambda) \\ &\propto \lambda^{n/2+\alpha-1}\exp\left(-\frac{1}{2}\left\|C^{-1/2}(Au-b-\gamma)\right\|^2\right. \\ &\quad \left. -\frac{\lambda}{2}u^T L u - \lambda\beta\right), \end{aligned} \quad \textbf{(10)}$$

from which we compute samples using a Gibbs sampler (Gelman 2004). The mean of the samples is taken as the reconstruction x, and the uncertainty is measured either by the pointwise standard deviation of the sample or by computing 95% credibility bands.

Figure 1a shows a PSF computed for an x-ray radiograph along with an image of a lead step wedge (Figure 1b). The step wedge is used to compute how much of the x-ray energy is transmitted through different thickness of the lead. The vertical cross section of the image (Figure 1c) shows the relative intensities of light passing through the different thicknesses of the object. (The intensity scale has been normalized, giving relative rather than absolute values.)

Figure 2 presents the Poisson-TV reconstruction for the step wedge cross section in Figure 1. The edge information is clear in the reconstruction. In fact, this would make an excellent reconstruction, if it led to a direct calculation of the uncertainties associated with it. To do so, we construct the prior matrix L as described above and sample from the posterior distribution. Figure 3 shows the reconstruction results for the sampling scheme along with the histogram of the regularization parameter for the samples. As can be seen in Figure 3a, the reconstruction has much sharper edges than the blurred, noisy data, and it captures all of the scales except the smallest. (Note that the image is plotted in a logarithmic scale, so each step is at different scale from the others.) By sampling the signal we obtain error estimates on x, which are plotted in this case as 95% credibility bounds, shown as dotted lines. The regularization parameter is also sampled, which means that it is not necessary to know its value precisely ahead of time. Using the mean of the λ samples as the correct value and the standard

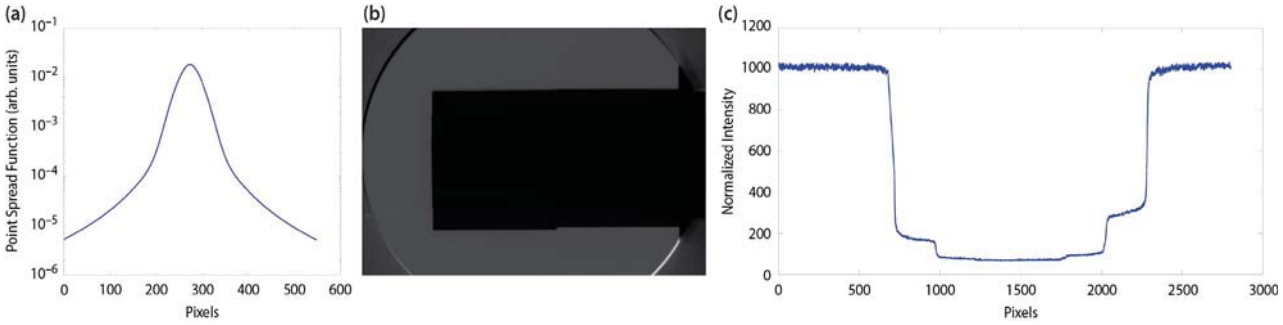

Figure 1. (a) Measured and normalized point spread function in logarithmic vertical scale and linear horizontal scale in pixels, (b) measured radiograph of a lead step wedge used for determining object densities, and (c) vertical lineout from the radiograph in linear, normalized intensity scale with linear horizontal scale in pixels

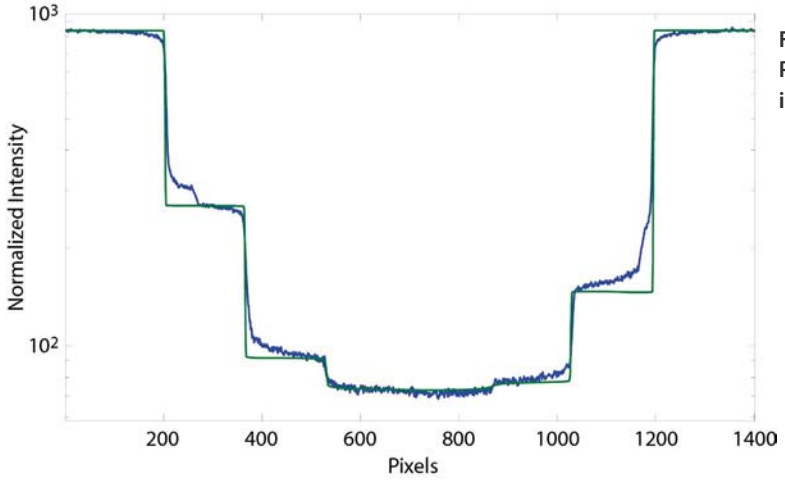

Figure 2. Step wedge cross section (blue) with Poisson-TV reconstruction (green). The edge information is evident.

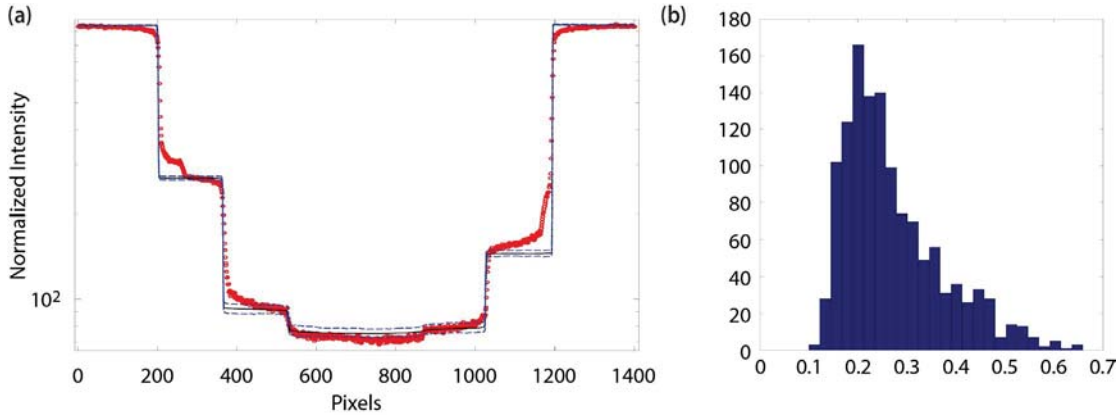

Figure 3. (a) The radiograph step wedge cross section (red) with sampling-based reconstruction (blue) and 95% credibility bounds (blue, dotted) and (b) the histogram of samples for the precision parameter

deviation as the uncertainty yields λ = 1.14 ±0.04. Further details of this method and the results can be found in Howard (2013).

Edge Localizing Abel Inversion with UQ

The density of an object that is radially symmetric about a central axis is given by the Abel transform,

$$A(u)(t) = 2\int_t^R \frac{ru(r)}{\sqrt{r^2 - t^2}\,dr} := b, \qquad \textbf{(11)}$$

where R is the maximum radius of the object, emanating out from the axis of symmetry; $u(r)$ is the density of the object; and b is the areal density of the object (Bracewell 1978). This is important in x-ray radiography, but it is fundamental to the processing of images from proton radiography. The areal density b can be computed from image intensities, either using a computed transfer curve or using the approximation $b \approx -\log(I/I_0)$, where I is the image intensity and I_0 is the maximum intensity across the image. Since A is again a linear operator as a function of u, the sampling scheme from the previous section can be applied. Once again we are interested in the edge information in the image data, because the features of greatest interest are the boundaries between regions of the object of different densities; therefore, we regularize using the total variation of the signal and use the algorithms described in Asaki (2005, 2006).

The most important quantity of interest in this application is the set of locations of the boundaries between objects (or regions of a single object) of different densities, so it is essential to accurately quantify uncertainties in the boundary location. Thus, rather than simply sampling around the precision matrix L, we developed a novel technique for sampling the precision matrix as well. This allows us to understand not only the uncertainty in the computed solution but also the uncertainty in our prior density assumption. The Bayesian formulation in this case is given by

$$p(u, L, \lambda|b) \propto p(b|u, \lambda)p(\lambda)p(u|L)p(L). \qquad \textbf{(12)}$$

The prior distribution on λ is chosen, as above, to follow a gamma distribution with parameters α and β. Rather than the Poisson likelihood, in this case we use the least squares likelihood, giving

$$p(b|u, \lambda) \propto \lambda^{n/2} \exp\left(-\frac{\lambda}{2}\|Au - b\|^2\right). \qquad \textbf{(13)}$$

Assuming that u follows a normal distribution with 0 mean and covariance L,

$$p(u|L) \propto |L|^{1/2} \exp\left(-\frac{1}{2}u^T Lu\right), \qquad \textbf{(14)}$$

and we choose a Wishart distribution on L (DeGroot 1970, Bernardo 1994),

$$p(L) \propto |L|^{(\nu-n-1)/2} \exp\left(-\frac{1}{2}\text{trace}\left(\Delta^{-1}L\right)\right), \qquad \textbf{(15)}$$

where Δ is a positive-definite scale matrix and we choose $\nu = n + 1$. Again a Gibbs sampler is used to compute the samples; the mean of the samples is taken as the solution x; and the standard deviation of the samples or 95% credibility bounds are taken as the measure of uncertainty.

Figure 4 shows an x-ray radiograph of a cylindrically symmetric object with annular sections of different materials. Figure 4b shows the areal density corresponding to a 1-D horizontal cross section through the middle of the image, and Figure 4c shows the least squares–TV reconstruction. The reconstruction captures the density boundaries quite well, and it is used to construct the L matrix around which we also sample.

Figure 5 shows the results of the u sampling along with the histogram of the sample values of λ. Note that the result still captures the edge features that the least squares–TV solution captured, but this method has also provided 95% credibility bounds around the solution (dotted lines in Figure 5a). The histogram of λ values is approximately symmetric about a single peak, which is further evidence that the sampling scheme has converged. In this case, the estimated value is $\lambda = 1.53 \times 10^3 \pm 90$.

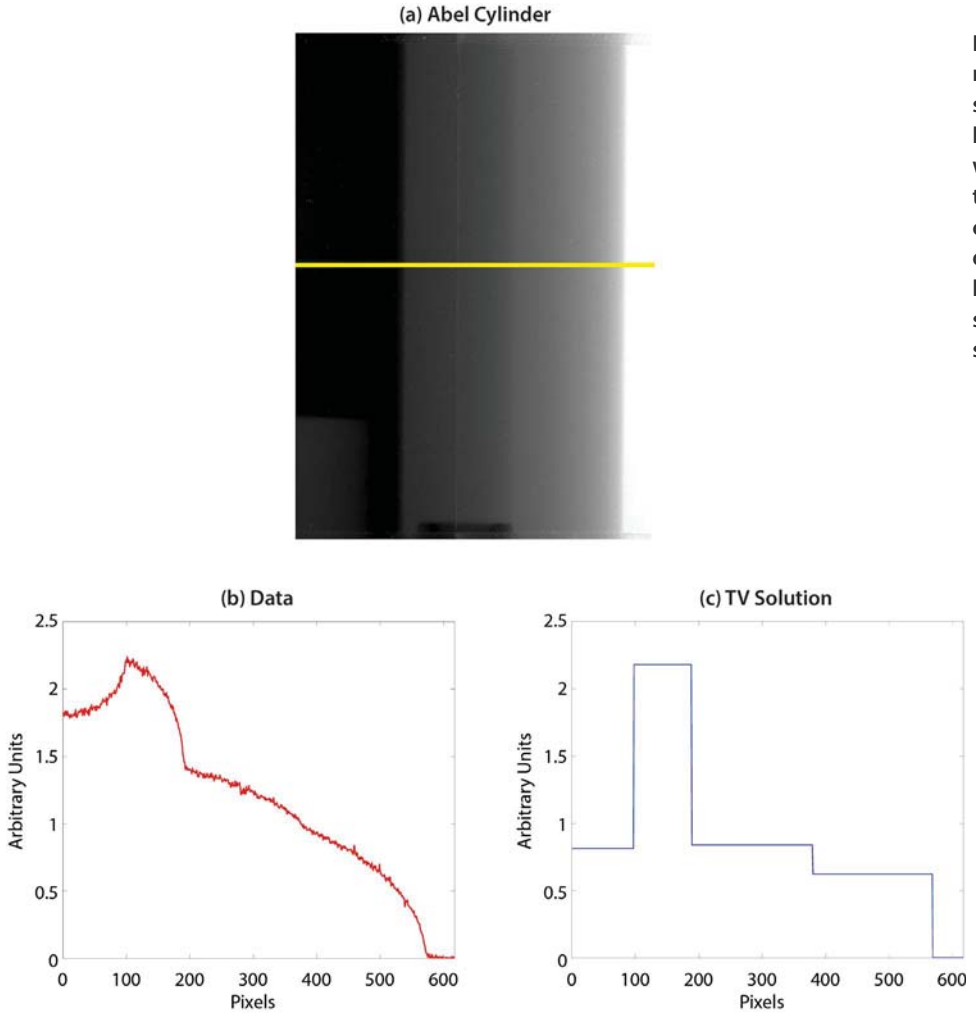

Figure 4. (a) An x-ray radiograph of a cylindrically symmetric object with a horizontal cross section, where the axis of symmetry of the object is the left boundary of the image; (b) the areal density computed from the highlighted horizontal cross section; and (c) the least squares–TV solution

Figure 6 shows the sampling results for a fully 2-D reconstruction of a subset of the image shown in Figure 4. The values of the standard deviation vary across the image from 0.002 to 0.004, with the relative standard deviation being about 1% of the computed value. In this case we do not plot the histogram for the distribution on λ, but the estimate is $\lambda = 2.66 \times 10^5 \pm 0.04 \times 10^5$. The standard deviation being less than 1.5% of the mean of the samples indicates that the desired value of λ has been correctly computed.

Reconstructing the Spot Shape and Size for a Pulsed Power X-Ray Source

In order to fully understand the blurring mechanism of any x-ray imaging system, it is important to be able to quantify the spatial distribution of the radiation source (often called "spot reconstruction"). A common technique is to radiograph an object with a square aperture larger than the source size and to analyze the penumbra in the image caused by the object's edge. Typically, we use an object known as an L rolled edge (LRE), which has a square aperture with a beveled surface to limit x-ray scattering through the object. Given a finite size source $x(r,s)$, a model for the exposure $A(x)(t,y)$ collected at the detector plane when imaging an LRE is given by

$$A(x)(t,y) = k \int_{t'}^{t''} \int_{y'}^{y''} x(r,s)\, dr\, ds, \qquad (16)$$

where t' and y' are given by

$$t' = t_c(1 + 1/m) - t/m \qquad (17)$$

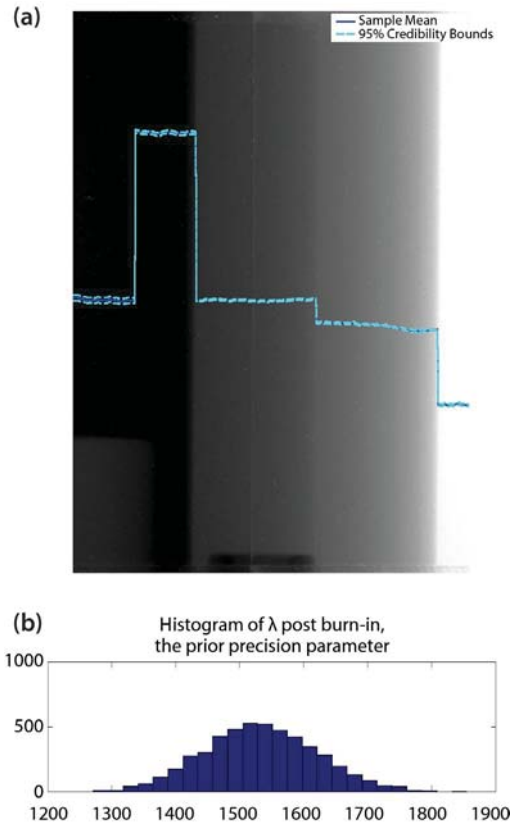

Figure 5. (a) The mean of the computed samples overlaid on the original image with the 95% credibility bounds and (b) the histogram of the samples of the precision parameter λ

and

$$y' = y_c(1 + 1/m) - y/m, \qquad \textbf{(18)}$$

where m is the magnification, and (t_c,y_c) are coordinates for a corner of the aperture (Barnea 1994). The magnification can be computed as $m = l_d/l_s$, where l_s and l_d are the distances from the aperture to the source and from the aperture to the detector, respectively. This model allows for spot reconstruction using the methods discussed in the previous sections.

Figure 7b shows a synthetically generated radiograph of an LRE generated from the radiation source distribution shown in Figure 7a. In practice, the source x

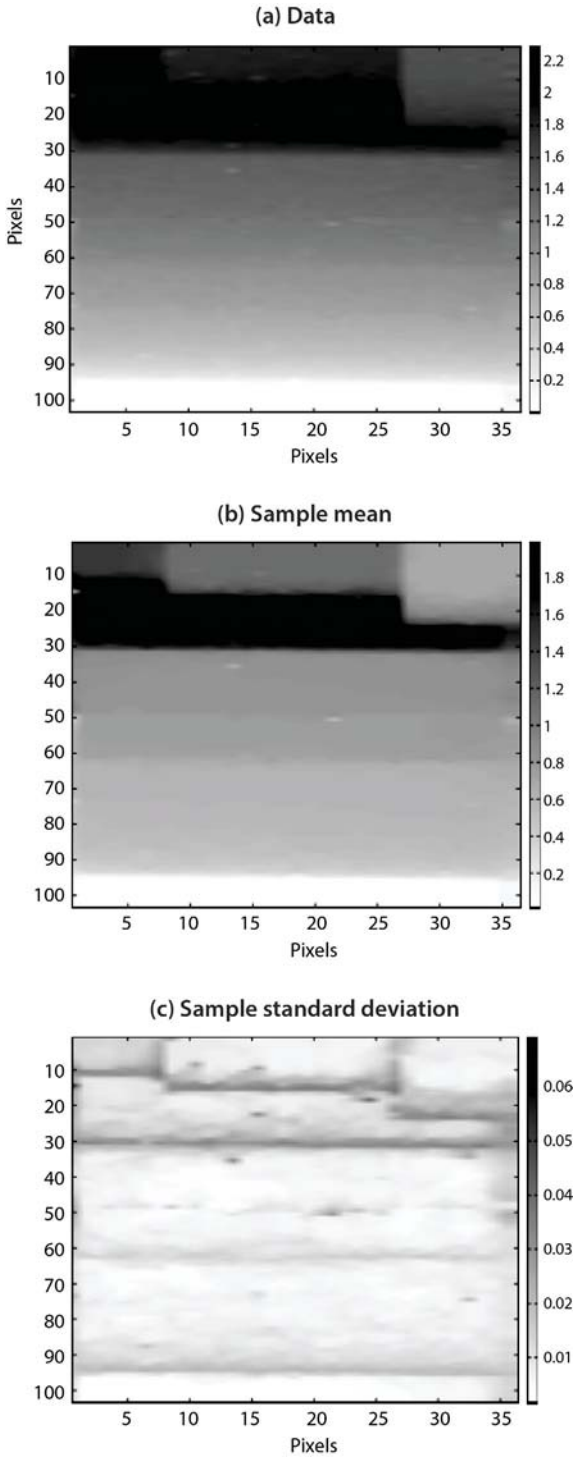

Figure 6. (a) A section of the image shown in Figure 4 (rotated), (b) the mean of the computed samples, and (c) the pointwise standard deviation of the samples. The color bars, in arbitrary units, show relative values.

(Figure 7a) is the unknown and must be reconstructed from the radiograph (Figure 7b). Using the least squares likelihood, the reconstructed spot is given by

$$x = \underset{u}{\operatorname{argmin}} \int_\Omega |Au - b|^2 \, d\Omega + \lambda \int_\Omega |\nabla u|^2 \, d\Omega, \tag{19}$$

where again λ is the regularization parameter. This regularization is called H^1-regularization, which enforces a smoothness prior. The prior density of u in this case uses the diffusion operator

$$L = D_x^T D_x + D_y^T D_y \tag{20}$$

instead of the TV formulation for L, in order to sample smooth solutions.

Figure 8 shows the results of sampling from the simulated radiograph in Figure 7b. The mean of the spot reconstructions is shown in Figure 8a; Figure 8b shows the pointwise standard deviation of the samples; and Figure 8c shows histograms of both precision parameters and the resulting regularization parameter. The mean sample (Figure 8a) provides an excellent reconstruction of the true spot that generated the radiograph, and the true spot falls within the uncertainty bands.

To further validate these methods, we include an example generated by the radiation transport code MCNP, which was developed at LANL (Briesmeister 2000). This code has been well vetted through widespread use and is a standard modeling tool for radiation transport. In this example, MCNP was used to simulate an LRE radiograph generated with a uniform spot with a radius 2.5 mm. Because the spot is uniform, we seek the solution x_{LTV} to the TV-regularized functional with least squares data fidelity given by

$$x_{LTV} = \underset{u}{\operatorname{argmin}} \int_\Omega |Au - b|^2 \, d\Omega + \lambda \int_\Omega |\nabla u| \, d\Omega. \tag{21}$$

Using the solution x_{LTV}, we compute the TV formulation for the precision matrix L and sample accordingly. Figure 9a corresponds to the radiograph created with MCNP, Figure 9b is the mean of the computed samples, and Figure 9c is the pointwise standard deviation. Using the source magnification from the experiment, we know that the pixel width at the source is approximately 0.54 mm and the mean reconstructed spot has a 2.43 mm radius. The relative standard deviation varies from 0 to approximately 3.5 and is about 4.3% near the reconstructed spot. The histograms for the regularization parameter are not shown, but the estimate is $\lambda = 5.65 \times 10^{-4} \pm 1 \times 10^{-6}$.

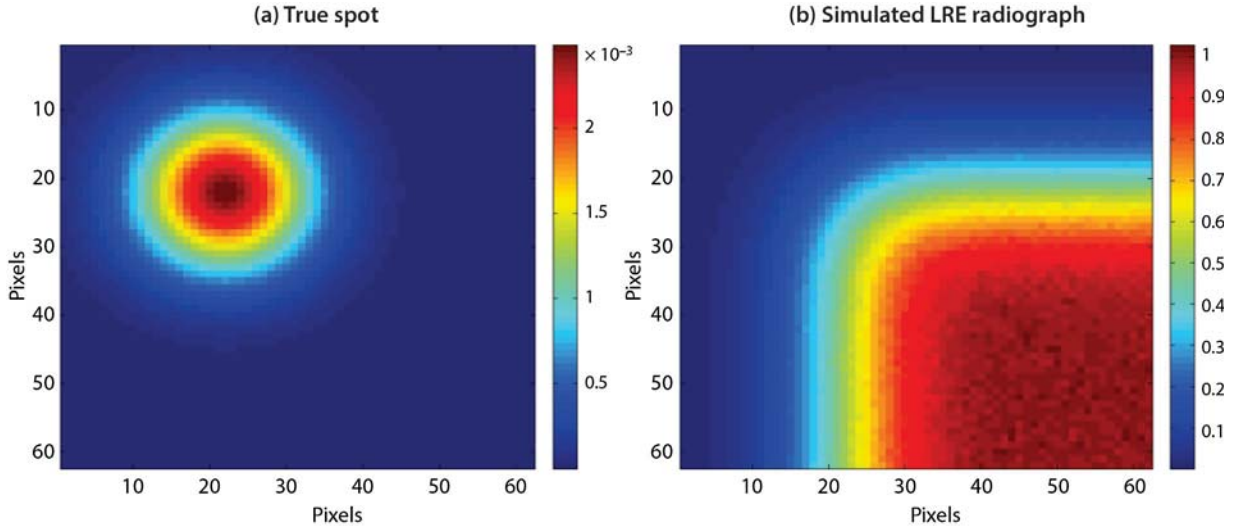

Figure 7. (a) A synthetically generated radiation source profile and (b) a simulated radiograph of an LRE

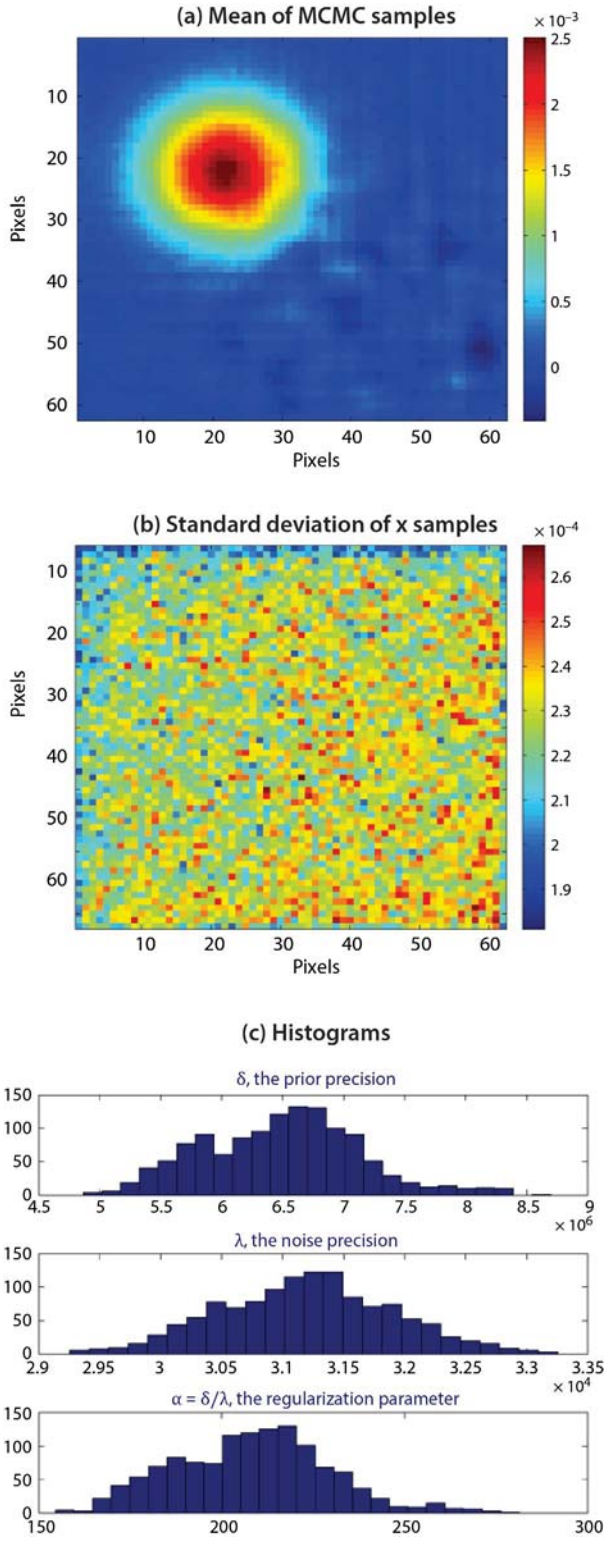

Figure 8. (a) The mean of the computed samples, (b) the pointwise standard deviation of the samples (the color bars show arbitrary intensity units), and (c) histograms of the precisions δ and λ and the regularization parameter α = δ/λ

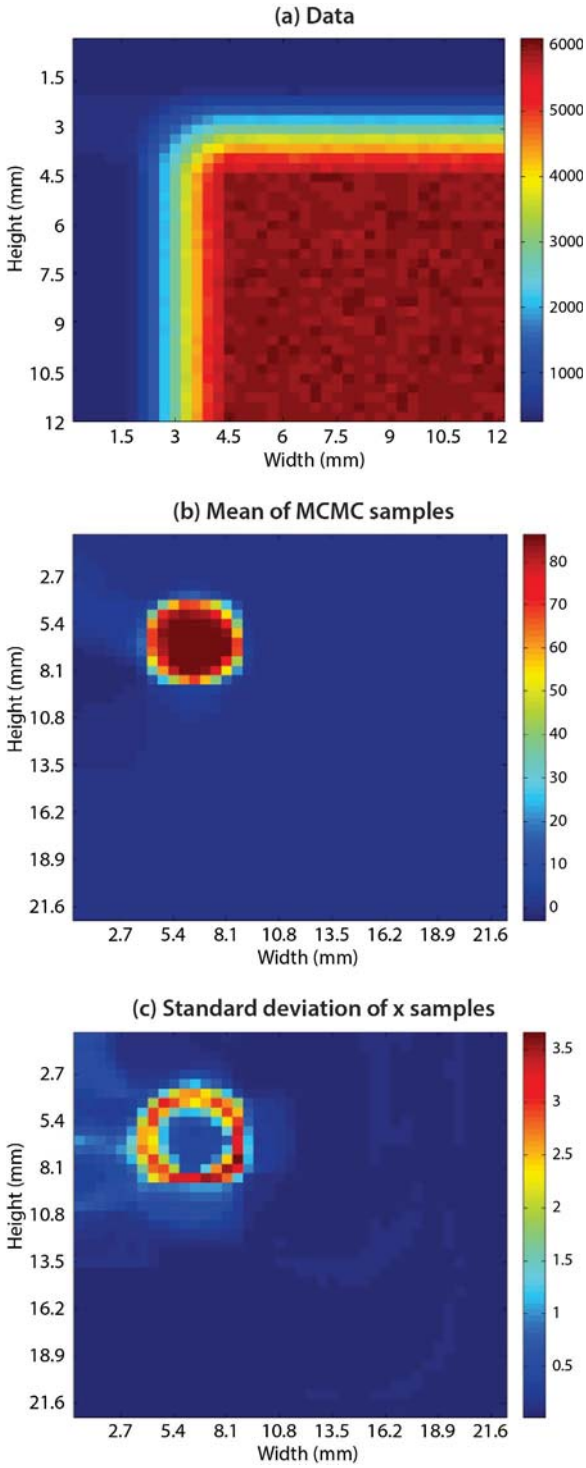

Figure 9. (a) A simulated radiograph created with MCNP, (b) the mean of the computed samples, and (c) the pointwise standard deviation of the samples (color bars show intensity in arbitrary units)

Conclusion

In security science–driven quantitative radiography, it is essential to be able to assign meaningful uncertainties to quantities computed via image processing algorithms. In this work we have presented sampling schemes for linear inverse problems that reconstruct the data—capturing the features of interest—and give estimates of the errors in the reconstruction. One scheme is designed around using a total variation regularized solution as the precision matrix for a Gaussian prior, and the second scheme extends that by also sampling the precision matrix itself. These schemes result in uncertainty estimates on the computed solution as well as on the assumed prior. This is a significant advance in radiography image processing, and the results shown from example x-ray radiographs demonstrate the success of the approach for deconvolution, Abel inversion, and the reconstruction of an x-ray source spot.

Acknowledgments

The authors would like to thank Todd Haines (LANL), Timothy Webb (Sandia National Laboratories), Stephen Lutz (Keystone), and Russell Howe (NSTec) for their helpful comments and suggestions on the project.

References

Asaki, T. J., R. Chartrand, K. R. Vixie, B. Wohlberg, "Abel inversion using total-variation regularization," *Inverse Problems* **21** (2005) 1895–1903.

Asaki, T. J., P. R. Campbell, R. Chartrand, C. E. Powell, K. R. Vixie, B. E. Wohlberg, "Abel inversion using total variation regularization: Applications," *Inverse Problems in Science and Engineering* **14**, 8 (2006) 873–885.

Bardsley, J. M., A. Luttman, "Total variation-penalized Poisson likelihood estimation for ill-posed problems," *Adv. Comp. Math.* **31** (2009) 35–59.

Bardsley, J. M., "Gaussian Markov random field priors for inverse problems," *Inverse Problems and Imaging* **7**, 2 (2013) 397–416.

Barnea, G., "Penumbral imaging made easy," *Rev. Sci. Instrum.* **65**, 6 (1994) 1949–1953.

Bernardo, J. M., A. F. M. Smith, *Bayesian Theory*, John Wiley & Sons, New York, 1994, 13–15.

Bracewell, R. N., *The Fourier Transform and Its Applications*, 2nd edition, McGraw-Hill College, Blacklick, Ohio, 1978, 250–275.

Briesmeister, J. F., "MCNP-A General Monte Carlo N-Particle Transport Code, Version 4C," LA-13709-M, Los Alamos National Laboratory, Los Alamos, New Mexico, 2000.

Clarke, A., et al., "Proton radiography peers into metal solidification," *Sci. Rep.* **3**, 2020 (2013) 1–6.

DeGroot, M. H., *Optimal Statistical Decision*, McGraw-Hill, New York, 1970, 327–334.

Gamerman, D., *Markov Chain Monte Carlo: Stochastic Simulation for Bayesian Reference*, Chapman and Hall/CRC, London, 1997, 119–155.

Gelman, A., J. B. Carlin, H. S. Stern, D. B. Rubin, *Bayesian Data Analysis*, 2nd edition, Chapman and Hall/CRC, London, 2004, 78–80.

Hansen, P. C., J. G. Nagy, D. P. O'Leary, *Deblurring Images: Matrices, Spectra, and Filtering*, SIAM, Philadelphia, 2006, 71–86.

Howard, M., A. Luttman, M. Fowler, "Sampling-based uncertainty quantification in deconvolution of x-ray radiographs," National Security Technologies, LLC, Las Vegas, Nevada, 2013.

Smith, J., et al., "Cygnus dual beam radiography source," *Proc. IEEE Pulsed Power Conf.* (2005) 334–337.

Smith, J., D. Nelson, E. Ormond, I. Molina, G. Corrow, M. Hansen, D. Henderson, S. Lutz, C. Mitton, "Cygnus performance in subcritical experiments," *Proc. 16th IEEE International Pulsed Power Conf.* **2** (2007) 1089–1094.

Vogel, C. R., *Computational Methods for Inverse Problems*, SIAM, Frontiers in Applied Mathematics, Philadelphia, 2002, 129–142.

Ziock, H.-J., et al., "The proton radiography concept," LA-UR-98-1368, Los Alamos National Laboratory, Los Alamos, New Mexico, 1998.

MPDV and Large Data Set Statistics

NLV-01-13 | Continued from FY 2012 | Continuing in FY 2014 | Year 2 of 2

Eric Machorro,[1,a] Aaron Luttman,[a] Jerome Blair,[b] Nathan Sipe,[a] and Michael Peña[a]

Photonic Doppler velocimetry (PDV) is a technique for indirectly measuring the velocity of a surface moving at very high speeds; in PDV, laser light is reflected off the surface and an oscilloscope measures the beat frequency of the Doppler-shifted light against the original light. There are established methods for computing surface velocity and position from the voltages measured by the oscilloscope, but recent research has focused on methods for estimating the uncertainties in the calculated result. We have established a three-phase approach to developing methods for quantifying uncertainties in PDV: (1) development and theoretical analysis of statistical methods for computing surface velocities and positions from voltage measurements, (2) design and fielding of laboratory experiments to benchmark PDV against high-speed video, and (3) computational analysis and interpretation of experimental results. The work presented here spans the end of the first phase through the beginning of the third phase, with the description of a mathematical formulation for estimating the bias and random errors in velocity calculations, continuing with the description of two controlled laboratory experiments that were fielded with PDV and high-speed imagery, and concluding with preliminary analysis of some experimental data. The results show that the experiments were well designed for analyzing the techniques used in PDV analysis, and the collected data show that our newly developed methods perform as well as the classical techniques, yet provide error bars and avoid the classic problems associated with picking the "right" analysis window. Subsequent planned experiments will show that these new methods will outperform the classic approaches.

[1] machorea@nv.doe.gov, 702-295-5352
[a] North Las Vegas; [b] Keystone International, Inc.

Background

Photonic Doppler velocimetry (PDV) is an interferometer that measures the velocity of surfaces moving at high speeds (Strand 2006), and it has become one of the most important diagnostic tools in shock physics experimentation (Holtkamp 2006), including in the nation's subcritical nuclear experimentation program. Fundamentally, a laser beam shines on a surface, and both the original laser light and the Doppler-shifted reflected light are combined. The associated beat frequency is measured on a digital oscilloscope, and the voltage data are then used to determine the surface velocity and position. The basic mathematical model is that the surface velocity at a given time is proportional to the dominant frequency in the signal near that time instance, so the most common approach to determining surface velocity at a given time is to compute the short-time Fourier transform of the signal, using a window of a chosen length centered at that point in time (Ao 2010). Additional description and background can be found in Machorro (2013).

Project

Given the importance of PDV measurements and associated calculations to large-scale experiments, it is essential that all computations have meaningful, mathematically rigorous, and statistically justified error bars associated with them. To that end, we developed two new techniques for computing surface velocity: statistics-based spline fitting (SBSF) and local polynomial approximation (LPA). The algorithmic details of both methods are described below; LPA also required the development of an entirely new mathematical theory to support it. The details of this mathematical theory, generalizing a previous result called the Peano kernel theorem (PKT) (Peano 1913, Sard 1963), are also documented below. Given the new algorithms, it was necessary to design controlled experiments in which PDV could be fielded and compared to other diagnostics, and the results of two such experiments, one involving a magnetically driven oscillating beam and one showing the deformation of impacted steel plates, are presented below.

Statistics-Based Spline Fitting and Local Polynomial Approximation

SBSF and LPA, though quite different, share some common features. In both, the measured signal as a function of time and a region of interest (ROI) are determined by the user. Both provide an approximation of the phase and amplitude of the signal defined by the ROI as a function of time using the same algorithm. This algorithm uses a complex spectrogram (CSGM) as opposed to the real-valued spectrogram used by other algorithms for analyzing PDV data (see Figure 4). This CSGM is calculated for every data point in the original data. The phase produced by this algorithm is quite noisy, because the amount of filtering done is the minimum necessary to get reliable results. Both methods use the same algorithm based on a noise model for the oscilloscope, obtained from the user-defined noise ROI on the spectrogram, for producing a noise model for the phase φ_k. This phase noise model depends on the estimated amplitude A_k of the signal (which changes with time) and on the oscilloscope complex white-noise estimate η_k. The model uses a low-noise approximation, which is valid for a signal-to-noise ratio (SNR) of 4 or more, and is given as

$$data_k \approx \varphi_k + \eta_k / A_k , \quad (1)$$

where k = 1…N corresponding to times $\left\{t_{k_o+k}\right\}_{k=1}^{N}$, and where $\varphi(t_k) = \varphi_k$ represents the discrete measurement of the phase over time. When the SNR is less than this, there is another term in the phase noise model that has very different statistical properties (Machorro 2011). This corresponds to when the term η_k/A_k in Equation 1 jumps a factor of 2π. This is not yet incorporated into any analysis programs.

The LPA Method

For each time, t, for which an output value is desired, a polynomial is fit to the phase estimate in an interval of length T_{fit} surrounding t. The displacement (velocity) at t is obtained by multiplying the value (derivative) of the polynomial at t by the wavelength divided by π. The fit is a weighted least-squares fit with the weight maximum at the center of the interval and going to zero at the ends. This weighting is multiplied by the inverse of the estimated variance of the phase at each point. The degree of the polynomial is fixed at 2 for displacement and 3 for velocity. Varying the value of T_{fit} varies the amount of smoothing performed on the data, with larger values of T_{fit} yielding more smoothing.

There are two types of errors associated with the smoothing method. First, there is the random error. The random errors in the phase estimate propagate through the smoothing to yield a random error in the computed displacement or velocity value. The standard deviation of this error decreases as T_{fit} increases. The other type of error is the bias. This is the error resulting from the fact that the true phase is not exactly a polynomial in the interval over which the fit is done. This error increases as T_{fit} increases. The combined error from the two sources is a minimum when the two error magnitudes are approximately equal.

An estimate of the magnitude of each of these errors is made and used to produce error bars and to find an optimum value for T_{fit}. The calculation of the random component of the error is a standard statistical calculation. The estimate of the bias error is based on the PKT, which yields

$$e_b[\phi] = \int_{-T_{fit}/2}^{T_{fit}/2} K(t,\tau)\phi^{(n)}(\tau)d\tau, \quad \textbf{(2)}$$

where ϕ is the phase shift, n = 2 for displacement and 3 for velocity, and K is the Peano kernel. In practice, ϕ is only known approximately, so we only estimate the upper bound on the bias error given by

$$|e_b| \le E_b = \int_{-T_{fit}/2}^{T_{fit}/2} |K(t,\tau)|\,|\phi^{(n)}(\tau)|d\tau. \quad \textbf{(3)}$$

The function $K(t,\tau)$ is evaluated for all relevant values of t and τ by methods developed at National Security Technologies, LLC (NSTec).

A difficult part of this approach is estimating the 2nd or 3rd derivative of ϕ using only the data. The estimate of ϕ is noisy, and the noise has a very large influence on the estimation of derivatives. A goal of this year's work was to solve this problem—to produce an algorithm that resulted in an n^{th} derivative estimate that is usable in this formula. The algorithm developed involves fitting n^{th} degree polynomials (which have constant n^{th} derivatives) to many intervals within the data domain and piecing together the results to get an upper bound for the absolute value of the n^{th} derivative at each point. For smaller interval lengths the noise has a much larger influence than the signal, so for each interval a statistical test is made to determine if the resulting n^{th} derivative estimate is likely due to noise. If it is, the n^{th} derivative estimate for that interval is not used.

This algorithm developed for n^{th} derivative estimation has had good success but is not yet ready for routine use in PDV analysis. It works very well for simulated data where the noise statistical properties are the same as those currently assumed in the PDV analysis. When used for experimental PDV data, it tends to greatly overestimate the n^{th} derivative. This is likely due to the neglected term in the current noise model. This problem was solved for the example data by setting a lower limit on the length of the interval used for the n^{th} derivative estimate. This lower limit was the smallest value for which the obtained estimate was of the same magnitude as an estimate obtained from the spline fit.

The SBSF Method

The SBSF method uses the same data and error model as LPA, but it produces varying smoothing as a function of time using a different mechanism. It performs a global weighted-least-squares fit to the phase data by a cubic spline function. A cubic spline function has knots $\{T_k : T_k<T_{k+1}\}$, which are time points between which the function is a cubic polynomial and at which it has two continuous derivatives. The third derivative has jumps at the knots. The amount of smoothing performed near time t is controlled by the quantity $\Delta(t)$, the length of the interval starting at the knot immediately before t and ending at the knot immediately after t. This plays the same role as $T_{\text{fit}}(t)$ does in the LPA method.

As in the LPA method, $\Delta(t)$ is adjusted to give a good trade-off between the random error and the bias. The random error is a somewhat straightforward statistical calculation. The estimation of the bias error uses a method developed at NSTec that has been previously published in reports and conference proceedings (Blair 2007).

Comparison of the Two Methods

Currently the computation time for the LPA method is 10 to 50 times longer than for the SBSF method. This is not inherent in the methods but results from the fact that the SBSF method has been in use for 8 years and has been optimized for efficiency on larger data sets. Both methods produce consistent results and error bars. The LPA method is much easier to analyze mathematically and the programming is more straightforward. Both methods produce random error estimates for PDV data that tend to be too small because of the

neglected term in the error model. Correctly incorporating the additional error term will be easier for the LPA method.

Generalizations of the Peano Kernel Theorem

One of the most important advances of the LPA method is how it distinguishes between the errors due to the random noise in the signal and the errors due to the fitting bias (i.e., because the signal is not locally exactly a polynomial). To compute the bias errors, a generalized form of the PKT, which was developed from a classical result in numerical quadrature (Peano 1913), is used. The idea is that if Q is a quadrature rule that exactly integrates polynomials of degree $n-1$ on a bounded interval $[a,b]$, then there exists a kernel K, depending only on T, such that

$$e(f) = Q(f) - \int_a^b f(t)dt = \int_a^b K(t) f^{(n)}(t)dt. \qquad (4)$$

In our most recent work, we have generalized the PKT from the class of linear functionals on $C^n([a,b])$ to the class of Laplace transformable tempered distributions of exponential decay. In particular, it is not necessary that the functionals being approximated have compact support. The generalized result is proven using an approach that provides a formula for computing K in the Fourier domain, which can be more computationally tractable and efficient in many cases. In the case of PDV analysis, the interval $[a,b]$ corresponds to the fitting interval $[-T_{\text{fit}}/2, T_{\text{fit}}/2]$ discussed earlier, and $K^{(n)}$ is the error kernel for the bias error.

Vibrating Beam Experiment—Comparing PDV to High-Speed Video

Another important component of analyzing methods for extracting velocities from PDV measurements is to compare calculations from PDV measurements to those of other diagnostics. Work has been done comparing PDV to VISAR (Dolan 2010), but there have been few experiments comparing PDV to high-speed imagery for basic error analysis. We designed an experiment as a proof-of-principle exercise, comparing PDV velocity and position calculations with the Interpolated FFT (IpFFT) method to velocity and position calculations from high-speed video.

Experimental Setup

The block diagram of the experimental setup is shown in Figure 1. A length of packing band was fixed at each end and held under tension using optical mounting hardware and a ratchet, and linear driver optical plates were used to adjust the band tension. At ¼ of the length on either side of the midpoint, DC electromagnets were placed below the band. Directly above and centered to each of the electromagnets, two disc neodymium magnets, 0.25 inches in diameter, were placed above and below so that the band was between the magnets. The leads of each electromagnet were connected in parallel to the output of a stereo receiver, and a Stanford Frequency (function) Generator was used as the input signal for the stereo receiver. The frequency output was adjusted until maximum displacement at the highest frequency was achieved.

To measure the beam surface velocity, PDV probes were placed in a holder directly above a section of the packing band (see Figure 2a). Two Phantom V711 cameras captured the high-speed video data. A single line of sight was used through a combination of beam splitters so the illumination source and both cameras would be as coincident along that line of sight without obstruction due to any one of the three. This made possible the elimination of shadows on the background, enhancing the contrast of the band.

The band was oscillated by adjusting the frequency of the Stanford Frequency Generator output and adjusting the power using the stereo receiver. A third electromagnet was placed over one of the neodymium magnet pairs to act as a pickup in order to measure the oscillation frequency. The goal was to find the highest frequency of oscillation with maximum displacement. The trigger output of the camera, frame rate, band pickup signal, and multiplexed PDV (MPDV) oscilloscope signals were all recorded onto one oscilloscope for diagnostic and timing purposes.

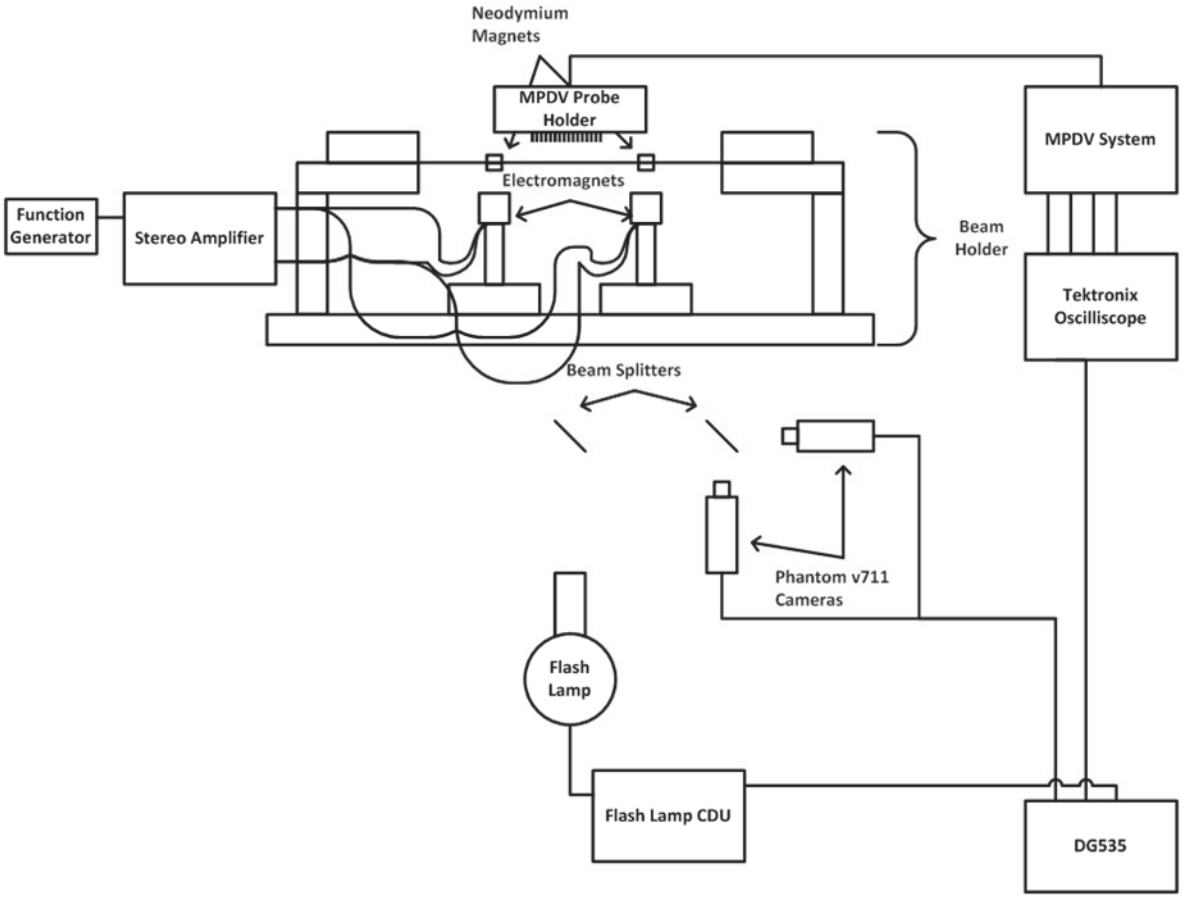

Figure 1. Block diagram for vibrating beam oscillator

Experimental Results

As can be seen in Figure 2b, the PDV probes look down on the band, each at its own angle. In order to account for this, the band is covered by an auto-reflective tape, which reflects all incident light from the probe directly back to the probe regardless of the angle of the probe to the surface of the band relative to normal. Figures 2c and 2d show the computed band position using the video (red) and the PDV (green). The PDV velocities were computed using the IpFFT method, and the displacements were computed by integrating the velocity curves. These calculated displacements include only the motion component along each probe axis and neglect any lateral motion. The camera positions were computed by extracting the image data along the pointing lines of the PDV probes (as shown in Figure 2b) and calculating the point of maximum absolute gradient. This corresponds to the top of the oscillating beam. This is done for each frame in the video sequence, giving a time series of beam positions. The time series is then smoothed using a Gaussian filter.

Figure 3 shows the time traces for Probes 1, 2, 8, and 9, with the displacements computed from the camera data at the location of the PDV probe in blue and the positions calculated from the PDV in green. As can be seen, the frequencies of oscillation for the PDV and camera results are very close, but the amplitudes differ significantly, sometimes by as much as 100%. The linear size of a pixel in mm at the object plane was calibrated to 0.1832 mm, and both the PDV and the camera data were normalized to have a mean displacement of 0 mm.

One of the most important quantities of interest is the maximum displacement of the beam, and Table 1

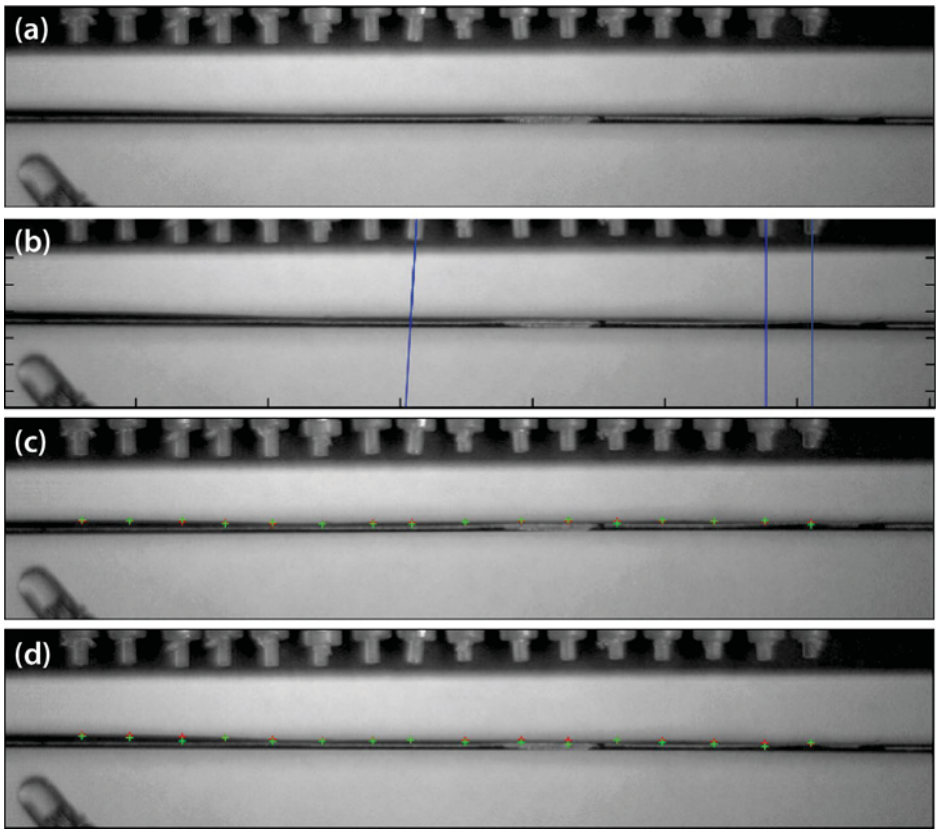

Figure 2. (a) An image from the video sequence, showing the PDV probes pointing down on the beam; (b) blue lines showing pointing vectors of PDV Probes 1, 2, and 9 (right to left); (c) image 1000 in the video sequence, at 16.7 ms, with camera (red) and PDV (green) position estimates overlaid; and (d) image 5000 in the video sequence, at 83.3 ms, with camera (red) and PDV (green) position estimates overlaid

Table 1. The maximum beam displacement in mm, as computed from the camera data and the PDV data, as well as the percent difference

Probe	Camera (mm)	PDV (mm)	Relative Difference (%)
1	1.649	2.2	33.43
2	1.72	2.378	38.24
3	1.63	2.001	22.73
4	1.478	1.880	27.18
5	1.451	1.996	37.59
6	1.429	2.161	51.27
7	1.353	1.882	39.07
8	1.267	1.601	26.29
9	1.251	1.700	35.86
10	1.248	1.297	3.89
11	1.076	1.236	14.88
12	1.032	1.497	45.05
13	0.908	1.613	77.67
14	0.916	1.753	91.42
15	0.777	1.406	81.02
16	0.782	1.109	41.80

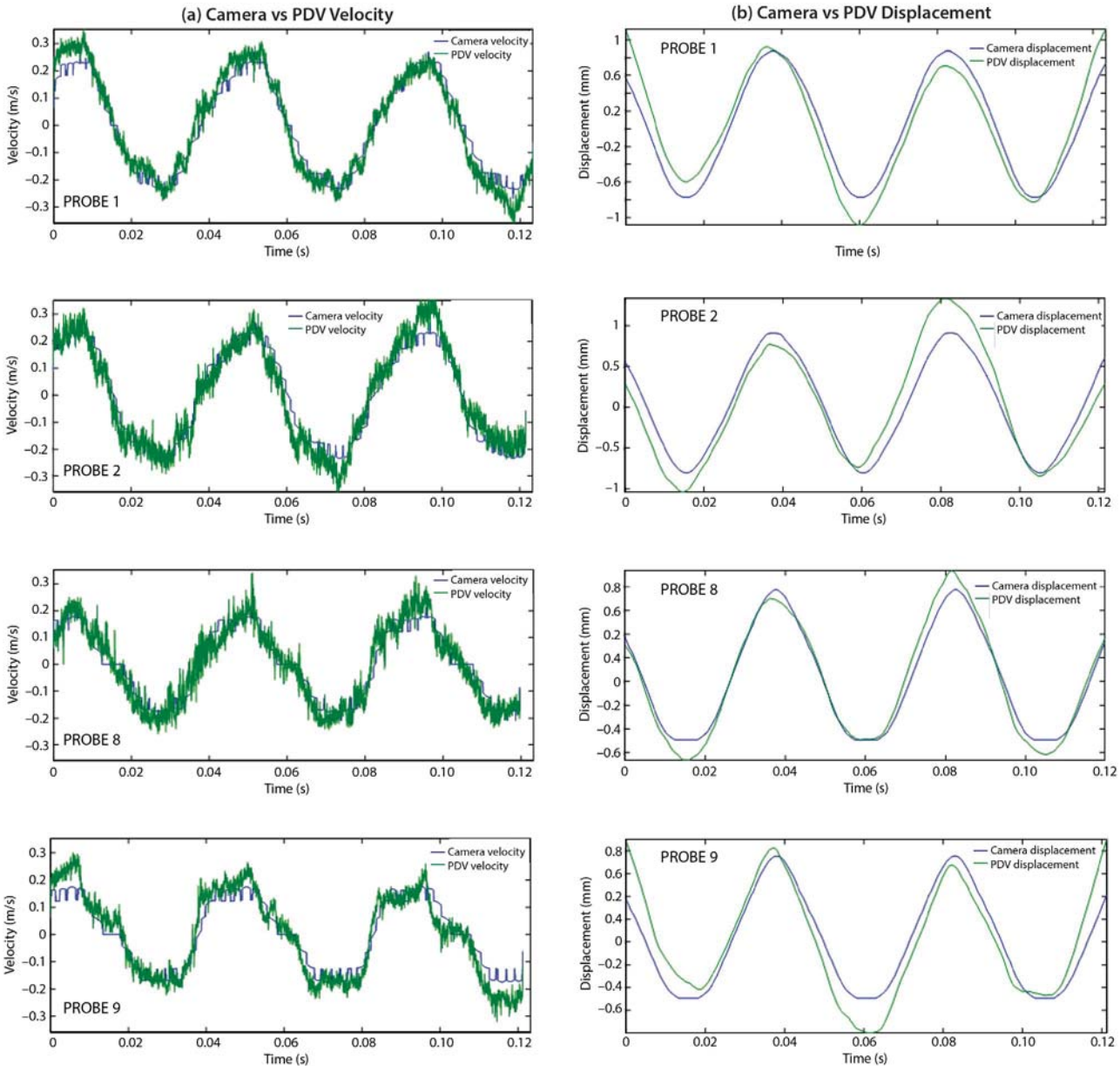

Figure 3. (a) Camera and PDV velocity and (b) displacement estimates over time for Probes 1, 2, 8, and 9 indicate that there are significant differences between the displacement computed from the video data versus computed from PDV data. The horizontal axis is time in seconds, and the vertical axes are velocity in m/s and displacement in mm.

shows the calculated maximum displacement from the camera and the PDV at the locations of each PDV probe. There are two important things to note from these data. First, there is a clear trend in lower displacement for higher-numbered probes. This is expected because the beam is being magnetically driven only from one side—near where Probe 1 is located—so the system energy is dissipated across the beam, causing the opposite side of the beam to oscillate with energy and therefore with less amplitude. Second, there are significant differences between the maximum displacement computed from the video data and that computed from the PDV data. There are two major possible reasons for this, and there are other potential issues with the data comparison: (1) the time sampling rate of the camera data is far less than the

sampling rate of the PDV measurements, and (2) the comparison depends on the ability to accurately locate the position in the camera data where a given PDV probe is actually pointing. This is clearly limited by the spatial resolution of the camera data, but it is also limited by the accuracy to which we can infer the pointing direction of the PDV lasers, which we can only do by analyzing the orientation of the probe and not by calculating deviations of the laser from that angle. The result is that the mean maximum displacement across the probes is 1.248 mm from the high-speed video and 1.731 mm from the PDV data.

The first experimental comparison of PDV and high-speed video shows that the two diagnostics can be compared systematically and that they are able to capture the same coarse-scale features. Nonetheless, in order for a more accurate comparison, it is necessary to increase the spatial and temporal resolutions of the video data and to compare in experiments where the measured velocities are higher than those seen here.

Two-Stage Gas Gun Experiments—Comparing PDV Methods to Each Other and to High-Speed Video

The results of the vibrating beam experiment showed that PDV can be compared to high-speed video, and the next step was to perform a test at much higher velocities than were possible for the vibrating beam. An excellent candidate for such a study was to analyze the velocity of the surface of a steel plate after impact by a high-velocity projectile. Such a plastic deformation study was already being performed by researchers from National Security Technologies, LLC, and the University of Nevada, Las Vegas (UNLV), and the data from that set of experiments was adapted for use in this study. See Becker (2014) for a complete description of the experimental setup and diagnostics details.

Our analysis in this case involved extracting PDV velocities using the IpFFT, SBSF, and LPA methods, extracting a position profile from the camera data, and simulating the plate deformation using the ALEGRA hydrodynamics code (Rider 2008). Each of the PDV methods start from the spectrogram of the data, which is shown in Figure 4. In this case, two probes were combined on a single oscilloscope channel, but for clarity only one of the two signals is shown. The high-speed video was captured at 220,000 frames per second with 302 µm pixels, and the location of the deforming surface was calculated by segmenting each video frame in order to determine the boundaries of a black region that developed behind the surface. This can be seen in Figure 5,

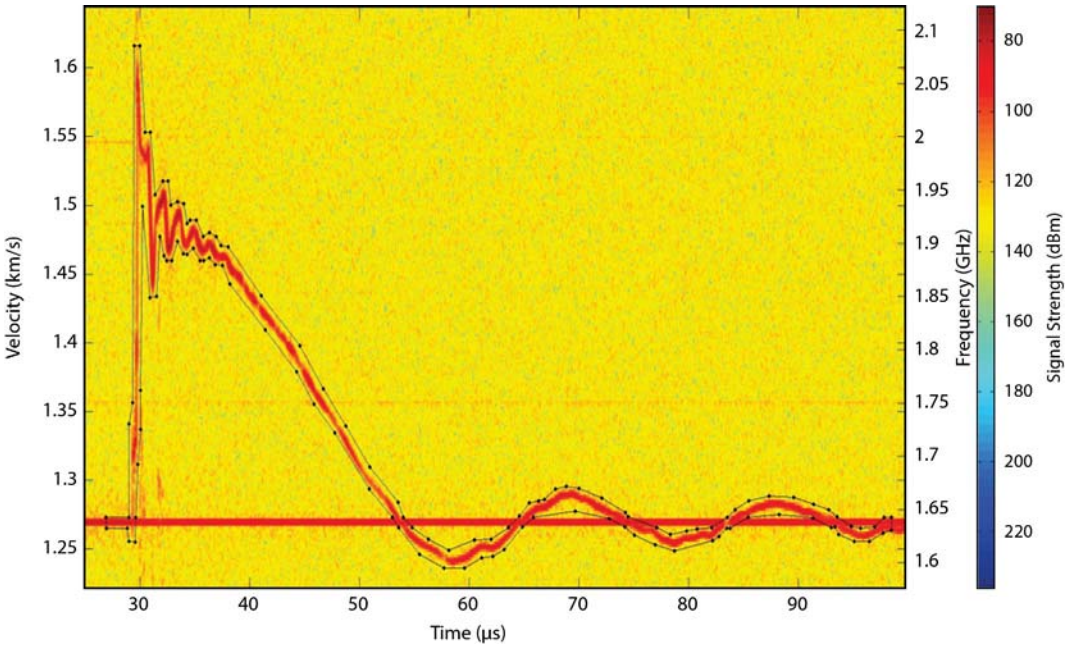

Figure 4. Real-valued spectrogram for Run 5 of the gas gun experiment. The black polygon delineates the region of interest (ROI) to be extracted. Vertical axis has units of velocity in km/s.

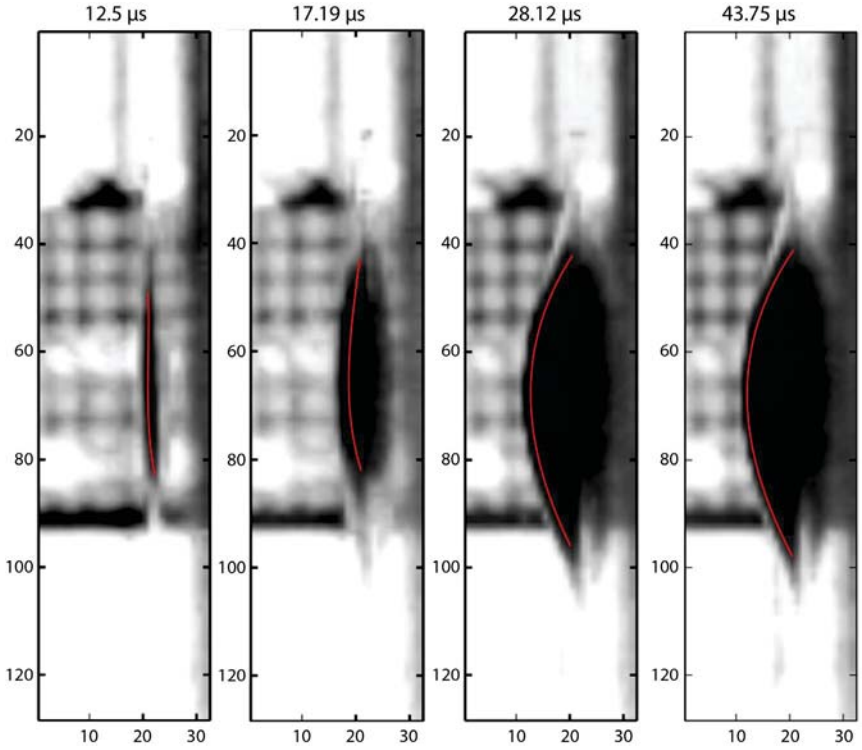

Figure 5. Impacted metal plate bulging out the back side at times 12.5, 17.19, 28.12, and 43.75 µs. The leading edge of the bulge, as extracted using the algorithms described here, is also shown (in red). Units are in image pixels.

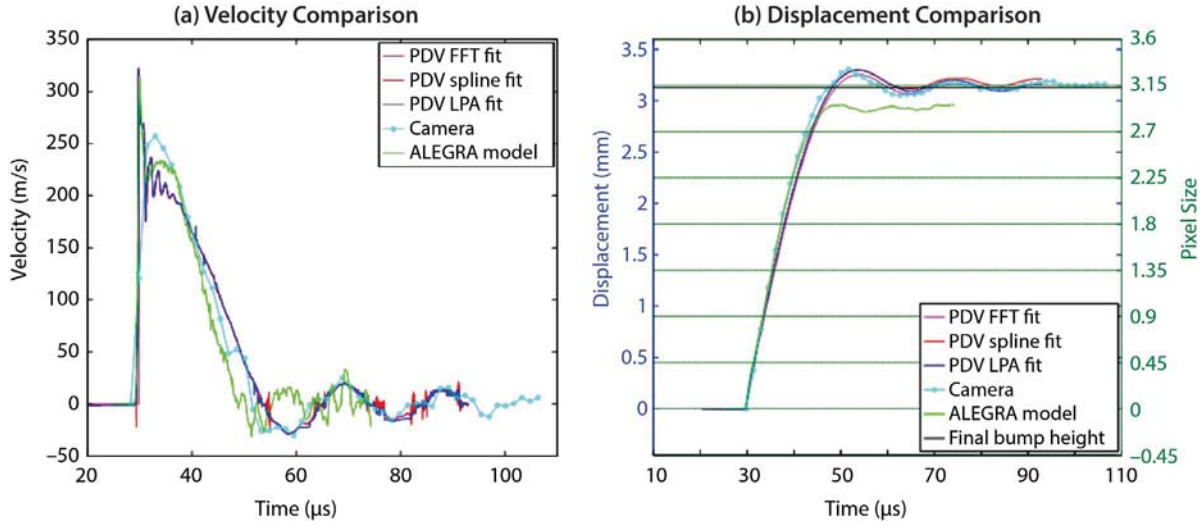

Figure 6. Comparison of PDV methods and high-speed video on Run 5 for (a) surface velocity and (b) displacement. The PDV FFT fit is based on the IpFFT described above, where we used a window length (duration) of 409.6 ns.

where four video frames are shown with the extracted surface, at times 12.5, 17.19, 28.12, and 43.75 µs. Given the pixels that formed the boundary of the black region behind the surface, the surface was computed by fitting a cubic polynomial to the boundary points normal to the surface to extract the surface position at sub-pixel accuracy. The camera velocity is computed by differentiating the position, and the PDV displacements were computed by integrating the velocity.

The computed velocities and displacements are shown in Figure 6a for all three PDV methods, the camera

Table 2. Velocities and displacements at times corresponding to important features in the PDV and camera traces. The peak velocity and displacement, and the corresponding times, as well as the times, velocities, and displacements corresponding to peaks in the "breathing" phase are included.

	Jump-Off Time (μs)	Max Velocity (m/s)	Time at Max (μs)	1st Low Velocity (m/s, breathing)	1st Low Velocity Time (μs, breathing)	1st High Velocity (m/s, breathing)	1st High Velocity Time (μs, breathing)	2nd Low Velocity (m/s, breathing)	2nd Low Velocity Time (μs, breathing)
SBSF	29.32	322.7	29.77	–29.11	58.43	19.77	69.30	–15.77	78.62
LPA	28.99	321.4	29.77	–28.81	58.49	19.89	69.43	–17.03	78.70
FFT	29.79	316.3	29.78	–29.28	58.48	19.72	69.36	–15.73	78.70
Camera	28.25	257.1	32.94	–30.62	59.5	25.27	68.88	–15.62	78.25
ALEGRA	29.98	314.6	29.84	–31.47	51.43	16.43	58.91	–21.72	62.29
	2nd High Velocity (m/s, breathing)	2nd High Velocity Time (μs, breathing)	Final Displacement (mm)	Max Displacement (mm)	Time at Max Displacement (μs)	1st Low Displacement (mm, breathing)	1st Low Displacement Time (μs, breathing)	2nd Low Displacement (mm, breathing)	2nd Low Displacement Time (μs, breathing)
SBSF	12.84	87.98	3.18	3.30	53.33	3.12	65.35	3.15	84.67
LPA	13.81	87.65	3.15	3.30	53.35	3.09	65.34	3.10	84.27
FFT	12.87	87.67	3.13	3.25	53.28	3.07	65.61	3.10	85.05
Camera	15.61	89.19	3.18	3.31	51.69	3.05	62.63	3.11	82.94
ALEGRA	33.17	74.30	2.93	2.96	73.74	2.89	55.39	2.91	66.27

data, and the ALEGRA simulation. The time sampling of the PDV is a factor of 367 greater than the sampling of the camera, so the camera is not able to accurately capture the initial highest velocity or the oscillations that occur immediately after the pull back from the peak velocity. Each of the computational methods for extracting velocity from the PDV data show nearly the same jump-off time and peak velocity, and they all capture the oscillations after the pull back. The ALEGRA simulation shows a jump-off time that is too early and a peak velocity that is too low, and it completely fails to capture the oscillations of the surface in the 30–40 μs time range. More generally, the ALEGRA simulation shows the same general features as the other reconstructions, but on a shorter timescale. In some sense the ALEGRA model predicts the dynamics will be faster than the data show.

The different PDV velocity extraction techniques show very similar behavior, except that the IpFFT method suggests an earlier jump-off time (Table 2) and the SBSF results are noisier than the others. One of the interesting features that we see in all of the data are the velocity local maxima around 70 and 90 μs and the corresponding local minima around 60 and 80 μs. The local minima are times of negative velocity, which show that the surface is actually retracting from its most displaced position, features that can also be seen in Figure 6b. This phenomenon is called "breathing." Along with the displacement time series for each PDV method, the camera data, and the ALEGRA simulation, the final displacement as physically measured by the machine shop on the metal plate is shown, just above 3 mm. Note that all of the PDV techniques and the camera data indicate a final displacement that is nearly equal to the measured value; only the ALEGRA simulation fails to capture the final displacement accurately.

This experiment shows that high-speed video can accurately capture all of the same dynamics that PDV analysis techniques can capture, as long as they are on time scales appropriate to the sampling rate of the video. It also shows that there are differences among the results computed from the different PDV analysis techniques. These differences form the basis of the third component of this project, which is the subject of our ongoing work.

Conclusion

Carefully calibrated and cross-timed data have been collected from the two very different experimental setups using MPDV and a high-speed camera: a vibrating plastic beam and two-stage gas gun. It became clear in analyzing the PDV data from these experiments that a previously investigated source of error, the capture error, will need to be modeled. This will be explored next fiscal year in the SDRD project "MPDV Data Analysis and Uncertainty Quantification (UQ) for Large-scale Data Sets" (NLV-15-14) and to a lesser degree in the project "Plastic Deformation Study Using Light Gas Gun" (NLV-14-14). This year the vast differences in speed and time scales for these two experimental setups have been very helpful in evaluating PDV techniques for estimating speed and providing error bars. Building on the collaborations with the UNLV gas gun, we expect to record even higher-fidelity data that will help assess PDV techniques for measuring displacement and 1-D reconstruction of the impact profile.

In addition to the several improvements to the SBSF technique developed in FY 2013 that made it practical in handling the large data sets associated with MPDV measurements, several fundamental mathematical and statistical results were finalized. The premier result is a generalization of the Peano Kernel Theorem. Although it is applied here to develop error bars for LPA and MPDV analysis, the result is a generalization to the fundamental underpinnings of both finite-elements simulations and adaptive mesh-refinement techniques that are used across the complex. The PKT is the seminal result in a class of theorems that says that if *any* quadrature, statistical, or finite-element technique is exact when applied to problems whose true solution is a polynomial of degree n–1 (as most are), then the error in the approximate solution is in proportion to the n^{th} derivative. A generalization to the

much more widely known, higher-dimensional extension known as the Bramble-Hilbert lemma is expected to be forthcoming next fiscal year.

Another statistical tool that was developed this year was the LPA variable-windowing algorithm. Although it is computationally quite expensive, it automatically picks the optimal window size for doing local-polynomial fitting where the optimal window size is the one that minimizes the sum of the square of the bias error and the random error. The applications to PDV analyses are quite clear: aside from error analyses, one of the main problems in PDV analysis is picking the best window length for FFT analyses. Heretofore, there has not been any tool available to do this in anything other than a manner that is ad hoc and based on best professional judgment. More generally, however, there are applications across the entire field of statistics and non-parametric regression that could benefit from this technique.

Acknowledgments

The authors would like to thank Marylesa Howard, Edward Daykin, Stephen Mitchell, Steven Gardner, C. Y. Tom, Rand Kelly, Brendan O'Toole (UNLV), Mohammed Trabia (UNLV), Steve Becker, Robert Hixson, Tim Meehan, and Kristen Crawford for helpful suggestions on the project and for helping to design and field the experiments.

References

Ao, T., D. Dolan, "SIRHEN: A data reduction program for photonic Doppler velocimetry measurements," SAND2010-3628, Sandia National Laboratories, Albuquerque, New Mexico, 2010.

Becker, S., et al., "Plastic deformation study using a light gas gun," Site-Directed Research and Development, FY 2013, National Security Technologies, LLC, Las Vegas, Nevada, 2014, [37–49].

Blair, J., "Error estimates derived from the data for least-squares spline fitting," *Proc. Inst. & Meas. Tech. Conf.*, Warsaw, Poland (2007) 1–6.

Dolan, D. H., "Accuracy and precision in photonic Doppler velocimetry," *Rev. Sci. Instrum.* **81**, 5 (2010) 053905.

Holtkamp, D. B., "Survey of optical velocimetry experiments – Applications of PDV, a heterodyne velocimeter," *Proc. 2006 Conf. Megagauss Magnetic Field Generation*, Santa Fe, New Mexico (2006) 119–128.

Machorro, E., J. Blair, "Phase error and the capture effect," Presentation, 6th Annual PDV Workshop, Livermore, California, November 3–4, 2011.

Machorro, E., J. Blair, A. Luttman, E. Daykin, "Uncertainty estimation techniques for high-density 1-D MPDV imaging diagnostic," *Site-Directed Research and Development*, FY 2012, National Security Technologies, LLC, Las Vegas, Nevada, 2013, 169–176.

Peano, G., "Resto delle formulae di quadrature espresso con un integrale definite," *Atti Reale Accademia dei Lincei, Rend.* **22** (1913) 562–569.

Rider, W. J., et al., "ALEGRA: An arbitrary Lagrangian-Eulerian multimaterial, multiphysics code," *Proc. 46th AIAA Aero. Sci. Meeting*, Reno, Nevada (2008) 1–39.

Sard, A., *Linear Approximation*, Mathematical Surveys No. 9, American Mathematical Society, S. Providence, Rhode Island, 1963, 451–453.

Strand, O. T., D. R. Goosman, C. Martinez, T. L. Whitworth, W. W. Kuhlow, "Compact system for high-speed velocimetry using heterodyne techniques," *Rev. Sci. Instrum.* **77**, 8 (2006) 083108.

Maximum Likelihood Estimation and Uncertainty Quantification for Signals with Poisson-Gaussian Mixed Noise

LO-03-13 | Continued in FY 2014 | Year 1 of 1

Michał Odyniec,[1,a] Aaron Luttman,[b] and Jerome Blair[b]

The goals of this project were to develop new algorithms (and refine existing ones) for analyzing signals modeled by Poisson-Gaussian mixed noise and to apply these algorithms to relevant NNSA applications, such as neutron time-of-flight analysis of data from the National Ignition Facility and special nuclear material detection. Ultimately, we found our research to be relevant to several more NNSA activities including advanced radiography analysis, radiance measurements, and time-of-flight studies for dense plasma focus experiments. Consequently, the project grew to meet the emerging opportunities to use it in other areas, with these applications dictating which parts of the algorithms and theory should be developed. During the first year of the project, we developed computational and statistical methods tailored to the Poisson-Gaussian mixed-noise environment to improve signature, signal, and image reconstructions from mixed-noise data. We also mathematically modeled the propagation of uncertainty through the mixed-noise reconstruction process. This work provided the first Poisson maximum likelihood estimation signal reconstruction algorithms for NSTec applications, and we believe it is the first to systematically perform uncertainty quantification.

[1] odyniem@nv.doe.gov, 925-960-2630
[a] Livermore Operations; [b] North Las Vegas

Background

Signal reconstruction from contaminated measurements is relevant to many NNSA applications, namely neutron time-of-flight (NToF) measurements at Lawrence Livermore National Laboratory (LLNL) and Sandia National Laboratories (SNL), radiance studies at the Special Technologies Laboratory (STL), and radiography at LLNL and the Nevada National Security Site. The processes that we are analyzing are of the counting kind and are therefore Poisson stochastic processes. Furthermore, during measurements, they all suffer from Gaussian instrumentation noise. Problems of that type are naturally modeled as

$$z = H \cdot Poiss(x(u)) + \mathrm{N}(0,\sigma^2), \quad (1)$$

where z denotes the measured data, and H is a linear (convolution) operator modeling the measurement system; at this stage we assumed the measurement system to be ideal. The mean of the Poisson process is the "true" signal $x(u)$ with unknown parameters u. Our aim was to investigate the "best" ways to recover these parameters.

We also considered an important special case that usually requires regularization, where the parameter dependence is linear:

$$z = Poiss(Au) + \mathrm{N}(0,\sigma^2). \quad (2)$$

Within National Security Technologies, LLC (NSTec), there are many projects that require this type of signal reconstruction. Our work provided the first Poisson maximum likelihood estimation (MLE) signal reconstruction algorithms for NSTec applications, and we

believe it is the first to systematically perform uncertainty quantification (UQ) through the reconstruction process.

Project

We developed computational and statistical methods tailored to the Poisson-Gaussian mixed-noise environment to improve signature, signal, and image reconstructions from mixed noise data. We also mathematically modeled the propagation of uncertainty through the mixed-noise reconstruction process.

Specifically, we developed the following:

a. A Poisson-based method for deconvolution with sampling (linearized Poisson) and edge enhancements, which included a new technique for boundary artifacts in inverse problems (Bardsley 2013)

b. Radon transform numerical reconstruction (Luttman 2013)

c. Explicit results for NToF measurements that provide insight into measurement setup (Odyniec 2013a, 2013b)

Deconvolution and Elimination of Boundary Artifacts

When measurements are dominated by Poisson noise, the most natural measure of error when reconstructing the signal is the Poisson likelihood

$$L_z(Au) := \int_\Omega \big(Au - z\log(Au)\big)d\Omega, \tag{3}$$

where it is assumed that both u and Au are strictly positive. In this case, solving Equation 2 reduces to solving the minimization problem

$$x = \underset{u}{\operatorname{argmin}} \int_\Omega Au - z\log(Au)\,d\Omega + \int_\Omega |\nabla u| d\Omega, \tag{4}$$

where the second term on the right is known as "total variation regularization" and enhances edges and corners in the signal. It was shown that this optimization is well-posed, having a unique solution for every weighting of the regularization (Bardsley 2009). The result was compared with the classical Tikhonov reconstruction, with a cost function of

$$x = \underset{u}{\operatorname{argmin}} \int_\Omega \big((Au - z)^2 + \alpha u^2\big)\,d\Omega. \tag{5}$$

Figure 1a shows Tikhonov reconstruction for a synthetically generated signal, and Figure 1b shows the new reconstruction. The original ("unknown") signal is shown in blue, the measured data in red dots, and the reconstructed signal in green. Our reconstruction removed oscillations in the noisy signal, sharpened the jumps (edges), and captured all signal scales.

We also developed a Markov Chain Monte Carlo (MCMC) sampling scheme with a data-driven approach to dealing with boundary artifacts in deconvolution problems. The approach retained computational efficiency by assuming a periodic boundary condition on the extended domain. The MCMC method sampled the unknown object x, as well as the noise precision, making regularization parameter selection unnecessary. Moreover, in the Poisson noise case, we extended our framework by using a Gaussian approximation of the negative-log Poisson likelihood. We illustrated the method by several synthetic examples and also by x-ray radiography; the sampling scheme worked well in all of them, and boundary artifacts were negligible in the associated reconstructions (Bardsley 2013).

NToF Reconstruction

Neutron tomography is a method for analyzing neutron creation events from detector data. Given a source emitting neutrons, one wishes to determine the neutron flux from the source as well as the energy (or velocity) spectrum of the neutrons being emitted. In controlled fusion, the temperature of the plasma is one of the most important properties for understanding the efficiency of the reaction and is proportional to the variance of the time-dependent energy distribution, which is also an important quantity to compute in its own right.

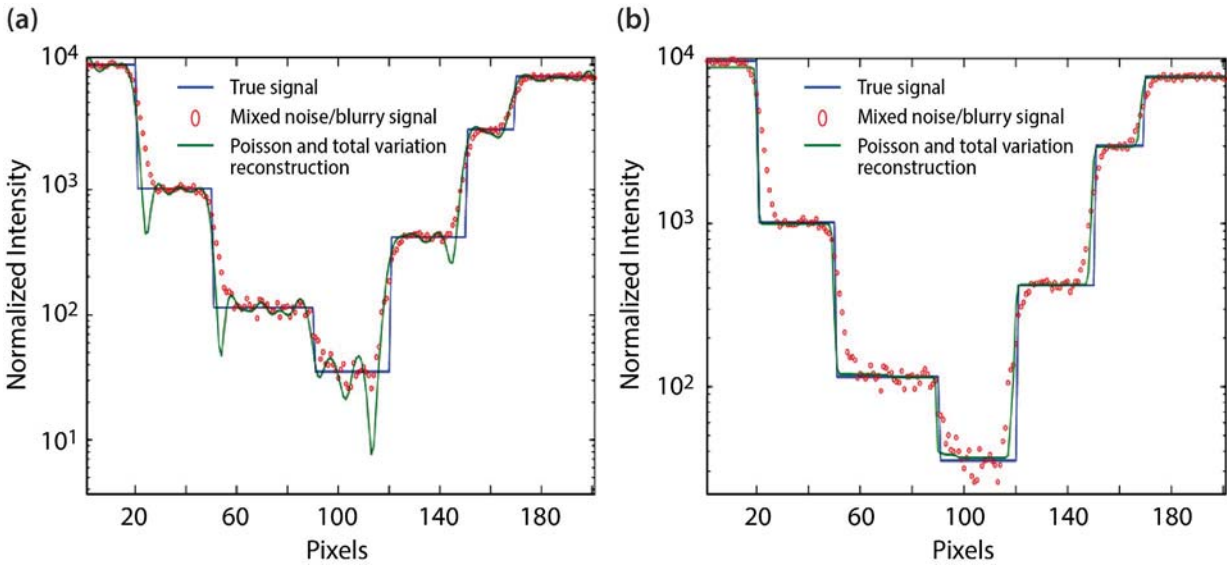

Figure 1. Comparison of a (a) classical Tikhonov reconstruction and (b) our signal reconstruction with new cost function that removed oscillations in the noisy signal, sharpened the jumps (edges), and captured all signal scales

Because neutrons of different energies travel at different speeds, time-of-flight principles allow us to reconstruct the velocity distribution. Assuming that all neutrons are created instantaneously, the detected signal used to reconstruct velocity profiles can also yield energy distribution information. In our approach we allowed for non-instantaneous neutron creation, and have added two important additional parameters: the center and spread and the time distribution for neutron creation. Reconstructing these parameters required multiple detectors placed at different distances from the source.

We devised a model for neutron creation based on physical principles (Lehner 1967, Brysk 1973) and, using the Radon transform, derived the corresponding model for the neutron detector signals (Luttman 2013). We also developed several explicit formulae that expressed variances of interest in terms of the measurement setup. These included explicit formulae for the ratio of mixed noise variances (Equation 7), for the variances of plasma temperature variance and of signal timing and width (Equations 8–10). To our knowledge this is the first time that reasonably general and explicit formulae for neutron creation have been developed (Odyniec 2013a, 2013b).

Our Model

If t is the time at which a particle is emitted, t' is the time at which the particle is detected, D is the distance from the source to the detector, and E is the particle energy level, the goal is to reconstruct the time-dependent energy distribution, $\tilde{f}(E, t)$, and the corresponding velocity distribution, $f(v, t)$, from the flux function, $S(D, t')$, which combines the detector measurements.

Reconstructing particle energy spectra from measured data is a well-studied problem, and neutron spectroscopy in particular has been an active area of research for several decades (Lehner 1967, Brysk 1973, Ballabio 1998). The basic mathematical model for time-of-flight–based spectroscopy is given by

$$S(D,t') := \int_0^\infty f(v,t'-D/v)\,dv. \quad \textbf{(6)}$$

Tomography for NToF Reconstruction

In this approach we recovered parameters and their uncertainties numerically. Neutron creation in a deuterium-deuterium fusion reaction was modeled as Gaussian in creation energy and creation time. The model was propagated through the Radon transform to give a formulation for the signal at the detector

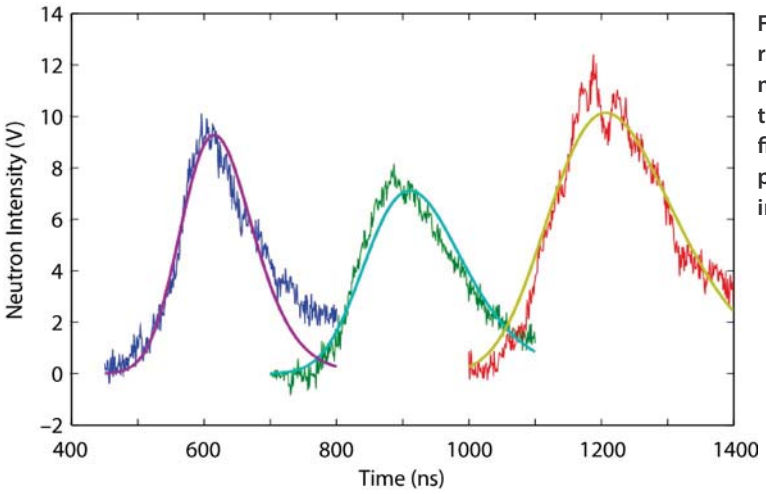

Figure 2. Comparison of measured and reconstructed signal in DPF experiment. The three noisy traces are measured neutron signals, and the corresponding smooth traces are the model fits corresponding to Equation 6. The fundamental parameters describing the fusion reaction can be inferred directly from the data fits.

(Equation 6). Due to an insufficient number of detectors or high levels of noise in the data, inverting the integral operator is ill-posed. We developed a parametric model for the energy distribution of fusion neutrons and derived the corresponding model for the signals seen at the detectors. Fitting model parameters to the detected signals, we obtained plasma temperature and the neutron energy spectrum. In Luttman (2013) we derived the form of the detector signal based on a classical model for neutron energy, analyzed the numerical properties of the data fitting, and demonstrated the method on experimental data from the NSTec dense plasma focus (DPF) laboratory in North Las Vegas. We also computed uncertainties in the parameters. Figure 2 shows the signals at three detectors at distances 14, 21, and 28 m from the source, positioned straight out from the source, parallel to the anode. The noisy curves are the measured voltages on an oscilloscope that correspond to neutrons being collected at the detector. The three corresponding smooth curves are the fitted model curves (Luttman 2013). For the data shown in Figure 2, the parameters describing the neutron creation computed with numerical uncertainty shown were as follows:

peak energy	E_0 = 2.8 ±0.02 MeV
peak creation time	t_0 = 18 ±3.2 nsec
energy spread	s_E^2 = 0.2 ±0.011 MeV^2
creation time spread	s_t^2 = 828 ±195 nsec^2

The peak energy being larger than 2.45 MeV indicates that the fusion reaction occurs in a reference frame that is moving towards the detectors. The creation time spread being 828 ns indicates that the duration of neutron creation is approximately 60 ns, which agrees with other estimates of the duration of the reaction.

Explicit Formulae for Uncertainties in NToF

We also looked for uncertainties of the NToF parameters analytically. Specifically we found (1) an estimate of the relative effect of the counting versus the instrument uncertainty and (2) an estimate of parameter uncertainties in our model. Both results were obtained independently of calculation of the parameter values from measured data and consequently became a tool in planning a measurement setup (Odyniec 2013a, 2013b).

The first result presents explicitly the ratio of uncertainties of the counting (Poisson) process versus the Gaussian (measurement) process in terms of the oscilloscope and detector parameters

$$\frac{\sigma_{P\max}^2}{\sigma^2} \approx \frac{5\sqrt{kT}}{N_0} \cdot \frac{2^{2 \cdot ENOB}}{\Delta t} \cdot \frac{D^3}{\alpha \cdot A}, \qquad (7)$$

where $ENOB$ denotes the number of effective bits.

Note that in the right-hand side of Equation 7, the first ratio describes plasma properties that we know approximately even before measurements are performed, the second ratio describes the properties

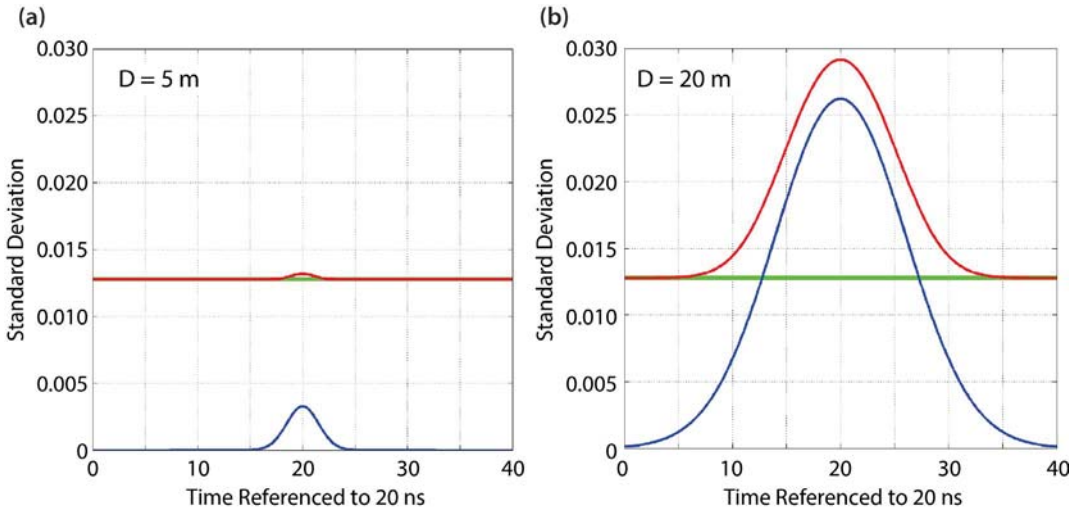

Figure 3. Standard deviations of Poisson (blue), Gaussian (green), and total (red) noise at a distance of (a) 5 m and (b) 20 m

of the oscilloscope, and the third describes the properties and placement of the detector. Therefore, without performing measurements and having only rough values of the parameters of interest, we know how to choose the oscilloscope settings and how to choose and place the detector.

The relative sizes of two uncertainties are illustrated in Figure 3. It shows standard deviation errors, referred to hereafter simply as "errors," of Gaussian (measurement) process, of Poisson process, and of their sum versus time, which is arbitrarily referenced to 20 ns. The measurement error (green line) is constant, depending only on oscilloscope parameters. The Poisson error (blue line) is proportional to the square root of the signal oscilloscope readout; the proportionality factor depends on the number of neutrons arriving at the detector. The total (red line) is little affected by Poisson noise at the distance of D = 5 m (Figure 3a). Only when the distance increases (and the number of detected particles diminishes), does the Poisson noise start to matter (Figure 3b). Thus, it follows that at distances of a few meters our errors are determined by the oscilloscope's performance.

We further developed explicit formulae for parameter variances obtained independently of the calculation of the parameter values and expressed them in terms of the measurement setup. Our model assumed that neutrons are not created instantaneously. Thus the parameters of interest include not only the plasma temperature kT, but also the time reference t_n, and the spread w_n of the profile of neutron creation intensity. The explicit formulae of their uncertainties (standard deviations) are:

$$\sigma_{t_n} = \sigma_{t_0} \approx 0.246 \cdot kT^{1/4} \cdot D^{1/2} \cdot \Delta t^{1/2} \cdot \sigma \quad \textbf{(8)}$$

$$\sigma_{w_n} = \frac{0.0117}{w_n} \sigma \cdot kT^{3/4} \cdot \Delta t^{1/2} \cdot D_1^{3/2} \cdot f_{w_n}\left(D_2/D_1\right) \quad \textbf{(9)}$$

$$\sigma_{kT} = 7.5 \cdot kT^{3/4} \cdot \sigma \cdot \Delta t^{1/2} \cdot D_1^{-1/2} \cdot f_{kT}\left(D_2/D_1\right). \quad \textbf{(10)}$$

As in Equation 7, the standard deviations of parameters of interest are expressed in terms of the choice, settings, and placement of the detector and the oscilloscope. Consequently, the method serves as a tool in planning a measurement setup.

In particular, Equations 9 and 10 provide an insight into the optimal detector placement. They tell us that the optimal placement of the two detectors is about 1 m for the closer detector and about 8 m for the farther one. Indeed, the minimum feasible detector distance is about 1 m; on the other end the counting error is negligible up to 8 m. Additionally, the coefficients f_{kT} and f_{w_n} flatten at the ratio x = 8 (Figure 4) so that a further increase of the second distance would provide little gain in accuracy. This conclusion, that extremal detector placement is the optimal one, is intuitively convincing because we want to disentangle the creation time and the time of flight. Therefore, we need one detector to be "least" affected by the time of flight (i.e., placed "close" to the source) and the other detector the "most" affected (i.e., placed "far" from) the source.

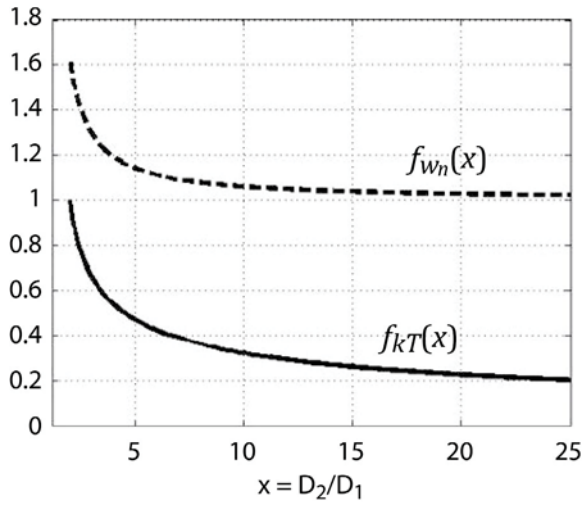

Figure 4. Dependence of the coefficients $f_{kT}(x)$ and $f_{w_n}(x)$, from Equations 9 and 10, on a distance ratio (Odyniec 2013b)

Example

Consider a numerical example with "typical" deuterium-tritium fusion reaction parameters: plasma temperature of kT = 16 keV, and neutron creation intensity width of w_n = 0.02 ns (Jacoby 2013). Let the measuring oscilloscope have the time step Δt = 0.01 ns (which is the state-of-the-art value in the year 2013) and the effective number of bits $ENOB$ = 5.5 (which translates into σ = 0.013).

Note that for closely spaced detectors D_1 = 1 m, D_2 = 2 m, we have:

$$kT = 16 \cdot \left(1 \pm 5 \cdot 10^{-3}\right) \text{keV} \quad \textbf{(11)}$$

$$w_n = 2 \cdot 10^{-2} \cdot (1 \pm 0.56) \text{ns}. \quad \textbf{(12)}$$

Applying our findings and moving the second detector to D_2 = 8 m, we get:

$$kT = 16 \cdot \left(1 \pm 2.3 \cdot 10^{-3}\right) \text{keV} \quad \textbf{(13)}$$

$$w_n = 2 \cdot 10^{-2} \cdot (1 \pm 0.35) \text{ns}, \quad \textbf{(14)}$$

with significantly reduced uncertainties on both measurements.

The example shows that with a simple extraction based on only two detectors (when signals considered are Gaussian), the plasma temperature can be determined with an uncertainty below 1% and neutron creation spread with a very reasonable uncertainty. Moreover, with properly positioned detectors, the latter reaches 35%. This is an unexpected and quite impressive result considering that the creation width is orders of magnitude smaller (20 ps) than the width of the received signal (10 ns).

Conclusion

We have invented and refined the theoretical properties of the mixed noise of MLE methods and of signal reconstruction. We also developed a neutron creation model with a non-instantaneous neutron creation profile that resulted in calculation of plasma parameters and their uncertainties. Our work included a numerical analysis based on the Radon transform and also a derivation of explicit formulae that allowed us to plan the measurement setup before simulations or measurements were performed. As our research progressed, we found new areas that would benefit from our efforts, such as uncertainty in radiance experiments using photomultipliers (of interest to STL), noise in neutron radiography (of interest to LLNL), and advanced models of neutron creation in NToF (of interest to LLNL and SNL). Some results

have been published (Odyniec 2013a), and the others (Bardsley 2013, Luttman 2013, Odyniec 2013b) have been submitted for peer review.

In FY 2014, when this project continues, we will generalize our approach to include non-homogeneous and filtered Poisson processes, which include system response analysis. This future work will allow us to compare our results with actual experiments. We will also continue investigating regularization methods in UQ analysis, such as generalizing the results of Bardsley 2013 to nonlinear problems.

Acknowledgments

We would like to thank Tim Meehan (North Las Vegas) for sharing the DPF data and helpful comments on DPF, Brandon La Lone (STL) for helpful comments and data on radiance, Barry Jacoby (LLNL) and Mark Lowry (LLNL) for helpful discussions of NToF, David Fittinghoff (LLNL) for helpful discussions on radiography, and Heikki Haario (Lappeenranta University of Technology) for helpful comments and sharing his MCMC programs.

References

Ballabio, L., J. Källne, G. Gorini, "Relativistic calculation of fusion product spectra," *Nucl. Fusion* **38**, 11 (1998) 1723.

Bardsley, J. M., Luttman, A., "Total variation-penalized Poisson likelihood estimation for ill-posed problems," *Adv. Comput. Math* **31** (2009) 35–59.

Bardsley, J., A. Luttman, "A Bayesian method for dealing with edge effects," *Linear Algebra and Its Applications*, submitted October 2013.

Brysk, H., "Fusion neutron energies and spectra," *Plasma Phys.* **15**, 7 (1973) 611–617.

Jacoby, B., private communication, 2013.

Lehner, G., F. Pohl, "Reaction neutrons used for plasma diagnostic purposes," *Zeitschrift für Physik* **207** (1967) 83–104.

Luttman, A., M. Odyniec, N. Shlayan, J. Blair, E. Machorro, P. Kachroo, "A model-based approach to fusion neutron spectroscopy," *IEEE Trans. Plasma Sci.*, submitted October 2013.

Odyniec, M., J. Blair, "Effect of the measurement vs. the counting errors on parameters' covariance in neutron tomography analysis," *Proc. SOFE Conf.*, Symposium on Fusion Engineering (SOFE) 2013, San Francisco, 2013a, 1–6.

Odyniec, M., J. Blair, "Parameters' covariance in neutron time of flight analysis – Explicit formulae," *IEEE Trans. Plasma Sci.*, submitted July 2013b.

This page left blank intentionally

Power Automation System (PAS) Vulnerability Assessment in Smart Grid

RSLN-04-13 | Continued in FY 2014 | Year 1 of 2

Ki Park[1,a] and Yoohwan Kim[b]

The electrical power grid is controlled by supervisory control and data acquisition (SCADA) control devices. Unfortunately, many of these devices are exposed to physical attacks. In this environment, security key theft and malware injection attacks are very dangerous because attackers can inject malicious commands to bring down the power grid or propagate malware to other SCADA devices or control centers. This 2-year research is developing a new cryptographic scheme and processor architecture to prevent those attacks. In this approach, the erasable programmable read-only memory does not contain any security key material; thus, no security key material is revealed to the attacker if the storage device is stolen or compromised. If the attacker tries to replace the firmware with malware, the malware code will not be executed because it does not pass the integrity verification process. With the proposed approach, the damage is limited only to the targeted SCADA machine, and it will not propagate to other devices. For year 2, a prototype architecture will be developed for a proof-of-concept demonstration.

[1] parkkh@nv.doe.gov, 702-295-8022
[a] Remote Sensing Laboratory–Nellis; [b] University of Nevada, Las Vegas

Background

The modern power grid is composed of generation, transmission, and distribution subsystems. In all subsystems, the electrical power flow is controlled by supervisory control and data acquisition (SCADA) devices at each substation. Different types of SCADA devices are used, such as remote terminal units or intelligent electronic devices. At the control center, master terminal units, energy management systems, and human-machine interfaces are employed (Wei 2011). They communicate with each other via remotely controlled SCADA protocols. The master stations may be further connected to incorporate IT systems over the Internet or private communication lines. The vulnerability domain can be divided into the following four categories:

1. Attack on physical power systems: The physical system can be damaged by a variety of physical attacks, such as manually tripping relays, cutting wires, flooding, destroying sensors, or using explosives.

2. Attack on SCADA devices: SCADA systems are essentially typical desktop computers running commercial operating systems, such as Microsoft Windows. Over 60% of SCADA systems are running Windows operating systems. They are often unpatched for extended periods of time and have numerous vulnerabilities. The associated application software could contain numerous vulnerabilities. They can be exploited locally or remotely.

3. Attack on SCADA protocols: SCADA systems run specialized protocols that are different from the ones used in traditional IT systems, such as transmission control protocol/Internet protocol (TCP/IP). While newer protocols provide advanced security features, legacy protocols still widely used in the field are vulnerable to even primitive attacks.

4. Attack on Internet protocols: When SCADA systems are connected directly (or indirectly) to the Internet via a corporate network, they can be exposed to the same type of attacks as typical IT systems.

As for the power automation system (PAS) vulnerability analysis, we are particularly interested in the physical attacks. On the distribution side, there are many devices that are controlled by computing devices, such as smart meters, smart thermostats, or smart appliances. These devices are physically exposed to a variety of attacks. The storage devices are most vulnerable, but the processor can be protected to a greater degree with tamper-resistive protection mechanisms. The storage device contains sensitive data and needs to be programmable at the time of deployment, upgradable in the field, or physically replaceable. Therefore, storage devices, such as electrically erasable programmable read-only memory (EEPROM), erasable programmable read-only memory (EPROM), Flash ROM, or secure digital (SD) cards, are physically separated from the processor to make deployment and maintenance easier.

However, the data stored in the storage device can be read not only by the processor, but also by anyone who has a means of access to the physical device. Even with tamper-resistive protection, such as epoxy, it is still possible to reverse engineer the hardware chips (Laurie 2013). Once the bits are exposed, the sensitive material can be recovered by the attackers. Because the bit values in cryptographic keys are highly randomized, they have high entropy (Ji-Zhong 2012). With entropy analysis, potential keys can be easily identified (Figure 1).

One possible attack is the theft of the security key material. Controller devices are essentially computers that are composed of a processing element and a storage unit. The firmware (control software) and security key material need to be stored in non-volatile memory (NVM) such as EPROM, EEPROM, or Flash memory, called EPROM collectively in this report. When attackers have physical access to the controller device, they can remove the EPROM, read its content, and retrieve the security key material. Once the security key is stolen, messages can be decrypted or bogus messages can be encrypted. Another concern is malware injection. Most of these controller devices are commercially available, allowing attackers to write new firmware that performs malicious actions. When the controller devices are physically exposed to the attacker, the attacker can remove the EPROM, replace its original firmware with malware (or simply swap in a different EPROM), and let it run. It could interfere with the SCADA operation or infect other controllers.

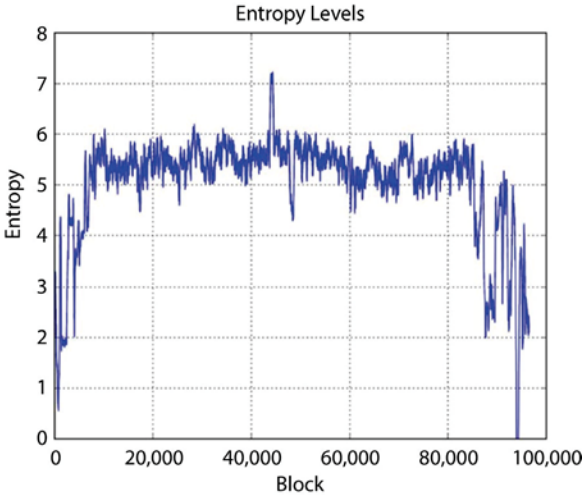

Figure 1. Identifying the cryptographic key with entropy analysis

Project

This project investigates cyber threats on the PAS in Smart Grid and identifies vulnerabilities associated with such attacks. In FY 2013, this 2-year SDRD project focused on developing a cyber attack model and vulnerability assessment capability. With successful attack observations in the first year, a prototype field-programmable gated array (FPGA) board with new protection architecture will be developed in the second year.

Power Grid Vulnerability Simulation

In order to show the impact of security key theft and malware injection threats, a power grid model from the IEEE 24-bus Reliability Test System (Grigg 1999) is utilized (Figure 2). Without any protection, the attackers can disable not only the first compromised substation 17 but also remotely corrupt other adjacent buses (16 and 18), thus creating cascading failures throughout the power grid.

Although our methodology does not prevent a physical attack to destroy the control devices, the proposed scheme can protect the substations from the security key theft attack, eavesdropping and message fabrication attacks, and man-in-the-middle attacks, thereby offering critical protection for the modern power grid communication infrastructure at a reasonably low cost.

Current Approach and Issues

Typical cryptographic approaches cannot solve these attack problems because once the attacker has unfettered access to the hardware, all the cryptographic data can be compromised. For example, Kerberos uses a data item called ticket, which carries the authentication information (Garman 2003). The tickets are encrypted under temporary session keys, so there is no risk of revealing private keys. Although Kerberos is well suited for distributed environments, the private keys are still stored in the individual machine. There must be a physical protection solution for the keys.

The above problems are not unique to SCADA systems. All computing devices suffer from the same kind of attacks, and the industry has been working to find a solution. The Trusted Computing Group has developed trusted platform module (TPM) architecture, which stores confidential data and processes them securely. The TPM architecture has been very widely used

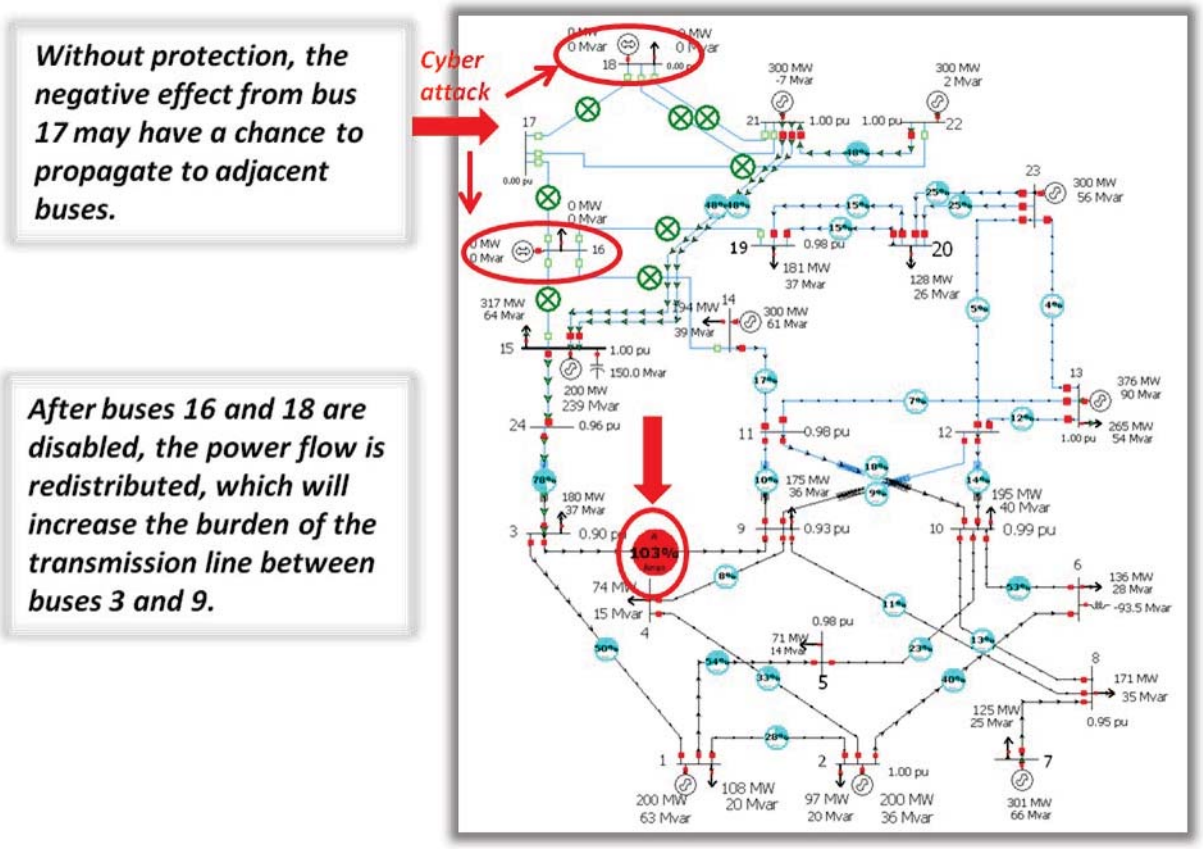

Figure 2. Cascading bus failure without protection

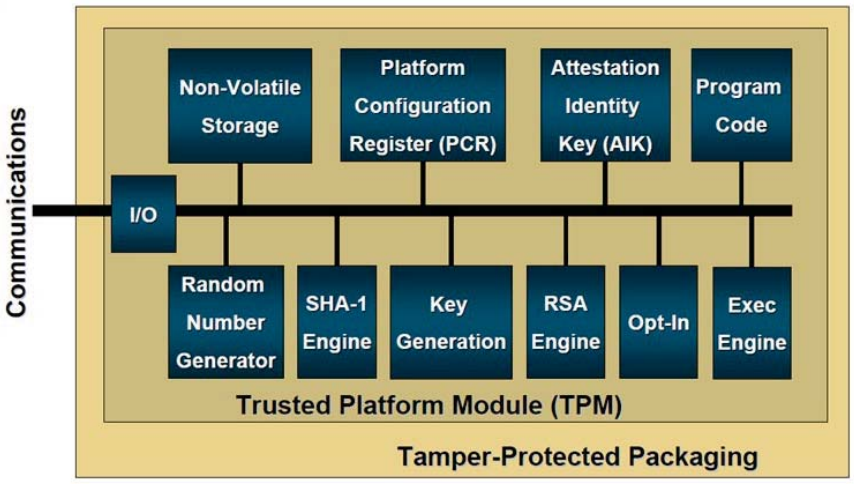

Figure 3. TPM chip architecture stores confidential data and processes them separately (George 2005)

in over 600 million installations. Nowadays there is an effort to move the TPM to the SCADA domain (O'Halloran 2013). Figure 3 shows the basic TPM architecture (George 2005).

The nature of this TPM security chip ensures that information, including keys, passwords, and digital certificates, stored within are made more secure from external software attacks and physical theft. All cryptographic functions are performed on the chip. TPM is an implementation of a root of trust model that is integrated into the boot process to establish trust level and gather measurement about the running environment for trusted reporting. Hence, TPM is typically affixed to the motherboard of a computing system (Infineon 2007).

Despite its advantages and well-established performance, there are some obstacles with TPM. In a SCADA environment, the program codes are commonly stored in an external storage. This makes it easier to upgrade the software by simply replacing the storage hardware module. On the other hand, in a TPM environment, the software must be stored in the TPM chip in an encrypted format, which lowers the flexibility. If the software and data grow beyond the size of the TPM storage size, the whole circuit board must be replaced. On the other hand, if the software is stored in external storage, only the storage unit should be replaced. Second, because TPM is a separate chip, the communication between the main processor and TPM can be intercepted if all the hardware is accessible to the attacker. If the main processor and its RAM are not protected, the data can be read by sophisticated equipment. In other words, both the TPM and main processor need to be in the same tamper-protected packaging. Without the main processor, the execution unit is too primitive to execute the entire control software for the SCADA system. The cryptographic keys in TPM devices are embedded by the factory, which requires that a manufacturer be completely trustworthy. We need a solution that frees the SCADA operators from the TPM manufacturers and executes the software without worry of key theft while maintaining low cost.

Framework for Protecting Key Material

Instead of EPROM, we propose to store the key material within the processor. With new and simpler microcontroller architecture, we can create a small NVM within the microcontroller and store the key material there. However, without any adequate protection, the attacker can remove the chip and retrieve the stored values by physical attack. Therefore, tamper-protective packaging is needed. Instead of a full-blown cryptographic execution unit, we propose an enhanced processor architecture with two new instructions (*Set* and *Gen*) as shown in Figure 4.

There are two NVM sections in the new chip: invisible NVM (I-NVM) and visible NVM (V-NVM), where *visible* means it is accessible from the program, not observable by the attacker. They have the following features:

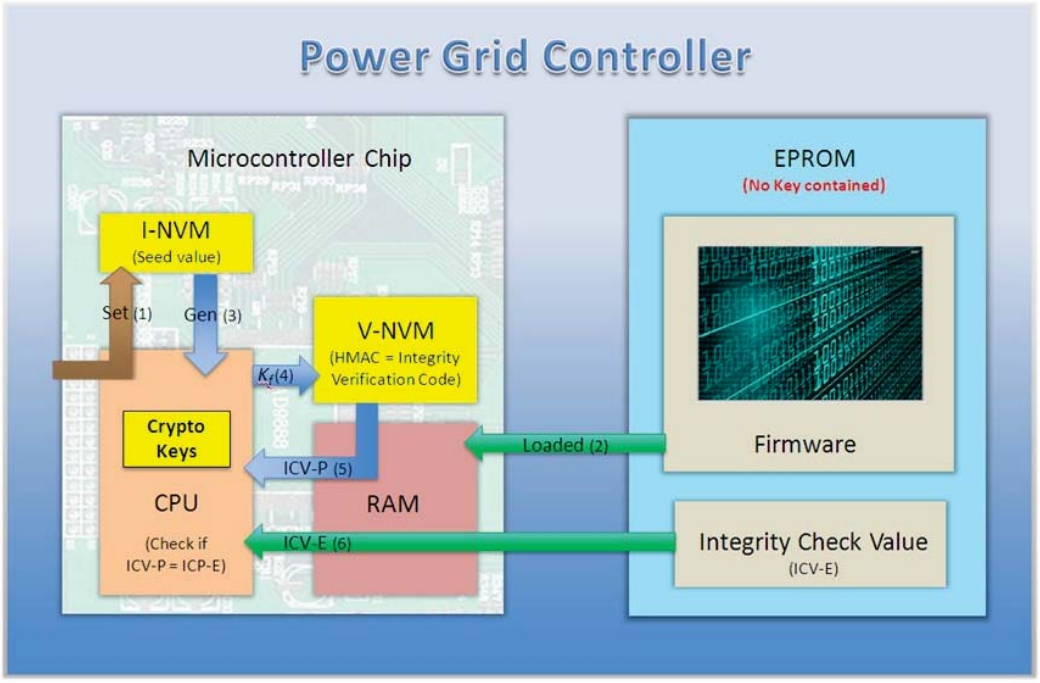

Figure 4. Components and their relationships in the proposed scheme

- I-NVM contains a small number called the seed value, which will be used for deriving keys. The size of I-NVM is small, e.g., 4 to 8 bytes. The content of I-NVM cannot be accessed at all by any means. There is no memory address or machine instruction to read the value. Only two types of operations are allowed for I-NVM, *Set* and *Gen*. The *Set* instruction initializes the memory with a certain value called seed. The *Gen* instruction reads the seed value and generates a sequence of pseudo-random numbers. The algorithm for the *Gen* instruction is embedded in the processor.

- V-NVM contains a normal code segment that can be accessed by the processor. This memory region is accessible from the outside. However, the code segment contained here is preconfigured at the factory and cannot be changed by the software. In other words, V-NVM is ROM, not EPROM. This memory contains the code segment to read and verify the integrity of the firmware in the EPROM when the system is powered up.

This new architecture provides three important benefits: (1) no key material is stored in the EPROM, so theft of the memory content is impossible; (2) it provides better firmware content protection, enforcing an integrity check by the processor; and (3) there is better utilization of protected memory, as it needs only a small modification in the existing processor architecture and no design changes at the board level.

For further discussion, we make the following assumptions:

- EPROM is used to represent the storage unit, such as EEPROM, Flash ROM, or SD card.

- Anyone (including the attackers) can read and write in any memory address directly in the EPROM after removing it from the SCADA system.

- The RAM is enclosed within the tamper-protective microcontroller package, so the attacker cannot read or write on it while the processor is up and running. Likewise, the communication between the CPU and memory cannot be captured from the outside.

- Even if the tamper-protective packaging is compromised, the attacker can read only the V-NVM section within the microcontroller, but not the I-NVM section.

- Unlike the TPM-based system, there is no separate TPM unit.
- I-NVM section is not accessible through the Joint Test Action Group (JTAG) or In-Circuit Serial Programming (ICSP) interfaces.

Firmware Installation or Upgrade Process

The firmware installation process illustrated in Figure 5 describes the flow of generating the message authentication code (MAC) value. The control center and the SCADA devices share the same seed value. From the seed value, a hash key (K_f) is generated by running the *Gen( )* algorithm. By using the firmware integrity verification key (K_f), the firmware runs through a hash-based message authentication code (HMAC) process, and the MAC value for the integrity check value in EPROM (ICV-E) is generated. Then it is stored in the EPROM.

ICV-E = Hash (Firmware, K_f)

The firmware and the ICV-E value are then written on the storage unit of each controller unit. Because the attacker cannot obtain K_f, it would be unfeasible for the attacker to generate the correct ICV-E.

Sequence of Operation

The code verification process is a reverse process of the firmware installation process. The authenticity of the firmware is checked by the steps below:

1. The seed value is set during the initial field-deployment stage.
2. The authentication code reads the firmware in EPROM and loads it in the RAM.
3. The authentication code executes the *Gen* instruction to derive the firmware integrity verification key, K_f.
4. The authentication code in V-NVM executes to calculate HMAC (firmware, K_f) value.
5. The integrity check value in processor (ICV-P) is obtained.
6. ICV-E is read from the EPROM for comparison.
7. If ICV-E = ICV-P, the firmware is valid. If the firmware is valid, the control is transferred to the loaded firmware in the RAM.

Even if the firmware is modified or replaced with malware by an attacker, the ICV-E value is likely to be wrong and will not pass the verification process.

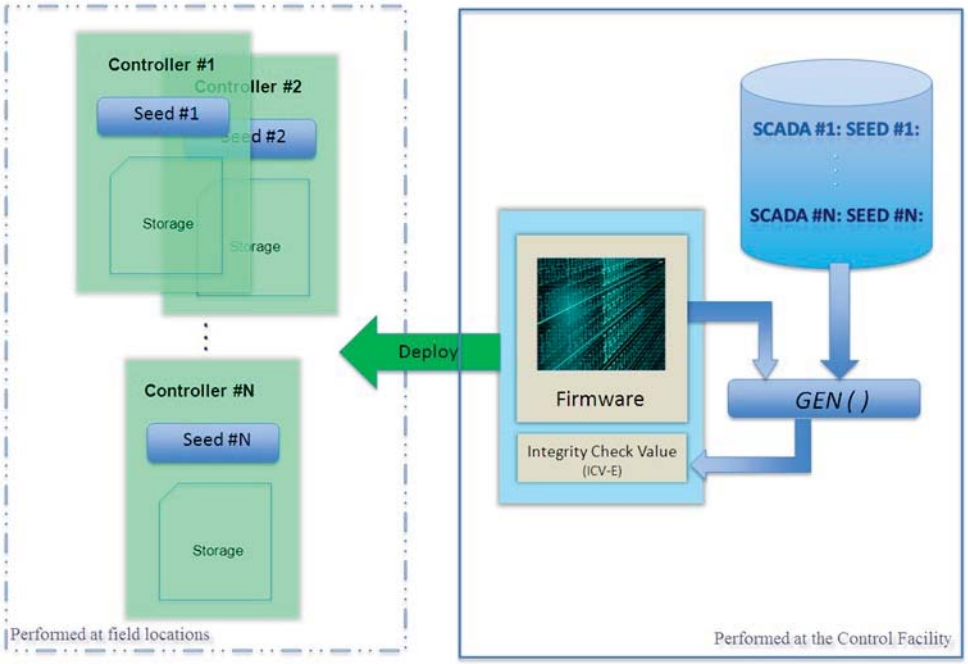

Figure 5. Firmware installation process for generating the message authentication code

This code verification process is very important for protecting key material. Obviously, an executable program can access the information inside the RAM. Although the seed value in I-NVM is not readable directly, derived key values get stored in the RAM, which can be read by the program. Attackers can write a code to run the *Gen* instruction to generate the cryptographic key and attempt to export it out of the CPU. However, with the code verification process, such a malicious operation is prevented in the first place.

Security Analysis

Disruptive cyber attacks are becoming more damaging as the growing interdependence of the communications and energy-delivery infrastructures creates vulnerabilities and increases the likelihood of wide-ranging consequences. The attacker can launch the following types of attacks, but their adverse impacts on the grid operations can be successfully minimized.

Theft of EPROM

The attacker may remove the EPROM, read the content, reverse engineer, and try to update it with malicious code. However, the EPROM does not have any key material. The attacker cannot extract the key after stealing the EPROM.

Illegal Firmware Update in the EPROM

The attacker can simply replace the existing EPROM with another EPROM containing malware. But in order to make the malware run in the new EPROM, the attacker needs to shut down the controller and reboot it. Upon reboot, the processor will try to authenticate, and without proper ICV-E value, it will fail. The only way for the attacker to obtain the correct ICV-E is to have the seed value and run the *Gen* instruction. Even though the *Gen* instruction's algorithm is open to the public, the seed value is not, making it very difficult to create a correct ICV-E.

Theft of the CPU

The seed value and the keys are protected by multiple methods. First, the microcontroller and the memory are in a tamper-protected package. Second, if the package is compromised, the I-NVM is not accessible by any method. I-NVM does not have a memory address, so it cannot be retrieved by a typical program. On the other hand, the attacker may read the V-NVM content, but the V-NVM does not contain any confidential information other than the already well-known code segment. To access the memory online, the attacker needs to run a new firmware program, but it has to pass the verification process, which will fail without a correct ICV-E value.

Unauthorized Change of the Seed Value

The seed value is set when the SCADA device is initially deployed, but it may also need to be updated during field operation. In order to accommodate version upgrades, the firmware has a function to accept a new seed value and update the I-NVM with it. During the upgrade, new firmware and a new MAC value should be written on the EPROM. Once the I-NVM updates, the SCADA controller shuts down and reloads the new firmware from the EPROM. When the attacker has physical access to the SCADA device, he or she can attempt to change the seed value. However, as soon as the seed value is modified, the system will shut down and try to reboot. At that point, the new code will not pass the integrity verification process due to a wrong ICV-E value generated with a fabricated seed value.

Cryptographic Algorithms

In the proposed processor architecture, there are two new instructions, *Set* and *Gen*. The *Set* instruction writes a value in the I-NVM. This seed value needs to be at least 128 bits long. Once the value is written, the *Gen* instruction can produce key values. The *Gen* instruction implements a hash function, where a newly developed secure hash algorithm (SHA-3) can be used. SHA-3 is the most recent hash algorithm adopted as a new standard by the National Institute of Standards and Technology (NIST) in 2013 (NIST 2013). It is known to be very fast, with a reported average speed of 12.5 cycles per byte on an Intel Core 2 processor. It can produce 224-, 256-, 384-, and 512-bit hash values.

Because reusing a single key increases vulnerability, separate keys should be used for different purposes. These keys are derived from the *Gen* instruction. To produce multiple key values, the *Gen* instruction takes an input as an index value as shown in Figure 6. This index value is prepended to the seed value in I-NVM, and together they become the input for the SHA-3 hash function.

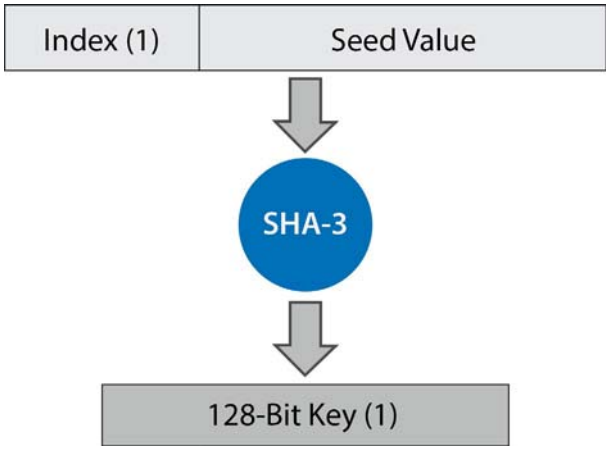

Figure 6. Generating a key value 1 with index 1 and a seed value

For example, *Gen (1)* produces K_f, *Gen (2)* produces K_p, and so on, for the following keys.

1. Firmware integrity verification key, K_f
2. Decryption key for private key, K_p
3. Authentication key (client to server), K_{a1}
4. Authentication key (server to client), K_{a2}
5. Encryption key (client to server), K_{e1}
6. Encryption key (server to client), K_{e2}
7. Integrity key (client to server), K_{i1}
8. Integrity key (server to client), K_{i2}

All the key sizes are 128 bits, so we can use a 224-bit version of SHA-3 and use the first 128 bits from the hash output.

Keyed HMAC

A keyed HMAC is a specific construction for calculating a MAC involving a cryptographic hash function in combination with a secret cryptographic key (Krawczyk 1997). It operates as

$$HMAC\,(K,m) = H\,((K \oplus opad) \,||\, H \times ((K \oplus ipad) \,||\, m)), \quad \textbf{(1)}$$

where

- H is a cryptographic hash function,
- K is a secret key padded to the right with extra zeros to the input block size of the hash function, or the hash of the original key if it is longer than that block size,
- m is the message to be authenticated,
- $||$ denotes concatenation,
- $\oplus$ denotes exclusive or (XOR),
- $opad$ is the outer padding (0×5c5c5c…5c5c, one-block-long hexadecimal constant), and
- $ipad$ is the inner padding (0×363636…3636, one-block-long hexadecimal constant).

Mutual Authentication

The SCADA device and the SCADA control center must verify the authenticity of each other. This can be done by using the shared authentication key. The loaded firmware generates the necessary keys for this purpose by running *Gen (3)* and *Gen (4)*, which produces K_{a1} and K_{a2}, respectively (Figure 7).

The SCADA control center and individual SCADA device have the same seed value, and they generate the same keys K_{a1} and K_{a2} using the above process. To ensure that both parties are legitimate, they perform the following mutual authentication procedure by exchanging nonce values (N_C, N_S). A nonce is a random number used once, chosen by the control center and the SCADA device.

1: SCADA → Control Center : { ID_S || N_S }

2: Control Center → SCADA : { $E(K_{a2}, N_S \,||\, N_C)$ }

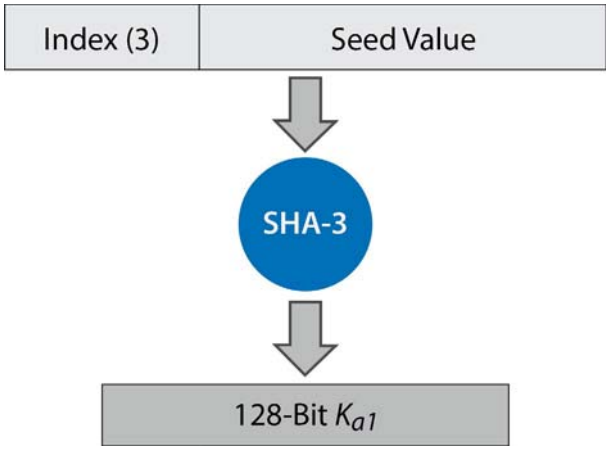

Figure 7. Generating a key for firmware authentication

3: SCADA → Control Center : { $E(K_{a1}, N_c)$ }

If the nonce is properly replied back, the sender knows that the other party has the correct key.

Encrypted Communication

After the SCADA device and control center are mutually authenticated, they can secure data communication. Both generate the encryption keys by *Gen (5)* and *Gen (6)*. The data payload (*D*) is encrypted in the following fashion:

- From SCADA device to the control center: { $E(K_{e1}, D)$ }
- From the control center to SCADA device: { $E(K_{e2}, D)$ }

The encryption algorithm is included in the firmware. It implements the various block cipher algorithms in cipher block chaining mode or counter mode.

Conclusion

The SCADA device in the electrical power grid is vulnerable to physical attack that leads to key theft and malware injection. Once malware is injected in a SCADA device, it can inject false sensor data and malicious commands, affecting other SCADA devices, causing a cascade effect in the entire power grid, which could lead to a blackout. We have demonstrated the effect of malicious command with a PowerWorld simulation (Figure 2). To protect the key material and firmware, a physical protection method combined with a cryptographic scheme is necessary. The current solution of using a TPM is inadequate in the SCADA environment because the communication between the TPM and main processor is not secure and not flexible for maintenance.

Our simple scheme, which can be applied to large-scale PAS, can protect the key material and firmware manipulation. In the scheme we are developing, the storage device does not contain any security key material; therefore, no key material is revealed to the attacker if the storage device is stolen. All firmware is authenticated using a keyed HMAC, so the malware code cannot be executed because it cannot pass the integrity verification process. The attacker can still damage a single SCADA device when he or she has physical access to it, but the damage is limited only to a single SCADA device and does not spread.

With successful attack observations in the first year, an FPGA board with new protection architecture will be developed in the second year.

References

Garman, J., *Kerberos: The Definitive Guide*, O'Reilly Media, Sepastopol, California, 2003.

George, P., "The Trusted Platform Module Specifications," http://courses.cs.vt.edu/cs5204/fall10-kafura-BB/Papers/TPM/Intro-TPM-slides-2.pdf (2005), accessed September 5, 2013.

Grigg, C., et al., "The IEEE Reliability Test System-1996. A Report Prepared by the Reliability Test System Task Force of the Application of Probability Methods Subcommittee," *IEEE Trans. Power Systems* **14**, 3 (1999) 1010–1020.

Infineon Technology, "Infineon first to release Windows Vista ready TPM v1.2 management suite for simple manageability of trusted platforms in enterprise environments," http://www.presseagentur.com/infineon/detail.php?pr_id=1201&lang=en (January 23, 2007), accessed September 5, 2013.

Ji-Zhong, L., J. Lie-Hui, Y. Qing, X. Yao-Bin, "Hybrid method to analyze cryptography in software," *2012 Fourth International Conference on Multimedia Information Networking and Security* (2012) 930–933.

Krawczyk, H., M. Bellare, R. Canetti, "HMAC: Keyed-hashing for message authentication," http://tools.ietf.org/html/rfc2104 (1997), accessed September 5, 2013.

Laurie, A., Z. Franken, "Decapping chips the easy hard way," DEF CON 2013.

NIST, "SHA-3 standardization," http://csrc.nist.gov/groups/ST/hash/sha-3/sha-3_standardization.html (2013), accessed September 5, 2013.

O'Halloran, S., "Improving SCADA and industrial control systems," http://www.foodengineeringmag.com/articles/print/90314-improving-scada-and-industrial-control-systems (February 26, 2013), accessed February 26, 2013.

Wei, D., Y. Lu, M. Jafari, P. M. Skare, K. Rohde, "Protecting smart grid automation systems against cyberattacks," *IEEE Trans. Smart Grid* **2**, 4 (2011) 782–795.

Photonics

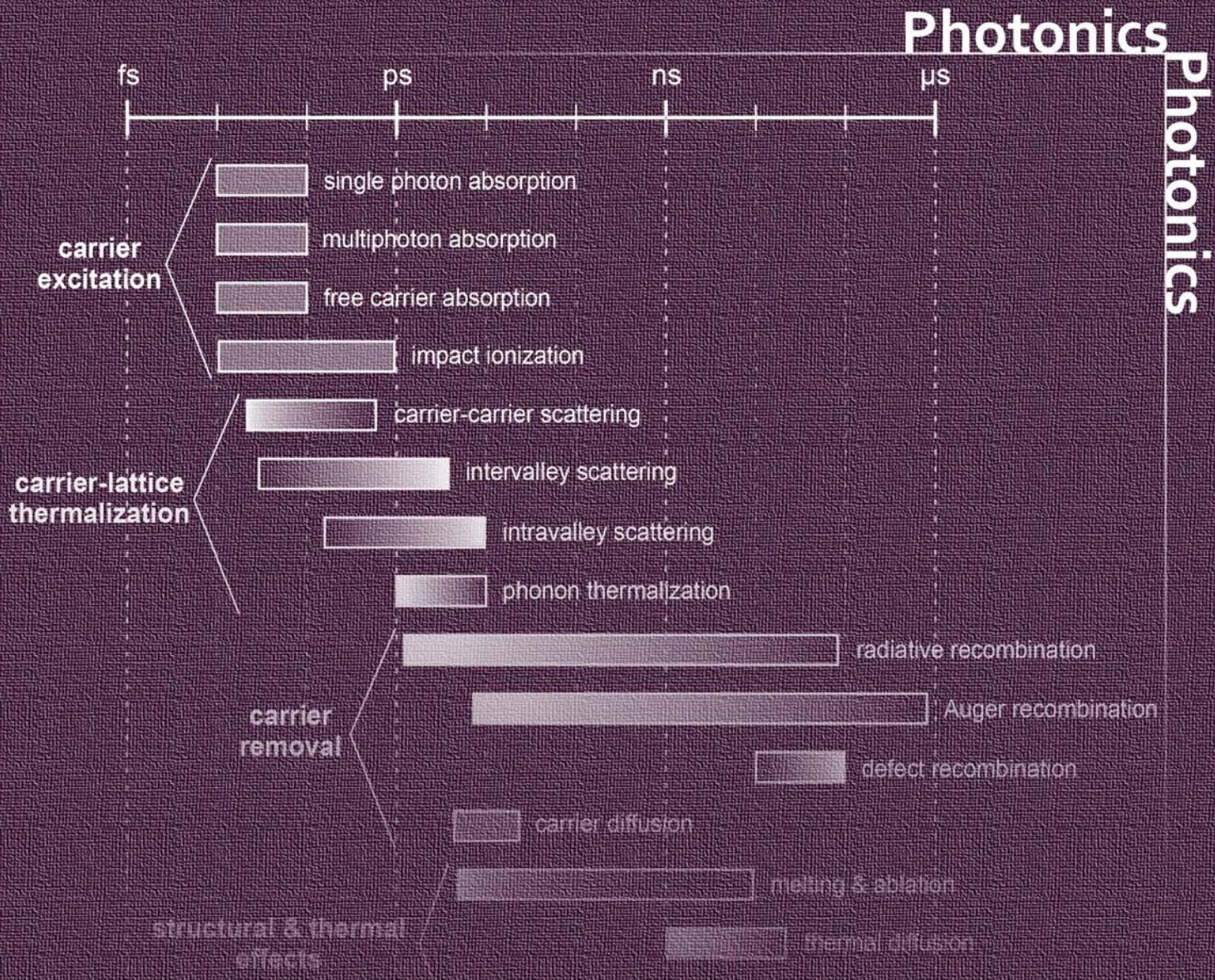
Photonics
fs
ps
ns
μs
carrier excitation
single photon absorption
multiphoton absorption
free carrier absorption
impact ionization
carrier-lattice thermalization
carrier-carrier scattering
intervalley scattering
intravalley scattering
phonon thermalization
carrier removal
radiative recombination
Auger recombination
defect recombination
carrier diffusion
melting & ablation
structural & thermal effects
thermal diffusion

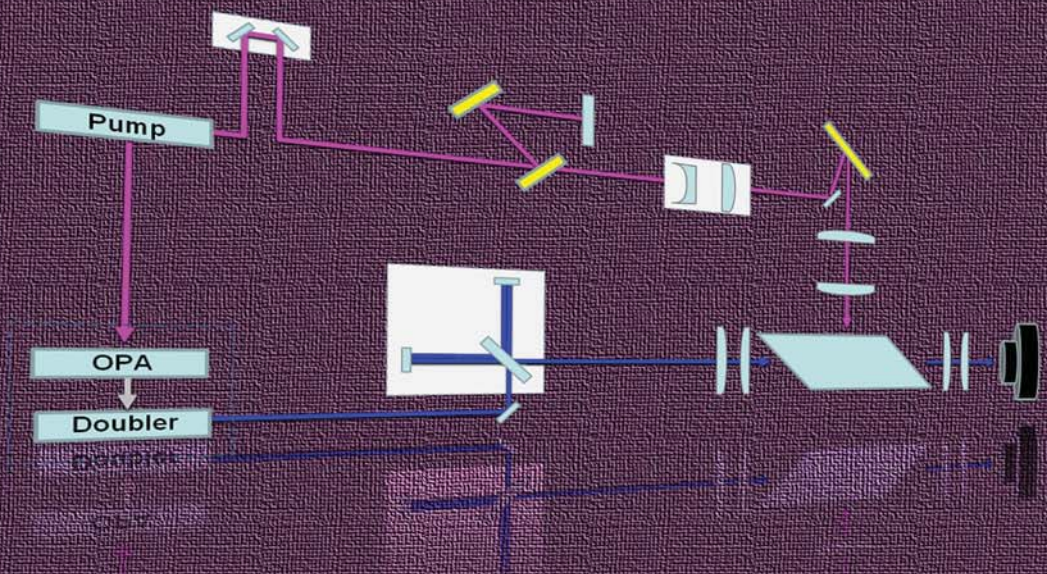
Pump
OPA
Doubler

Study of Radiation-Induced Refractive Index Change in GaN for Ultrafast Scintillator Applications

LAO-08-13 | Year 1 of 1

Kristina Brown,[1,a] Paul Steele,[b] and Alden Curtis[a]

Despite extensive research on new scintillator materials, the essential mechanism of energy absorption, excitation, and photoemission has remained unchanged for over 50 years. Recently, a new class of semiconductor detector that changes its refractive index when subjected to radiation (called the radoptic effect), has been developed and shows promise for applications that need to resolve ultrafast phenomena. Our project investigated the suitability of four such semiconductors for use as high-speed radiation-sensing devices. The materials were thinned, polished, and optically excited in a Fabry-Perot configuration. While index shifts were observed in the indium phosphide samples at incident energy densities of 8.5 μJ/mm², the gallium nitride samples, at approximately 1 μJ/mm², were deemed inadequate to our purpose. A portion of this work is being further studied in conjunction with an FY 2014 hyperchromatic lens and plenoptic camera project.

[1] brownkk@nv.doe.gov, 505-663-2083
[a] Los Alamos Operations; [b] Lawrence Livermore National Laboratory

Background

High-energy density physics, materials studies, and inertial confinement fusion experimenters have long desired ultrafast scintillators to avoid problems with detector coincidence and pileup. Conventional scintillators rely on excitation and decay or transport of charge carriers before light can be detected, placing inherent limits on the speed of detection. Using a phenomenon other than scintillation may allow for increased detection speed. Increased speeds may enable new diagnostic methodologies and facilitate diagnostics at facilities such as the National Ignition Facility, the Advanced Photon Source, the Z machine, and the proposed Matter-Radiation Interactions in Extremes facility. Multiple materials that exhibit the radoptic effect, by which refractive index is modified by incident radiation, have been investigated and developed by Lawrence Livermore National Laboratory (LLNL) (Baker 2012). LLNL has demonstrated gallium arsenide devices with picosecond speeds through the use of hydrogen ion implantation to increase the rate of carrier recombination. This study investigated the possibility of even higher detector speed and sensitivity by utilizing different semiconductors as radoptic sensors.

Project

The radoptic effect occurs when an ionizing photon or particle impinges on a semiconductor, creating electron-hole pairs in its path (Figure 1). The excited charge carriers induce a change in the refractive index in the region of the material in which they are formed. The material may then be probed with an optical probe beam, and an interferometer used to determine the change in refractive index (Figure 2). To optimize for sensitivity, we used a Fabry-Perot configuration for the interferometer. The reflection spectra of Fabry-Perot cavities have pronounced dips (or resonances)

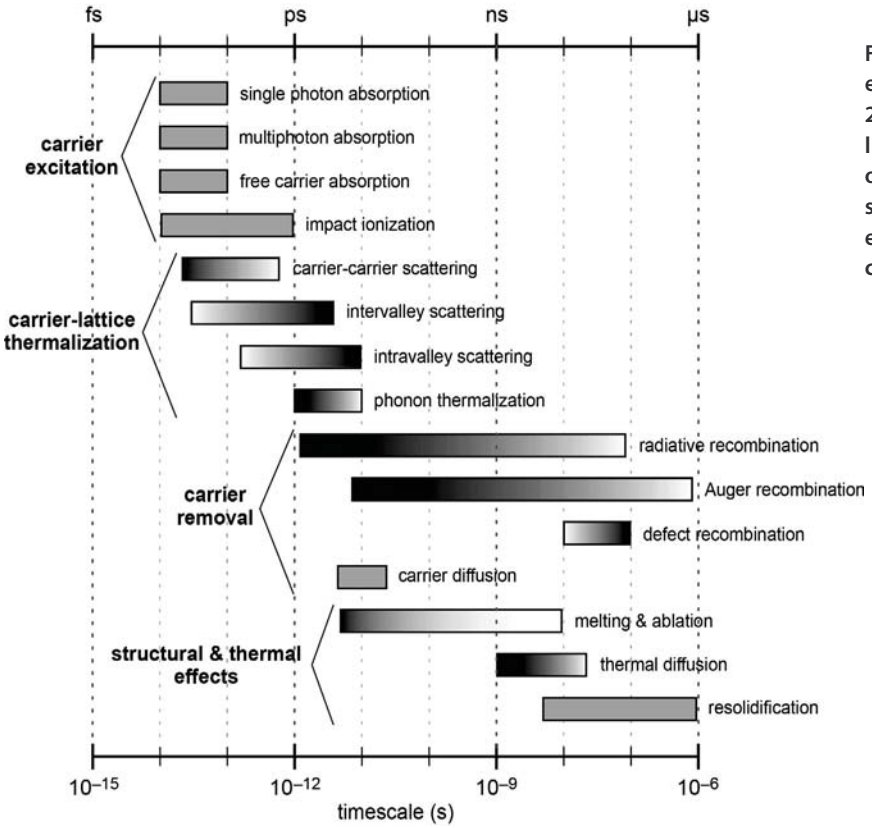

Figure 1. Characteristic time scales for electron and lattice processes (Callan 2001). Conventional scintillators are limited by carrier recombination or carrier transport in the case of semiconductor detectors. The radoptic effect allows interrogation of charge carriers in situ.

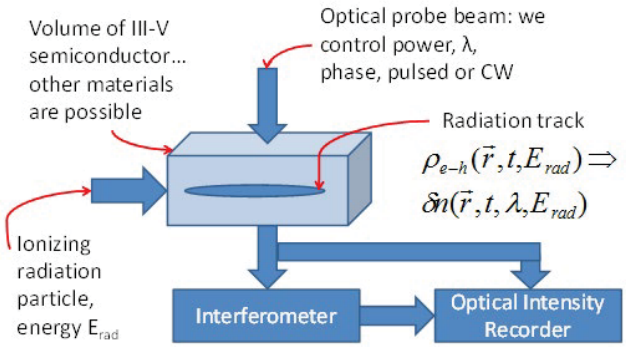

Figure 2. Conceptual illustration of radoptic effect. Achievable optical index changes in the radiation track are *δn* ~0.01 to 0.1 (Lowry 2004).

at certain wavelengths. The positions of these resonances are directly related to the optical thickness of the cavities. An index change in the cavity material changes the optical thickness of the cavity and hence the position of the cavity resonances. By measuring the position of the resonances in a pump-probe experiment, we can determine the index of refraction very accurately and with very high temporal resolution. The probe pulse, due to its fast duration, is inherently high bandwidth, and it is this bandwidth that allows a spectrum to be obtained.

We originally planned to study gallium nitride (GaN) as the relevant literature (Ye 1999, Stanton 2001) hinted that it could exhibit a faster rise time than other radoptic materials. However, carrier excitation is a complicated process and the literature is inconsistent on the matter. Rise time (excitation) and decay time (recombination) depend on the wavelength of the pump, since hot electrons, for example, have longer relaxation times than optically excited electrons. Also, the magnitude of the index change is dependent on the spectral proximity of the probe laser to the band edge. Ultimately, our team decided to test undoped GaN, magnesium-doped gallium nitride (GaN:Mg), undoped indium phosphide (InP), and sulfur-doped indium phosphide (InP:S) due to results published by Dvorak (1995), Martin (1995), Pačebutas (2001), Gonzalez (2009), and Pinos (2009).

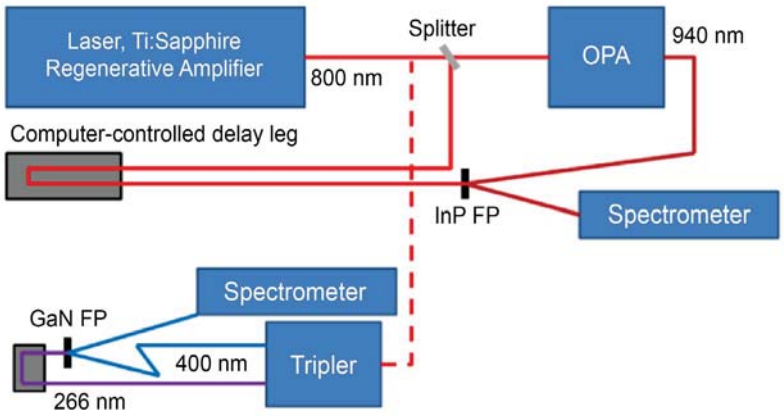

Figure 3. Experimental setup. A Ti:Sapphire laser is used to produce both the pump and probe beams for each material. For the InP experiments, the 800 nm beam was used as a pump while the 940 nm beam produced by the OPA probed the Fabry-Perot interferometer. A delay leg adjusted the time at which the pump illuminated the material and the index shift was expected. For the GaN experiments, the beam was passed through a doubler/tripler to create a 266 nm pump (also adjusted with delay leg) and 400 nm probe.

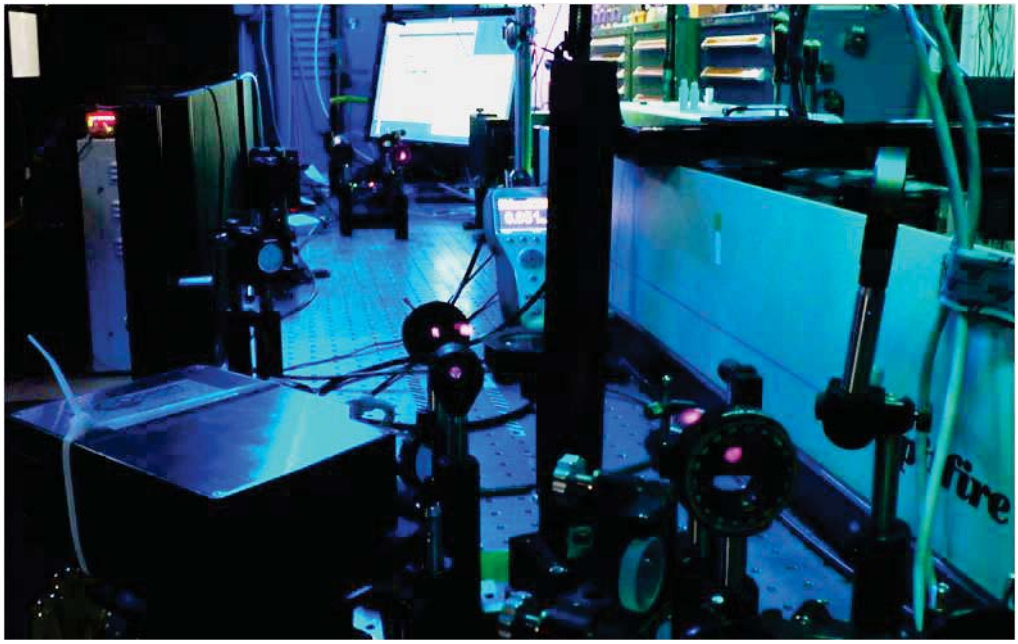

Figure 4. Pump-probe InP experiment. The 940 nm probe laser illuminates a sample while an 800 nm pump beam is passed through a computer-controlled delay leg before impinging on the sample.

For this experiment, a Ti:Sapphire laser with a regenerative amplifier created pulses that were used for both pump and probe (Figure 3). For the InP samples, an 800 nm beam was used for the pump; the beam was sent through an optical parametric amplifier (OPA), and the resultant 940 nm beam was used as the probe (Figure 4). The GaN experiments required higher-energy photons to excite the material, so a frequency doubler and tripler created a 400 nm probe and 266 nm pump, respectively. For each experiment, a computer-controlled delay leg adjusted the time at which the pump pulse would arrive at the sample, and the spectrometer recorded probe spectra at each length of delay. As such, the samples' responses were recorded as a function of delay time.

All of the materials studied were prepared for use in an etalon and made as thin as possible to maximize the areal density of created charge carriers, which maximizes the shift in the Fabry-Perot resonances. This has the added benefit of increasing the spread between each resonance. The undoped InP samples were solid, uncoated InP wafers from MTI-XTL and were thinned to 33 µm. The InP:S samples shattered while undergoing thinning to between 9 and 20 µm.

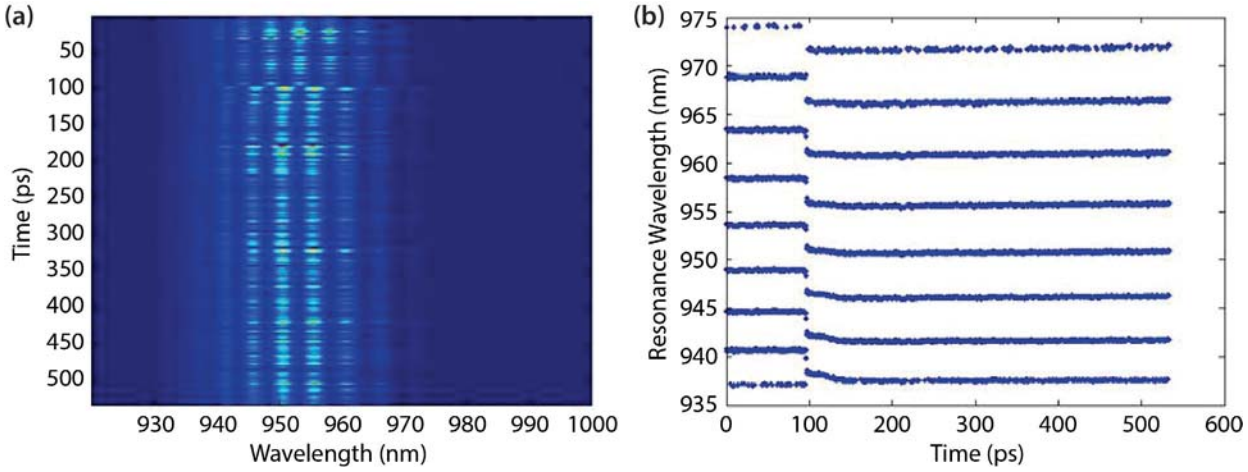

Figure 5. (a) A scan of the undoped InP Fabry-Perot cavity, with intensity displayed as color so the Fabry-Perot resonances can be viewed. The resonances are then extracted by a peak-finding algorithm and (b) displayed separately. The abrupt index change can be seen at approximately 100 ps in both plots.

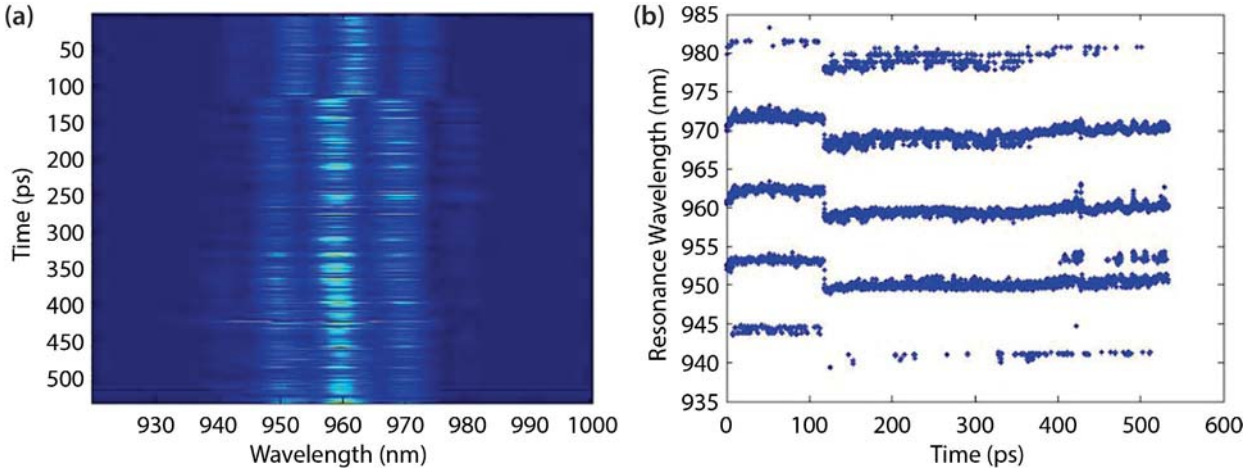

Figure 6. (a) A scan of the InP:S sample displays the same effect as the InP sample in Figure 5. The Fabry-Perot resonances (b) are spaced further apart due to differing sample thicknesses. The index change can be seen just after 100 ps in both plots.

As the experiment required approximately 1 mm^2 of material, the shards were still usable and so mounted inside 1-inch fender washers before being set in filter mounts. The GaN samples were epitaxially grown on a sapphire substrate (also purchased from MTI-XTL) and did not need to be thinned. The GaN and GaN:Mg layers were 5 µm and 3 µm thick, respectively. It is worth noting that epitaxially grown material exhibits a lattice mismatch between the grown GaN and the sapphire substrate (cubic lattice constants are 7.78 and 18.85, respectively, according to Akasaki (1997), which may create internal stresses that alter the material properties and performance.

The received signal depends on several parameters. The strength of the index change depends on the intensity of the pump beam, so the pump beam must be tightly focused. Because the probe detects the average change over the area of the beam, it was important to focus the probe beam with great care, as well as to precisely overlay it on the pump beam. The resolution

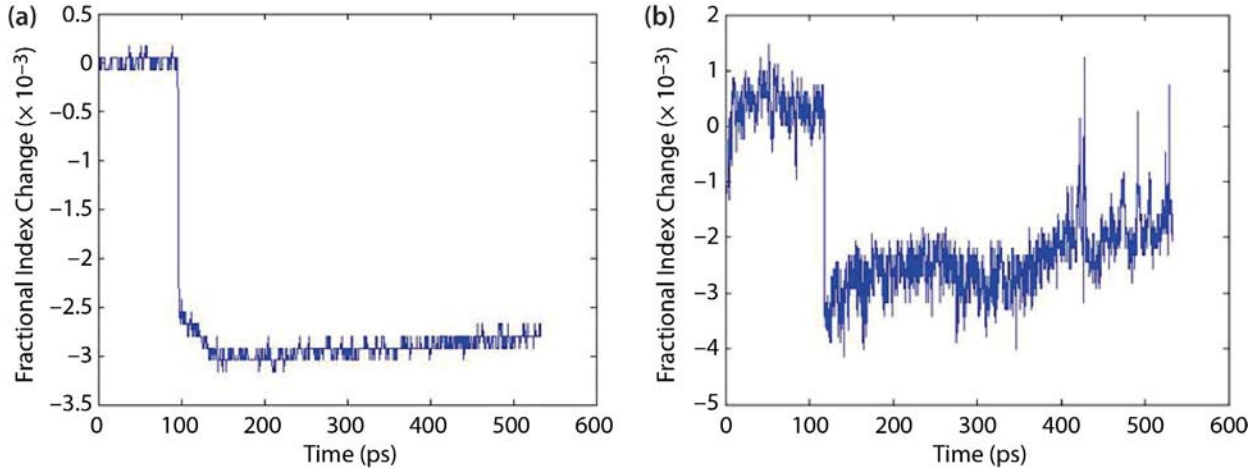

Figure 7. Fractional index change of (a) InP and (b) InP:S. A central Fabry-Perot resonance is selected, and the first 100 points are averaged to give a baseline value for the refractive index, which is then used to calculate the fractional index change $\delta n/n = \delta\lambda/\lambda$.

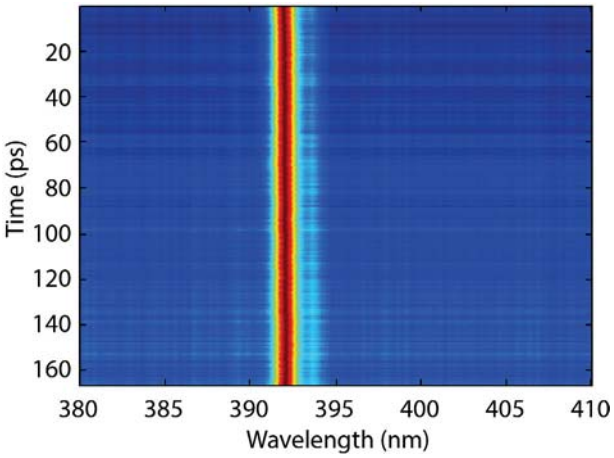

Figure 8. GaN:Mg data show that any index change is smaller than the spectral instabilities of the probe laser. Only one resonance peak (shown in red) is clearly visible, and we do not see a clear shift at any one time. While this material should have an index shift, energy density of approximately 1 μJ/mm² was not sufficient to produce it visibly, so this material is unlikely to be a good candidate for radoptic detection.

of the spectrometer is also a critical parameter. For the GaN samples, we had a free spectral range from 5 to 10 nm, with an initial spectrometer resolution of 0.2 nm, so there were only 25–50 pixels covering each resonance. Upgrading the spectrometer to one with resolution of 0.04 nm gave us 125–250 pixels in each free spectral range, allowing us to detect a much smaller shift.

For the InP samples, the full power of the pump laser was used; it measured around 360 μJ per pulse, 60 μJ of which was accepted into the 3 mm diameter iris, yielding 8.5 μJ/mm² impinging on the sample in each pulse. Unfortunately, the pump laser was not stable enough to observe a clean shift, so results for energy densities lower than 8.5 μJ/mm² are not included here. The spectrometer scans were overlaid, and a peak-finding algorithm was used to track the shift in the peaks (Figures 5 and 6). Finally, the fractional index shift ($\delta n/n = \delta\lambda/\lambda$) was calculated (Figure 7).

For the GaN and GaN:Mg samples, we used a pump laser wavelength of 267 nm, and the experiments were repeated on two occasions. For the first experiment, the energy was optimized for a 400 nm probe, but unfortunately no shift was observed. We believe that the lack of shift is a consequence of the coarse resolution of the spectrometer used. The second experiment employed the upgraded spectrometer, but unfortunately the laser had in the interim been tuned to 780 nm for other experiments, resulting both in lower conversion efficiency to second and third harmonics

(390 nm and 260 nm) and in unavoidable clipping of the beams within the tripler. It was difficult to measure the energy incident on the GaN and GaN:Mg samples, but the best estimate was less than 1 μJ for a spot size of 1 mm^2. This energy produced no detectable index change, or a shift that was smaller than the spectral instability of the probe laser (Figure 8).

This experiment would be greatly improved were we to use a beam splitter and a second spectrometer on the probe line to normalize output by input intensity. While a radiometer could accomplish this, the spectrometer would have the added advantage of being able to see additional spectral artifacts in the beam. Another improvement would be in sample preparation; epitaxially grown samples with distributed Bragg reflectors on each side would have enhanced the signal by using thinner material while increasing the sharpness and definition of the resonance peaks.

Conclusion

This SDRD effort investigated the suitability of four semiconductors for use as high-speed radiation-sensing devices: InP, InP:S, GaN, and GaN:Mg. The materials were thinned, polished, and tested in a pump-probe configuration. Index shifts were observed in the InP samples at 8.5 μJ/mm^2 but not in the GaN samples at approximately 1 μJ/mm^2. We intend to publish results in SPIE or IEEE conference proceedings. More materials research is needed to accurately predict the superior materials for radoptic sensors; however, much of the knowledge we obtained will improve fast x-ray detector design efforts. A portion of this research is being continued in conjunction with a hyperchromatic lens and plenoptic camera project, an FY 2014 SDRD effort (LAO-12-14, "Ultrafast All-Optical Framing Technology").

Acknowledgments

We would like to thank Steve Vernon and Rick Stewart for their help with radoptic theory, Susan Haynes for her laboratory wizardry, Dan Frayer for help with project management and organization, and Stuart Baker for help with project focus and consultation.

References

Akasaki, I., H. Amano, "Crystal growth and conductivity control of group III nitride semiconductors and their application to short wavelength light emitters," *Japanese Journal of Applied Physics* **36** (1997) 5393–5408.

Baker, K. L., R. E. Stewart, P. T. Steele, S. P. Vernon, W. W. Hsing, "Ultrafast semiconductor x-ray detector," *Appl. Phys. Lett.* **101**, 3 (2012) 031107.

Callan J. P., A. M.-T. Kim, C. A. D. Roeser, E. Mazur, "Ultrafast dynamics and phase changes in highly excited GaAs," in *Semiconductors and Semimetals, Ultrafast Physical Processes in Semiconductors,* Volume 67, K. T. Tsen, ed., Academic Press, London, 2001, 151–203.

Dvorak, M. D., B. L. Justus, "Z-scan studies of nonlinear absorption and refraction in bulk, undoped InP," *Opt. Commun.* **114**, 1–2 (1995) 147–150.

Gonzalez, L. P., J. M. Murray, S. Krishnamurthy, S. Guha, "Wavelength dependence of two photon and free carrier absorptions in InP," *Opt. Express* **17**, 11 (2009) 8741–8748.

Lowry, M. E., C. V. Bennett, S. P. Vernon, R. Stewart, R. J. Welty, J. Heebner, O. L. Landen, P. M. Bell, "X-ray detection by direct modulation of an optical probe beam—Radsensor: Progress on development for imaging applications," *Rev. Sci. Instrum.* **75**, 10 (2004) 3995–3997.

Martin, P., E. M. Skouri, L. Chusseau, C. Alibert, H. Bissessur, "Accurate refractive index measurements of doped and undoped InP by a grating coupling technique," *Appl. Phys. Lett.* **67**, 7 (1995) 881-883.

Pačebutas, V., A. Stalnionis, A. Krotkus, T. Suski, P. Perlin, M. Leszczynski, "Picosecond Z-scan measurements on bulk GaN crystals," *Appl. Phys. Lett.* **78**, 26 (2001) 4118–4120.

Pinos, A., S. Marcinkevicius, M. Usman, A. Hallen, "Time-resolved luminescence studies of proton-implanted GaN," *Appl. Phys. Lett.* **95**, 11 (2009) 112108.

Stanton, N. M., A. J. Kent, A. V. Akimov, P. Hawker, T. S. Cheng, C. T. Foxon, "Energy relaxation by hot electrons in n-GaN epilayers," *J. Appl. Phys.* **89**, 2 (2001) 973–979.

Ye, H., G. W. Wicks, P. M. Fauchet, "Hot electron relaxation time in GaN," *Appl. Phys. Lett.* **74**, 5 (1999) 711–713.

Ultrafast All-Optical Framing Technology

LAO-02-13 | Continued in FY 2014 | Year 1 of 2

Daniel Frayer[1,a]

Current methods of recording multiple-frame images at short time scales are limited by electro-optic tube physics and radiometry. This investigation sought an all-optical methodology for the capture of a high number of quasi-continuous effective frames of 2-D data at very short time scales, with improvement over existing framing camera technology in terms of short recording windows and number of frames. Our concept combines a chirped laser pulse that encodes temporal phenomena onto wavelength, a strong hyperchromatic lens to map wavelength onto axial position, and a recording technology, such as holography or plenoptic imaging, to capture the resultant images and their axial locations. A novel lens was designed to maximally separate focal position as a function of wavelength, and the fabricated lens assembly was qualified as meeting design requirements. Criteria were defined for characteristics of the input chirped pulse. An arrangement was made with Raytrix GmbH to obtain a customized plenoptic camera to optimally record spectral data and reconstruct temporal images. The work will continue in FY 2014 through a proposed experimental demonstration in collaboration with the University of Texas at Austin and investigation into new temporal and phenomenological regimes.

[1] frayerdk@nv.doe.gov, 505-663-2090
[a] Los Alamos Operations

Background

Currently, fast imaging at the nanosecond scale is accomplished using electro-optic tube framing cameras, multiple-camera systems, or electro-optic tube streak cameras. Each of these technologies is limited. Electro-optic tube framing cameras are limited by tube physics in terms of the number of frames, the integration time of each frame and the time between frames (both in tens of ns), and phosphor efficiency. Multiple-camera systems are limited in the number of frames and in corresponding radiometric efficiency. Streak cameras can obtain integration time and temporal resolution much better than either, but at the cost of an entire spatial dimension of data. There is currently no method for obtaining multiple-frame 2-D images at the nanosecond scale or shorter, so any attempt to obtain information on materials at these time scales is limited to exotic single-frame imaging or non-imaging methods.

An all-optical recording methodology, i.e., one that does not require conversion of signal photons to electrons, would not be subject to the restrictions imposed by electro-optic tube physics, and could demonstrate improved performance by several metrics: system efficiency, total recording time, and number of frames. However, phenomena that allow for fast manipulation of optical signals, such as the electro-optic Kerr and Pockels effects, while approaching nanosecond speeds, are insufficiently sensitive and cannot be utilized to produce a high number of frames. The proposed methodology employs an

ultrafast phenomenon in common usage, namely a laser pulse that has been dispersively lengthened such that wavelength is a function of time, i.e., chirped. Active illumination with such a pulse would effectively map time onto wavelength. The methodology incorporates a hyperchromatic lens, designed to maximize the change in the position of its focus as a function of incident illumination wavelength, to produce images of an object illuminated by the chirped pulse at differing axial locations (Novak 2005). Whereas the resulting axially stacked images would not be recordable using a standard intensity-recording camera, the methodology employs a depth-sensitive recording mechanism: either a vector-recording plenoptic camera to capture at once both the images in the volume and their relative positions within the volume or, alternatively, a holographic recording medium. A schematic of the proposed methodology is shown in Figure 1. Previous methodologies for high-speed data capture have acquired multiple images via mapping space onto time using wavelength and dispersion (Goda 2009) and continuous non-imaging data via encoding onto chirped pulses (Bolme 2007). Hyperchromats have recently been proposed in confocal microscopy and hyperspectral imaging (Hillenbrand 2012a, 2012b). However, no existing methodology employs chirped pulses to map 2-D imaging information onto color to produce continuous images of ultrafast events.

Project

The three components of the technology (lens, chirped laser, and recording system) followed three separate parallel paths of inquiry: (1) design of a hyperchromatic lens with maximal dependence of axial focal position on wavelength, representative magnification, and an appropriate design wavelength and minimal spectral width; (2) investigation into the availability of laser sources with appropriate center wavelength, spectral shape and width, and dispersed length; and (3) investigation into recording methods. Each of these three paths were expected to inform the others; e.g., limits on laser bandwidth at a given center wavelength might provide input criteria for longitudinal chromatic dispersion in the hyperchromatic lens design, and material and manufacturing constraints on optical elements might inform the search for existing lasers or new laser development. At the same time, the potential for experiments was investigated.

Design

Initial design requirements included a field of view of less than 5 mm, under the assumption that magnifying achromatic optics could be used to relay an image of an actual phenomenon of interest to the object plane of the hyperchromat, and a magnification of between 5x and 10x, to enable higher longitudinal chromatic dispersion while maintaining a reasonable

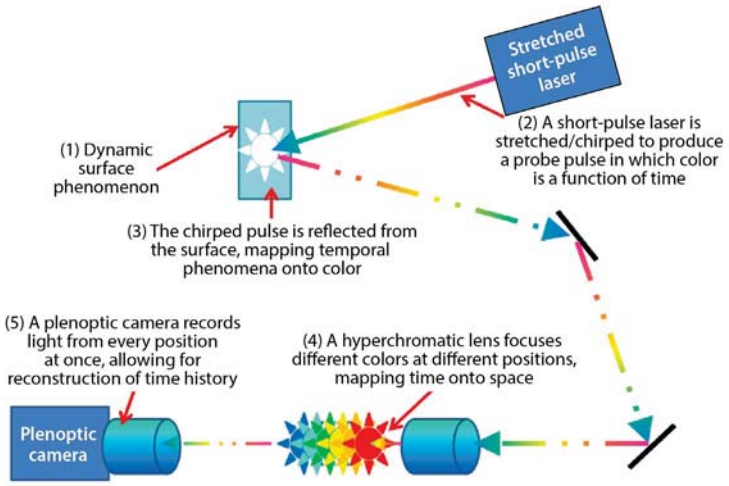

Figure 1. Proposed methodology as employed as an experimental diagnostic

final image size. Early designs employed only high material dispersion present in specialty glasses used to make refractive components, and converged on multiple-element telephoto-type configurations. The greatest achieved longitudinal chromatic dispersion using this approach was ~250 µm/nm, requiring 40 nm of incident illumination spectrum to achieve 10 mm of shift in the back focal plane with diffraction-limited imaging performance. This dispersion was considered too low for two reasons: namely, spectral bandwidth in laser pulses tends to be in the 1 to 10 nm regime, and plenoptic cameras were considered unlikely to resolve more than two frames in such a short image volume.

As such, we abandoned the refractive-only design and pursued a new design that incorporates hybrid diffractive components. Hybrid diffractive elements have at least one surface with a diffractive pattern that varies with position on the surface, thereby inducing change in the optical wavefront as a function of position. These diffractive patterns have significantly higher dispersion than even the highest dispersion glasses. Although they can induce arbitrary wavefronts, they are limited to relatively low power by manufacturing and material constraints, and so require additional refractive components. Communications with Apollo Optical Systems of West Henrietta, New York, resulted in iterative design changes to produce a hybrid diffractive element within manufacturability constraints.

Initially our design specified a 515 nm center wavelength, as this wavelength may be readily obtained in short-pulse lasers incorporating ytterbium dopants, while sufficiently avoiding the 532 nm light already employed in many optical systems, such as high-speed velocimetry. However, investigations into laser sources and potential experiments (as will be discussed below) led to a final design at 532 nm. The final design uses two identical custom diffractive elements that maximize dispersion within manufacturing constraints; these were designed to be fabricated from acrylic plastic and did not incorporate surfaces with refractive power. The final design resulted in a longitudinal chromatic dispersion of nearly 9 mm/nm, more than 30 times higher than that achievable with glass dispersion alone. As a point of reference, the optical system will spread the focal planes for the complete visible spectrum over more than 1.5 m of axial distance. The dispersion curve for the final system is shown in Figure 2, engineered to provide maximum and near-flat dispersion at 532 nm. The final optical design is shown in Figure 3. The optomechanical mounting hardware is shown in Figure 4.

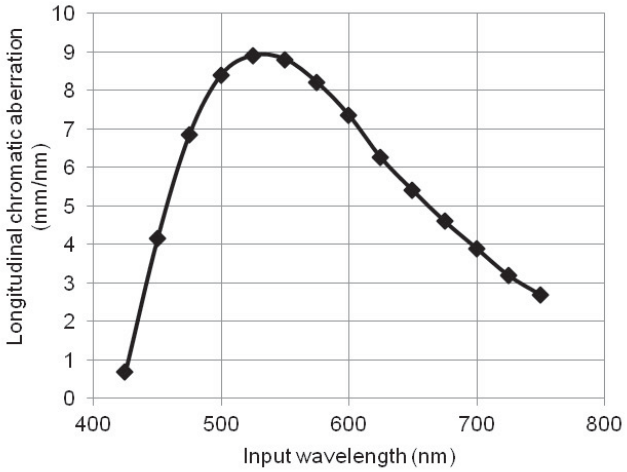

Figure 2. The dispersion curve for the final optical design provides maximum and near-flat dispersion at 532 nm

As expected from the refractive-only design, the final design has a telephoto configuration, with a first set of optical elements with total positive power, and a second set of elements with total negative power; the resulting magnification is –7.5 and constant for a bandwidth of 5 nm. The positive set of elements incorporates the two diffractive elements, each of which has a clear aperture of 25 mm and a focal distance of 106.4 mm, as well as the system aperture stop. It should be noted that although the system contains nine discrete optical elements, three of them have virtually no power. These three elements, as well as the remaining four non-diffractive elements, are menisci that minimize astigmatism induced by the diffractive elements. The final design provides near-diffraction-limited imaging, with a maximum optical resolution of approximately 53 line-pairs per mm (lp/mm) at 20%

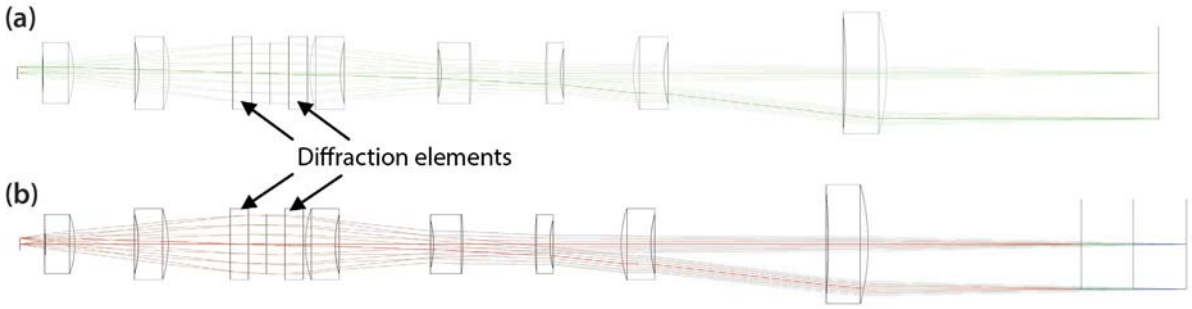

Figure 3. Final optical design, shown with (a) the center wavelength alone and (b) 5 nm bandwidth. Arrows indicate diffractive elements.

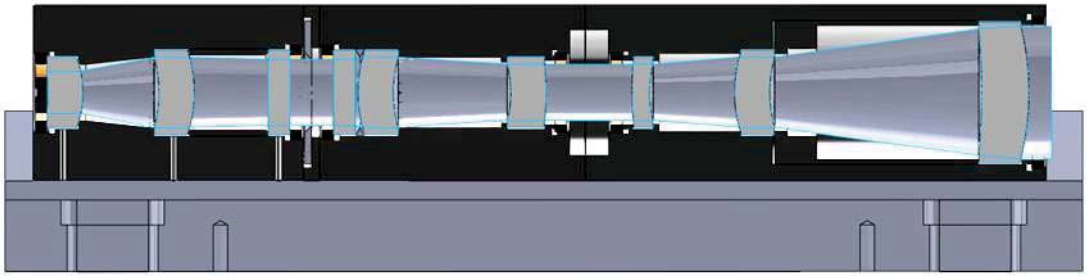

Figure 4. Optomechanical housing, with lenses indicated, designed to meet strict optical positioning and orientation tolerances while minimizing stray light reflections

contrast across the 5 nm bandwidth. A tolerancing analysis for manufacturing resulted in an expected maximum resolution of greater than 35 lp/mm.

The diffractive components for assembly were ordered from Apollo Optical Systems, and the refractive components from Optimax Systems, Inc., of Ontario, New York. The optomechanical housing for the components was ordered from Zero Hour Parts of Ann Arbor, Michigan. The lenses and housing were assembled at Los Alamos Operations. The final assembly was characterized for imaging performance and longitudinal chromatic aberration using a resolution pattern and multiple illumination sources: an incandescent source, both by itself and with multiple narrow-band filters, and a laser at 522.8 nm. A photograph of the bench-top setup as well as an image captured using broadband illumination and a diffuse reflector placed at a location of green focus are shown in Figure 5. Images were captured using a CCD camera. It should be noted that the camera lens used did not allow for focal adjustment, so the image on the right is defocused; the image at the employed wavelength was a negative image, and the camera could not be adequately positioned to account for this fact. As can be seen in Figure 6b, resolution element 5 in group 5 (with a resolution of 50.8 lp/mm) is clearly visible; however, the illumination source and the edges of the resolution pattern caused a high level of structured background noise (visible in Figure 6), rendering a quantified resolution limit difficult to obtain from the images. Nevertheless, it may be qualitatively stated that the assembly appears capable of imaging at near the diffraction limit and well above the toleranced-for and acceptable threshold. The positions of the various image planes matched those expected from the design, so the lens may be also qualified as meeting the designed longitudinal chromatic aberration.

Laser Illumination

We initially conceived of this imaging methodology as complementary to existing diagnostic techniques and at time scales relevant to experiments in shock and

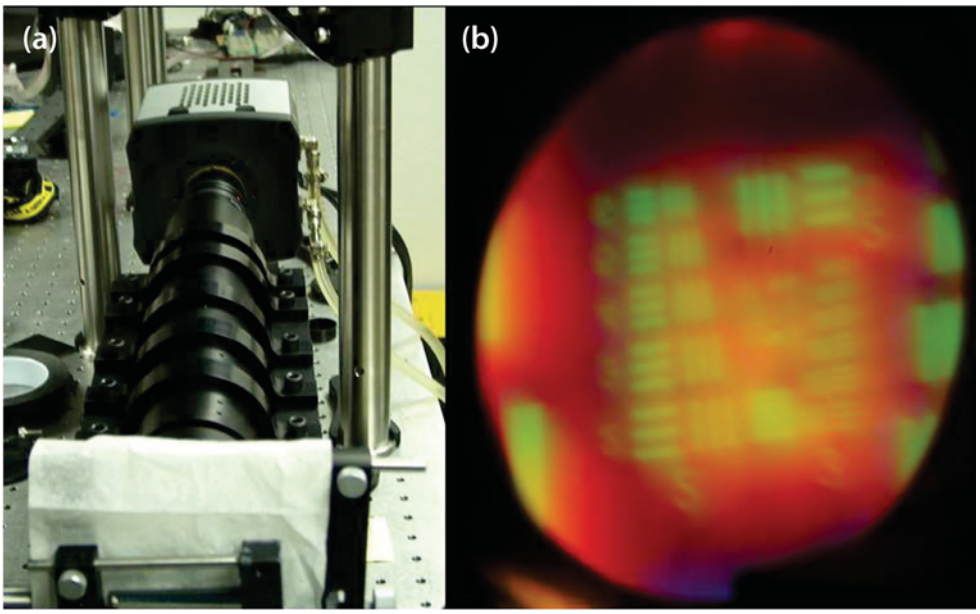

Figure 5. (a) Bench-top setup and (b) sampled broadband image. The broadband image was taken at the focal position for a specific wavelength in the green portion of the spectrum, while other portions of the spectrum are significantly defocused, their optimal focal positions lying elsewhere along the optical axis.

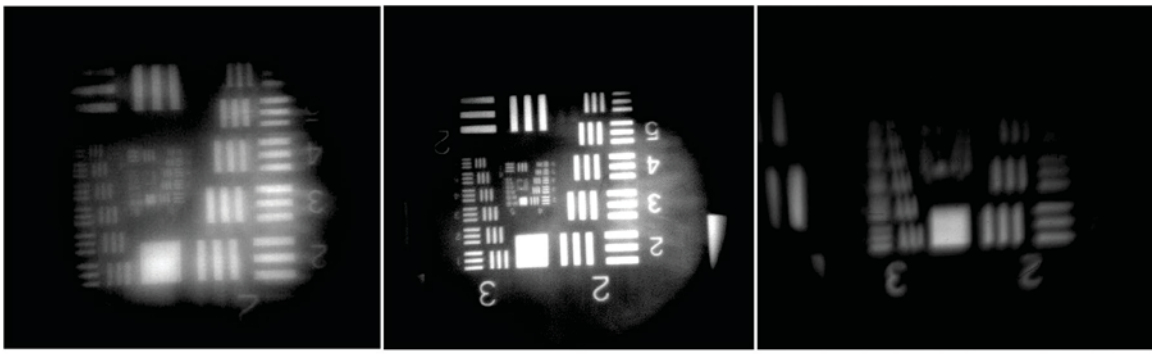

(a) Blue: 357.3 nm
Image at 990 mm

(b) Green: 522.8 nm
Image at 195 mm

(c) Yellow: 571.1 nm
Image at 0 mm

Figure 6. Images captured using different illumination wavelengths and camera positions indicate imaging performance and longitudinal displacement match the design model

dynamic materials. As the hyperchromatic lens and recording medium are agnostic to the dimension of time, recording length is determined entirely by the temporal characteristics of the illumination source. An investigation with the technical staff at Fianium Ltd., a maker of short-pulse fiber lasers, determined that their fiber laser technology could not be practically employed to produce pulses of the necessary length; fiber dispersion could not be employed because of high absorption in the visible spectrum, and grating dispersion could not be used because of the very large gratings necessary for chirping beyond 100 ps. An alternate approach using supercontinuum generation was also pursued, but it produced insufficient energy per pulse to be viable. For phenomena relevant to the <100 ps regime, electronic jitter in the timing and firing

system would render a stand-alone laser impractical, as the jitter would be at least as large as the temporal window of interest.

Discussions with multiple scientists at the University of Texas at Austin (UTA) provided a possible separate path for illumination. Several lasers on the UTA campus are used in ultrafast materials studies; for example, phenomena generated by pulses shorter than 200 fs incident on various materials are studied at the Petawatt laser facility. These lasers are occasionally split into pump/probe configurations—the pump beam is used to generate phenomena, while the probe beam may be independently timed, stretched, and frequency-doubled for diagnostic use. These lasers operate at 1064 nm, with probe beams capable of operating at a frequency-doubled 532 nm. Fielding a system based on this project's methodology on an experiment using a frequency-doubled, chirped probe beam to investigate phenomena generated by a 1064 nm pump pulse would experimentally validate the proposed methodology, while also being of significant interest to researchers at UTA. As mentioned above, system timing is determined only by the illumination signal. For an experiment involving phenomena generated by sub-picosecond pulses, a pump that is stretched to multiple picoseconds would exhibit a clean chirp, i.e., a pulse in which a single wavelength is only present at a given instant, providing data that are temporally non-convolved; as both pump and probe are split from the same beam line, no jitter would be present.

Other options for future development were also considered, as imaging diagnostics on ultrashort high-energy laser facilities is a small niche application. A total pulse with a clean chirp, of duration above 1 ns, could be achieved by a suite of short-pulse laser diodes of closely spaced wavelengths. This option would offer the advantage of arbitrary timing above a minimum floor, but also be disadvantaged by a small number of lasers and a relatively high floor, perhaps above 10 ns. A 1550 nm ultrashort pulse with high bandwidth could be chirped using low-loss optical fiber and then tripled. We must consider that any option for illumination that would allow this methodology to be used on nanosecond and greater time scales would require a significant future internal or external development effort.

Recording

The initial proposal for this research saw digital holography as the most likely recording means for the proposed methodology. Before the project began, however, it became clear that using holography would tightly constrain experimental design and require significant development of a reconstruction algorithm. At the same time, a new possibility emerged: commercially available plenoptic (or light-field) cameras. Plenoptic cameras employ image-plane lenslet arrays and considerable oversampling to achieve measurement of light as intensities and direction vectors, rather than merely intensity. Therefore, digital refocus of images, reconstruction of scenes in 3-D, and, to some extent, digital determination of the longitudinal position of a given object point are possible. Using a plenoptic camera would obviate the disadvantages of holographic methods. Such a camera from Raytrix GmbH of Kiel, Germany, was already in the possession of the Special Technologies Laboratory (STL). During June 2013, the camera was tested in multiple configurations to determine the viability of the camera in this project's methodology.

Initial tests, using a Nikon macro zoom lens, representative of the type required by the hyperchromatic lens, were performed with opaque objects separated longitudinally by less than the total image volume produced by the hyperchromat, and laterally so that one object did not obscure the other. The combination of the Raytrix camera and its reconstruction algorithm were determined to be unable to distinguish objects separated longitudinally by less than 1 mm. Another set of tests was performed using an optical setup that mimicked the image volume the hyperchromat would actually produce, namely a set of longitudinally stacked images, each of which do not obscure the information from any other. The setup used a beam splitter and identical resolution targets to allow the camera to see what appeared to be one resolution target in front of the other by an adjustable distance

but did not obscure it. The apparent longitudinal distance was varied between 1 and 50 mm. The reconstruction algorithm proved capable of digitally refocusing on one or the other, but could not determine the spatial separation quantitatively or even qualitatively, as its depth analysis function saw them both as existing at the same distance from the camera. As such, the off-the-shelf version of the camera and algorithm were deemed insufficient for adequate recording of the image volume produced by the hyperchromat. Discussions with the technical staff at Raytrix have led to the procurement of a version of their camera with customized lenslet array and customized reconstruction algorithm that will optimize it for the optical characteristics of the image volume produced by the hyperchromat, and allow for reconstruction of stacks of apparently transparent objects, two requirements for application to this project's methodology.

Conclusion

This project investigated a novel methodology for the capture of information from high-speed experiments. The methodology incorporates an optical illumination source for which wavelength is dependent on time, a hyperchromatic lens that images information at different wavelengths at longitudinally separated focal planes, and a recording methodology that allows for the capture of 3-D optical information. Optical design and assembly successfully produced a hyperchromatic lens that longitudinally displaces image planes by 9 mm/nm of incident illumination with near-diffraction-limited imaging performance. Illumination needs do not allow for recording over temporal windows of greater than 100 ps using commercially available light sources, but the methodology may be used for chirped probe beams generated in conjunction with pump beams at high-energy ultrashort laser facilities like those at UTA. The off-the-shelf version of the plenoptic camera produced by Raytrix, while capturing the relevant depth information, does not reproduce actual image depth, but the company is developing a customized version that will do this.

Future Development

This project has been awarded a second year of investigation. Several paths of inquiry should be pursued for further development. Using the procured customized camera, the entire system should be experimentally validated at a laser facility capable of the pump/probe generation capabilities discussed previously. Development of novel illumination sources, as proposed above, should be pursued to extend the usefulness of this methodology into longer time scales. Methods of mapping other types of information (including self-generated optical or x-ray radiation) should be investigated, as these may remove the limitations imposed by the need for active illumination.

Acknowledgments

We would like to thank Morris Kaufman and Jaylene Martinez (LAO) for optomechanical design support; and Rachel Haynes and Rod Tiangco (STL) for camera testing support; as well as the technical staffs of Fianium Ltd. and Raytrix GmbH, for their contributions to this work.

References

Bolme, C. A., S. D. McGrane, D. S. Moore, D. J. Funk, "Single shot measurements of laser driven shock waves using ultrafast dynamic ellipsometry," *J. Appl. Phys.* **102** (2007) 033513.

Goda, K., K. Tsia, B. Jalali, "Serial time-encoded amplified imaging for real-time observation of fast dynamic phenomena," *Nature* **458** (April 2009) 1145–1149.

Hillenbrand, M., B. Mitschunas, C. Wenzel, A. Grewe, X. Ma, P. Feßer, M. Bichra, S. Sinzinger, "Hybrid hyperchromats for chromatic confocal sensor systems," *Advanced Optical Technologies* **1**, 3 (2012a) 187–194.

Hillenbrand, M., A. Grewe, M. Bichra, B. Mitschunas, R. Kirner, R. Weiß, S. Sinzinger, "Chromatic information coding in optical systems for hyperspectral imaging and chromatic confocal sensing," *Proc. SPIE* **8550** (2012b) 85500D.

Novak, J., A. Miks, "Hyperchromats with linear dependence of longitudinal chromatic aberration on wavelength," *Optik* **116**, 4 (2005) 165–168.

This page left blank intentionally

Solid-State IR Fast Streak Based on Beam Deflection

SO-01-13 | Year 1 of 1

Amy Lewis,[1,a] Daniel Frayer,[b] Andrew Mead,[c] John E. Heebner,[d] and Susan M. Haynes[d]

The aim of this project was to develop a new, fast, solid-state photon-based deflector capable of 1 ns of record length and sensitivity at wavelengths above 900 nm for infrared imaging applications and infrared spectroscopy. The work leverages the Lawrence Livermore National Laboratory's serrated light illumination for deflection-encoded recording (SLIDER) deflector but improves upon its performance with a 6x record length. The experimental data indicate an effective sampling rate of 125 GS/s and a resolution of 60 ps. Modeling indicates the potential for improving this to 10 ps. Applications as a streak system or spectrometer are possible.

[1] lewisae@nv.doe.gov, 505-284-1417
[a] Sandia Operations; [b] Los Alamos Operations; [c] Livermore Operations; [d] Lawrence Livermore National Laboratory

Background

Near-IR measurements are important for pyrometry, streak, and spectrometry applications for dynamic temperature measurements and weapons component testing. Current streak technology suffers from poor quantum efficiency as a result of limited photocathode materials and poor responsivity in wavelengths above about 900 nm. Typical pyrometry measurements include 35 µs record lengths and 13 ns temporal resolution using indium antimonide and mercury cadmium telluride IR detectors combined with oscilloscope recording. Desire exists to increase the temporal resolution to better understand bulk temperature changes of dense materials experiencing shock-induced phase changes.

In 2010, a member of our project team, John Heebner (Sarantos 2010), demonstrated a novel optical deflection mechanism that could be used to deflect a beam of light at picosecond time scales. The deflection was based on the dynamic imprinting of prisms via nonlinear optical effects in a solid-state waveguide. Related previous attempts at this had failed largely because the traditional mechanisms used to deflect beams of light are either too slow (electro-optic, acousto-optic, liquid crystal effects) or too weak (Kerr effect). The team recognized that nonlinear optical effects in semiconductors can be strong and have fast rise times but are often overlooked for picosecond operation due to long recovery times dominated by electron-hole recombination. Rather than seeing this as an obstacle, the long persistence was turned into a feature by taking advantage of time-of-flight of the signal through the waveguide. With this implementation, the planar waveguide is instantaneously illuminated by a pump beam that is patterned with a sequence of prisms. The signal experiences a distributed deflection that is finely discretized over a large number of thin prisms. Because the prism array is created while the signal is in transit through it, later portions of the signal propagate through more prisms. The signal thus deflects in linear proportion to its time delay. The swept beam is then focused onto a conventional camera that records the spatially swept representation of the temporal signal. The serrated light illumination for deflection-encoded recording (SLIDER) achieved a 1 ps resolution over a record length of 100 ps. For applicability to streak applications, longer record lengths would be necessary.

Project

In discussions between National Security Technologies, LLC, and Lawrence Livermore National Laboratory (LLNL), multiple novel approaches for extending the record from 100 ps to 1 ns were developed and considered based on technical feasibility and project risk. These approaches and considerations are summarized and compared with option 1, the baseline SLIDER approach, in Table 1. In the baseline approach, a 100 fs pump pulse instantaneously excites electron-hole pairs, which remain excited for many nanoseconds, creating a change in the refractive index that activates all the prisms simultaneously for the duration of the sweep. Distributed deflection is achieved simply through time-of-flight, as the early part of the record traverses the waveguide without seeing many prisms activated by the pump while the later part experiences all of them activated. As a result the length of the chip practically limits the record length to approximately 100 ps. In option 2, a single prism deflector has an index response that is directly proportional to the intensity, as opposed to integrating. This sounds attractive, but a single thin prism cannot provide many waves of tilt before the index saturates, limiting the number of resolvable spots. Option 3a requires a triangular pulse and an instantaneous material response, both requirements presenting practical implementation challenges. Option 3b requires a prescribed (exact) material response time that is difficult to engineer. For this effort, we selected option 3c, a traveling wave SLIDER deflector. An ideally flat, long pump excites the electron-hole pairs, effectively ramping up the index in a linear manner continuously. Many prisms are used to achieve the deflection, but they are synchronously turned on as the signal front passes through the device. Thus, this mechanism behaves like the single prism option, but one in which the tilt contributions from all of the prisms are cumulatively added.

Novel Extension: Traveling Wave SLIDER Mechanism

Approaches 3a, 3b, and 3c differ from option 1, baseline SLIDER, in pumping methodology. Approach 3c was agreed upon as presenting the highest technical feasibility and lowest risk. The associated methodology is illustrated in Figure 1. Our pump geometry sought

Table 1. Technical approaches and considerations (SLIDER variants targeting 1 ns record with 10 ps resolution)

		Record limit	Pump pulse space-time profile	Pump pulse temporal profile	Index (Carrier) Recovery time
1	**Baseline SLIDER** Short pump + time-of-flight through prism array	100 ps limited by chip length	Normal, no skew required	Short pulse < 1 ps	No material conditioning required $\tau_{RC} > \Delta t_{record}$
2	**Single prism** with increasing index	10 ps limited by carrier saturation	Normal, no skew required	Stretched pulse ~ 1 ns	No material conditioning required $\tau_{RC} > \Delta t_{record}$
3a	**Traveling wave SLIDER** Pump driven directly	Controlled directly by pump	Space-time skew required for traveling wave	Stretched, shaped (triangular ramped) pulse ~ 1 ns	Material conditioned fast $\tau_{RC} < \delta t_{resolution}$
3b	**Traveling wave SLIDER** Material recovery driven	Controlled directly by material recovery	Space-time skew required for traveling wave	Short pulse < 1 ps	Recovery set precisely $\tau_{RC} = \Delta t_{record}$
3c	**Traveling wave SLIDER** Pump driven indirectly	Controlled indirectly by pump + integrating response	Space-time skew required for traveling wave	Stretched pulse ~ 1 ns	No material conditioning required $\tau_{RC} > \Delta t_{record}$

Red: Completely novel; higher project risk
Yellow: Increased complexity; risks mitigated by prior experience or effort
Green: Previously demonstrated; manageable complexity

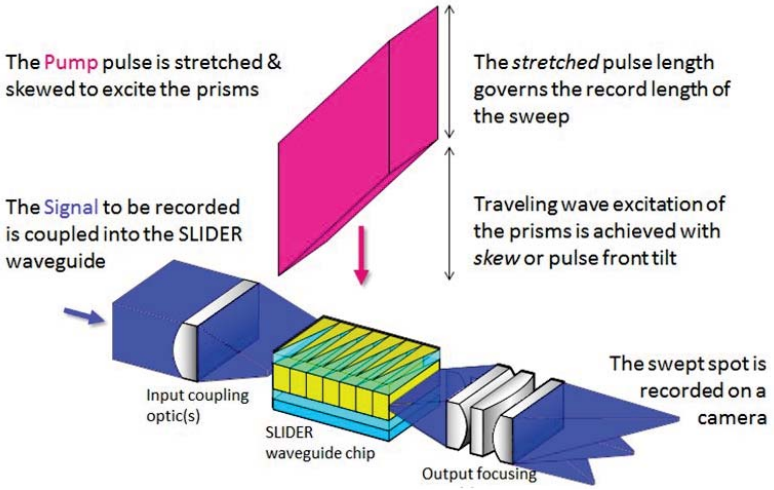

Figure 1. Our traveling wave SLIDER mechanism design would extend the SLIDER record length at least six-fold, from 100 ps to at least 600 ps

to extend the SLIDER record length at least six-fold, from 100 ps to at least 600 ps. In the illustration, the signal to be recorded (blue) is coupled through a cylindrical focusing lens into the guiding layer of a planar waveguide. While the signal is in transit through the waveguide, an array of prisms is imprinted in the guiding layer by illuminating from the top with a specially formatted pump laser pulse. This pump pulse is stretched in time to 1 ns and skewed to ensure that the leading edges of the signal and pump pulse travel down the waveguide with the same velocity. The pump pulse first passes through a lithographically defined pattern of prisms on top of the upper cladding layer of the waveguide chip. The inverse pattern is then effectively imprinted in the guiding layer through refractive index changes caused by the excitation of electron-hole pairs. These changes are cumulative, resulting in a series of effective prisms with a refractive index that varies monotonically in time.

Modeling

To assess the predicted performance of the traveling wave SLIDER concept, multiple models were constructed for the various subsystems required to participate in an experiment. To predict the required pump fluences and energies required to drive the SLIDER deflection, we leveraged previously developed simulations that were anchored to experiments. To model and design a stretcher for extending the pulse width of a pump pulse from 100 fs to 1 ns, we used an analytic model based on Treacy's (1963) formulation. Finally, to model the creation of a pulse-front tilt or skew that would lead to a traveling wave synchronization of the signal and pump, we implemented both analytic expressions and a 1-D space + time splitstep beam propagation simulation. The results of these models were used to inform the design and procurement of components for a proof-of-concept experiment.

Proof-of-Concept Experiment

To test the new SLIDER concept, we implemented a previously fabricated planar waveguide consisting of a gallium arsenide (GaAs) guiding layer surrounded by aluminum gallium arsenide (AlGaAs) cladding layers. Figure 2 illustrates the experimental beam-path architecture. A Ti:Sapphire regenerative amplifier provided a 150 fs pump pulse that was split and used to create (1) the SLIDER prisms (at 800 nm or any absorbing wavelength below the GaAs band edge of 870 nm) and (2) a test signal. The pump was stretched in time by 4 orders of magnitude from 100 fs to 1 ns using a double-pass, two-diffraction grating arrangement. It was then flattened spatially from a Gaussian beam to a circular flat-top pulse using an off-the-shelf multi-element aspheric lens system. Finally, it was tilted across space and time by diffracting from a grating in the Littrow configuration and imaged onto the top surface of the SLIDER chip.

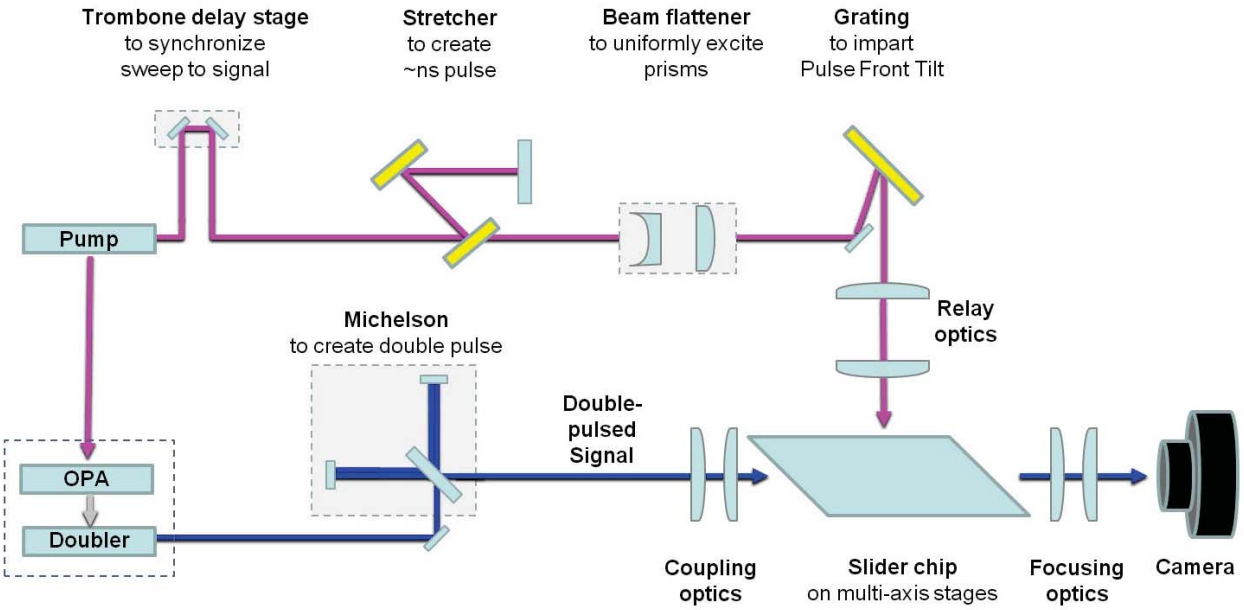

Figure 2. The experimental beam-path architecture, showing the pathways for the SLIDER pump beam (upper, magenta) and test signal beam (lower, blue)

The signal was created using an optical parametric amplifier (OPA) and an interferometer. The OPA was pumped with a portion of the beam from the regenerative amplifier, and used to generate a 1880 nm idler beam. The idler beam was subsequently frequency doubled to 940 nm to allow transmission through the GaAs waveguide. The 940 nm signal was then passed through a Michelson interferometer in order to create a double-pulse test pattern with a relative delay of 500 ps. Figure 3 shows overlaid oscilloscope recordings of the pump and signal waveforms.

Expected Results

We first recorded the signal and pump pulses on a conventional oscilloscope. Recording the dual signal pulses on an oscilloscope was useful for calibrating the relative delay between the pulses. Recording the pump pulse was useful for adjusting the grating separation in the stretcher. Moving on to the traces on the camera, upon adjusting the delay between the pump and signal pulses, we expected to see the two pulses overlap at the start of the record (prior

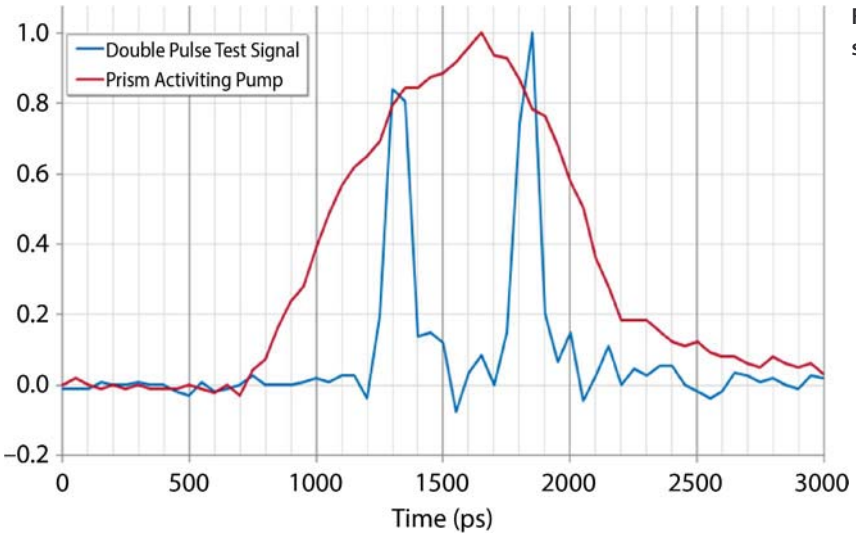

Figure 3. Oscilloscope traces for the stretched pump and test signal pulses

to the arrival of the pump pulse), then be separately resolved, and finally overlap at the end of the record. As the pulses are deflected, an overall attenuation was also expected as the creation of electron-hole pairs is accompanied by free-carrier absorption.

Figure 4 shows the recorded data in the form of signal versus time, for varying delays between the pump and signal beams. The first trace at 0 ps offset between pump and signal clearly shows that both pulses overlap at the start of the record. In subsequent traces, the later pulse separates from the earlier one, becoming individually resolved. The spot fidelity is compromised in the experiment due to the presence of a pedestal and ghost reflection. The pedestal results from imperfections in both the incoming beam and the waveguide facet that scatters light prior to the lenses that focus it on the camera's focal plane array. The ghost overlapping with the start of the record results from double-bounce reflections from the two end facets. An improved focal spot fidelity could be achieved by spatially filtering the signal beam and improving the cleaves on the end facets of the waveguide. Anti-reflection-coated end facets could remove the static ghost.

Additional development is needed for the implementation of this approach in an actual diagnostic instrument. The complexity, size, and cost of the pump laser system needs to be reduced, perhaps by way of a compact fiber laser. Additional improvements as mentioned above are required to bring the temporal resolution to 100:1 from the current 10:1. An imaging instrument would require significant research in manufacturing waveguides that are stacked vertically and in simultaneously pumping them. Any application imaging broadband signal light would require a substantial effort in optical engineering and/or material science to mitigate time-dependent chromatic aberration induced by the dispersion in the refractive index of the prisms. A spectroscopic application would require the least development and may be considered the most promising potential application. Such an instrument could be achieved with the incorporation of a grating downstream of the deflector to separate wavelengths orthogonally to the sweep axis, thus negating the need for multi-waveguide development and a dispersion-correction apparatus.

Conclusion

This project resulted in the identification of a novel prism excitation mechanism for beam deflection that enables extension of the original SLIDER concept to longer record lengths. An experimental validation was performed. A 6x increase in record length was achieved. The data indicate an effective sampling rate of 125 GS/s and a resolution of 60 ps. Modeling

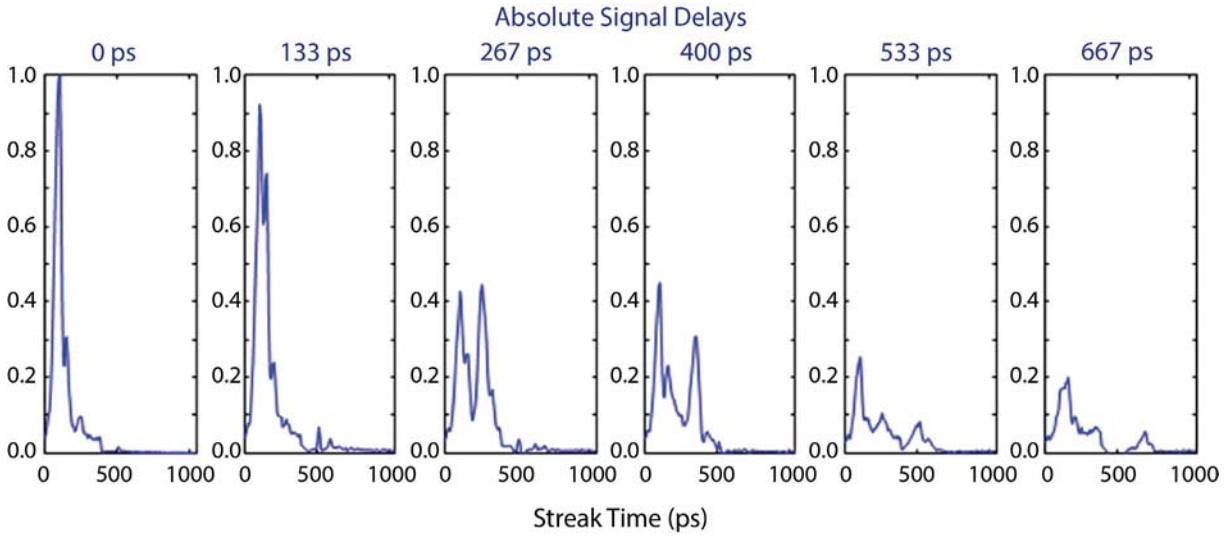

Figure 4. Recorded deflection data, showing the record length extension to 600 ps

indicates the potential for improving this to 10 ps. Applications as a streak system or spectrometer are possible. Additional work is required to convert the lab demonstration into an instrument.

Acknowledgments

Our project team would like to acknowledge LLNL's prior contribution to this technology and use of the hardware and facilities from the existing design.

References

Sarantos, C. H., J. E. Heebner, "Solid-state ultrafast all-optical streak camera enabling high-dynamic-range picosecond recording," *Opt. Lett.* **35** (2010) 1389–1391.

Treacy, E. B., "A 21-centimeter traveling-wave maser," Technical Report No. 401, Cruft Laboratory, Harvard University, Cambridge, Massachusetts, January 22, 1963.

Appendix

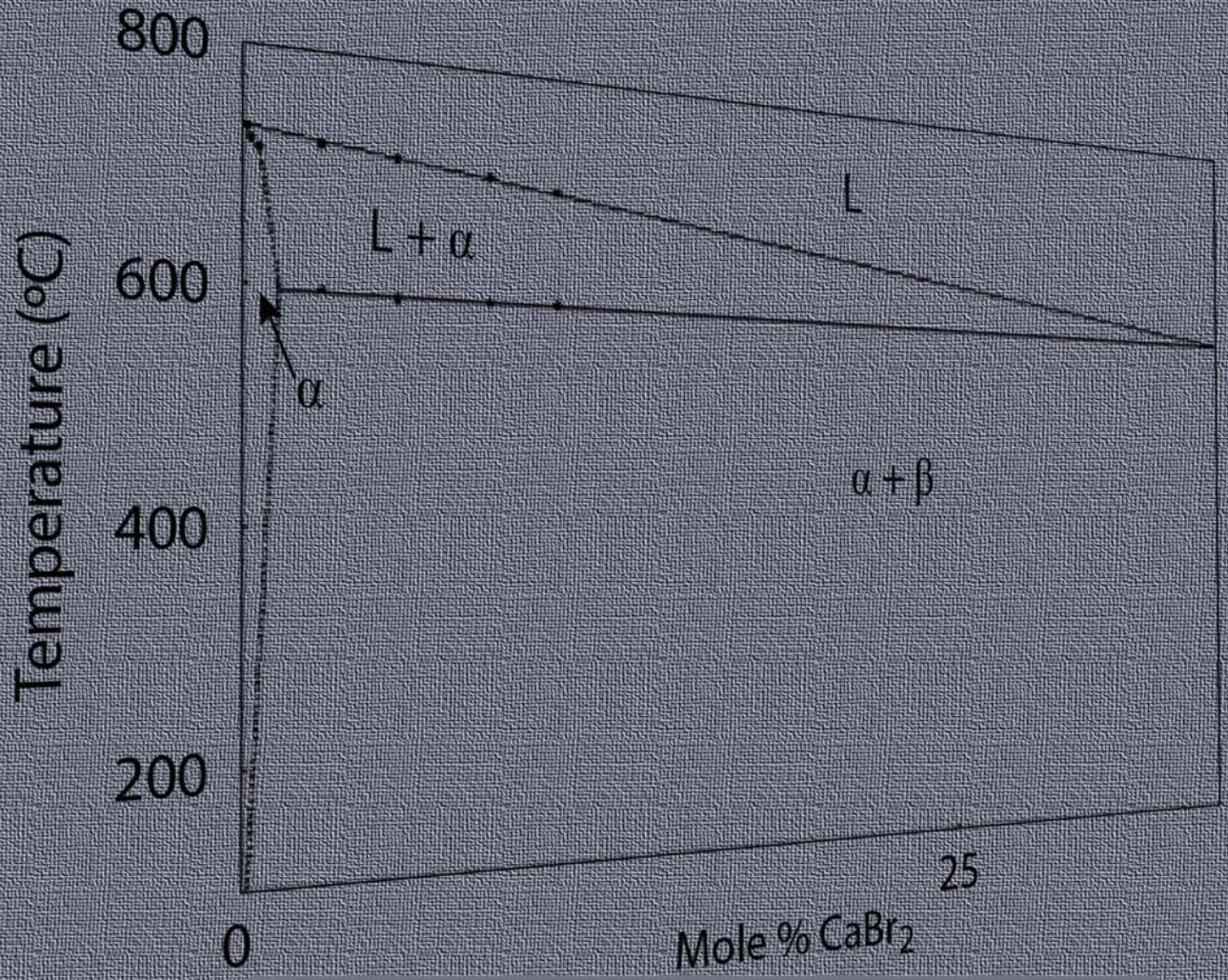
800
600
400
200
Temperature (°C)
L
L + α
α
α + β
0
25
Mole % CaBr2

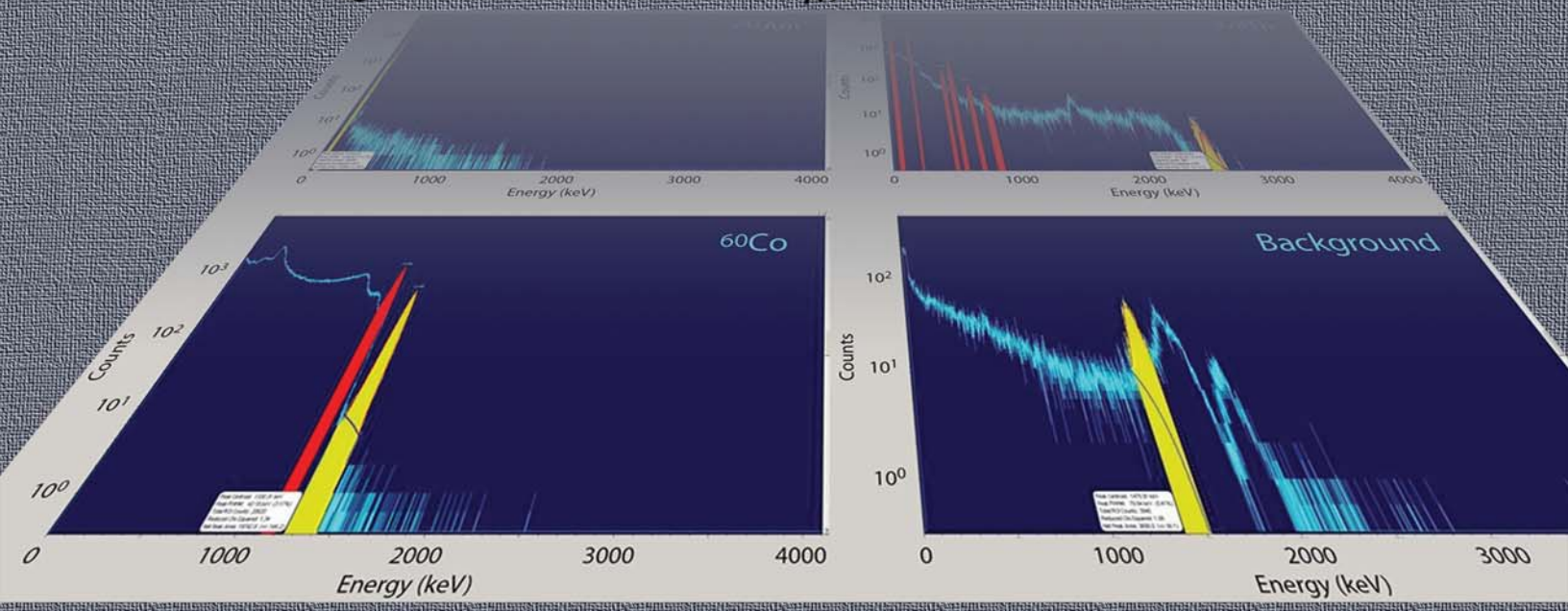
60Co
Background
Counts
Energy (keV)
0
1000
2000
3000
4000

Low-Cost Cerium Bromide Alloys

RSL-08-12-13 | Continued from FY 2012 | Year 2 of 2 Addendum

Paul Guss,[1,a] Thomas Stampahar,[a] Michael E. Foster,[b] Bryan M. Wong,[b] F. Patrick Doty,[b] Pin Yang,[b] Kanai Shah,[c] Michael R. Squillante,[c] Urmila Shirwadkar,[c] Rastgo Hawrami,[c] Josh Tower,[c] Sanjoy Mukhopadhyay,[d] and Ding Yuan[e]

During FY 2012 the Remote Sensing Laboratory (RSL) developed an aliovalently calcium-doped cerium tribromide crystal with 3.2% resolution. This short extension project, completed in FY 2013, allowed RSL to complete the crystal assessment and enabled Sandia National Laboratories to calculate predictive performance and physical characteristics using a proven density functional theory formalism for a less dilute doping (original crystal cracked due to too much calcium). Results are reported for the work done to map the detector performance, characteristics, calcium doping concentration, and crystal strength.

[1] gusspp@nv.doe.gov, 702-295-8095
[a] Remote Sensing Laboratory–Nellis; [b] Sandia National Laboratories; [c] Radiation Monitoring Devices, Inc.;
[d] Remote Sensing Laboratory–Andrews; [e] North Las Vegas

Background

In September 2012 Dynasil Radiation Monitoring Devices, Inc. (RMD), prepared an aliovalently calcium-doped cerium tribromide ($CeBr_3$:Ca^{2+}) crystal according to careful theoretical modeling and delivered the crystal to the Remote Sensing Laboratory (RSL) for assessment and evaluation (Figure 1). $CeBr_3$:Ca^{2+} has a hexagonal crystal structure identical to uranium trichloride (UCl_3). Hexagonal crystals may fracture easily; therefore, their manufacturing yield may be low, making the reliability of large crystals questionable (Doty 2007, 2011). Significant gains in the practical scale for $CeBr_3$ scintillators may be realized by increasing fracture toughness of the crystals (Guss 2013). Aliovalent substitution, in which a host ion is replaced with an ion of different valence (e.g., Ca^{2+} for Ce^{3+} in $CeBr_3$) is a more potent method of strengthening than isovalent substitution (i.e., replacing a fraction of ions with like-valence ions). In this approach, the formation of intrinsic defects necessary to maintain charge neutrality results in complexes with long-range interactions in the crystal. The resulting increase in hardening rate can be explained in terms of elastic interaction with dislocations (Pletka 1977).

Because $CeBr_3$ already exhibits superior scintillation characteristics (Shah 2005), the alloying element(s) used to strengthen the crystal must not degrade the scintillation properties. Aliovalent alloying provides more strengthening than isovalent alloying. The solid solution strengthening based on lattice distortions due to some small concentration of dopant can be approximated as

$$\tau = \gamma \cdot G c^{1/2}, \quad (1)$$

where G is the shear modulus, c is the concentration of solute in atomic fraction, and γ is a proportionality constant (Courtney 2000, Harrison 2010). For spherically symmetric distortions, such as those found in isovalent alloying, γ typically takes on values that are significantly smaller than unity, on the order of 10^{-4} to 10^{-6}. For tetragonal lattice distortions, such as those

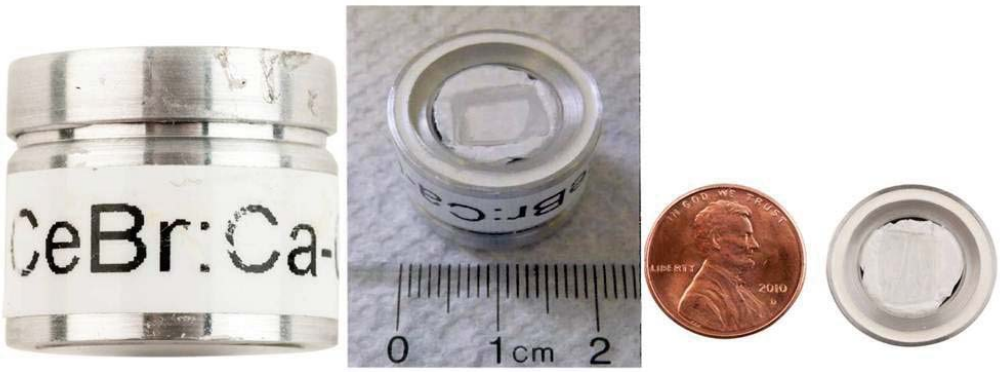

Figure 1. Packaged scintillator of 1.9% Ca^{2+}-doped $CeBr_3$

created from solute atoms of a different valence, γ can be nearly unity. Therefore, aliovalent alloying is more effective for a given concentration of solute (Harrison 2010).

Electronic valence effects exert a powerful influence on material and optical properties. In particular, aliovalent substitution has improved a variety of technologies, such as gadolinium titanate ($Gd_2Ti_2O_7$) ion conductors for solid fuel cells; gallium indium oxide ($GaInO_3$) transparent conductors for solar cells; rechargeable batteries; thermoelectric devices; lead zirconate titanate ($Pb[Zr_{(x)}Ti_{(1-x)}]O_3$), or piezoelectric ceramics; and cubic zirconium dioxide (ZrO_2) crystals. Among scintillating materials, $CeBr_3$ single crystals have shown superior scintillating properties, and large $CeBr_3$ crystals critically enable improved identification of radioisotopes. Unfortunately, fracture during synthesis complicates the growth of $CeBr_3$ crystals in sizes large enough to be used to identify radioisotopes. Aliovalent substitution may strengthen the material without significantly degrading the scintillating properties (Harrison 2010). An optimized material design, however, has not been achieved due to a large number of possible aliovalent combinations. Most empirical atomistic simulations can approximately account for charge variation but not electronic valence effects. These simplistic simulations cannot correctly reveal aliovalent phenomena such as the valence-compensating interstitials or vacancies.

From a theoretical point of view, one would like to explore a computational design beforehand to predict the effect of aliovalent doping on the mechanical and optical properties of these materials before they are used in experiments. Wong (2009, 2010) showed in previous theoretical studies that first-principles-based approaches were necessary to accurately predict effects due to defects and radiation. Although there has been great progress in resolution-of-the-identity techniques for computationally intensive coupled cluster methods, these wavefunction-based approaches are still computationally much more demanding than density functional theory (DFT) methods. Our DFT results for both the pure $CeBr_3$ primitive cell and the (divalent) calcium-doped "supercell," which includes 200 atoms and well over 1000 electrons, were based on spin-polarized, generalized gradient approximation (GGA) methods (Perdew 1996, 1997; Hua 1997) using Projector-Augmented-Wave (PAW) pseudopotentials (Blöchl 1994, 2001). It was discovered that the inclusion of a Hubbard U DFT correction (Anisimov 1991, 1997; Kulik 2008), often denoted as DFT+U, was essential for obtaining accurate band structures and band gaps. Within the Hubbard DFT approach, an onsite penalty function is placed on the *f* electrons for each of the cerium (Ce) atoms to prevent spurious over-delocalization of the electrons.

Theoretical Background

Based on the Hohenberg-Kohn theorem (Hohenberg 1964), which relates electron densities with the external electrostatic potential, DFT can be applied to any quantum-mechanical situation. As is the case for all DFT formalisms, i.e., for both orbital-free DFT and the Kohn-Sham orbital-dependent approach used here (Kohn 1965, Kümmel 2008), this limitation arises from approximations to the (still unknown) exact exchange-correlation functional. As shown by several groups including ours, the use of

conventional exchange-correlation functionals results in severely underestimated band gaps and incorrect asymptotic potential energy surfaces resulting from electron-transfer self-interaction (Li 2007, Wong 2010). The conventional approach for handling these systems (at least for molecules) is to use Møller-Plesset perturbative theory (MP2) (Møller 1934) in conjunction with highly correlated coupled-cluster singles and doubles plus perturbative triples method (CCSD(T)) to estimate electronic energies (Valeev 2008). However, the computational cost of CCSD(T) methods (Mackie 2011) is too high for routine application to molecules larger than about 30 atoms. Recognizing the shortcomings of conventional functionals, major methodological progress has been made in DFT techniques, which incorporate a strong intra-atomic interaction in a (screened) Hartree-Fock-like manner, as an onsite replacement of GGA (Perdew, 1996, 1997; Hua 1997). The DFT results for both the pure $CeBr_3$ primitive cell and the (divalent) Ca^{2+}-doped supercell were based on spin-polarized, GGA methods using PAW pseudopotentials (Blöchl 1994) calculated by the Vienna Ab-initio Simulation Package (VASP) (2012). The inclusion of a Hubbard DFT correction was essential for obtaining accurate band structures and band gaps (Guss 2013). This formalism is essential for the Ce-based materials studied here, as conventional GGAs fail to describe systems with localized (strongly correlated) *d* and *f* electrons, which manifests itself in the form of unrealistic one-electron energies due to spurious self-interaction. This rotationally invariant approach has been further modified and applied in many forms by Liechtenstein (1995) and Dudarev (1998) and used here.

Project

Calculations

Our DFT results for both the pure $CeBr_3$ primitive cell and the (divalent) calcium-doped supercell were based on the Perdew-Burke-Ernzerhof (PBE) GGA functional using PAW pseudopotentials. The PBE GGA is used for the exchange and correlation correction (Blöchl 1994, 2001; Perdew 1996, 1997). Inclusion of a Hubbard DFT+U correction for the *f*-electrons on Ce was essential for obtaining accurate band structures and band gaps. Within the Hubbard DFT approach, an onsite penalty function is placed on the *f*-electrons for each of the Ce atoms to prevent spurious over-delocalization of the electrons. Geometry optimizations of both the ions and the unit cell were carried out. In the point-defect calculations, a large 3 × 3 × 3 supercell was used; therefore, a smaller 2 × 2 × 2 gamma-centered Monkhorst–Pack grid (Monkhorst 1976) was used. Using the converged geometry, we then evaluated the cohesive energy (E_{coh}) of the calcium-doped $CeBr_3$ material. E_{coh} is defined as the energy required to break the atoms of the solid into isolated atomic species, a measure of the strength of the material. E_{coh} is given by

$$E_{coh} = E_{solid} - \sum_i E_i^{atom}, \quad \textbf{(2)}$$

where the summation index, i, represents all the different atoms that constitute the solid. For the calcium-doped 3 × 3 × 3 $CeBr_3$ supercell, we obtained a cohesive energy of –3.66 eV/atom. The electronic structures and optical properties of both the undoped and the calcium-doped $CeBr_3$ crystal may be derived using a k-point grid generated according to the Monkhorst–Pack scheme (Monkhorst 1976), for sampling of the Brillouin zone (Brillouin 1930). The optical properties of $CeBr_3$ can be determined by the frequency-dependent dielectric function $\varepsilon(\omega) = \varepsilon_1(\omega) + i\ \varepsilon_2(\omega)$ that is mainly connected with the electronic structures. The imaginary part $\varepsilon_2(\omega)$ of $\varepsilon(\omega)$ may be calculated from the momentum matrix elements between the occupied and unoccupied states within selection rules:

$$\varepsilon_2(\omega) = [2e^2\pi/(\Omega\ \varepsilon_0)]\ \Sigma_{k,v,c}\ |\langle \Psi^c{}_k | \hat{u}\cdot r | \Psi^v{}_k \rangle|^2 \times \delta(E^c{}_k - E^v{}_k - E), \quad \textbf{(3)}$$

where ω is the light frequency, and e is the electronic charge. $\Psi^c{}_k$ and $\Psi^v{}_k$ are the conduction and valence band wavefunctions at k, respectively. The real part $\varepsilon_1(\omega)$ of the dielectric function $\varepsilon(\omega)$ can be derived from the imaginary part $\varepsilon_2(\omega)$ using the Kramers–Kronig dispersion equation. Other constants can be derived from $\varepsilon_1(\omega)$ and $\varepsilon_2(\omega)$ (Saha 2000, Li 2007).

Structure Determination and Electronic Properties

We have carried out a series of DFT calculations taking into account both ferromagnetic and antiferromagnetic behaviors, and we also performed a high-level calculation (using the HSE06 hybrid functional) (Heyd 2003, Krukau 2006) to understand and predict the band gap of this material. The energy band structure, shown in Figure 2, is calculated along the path that contains the highest number of high-symmetry points of the Brillouin zone, namely Γ → A → H → K → Γ → M → L → H. Our structures are in reasonable agreement with experiments (Zachariasen 1948a, 1948b; Sato 1976; Park 1993). The zero energy is set to the Fermi level (Kittel 1980). The lowest bands around −36 eV consist of *5s* states of Ce. The Ce *5p* states are located at around −19 eV. The bands around −16 eV are derived from the *4s* states of bromine (Br). The energy bands in the range from −6 to −2 eV correspond to the *4p* states of Br that decide the top of the valence band. There are more peaks near 2 and −18 eV for the pure $CeBr_3$ supercell. Results are in agreement with $CeCl_3$ data. Above the Fermi level, the conduction band consists of the *4f* and *5d* states of Ce. The *4f* states have a sharp peak due to the strong localization character of the *4f* states. If the *4f* electron is kept in the core, the calculated result agrees with other experiments (Skorodumova 2001, Li 2007).

In addition, a partly filled *f* band situated right at the Fermi level was found. This discrepancy from an experiment by Park (Park 1993, Vetere 2000) may arise from the different treatment method of the *4f* states of Ce. If the *4f* electron is kept in the core, the calculated result was found to be in agreement with the experimental results (Skorodumova 2001). Otherwise, because of the localized character of the *f* states, the unpaired electron cannot lead to metallic behavior, with its effective mass tending toward infinity (Goubin 2004). Therefore, $CeBr_3$ is an insulator (Li 2007).

In order to understand how the defect influences the electronic density of states (DOS), we also evaluated the DOS for both the pure, undoped $CeBr_3$ material and the calcium-doped supercell (Figures 3 and 4). Comparing Figures 3 and 4, we notice that several peaks near 2 and –18 eV disappear for the calcium-doped compound. These differences are undoubtedly due to the presence of the calcium atom and its distortion of the electronic environment around this dopant. Finally, using the converged DOS results, we computed the optical properties of these compounds by evaluating the real parts of the frequency-dependent dielectric tensor (Figures 5 and 6).The dielectric function of $CeBr_3$ is calculated based on its electronic structure. $\varepsilon_1(\omega)$ is a function of the photon energy. The imaginary part $\varepsilon_2(\omega)$ of the dielectric function is connected with the energy band structure, but correlates with the real part $\varepsilon_1(\omega)$ of the dielectric function. The first peak at 1 eV observed for the pure $CeBr_3$ supercell is not evident for the Ca^{2+}-doped $CeBr_3$ supercell. The peak at 3 eV corresponds to the transition $4f^1 \rightarrow 5d^0$ of Ce. The main peaks of about 4 eV may be ascribed

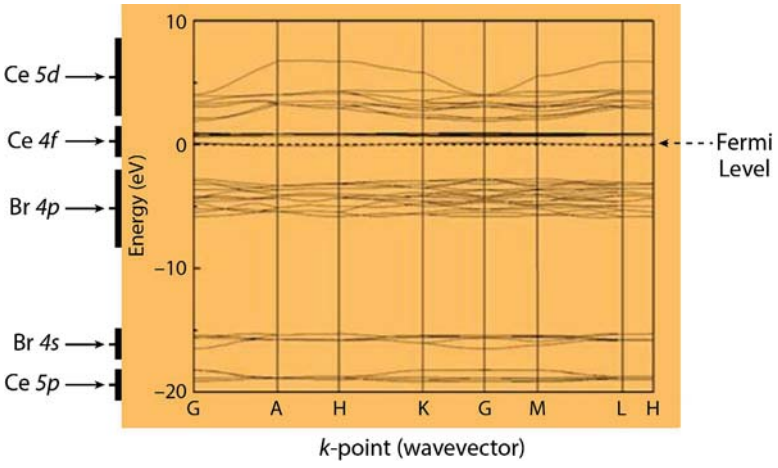

Figure 2. Band structure of $CeBr_3$ in a hexagonal crystal lattice. Plotted is the energy vs. *k*, where *k* is the wavevector that gives the phase of the atomic orbitals as well as the wavelength of the electron wavefunction (crystal momentum). The band structure corresponds to the Brillouin zone for the $CeBr_3$ hexagonal crystal lattice. The Fermi energy level is shifted to the valence band maximum at zero.

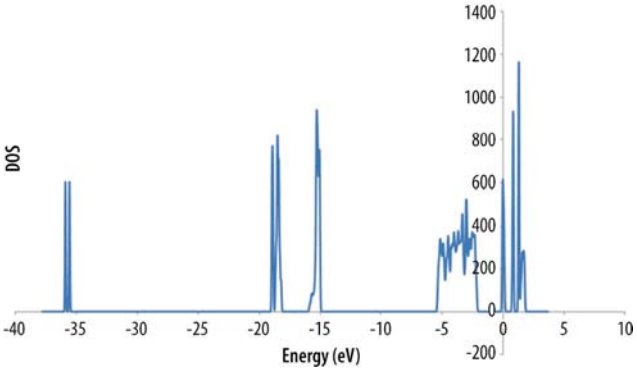

Figure 3. The energy band structure and electronic partial density of states around the Fermi level for the 3 × 3 × 3 pure $CeBr_3$ supercell

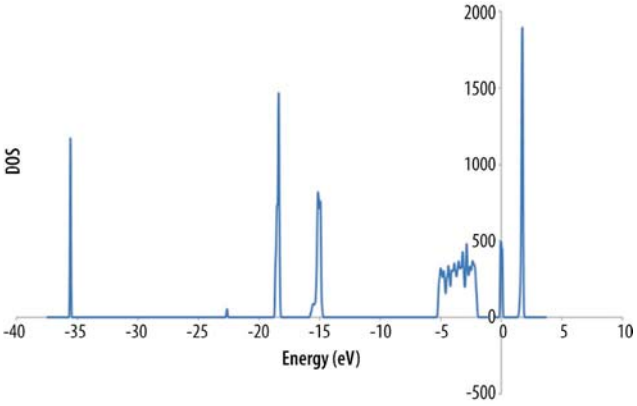

Figure 4. The energy band structure and electronic partial density of states around the Fermi level for the 3 × 3 × 3 Ca^{2+}-doped $CeBr_3$ supercell

to the transition from the Br *4p* valence band (VB) to the Ce *5d* conduction band (CB). The peaks near 20 eV correspond mainly to the transition of inner electron excitation from Ce *5p* VB to CB (Li 2007).

Although the optical responses in Figures 3 and 4 are similar, there are noticeable differences at 5 and 20 eV with a much stronger variation near 5 eV for the pure $CeBr_3$ material. We note, in passing, that these effects would probably be more significant if a higher calcium-doping level were used (i.e., one calcium atom for every four cerium atoms). Furthermore, understanding how to modulate this distortion in electron density (which results in other spectroscopic observables) with other types of dopants would enable us to maximize their theoretical energy resolution for spectroscopy applications, using an experimental approach guided by predictive modeling.

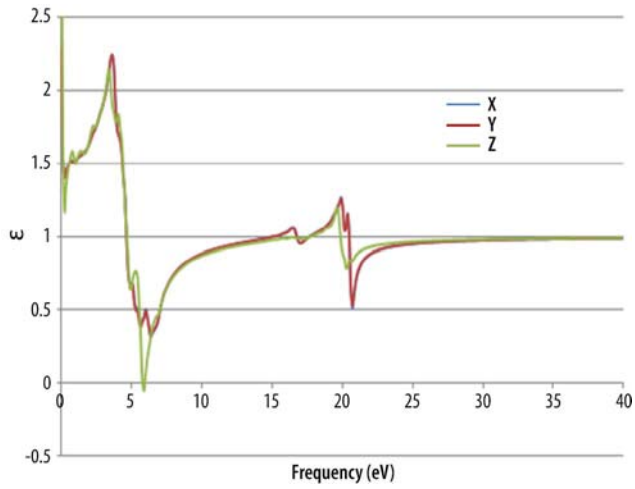

Figure 5. Real parts $\varepsilon_1(\omega)$ of the dielectric tensor for the 3 × 3 × 3 pure $CeBr_3$ supercell, where $\varepsilon(\omega) = \varepsilon_1(\omega) + i\,\varepsilon_2(\omega)$, and ω is the light frequency

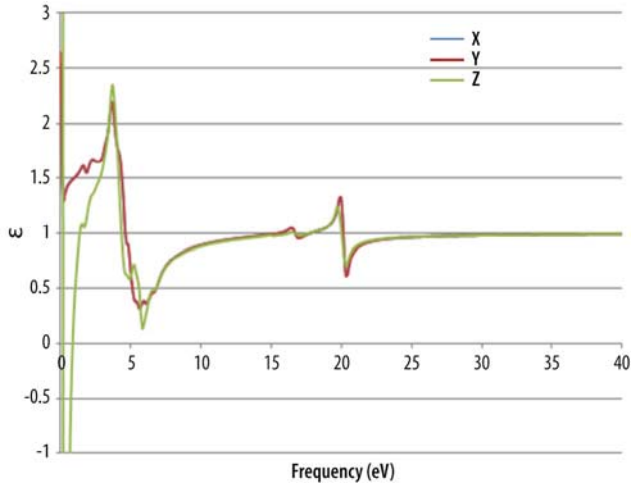

Figure 6. Real parts $\varepsilon_1(\omega)$ of the dielectric tensor for the 3 × 3 × 3 Ca^{2+}-doped $CeBr_3$ supercell, where $\varepsilon(\omega) = \varepsilon_1(\omega) + i\,\varepsilon_2(\omega)$, and ω is the light frequency

Experimental Approach

We sought to achieve ultralow activity and high-strength cerium bromide ($CeBr_3$) scintillators through a program of refining and alloying with aliovalent strengthening agents (substituents with a different valence than the host lattice). $CeBr_3$ is a self-activated lanthanide scintillator, which has received considerable recent attention (Shah 2005) due to proportionality and energy resolution for gamma spectroscopy far superior to thallium-doped sodium iodide (NaI:Tl).

Because the material possesses no intrinsic radioactivity, $CeBr_3$ has a high potential to outperform scintillators such as cerium-activated lanthanum tribromide or lanthanum-based elpasolites (Guss 2009), making it an excellent candidate for gamma spectrometers for passive detection and identification of special nuclear material (Shah 2004, Guss 2010). However, due to its hexagonal crystal structure (UCl_3), pure $CeBr_3$ can fracture during crystal growth, detector fabrication, and subsequent use under field conditions, thus impacting manufacturing yield and reliability for large crystals (Doty 2008).

Aliovalent substitution, in which a host ion is replaced with an ion of different valence (e.g., Cd^{2+} for Ce^{3+} in $CeBr_3$), is a more potent method of strengthening than isovalent substitution (i.e., replacing a fraction of ions with like-valence ions). The formation of intrinsic defects necessary to maintain charge neutrality results in complexes with long-range interactions in the crystal. The resulting increase in hardening rate can be explained in terms of elastic interaction (tetragonal distortion) with dislocations (Pletka 1977). Concentration levels necessary to increase the yield strength by an order of magnitude may be in the 100–500 ppm range (0.01%–0.05%) for aliovalent substitution, whereas isovalent substitution may require 10%–50% to achieve the same effect.

For these reasons, aliovalent substitution was chosen to improve the strength of $CeBr_3$. Sandia National Laboratories (SNL) demonstrated success with this approach, achieving a dramatic reduction of fracture in aliovalent alloys compared with pure $CeBr_3$ crystals (Harrison 2010). Prototype ingots were compounded with the addition of 2% of $CaBr_2$ added to a high purity $CeBr_3$ charge in a closed ampoule before melting and solidification in a gradient-freeze process. Pure $CeBr_3$ ingots solidified under these conditions were severely fractured, yielding only centimeter-size shards. The lesson learned was that 2% was too high of a charge for the calcium. Therefore, we needed to perform mass analysis of the material and recalculate the DFT with a lower charge of calcium. We also performed an assessment of the spectroscopic performance of the $CeBr_3$:Ca shards delivered by RMD to RSL.

Experiment

The 2% calcium-doped $CeBr_3$:Ca crystallite was grown and packaged by RMD and delivered to RSL in late September 2012. Several minor tasks remained to complete characterization of the calcium-doped crystal. SNL performed DFT model calculations with less dilute doping (i.e., something less than 2%) of calcium in $CeBr_3$. This helped assess what doping concentration would lead to changes in optical and mechanical properties. RMD assessed crystal growth strategies for performing growth with lower concentrations of calcium. RSL assessed the RMD crystal delivered on September 27. RSL acquired spectra with different isotopes using the RMD crystal using the techniques described by Guss (2011, 2013). The emission spectrum for this crystallite is shown in Figure 7. Figure 8 shows a light output measurement for the crystallite estimated at 65,200 photons per MeV based on comparison to the bismuth germanium oxide (BGO) light yield.

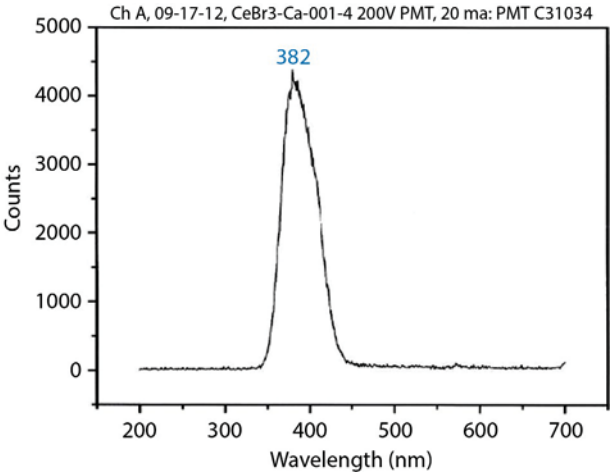

Figure 7. Emission spectrum measured with 6 mm × 2 mm 1.9% Ca^{2+}-doped $CeBr_3$ crystal in the permanent canister

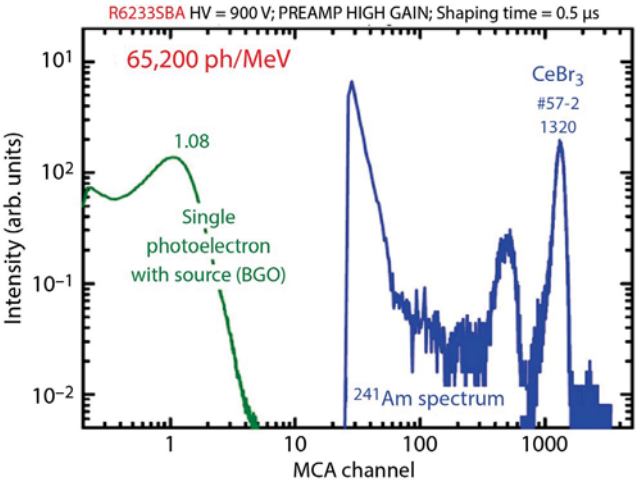

Figure 8. Light output measurement relative to BGO indicates 65,200 photons per MeV for Ca^{2+}-doped $CeBr_3$ crystal in the permanent canister

Proportionality of light yield is one area of performance that Ce-doped and Ce-based lanthanide halides excel. Maintaining proportionality is key to producing a strengthened, high-performance scintillator. Relative light yield proportionality was measured for both doped and undoped samples of $CeBr_3$ to ensure no loss in performance was incurred by aliovalently doping the crystal. The light output and proportionality, however, appear to be similar to $CeBr_3$. There was a reduced yield at low energy. Relative light yield proportionality measurements suggest that dopants do not significantly affect proportionality at higher energies. A plot of light yield proportionality for a doped sample is shown in Figure 9.

RSL completed additional testing and evaluation of the new crystal as well as the assessment of benchmarking spectroscopy. Results are summarized in Figure 10, which present energy resolution as a function of energy. Typical spectroscopy results using a ^{137}Cs radiation source are shown in Figure 11 for our crystallite. We obtain 4.5% for the packaged crystallite. More spectra are presented in Figure 12 for ^{241}Am, ^{60}Co, ^{228}Th, and background to exemplify $CeBr_3$:Ca over a broader energy range. The radiation source spectra were acquired for exactly 3600 s with the radiation source in contact with the crystal face using typical source strengths of several µCi. The laboratory background acquisition time was 3×10^5 s. Obviously, the packaging of the crystallite impacted the performance of $CeBr_3$:Ca.

Figures 13 and 14 present a comparison of the ^{137}Cs radiation source spectra and proportionality before and after packaging and sealing into the hermetically sealed canister sent to RSL. A slight degradation in performance is associated with the permanent package of the crystal.

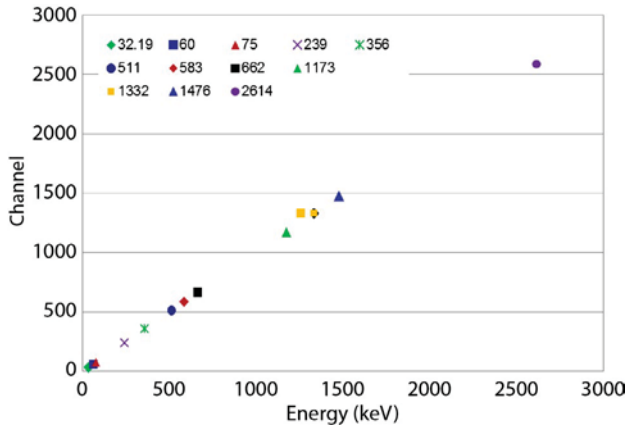

Figure 9. Relative light yield proportionality of 1.9% nominally Ca^{2+}-doped $CeBr_3$

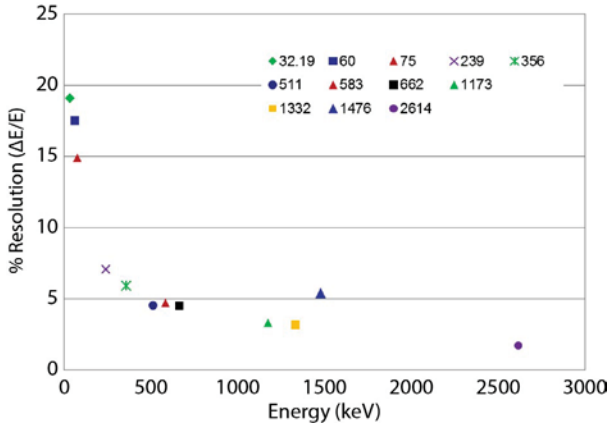

Figure 10. Energy resolution of 1.9% nominally Ca^{2+}-doped $CeBr_3$

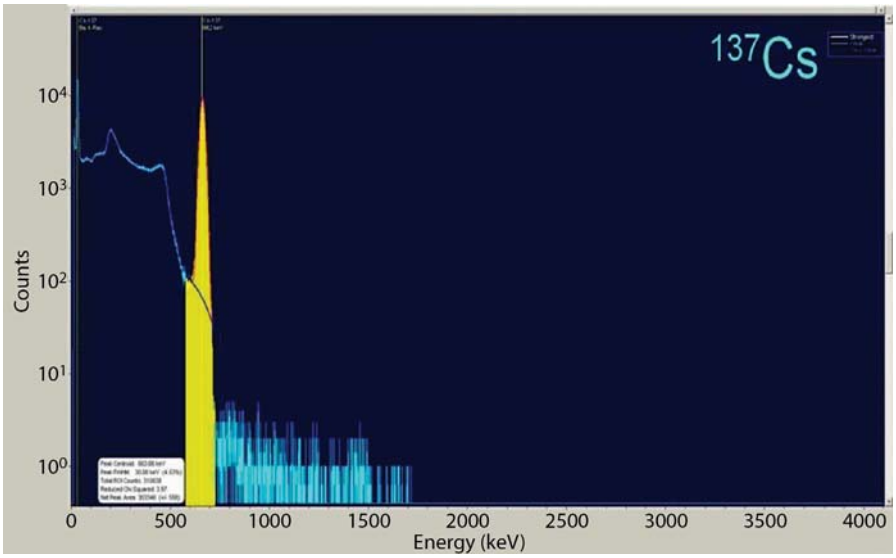

Figure 11. ^{137}Cs spectrum with 1.9% Ca^{2+}-doped $CeBr_3$ in the permanent canister (4.5%)

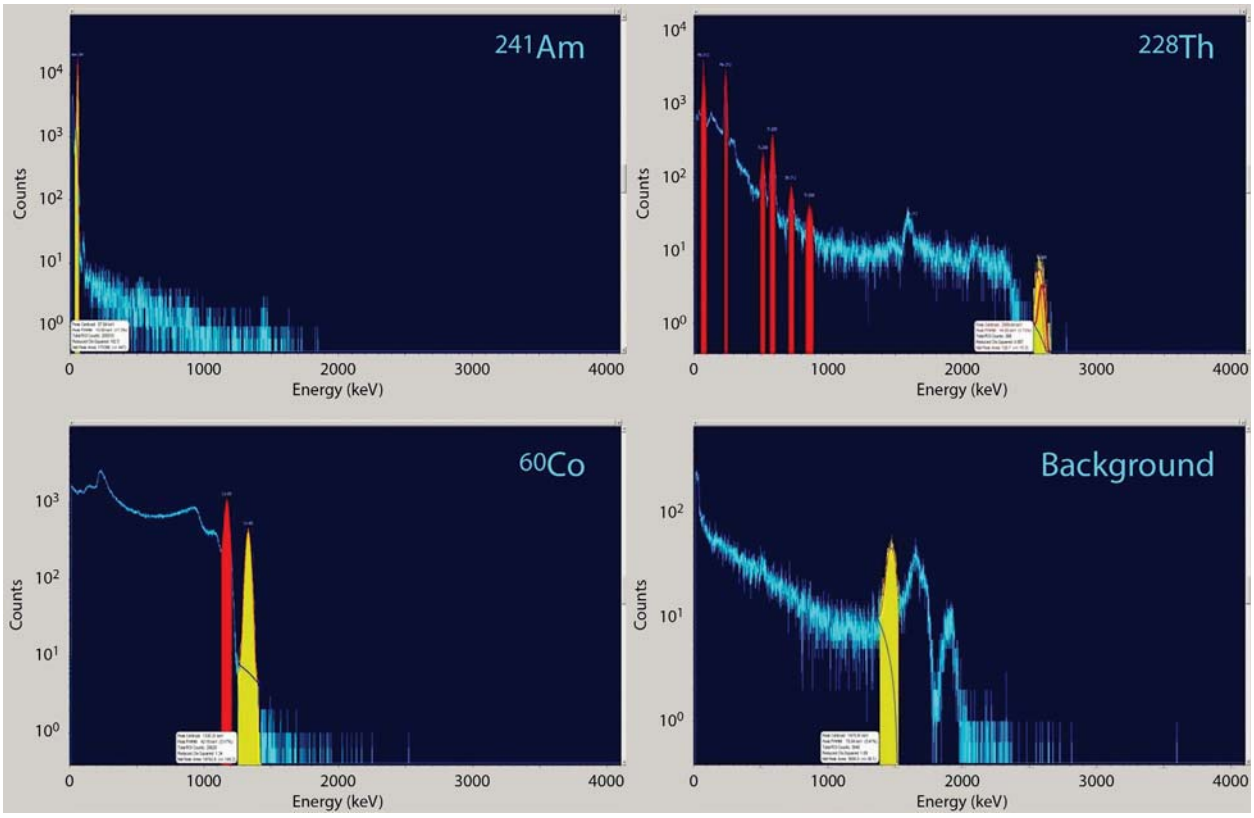

Figure 12. ^{241}Am, ^{228}Th, ^{60}Co, and background spectrum with 1.9% Ca^{2+}-doped $CeBr_3$ in the permanent canister

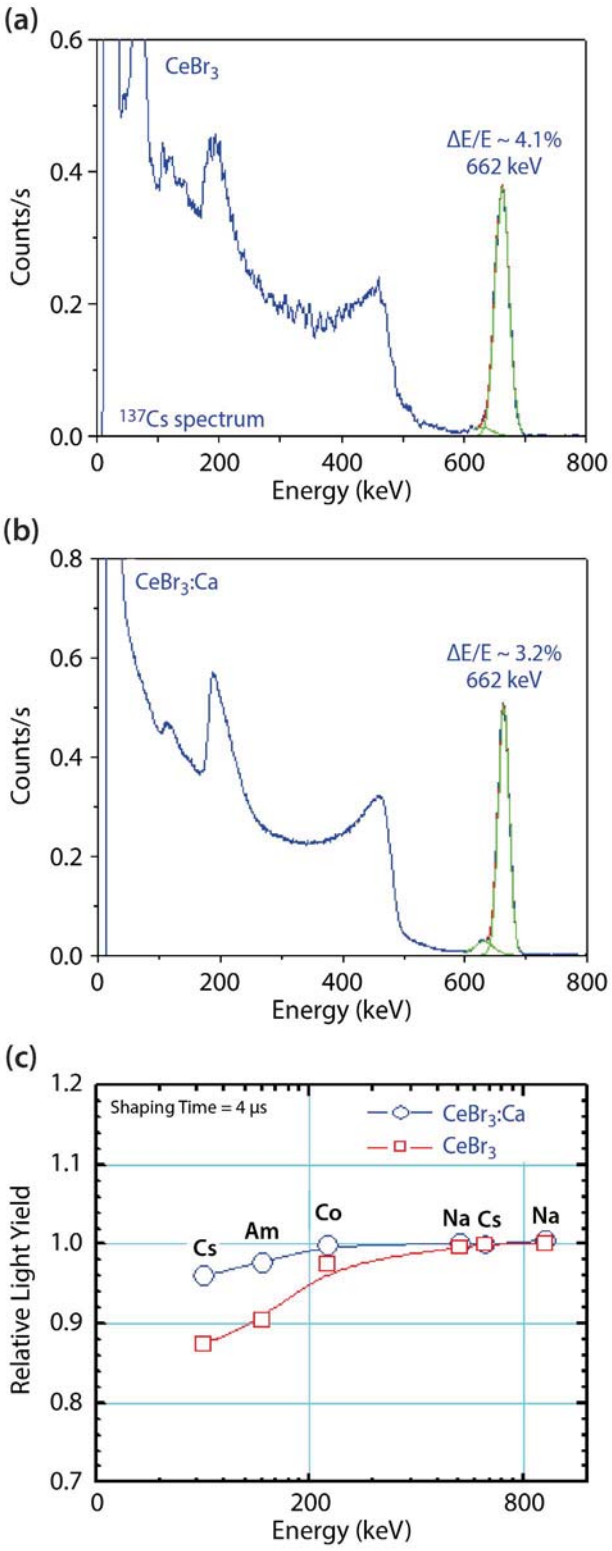

Figure 13. (a) 662 keV spectrum with standard $CeBr_3$ with ~4% FWHM, (b) 662 keV spectrum with $CeBr_3$:Ca^{2+} with ~3.2% FWHM, and (c) proportionality plots showing improved proportionality of $CeBr_3$:Ca over standard $CeBr_3$

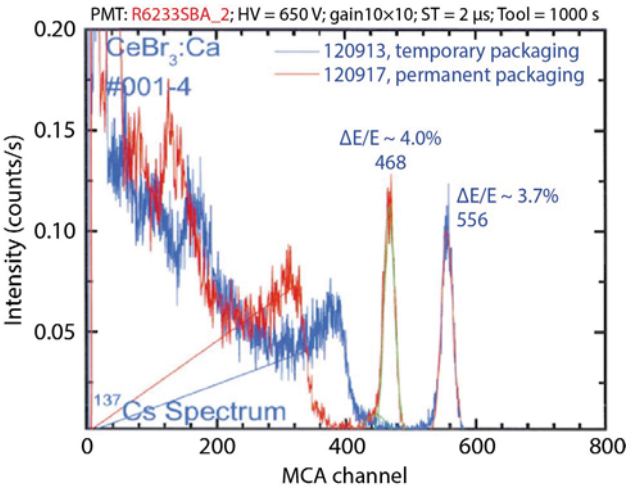

Figure 14. Comparison of measurements with the 1.9% Ca^{2+}-doped $CeBr_3$ crystal in temporary test canister (3.7%) versus the permanent canister (4.0%)

Solubility of $CaBr_2$ in $CeBr_3$

We have measured the calcium concentration in the $CeBr_3$ by the inductively coupled plasma mass spectrometry (ICP-MS) technique from the crystals prepared by RMD. ICP-MS is a type of mass spectrometry capable of detecting metals and several non-metals at concentrations as low as one part in 10^{12} (part per trillion). SNL performed the ICP-MS. SNL also calculated a DFT model with less dilute doping (i.e., something less than 2%) of calcium in $CeBr_3$. SNL analyzed the concentration of calcium in the crystals. Referring to Table 1, we used the average calcium weight % concentration, x = 0.000214, in our complex of $Ce_{(1-x)}Ca_xBr_{(3-x)}$, to evaluate the formula for atomic percentage:

$$\begin{aligned}\text{Atomic \%} &= 40.078x/[(140.116\,(1-x) \\ &\quad + 40.078x + 79.904\,(3-x)] \\ &= 0.00228 = 0.228\%\end{aligned} \qquad \textbf{(4)}$$

Based on our measurements, using three different samples (~0.2 grams), we have three consistent data sets indicating that the calcium concentration in these crystals is 0.0214 ±0.0102 wt.% (one σ) by weight, which corresponds to an atom percentage of 0.228 at.%. This value seems to be much less than the batch formulation. We do not know for certain if there is

Table 1. ICP-MS assays for Ca^{2+}-doped $CeBr_3$; nominal composition 2 wt.% $CaBr_2$ in $CeBr_3$

Sample	Calcium Concentration (wt.%)	95% Confidence Limit (wt.%)
#1	0.0238	0.0014
#2	0.0212	0.0015
#3	0.0192	0.0015

a solubility limit or a composition gradient in the ingot (sampling). Our data will be used to extract the solubility limit.

The objective of this portion of the task was to experimentally determine the solubility of $CaBr_2$ in the intrinsic scintillator $CeBr_3$. Our initial approach attempted equilibrium solid-state diffusion at several elevated temperatures for various amounts of time to allow Ca^{2+} to diffuse into the cerium bromide lattice, followed by chemical analysis to determine solubility limit and the activation energy for diffusion. However, this approach resulted in partial melting/fusion of the samples; therefore, a set of differential scanning calorimetric (DSC) measurements were performed and combined with our existing segregation data from crystal growth to build a working-phase diagram in the $CeBr_3$-rich region.

The chemical analysis of three $CeBr_3$ samples from a nominal 2% ingot grown by RMD is summarized in Table 1. The ICP-MS was used to determine as-grown concentrations of calcium with approximately 5% precision. Assuming the growth conditions were near equilibrium, an estimate for the segregation coefficient K_{eff} is $C_S/C_L = 0.11$. Therefore, the slope of the solidus line near 2% $CaBr_2$ in the liquid can be estimated by establishing a liquidus line from melting point data.

Table 2 is a tabulation of DSC data taken on samples in the composition range of 0%–10% $CaBr_2$ by mole. While the measured melting temperature $\mathbf{T_m}$ for the pure $CeBr_3$ sample appears anomalous and is in poor agreement with the literature, the mixtures show linear trends, including an apparent eutectic temperature $\mathbf{T_e}$ near 597°C for calcium concentrations ≥ 2.35%.

Table 2. DCS results for $CeBr_3$–$CaBr_2$ mixtures in the range 0–10 mole %

Mole % $CaBr_2$	T_m (°C)	T_e (°C)
0	715.3	--
0.2	732.1	--
2.35	721.8	598.3
4.65	715.2	595.4
7.63	706.8	596.2
9.85	697.3	597.0

All results are plotted in Figure 15, on which approximate solidus, liquidus, and eutectic lines have been constructed. Not plotted are some additional data taken at 20% and 30%, which indicate the liquidus continues the near-linear trend. Note that our current experimental upper bound for the solid solubility is the data point at 2.35%, which must lie well within the α+β field, since the eutectic temperature $\mathbf{T_e}$ was detected. This concentration is considerably less than the intersection of the extrapolated solidus and the eutectic temperature; therefore, the solidus line is clearly nonlinear and probably exhibits retrograde solubility well below the melting point of pure $CeBr_3$, as is commonly observed for sparingly soluble impurities in other systems. This behavior can be characterized as a variation of the segregation coefficient with temperature, as analyzed by Hall (1957). For example, the maximum solid solubility for sparingly soluble impurities in silicon and germanium follow a simple empirical correlation with k_0, the limiting equilibrium segregation coefficient, as $C_L \rightarrow 0$: $C_{S,max} = k_0/10$ (Fischler 1962). Based on this relation, the solidus was arbitrarily extrapolated to $k_{eff}/10 = 1.1\%$ at the eutectic temperature to estimate the minimum extent of the eutectic line towards the $CeBr_3$ side of the phase diagram (Figure 15).

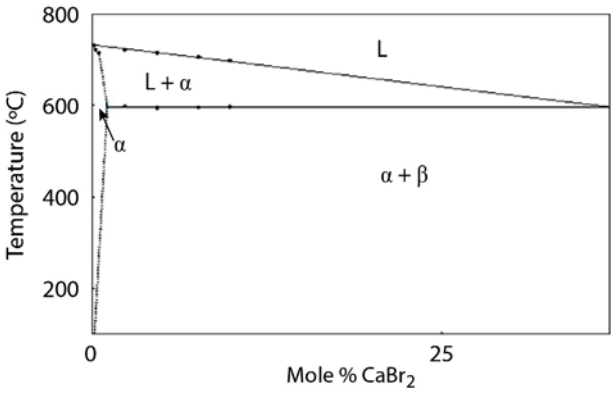

Figure 15. Phase diagram for $CeBr_3$–$CaBr_2$

It should be noted that the eutectic composition extrapolated from the points plotted is near 37% calcium; however, the nominal 20% and 30% data indicate it could be near 50%. More experiments are needed to accurately determine both the eutectic composition and the β phase, which could reasonably be expected to be a ternary such as $CaCeBr_5$ or Ca_2CeBr_7.

Discussion

SNL performed microhardness measurements to see if the aliovalent approach hardened the crystal as expected. Microhardness (Vickers hardness [Smith 1922]) and indentation toughness of these samples were measured. Due to the size limitation, we could not obtain sufficient statistics and confidence on these measured values. Therefore, we do not report the results here. Future work should include studies in correlation between sheer strength and Ca^{2+} concentration.

Based on the recent literature on strengthening mechanisms (Sinha 1977), there are compelling requirements to research and share several ideas, questions, and answers. Sinha's paper on aliovalent strengthening of CaF_2 attempts to determine mechanisms for low and high temperature. Sinha and Nicholson (1977) found that Y(III) gave an order of magnitude greater increase in critical resolve shear stress than Na(I). They conclude the long-range retarding force on dislocations at high temperature is likely due to the induced reorientation of Na(I)/F-vacancy or Y(III)/F-interstitial dipoles in the stress fields of moving dislocations (Snoek effect). This suggested role of the Snoek effect (Snoek 1941) is in accord with analysis of the athermal regime in recent papers on Y-stabilized zirconia and other materials (Baither 1997, Lassila 2002, Shah 2005, Mercer 2007, Armengol 2008, Martin 2008, Taherabadi 2008, Gan 2010, Harrison 2010). If the authors are correct that anion interstitials balance the charge for the higher valence cation, then the difference in strength may be related to the higher mobility of interstitials. The interstitial fluoride ion in CaF_2 may be more plausible than interstitial bromide; however, the $CeBr_3$ crystal structure does have large open channels. We examined whether the M(IV)/Br-interstitial seems like a feasible complex in $CeBr_3$. Because the athermal (high-temperature) regime is probably more important during crystal growth, future work should explore if it makes sense to place more emphasis on M(IV) cations silicon, tin, lead, titanium, zirconium, hafnium, rhenium, molybdenum, cerium, thorium, protactinium, uranium, neptunium, and plutonium.

The paper "Ca^{2+}-Doped $CeBr_3$ Scintillating Materials" was submitted to the *Journal of Applied Physics*. This work was presented at the August 2013 SPIE conference in San Diego, California.

Conclusion

To summarize, new DFT simulations demonstrate a capability for predicting properties of doped $CeBr_3$ materials that is unavailable elsewhere but is critically needed to study the property-limiting valence phenomena in ionic compounds. During this project, we assessed concentrations and the solubility limit. RSL benchmarked the Ca^{2+}-doped $CeBr_3$ crystal. The Ca^{2+}-doped $CeBr_3$ crystal has improved energy resolution (i.e., 3.2%) and linearity over the pure $CeBr_3$ crystal.

Acknowledgments

We would like to thank RMD for production of the crystal, and acknowledge Marlene Bencomo (University of New Mexico) for performing the series of

equilibrium diffusions of cleaved $CeBr_3$ flakes in contact with $CaBr_2$ powder at five temperatures, followed by ICP-MS to analyze the equilibrium concentrations.

References

Anisimov, V. I., J. Zaanen, O. K. Andersen, "Band theory and Mott insulators: Hubbard U instead of Stoner I," *Phys. Rev. B* **44**, 3 (1991) 943–954.

Anisimov, V. I., F. Aryasetiawan, A. I. Lichtenstein, "First-principles calculations of the electronic structure and spectra of strongly correlated systems: the LDA+U method," *J. Phys.: Condens. Matter* **9** (1997) 767–808.

Armengol, S., "Caracterización Microestructural de un recubrimiento de YSZ para aplicaciones biomédicas," IV. Latin American Congress on Biomedical Engineering 2007, Bioengineering Solutions for Latin America Health, *IFMBE Proc.* **18** (2008) 671–675.

Baither, D., B. Baufeld, U. Messerschmidt, M. Bartsch, "HVEM high-temperature in situ straining experiments on cubic zirconia single crystals," *Mater. Sci. Eng.* **A233** (1997) 75–87.

Blöchl, P. E., "Projector augmented-wave method," *Phys. Rev. B* **50**, 24 (1994) 17953–17979.

Blöchl, P. E., C. J. Först, J. Schimpl, "Projector augmented wave method: Ab-initio MD with full wave functions," Clausthal University of Technology Germany (25 November 2001), *Bull. Mater. Sci.* **26**, 1 (January 2003) 33–41.

Brillouin, L., "Les électrons dans les métaux et le classement des ondes de De Broglie correspondantes," *Comptes Rendus Hebdomadaires des Séances de l'Académie des Sciences* **191** (1930) 292–299.

Courtney, T. H., *Mechanical Behavior of Materials*, 2nd edition, Waveland, Long Grove, Illinois, 2000, 232.

Doty, F. P., D. McGregor, M. Harrison, K. Findley, R. Polichar, "Structure and properties of lanthanide halides," *Proc. SPIE* **6707** (2007) 670705:1–11.

Doty, F. P., D. McGregor, M. Harrison, K. Findley, R. Polichar, P. Yang, "Basic materials studies of lanthanide halide scintillators," *Proc. Mat. Res. Soc.* **1038** (2008) 1–8.

Doty, F. P., "Fracture resistant lanthanide scintillators," U.S. Patent 7,683,572 B1, filed November 8, 2007, and issued March 23, 2010.

Dudarev, S. L., G. A. Botton, S. Y. Savrasov, C. J. Humphreys, A. P. Sutton, "Electron-energy-loss spectra and the structural stability of nickel oxide: An LSDA+U study," *Phys. Rev. B* **57**, 3 (1998) 1505–1509.

Fischler, S., "Correlation between maximum solid solubility and distribution coefficient for impurities in Ge and Si," *J. Appl. Phys.* **33**, 4 (1962) 1615.

Gan, Y. X., S. V. Pothula, M. J. Franchetti, "Plasticity of nanoporous Ni/YSZ anode: A numerical analysis," *ASME 8th International Conference on Fuel Cell Science, Engineering and Technology Proc.* **2** (2010) 153–158.

Goubin, F., X. Rocquefelte, D. Pauwels, A. Tressaud, A. Demourgues, S. Jobic, Y. Montardi, "The dielectric function of LnSF rare-earth fluorosulfides (Ln=La, Ce): Experiment and theory," *J. Solid State Chem.* **177**, 8 (2004) 2833–2840.

Guss, P. P., M. Reed, D. Yuan, A. Reed, S. Mukhopadhyay, "$CeBr_3$ as a high-resolution gamma-ray detector," *Nucl. Instrum. Methods Phys. Res. A* **608**, 2 (2009) 297–304.

Guss, P. P., M. Reed, D. Yuan, M. Cutler, C. Contreras, D. Beller, "Comparison of $CeBr_3$ with $LaBr_3$:Ce, $LaCl_3$:Ce, and NaI:Tl detectors," *Proc. SPIE* **7805** (2010) L-1.

Guss, P. P., R. Guise, S. Mitchell, S. Mukhopadhyay, D. Lowe, R. O'Brien, D. Yuan, "Nanostructured Lanthanum Halides and $CeBr_3$ for Nuclear Radiation Detection," *Nevada National Security Site-Directed Research and Development*, FY 2010, National Security Technologies, LLC, Las Vegas, Nevada, 2011, 55–64.

Guss, P., B. Wong, M. Foster, F. P. Doty, K. Shah, M. Squillante, J. Glodo, D. Yuan, "Low-Cost Cerium Bromide Alloys," *Site-Directed Research and Development*, FY 2012, National Security Technologies, LLC, Las Vegas, Nevada, 2013, 11–19.

Hall, R. N., "Variation of the distribution coefficient and solid solubility with temperature," *J. Phys. Chem. Solids* **3**, 1–2 (1957) 63–73.

Harrison, M. J., P. Ugorowski, C. Linnick, S. Brinton, D. S. McGregor, F. P. Doty, S. Kilpatrick, D. F. Bahr, "Aliovalent doping of $CeBr_3$," *Proc. SPIE* **7806** (2010) 78060M–78060M-14.

Heyd, J., G. E. Scuseria, M. Ernzerhof, "Hybrid functionals based on a screened Coulomb potential," *J. Chem. Phys.* **118** (2003) 8207.

Hohenberg P., W. Kohn, "Inhomogeneous electron gas," *Phys. Rev.* **136**, 3B (1964) B864–B871.

Hua, X., X. Chen, W. A. Goddard, "Generalized generalized gradient approximation: An improved density-functional theory for accurate orbital eigenvalues," *Phys. Rev. B* **55**, 24 (1997) 16103–16109.

Kittel, C., H. Kroemer, *Thermal Physics*, 2nd edition, W. H. Freeman, New York, New York, 1980, 357.

Kohn W., L. J. Sham, "Self-consistent equations including exchange and correlation effects," *Phys. Rev.* **140**, 4A (1965) A1133–A1138.

Krukau, A. V., O. A. Vydrov, A. F. Izmaylov, G. E. Scuseria, "Influence of the exchange screening parameter on the performance of screened hybrid functional," *J. Chem. Phys.* **125** (2006) 224106-1–224106-5.

Kulik, H. J., N. Marzari, "A self-consistent Hubbard U density-functional theory approach to the addition-elimination reactions of hydrocarbons on bare FeO+," *J. Chem. Phys.* **129**, 13 (2008) 134314.

Kümmel, S., L. Kronik, "Orbital-dependent density functionals: Theory and applications," *Rev. Mod. Phys.* **80**, 1 (2008) 3–60.

Lassila, D. H., A. Goldberg, R. Becker, "The effect of grain boundaries on the athermal stress of tantalum and tantalum-tungsten alloys," *Metallurgical and Materials Transactions* **33A**, 11 (November 2002) 3457–3464.

Li, C., B. Wang, R. Wang, H. Wang, "First-principles studies on the electronic and optical properties of $CeCl_3$ and $CeBr_3$," *Solid State Communications* **144**, 5–6 (2007) 220–224.

Liechtenstein, A. I., V. I. Anisimov, J. Zaanen, "Density-functional theory and strong interactions: Orbital ordering in Mott-Hubbard insulators," *Phys. Rev. B* **52**, 8 (1995) R5467–R5470.

Mackie, I. D., G. A. Dilabio, "Approximations to complete basis set-extrapolated, highly correlated non-covalent interaction energies," *J. Chem. Phys.* **135**, 13 (2011) 134318–134318-10.

Martin, H., R. Pippan, "Athermal and thermal limits of the grain refinement by SPD," *Materials Science Forum* **584-586** (2008) 938–943.

Mercer, C., J. R. Williams, D. R. Clarke, A. G. Evans, "On a ferroelastic mechanism governing the toughness of metastable tetragonal-prime (*t'*) yttraia-stabilized zirconia," *Proc. R. Soc. A* **463**, 2081 (May 8, 2007) 1393–1408.

Møller, C., M. S. Plesset, "Note on an approximation treatment for many-electron systems," (abstract) *Phys. Rev.* **46**, 7 (1934) 618–622.

Monkhorst, H. J., J. K. Pack, "Special points for Brillouin-zone integrations," *Phys. Rev. B* **13**, 12 (1976) 5188–5192.

Park K. H., S.-J. Oh, "Electron-spectroscopy study of rare-earth trihalides," *Phys. Rev. B* **48**, 20 (1993) 14833–14842.

Perdew, J. P., K. Burke, M. Ernzerhof, "Generalized gradient approximation made simple," *Phys. Rev. Lett.* **77**, 18 (1996) 3865–3868.

Perdew, J. P., K. Burke, M. Ernzerhof, "Errata (Generalized gradient approximation made simple)," *Phys. Rev. Lett.* **78**, 7 (1997) 1396(E).

Pletka, B. J., T. E. Mitchell, A. H. Heuer, "Solid solution hardening of sapphire (α-Al_2O_3)," *Physica Status Solidi* **39**, 1 (1977) 301–311.

Saha, S., T. P. Sinha, "Electronic structure, chemical bonding, and optical properties of paraelectric $BaTiO_3$," *Phys. Rev. B* **62**, 13 (2000) 8828–8834.

Sato, S., "Optical absorption and x-ray photoemission spectra of lanthanum and cerium halides," *J. Phys. Soc. Japan* **41**, 3 (1976) 913–920.

Shah, K. S., J. Glodo, M. Klugerman, W. M. Higgins, T. Gupta, P. Wong, "High energy resolution scintillation spectrometers," *IEEE Trans. Nucl. Sci.* **51**, 5 (2004) 2395–2399.

Shah, K. S., J. Glodo, W. Higgins, E. V. D. van Loef, W. W. Moses, S. E. Derenzo, M. J. Weber, "$CeBr_3$ scintillators for gamma-ray spectroscopy," *IEEE Trans. Nucl. Sci.* **52**, 6 (2005) 3157–3159.

Sinha, M. N., P. S. Nicholson, "Effect of impurities on the strengthening of CaF_2 single crystals," *J. Mat. Sci.* **12**, 7 (1977) 1451–1462.

Skorodumova, N. V., R. Ahuja, S. I. Simak, A. Abrikosov, B. Johansson, B. I. Lundqvist, "Electronic, bonding, and optical properties of CeO_2 and Ce_2O_3 from first principles," *Phys. Rev. B* **64** (2001) 115108-1–115108-9.

Smith, R. L., G. E. Sandland, "An accurate method of determining the hardness of metals, with particular reference to those of a high degree of hardness," *Proceedings of the Institution of Mechanical Engineers* **I** (1922) 623–641.

Snoek, J., "Effect of small quantities of carbon and nitrogen on the elastic and plastic properties of iron," *Physica* **8**, 7 (1941) 711–733.

Taherabadi, L., J. E. Trujillo, T. Chen, J. R. Porter, M. L. Mecartney, "Observation of dislocation assisted high temperature deformation in mullite and mullite composites," *J. European Ceramic Soc.* **28** (2008) 271–376.

VASP, Vienna Ab-initio Simulation Package, What is VASP? http://cmp.univie.ac.at/research/vasp/, accessed December 12, 2013.

Valeev, E. F., T. D. Crawford, "Simple coupled-cluster singles and doubles method with perturbative inclusion of triples and explicitly correlated geminals: The $CCSD(T)_{R12}$ model," *J. Chem. Phys.* **128** (2008) 244113.

Vetere, V., C. Adamo, P. Maldivi, "Performance of the 'parameter free' PBE0 functional for the modeling of molecular properties of heavy metals," *Chem. Phys. Lett.* **325**, 1–3 (2000) 99–105.

Wong, B. M., "Optoelectronic properties of carbon nanorings: Excitonic effects from time-dependent density functional theory," *J. Phys. Chem. C* **113**, 52 (2009) 21921–21927.

Wong, B. M., T. H. Hsieh, "Optoelectronic and excitonic properties of oligoacenes: Substantial improvements from range-separated time-dependent density functional theory," *J. Chem. Theory Comput.* **6**, 12 (2010) 3704–3712.

Zachariasen, W. H., "Crystal chemical studies of the 5f-series of elements. I. New structure types," *Acta. Crystallogr.* **1**, 5 (1948a) 265–268.

Zachariasen, W. H., "The UCl_3 type of crystal structure," *J. Chem. Phys.* **16**, 3 (1948b) 254.


SDRD
SITE DIRECTED RESEARCH & DEVELOPMENT